



The
University
Of
Sheffield.

The Behaviour of Cold-Formed Steel Built-up Structural Members

(Volume I)

By:

Francisco Javier Meza Ortiz

A thesis submitted in partial fulfilment of the requirements for the degree of
Doctor of Philosophy

The University of Sheffield
Faculty of Engineering
Department of Civil & Structural Engineering

September 2018

Abstract

Cold-formed steel sections offer many benefits to construction, such as a high strength-to-weight ratio, an ease of handling, transportation and stacking, and important sustainability credentials. For these reasons their range of application has rapidly expanded from being mainly used as secondary members in steel structures to an increasing use as primary members. This trend in construction is exerting an increased demand on cold-formed steel structural members in terms of the span length and the load carrying capacity they need to provide. A common and practical solution to address these new demands consists of creating built-up sections by connecting two or more individual sections together using fasteners or spot welds. However, a lack of understanding of the way these sections behave and a gap in specific design provisions has prevented the exploitation of the real potential which these types of sections can offer.

This research aims to develop an improved understanding of the behaviour, stability and capacity of built-up cold-formed steel members in compression and bending, paying special attention to the various interactions resulting from cross-sectional instabilities, buckling of the individual components in between connector points and global buckling of the built-up member, as well as the role played by the connector spacing in these interactions.

To this end, a series of experiments on built-up beams and columns was carried out. A total of 20 stub column tests were completed with four different built-up geometries, each constructed from four individual components assembled with either bolts or self-drilling screws at varying spacings. The columns were tested between fixed end conditions and were designed to exclude global instabilities of the built-up specimens. In addition, 24 long column tests with almost identical built-up cross-sectional geometries, assembled with the same types of connectors, were also conducted. The columns were compressed between pin-ended boundary conditions and the load was applied with eccentricities of $L/1000$ or $L/1500$. Each built-up geometry was tested with three different connector spacings, and this time the columns were designed to exhibit global buckling of the whole column in addition to cross-sectional buckling of the components and possible buckling of the components in between connector points. A series of 12 beam tests was also carried out for two different cross-sectional geometries, constructed from multiple channel sections and connected with bolts at varying spacing. The built-up beams were tested in four-point bending, with lateral restraint provided at the locations where the concentrated loads were applied in order to avoid global instability. All tests on columns and beams showed that the different components of the built-up geometry mutually restrained each other while buckling, relative to their individually preferred buckled shapes, and that while the connector spacing may significantly affect the amount of restraint they exert on each other, its effect on the ultimate capacity is considerably less. The material properties of all tested specimens were determined by means of coupon tests taken from the corners and flat portions of the constituent sections, while detailed measurements of the geometric imperfections of each specimen were carried out using a laser displacement sensor mounted on a specially designed measuring rig. In addition, the mechanical behaviour of the connectors used to assemble the built-up specimens was determined by means of single lap shear tests.

Detailed finite element models were created of the built-up beams and columns, which included the material non-linearity obtained from the tensile coupons, the geometric imperfections recorded on the actual specimens and the connector behaviour obtained from the single lap shear tests. The models were first validated against the data gathered from the experimental programmes and were further used in parametric studies, in which the sensitivity of the ultimate capacity to contact between the components and to the connector spacing was investigated. The numerical studies revealed that the effects of both contact between the components and the connector spacing on the ultimate capacity was most pronounced when the connector spacing was shorter than the natural local buckle half-wave length of the components. However, this range of connector spacings may prove impractical in construction due to the large amount of labour it requires.

Acknowledgements

I would like to express my deepest gratitude to Dr. Jurgen Becque for the opportunity he gave me to do this Ph.D under his supervision. His guidance, support and trust during the development of this work have been key to its successful completion. I feel that what I have learned from his values and approach to research have helped me to become a better researcher.

Thanks to the EPSRC [Grant EP/M011976/1] for making some funding available for a project related to this research.

My thanks goes to the technicians Christopher Todd, Paul Blackburn and Robin Markwell for their support and insight in the preparation of the experiments, and for their patience and good humour while introducing me to the Yorkshire dialect. Thanks also to future Dr. Seyed Mohammad Mojtabaei for his kind and selfless help in the laboratory.

I would also like to thank my partner Maria Kelly for the immense support, care and patience she gave me during my studies. She has also had to take much of the burden of me completing this thesis by filling my absence in many day-to-day responsibilities. This work could not have been possible without her. Thanks to my daughter for putting up with my long working hours, especially during the last few months. Your smile have been a great source of encouragement to me during the drawn-out writing up period.

Finally, I would like to take the liberty to thank my mother, Julia, my father, Fernando, and my brother, Rodrigo in my native language (Spanish):

Gracias por el apoyo que me han dado durante mis estudios. Soy consciente del sacrificio que han tenido que hacer durante este tiempo, teniendo que a veces callar lo que más cuesta para asegurar que terminase mis estudios. Gracias mamá por haber venido durante estos últimos meses a ayudarme en casa. Realmente no sé cómo hubiese podido escribir esta tesis sin tu ayuda.

Table of Contents

Abstract	i
Acknowledgements	ii
Table of Contents	iii
List of Figures	x
List of Tables	xxv
List of Symbols	xxx
Chapter 1	1
1.1. Background.....	1
1.2. Objectives and scope.....	4
1.3. Thesis layout	5
1.4. Publications.....	7
Chapter 2	9
2.1. Material properties of cold-formed steel.....	9
2.1.1 Mechanical properties	9
2.1.2 Residual stresses	11
2.2. Geometric imperfections.....	13
2.3. Instabilities in thin-walled members	15
2.3.1 Local buckling	16
2.3.2 Distortional buckling	19
2.3.3 Global buckling.....	20
2.3.4 Buckling interaction.....	21
2.4. Elastic stability analysis of thin-walled CFS members.....	22
2.4.1 Finite element method (FEM).....	22
2.4.2 Finite strip method (FSM).....	22

2.4.3 Compound strip method (CSM)	23
2.4.4 Generalised Beam Theory (GBT).....	24
2.5. Design Methods.....	24
2.5.1 Effective with method	24
2.5.2 Direct Strength Method (DSM).....	27
2.5.3 Erosion of Critical Bifurcation Load (ECBL)	30
2.6. Design codes.....	31
2.6.1 Eurocode 3 (EC3).....	31
2.6.2 North American Specification (NAS)	32
2.7. Previous research on CFS built-up members	35
2.7.1 Modified slenderness ratio.....	35
2.7.2 Extending the DSM to the design of built-up members	36
2.7.3 Additional research on built-up members	39
2.8. Numerical modelling of CFS built-up members using Abaqus.....	40
2.8.1 Abaqus solvers for non-linear buckling analysis.....	40
2.8.2 Solving a non-linear problem with Abaqus/Standard General Statics solver.....	41
2.8.3 Stabilization schemes and solution control in Abaqus/Standard	43
2.8.4 Contact interaction.....	48
2.8.5 Mesh-independent fasteners	50
2.8.6 Fastener coordinate system.....	53
Chapter 3.....	55
3.1. Introduction	55
3.2. Labelling.....	57
3.3. Material Properties	58
3.3.1 Flat coupons.....	58
3.3.2 Corner coupons.....	60
3.3.3 Coupon test procedure and results.....	62
3.4. Section design and geometry.....	65
3.4.1 Design of built-up column 1	67
3.4.2 Design of built-up column 2.....	68

3.4.3 Design of built-up columns 3 and 4	69
3.5. Cross-section assembly and specimen preparation	70
3.6. Imperfection Measurements.....	76
3.6.1 Imperfection measuring rig.....	76
3.6.2 Measuring process	77
3.6.3 Imperfection measurement results	86
3.7. Test Set up.....	88
3.7.1 Introduction.....	88
3.7.2 Instrumentation	89
3.7.3 Test procedure.....	92
3.8. Test results	93
3.8.1 Strain gauge readings	93
3.8.2 Deformed shape	95
3.8.3 Critical buckling stresses	104
3.8.4 Ultimate load.....	113
3.9. Summary and conclusions	117
Chapter 4	121
4.1. Introduction.....	121
4.2. Labelling	122
4.3. Material Properties.....	122
4.3.1 Flat coupons	123
4.3.2 Corner coupons	123
4.3.3 Coupon testing and results	125
4.4. Section Design and geometry	126
4.5. Cross-section assembly and specimen preparation	130
4.6. Imperfection Measurements.....	133
4.7. Test Set up.....	139
4.7.1 Introduction.....	139
4.7.2 Boundary conditions	140
4.7.3 Instrumentation	142

4.7.4 Test procedure	144
4.8. Test results.....	144
4.8.1 Deformed shape.....	144
4.8.2 Critical buckling stress and shear force at the connectors	157
4.8.3 Ultimate capacity	162
4.9. Summary and conclusions	166
Chapter 5.....	169
5.1. Introduction	169
5.2. Labelling	171
5.3. Material Properties	171
5.3.1 Flat coupons.....	172
5.3.2 Corner coupons.....	173
5.3.3 Coupon testing and results.....	175
5.4. Section design and geometry	177
5.4.1 Design of built-up column 1	178
5.4.2 Design of built-up column 2.....	180
5.4.3 Design of built-up columns 3 and 4.....	181
5.5. Cross-section assembly and specimen preparation.....	183
5.6. Imperfection Measurements	190
5.6.1 Imperfection measuring rig	190
5.6.2 Measuring process	191
5.6.3 Imperfection measurement results.....	201
5.6.4 Measuring rig accuracy	224
5.7. Test Set up	233
5.7.1 Introduction	233
5.7.2 Pin-ended supports	234
5.7.3 Instrumentation.....	236
5.7.4 Test procedure	241
5.8. Test results.....	241
5.8.1 Strain gauge readings	241

5.8.2 Deformed shape	248
5.8.3 Critical buckling stresses	262
5.8.4 Ultimate load.....	269
5.9. Summary and conclusions	277
5.9.1 Conclusions regarding the imperfection measurements.....	278
5.9.2 Conclusions regarding the column tests results	280
Chapter 6	282
6.1. Introduction.....	282
6.2. Labelling	283
6.3. Specimen geometry and preparation.....	283
6.4. Material Properties.....	287
6.5. Test Set-up	287
6.5.1 Transducers	288
6.5.2 Digital image correlation	288
6.6. Test results	290
6.6.1 Ultimate capacity and failure mode	290
6.6.2 Comments on the LVDT arrangement.....	298
6.6.3 DIC accuracy	300
6.7. Summary and conclusions	303
Chapter 7	306
7.1. Introduction.....	306
7.2. Details of the FE models.....	307
7.2.1 Boundary conditions	307
7.2.2 Geometric imperfections.....	308
7.2.3 Material properties	309
7.2.4 Contact interaction	313
7.2.5 Connector modelling.....	314
7.2.6 Type of analysis	316
7.2.7 Overcoming convergence issues in Abaqus/Standard	316

7.2.8 Mesh analysis	324
7.3. FE model verification	329
7.3.1 Ultimate load	329
7.3.2 Deformed shape.....	332
7.3.3 Critical buckling stresses	337
7.4. Parametric study	338
7.4.1 Effect of fastener modelling	338
7.4.2 Connector spacing and contact interaction	345
7.5. Summary and conclusions	352
Chapter 8.....	356
8.1. Introduction	356
8.2. FE modelling details.....	357
8.2.1 Boundary conditions.....	357
8.2.2 Geometric imperfections	361
8.2.3 Material properties.....	363
8.2.4 Contact interaction.....	364
8.2.5 Connector modelling	365
8.2.6 Type of analysis.....	366
8.2.7 Stabilization study	366
8.2.8 Mesh analysis	370
8.3. Detailed FE model: verification	374
8.3.1 Ultimate moment capacity.....	374
8.3.2 Deformed shape.....	376
8.3.3 Critical buckling stresses	379
8.4. Simplified FE model: verification	382
8.4.1 Ultimate moment capacity.....	382
8.4.2 Deformed shape and critical buckling stresses	384
8.5. Parametric study	386
8.5.1 Effect of fastener modelling	386
8.5.2 Connector spacing and contact interaction	390

8.6. Summary and conclusions	397
Chapter 9	400
9.1. Introduction.....	400
9.2. Details of the FE models.....	401
9.2.1 Boundary conditions	401
9.2.2 Geometric imperfections.....	402
9.2.3 Material properties	403
9.2.4 Contact interaction	405
9.2.5 Connector modelling.....	406
9.2.6 Type of analysis	406
9.2.7 Overcoming convergence issues in Abaqus/Standard	406
9.2.8 Stabilization study.....	407
9.2.9 Mesh analysis.....	414
9.3. FE model verification	418
9.3.1 Ultimate load.....	418
9.3.2 Deformed shape	421
9.3.3 Critical buckling stresses	429
9.4. Parametric study.....	432
9.4.1 Effect of fastener modelling.....	432
9.4.2 Connector spacing and contact interaction	435
9.5. Summary and conclusions	440
Chapter 10	444
10.1. Summary and conclusions	444
10.1.1 Experimental studies	444
10.1.2 Numerical studies.....	448
10.2. Recommendations for future work	450
References.....	454

List of Figures

Figure 1.1: CFS used as secondary steelwork: a) roof purlins in a steel structure (http://www.rki-bg.com [accessed on August 2018]); b) beams in a mezzanine floor; c) wall cladding (http://www.bw-industries.co.uk [accessed on August 2018])	2
Figure 2.1: Effect of strain hardening and strain aging on the stress-strain characteristic of structural steel.....	10
Figure 2.2: Buckling behaviour of a perfect and imperfect plate: a) Force vs. lateral deflection; b) average stress vs. strain	18
Figure 2.3: Effective width concept	25
Figure 2.4: Reduction factor ρ against relative plate slenderness λp	26
Figure 2.5: The interactive buckling mode based on the ECBL theory	30
Figure 2.6: Tensile force in the connectors of a flexural member composed of back-to-back channels (AISI, 2016b).....	34
Figure 2.7: Iteration process in a time increment	42
Figure 2.8: Mesh independent fasteners	51
Figure 2.9: Methods used to locate the fastening points with a point-based or a discrete fastener	53
Figure 2.10: Global and fastener coordinate systems.....	54
Figure 3.1: Built-up cross sections	57
Figure 3.2: a) M6 bolts, b) M5.5 self-drilling screws.....	57
Figure 3.3: Flat coupon dimensions	58
Figure 3.4: a) Flat coupons before testing, b) Flat coupon during testing.....	59
Figure 3.5: Corner coupon dimensions.....	60
Figure 3.6: Corner coupons and square block arrangement	61
Figure 3.7: a) Corner coupons before testing, b) Pair of corner coupons during testing	61
Figure 3.8: Photograph of the cross-section of corner coupon T10412-a	62
Figure 3.9: T15414-a Flat coupon test results	63
Figure 3.10: Stress-strain curve of flat and corner coupons belonging to section T12012	65
Figure 3.11: Bending deformations in corner coupons	65
Figure 3.12: Nomenclature used to refer to the dimensions of the component sections	66
Figure 3.13: Signature curve of the components of built-up column 1	68
Figure 3.14: Signature curve of the components of built-up column 2.....	69
Figure 3.15: Signature curve of the components of built-up columns 3 and 4.....	70
Figure 3.16: Location of connectors in a) geometry 1 and b) geometry 2	73
Figure 3.17: Images of built-up columns 1 and 2 during and after assembly.....	74
Figure 3.18: Location of connectors in a) geometry 3 and b) geometry 4	74

Figure 3.19: Images of built-up columns 3 and 4 during and after assembly	75
Figure 3.20: a), c) and d) Mould made with modelling clay and cardboard, b) Column set in resin.....	76
Figure 3.21: a) and b) Traverse system for measuring imperfections, c) Trolley, d) Laser sensor	77
Figure 3.22: Location of the imperfection measurements in built-up column 1	79
Figure 3.23: Measurement of the imperfections of built-up column 1	79
Figure 3.24: Location of the imperfection measurements in built-up column 2.....	80
Figure 3.25: Measurement of the imperfections of built-up column 2	80
Figure 3.26: Location of the imperfection measurements in built-up column 3.....	82
Figure 3.27: Location of the imperfection measurements in the lipped channels of built-up column 3	82
Figure 3.28: Measurement of the imperfections of built-up column 3	83
Figure 3.29: Location of the imperfection measurements in built-up column 4.....	84
Figure 3.30: Location of the imperfection measurements in the plain channels of built-up column 4	84
Figure 3.31: Measurement of the imperfections of built-up column 4	85
Figure 3.32: Typical web imperfections of channel T15414-2 in built-up column 1	86
Figure 3.33: Typical web imperfections of channel S11012-9 in built-up column 4	87
Figure 3.34: Typical flange imperfections of channel T15414-2 in built-up column 2.....	87
Figure 3.35: Plaster used to correct misalignment between the platen of the machine and the column end plate	89
Figure 3.36: Location of strain gauges in a) SC1, b) SC2, c) SC3 and d) column 4	89
Figure 3.37: Arrangement of LVDTs to measure axial deformation.....	90
Figure 3.38: a), b), c) and d): Potentiometer frame, e) Potentiometer used to record out-of-plane deformations, f) LVDTs used to record axial deformation of the column.....	91
Figure 3.39: Potentiometer arrangement for a) column 1, b) column 2.....	92
Figure 3.40: Potentiometer arrangement for a) column 3, b) column 4.....	92
Figure 3.41: Axial load vs compressive strain in column SC1-2a.....	93
Figure 3.42: Axial load vs compressive strain in column SC2-2a.....	94
Figure 3.43: Axial load vs compressive strain in column SC3-2a.....	94
Figure 3.44: Axial load vs compressive strain in column SC4-2a.....	95
Figure 3.45: Deformed shape approaching ultimate load in a) SC1-2a, b) SC1-3a, c) SC1-5a..	97
Figure 3.46: Final deformed shape at end of test in a) SC1-2a, b) SC1-3a, c) SC1-5a	97
Figure 3.47: Deformed shape approaching ultimate load in a) SC2-2a, b) SC2-4a, c) SC2-6a..	98
Figure 3.48: Final deformed shape at end of test in a) SC2-2a, b) SC2-4a, c) SC2-6a	99
Figure 3.49: Deformed shape approaching ultimate load in a) SC3-2a, b) SC3-2b, c) SC3-5a, d) SC3-5b	101

Figure 3.50: Final deformed shape at end of test in a) SC3-2a, b) SC3-2b, c) SC3-5a, d) SC3-5b	101
Figure 3.51: Deformed shape approaching ultimate load in a) SC4-2a, b) SC4-2b, c) SC4-5a, d) SC4-5b.....	103
Figure 3.52: Final deformed shape at end of test in a) SC4-2a, b) SC4-2b, c) SC4-5a, d) SC4-5b	103
Figure 3.53: Force against lateral deflection curve for: a) a channel; b) a plate	104
Figure 3.54: Post-buckling change of stiffness in column SC1-2a recorded with strain gauges	106
Figure 3.55: Axial load vs lateral displacements in SC1-2a.....	107
Figure 3.56: Axial load vs lateral displacements in SC2-2a.....	109
Figure 3.57 Axial load vs lateral displacements in SC2-4a.....	109
Figure 3.58: Axial load vs lateral displacements in SC3-5a.....	111
Figure 3.59: Axial load vs lateral displacements in SC4-5b	113
Figure 3.60: Axial load vs axial displacements in SC2-4a	114
Figure 3.61: Axial load vs. deformation curves: geometry 1	114
Figure 3.62: Axial load vs. deformation curves: geometry 2	115
Figure 3.63: Axial load vs. deformation curves: geometry 3	116
Figure 3.64: Axial load vs. deformation curves: geometry 4	117
Figure 4.1: Built-up cross-sections.....	122
Figure 4.2: Flat coupon during testing.....	123
Figure 4.3: Corner coupon dimensions.....	124
Figure 4.4: Pair of corner coupons during testing	124
Figure 4.5: T12915 Corner coupon test results	125
Figure 4.6: Nomenclature used to refer to the dimensions of the component sections	127
Figure 4.7: Stress distribution within component sections for elastic stability analysis	128
Figure 4.8: Signature curve of the components of geometry 1.....	129
Figure 4.9: Signature curve of the components of geometry 2.....	130
Figure 4.10: Location of connectors in geometry 1 beams	132
Figure 4.11: Location of connectors in geometry 2 beams	132
Figure 4.12: Built-up beams during and after assembly.....	133
Figure 4.13: Locations of the imperfection measurements in geometry 1	135
Figure 4.14: Measurement of the imperfections in geometry 1.....	136
Figure 4.15: Locations of the imperfection measurements in geometry 2	136
Figure 4.16: Measurement of the imperfections in geometry 2.....	137
Figure 4.17: Imperfections in the web of channel T12915-6 (geometry 1).....	138
Figure 4.18: Imperfections of a flange of channel T10412-1 (geometry 2)	139
Figure 4.19: 4-point bending test rig	139

Figure 4.20: Laterally restraining assembly.....	140
Figure 4.21: Loading devices: a) Pin support, b) Roller support	141
Figure 4.22: Distribution of the LVDTs along the test specimen	142
Figure 4.23: Location of the LVDTs within the cross-section.....	142
Figure 4.24: Potentiometer lay-out within the cross-sections	143
Figure 4.25: Location of the potentiometers along the test specimens	143
Figure 4.26: Top channel in specimen B1-3b displaying buckles with different half-wave lengths.....	145
Figure 4.27: Deformed shape of specimen B1-0a: a) before peak load, b) after peak load.....	146
Figure 4.28: Deformed shape of specimen B1-0b: a) before peak load, b) after peak load.....	146
Figure 4.29: Deformed shape of specimen B1-2a: a) before peak load, b) after peak load.....	147
Figure 4.30: Deformed shape of specimen B1-2b: a) before peak load, b) after peak load.....	147
Figure 4.31: Deformed shape of specimen B1-3a: a) before peak load, b) after peak load.....	148
Figure 4.32: Deformed shape of specimen B1-3b: a) before peak load, b) after peak load.....	148
Figure 4.33: Plastic hinge in B1-2a: a) Top channel b) Channels comprising the web	149
Figure 4.34: Asymmetric plastic hinge in built-up specimens a) B1-0b b) B1-2b	149
Figure 4.35: Axial load vs lateral displacements (B1-2a).....	150
Figure 4.36: Axial load vs lateral displacements (B1-3a).....	151
Figure 4.37: Deformed shape of specimen B2-0a: a) before peak load, b) after peak load.....	153
Figure 4.38: Deformed shape of specimen B2-0b: a) before peak load, b) after peak load.....	153
Figure 4.39: Deformed shape of specimen B2-2a: a) before peak load, b) after peak load.....	154
Figure 4.40: Deformed shape of specimen B2-2b: a) before peak load, b) after peak load	154
Figure 4.41: Deformed shape of specimen B2-3a: a) before peak load, b) after peak load.....	155
Figure 4.42: Deformed shape of specimen B2-3b: a) before peak load, b) after peak load.....	155
Figure 4.43: Yield line mechanism in B2-2a: a) Top channel, b) Channels comprising the web	156
Figure 4.44: Axial load vs lateral displacements of B2-0a	156
Figure 4.45: Axial load vs lateral displacements of B2-3b.....	157
Figure 4.46: Distance between the centroid of the top channel and the centroid of the built-up cross-section 1.....	158
Figure 4.47: Slip at specimen end between the components of built-up beam 1	161
Figure 4.48: Slip at specimen end between the components of built-up beam 2.....	162
Figure 4.49: Moment vs relative deflection at mid-span (B1-2a).....	163
Figure 4.50: Moment vs relative deflection at mid-span of specimens with geometry 1	163
Figure 4.51: Ultimate capacity vs connector spacing of specimens with geometry 1	164
Figure 4.52: Moment vs relative deflection at mid-span of specimens with geometry 2	165
Figure 4.53: Ultimate capacity vs connector spacing of specimens with geometry 2	165
Figure 5.1: Built-up cross sections.....	170

Figure 5.2: a) Flat coupons before testing, b) Flat coupon during testing	172
Figure 5.3: a) Corner coupons before testing, b) Pair of corner coupons during testing	174
Figure 5.4: static stress–strain curve for flat coupons T15414(l) and T15414(s).....	176
Figure 5.5: Nomenclature used to refer to the dimensions of the component sections	177
Figure 5.6: Signature curve of the components of built-up column 1	180
Figure 5.7: Signature curve of the components of built-up column 2	181
Figure 5.8: Signature curve of the components of built-up columns 3.....	182
Figure 5.9: Signature curve of the components of built-up columns 4.....	183
Figure 5.10: Nomenclature used to refer to the dimensions of the component sections	184
Figure 5.11: Location of connectors in a) geometry 1 and b) geometry 2	186
Figure 5.12: Built-up columns 1 and 2 during and after assembly.....	187
Figure 5.13: Location of connectors in a) geometry 3 and b) geometry 4	187
Figure 5.14: Built-up columns 3 and 4 during and after assembly.....	188
Figure 5.15: a) and b) Endplate welded to the columns; c) welding process d) scribed lines on specimen and endplate;.....	189
Figure 5.16: Typical flange distortion at the end of channel T15414 in specimens: a) LC2-2b; b) LC2-4b.....	190
Figure 5.17: Imperfection measuring rig	191
Figure 5.18: Imperfections measured in plain and lipped channels	194
Figure 5.19: Imperfection measurements on the individual channels	195
Figure 5.20: Location of the imperfection measurements in built-up column 1	196
Figure 5.21: Measurement of the imperfections of built-up column 1	197
Figure 5.22: Location of the imperfection measurements in built-up column 2	198
Figure 5.23: Measurement of the imperfections of built-up column 2.....	198
Figure 5.24: Location of the imperfection measurements in built-up column 3	200
Figure 5.25: Measurement of the imperfections of built-up column 3.....	200
Figure 5.26: Location of the imperfection measurements in built-up column 4	201
Figure 5.27: Measurement of the imperfections of built-up column 4.....	201
Figure 5.28: Imperfection components and bearing deformations along the web of channel S11012-7	203
Figure 5.29: Imperfection components and bearing deformations along the web of channel T13014-2	203
Figure 5.30: Undulating imperfection component along the left flange of channel S11012-2 .	204
Figure 5.31: Imperfection profile recorded along the left flange of specimens of each type of channel.....	204
Figure 5.32: Imperfection profile along the flanges of channels T13014-2 and T12012-2.....	205
Figure 5.33: Imperfection profile along the web, flanges and lips of channel S11012-3.....	206
Figure 5.34: Imperfection distribution along the web of channels T13014 after assembly	208

Figure 5.35: Imperfection profile along the web of channels T15414 after assembly.....	209
Figure 5.36: Imperfection profile along the web of channels S11012 after assembly	209
Figure 5.37: Imperfection profile along one of the flanges of channels T15414-1, T15414-5 and T15414-9 after the assemblage	210
Figure 5.38: Average PSD of the web imperfections of channels T13014 before and after the assemblage	212
Figure 5.39: Average PSD of the web imperfections of channels T15414 before and after the assemblage	213
Figure 5.40: Average PSD of the web imperfections of channels T7914 before and after the assemblage	213
Figure 5.41: Average PSD of the web imperfections of channels T12012 before and after the assemblage	214
Figure 5.42: Average PSD of the flange imperfections of channels S11012 before the assemblage	214
Figure 5.43: Average PSD of the web imperfections of channels S11012 before and after the assemblage	215
Figure 5.44: Average PSD of the flange imperfections of channels T15414 before and after the assemblage	215
Figure 5.45: Average PSD of the flange imperfections of channels T12012 before and after the assemblage	216
Figure 5.46: Average PSD of the flange imperfections of channels S11012 before and after the assemblage	216
Figure 5.47: Minor axis global imperfection of a representative specimen of each type of channel before the assemblage.....	217
Figure 5.48: Minor axis global imperfections of channels T12012 before the assemblage.....	217
Figure 5.49: Major axis global imperfections of a representative specimen of each type of channel before the assemblage.....	218
Figure 5.50: Minor axis global imperfections of channels T12012 after the assemblage.....	220
Figure 5.51: Minor axis global imperfections of channels S11012 after the assemblage.....	220
Figure 5.52: Minor axis global imperfections of channels T15414 after the assemblage.....	221
Figure 5.53: Minor axis global imperfections of channels T7914 after the assemblage.....	221
Figure 5.54: Global imperfection of channels T13014 before and after the assemblage.....	222
Figure 5.55: Global imperfection of channels T15414 before and after the assemblage.....	222
Figure 5.56: Global imperfection of channels T7914 before and after the assemblage.....	222
Figure 5.57: Global imperfection of channels T12012 before and after the assemblage.....	223
Figure 5.58: Global imperfection of channels S11012 before and after the assemblage.....	223
Figure 5.59: Calibration of the imperfection measuring rig	225

Figure 5.60: Imperfections of the guiding system along the measuring lines of the web of channels T12012.....	226
Figure 5.61: Flexural and torsional deformations due to self-weight.....	226
Figure 5.62: Measured channel positions to check accuracy of the measuring rig	227
Figure 5.63: Imperfections of the web of channel T12012-26 measured in four different positions.....	228
Figure 5.64: $\Delta_{Imp,L_i}(x)$ obtained in the web of channel T12012-26	229
Figure 5.65: Δ_{Imp,L_i} obtained in the web of channel T12012-26 after removing the self-weight deflections	230
Figure 5.66: Maximum imperfection difference obtained in the web of channel T12012-26 after removing the self-weight deflections	231
Figure 5.67: Maximum imperfection difference obtained in the web of channel T12012-25 after removing the self-weight deflections	232
Figure 5.68: Maximum imperfection difference obtained in the web of channel T7914-13 after removing the self-weight deflections	232
Figure 5.69: Test set-up	234
Figure 5.70: a) and b) components of top support; c) and d) components of bottom support...	235
Figure 5.71: a) alignment between scribed lines; b) bottom support bolted to the specimen....	235
Figure 5.72: Location of LVDTs G1 and G2 for: a) LC1; b) LC2; c) LC3 and d) LC4	237
Figure 5.73: Location of potentiometers W-1 and W-2	238
Figure 5.74: Schematic representation of the aluminium frame holding potentiometers <i>D1</i> and <i>D2</i>	239
Figure 5.75: Aluminium frame attached to a specimen with geometry 4.....	239
Figure 5.76: Location of strain gauges in a) LC1, b) LC2, c) LC3 and d) LC4	240
Figure 5.77: Strain gauge lay-out for each geometry	240
Figure 5.78: Displacement rate achieved in specimen LC1-8a	241
Figure 5.79: Axial load vs compressive strain in column LC1-2a	242
Figure 5.80: Axial load vs compressive strain in column LC2-2a	242
Figure 5.81: Axial load vs compressive strain in column LC3-2a	243
Figure 5.82: Axial load vs compressive strain in column LC4-2a	243
Figure 5.83: Strain gauge locations and distance between left and right channel webs	244
Figure 5.84: Axial load vs initial eccentricity at mid-height for column LC4-8a	247
Figure 5.85: Deformed shape approaching ultimate load in a) LC1-2a, b) LC1-2b, c) LC1-3a, d) LC1-3b, e) LC1-8a, f) LC1-8b	250
Figure 5.86: Final deformed shape at end of test in a) LC1-2a, b) LC1-2b, c) LC1-3a, d) LC1-3b, e) LC1-8a, f) LC1-8b.....	251
Figure 5.87: Plastic yield line mechanism in a) LC1-3a, b) LC1-3b.....	251
Figure 5.88: Plastic yield line mechanism in LC2-6b	252

Figure 5.89: Deformed shape approaching ultimate load in a) LC2-2a, b) LC2-2b, c) LC2-6a, d) LC2-6b, e) LC2-4a, f) LC2-4b.....	254
Figure 5.90: Final deformed shape at end of test in a) LC2-2a, b) LC2-2b, c) LC2-6a, d) LC2-6b, e) LC2-4a, f) LC2-4b	255
Figure 5.91: Deformed shape approaching ultimate load in a) LC3-2a, b) LC3-2b, c) LC3-3a, d) LC3-3b, e) LC3-8a, f) LC3-8b.....	257
Figure 5.92: Yield line mechanism in a) LC3-2b, b) LC3-8b.....	257
Figure 5.93: Final deformed shape at end of test in a) LC3-2a, b) LC3-2b, c) LC3-3a, d) LC3-3b, e) LC3-8a, f) LC3-8b	258
Figure 5.94: Synchronicity between the local buckling pattern of the lipped and plain channels in a) LC3-8a, b) LC3-8b	258
Figure 5.95: Deformed shape approaching ultimate load in a) LC4-2a, b) LC4-2b, c) LC4-3a, d) LC4-3b, e) LC4-8a, f) LC4-8b.....	260
Figure 5.96: Distortional buckling in lipped channel on compression side as yield lines formed in a) LC4-2b, b) LC4-3b	260
Figure 5.97: Yield line mechanism in column a) LC4-2b, b) LC4-8b, c) LC4-8a	261
Figure 5.98: Final deformed shape at end of test in a) LC4-2a, b) LC4-2b, c) LC4-3a, d) LC4-3b, e) LC4-8a, f) LC4-8b	261
Figure 5.99: Axial load vs lateral displacements of LC1-2b	263
Figure 5.100: Axial load vs lateral displacements of LC2-2a.....	265
Figure 5.101: Axial load vs lateral displacements of LC2-4b	265
Figure 5.102: Axial load vs lateral displacements of LC3-2b	267
Figure 5.103: Axial load vs lateral displacements of LC3-8a.....	268
Figure 5.104: Axial load vs lateral displacements of LC4-2b	269
Figure 5.105: Axial load vs axial displacements of LC3-2b.....	270
Figure 5.106: Axial load vs. axial deformation curves: geometry 1	272
Figure 5.107: Axial load vs. lateral deflection curves: geometry 1	272
Figure 5.108: Axial load vs. axial deformation curves: geometry 2	273
Figure 5.109: Axial load vs. lateral deflection curves: geometry 2	274
Figure 5.110: Axial load vs. axial deformation curves: geometry 3	275
Figure 5.111: Axial load vs. lateral deflection curves: geometry 3	275
Figure 5.112: Axial load vs. axial deformation curves: geometry 4.....	276
Figure 5.113: Axial load vs. lateral deflection curves: geometry 4	277
Figure 6.1: Connector specimens fabricated for each built-up geometry	284
Figure 6.2: Nominal dimensions of steel plate	285
Figure 6.3: Single lap shear test set-up	287
Figure 6.4: a) BCS14-14a and b) SCS12-12b.....	288
Figure 6.5: Camera and lamp arrangement for DIC	290

Figure 6.6: Load-elongation curve of specimens BCS24-14.....	291
Figure 6.7: Load-elongation curve of specimens BCS15-15.....	292
Figure 6.8: Load-elongation curve of specimens BCS14-12.....	292
Figure 6.9: Load-elongation curve of specimens BCS15-12.....	292
Figure 6.10: Load-elongation curve of specimens BCS14-20/SCS14-20	293
Figure 6.11: Load-elongation curve of specimens BCS14-14/SCS14-14	294
Figure 6.12: Load-elongation curve of specimens SCS12-12/BCS12-12	294
Figure 6.13: Small gap between steel sheets of specimen SCS14-14	295
Figure 6.14: Load-elongation curve of all screwed specimens	295
Figure 6.15: Deformed shape of a) BCS24-14b; b) BCS15-15c	296
Figure 6.16: Deformed shape of a) BCS12-14c; b) BCS12-14a	296
Figure 6.17: Deformed shape of a) BCS14-20b; b) SCS14-20c	297
Figure 6.18: Deformed shape a) BCS14-14b; b) SCS14-14c.....	297
Figure 6.19: Deformed shape of a) SCS12-12a; b) BCS12-12c.....	297
Figure 6.20: Force vs displacement curve of specimen BCS15-12c	299
Figure 6.21: Source of error in LVDT readings	299
Figure 6.22: Load vs deformation curve obtained from LVDTs and Ncorr v1.2 for specimen BCS15-15a	301
Figure 6.23: Difference between Ncorr v1.2 and average LVDT measurements	302
Figure 6.24: Difference between deformations obtained from Jones' DIC and LVDTs.....	302
Figure 6.25: Load vs deformation curve obtained from LVDTs and Jones' DIC code for specimen SCS12-12a.....	303
Figure 7.1: Built-up cross-sections.....	307
Figure 7.2: Location of measured imperfections in stub columns.....	308
Figure 7.3: Interpolated imperfections	309
Figure 7.4: FE models including amplified out-of-plane imperfections	309
Figure 7.5: Corner coupon width.....	311
Figure 7.6: Bilinear and actual stress-strain curve.....	311
Figure 7.7: Effect of material modelling approach on predicted column response: a) SC1-5b; b) SC2-6a; c) SC3-5b; d) SC4-5a	312
Figure 7.8: Master and slave role in contact interaction.....	314
Figure 7.9: PLANAR connector element	315
Figure 7.10: Contact stabilization in columns SC1-2b: a) Dissipated energy over total strain energy; b) Load-axial shortening curve.....	320
Figure 7.11: Contact stabilization in columns SC2-2b: a) Dissipated energy over total strain energy; b) Load-axial shortening curve.....	320
Figure 7.12: Contact stabilization in columns SC3-2a: a) Dissipated energy over total strain energy; b) Load-axial shortening curve.....	320

Figure 7.13: Load-lateral displacement curve of plate sections in column SC1-2b for different scale factors.....	321
Figure 7.14: Automatic stabilization in columns SC1-2b: a) Dissipated energy over total strain energy; b) Load-axial shortening curve	323
Figure 7.15: Automatic stabilization in columns SC2-2b: a) Dissipated energy over total strain energy; b) Load-axial shortening curve	323
Figure 7.16: Automatic stabilization in columns SC3-2a: a) Dissipated energy over total strain energy; b) Load-axial shortening curve	323
Figure 7.17: Automatic stabilization in columns SC4-2a: a) Dissipated energy over total strain energy; b) Load-axial shortening curve	324
Figure 7.18: Effect of mesh size and element type on the ultimate load and total CPU time for columns SC1	328
Figure 7.19: Effect of mesh size and element type on the ultimate load and total CPU time for columns SC2	328
Figure 7.20: Effect of mesh size and element type on the ultimate load and total CPU time for columns SC3	329
Figure 7.21: Numerical and experimental load vs. axial shortening curves of columns SC1...	330
Figure 7.22: Numerical and experimental load vs. axial shortening curves of columns SC2...	331
Figure 7.23: Numerical and experimental load vs. axial shortening curves of columns SC3...	331
Figure 7.24: Numerical and experimental load vs. axial shortening curves of columns SC4...	332
Figure 7.25: Deformed shape of SC1-2a: a) before peak load; b) after peak load.....	333
Figure 7.26: Deformed shape of SC1-5a: a) before peak load; b) after peak load.....	333
Figure 7.27: Deformed shape of SC2-2a: a) before peak load; b) after peak load.....	333
Figure 7.28: Deformed shape of SC2-6a: a) before peak load; b) after peak load.....	334
Figure 7.29: Deformed shape of SC3-5a: a) before peak load; b) after peak load.....	334
Figure 7.30: Deformed shape of SC4-5a: a) before peak load; b) after peak load.....	334
Figure 7.31: Experimental and numerical axial load vs lateral displacement curves of SC1-3b	335
Figure 7.32: Experimental and numerical axial load vs lateral displacement curves of SC2-2a	335
Figure 7.33: Experimental and numerical axial load vs lateral displacement curves of SC3-2a	336
Figure 7.34: Experimental and numerical axial load vs lateral displacement curves of SC4-5b	336
Figure 7.35: Amplified deformed shape of one of the lipped channels of: a) SC3-2a; b) SC4-2a	337
Figure 7.36: Ultimate load comparison for different connector modelling approaches	340
Figure 7.37: Maximum connector shear force	341

Figure 7.38: Maximum connector slip	341
Figure 7.39: FE models: deformed shape of SC1-2a.....	342
Figure 7.40: FE models: deformed shape of SC1-3a.....	343
Figure 7.41: FE models: deformed shape of SC1-5a.....	343
Figure 7.42: Load-lateral displacement curves from Hinge and Planar FE models of SC1-5b.	343
Figure 7.43: FE models: deformed shape of SC2-6a.....	344
Figure 7.44: Load-lateral displacement curves from Hinge and Planar FE models of SC2-6a.	344
Figure 7.45: FE models with varying number of connectors and Tie constraint for column SC3	345
Figure 7.46: Load-axial deformation curve of SC1: a) with contact; b) without contact.....	346
Figure 7.47: Load-axial deformation curve of SC2: a) with contact; b) without contact.....	346
Figure 7.48: Load-axial deformation curve of SC3: a) with contact; b) without contact.....	346
Figure 7.49: Load-axial deformation curve of SC4: a) with contact; b) without contact.....	347
Figure 7.50: Ultimate load vs. connector spacing obtained from FE models: a) with contact; b) without contact	348
Figure 7.51: Amplified buckled shape of columns SC1	349
Figure 7.52: Amplified buckled shape of columns SC2.....	349
Figure 7.53: Amplified buckled shape of columns SC3.....	350
Figure 7.54: Gap formation between the web of the plain channels and the flanges of the lipped channels in columns SC3.....	351
Figure 7.55: Amplified buckled shape of two of the components of columns SC4	351
Figure 7.56: Effect of contact interaction on the ultimate capacity	352
Figure 8.1: Built-up cross-sections	356
Figure 8.2: Loading and support conditions in test set-up.....	358
Figure 8.3: Loading and support conditions in FE model	358
Figure 8.4: Modelling of the loading points of beam: a) B1; b) B2	359
Figure 8.5: End support modelling of beam B1	360
Figure 8.6: End support modelling of beam B2	360
Figure 8.7: Boundary conditions in simplified FE models.....	361
Figure 8.8: Location of the imperfection measurements	362
Figure 8.9: Interpolated imperfections	362
Figure 8.10: Beam B2 FE model incorporating out-of-plane imperfections (amplified x50) ...	362
Figure 8.11: Effect of material properties modelling approaches on beams: a) B1-3a; b) B2-3a	364
Figure 8.12: Master and slave surfaces in contact interaction.....	365
Figure 8.13: Dissipated viscous energy relative to total strain energy using Stabilization 3 in beams B1	368

Figure 8.14: Dissipated viscous energy relative to total strain energy using Stabilization 2 and Stabilization 3 in beams B2	368
Figure 8.15: Dissipated viscous energy relative to total strain energy using Stabilization 1 and Stabilization 3 in beams B2	369
Figure 8.16: Moment-deflection curve using Stabilization 1 and Stabilization 3 in beams B2	369
Figure 8.17: Effect of mesh size on the ultimate moment and total CPU time for beam B1	372
Figure 8.18: Effect of mesh size on the ultimate moment and total CPU time for beam B2	373
Figure 8.19: Mesh 3A configuration in beam B1	373
Figure 8.20: Mesh 3A configuration in beam B2	373
Figure 8.21: Mesh 3B configuration in beam B1	374
Figure 8.22: Moment vs. mid-span deflection curve obtained from tests and detailed FE models for beams B1	375
Figure 8.23: Moment vs. mid-span deflection curve obtained from tests and detailed FE models for beams B2	375
Figure 8.24: Deformed shape of B1-0b: a) before peak load (amplified); b) after peak load...	376
Figure 8.25: Deformed shape of the web channels of B1-0b at the peak load.....	377
Figure 8.26: Deformed shape of B1-2b: a) before peak load (amplified); b) after peak load...	377
Figure 8.27: Deformed shape of B1-0b: a) before peak load (amplified); b) after peak load...	377
Figure 8.28: Deformed shape of B2-0b: a) before peak load (amplified); b) after peak load...	378
Figure 8.29: Deformed shape of B2-2b: a) before peak load (amplified); b) after peak load...	378
Figure 8.30: Deformed shape of B2-3b: a) before peak load (amplified); b) after peak load...	379
Figure 8.31: Axial load vs lateral displacements curve of B1-0b obtained from the test and the detailed FE model	380
Figure 8.32: Axial load vs lateral displacements curve of B1-2b obtained from the test and the detailed FE model	380
Figure 8.33: Axial load vs lateral displacements curve of B2-2b obtained from the test and the detailed FE model	381
Figure 8.34: Axial load vs lateral displacements curve of B2-3b obtained from the test and the detailed FE model	381
Figure 8.35: Moment vs. mid-span deflection curve obtained from tests and simplified FE models for beams B1	383
Figure 8.36: Moment vs. mid-span deflection curve obtained from tests and simplified FE models for beams B2	383
Figure 8.37: Axial load vs lateral displacements of B1-0b obtained from the tests and the simplified FE models	384
Figure 8.38: Axial load vs lateral displacements of B1-2b obtained from the tests and the simplified FE models	385

Figure 8.39: Axial load vs lateral displacements of B2-2b obtained from the tests and the simplified FE models.....	385
Figure 8.40: Axial load vs lateral displacements of B2-3b obtained from the tests and the simplified FE models.....	386
Figure 8.41: Ultimate moment comparison for different connector modelling approaches.....	387
Figure 8.42: Shear forces in the connectors: a) B1-2a; b) B2-2a	388
Figure 8.43: Failure mode of beam B1-2a:a) PLANAR model; b) Validated model.....	389
Figure 8.44: Failure mode of beam B2-2a:a) PLANAR model; b) Validated model.....	389
Figure 8.45: Moment vs. mid-span deflection of B1: a) with contact; b) without contact.....	390
Figure 8.46: Moment vs. mid-span deflection of B2: a) with contact; b) without contact.....	391
Figure 8.47: Ultimate load vs. connector spacing for FE models: a) with contact; b) without contact	392
Figure 8.48: Deformed shape of beam B2-0: a) with contact; b) without contact	393
Figure 8.49: Amplified buckling deformed shape of beams B1	395
Figure 8.50: Amplified buckled shape of beams B2	396
Figure 8.51: Signature curve top channel in: a) B1-3; b) B2-3	396
Figure 8.52: Effect of contact interaction on the ultimate capacity.....	397
Figure 9.1: Built-up cross-sections	401
Figure 9.2: FE model boundary conditions	402
Figure 9.3: Location of measured imperfections in stub columns.....	403
Figure 9.4: Interpolated imperfection.....	403
Figure 9.5: Effect of material properties modelling approaches on columns: a) LC1-8a; b) LC2-6a; c) LC3-2a; d) LC4-3a	404
Figure 9.6: Master and slave role in contact interaction.....	405
Figure 9.7: Contact stabilization in columns LC1: a) Dissipated energy over total strain energy; b) Load-axial shortening curve.....	409
Figure 9.8: Contact stabilization in columns LC2: a) Dissipated energy over total strain energy; b) Load-axial shortening curve.....	409
Figure 9.9: Contact stabilization in columns LC3: a) Dissipated energy over total strain energy; b) Load-axial shortening curve.....	410
Figure 9.10: Contact stabilization in columns LC4: a) Dissipated energy over total strain energy; b) Load-axial shortening curve.....	410
Figure 9.11: Load-lateral displacement curves of plate sections in column LC1-2a for different scale factors	410
Figure 9.12: Automatic stabilization in columns LC1: a) Dissipated energy over total strain energy; b) Load-axial shortening curve.....	413
Figure 9.13: Automatic stabilization in columns LC2: a) Dissipated energy over total strain energy; b) Load-axial shortening curve.....	413

Figure 9.14: Automatic stabilization in columns LC3: a) Dissipated energy over total strain energy; b) Load-axial shortening curve	413
Figure 9.15: Automatic stabilization in columns LC4: a) Dissipated energy over total strain energy; b) Load-axial shortening curve	414
Figure 9.16: Effect of mesh size on the ultimate load and total CPU time for columns LC1...	417
Figure 9.17 Effect of mesh size on the ultimate load and total CPU time for columns LC2....	417
Figure 9.18: Effect of mesh size on the ultimate load and total CPU time for columns LC3...	418
Figure 9.19: Numerical and experimental load vs. axial shortening curves of columns LC1 ..	419
Figure 9.20: Numerical and experimental load vs. axial shortening curves of columns LC2 ..	420
Figure 9.21: Numerical and experimental load vs. axial shortening curves of columns LC3 ..	420
Figure 9.22: Numerical and experimental load vs. axial shortening curves of columns LC4 ..	421
Figure 9.23: Comparison of the buckled shape: a) LC1-2a; b) LC1-3a; c) LC1-8a	422
Figure 9.24: Comparison of localized plastic deformations: a) LC1-2a; b) LC1-2b	423
Figure 9.25: Comparison of localized plastic deformations: a) LC1-3b; b) LC1-8b	423
Figure 9.26: Comparison of the buckled shape: a) LC2-2b; b) LC2-6a; c) LC2-4a	424
Figure 9.27: Comparison of localized plastic deformations: a) LC2-2b; b) LC2-6b	425
Figure 9.28: Comparison of the buckled shape: a) LC3-2a; b) LC3-3b; c) LC3-8b	426
Figure 9.29: Comparison of localized plastic deformations: a) LC3-2a; b) LC3-8a	426
Figure 9.30: Comparison of the buckled shape: a) LC4-2a; b) LC4-3b; c) LC4-8b	427
Figure 9.31: Deformed shape of lipped channel on compression side.....	428
Figure 9.32: Comparison of localized plastic deformations: a) LC4-2b; b) LC4-3b; c) LC4-8b	428
Figure 9.33: Experimental and numerical axial load vs lateral displacement curves of LC1-3a	430
Figure 9.34: Experimental and numerical axial load vs lateral displacement curves of LC2-6b	430
Figure 9.35: Experimental and numerical axial load vs lateral displacement curves of LC3-3a	430
Figure 9.36: Experimental and numerical axial load vs lateral displacement curves of LC4-3b	431
Figure 9.37: Ultimate load comparison for different connector modelling approaches	433
Figure 9.38: Maximum connector slip	433
Figure 9.39: Maximum connector slip	434
Figure 9.40: Failure mode in PLANAR FE model: a) LC1-8a; b) LC2-6a; c) LC3-8a; d) LC4-8a	435
Figure 9.41: Load-axial deformation LC1: a) with contact; b) without contact	436
Figure 9.42: Load-axial deformation LC2: a) with contact; b) without contact	436
Figure 9.43: Load-axial deformation LC3: a) with contact; b) without contact	436

Figure 9.44: Load-axial deformation LC4: a) with contact; b) without contact..... 437

Figure 9.45: Ultimate load vs. connector spacing for FE models: a) with contact; b) without contact 439

Figure 9.46: Effect of contact interaction on the ultimate capacity 440

Figure 10.1: Arrangements of two 2D laser sensors taking measurements in the vertical direction..... 452

Figure 10.2: Arrangements of two 2D laser sensors taking measurements in a horizontal direction..... 452

List of Tables

Table 3.1: Measured dimensions of flat coupons.....	59
Table 3.2: Measured area of corner coupons	62
Table 3.3: Material properties of tensile coupons	64
Table 3.4: Nominal dimensions of the component sections	66
Table 3.5: Predicted buckling stress of built-up column 1.....	68
Table 3.6: Predicted buckling stress of built-up column 2.....	69
Table 3.7: Predicted buckling stress of built-up columns 3 and 4	70
Table 3.8: Measured dimensions of built-up column 1.....	71
Table 3.9: Measured dimensions of built-up column 2.....	71
Table 3.10: Measured dimensions of built-up column 3.....	72
Table 3.11: Measured dimensions of built-up column 4.....	72
Table 3.12: Maximum and averaged imperfection measurement	88
Table 3.13: Buckling stresses of the components of geometry 1	107
Table 3.14: Buckling stresses of the components of geometry 2.....	110
Table 3.15: Buckling stresses of the different components of geometry 3	110
Table 3.16: Buckling stresses of the different components of geometry 4	112
Table 3.17: Ultimate loads: geometry 1.....	115
Table 3.18: Ultimate loads: geometry 2.....	115
Table 3.19: Ultimate loads: geometry 3.....	116
Table 3.20: Ultimate loads: geometry 4.....	117
Table 4.1: Measured dimensions of flat coupons.....	123
Table 4.2: Measured area of corner coupons	124
Table 4.3: Material properties of tensile coupons	126
Table 4.4: Nominal dimensions of the component sections	127
Table 4.5: Predicted buckling stresses of the components of geometry 1	129
Table 4.6: Predicted buckling stresses of the components of geometry 2	130
Table 4.7: Measured dimensions of geometry 1 specimens	131
Table 4.8: Measured dimensions of geometry 2 specimens	131
Table 4.9: Maximum and averaged imperfection measurement	137
Table 4.10: Shear force in shear span connectors of specimens with geometry 1	159
Table 4.11: Buckling stresses of the top channel of specimens with geometry 1	160
Table 4.12: Shear force in shear span connectors of specimens with geometry 2	161
Table 4.13: Buckling stresses of the top channel of specimens with geometry 2	161
Table 4.14: Ultimate capacity of built-up beam 1.....	164
Table 4.15: Ultimate capacity of built-up beam 2.....	166

Table 5.1: Measured dimensions of flat coupons	173
Table 5.2: Measured area of corner coupons.....	174
Table 5.3: Material properties of tensile coupons	175
Table 5.4: Nominal dimensions of the component sections	177
Table 5.5: Predicted buckling stress of built-up column 1	179
Table 5.6: Predicted buckling stress of built-up column 2	181
Table 5.7: Predicted buckling stress of built-up columns 3.....	182
Table 5.8: Predicted buckling stress of built-up columns 4.....	183
Table 5.9: Measured dimensions of built-up column 1	184
Table 5.10: Measured dimensions of built-up column 2	184
Table 5.11: Measured dimensions of built-up column 3	184
Table 5.12: Measured dimensions of built-up column 4	185
Table 5.13: Average thickness of zinc coating.....	185
Table 5.14: Statistical values of the out-of-plane imperfection of the channels before the assemblage.....	207
Table 5.15: Statistical values of the out-of-plane imperfections of the channels after the assemblage.....	210
Table 5.16: Statistical values of the global imperfection of the channels before the assemblage	219
Table 5.17: Statistical values of the global imperfection of the channels after the assemblage	224
Table 5.18: Imperfection difference obtained in channels measured in positions 1, 2, 3 and 4	233
Table 5.19: Global flexural imperfection difference in channels measured in positions 1, 2, 3 and 4	233
Table 5.20: Vertical location of potentiometers $L1$, $L2$, $L3$ and $L4$	237
Table 5.21: Stress difference between left and right channel	245
Table 5.22: Accuracy assessment of load eccentricity	247
Table 5.23: Buckling stresses of the different components of geometry 1.....	264
Table 5.24: Buckling stresses of the different components of geometry 2.....	266
Table 5.25: Buckling stresses of the different components of geometry 3.....	266
Table 5.26: Buckling stresses of the different components of geometry 4.....	268
Table 5.27: Ultimate loads: geometry 1	273
Table 5.28: Ultimate loads: geometry 2	274
Table 5.29: Ultimate loads: geometry 3	275
Table 5.30: Ultimate loads: geometry 4	277
Table 6.1: Measured width and thickness of steel plates.....	286
Table 6.2: Ultimate capacity and failure mode of test specimens	298
Table 6.3: Comparison between DIC and LVDTs	301
Table 7.1 Difference in ultimate load relative to FE model with actual material properties.....	313

Table 7.2: Ultimate load comparison with contact control schemes.....	318
Table 7.3: Ultimate load comparison with automatic stabilization schemes	322
Table 7.4: Mesh configuration for built-up column 1	325
Table 7.5: Mesh aspect ratios in built-up column 1	325
Table 7.6: Mesh configuration for built-up column 2.....	326
Table 7.7: Mesh aspect ratios in built-up column 2.....	326
Table 7.8: Mesh configuration for built-up column 3.....	326
Table 7.9: Mesh aspect ratios in built-up column 3.....	326
Table 7.10: Effect of element type and mesh size on the ultimate load and total CPU time for columns SC1	327
Table 7.11: Effect of element type and mesh size on the ultimate load and total CPU time for columns SC2	327
Table 7.12: Effect of element type and mesh size on the ultimate load and total CPU time for columns SC3	327
Table 7.13: Numerical and experimental ultimate loads of columns SC1	330
Table 7.14: Numerical and experimental ultimate loads of columns SC2.....	330
Table 7.15: Numerical and experimental ultimate loads of columns SC3.....	331
Table 7.16: Numerical and experimental ultimate loads of columns SC4.....	331
Table 7.17: Numerical and experimental buckling stresses of the components of columns SC1	337
Table 7.18: Numerical and experimental buckling stresses of the components of columns SC2	338
Table 7.19: Numerical and experimental buckling stresses of the components of columns SC3	338
Table 7.20: Numerical and experimental buckling stresses of the components of columns SC4	338
Table 8.1: Difference in ultimate moment with respect to FE model with actual material properties	364
Table 8.2: Mesh configurations for built-up beam 1.....	370
Table 8.3: Mesh configurations for built-up beam 2.....	370
Table 8.4: Maximum aspect ratios in built-up beams 1 and 2	371
Table 8.5: Effect of mesh size on the ultimate load and total CPU time for beam B1	371
Table 8.6: Effect of mesh size on the ultimate load and total CPU time for beam B2	371
Table 8.7: Ultimate moment capacity obtained from tests and detailed FE models for beams B1	374
Table 8.8: Ultimate moment capacity obtained from tests and detailed FE models for beams B2	375

Table 8.9: Buckling stresses of the top channel of beams B1 obtained from the tests and the detailed FE models	380
Table 8.10: Buckling stresses of the top channel of beams B2 obtained from the tests and the detailed FE models	382
Table 8.11: Ultimate moment capacity obtained from tests and simplified FE models for beams B1	382
Table 8.12: Ultimate moment capacity obtained from tests and simplified FE models for beams B2	383
Table 8.13: Buckling stresses of the top channel of beams B1 obtained from the tests and the simplified FE models.....	385
Table 8.14: buckling stresses of the top channel of beams B2 obtained from the tests and the simplified FE models.....	386
Table 8.15: Failure modes beams B1 and B2.....	391
Table 9.1: Difference in ultimate load with respect to FE model with actual material properties	405
Table 9.2: Ultimate load comparison with contact control schemes	408
Table 9.3: Ultimate load comparison with automatic stabilization schemes.....	412
Table 9.4: Mesh configuration for column LC1	415
Table 9.5: Mesh aspect ratio in column LC1.....	415
Table 9.6: Mesh configuration for columns LC2	415
Table 9.7: : Mesh aspect ratio in columns LC2.....	415
Table 9.8: Mesh configuration for column LC3.....	415
Table 9.9: Mesh aspect ratio in columns LC3	416
Table 9.10: Effect of the mesh size on the ultimate load and total CPU time for columns LC1	416
Table 9.11: Effect of the mesh size on the ultimate load and total CPU time for columns LC2	416
Table 9.12: Effect of the mesh size on the ultimate load and total CPU time for columns LC3	416
Table 9.13: Numerical and experimental ultimate loads of columns LC1	419
Table 9.14: Numerical and experimental ultimate loads of columns LC2	419
Table 9.15: Numerical and experimental ultimate loads of columns LC3	420
Table 9.16: Numerical and experimental ultimate loads of columns LC4	421
Table 9.17: Numerical and experimental buckling stresses of the components of columns LC1	431
Table 9.18: Numerical and experimental buckling stresses of the components of columns LC2	431

Table 9.19: Numerical and experimental buckling stresses of the components of columns LC3	431
Table 9.20: Numerical and experimental buckling stresses of the components of columns LC4	432
Table 9.21: Failure modes in columns LC1	437
Table 9.22: Failure modes in columns LC2	437
Table 9.23: Failure modes in columns LC3	438
Table 9.24: Failure modes in columns LC4	438

List of Symbols

Latin letters

A :	Area
$A_{built-up}$:	Cross-sectional area of a built-up geometry
A_{cons} :	Constant imperfection component
A_{eff} :	Effective area
A_{topch} :	Area of the top channel in a built-up geometry
A_{und} :	Undulating imperfection component
b :	Flange width of a channel section
b_c :	Width of tensile coupon gauge length
c :	Damping factor
c_a :	Displacement correction for iteration a
c_d :	Damping coefficient
$d_{SG,x}$:	Distance between centre lines of strain gauges in the x-direction
$d_{SG,y}$:	Distance between centre lines of strain gauges in the y-direction
d_w :	Distance between the web of two opposite channels in a built-up specimen
D :	Flexural rigidity of the plate
$e_{0,mid}$:	Initial eccentricity at mid-height obtained from the nominal eccentricity applied at the column end and the global imperfection at mid-height
$e_{0,SG}$:	Initial eccentricity at mid-height obtained from strain gauges
E :	Young's modulus
f_x :	Compressive stress in x-direction
F :	Force
F_v :	Stabilizing viscous forces
F_y :	Squash load

g :	Distance between the two rows of connectors nearest to the top and bottom flange of a channel
h :	Web width of a channel section or width of the plate sections
I :	Second moment of area
I_a :	Internal forces for iteration a
$I_{built-up,xx}$:	Second moment of area of a built-up cross-section about the horizontal axis through its centroid
k_σ :	Buckling coefficient for plates
KL/r :	Slenderness ratio
$(KL/r)_o$:	Global slenderness of a built-up cross-section about its minor axis
l :	Lip width of a channel section
L :	Specimen length
L_{cr} :	Effective length
L_p :	Buckling half-wave length of the plate sections
m :	Distance from the shear centre of a channel to the mid-plane of the web
M :	Bending moment
M^* :	Artificial mass matrix with unit density
M_{crd} :	Elastic distortional buckling moment
M_{crl} :	Elastic local buckling moment
M_{nd} :	Ultimate moment capacity against distortional buckling
M_{nl} :	Ultimate moment capacity against local buckling
M_y :	Moment that causes first yielding
N :	is equal to $A_{eff}f_y$ in ECBL
\bar{N} :	is equal to N/N_{pl}
N_{cr} :	Flexural buckling load
N_{pl} :	is equal to $Q \cdot A_{eff}f_y$ in ECBL
P :	External forces
P_{crd} :	Elastic distortional buckling load

P_{crI} :	Elastic local buckling load
P_{nd} :	Ultimate load against distortional buckling
P_{nl} :	Ultimate load against local buckling
P_s :	Factored concentrated load or reaction in a built-up beam
q :	Design load on a beam for the purpose of determining the maximum connector spacing
Q :	ratio between the effective area and the gross area in ECBL
r_i :	Minimum radius of gyration
r_{int} :	Internal radii of a channel section
R_a :	Force residual for iteration a
s :	Connector spacing
S_{ampl} and S_{incr} :	Time-dependent scale factors
S_{const} :	Constant scale factor
S_{gap} :	Gap-dependent scale factor
S_{iter} :	Iteration-dependent scale factor
S_{max} :	Maximum connector spacing
S_{span} :	Length of the shear span in beams specimens
S_{tang} :	Constant scale factor for tangential stabilization
t :	Plate thickness; thickness
$T_{connector}$:	Connector local coordinate system
$T_{conn.orientation}$:	Connector orientation relative to fastener coordinate system
$T_{fastener}$:	Fastener local coordinate system
T_r :	Required tensile strength of the connection in a built-up beam
T_s :	Factored strength of the connection in tension
v :	Vector of nodal velocities
v_{relN} :	Relative normal velocity between nearby points
v_{relT} :	Relative tangential velocity between nearby points

V :	Vertical shear force
V_{con} :	Shear force at the connector
V_{slip} :	Slip shear force at the connectors
w :	plate deflection
y :	Vertical distance of a point in a cross-section to the centroid
\bar{y} :	Distance from the centroid of the top channel to the centroid of the built-up cross-section

Greek letters

α :	Imperfection factor
$\delta_{flanges}$:	Cross-sectional imperfection along the flanges of the channels
$\delta_{flanges,L}$:	Local imperfection along the flanges of the lipped channels
$\delta_{global,m}$:	Global flexural imperfection of the channel about its minor axis
$\delta_{global,M}$:	Global flexural imperfection of the channel about its major axis
δ_{lips} :	Local imperfection along the lips of the lipped channels
δ_{plate} :	Global imperfection along the plate sections
δ_{web} :	Cross-sectional imperfection along the web of the channels
$\delta_{r,mid}$:	Beam mid-span deflection measured relative to the deflections at the loading points
$\Delta_{Imp,L_i}(x)$:	Cross-sectional imperfection difference
ΔP :	Incremental external forces
Δu_a :	Incremental displacement at the nodes for iteration a
$\Delta \delta_{global,m}$:	Minor axis global imperfection difference
ε :	Engineering strains
ε_c :	Average strain on the compression side of a built-up geometry obtained from strain gauges
ε_f :	Elongation after fracture

ε_i :	Average strain on the tension side of a built-up geometry obtained from strain gauges
ε_T :	True strains
ε_T^{Pl} :	True plastic strains
λ :	Slenderness factor
$\bar{\lambda}$:	Non-dimensional slenderness
$\bar{\lambda}_p$:	Reduced plate slenderness
λ_d :	Distortional slenderness
λ_l :	Local slenderness
ν :	Poisson's ratio
ξ :	Accuracy of imperfection measurement
ρ :	Effective width reduction factor
σ :	Engineering stresses
$\sigma_{0.2\%}$:	0.2 % proof strength
σ_{cr} :	Elastic buckling stress for local, distortional or global buckling
$\sigma_{L,avg}$:	Average stress in a cross-section obtained from the column load
$\sigma_{SG,avg}$:	Average stress in a cross-section obtained from strain gauges
$\sigma_{SG,ch,L}, \sigma_{SG,ch,R}$:	Stress in the left/right channel obtained from strain gauges
σ_{stab} :	Stabilizing stress normal to the surfaces
σ_T :	True stresses
σ_u :	Ultimate tensile stress
τ_{stab} :	Stabilizing stress tangent to the surfaces
v :	Maximum imperfection
ψ :	Maximum erosion factor in ECBL

Chapter 1

Introduction

1.1. Background

Cold-formed steel (CFS) sections with thicknesses ranging between 0.5 mm to 6 mm have traditionally been used as secondary steelwork in buildings. Common examples include roof purlins and wall girts consisting of lipped channels, sigma or zed sections, as well as wall and roof cladding made of profiled sheets with thicknesses of up to 1.5 mm (see Figure 1.1). CFS sections have also been used in mezzanine floors and as steel framing in light industrial and commercial buildings (Dubina et al., 2012).

Depending on the quantity, length and complexity of the sections, they can be produced by roll forming or brake-pressing. In roll forming, a continuous strip of steel is passed through a series of rolls which progressively deform it until the desired shape is achieved. This technique is preferred when large quantities of a given shape have to be fabricated. In contrast, in the press-braking procedure each bend of the cross-section is produced by folding the sheet along its full length when it is pressed against a shaped die. This technique is used for low volume productions and for lengths of up to 8 m. Improvements in manufacturing technology have allowed increasing production speeds and have enabled steel strips of up to 25 mm thickness to be roll formed, while sheets of up to 12.5 mm thickness can be brake-pressed. Also, improvements in the application of zinc coatings to CFS sections have improved their corrosion resistance.

These improvements, together with the advantages originating from the slender nature of these sections have significantly widened their range of applications. Due to their shape, they can often be nested when stored, allowing for compact packing and reducing the cost of transportation. They are also easily handled, with single members and sub-frames easily put in place by operators, facilitating rapid construction. In addition, CFS sections are sustainable as they have a long service life and can be easily re-used or recycled, minimising waste generation.



Figure 1.1: CFS used as secondary steelwork: a) roof purlins in a steel structure (<http://www.rki-bg.com> [accessed on August 2018]); b) beams in a mezzanine floor; c) wall cladding (<http://www.bw-industries.co.uk> [accessed on August 2018])

The efficient use of the material in CFS sections also leads to a high strength-to-weight ratio, offering on the one hand a reduced carbon footprint, while on the other hand providing a more economical solution by reducing the self-weight of the structure. This issue is not just important for reducing the total cost of a building, but can also be essential in cases where it is necessary to add a new storey to a building, minimising the added load on the existing structure and its foundations.

CFS sections also provide a great flexibility of cross-sectional profiles and sizes, which means that their geometry can easily be tailored to satisfy specific demands.

The above reasons are leading to an increasing use of thin-walled structural steel, not just as secondary members, but also as primary load-bearing members, with the CFS industry consequently experiencing a drive towards producing sections that can provide larger spans and

resist higher loads. Examples of this evolution are multi-storey buildings and portal frames constructed entirely out of CFS (Schafer, 2011; Zhang and Rasmussen, 2014).

On the other hand, the reduced wall thickness of CFS sections makes them more prone to being affected by cross-sectional instabilities such as local and distortional buckling. These cross-sectional instabilities originate in addition to the global instabilities which are common to the traditionally used hot-rolled sections. The various instabilities can interact with each other, further reducing the ultimate capacity of CFS sections. Moreover, due to the nature of the fabrication process, the cross-sectional shapes that can be cold-formed are commonly mono-symmetric or point-symmetric, with double symmetry difficult to obtain.

A logical solution to increase the load carrying capacity of CFS members is joining two or more sections together by means of welding or fasteners, such as bolts, rivets or screws to form a built-up section. A wider range of cross-sectional shapes can thus be obtained using the currently available single shapes and be tailored to meet specific requirements. In addition, doubly symmetric cross sections can easily be constructed by joining single sections together, suppressing certain buckling modes which tend to occur in members with singly symmetric cross-sections, such as flexural-torsional buckling. Double symmetry also eliminates the shift of the effective centroid which single sections may experience when local or distortional buckling takes place. Additionally, closed sections can be constructed with increased torsional resistance. Since built-up sections can in principle be assembled on site, the advantages of ease of transportation and handling largely remain.

Despite the potential benefits built-up sections offer, the current major design codes (AISI, 2016a; CEN, 2006) provide at best only limited provisions for certain specific types of built-up sections, with Europe lagging behind in this area. Both the Eurocode (EC3) and the North American Specification (NAS) have traditionally been based on the Effective Width Method (EWM) to address the design of thin-walled members which are susceptible to cross-sectional instabilities. This design approach may become iterative and time consuming. This provided an incentive for the American code to introduce the Direct Strength Method (DSM) more than a decade ago. The DSM has managed to reduce the tediousness of the design process and has fuelled new research in this field. However, it is currently limited to single sections. It is the author's opinion that the European design guidelines need to be improved in order to provide a timely response to new practical developments in the CFS construction industry, as well as to mobilize the potential for future innovation, particularly with respect to built-up sections. This can be achieved by taking advantage of new design methods such as the DSM, which can potentially be modified or extended to apply to built-up sections. Before this stage can be achieved, however, a more fundamental study of the stability and behaviour of built-up sections is required, which is what this thesis aims to provide.

1.2. Objectives and scope

This research aims to contribute towards the understanding of the buckling behaviour and capacity of CFS built-up members, paying special attention to the coupled instabilities resulting from interaction between cross-sectional instabilities of the components, buckling of the individual components between connector points and global instabilities of the entire built-up member. The objectives of this research are to:

- carry out experimental work on CFS built-up members, in particular to:
 1. design and conduct 20 stub column tests with four different cross-sectional geometries to investigate the cross-sectional compressive behaviour and capacity. The columns are assembled with either screws or bolts at varying spacings in order to study the influence of the connector type and spacing on the buckling behaviour and capacity of the built-up specimens.
 2. design and conduct 24 long column tests, covering the same four cross-sections, with varying connector spacings to investigate the interaction between buckling of the individual components in between connector points, cross-sectional instabilities and global buckling of the built-up member, paying special attention to the effect of the connector spacing on the nature of the buckling interaction and the load carrying capacity.
 3. design and conduct 12 four-point bending tests on beams with two different cross-sectional geometries, assembled with varying connector spacings, to investigate the cross-sectional bending moment capacity, paying especial attention to the local buckling interaction between the individual components and the role of the connector spacing in this interaction. The beams are tested with lateral restraints at the loading points to avoid global instability.
 4. conduct coupon tests to determine the material behaviour of all the components used to assemble the built-up specimens.
 5. measure the geometric imperfections of the built-up specimens prior to testing. A state-of-the-art measuring system is developed for this purpose, satisfying the requirements related to the length of the specimens to be measured and the desired accuracy of the readings.
 6. carry out single lap shear tests to determine the behaviour of the connectors used in the built-up members.
- conduct numerical work on CFS built-up members, in particular to:

1. develop detailed finite element (FE) models of the tested specimens, incorporating the recorded geometric imperfections, the measured material properties and the experimentally determined connector behaviour data.
2. validate the FE models against the experimental data gathered from the laboratory tests.
3. conduct parametric studies using the validated models to investigate the effect of various parameters on the buckling response and strength of CFS built-up members, including the connector spacing and the presence of contact between the components.

1.3. Thesis layout

This thesis is divided into two volumes, with the first volume constituting the main text, which is divided into ten chapters. A brief overview of each chapter is given below:

Chapter 2 presents a review of the relevant literature in the field of cold-formed steel (CFS) built-up members. This includes a review of the different factors which affect the buckling behaviour of CFS members, the type of instabilities which are present in thin-walled members and the different numerical tools which can be used to determine their critical elastic buckling stresses. A review of the main codes currently available for the design of CFS members is also presented, highlighting their design philosophy and limitations for the design of built-up members. The chapter also includes a thorough review of the previous research on CFS built-up members and concludes with a summary of the key factors to take into account when developing finite element models to simulate the behaviour of CFS built-up members.

Chapter 3 presents an experimental programme on built-up CFS stub columns with four different cross-sectional geometries. The built-up columns were constructed from individual channels and plate sections, assembled with bolts or self-drilling screws at varying connector spacings. They were tested between fixed boundary conditions, avoiding global instabilities of the column. Test coupons were taken from the corners and flat portions of the sections in order to determine their material properties and detailed measurements of the geometric imperfections of each specimen were performed. The results of the compression tests are discussed in terms of the ultimate capacity of the columns, their deformed shape and the critical buckling stresses experimentally derived for some of their components.

Chapter 4 presents an experimental programme on built-up CFS beams with two different cross-sectional geometries. The specimens were tested in a four-point bending configuration, providing lateral restraints at the loading points to avoid global instability. The built-up

specimens were composed of plain channel sections assembled with bolts. The material properties of the test specimens were determined by means of coupon tests and the geometric imperfections were measured prior to testing. The results of the tests are examined in terms of the ultimate moment capacity of the beams, their deformed shape and the critical buckling stresses experimentally derived for some of their components.

Chapter 5 presents an experimental programme consisting of compression tests on long built-up columns with four different cross-sectional geometries. The columns were subjected to uniaxial compression between pin-ended boundary conditions, while applying the load with eccentricities of $L/1000$ or $L/1500$. The built-up sections were formed from channels and plate sections and were assembled with bolts or self-drilling screws. The connector spacing was varied between specimens. Test coupons were taken from the corners and flat portions of the sections in order to determine their material properties. In addition, the chapter presents the development of a state-of-the-art measuring system, which was used to record the geometric imperfections of the components of the long columns before and after they were assembled into their final configuration.

Chapter 6 presents a series of single lap shear tests carried out on the connectors used to assemble the built-up members discussed in Chapter 3, Chapter 4 and Chapter 5. The chapter also include an assessment of the reliability of Digital Image Correlation (DIC) for the measurements of in-plane deformations in CFS members by comparing the deformations of the connector test specimens recorded with this method to those recorded using LVDTs.

Chapter 7 describes the development of detailed finite element (FE) models of the stub columns presented in Chapter 3. The FE models included the initial geometric imperfections measured on the columns, the non-linear material behaviour obtained from tensile coupons and the connector behaviour obtained from the single lap shear tests. The models were verified against the experimental data gathered from the stub column tests and were further used in parametric studies.

Chapter 8 describes the development of both detailed and simplified FE models for the beams presented in Chapter 4. The FE models included the initial geometric imperfections measured on the beams and the non-linear material behaviour obtained from tensile coupons, as well as the connector behaviour obtained from the single lap shear tests. The models were verified against the experimental data gathered from the beam tests and the simplified models were further used in parametric studies.

Chapter 9 describes the development of detailed FE models of the long columns presented in Chapter 5. The FE models incorporated the initial geometric imperfections as measured on the columns and the non-linear material behaviour obtained from tensile coupons. In addition, the connector behaviour as measured in the single lap shear test was also incorporated into the FE

models. The models were verified against the experimental data gathered from the long column tests and were further used in parametric studies.

Chapter 10 presents the general conclusions drawn from the research and provides recommendations for future work.

The second volume of the thesis contains all the Appendices.

1.4. Publications

The following papers have resulted from the research presented in this thesis:

Meza, F., Becque, J. and Hajirasouliha, I. “Experimental Study of Cold-Formed Steel Built-up Columns” *Thin-Walled Structures*, [Accepted for publication].

Ye, J., Meza, F., Hajirasouliha, I., Becque, J., Shepherd, P. and Pilakoutas, K. “Experimental investigation of the cross-sectional bending capacity of cold-formed steel channels subject to local-distortional buckling interaction.” *Journal of Structural Engineering*, [Accepted for publication].

Meza, F., Becque, J. and Hajirasouliha, I. (2018) “Experimental investigation of slender cold-formed steel built-up columns.” *Eighth International Conference on Thin-Walled Structures*, Lisbon, Portugal.

Ye, J., Meza, F., Hajirasouliha, I. and Becque, J. (2018) “Experimental investigation of the bending capacity of CFS back-to-back channel sections.” *Eighth International Conference on Thin-Walled Structures*, Lisbon, Portugal.

Meza, F. and Becque, J. (2017). “Experimental and numerical investigation of cold-formed steel built-up stub columns.” *EUROSTEEL*, Copenhagen, Denmark.

Meza, F., Becque, J. and Hajirasouliha, I. (2016). “Experimental investigation of cold-formed steel built-up beams.” *Proceedings of the 7th International Conference on Coupled Instabilities in Metal Structures*, Baltimore, USA.

Meza, F., Cheng, S. and Becque, J. (2016). “Experimental investigation of the cross-sectional stability of cold-formed steel built-up columns.” *The International Colloquium on Stability and Ductility of Steel Structures*, Timisoara, Romania.

Meza, F., Becque, J. and Hajirasouliha, I. (2016). “Experimental investigation of the buckling interaction between individual components of a built-up steel beam.” *The Annual Postgraduate Research Conference*, Sheffield, UK.

Meza, F., Becque, J. and Hajirasouliha, I. (2015). “Experimental investigation of the buckling interaction between individual components of a built-up steel column.” *The Annual Postgraduate Research Conference*, Sheffield, UK.

Meza, F., Becque, J. and Hajirasouliha, I. (2015). “Experimental investigation of cold-formed steel built-up stub columns.” *Eighth International Conference on Advances in Steel Structures*, Lisbon, Portugal.

Chapter 2

Literature Review

2.1. Material properties of cold-formed steel

The production of cold-formed steel (CFS) starts with a hot-rolled steel slab, which is cold-reduced until a steel sheet of a desired thickness is obtained. The steel sheet is subsequently subjected to a heat treatment called annealing whereby the residual stresses induced during the cold-rolling process are removed. The sheets are then stored onto coils, ready to be transported to the final stage, where they can be folded into their desired shape by either roll-forming or press-braking at room temperature. These cold-forming operations can significantly affect the mechanical properties of cold-formed steel, while also introducing residual stresses and geometric imperfections in the final product which can have a significant impact on its strength and behaviour.

2.1.1 Mechanical properties

The change in the mechanical properties of cold-formed steel is characterised by an increase of the yield stress and ultimate strength, and a reduction of the ductility. Chajes et al. (1963) attributed this change in the stress-strain characteristic of cold-formed steel to three main phenomena, namely: strain hardening, strain aging and the Bauschinger effect. Figure 2.1 illustrates the effect of strain hardening and strain aging on a typical hot-rolled carbon steel. The effect of strain hardening results in an increase in the yield stress, while removing the typical yield plateau, and a decrease in ductility. Strain aging, on the other hand, produces increases in the yield stress and ultimate strength and a further decrease in ductility. Another aspect of strain aging in carbon steel, observed by Chajes et al. (1963), is the recovery of the yield plateau present in the virgin material before cold-work takes place. The Bauschinger effect is related to imperfections in the crystalline structure of the steel. It takes place immediately after the material is plastically deformed, resulting in an increase in the yield stress when the material is

unloaded and reloaded in the same direction as the initial prestrain, and a decrease when it is reloaded in the opposite direction.

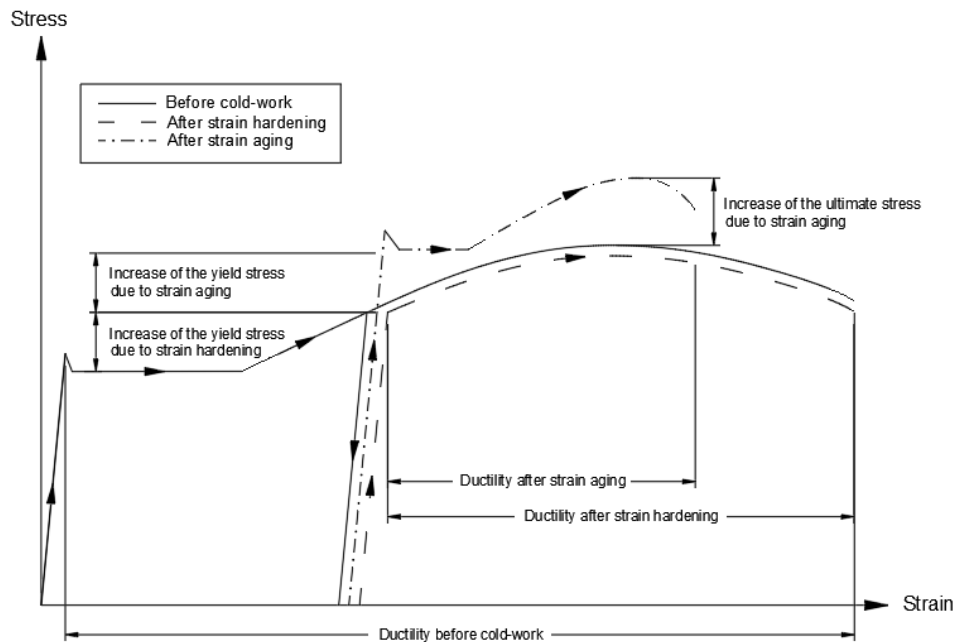


Figure 2.1: Effect of strain hardening and strain aging on the stress-strain characteristic of structural steel

Chajes et al. (1963) and Karren (1967) concluded that there are several factors which affect the extent to which the mechanical properties of the virgin material are affected by the cold-forming process. These include the chemical composition of the steel, its prior metallurgical history, its prior history of cold-working and the type and magnitude of plastic strains caused by the cold-working.

Since during the cold-forming process most of the strain hardening is introduced in the folded regions of the cross-section (where the amount of plastic straining is the largest), and it is in these regions where over time most of the strain aging take place, the mechanical properties in these regions may significantly differ from those in the flat regions. The amount of plastic strain introduced in the corner regions depends on the geometric characteristics of the corner. A low ratio of the inside corner radius to the thickness induces the highest amount of cold-working and therefore causes a larger increase in yield stress (Karren, 1967). Karren (1967) and Kenneth and Winter (1967) found that the increment in ultimate strength in the corner regions is relatively small compared to the increase in the yield stress. In addition, steel materials with a high ultimate strength to yield stress ratio were found to be more susceptible to undergoing large amounts of strain hardening and experience larger increment in the yield stress when they are plastically deformed. Karren (1967) also noted that the corner regions showed more gradual yielding than the flat portions of a CFS section, and that this gradual yielding was present even

after strain aging took place. Karren (1967) attributed this gradual yielding behaviour in the corner regions to the fact that, as the corner is formed, the various fibres located throughout the thickness are subjected to varying amounts of cold work, causing the yield stress of the fibres to also increase by different amounts and resulting in a gradual stress-strain curve.

On the other hand, Chajes et al. (1963) and Kenneth et al. (1967) also observed that the stress-strain curve of the flat portions may either have a sharp yield transition or show more gradual yielding, depending on the type of material used. Aging materials present stress-strain curves with sharper transitions than non-aging materials after having been subjected to cold work. Abdel-Rahman and Sivakumaran (1997) observed, after testing steels with nominal yield stresses of 345 MPa and 228 MPa, that the grade of steel may also have an effect on the sharpness of the yield transition of the material in the flat portions. Results from coupons tests showed that, while all coupons extracted from the sections with the highest steel grade experienced a gradual yielding behaviour, coupons cut from the sections with the lower grade showed either very sharp yielding or moderately sharp yielding behaviour.

While the specifics of the cold-forming method used in the manufacturing process make little difference in the enhancement of the yield stress and the ultimate strength in the corner regions of a cross-section, they can have an important effect on the properties of the flat portions (Kenneth et al., 1967). For example, roll-formed sections may undergo a significant enhancement of the mechanical properties of the flat portions as a result of the pressure exerted by the rollers. This was corroborated by Abdel-Rahman and Sivakumaran (1997), who observed that the yield stress and the ultimate strength in areas adjacent to the corners were generally higher than in the middle of the flat portions, producing a non-uniform enhancement of the mechanical properties. On the other hand, Abdel-Rahman and Sivakumaran (1997) also found that, away from the corner regions, the mechanical properties of the flat portions of the flanges and the web were almost identical. In the case of specimens which are press-braked, where the flat portions of the cross-section are only subject to straining due to the coiling and uncoiling process, the enhancement of the mechanical properties in these regions can be considered negligible. For these types of sections, Kenneth et al. (1967) suggested that the influence of the cold-working extends less than one sheet thickness from the corner.

2.1.2 Residual stresses

As a result of the forming process, residual stresses are introduced in CFS members. Determining the distribution and the magnitude of these residual stresses has attracted significant research interest in the past, as they may result in early yielding of certain areas of the cross-section and affect the way in which stresses are distributed. Many researchers have tried to experimentally quantify the magnitude of the residual stresses in cold-formed thin-walled members. Initially, experiments were based on strain measurements taken on the surface

of strips cut from the studied member. The measured surface strains were then converted into residual stresses using Hooke's Law (Batista and Rodrigues, 1992; Ingvarsson, 1975; Weng and White, 1990; Weng and Pekoz, 1990). Weng and Pekoz (1990) studied the magnitude and distribution of residual stresses in the longitudinal direction of lipped channels that were roll-formed or press-braked. They found that the residual stresses on opposite surfaces of the channel had opposite signs and assumed a simplistic linear variation of the residual stresses through the thickness. Later on, Key and Hancock (2006) experimentally demonstrated that this distribution is indeed non-linear.

Quach et al. (2004) suggested that the non-linear distribution of the longitudinal residual stresses through the thickness in the flat portions of CFS sections is mainly due to the coiling and uncoiling process. During coiling, the fibres closer to the surface of the steel sheet may undergo plastic bending while the fibres closer to central portion of the sheet undergo elastic bending. This introduces residual stresses and a residual curvature in the steel sheet. Additional residual stresses are reintroduced as the steel sheet is flattened due to the restraints imposed by the folds created during the forming process. Quach et al. (2004) found that the magnitude and distribution of these residual stresses are related to the coil diameter and found that the maximum diameter for which these residual stresses are introduced depends only on the material properties of the steel sheet.

Residual stresses originating from the forming process are mainly concentrated in the corner regions. Ingvarsson (1975) showed theoretically and experimentally that these residual stresses are not only introduced in the direction of bending, but also in the transverse direction (along the specimen length). In common CFS members the corners become fully plastic through their thickness when the steel sheet is bent into shape. Residual stresses are locked into the plate and after the forming load is released, they induce an elastic recovery of the plate known as springback. This results in a nonlinear distribution of the residual stresses through the thickness in the direction of the bent, which in turn, due to the plain strain condition and the Poisson's effect, results in a nonlinear residual stress distribution in the longitudinal direction of the member. Weng and White (1990) experimentally corroborated this non-linear distribution of the transverse residual stresses through the thickness when studying thick plates which were gradually cold-bent.

The specific method used in the forming process also has an effect on the magnitude of the residual stresses. Flexural residual stresses originating from a roll-forming process are larger than the ones originating from press-brake operations (Batista and Rodrigues, 1992; ECCS, 1978; Schafer and Pekoz, 1998). Numerous researchers have proposed different ways of modelling the residual stresses in CFS members. The first theoretical models to predict the magnitude and distribution of residual stresses only included the effect of the forming process itself (Ingvarsson, 1975; Rondal, 1987). More recently, Quach et al. (2004) presented an

analytical solution to predict the residual stresses originating from the coiling and uncoiling process. These residual stresses were included in an FE model that was used to simulate the residual stresses originating from press-brake operations (Quach et al., 2006). A set of algebraic equations was presented by Moen et al. (2008) which can be used to predict the residual stresses and the effective plastic strains in CFS members, taking into account each of the stages of the manufacturing process. Quach et al. (2010) also presented an advanced numerical approach to include the effect of residual stresses, as well as the effect of cold-working in a FE non-linear buckling analysis. In this study, both the residual stresses originating from the coiling-uncoiling process and the press-braking process were accounted for, and the plastic strains were predicted by a closed-formed analytical solution. Other researchers have opted to derive the residual stresses using FE by modelling the whole fabrication process (Pastor et al., 2013).

However, adequate incorporation of these residual stress predictions into numerical models is a complicated and time consuming process. At the same time, it is important to consider that residual stresses and the enhancement of the yield stress of the virgin material are consequences of the same fabrication process and that the effect of one tends to partially compensate for the effect of the other (Schafer et al., 2010; Schafer and Pekoz, 1998). For this reason, it has been common practice to ignore both effects when numerically modelling the behaviour of CFS members to predict their capacity. A more recommended approach is to include the combined effects of residual stresses and strain hardening by using the stress-strain characteristic obtained from tensile coupons extracted from the corners and the flat portions of the member. After the coupons are cut from the specimen they tend to curve longitudinally as a result of the release of longitudinal through-thickness bending residual stresses. However, after securing the coupons between the grips of the testing machine and applying the initial stages of loading, they are straightened to a state similar to the one before they were extracted from the specimen and the through-thickness residual bending stresses are almost fully reintroduced into the coupon before they are tested (Rasmussen and Hancock, 1993). This way of accounting for the combined effects of strain hardening and residual stresses has been successfully applied to model the non-linear buckling behaviour of CFS members by various researchers (Becque and Rasmussen, 2009a, 2008; Jiahui, 2014; Sivapathasunderam, 2009).

2.2. Geometric imperfections

Geometric imperfections are also introduced into CFS members as a result of the manufacturing process. These geometric imperfections are normally categorized into global imperfections and cross-sectional imperfections. Global imperfections include bowing, camber, warping and twisting, while cross-sectional imperfections are commonly divided into local and distortional imperfections. Zeinoddini and Schafer (2012) suggested that, while bowing imperfections are

largely a result of the coiling process, the other types of imperfections are mainly introduced during the cold-forming process.

The buckling response and the ultimate capacity of CFS members may show a considerable sensitivity to geometric imperfections. A probabilistic examination of the effect of geometric imperfections on the ultimate strength of members made of cold-formed steel was presented in (Schafer et al., 1998). The effect of geometric imperfections on the ultimate capacity depends on the type of failure mode. Thus, an element failing in distortional buckling is more likely to be affected by geometric imperfections than an element failing in the local mode (Pastor et al., 2014; Schafer, 2000). The effect of geometric imperfections on the ultimate capacity may also be accentuated when interaction between buckling modes takes place. Van der Neut (1969) demonstrated that both local and global imperfections can cause a severe reduction of the ultimate capacity when the local buckling load and the global buckling load are of similar magnitude.

Advanced numerical modelling has proven to be of great use to supplement experimental research. However, the reliability of numerical models depends to a great extent on the characterization of geometric imperfections. In order to accurately characterize the geometric imperfections of a member, both their magnitude and distribution should be considered. It should also be taken into account that when the critical buckling load of a member is approached, the imperfections in the shape of this buckling mode have the most pronounced effect on the response of the member (Rasmussen and Hancock, 1988).

It is common practice for the global geometric imperfections to be represented in the form of the flexural buckling mode. An amplitude of 1/1500 times the length of the column was proposed by (Bjorhovde, 1972), whereas a more conservative value of 1/1000 was suggested by the ECCS (1978). Cross-sectional imperfections are associated with local and distortional failure modes and their magnitude is typically defined as a function of the thickness or the width of the cross-section. Different scaling factors have been suggested to model cross-sectional imperfections, depending on whether the predominant type of failure is the local or the distortional buckling mode. For instance, Walker (1975) proposed an imperfection magnitude for local imperfections based on the thickness and the local slenderness of the cross-section, while Schafer and Pekoz (1998) and CEN (2009) proposed imperfection magnitudes which are proportional to the width of the web of the cross-section. Regarding the distortional imperfection Schafer and Pekoz (1998) suggested using an imperfection magnitude proportional to the thickness of the cross-section, while CEN (2009) recommends that the imperfection magnitude should be proportional to the flange width.

The behaviour predicted by an FE model can vary significantly depending on the magnitude of the geometric imperfections introduced. This was demonstrated in a study carried out on rack sections by Pastor et al. (2014), where an FE model was created using the first eigenmode from

a buckling analysis as the imperfect shape and the response of the member to different imperfection magnitudes proposed by various researchers was compared. The study showed differences in the predicted peak loads of up to 30%. Moreover, most of the existing geometric imperfection data which have been used to propose imperfection magnitudes consists of maximum imperfection measurements, typically taken at a few sparse points using straight edges and dial gauges or calipers. Schafer and Pekoz (1998) have argued that using the maximum imperfection values often leads to a conservative characterization of the geometrical imperfections in a member since these imperfection values do not necessarily follow the shape of a critical buckling mode of the member. This was proved by Dubina and Ungureanu (2002) in a study carried out on channel columns, which showed that the ultimate loads predicted by FE models in which the geometric imperfections were modelled using the maximum cross-sectional imperfection value and the critical local mode shape were 12% lower than those predicted by FE models in which the geometric imperfections were incorporated using the real distribution as measured on the channels.

A different approach consists of using an imperfection spectrum, which accounts for the randomness of the imperfections, as proposed by Zeinoddini and Schafer (2012). The imperfection spectrum was created by averaging the Fourier transform of the imperfection signal measured in 11 lipped channels by Schafer and Pekoz (1998).

Imperfection measuring techniques have also improved significantly in recent years. Becque and Rasmussen (2009b) used laser displacement sensors mounted on a frame to measure the geometric imperfections of lipped channels along five longitudinal lines (three lines along the web and one line along the lipped end of each flange). A similar measuring technique was also used by Sivapathasunderam (2009) to measure the geometric imperfections of a built-up LiteSteel beam. More recently, a laser-based scanning platform was presented by Zhao et al., (2017, 2015), which was able to measure and reconstruct the full-three dimensional imperfect geometry of a lipped zed section.

2.3. Instabilities in thin-walled members

Instabilities in thin-walled members can generally be categorized into three distinct buckling modes: local, distortional and global. These buckling modes may appear individually or they may interact with each other. Local and distortional buckling are referred to as cross-sectional instabilities because the cross-sections do not undergo any global displacements out of their original positions and the buckling stresses and resistances are independent of the member length, whereas global buckling modes, which involve displacements of the cross-sections as near rigid bodies out of their original positions, are referred to as member instabilities.

Local buckling involves plate bending deformations of the components of the cross-section, without translation of the corners and is characterized by a relatively short half-wavelength, which is comparable to the cross-sectional dimensions (Ådány, 2004). Out of the three different types of buckling modes encountered in thin-walled members, local buckling possesses the greatest post-buckling reserve strength.

Global buckling occurs at the longest half-wave length and is characterized by the deformation of the member with minimal distortion of its cross-section. Depending of the type of deformations and the type of loading, further sub-classes can be distinguished, such as: flexural buckling, torsional buckling, flexural-torsional buckling and lateral-torsional buckling (Ådány, 2004). As opposed to local buckling, global buckling hardly possesses any post-buckling capacity, and therefore, collapse is imminent once the member reaches the minimum of the lateral, torsional or lateral-torsional critical loads.

Distortional buckling occurs at half-wave lengths longer than those of local buckling, but shorter than those associated with global buckling. Hancock et al. (1994) stipulated that this buckling mode was characterized by a rotation of the flange at the flange/web junction or by the displacement of an intermediate stiffener normal to the plate in which it is located. Distortional buckling involves membrane displacements of the edge or intermediate stiffener and it may occur when the stiffener is not adequate at preventing the out-of-plane displacement of the element it supports. For this reason it was first referred to as ‘stiffener buckling’ by Timoshenko and Gere (1963) and Desmond et al. (1981). The post-buckling capacity of the distortional buckling mode is intermediate between those of local and global buckling.

2.3.1 Local buckling

Research on the stability of plates can be traced back to Saint-Venant (1883) who derived the differential equation which describes the elastic buckling behaviour of a thin plate subject to in-plane compressive stresses. Later on, Bryan (1891) applied the energy method to a simply supported plate of dimensions a and b , subject to a compressive load along the side b , and expressed that the work done by the external compressive load has to equal the elastic strain energy accumulated in the plate due to bending:

$$\Delta W = \Delta U \quad (2.1)$$

He thereby represented the deflected shape of the simply supported plate w by a Fourier series:

$$w = \sum \sum A_{mn} \sin \frac{m\pi}{a} x \sin \frac{n\pi}{b} y \quad (2.2)$$

Considering that the work done by the compressive load has to be equal to the strain energy in order for the plate to be in a stable equilibrium, he concluded that the plate should buckle with a

single half-wave in the direction orthogonal to the direction of the applied load and that the number of half-waves in the loading direction would depend on the length of the plate in that direction (Bryan, 1891). The value of the critical load obtained from the energy method can be written as:

$$N_{cr} = \frac{k_{\sigma} D \pi^2}{b^2} \quad (2.3)$$

Where D is the flexural rigidity of the plate and k_{σ} is the buckling coefficient of the plate, which depends on the a/b ratio and is equal to 4.0 for a simply supported plate.

In 1910, Timoshenko solved the problem of a compressed plate under different types of loading and boundary conditions by integrating Saint-Venant's equation, derived from thin plate theory (Timoshenko and Gere, 1963):

$$\frac{\partial^4 w}{\partial x^4} + 2 \frac{\partial^4 w}{\partial x^2 \partial y^2} + \frac{\partial^4 w}{\partial y^4} + \frac{f_x t}{D} \frac{\partial^2 w}{\partial x^2} = 0 \quad (2.4)$$

where w is the plate deflection, t is the thickness of the plate and f_x is the compressive stress applied in the longitudinal x -direction.

In addition, he used the energy method to obtain the critical load in cases where a closed form solution could not be achieved. A list of the values of the buckling coefficient k_{σ} for plates with different boundary conditions, including plates reinforced with stiffeners, is presented in Timoshenko and Gere (1963).

Lundquist et al. (1945) proposed calculating the critical load of plate assemblies based on the general solution provided by Timoshenko for plates simply supported along the loaded edges and with different boundary conditions along the longitudinal edges, while applying the principle of moment redistribution to the junctions between the different plates to account for the rotational stiffness of each plate. This resulted in an iterative process, which was deemed too cumbersome. Therefore, (Bleich, 1952) and Bulson (1970) opted for an approximate approach which solved the differential equations of each plate while satisfying the static and kinematic continuity conditions at the junctions between the different plate components of the cross-section.

The post-buckling behaviour of plates is characterized by a non-linear redistribution of the longitudinal stresses towards the stiffened edges of the plate. This behaviour was mathematically captured by von Karman in 1910 by modifying Saint-Venant's equation using large deflection theory. This resulted in the set of non-linear equations Eq. (2.5) and Eq. (2.6), known as von Karman's equations, which apply to elastic plates without geometric imperfections, where the buckling behaviour is characterized by a sudden out-of-plane deformation when the compressive force reaches the critical buckling load of the plate.

$$\frac{\partial^4 F}{\partial x^4} + 2\frac{\partial^4 F}{\partial x^2 \partial y^2} + \frac{\partial^4 F}{\partial y^4} = E \left[\left(\frac{\partial^2 w}{\partial x \partial y} \right)^2 - \frac{\partial^2 w}{\partial x^2} \frac{\partial^2 w}{\partial y^2} \right] \quad (2.5)$$

$$\frac{\partial^4 w}{\partial x^4} + 2\frac{\partial^4 w}{\partial x^2 \partial y^2} + \frac{\partial^4 w}{\partial y^4} = \frac{t}{D} \left[\frac{\partial^2 F}{\partial x^2} \frac{\partial^2 w}{\partial y^2} + \frac{\partial^2 F}{\partial y^2} \frac{\partial^2 w}{\partial x^2} - 2 \frac{\partial^2 F}{\partial x \partial y} \frac{\partial^2 w}{\partial x \partial y} \right] \quad (2.6)$$

In the above equations, F is the Airy stress function and E is the Young's modulus.

Von Karman's equations were modified by Marguerre (1938) to account for the presence of geometric imperfections. In this case the buckling behaviour is characterised by a smooth deformation process, which depends on the magnitude of the initial imperfections. Figure 2.2a illustrates the load vs. lateral deflection behaviour of a square plate simply supported along its four edges, with and without including geometric imperfections, and subject to a uniaxial compressive load. Figure 2.2b shows the average stresses against the average strains for the same plate and shows that for the case in which membrane deformations are unrestrained, once the load exceeds the critical buckling stress, the stiffness of the plate is reduced by 60 % (Bulson, 1970).

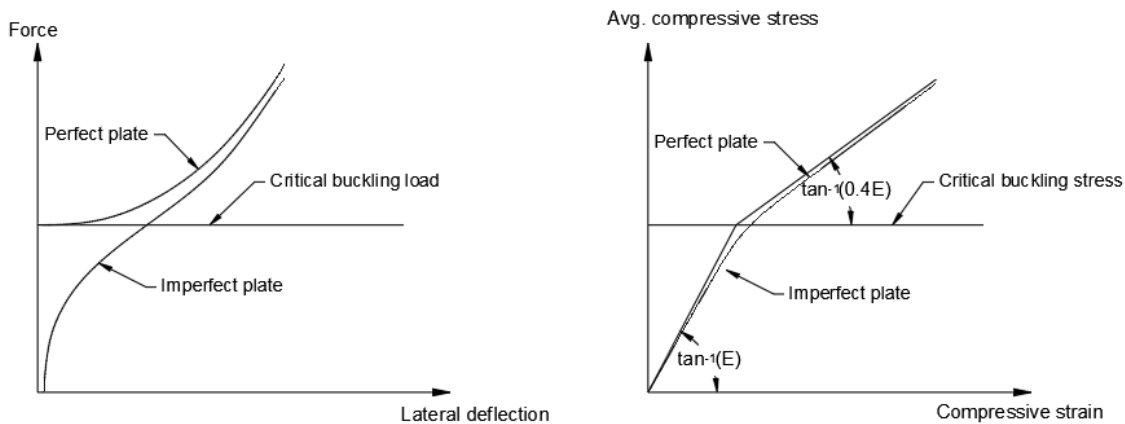


Figure 2.2: Buckling behaviour of a perfect and imperfect plate: a) Force vs. lateral deflection; b) average stress vs. strain

The solution to von Karman's equations is beyond reach, even for simple boundary conditions, making them impractical for design applications. For this reason, the 'effective width' concept was introduced by von Karman et al. (1932), in which the non-uniform post-buckling stress distribution is replaced by an equivalent uniform stress distribution over part of the plate. The effective width method is discussed in more detail in section 2.5.1.

2.3.2 Distortional buckling

Distortional buckling is governed by the rotational stiffness at the web/flange junction in members with edge stiffened flanges. The phenomenon of distortional buckling has been known since the 1940's. However, due to the complexity associated with describing it analytically, it was often ignored. It was not until the 1980's, with the advancement of new numerical methods such as the finite strip method (FSM), that researchers started gaining interest in this phenomenon (Schafer, 2000).

Making use of the finite strip method, Hancock (1985) developed a detailed design chart for computing the critical stress of the distortional buckling mode in rack sections with rear flanges. A few years later, a set of simplified equations were derived analytically by Lau and Hancock (1987) to calculate the distortional buckling stresses of lipped channel sections subject to compression. The model they used to derive the design equations considered the lipped flanges of the cross-section in isolation. The effect of the web was represented by a lateral and a rotational spring at the web/flange junction. Further research was also carried out on zed section columns by Charnvarnichborikarn et al. (1992). They modified the simplified equations derived by Lau and Hancock (1987) to calculate the elastic distortional buckling stresses of lipped zed sections under axial load. The model they used assumed that the web only provides vertical restraint to the lipped flanges and that the rotational and lateral restraint are negligible.

A model conceptually equivalent to the one used by Lau and Hancock (1987) was proposed by Schafer (1997) to calculate the elastic distortional buckling load, although the method used to represent the rotational restraint provided by the web to the lipped flange differed. A parametric study was carried out by Schafer (2000) to assess the accuracy of the various predictive equations for computing the distortional buckling load of zed and channel sections subject to pure compression. The study showed that both Lau and Hancock's (1987) and Schafer's (1997) equations predicted the distortional buckling load reasonably well, although Schafer's equation was slightly more accurate. The accuracy of the equations was also assessed against results obtained with the finite strip method.

Lau and Hancock's equation was adjusted by Hancock (1997) to compute the distortional buckling stress of flexural members made of zed and channel sections. This modified equation accounted for the stress gradient in the web and the different restraint the web provides to the flange due to the different buckling deformations it undergoes under flexural stresses. Schafer and Pekoz (1999) modified Hancock's closed-form solution to cover members in which distortional buckling initiates in the web.

The post-buckling capacity of the distortional buckling mode was studied in experimental tests carried out by Hancock (1985), Lau and Hancock (1988) and Lau and Hancock (1990). In these tests the distortional buckling stress was greater or equal to half the yield stress and the sections

showed no substantial post-buckling reserve capacity. On the other hand, test carried out by Kwon and Hancock (1992a; 1992b) and Bernard et al. (1993), in which the distortional buckling stress was significantly lower than the yield stress, showed a significant post-buckling reserve capacity.

2.3.3 Global buckling

The study of global instability of columns started with Leonhard Euler in 1744. He studied the case of an ‘ideal column’, assumed to be perfectly straight and subject to a concentrically applied compressive load. The column was fixed at the base and free at the upper end (Timoshenko and Gere, 1963). Euler recognized that the column always buckled about its weakest axis, and that the load at which the column buckled was inversely proportional to the square of its height.

Timoshenko and Gere (1963) studied Euler’s equation and expanded it to the cases of columns with different boundary conditions, leading to the general form of Euler’s equation, given as:

$$N_{cr} = \frac{\pi^2 EI}{L_{cr}^2} \quad (2.7)$$

In the above equation L_{cr} is the effective length of the column, which depends on its boundary conditions, EI is the flexural rigidity of the column, and N_{cr} is the flexural buckling load or Euler load. This is the most predominant type of global buckling in slender closed sections.

In addition to flexural buckling, thin-walled open cross-sections subject to an axial load may also be susceptible to a torsional or a flexural-torsional buckling mode due to their low torsional rigidity. Several researchers have investigated these types of global instabilities, including Goodier (1941), Timoshenko (1945), Vlasov (1961) and Fang and Winter (1965). The permissible types of global buckling depend on the type of cross-section. Doubly-symmetric and point-symmetric open cross-sections may be subject to a torsional buckling mode, in which the cross-section rotates about its shear centre. In the case of singly-symmetric shapes, the shear centre does not coincide with the centroid of the cross-section, and therefore the cross-section may buckle in a flexural-torsional mode by rotating about its shear centre and simultaneously bending about its minor axis.

In the case of slender flexural members bent about their major axis, the only possible global instability involves a simultaneous lateral deflection and twist. This type of instability is referred to as lateral-torsional buckling (Galambos, 1998; Vlasov, 1961).

2.3.4 Buckling interaction

The stability of thin-walled members may also be affected by interaction between any of the basic buckling modes previously described: local, distortional and global. This interaction typically reduces the capacity of the member below the capacities associated with the pure modes.

Interaction between local and global buckling has been extensively studied experimentally and theoretically since the 1950s and -60s (e.g. Fisher and Bijlaard (1953), Graves Smith (1967) and Van der Neut (1969)). After local buckling takes place the stiffness of the member in overall bending and torsion is significantly reduced, thereby reducing the global buckling load. Van der Neut (1969) also demonstrated that the interaction between local and flexural buckling becomes more pronounced when the local buckling load lies in the proximity of the flexural buckling load. In this case the interaction between local and flexural buckling becomes very sensitive to geometric imperfections. Additional research on local-global interaction can be found in (Davids and Hancock, 1986; Hancock, 1981; Kalyanaraman et al., 1977; Rasmussen, 2006)

The study of local-distortional interaction has much more recent origins. The first observation that both buckling modes can simultaneously occur in CFS sections is credited to Kwon and Hancock (1992b), who carried out compression tests on fixed-ended high-strength CFS lipped channel sections with and without intermediate stiffeners in the web. The authors observed significant post-buckling strength, even when the flange buckled locally while also deforming in the distortional mode, and initially concluded that the simultaneous presence of both modes did not appear to adversely affect the load carrying capacity. However, it was not until more than 10 years after the first observations of the possible coexistence of local and distortional buckling that the potentially adverse nature of their interaction was properly acknowledged by Yang and Hancock (2004), based on evidence obtained from tests performed by the authors on high-strength CFS lipped channels with intermediate stiffeners in the web and flanges, which were compressed between fixed-ends. Additional research on the interaction between local and distortional buckling in columns can be found in (Dinis and Camotim, 2015; Kwon et al., 2009; Kwon and Hancock, 1993; Schafer, 2002; Silvestre et al., 2009; Yap and Hancock, 2008; Young et al., 2013), while for beams it can be found in (Anbarasu, 2016; Dinis and Camotim, 2010; Martins et al., 2017). These studies revealed the ratio between the local and distortional buckling stresses to be one of the main factors affecting the reduction in ultimate strength produced by this interaction. Members in which the local and distortional buckling stresses of the section differed by less than 10% (referred to as ‘true interaction’) were found to be the most affected by local-distortional buckling interaction.

Interaction between distortional and global buckling is generally considered to be of less importance (Schafer, 2002), and significantly less research has been directed to study this phenomenon.

2.4. Elastic stability analysis of thin-walled CFS members

Determining the critical buckling stresses of thin-walled members by means of analytical solutions, which may be based on simplified models, may result in an unduly cumbersome task, especially when applied to local or distortional buckling modes. These solutions may also ignore critical mechanical features, such as inter-element equilibrium and compatibility (Schafer, 2006). Fortunately, advancements in computers now allow an elastic stability analysis of thin-walled members to be performed by means of numerical computational methods, such as the finite element method (FEM), the finite strip method (FSM) or generalized beam theory (GBT).

2.4.1 Finite element method (FEM)

Among the numerical methods, the finite element method is by far the most popular and general one, able to handle practically any cross-sectional geometry and arbitrary loading and support conditions. In the finite element method the member is discretized both within the cross-section and along its length, requiring a large number of degrees of freedom in order to provide an accurate prediction of the buckling stresses. This implies that a large number of candidate buckling modes are generated, among which the finite element method cannot automatically distinguish, leaving it to the user to identify the buckling modes. In addition, the finite element method is not able to directly calculate the critical load associated with a pure (local, distortional or global) buckling mode, limiting its applicability significantly in the stability analysis of thin-walled members (Adany and Schafer, 2006).

2.4.2 Finite strip method (FSM)

The finite strip method was initially developed by (Cheung, 1976). This numerical method provides the most widely used approach to examine all the possible instabilities in CFS members subject to longitudinal stresses caused by axial loading, bending or a combination of those two. In the finite strip method, a thin-walled member is discretized into a series of longitudinal strips. The stiffness of each strip is governed by Kirchhoff's thin plate theory for the bending behaviour and a plate stress condition for the membrane behaviour. The shape functions for the bending degrees of freedom employ a cubic polynomial in the transverse

direction and a sinusoid in the longitudinal direction, while the shape functions for the membrane degrees of freedom are linear in the transverse direction and sinusoidal in the longitudinal direction (Cheung, 1976; Schafer, 2006).

The finite strip method was modified by Adany and Schafer (2006) in order to decompose the buckling modes of thin-walled members into their pure global and distortional constituents. The method has been implemented in the open source software package CUFSM and has been further extended to provide a full modal decomposition which includes local, shear and transverse extension modes (Ádány and Schafer, 2008). The method is referred to as the constrained finite strip method because it employs a series of constraint equations to reduce the general deformation field provided by the finite strip method to the global, distortional, local, shear and transverse extension deformation fields. Initially, the applicability of the constrained finite strip method was limited to members with single-branched, open cross-sections and simply supported boundary conditions. However, this was later extended by Li and Schafer (2013) to cover general end conditions, and then by Ádány and Schafer (2014a, 2014b) to apply to members with arbitrary thin-walled cross-sectional geometries, including any flat-walled closed or open cross-sections and cross-sections containing both open and closed parts.

Despite these remarkable advancements in the applicability of the FSM, its range of application is still mostly limited to single sections. However, some attempts have been made to extend the FSM towards analysing built-up members by modelling the connector points as smeared multi-point constraints along the length of the member (Fratamico et al., 2018a, 2018b; Young and Chen, 2008) or as longitudinal stiffeners (Zhang and Young, 2015). However, these modelling approaches can only be considered approximations and can only provide an upper bound solution due to the discrete nature of the connector distribution in a built-up member.

2.4.3 Compound strip method (CSM)

The compound strip method was initially developed by Puckett and Cutkowski (1986) to incorporate the effect of the support conditions on a plate assembly using a direct stiffness approach. It has recently been used by Abbasi et al. (2018) to carry out the stability analysis of CFS built-up members assembled with discrete fasteners.

The CSM is an extension of the finite strip method in which the fasteners are represented by connector elements with adjustable translational and rotational stiffnesses. The connector elements can be placed anywhere within the strips and their end displacements and rotations are chosen such that they are compatible with the displacements of the connected strips. The stiffness matrix of each connector element is obtained by minimizing the strain energy with respect to the end displacements. The stiffness matrices of all the fasteners are then added to the total stiffness matrix in a direct stiffness approach.

The CSM is able to analyse built-up members with an arbitrary cross-sectional geometry and arbitrary fastener configuration, as well as general boundary conditions.

2.4.4 Generalised Beam Theory (GBT)

GBT is an effective method to analyse the elastic buckling behaviour of thin-walled members due to its intrinsic modal decomposition features. In GBT the displacement field is expressed as a linear combination of cross-section deformation modes with continuously varying amplitudes along the member length. As the method evolved, different cross-sectional deformation modes were added to the formulation. Schardt (1989) extended Vlasov's classical treatment by adding the distortional modes, Davies et al. (1994) and Davies and Leach (1994) included plate deformation modes to describe local instabilities, while Silvestre and Camotim (2003) added shear and transverse deformation modes. Due to the way in which the deformation field is decomposed in GBT, the buckling stresses associated with the pure buckling modes are directly provided.

Initially, GBT was only able to describe unbranched open cross-sections. However, Gonçalves et al. (2010) extended the method to arbitrary polygonal cross-sections, while Camotim et al. (2008) and Silvestre and Camotim (2003) extended it to thin-walled members with general loading and support conditions.

2.5. Design Methods

2.5.1 Effective width method

The effective width method is based on the concept that when the different plate elements which comprise the cross-section of a thin-walled member buckle locally, their effectiveness in carrying the load is reduced while the stresses shift towards the adjoining edges. The concept of an 'effective width' was introduced by von Karman et al. (1932) as a design tool that would simplify the complexity of equations (2.5) and (2.6), derived by the same author (Yu and LaBoube, 2010).

Von Karman's simplification is based on the assumption that the non-uniform distribution of stresses, which appears over the width of the plate as it develops its post-buckling strength can be replaced by an equivalent uniform stress applied over a fictitious effective width. The magnitude of the uniform stress is considered to be equal to the maximum non-uniform stress, which develops at the supported edges of the plate. In a plate supported along both longitudinal

edges the load is considered to be carried by two strips, one on each side of the plate (Karman et al., 1932), as depicted in Figure 2.3.

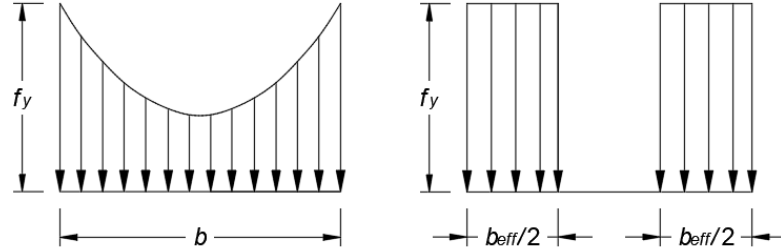


Figure 2.3: Effective width concept

The effective width is determined such that the non-uniformly distributed stress applied over the entire plate width equals the uniform stress carried by the two strips, as depicted in Figure 2.3. Therefore, the effective width can be written as:

$$b_{eff} = \rho \cdot b \quad (2.8)$$

Where b is the actual width of the plate and ρ is less than or equal to 1.

The critical buckling stress for a rectangular plate subject to a uniaxial compressive stress can be written as:

$$\sigma_{cr} = \frac{k_{\sigma} \pi^2 E}{12(1-\nu^2)(b/t)^2} \quad (2.9)$$

Where k_{σ} is a buckling factor which depends on the loading and support conditions of the plate and is equal to 4.0 for a plate simply supported along all four edges. E is the Young's modulus, ν is the Poisson's ratio, b is the width of the plate and t is the thickness.

According to Karman et al. (1932) since the plate is considered to fail when the magnitude of the uniform stress carried by its effective area equals the yield stress of the material, by replacing σ_{cr} with f_y and b with b_{eff} in Eq. (2.9) the effective width b_{eff} can be obtained as:

$$b_{eff} = \frac{\sqrt{k_{\sigma}} \cdot \pi}{\sqrt{12 \cdot (1-\nu^2)}} \cdot t \cdot \sqrt{\frac{E}{f_y}} \quad (2.10)$$

When designing a thin-walled member, the effective width method is applied to each plate element of the cross-section and their combined capacity constitutes the capacity of the cross-section. The effective width method thus provides a clear indication of which parts of the cross-section are effectively carrying the load and which parts are not contributing. However, the

calculation of the effective widths of the different plate elements of the cross-section does not consider the interaction between them and assumes boundary conditions for each plate which may not always agree with reality. In addition, the effective width method, as originally presented by von Karman, did not account for the detrimental effect of imperfections, such as the deviation from flatness of the plate. For this reason, Eq. (2.10) was modified to correlate with results from experimental tests carried out by Winter and Sechler in 1946 (Yu, 2000). This led to the well-known effective width equation which is nowadays used by the main design codes.

$$\rho = \frac{1}{\bar{\lambda}_p} \cdot \left(1 - \frac{0.22}{\bar{\lambda}_p} \right) \quad (2.11)$$

where $\bar{\lambda}_p$ is the reduced plate slenderness and is given by:

$$\bar{\lambda}_p = \sqrt{\frac{f_y}{\sigma_{cr}}} \quad (2.12)$$

Von Karman's equation (2.10) and Winter's equation (2.11) are depicted in Figure 2.4. It can be seen that for reduced slenderness values smaller than 0.673 the plate does not buckle and fails in compression with the whole cross-section yielding, whereas for greater values the plate fails by local buckling.

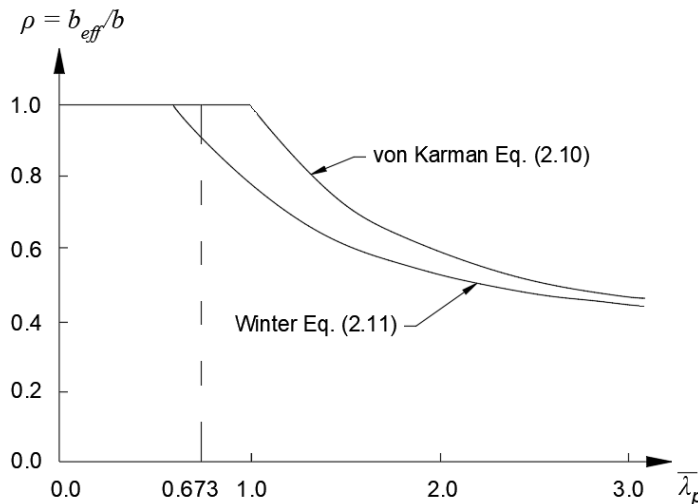


Figure 2.4: Reduction factor ρ against relative plate slenderness $\bar{\lambda}_p$

The effective width method provides a meaningful way to include the detrimental effect of local buckling of plate elements on the cross-sectional resistance and, through use of the effective section properties in the definition of a global slenderness, also on the capacity of the whole member to global buckling. However, the inclusion of distortional buckling is not straight-

forward. In addition, determining the effective width becomes increasingly more complicated as the number of plate elements in the cross-section increases, for instance, when internal stiffeners are added to the cross-section or when more complex cross-sections are used, limiting the opportunities for the optimization of cross-sections and discouraging design engineers from looking for new types of cross-sections for specific applications.

In addition, while the effective width method is able to provide satisfactory results for stiffened plate elements, it has been proved to provide results that are too conservative for both the strength and stiffness of unstiffened plate elements, such as the flanges of a plain channel section (Dubina et al., 2012). This has been attributed to the low value of the buckling factor k_σ (equal to 0.43) specified for these type of elements, which may lead to overly conservative predictions for sections with slender unstiffened flanges, especially when subject to stress gradients (Bambach and Rasmussen, 2002; Rasmussen, 1994; Rasmussen and Hancock, 1992).

2.5.2 Direct Strength Method (DSM)

The direct strength method is essentially an extension of the traditional approach used for the design of columns against global buckling to the situations where local or distortional buckling are the predominant failure modes. The method is based on proposing a relationship between the elastic buckling stresses (i.e. local, distortional and global), in combination with the yield stress of the member, and its ultimate capacity. This relationship is established through design curves which account for the post-buckling capacity of the various failure modes, their possible interaction with each other and their sensitivity to the initial geometric and material imperfections that may be present in the member. Based on the elastic buckling stresses and the yield stress a slenderness factor can be defined:

$$\lambda = \sqrt{\frac{f_y}{\sigma_{cr}}} \quad (2.13)$$

where σ_{cr} is the elastic buckling stress for local, distortional or global buckling. This slenderness factor can then be used in combination with the design curves for the different failure modes to determine the ultimate capacity of the member in local, distortional and global buckling.

The idea of using design curves to account for buckling modes other than global buckling can be credited to Hancock et al. (1994), who showed that there exists a relationship between the ultimate strength of thin-walled sections failing in a distortional buckling mode and their slenderness based on the distortional buckling stress. This conclusion was based on previous experimental research carried out at the University of Sydney on beams and columns made of channel, hat, rack, deck and zed sections. Hancock et al. (1994) proposed two sets of design curves, applicable for both CFS beams and columns undergoing distortional buckling. Later, an

additional strength curve was proposed by Hancock et al. (1996), this time specifically for flexural members undergoing distortional buckling.

The term ‘The Direct Strength Method’ was first introduced in the context of the design of beams by Schafer and Pekoz (1998). The proposed method was presented as an alternative to the traditional effective width approach. The authors presented three design curves for beams that were prevented from undergoing lateral-torsional buckling. The method was based on the results of 574 tests carried out on channels, hat, zed sections and trapezoidal decks with and without longitudinal stiffeners. The first strength curve used the same reduction factor ρ as the one proposed by Winter in the effective width method (Eq. (2.11)), but applied it to local buckling of the entire cross-section. The second curve was identical to the distortional buckling curve proposed by Hancock et al. (1996) and provided a reduction factor in case distortional buckling is the dominant type of failure. The third strength curve was a modification of the first curve to better correlate with the available experimental data (Schafer and Pekoz, 1998).

Eventually, the third curve proposed by Schafer and Pekoz (1998) became the Direct Strength design curve for beams failing by local buckling, while the design curve proposed by Hancock et al. (1996) became the Direct strength curve for beams failing by distortional buckling. For global buckling, the already existing strength curve for global buckling was retained.

The design strength curves for local and distortional buckling, as included in the current DSM for beams, are given by Eq. (2.14) and Eq. (2.15), respectively, for the slenderness ranges in which failure is governed by buckling instabilities.

$$\text{For } \lambda_l > 0.776 \rightarrow M_{nl} = \left[1 - 0.15 \left(\frac{M_{crl}}{M_y} \right)^{0.4} \right] \left(\frac{M_{crl}}{M_y} \right)^{0.4} M_y \quad (2.14)$$

$$\text{For } \lambda_d > 0.673 \rightarrow M_{nd} = \left[1 - 0.22 \left(\frac{M_{crd}}{M_y} \right)^{0.5} \right] \left(\frac{M_{crd}}{M_y} \right)^{0.5} M_y \quad (2.15)$$

In the above equations $\lambda_l = \sqrt{M_y/M_{crl}}$ and $\lambda_d = \sqrt{M_y/M_{crd}}$ are the local and distortional slenderness values for flexural members, respectively. M_y is the moment that causes first yielding of the cross-section, M_{crl} and M_{crd} are the elastic local and distortional buckling moments, respectively, and M_{nl} and M_{nd} are the capacities in local and distortional buckling, respectively.

A DSM for the design of columns was proposed by Schafer (2002) based on the results of 187 tests carried out on columns he collected from literature (Schafer 2002, 2000). The design curve proposed for local buckling was the same as the one used for beams, whereas for distortional

buckling the relevant design curve proposed by Hancock et al. (1994) was adopted. For global buckling, the existing curve for columns failing by global buckling was retained.

The design curves for local and distortional buckling, as included in the current DSM for columns, are given by Eq. (2.16) and Eq. (2.17), respectively, for the slenderness ranges in which failure is governed by buckling instabilities.

$$\text{For } \lambda_l > 0.776 \rightarrow P_{nl} = \left[1 - 0.15 \left(\frac{P_{crl}}{F_y} \right)^{0.4} \right] \left(\frac{P_{crl}}{F_y} \right)^{0.4} F_y \quad (2.16)$$

$$\text{For } \lambda_d > 0.673 \rightarrow P_{nd} = \left[1 - 0.22 \left(\frac{P_{crd}}{F_y} \right)^{0.5} \right] \left(\frac{P_{crd}}{F_y} \right)^{0.5} F_y \quad (2.17)$$

In the above equations $\lambda_l = \sqrt{F_y/P_{crl}}$ and $\lambda_d = \sqrt{F_y/P_{crd}}$ are the local and distortional slenderness values for compression members, respectively. F_y is the squash load, P_{crl} and P_{crd} are the elastic local and distortional buckling loads, respectively, and P_{nl} and P_{nd} are the capacities in local and distortional buckling, respectively.

The Direct Strength Method also takes into account possible interaction between local and global buckling in beams and columns by relating the elastic local buckling load (or moment) to the inelastic global buckling load (or moment), rather than to the squash load (or the moment which causes first yielding). The interaction between local and distortional buckling and between distortional and global buckling, on the other hand, is generally considered weak and is not included in the current formulation of the DSM (AISI, 2016a).

One of the main advantages of the DSM lies in its simplicity. This makes it a desirable alternative to the effective width method, which requires cumbersome calculations for cross-sections with more complex geometries. In addition, since the DSM does not require calculation of the effective cross-sectional properties, optimization of cross-sections by adding intermediate stiffeners can be achieved without implying additional complications in the design process. Also, interaction and compatibility of the deformations between the plate elements of a cross-section is accounted for in the DSM, since the elastic buckling stresses are obtained for the whole cross-section and not for the individual elements, as is the case in the effective width method.

On the other hand, it is important to point out that the DSM is a semi-empirical design method which is mainly based on the results of experiments. Therefore, the range of cross-sections which can reliably be designed using this method is limited to the geometries which were used to derive the design curves. A common example of cross-sections for which the DSM may not be suitable are those in which one part of the cross-section is noticeably more slender than the

others. For these cross-sections, the low critical buckling stress associated with the slender part of the cross-section may lead to overly conservative predictions, as the remaining capacity provided by the less slender unbuckled part of the cross-section is not taken into account (Schafer and Pekoz, 1998). This is, for example, the case for hat sections with wide compression flanges without stiffeners. For these types of cross-sections, the effective width method provides more realistic predictions.

A significant amount of research work is being dedicated to extending the applicability of the DSM to new cross-section types, including built-up members. A brief review of the research which has already been carried out in this field is included in section 2.7.2.

2.5.3 Erosion of Critical Bifurcation Load (ECBL)

The Erosion of the Critical Bifurcation Load (ECBL) method was proposed by Dubina and Ungureanu (2000) to account for the interaction between cross-sectional buckling (i.e. local or distortional buckling) and global flexural buckling in compression members. The method consists of relating the imperfection factor α which is included in the Ayrton-Perry formula to the maximum erosion in strength ψ , accounting for the effect of material and geometric imperfections, as well as the effect of buckling interaction. Figure 2.5 illustrates the maximum erosion which occurs when flexural buckling interacts with a cross-sectional buckling mode. The curve which represents the coupled instability mode follows the Ayrton-Perry formula, but is limited to $Q = A_{eff}/A$ to account for the effect of cross-sectional buckling, and is given by:

$$(Q - \bar{N})(1 - \bar{N}\bar{\lambda}^2) = \alpha(\bar{\lambda} - 0.2)\bar{N} \quad (2.18)$$

Where $\bar{N} = N / N_{pl}$, $\bar{\lambda}$ is the non-dimensional slenderness and α is the imperfection factor.

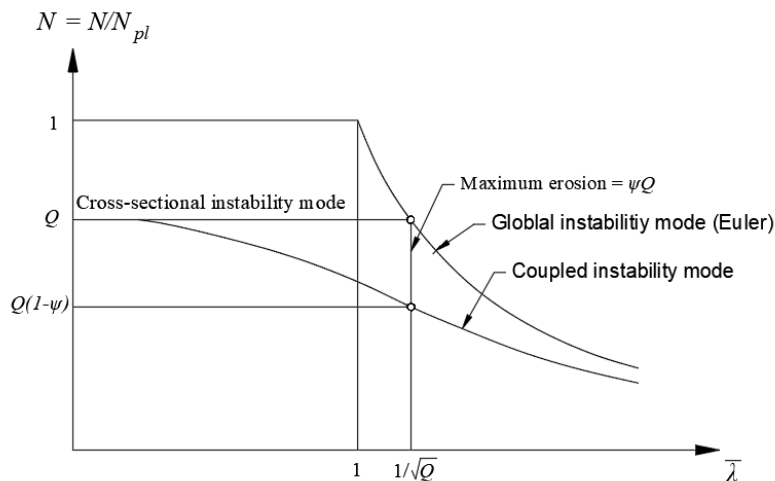


Figure 2.5: The interactive buckling mode based on the ECBL theory

Therefore, by equating Eq. (2.18) to $Q(1-\psi)$ at $\bar{\lambda}_c = 1/\sqrt{Q}$ the imperfection factor α can be obtained as a function of the erosion factor ψ :

$$\alpha = \frac{\psi^2}{1-\psi} \cdot \frac{\sqrt{Q}}{1-0.2\sqrt{Q}} \quad (2.19)$$

The imperfection factor calculated from Eq. (2.19) can then be introduced into the European column design curves, commonly used for hot-rolled sections (CEN, 2005), in order to adapt them to thin-walled CFS members accounting for the interaction between cross-sectional and global buckling (Dubina et al., 2012).

The main difficulty in this approach is to properly evaluate the erosion of the critical load in the ‘interactive slenderness range’. The authors have suggested that the evaluation of the erosion factor can be carried out by means of statistical analysis of compression tests on columns with slendernesses in the interactive buckling range, as well as non-linear numerical analyses of columns in the vicinity of the critical bifurcation point.

2.6. Design codes

2.6.1 Eurocode 3 (EC3)

The method adopted in Eurocode 3 (EC3) for the design of thin-walled CFS members susceptible to cross-sectional instabilities is based on the effective width concept. In EC3 the effect of local buckling is accounted for by using the provisions included in EN 1993-1-5 (CEN, 2009a) whereby the plate slenderness used in the effective width calculations is based on the yield stress, irrespective of whether global buckling takes place before any part of the cross-section reaches the yield stress. The interaction between local and global buckling is accounted for by using the effective cross-sectional area in the definition of the global slenderness, as specified in EN 1993-1-1 (CEN, 2005).

In the case of sections with edge or intermediate stiffeners, EN 1993-1-3 (CEN, 2006) provides specific provisions to incorporate the effect of distortional buckling in the calculation of the effective cross-sectional properties of the member. Distortional buckling results in a reduction of the effective thickness of both the stiffener and the adjacent part of the stiffened element. These provisions are based on the assumption that the stiffener behaves as a compression member with a continuous partial restraint, with a spring stiffness which depends on the flexural stiffness of the adjacent plane elements (CEN, 2006).

While the effective width approach included in EC3 has the advantage of being able to combine the effects of local and distortional buckling in the calculation of the effective cross-sectional properties of the member, the calculation procedure for stiffened cross-sections and cross-sections with more complex geometries becomes exceedingly complicated, especially if a more refined solution is sought, which may require several iterations.

2.6.1.1 EC3 provisions for built-up members

The provisions included in EC3 for built-up members are mainly focused on laced or battened built-up compression members, while for built-up compression members with chords in contact or closely spaced, the provisions are limited to giving a maximum allowable spacing between connectors (CEN, 2005). In addition, most of these provisions are only applicable to hot-rolled built-up members.

For thin-walled CFS built-up members, EN 1993-1-3 does not provide any specific design rules and only specifies the global buckling curve which should be used to determine the member buckling resistance for a limited number of open and closed cross-sectional geometries. No mention is made of whether those strength curves can be used for any type of open or closed cross-section, assembled from two or more individual sections with either identical or different cross-sectional geometries. There is also no guidance on the maximum connector spacing which should be used to assemble the built-up member or any indication of how the connector spacing or the type of connector may affect the ultimate capacity of the member. In addition, there is no consideration of how the individual components may interact with each other when buckling or how this interaction may affect the buckling response of the built-up member.

2.6.2 North American Specification (NAS)

The NAS (AISI, 2016a) has traditionally addressed the design of thin-walled CFS members through a variation of the Effective Width approach, which differs slightly from the one used in EC3. In the NAS, interaction between local and global buckling is treated by limiting the stress in the effective width calculations to the maximum compressive stress in the element when global buckling takes place. This global buckling stress is calculated using the gross section properties. In addition, in the NAS distortional buckling is treated as a limit state separate from local or global buckling.

In 2004, the NAS incorporated the Direct Strength Method (DSM) as an alternative design method, which was included in Appendix 1 of the specifications. In 2016, the DSM was moved to the main body of the specifications and is now considered an equivalent design method to the Effective Width approach (AISI, 2016b).

2.6.2.1 NAS provisions for built-up members

The provisions for built-up members included in the NAS can be used in conjunction with the effective width approach or the DSM. These provisions are scarce and apply to a limited number of built-up cross-sectional geometries consisting only of two identical components.

Provisions for built-up flexural members (AISI, 2016a)

The provisions for built-up flexural members included in (AISI, 2016a) only apply to I-shaped sections assembled from channels connected through their web in a back-to-back configuration. The provisions limit the maximum longitudinal connector spacing s_{max} to the following value:

$$s_{max} = \min \left\{ L/6; \frac{2gT_s}{mq} \right\} \quad (2.20)$$

where L is the span of the beam, g is the distance between the two rows of connectors nearest to the top and bottom flange, (see Figure 2.6), T_s is the factored strength of the connection in tension, m is the distance from the shear centre of one channel to the mid-plane of the web (see Figure 2.6) and q is the design load on the beam for the purpose of determining s_{max} . If the beam is subject to a uniformly distributed load, q should be taken as three times the uniformly distributed load. If the beam is subject to concentrated loads, q should be obtained by dividing the concentrated loads or reactions by the length of bearing. If the length of bearing is smaller than the longitudinal connector spacing, s , the required strength of the connections closest to the load or reaction should be calculated as follows:

$$T_r = P_s m / 2g \quad (2.21)$$

where P_s is the factored concentrated load or reaction and T_r is the required strength of the connection in tension.

The first requirement in Eq. (2.20) is an empirically determined limit to prevent excessive distortion of the top flange between connectors, while the second requirement in Eq. (2.20) is based on the fact that the shear centre of an individual channel is not contained in the plane of its web, and therefore, when a load is applied in the plane of the web, it produces a twisting moment in each channel about its shear centre. This generates a pull-out force in the connectors (AISI, 2016b).

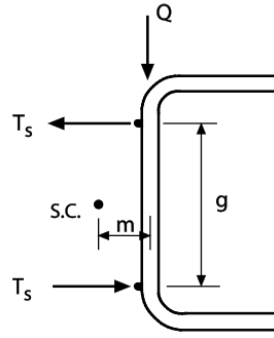


Figure 2.6: Tensile force in the connectors of a flexural member composed of back-to-back channels (AISI, 2016b)

Provisions for built-up compression members (AISI, 2016a)

The provisions included in (AISI, 2016a) for built-up members in compression apply only to members comprised of two sections in direct contact. The (AISI, 2016a) rules require that if global buckling of the built-up column introduces shear forces in the connectors between the components, the slenderness ratio KL/r , which is used in the calculation of the elastic global buckling stress, should be replaced by the modified slenderness ratio given by:

$$\left(\frac{KL}{r}\right)_m = \sqrt{\left(\frac{KL}{r}\right)_o^2 + \left(\frac{a}{r_i}\right)^2} \quad (2.22)$$

In the above equation $(KL/r)_o$ is the global slenderness ratio of the entire built-up cross-section about its minor axis, a is the intermediate fastener spacing and r_i is the minimum radius of gyration of the individual components of the built-up member.

The modified slenderness ratio accounts for the reduced shear rigidity of built-up members connected at discrete points and applies to columns failing in flexural or flexural-torsional buckling.

In addition, the (AISI, 2016a) provisions require the intermediate connector spacing, a , to be limited such that $a/r_i \leq 0.5(KL/r)_o$ to prevent failure of the individual components due to flexural buckling between connectors in the case that any one of the connectors becomes loose or ineffective. The intermediate connectors in any cross-section along the member are also required, as a group, to be able to transmit a force equal to 2.5 % of the ultimate capacity of the column. Additionally, the ends of the built-up member should be connected by a weld having a length of at least the maximum width of the member, or by connectors spaced longitudinally at less than 4 times the diameter of the connectors over a distance of at least 1.5 times the maximum width of the member, in order to prevent slip in the end connections.

It is worth noting that these provisions for built-up members in compression have mainly been derived from research on hot-rolled built-up members connected with bolts or welds (AISI,

2016b), and therefore, they do not necessarily reflect the behaviour of thin-walled members, in which cross-sectional instabilities often occur before global buckling takes place, and in which the material and geometric imperfections can differ substantially from those encountered in hot-rolled members.

2.7. Previous research on CFS built-up members

2.7.1 Modified slenderness ratio

The modified slenderness formula, as included in the (AISI, 2016a) provisions, was developed based on the experimental research of Zandonini (1985) on hot-rolled built-up struts consisting of back-to-back channels, connected to each other with intermediate welded or snug-tight bolted filler plates. In order to assess the applicability of the modified slenderness ratio to thin-walled CFS I-shaped columns, Stone and LaBoube (2005) carried out an experimental investigation consisting of 32 pin-ended compression tests on columns with four different cross-sectional dimensions. The columns were assembled from two identical lipped channels connected back-to-back with screws. The investigation showed that using the modified slenderness ratio resulted in conservative strength predictions, especially for the columns assembled with thicker channels. Whittle and Ramseyer (2009) also compared the predictions given by (AISI, 2016a) using the modified slenderness ratio to the results obtained from over 150 compressive tests on simply supported built-up box sections assembled from square lipped channels welded together in a toe-to-toe configuration at discrete intervals, and found them to be exceedingly conservative. It is worth pointing out, however, that the square lipped channels used to assemble the built-up specimens tested by Whittle and Ramseyer (2009) were relatively stocky, with width-to-thickness ratios ranging from 16 to 41, and therefore they did not exhibit local buckling. Reyes and Guzmán (2011) carried out compression tests on 48 built-up box sections made from two lipped channels welded together at discrete intervals, similar to those tested by Whittle and Ramseyer (2009). However, in this case the lipped channels had more slender cross-sections, with width-to-thickness ratios of the web which ranged from 50 to 67. The specimens were tested between fixed or flexible support conditions. The columns were relatively short, failing predominantly due to local buckling, and in the case of the specimen with the largest weld spacing, also by global buckling of the individual channels between the welds. The tests showed that, excluding the columns with the largest weld spacing, there was no statistical reduction in the ultimate capacity due to a larger connector spacing and therefore, the modified slenderness ratio was not applicable to these columns.

A simple design equation, which employed the modified slenderness ratio as one of the independent variables, was proposed by Piyawat et al. (2013) to predict the ultimate capacity of

doubly symmetric built-up tubular and I-shaped sections failing by distortional or global flexural buckling. The equation was developed by carrying out a regression analysis of a three-dimensional surface fitting the experimental and numerical data gathered in (Brueggen and Ranrseyel, 2005; Piyawat et al., 2011; Whittle and Ramseyer, 2009). However, the authors suggested that more compression tests on other practical built-up geometries were needed to further validate their proposed equation.

2.7.2 Extending the DSM to the design of built-up members

The inherent characteristic of the DSM of simply combining the elastic local, distortional, and global buckling stresses of thin-walled members in the calculation of the ultimate strength has prompted a significant amount of research to try and extend the applicability of the DSM to the design of built-up members. Most of the effort in extending the DSM to built-up members has been devoted to the way in which composite action between the individual components of the built-up geometry should be taken into account when calculating the elastic buckling stresses of the member, considering the limitations of the FSM in accounting for the discrete distribution of the connectors along the member.

The first attempt to incorporate composite action into the DSM equations can be attributed to Young and Chen (2008), who compared the predictions given by the DSM to the ultimate capacities obtained from a series of tests carried out on CFS built-up closed section columns. The built-up specimens were assembled from channels with intermediate web stiffeners connected at their flanges using self-tapping screws. The authors used the FSM to calculate the elastic critical buckling stresses required by the DSM using three different assumptions, which reflected different levels of composite behaviour. First, the individual channels were considered in isolation assuming no interaction between them. An intermediate level of interaction was incorporated by representing the connectors by smeared constraints along the column, while full composite action was modelled by considering the built-up geometry as one solid cross-section. Young and Chen (2008) showed that the ultimate capacities of the columns were intermediate between the predictions given by the DSM when considering the built-up cross-section as fully integral and the predictions assuming two independent profiles, suggesting that some level of composite action was present in the tested columns.

(Georgieva et al., 2012a, 2012b, 2012c, 2011) carried out an extensive experimental and numerical investigation to study the buckling behaviour of double-zed built-up columns and assessed the predictions of the DSM. The built-up columns were assembled with hot-rolled spacers bolted to the individual zed sections to restrict distortion of the cross-section at the interconnection points, and were designed to exhibit local, distortional and global buckling. The DSM was found to give conservative strength predictions for these members.

Zhang and Young (2012) also evaluated the suitability of the DSM to predict the ultimate capacity of built-up I-shaped compression members based on the results obtained from experiments. The specimens considered in the study were assembled from lipped sigma-channels connected back-to-back with self-tapping screws, and were designed to exhibit local, distortional and global buckling, as well as interaction between these buckling modes. As in (Young and Chen, 2008), the authors used the FSM to calculate the elastic cross-sectional buckling loads. However, this time they considered five different cases to represent the amount of composite behaviour which was experienced by the individual channels. In the first case, the channels were analysed in isolation, and therefore no composite action was considered. In the last four cases the entire built-up cross-section was considered as one solid cross-section and the different levels of composite action were represented by setting the thicknesses of the contact surfaces of the channels equal to 1.0, 1.2, 1.5 and 2.0 times the thickness of the individual channels. The study showed that the best agreement between the DSM predictions and the experimental results was achieved when assuming that the thickness of the channel webs in contact with each other was equal to 1.2 times the thickness of the individual channels, suggesting that some degree of composite behaviour was present in the tested specimens. Zhang and Young (2015) carried out parametric studies of the built-up geometries tested by Zhang and Young (2012) to assess the effect of the web and edge stiffeners on the buckling response of the built-up specimens. They also explored additional DSM approaches to predict the ultimate capacity, including one in which the effect of the composite action is included in the stability analysis by considering a channel in isolation with the connectors represented by longitudinal stiffeners.

A study similar to the one presented in (Zhang and Young, 2012), using the same five cases to represent the level of composite action, was carried out by Zhang and Young (2018) to evaluate the DSM predictions for built-up closed compression members with different types of web stiffeners. Two different built-up cross-sections were studied, both of them assembled with self-tapping screws. This study showed that good DSM predictions were obtained when the thicknesses of the contact surfaces in the built-up geometry were set equal to the thicknesses of the individual components, but also revealed some level of composite action in the tested built-up geometries. In this case, setting the thickness to 1.2 times the thickness of the individual components, however, as in the geometries tested by Zhang and Young (2012), resulted in slightly unsafe predictions.

Another experimental investigation of the structural response of CFS built-up I-sections was reported in (Lu et al., 2017). However, the built-up members tested by Lu et al. (2017) consisted of screw connected back-to-back lipped channels without web stiffeners. The authors concluded that there was clear evidence of ultimate strength erosion due to local-distortional and local-distortional-global interaction, and they subsequently proposed a novel direct strength based

method to account for these interactions. In addition, by comparing the ultimate capacities obtained for the built-up specimens with those obtained for the individual components, the authors showed that a significant amount of composite action could be achieved when the failure mode was governed by global buckling. They also concluded that when the failure mode of the tested columns was predominantly local or distortional buckling, the effect of composite action could be disregarded. Based on these observations, the authors decided to calculate the elastic cross-sectional buckling loads, required by the proposed DSM equations, using the FSM while considering the individual channels in isolation. However, to determine the elastic global buckling load they considered the built-up cross-section as one solid cross-section.

Fratamico et al. (2018b) also reported an experimental investigation of the buckling and collapse behaviour of screw connected back-to-back lipped channels. However, in this study the columns were seated in tracks, which provided a more realistic semi-rigid support condition. The authors assessed the effect of adding a group of connectors at each end of the column, as prescribed by (AISI, 2016a), and confirmed the importance of these end group fasteners (EGFs) in reducing the relative slip between the individual components and increasing the amount of composite action when flexural buckling takes place. The experimental study revealed that the benefit of adding the EGFs was more pronounced when global flexural buckling occurs without much participation of local buckling. Based on the experimental results, an extension of the DSM was proposed, in which the end support conditions were assumed to be fixed and the elastic buckling stresses were calculated using the FSM while modelling the connectors using the smeared constraint approach.

While most of the effort in extending the DSM to the design of built-up members has been concentrated on compression members, some research has also been dedicated to built-up flexural members. Wang and Young (2015) experimentally investigated the flexural behaviour of built-up CFS members with open and closed cross-sectional geometries and with circular web holes, with the aim of extending the DSM to the design of these types of members. The built-up geometries studied by Wang and Young (2015) consisted of an open cross-section formed by two lipped channels screw connected in a back-to-back configuration, and a closed cross-section assembled from two plain channels screwed together through their flanges. The authors explored different ways of calculating the elastic buckling stresses required by the DSM in order to account for the effect of the connectors and the web opening. The applicability of the DSM to the design of built-up flexural members was also assessed by Wang and Young (2016a, 2016b), who carried out an experimental and numerical investigation of flexural members with four different built-up cross-sectional geometries failing by cross-sectional instabilities. Each built-up geometry was assembled from two identical sections, screw connected either in a back-to-back configuration to form an open section, or connected through their flanges to form a closed section. The authors assumed in their analysis that the built-up geometries behaved as

one solid cross-section, and found that, while for some built-up geometries the DSM provided acceptable predictions, for other built-up geometries the predictions were either conservative or unsafe. The authors resolved to modify the DSM equations and proposed tailored DSM equations for each built-up geometry based on their experimental and numerical data.

A recently developed compound strip method (CSM) for the stability analysis of built-up members (Abbasi et al., 2018) was used in (Abbasi et al., 2017) to study the effect of the connectors spacing on the buckling behaviour of CFS built-up columns and to assess the applicability of the DSM to built-up members, based on the experimental results obtained in (Zhang and Young, 2012). The novelty of this study stemmed from the fact that the CSM is able to account for the discrete character of the connector points when computing the elastic buckling stresses of the built-up member. Using the CSM in numerical studies, the authors found that reducing the connector spacing enhanced the elastic local and global buckling stresses. In addition, an assessment of the DSM in which the elastic buckling stresses were obtained from the CSM revealed that the DSM predictions were fairly accurate in predicting the ultimate capacity of the built-up specimens tested by Zhang and Young (2012). However, the authors stressed the need to perform further comparisons to calibrate the DSM for a wider range of built-up sections with more complicated geometries.

2.7.3 Additional research on built-up members

Li et al. (2014) carried out a numerical and experimental investigation of built-up box section columns composed of two lipped channels with web stiffeners connected through their flanges with self-drilling screws. The researchers showed that local buckling of the individual components cannot effectively be restricted in a built-up member because its half-wave length is usually shorter than the connector spacing. They also indicated that some of the components of a built-up member may attract more load than the others due to a small difference in length, reducing the capacity of the member.

An experimental investigation was presented by Craveiro et al. (2016) on columns with open and closed built-up cross-sectional geometries. The tested columns were assembled from lipped and plain channels connected with self-drilling screws, constructing built-up geometries with up to four individual channels. The study revealed a significant degree of composite action, with the built-up geometries exhibiting ultimate capacities larger than those expected by simply adding up the contributions of the individual components. Liao et al. (2017) carried out an experimental and numerical investigation of multi-limb built-up stub columns with similar geometries as those tested by Craveiro et al. (2016) and found that the connector spacing had little impact on the ultimate capacity of the stub columns.

A significant research effort has also been focused on developing innovative built-up geometries. The built-up LiteSteel beam (LSB), consisting of two channels with hollow rectangular flanges connected back-to-back, has been investigated numerically and experimentally by (Jeyaragan and Mahendran, 2008a, 2008b). The authors found that the detrimental effect of lateral-distortional buckling, common in the single LSB, can be mitigated by connecting two LSB back-to-back, resulting in a moment capacity which is more than twice the capacity of the individual LSB section. The Modular Light-Weight Cold-formed beam (MLC beam) is another innovative built-up beam, consisting of two lipped channels with hollow flanges and a web containing beads and openings. The channels are laser welded together in a back-to-back configuration with reinforcing plates placed inside the flanges. The MLC beam was designed to provide a high resistance to lateral-torsional buckling and has been extensively investigated both numerically and experimentally (Dilorenzo et al., 2006; Landolfo et al., 2009, 2008; Lorenzo et al., 2004; Portioli et al., 2012).

2.8. Numerical modelling of CFS built-up members using Abaqus

This section is mainly based on Abaqus manual (Dassault Systemes, 2014).

2.8.1 Abaqus solvers for non-linear buckling analysis

Abaqus provides three different techniques for solving a non-linear buckling analysis.

The Modified Riks method has been successfully used by many researchers to predict the non-linear buckling behaviour of CFS members composed by a single section (Ashraf et al., 2006; Gardner and Nethercot, 2004; Li et al., 2013; Yan and Young, 2004; Young and Yan, 2004). This method can account for non-linear material properties and arbitrary boundary conditions, and can provide solutions irrespective of whether the response of the system is stable or unstable. However, in order for the Riks method to be applicable, the loads applied to the system must be proportional and the equilibrium path in the load-displacement space must be smooth and unbranched. In addition, in problems which involve contact non-linearity, such as buckling of a built-up member, the Riks analysis is most likely to terminate before the ultimate load of the member has been reached, since this method is not able to properly address the discontinuities associated with this type of non-linearity. A detailed description of the Modified Riks method can be found in (Dassault Systemes, 2014).

Another approach is to use the General Static method with the inclusion of artificial damping to stabilize the solution. This approach has proved to be very useful in determining the non-linear buckling response of built-up specimens in cases where the Modified Riks method has failed to converge (Becque, 2008; Piyawat, 2011). However, this approach should be used with caution,

as adding artificial damping in excess may significantly affect the solution and overestimate the ultimate capacity of the model.

The third approach is to use the Explicit Dynamic method, which treats the quasi-static buckling response as a dynamic problem. As this method does not attempt to converge to the exact solution, the specified time increment has to be sufficiently small to prevent the response predicted by this method from excessively deviating from the exact response. On the other hand, since no iterations are required, the computational cost of each increment is considerably lower than in the previous two methods. Also, to prevent inertial effects from affecting the response, the specified loading rate has to be limited, which in turn increases the number of increments needed. This typically requires several runs to find the optimum value of the loading rate. The Explicit Dynamic method always provides a solution. However, its validity needs to be scrutinized using the engineer's judgement.

Out of the three methods available in Abaqus to solve non-linear buckling problems, the General Static method is the most suitable one for problems involving contact discontinuities. These are likely to occur between components of a built-up member when it is subject to buckling instabilities. For this reason, the method used by the General Static solver to solve a non-linear problem is described in more detail in the next section.

2.8.2 Solving a non-linear problem with Abaqus/Standard General Statics solver

In a non-linear problem the stiffness matrix of the system changes as it deforms. For this reason, in order to determine the non-linear response of the system to certain loading conditions, the loading has to be expressed as a function of time and the simulation has to be divided into a series of time increments. In each time increment, Abaqus/Standard iteratively solves a static system of linear equations with an updated stiffness matrix of the system. By default, the General Static solver carries out this iterative process using the Newton-Raphson method. Abaqus/Standard adjusts the size of each increment depending on whether or not a converged solution is achieved after a series of iterations.

The Newton-Raphson method is represented for a single time increment in Figure 2.7, which illustrates the non-linear displacement response of a system to a given loading. At any time during the analysis, in order for the system to be in a static equilibrium, the total internal forces (I) must balance the external forces acting at each node (P).

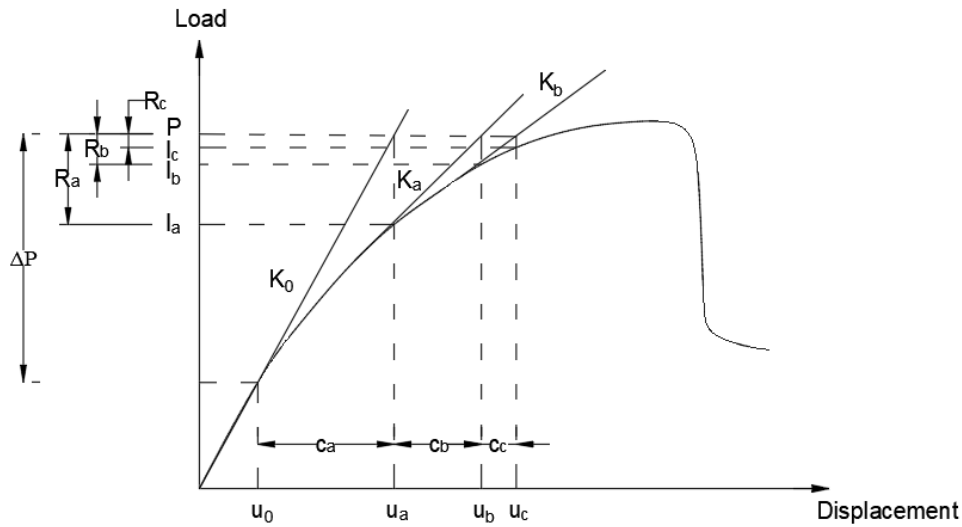


Figure 2.7: Iteration process in a time increment

Therefore, in a given time increment during the non-linear analysis, a small load increment ΔP applied at the beginning of the increment will result in the external forces P which must be balanced by the internal forces I_a . These internal forces are calculated based on the system configuration at $u_a = u_0 + c_a$, where c_a is referred to as the displacement correction for iteration a . c_a is determined using the system's tangent stiffness K_0 , which is based on the system configuration at u_0 , and P , as shown in Figure 2.7. In a non-linear problem I_a and P will never completely balance each other and therefore, Abaqus/Standard defines a force residual R_a for iteration a as:

$$R_a = P - I_a \quad (2.23)$$

This force residual R_a is compared to a tolerance value, which by default is equal to 0.5 % of a spatial average force computed over a number of nodes in the system, averaged over time. If R_a is less than this force residual tolerance at all nodes, Abaqus/Standard considers P and I_a to be in equilibrium. However, before the solution is accepted, Abaqus/Standard checks whether the final displacement correction c_a is less than 1 % of the total incremental displacement $\Delta u_a = u_a - u_0$. If this check is not satisfied, Abaqus/Standard performs another iteration. Similarly, if R_a is larger than the force residual tolerance value, Abaqus/Standard will try to balance the external and internal forces by performing iteration b , in which a new stiffness matrix is computed based on its updated configuration u_a . This stiffness matrix is used in combination with ΔP to determine the new displacement correction c_b for iteration b , which in turn is used to determine the new configuration of the system u_b and the internal forces I_b . As Figure 2.7 shows, if the solution converges within a given increment, each iteration will bring the external and internal forces closer to each other.

By default, Abaqus/Standard will continue performing iterations until either a maximum of 16 iterations are completed, or the force residual is less than the tolerance value while the displacement correction c is less than a fraction of the increment displacement Δu . If after 16 iterations the solution has not converged, Abaqus/Standard reduces the increment size to 25 % of its previous value and tries to find a converging solution for this smaller increment size. If the solution still does not converge, Abaqus/Standard will continue reducing the increment size until a converging solution is found, the minimum increment size specified is reached or a maximum of 5 consecutive reductions of the increment size have been carried out. If the solution still has not converged, Abaqus/Standard terminates the analysis prematurely. On the other hand, if during two consecutive increments the solution converges in fewer than 5 iterations, Abaqus/Standard will automatically increase the size of the next increment by 50 %. This ensures that in problems without severe convergence issues the solution can be reached in a reasonable time.

For non-linear problems with severe convergence issues Abaqus/Standard allows the user to change the default solution control parameters which govern the convergence criteria and the time incrementation algorithm. In addition to this, Abaqus/Standard offers a series of stabilization mechanisms, which can help to achieve convergence in cases where the solution tends to diverge.

2.8.3 Stabilization schemes and solution control in Abaqus/Standard

In a non-linear buckling analysis of a built-up member there are three sources of numerical instabilities which may prevent Abaqus/Standard from converging to the desired solution. The first source of instability is of a geometric character and originates from the very nature of the buckling phenomenon, which results in a local transfer of strain energy from one part of the built-up member to the neighbouring parts. The second source of instability is related to the material non-linearity and comes into effect after the proportionality limit of the material is exceeded due to material softening. The third source of non-linearity originates from the contact between the different components in the built-up member, which may lead to severe discontinuities in the model with gaps potentially opening up or closing and suddenly being unable/able to transfer pressures.

Abaqus/Standard includes two stabilization mechanisms which can be used with the General Static Solver to overcome these issues. The Automatic Stabilization scheme is mainly designed to address issues due to geometric non-linearity and material non-linearity, while the Contact Stabilization scheme focuses on smoothening the discontinuities introduced into the model by contact between nearby surfaces. Both stabilization mechanisms consist of adding artificial damping to the model to help stabilize it. In addition, Abaqus/Standard also allows the user to

modify some solution control parameters, which can prevent unnecessary cutbacks to the increment size during the simulation and can help prevent the solution from diverging in severely non-linear problems.

More details about the different options which can be used in a non-linear buckling analysis to help Abaqus/Standard converge to the desired solution are described below.

2.8.3.1 Automatic stabilization

The automatic stabilization mechanisms in Abaqus/Standard allow for the addition of artificial viscous forces into the global equilibrium equations solved in each increment:

$$P - I - F_v = 0 \quad (2.24)$$

In the above equation P and I are the external and internal forces acting at each node in the model and F_v are the stabilizing viscous forces which are added at each node. These viscous forces are obtained from

$$F_v = cM^*v \quad (2.25)$$

Where M^* is an artificial mass matrix calculated with unity density, c is a damping factor and v is the vector of nodal velocities. Therefore, if a region of the model has a tendency to undergo large displacements in a single increment, for instance due to sudden buckling, or a sudden loss of material stiffness, the local velocities at the nodes in that region generate viscous forces which dissipate part of the strain energy released. Regions in the model which are stable (i.e. which undergo small displacements in said increment) generate low viscous forces and, therefore, the artificial damping in those regions has little or no effect.

The damping factor c can be constant over the whole analysis step. In this case, Abaqus/Standard allows the user to specify the damping factor directly. Alternatively, Abaqus/Standard can calculate it automatically based on the ‘dissipated energy fraction’ which is the ratio between the energy dissipated during a given increment and the strain energy extrapolated based on the first increment of the step. The default value of the dissipated energy fraction is 2.0×10^{-4} .

Alternatively, Abaqus/Standard offers an adaptive automatic stabilization scheme, in which the damping factor can vary spatially and with time. This is the preferable approach as it reduces the effect the artificial forces may have on the response of the system. When this option is selected, the amount of artificial damping introduced into the model is controlled by the convergence history and the ratio of the energy dissipated by viscous damping to the total strain energy. If the convergence behaviour is problematic, Abaqus/Standard automatically increases the damping factor. Abaqus/Standard tries to limit the ratio of the energy dissipated by the

artificial forces to the total strain energy by imposing an accuracy tolerance. If this tolerance is exceeded, Abaqus/Standard adjusts the damping factor in each individual element so that the accuracy tolerance is satisfied both at the global and the local (element) level. Abaqus/Standard also restricts the ratio of the incremental value of the stabilization energy to the incremental value of the strain energy in each increment to ensure that this value does not exceed the accuracy tolerance. By default, the accuracy tolerance used with the adaptive automatic stabilization scheme is set to 0.05. However, this value can be adjusted to the specifics of the model.

To ensure that the artificial damping forces introduced into the model are not excessively large and distort the solution, Abaqus recommends performing a post-analysis to ensure that the energy dissipated by viscous damping (ALLSD) is negligible compared to the total strain energy (ALLIE).

2.8.3.2 Contact stabilization

The contact stabilization (or contact control) scheme is also based on the addition of viscous damping to help stabilize the model. The main difference with respect to the automatic stabilization scheme is that, in this case, artificial viscous stresses are applied at the slave nodes of a contact interaction to oppose the incremental relative motion between nearby surfaces. Contact stabilization can be specified for particular surfaces where contact is likely to occur. By default, the viscous stresses are automatically calculated for each contact constraint. However, Abaqus/Standard also allows the user to specify the damping coefficient directly. The first approach is a more robust solution as, in this case, the damping stresses are automatically adjusted over the step and are increased when severe contact discontinuity is present and reduced when contact between the surfaces is stable.

The viscous stresses determined by the contact stabilization scheme can be decomposed in to a stress normal to the interacting surfaces (σ_{stab}) and a tangential stress (τ_{stab}). These are given by:

$$\sigma_{stab} = s_{const} s_{iter} s_{ampl} s_{gap} c_d v_{relN} \quad (2.26)$$

$$\tau_{stab} = s_{const} s_{iter} s_{ampl} s_{gap} s_{tan g} c_d v_{relT} \quad (2.27)$$

where c_d is the damping coefficient which is automatically calculated by Abaqus/Standard for each contact constraint based on the stiffness of the respective elements and the time step. v_{relN} and v_{relT} are the relative normal and tangential velocities, respectively, between nearby points on opposing contact surfaces. s_{iter} is a scale factor which varies across iterations, allowing for larger viscous stresses during the early iterations of an increment and reducing them during later iterations to minimize the effect of the contact stabilization on the desired solution. s_{ampl} and s_{incr} are time-dependent scale factors which reduce the effect of the contact stabilization as the

analysis progresses. s_{gap} is a scale factor which controls the magnitude of the viscous stresses based on the distance between the slave and master nodes, with it being maximal when a zero gap distance exists between the slave and master node and being equal to zero when this distance is larger than a characteristic surface dimension. The two scale factors s_{const} and s_{tang} are constant factors which allow the Abaqus user to adjust the computed viscous stresses. This provides great flexibility in cases where the automatically calculated contact stabilization is not adequate.

As Eq. (2.26) and Eq. (2.27) show, the scale factor s_{const} applies to both normal and tangential stabilization, while s_{tang} only applies to tangential stabilization. This means that the viscous contact stresses can be controlled separately in order to stabilize the relative motion of the surface nodes in the normal and the tangential directions of the surfaces. This is important especially when the relative tangential motion between nearby surfaces is large, as may be the case when the component sections of a built-up member buckle. In this case tangential contact stabilization may absorb significant energy, and therefore it may be preferable to set the tangential viscous stresses to zero. Normal contact stabilization, on the other hand, is much less likely to absorb significant energy and therefore tends to have less influence on the results.

Contact stabilization can be activated in Abaqus/Standard by using the *CONTACT STABILIZATION or *CONTACT CONTROL keywords. Both options provide a similar contact stabilization option, with the main difference between them being the default values given to some of the scale factors used to calculate the viscous stresses.

As for the automatic stabilization scheme, care must be taken to ensure that the viscous damping does not significantly alter the response of the system. This can be achieved by performing a post-analysis check to ensure that the dissipated stabilization energy (ALLSD) is significantly smaller than the total strain energy of the system (ALLIE).

2.8.3.3 Solution Control Parameters

The Solution Control Parameters can be used to modify the convergence control algorithm Abaqus uses to solve a non-linear analysis, as well as the time incrementation scheme. However, modification of the solution control parameters may significantly affect the accuracy of the solution and/or the computational speed. For most analyses the solution control parameters need not be changed. However, there are cases where the solution procedure may not be able to converge with the default controls and it is necessary to change certain control parameters.

Displacement correction control

As mentioned in section 2.8.2, before Abaqus/Standard accepts the solution obtained for a given increment as a sufficiently close approximation of the exact solution, it checks whether the

largest displacement correction at the nodes is a small fraction of the total displacement increment. The limit for this ratio is given by C_n^α , which by default is equal to 0.01. Some analyses may not require such accuracy, and therefore Abaqus/Standard allows the user to increase the value of C_n^α , or even to remove this check by setting C_n^α to 1.

Time incrementation parameters

I_0 and I_R are the most significant time incrementation parameters, since they have a direct effect on convergence. However, they do not affect the accuracy of the solution. In non-linear analyses which are performed using the Newton-Raphson method the solution can be expected to converge quadratically if the estimate of the solution is within the radius of convergence. However, there are some problems in which quadratic convergence may not be achieved, for example, if the Jacobian is not exact. In addition, monotonic convergence may also not be achieved in problems in which various sources of non-linearity, such as contact, material or geometric non-linearity, interact with each other. Abaqus/Standard carries out regular checks to see the rate at which the residual forces are decreasing. If Abaqus/Standard detects that quadratic convergence is not being achieved it may reduce the time increment to enforce a quadratic convergence.

I_0 specifies the number of equilibrium iterations carried out before Abaqus/Standard checks whether the residuals are not increasing in two consecutive iterations. The default value for I_0 is 4. However, it may be necessary to increase this parameter if the initial convergence is non-monotonic. Similarly, I_R specifies the number of equilibrium iterations after which Abaqus/Standard checks whether the convergence happens at a logarithmic rate. The default value for I_R is 8. Abaqus/Standard recommends increasing the values of these two time incrementation parameters to $I_0 = 8$ and $I_R = 10$ in problems with severe discontinuities, in order to avoid premature cutbacks of the time increment.

'Line search' algorithm

The 'line search' algorithm is an option included in Abaqus/Standard to improve the robustness of the Newton-Raphson and quasi-Newton methods. In severely non-linear problems the Newton-Raphson algorithms may diverge during equilibrium iterations where residuals are large. The line search algorithm detects these situations automatically and scales the correction to the computed solution using a line search scale factor, s^{ls} , which helps to prevent divergence. The scale factor s^{ls} is obtained through an iterative process which minimizes the component of the residual vector in the direction of the correction vector. The accuracy of s^{ls} depends on several control parameters, with the most important ones being N^{ls} which is the number of line search iterations that are performed, and η^{ls} , which indicates the minimum change of s^{ls} between iterations before the line search algorithm stops. By default, when Abaqus/Standard uses the Newton-Raphson method, N^{sl} is set to zero (i.e. the line search algorithm is deactivated). When

using the quasi-Newton's method N^{sl} is set to 5 and η^{sl} is set to 0.1. N^{sl} can be increased, for example to 20, to allow for more line search iterations, while η^{sl} can be reduced, for example to 0.01, to request more accuracy in the line search factor s^{sl} . The additional computational cost the line search algorithm requires may be compensated by a reduction in the number of non-linear increments and a reduction in increment cutbacks.

2.8.4 Contact interaction

Abaqus/Standard offers two approaches for modelling surface-based contact interactions, namely: the general contact implementation and the contact pair implementation. Both approaches have very similar capabilities, with the main differences lying primarily in the user interface, the default numerical settings and the available options for defining the contact interaction. Abaqus/Standard provides several contact formulations that can be used in a contact simulation. Each formulation is based on the choice of a contact discretization, a tracking approach, and assignment of 'master' and 'slave' roles to the contact surfaces.

Two contact discretization approaches are available in Abaqus/Standard to model contact. The first one is the node-to-surface discretization approach, in which the nodes of one of the contact surfaces (slave surface) are constrained to not penetrate the other (master) surface. This is achieved by creating projection points on the master surface which interact with the slave nodes. Each contact condition involves a single slave node and a group of nearby master nodes which are used to define the projection point. In the node-to-surface approach the nodes of the master surface can, in principle, penetrate the slave surface. In addition, as the constraints are applied directly to the slave nodes, the contact forces tend to concentrate at these slave nodes. The other option is to use the surface-to-surface discretization formulation, in which the contact conditions are enforced in an average sense over regions nearby the slave nodes rather than at the individual slave nodes themselves. With this approach, although some small penetration may occur at some individual nodes, large undetected penetration of master nodes into the slave surface is not an issue. The surface-to-surface discretization approach tends to provide more accurate stress and pressure results than the node-to-surface approach. However, since the surface-to-surface approach generally involves a larger number of slave nodes in each contact constraint than the node-to-surface approach, its computational cost tends to be higher.

For each type of contact discretization, Abaqus/Standard offers the finite-sliding and the small-sliding tracking approaches to account for the relative motion of the two interacting surfaces. The finite-sliding approach allows for any arbitrarily large relative separation, sliding and rotation of the contact surfaces, while the small-sliding approach assumes that, although the surfaces may undergo arbitrarily large rotations, each slave node interacts with the same local area of the master surface throughout the analysis. With the small-sliding approach,

Abaqus/Standard does not have to monitor slave nodes for possible contact along the entire master surface, which is why this tracking approach generally leads to less computationally expensive solutions than the finite-sliding approach.

The general contact implementation only uses the surface-to-surface formulation in combination with the finite-sliding tracking approach. The contact pair implementation, on the other hand, by default uses the node-to-surface contact formulation with the small-sliding tracking approach, although it also allows the user to opt for any possible combination of the node-to-surface or surface-to-surface formulation with the small-sliding or finite-sliding tracking approach.

Regardless of the contact algorithm selected, the first step in defining a contact interaction between element-based deformable surfaces is to specify the surfaces which will be involved in the contact interaction. Alternatively, the general contact implementation offers an all-inclusive self-contact definition in which Abaqus/Standard automatically includes all exterior element faces, with the exception of faces belonging to cohesive elements, for potential contact. This is a simple way of defining the contact domain. However, it may result in a more computationally demanding solution since in this case, contact between elements which are not realistically able to be in contact with each other is also accounted for.

Once the contact surfaces have been specified, their properties have to be defined. In the case of contact between shell elements, these include, for example, the contact thickness of the shell and any possible offsets in the contact surface. The general contact formulation automatically accounts for the thickness associated with shell-like surfaces, defining contact on the outer faces. With the contact pair implementation, the shell thickness and any offsets are only accounted for when the surface-to-surface contact formulation is selected. In addition, when defining contact between two surfaces, the general contact formulation automatically accounts for any possible contact between the edge of one of the surfaces and the other surface. In this case, the surface-to-surface contact formulation is used as the primary formulation, while the edge-to-surface formulation is used as a supplementary formulation which uses the penalty enforcement method and only involves the displacement degrees of freedom of the edge nodes. The contact pair implementation also allows for edge-to-surface contact interaction. However, this type of interaction has to be defined separately.

The next step is to define the contact property model which governs the behaviour of the surfaces when they are in contact. The default contact property model in Abaqus/Standard assumes a ‘hard’ contact in the normal direction and a frictionless contact in the tangential direction. However, other types contact property models can be defined such as a ‘softened’ contact relationship in the normal direction or different types of friction models in the tangential direction. The latter include a penalty formulation which uses the Coulomb friction model or the ‘rough’ formulation, which assumes that, once the surfaces are in contact, they cannot slide. Three constraint enforcement methods are available in Abaqus/Standard to define normal

contact, namely: the direct method, the penalty method and the augmented Lagrange multiplier method. The direct method strictly enforces a given pressure-overclosure behaviour in each constraint and is the only method that can be used for softened pressure-overclosure relationships. The penalty method is the default method used for hard contact when the finite-sliding surface-to-surface formulation is selected. This method approximates hard pressure-overclosure behaviour by allowing a limited amount of penetration and calculates the contact pressure based on the amount of penetration. The augmented Lagrange formulation is similar to the penalty method but uses an augmentation iteration scheme when a specified penetration tolerance is exceeded. This reduces the amount of penetration, improving the accuracy of the hard pressure-overclosure approximation. The augmented Lagrange method is used by default for self-contact with the node-to-surface formulation if the hard pressure-overclosure relationship is selected.

Finally, it is also important to specify the way in which the initial overclosures (at the beginning of the analysis) in a contact interaction should be resolved. General contact, by default, eliminates initial overclosures by adjusting the position of the slave nodes without generating any stress or strain in the model. The contact pair formulation, on the other hand, by default solves the initial overclosures during the first increment by treating them as ‘interference fits’, in which the penetration of the slave nodes into the master surface is resolved by the generation of stresses and strains in the model. It is important to mention that only those slave nodes which penetrate into the master surface over a distance smaller than an overclosure tolerance calculated by Abaqus/Standard are repositioned. The philosophy behind this is that the default initial adjustments are intended to correct only minor mismatches associated with the generation of the mesh. Therefore, if the overclosures are larger than the calculated tolerance, an exclusion zone is automatically generated and the contact interaction between these surfaces is removed. Abaqus/Standard offers alternative contact initialization methods to solve initial overclosures between contact surfaces. For example, a more robust option to solving all the initial overclosures in the first increment is to use the shrink-fit method to gradually resolve the overclosures over multiple increments. This may be useful when there are large overclosures in the model which cannot be solved in a single increment. In addition, Abaqus/Standard allows the user to increase the search zones for strain-free or interference fit adjustment when the default overclosure tolerance is not appropriate.

2.8.5 Mesh-independent fasteners

Mesh-independent fasteners make use of position points to define a point-to-point connection between two or more surfaces. The fasteners can be located anywhere between the surfaces to be connected, irrespective of the location of the nodes. The location of the fastening points is defined by either specifying an attachment point or an attachment line. The fastening points are

connected to the neighbouring nodes on each surface with distributing coupling constraints, as illustrated in Figure 2.8. Different weighting options can be used to apply these constraints, making use of the distances of the coupling nodes to the fastening point. By default, Abaqus uses the uniform weighting scheme. However, this can be changed to a scheme in which the importance of the constraints provided by the neighbouring nodes decreases with distance following a linear, quadratic, or cubic polynomial weight distribution. Depending on the weighting function selected, the characteristic length of the connected facets and the geometric properties of the fastener, Abaqus/Standard defines a region of influence, which determines the number of coupling nodes that are associated with the fastening points. For a given mesh and weighting scheme, the region of influence can be modified manually by changing the physical fastener radius, although it will always include a minimum of three coupling nodes.

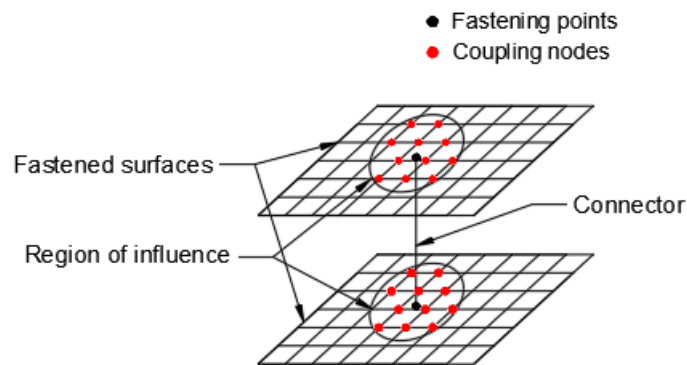


Figure 2.8: Mesh independent fasteners

Mesh-independent fasteners can be defined using either connector elements or Beam Multi-point Constrains (MPCs). BEAM MPCs can be used to model perfectly rigid connectors between the fastened surfaces by eliminating all the translational and rotational degrees of freedoms of one of the fastening points. This approach has the advantage of reducing the size of the model. However, it does not allow any output of the connector such as forces or deformations. Also, since the constraints are imposed by eliminating the degrees of freedom of one of the fastening nodes, it is not possible to model more complex connector behaviour, which can include, for example, slip between the connected surfaces or bearing deformations of the surfaces around the connectors. To model more complex connector behaviour Abaqus/Standard includes the option of using connector elements (CONN3D2), which use Lagrange multipliers to enforce kinematic constraints between the fastening nodes. This allows for a more flexible and tailored modelling of the connectors, since kinematic constraints can be applied to specific components of relative motion between the fastening nodes. This allows, for example, to model the effects of elasticity and plasticity in the connectors and the surrounding surface or local friction at the connector. In addition, connector elements provide output of the

different variables that are included in the definition of the connector behaviour, such as forces or relative displacements between the fastening nodes.

2.8.5.1 Fastener types

Mesh-independent fasteners can be created using point-based fasteners, discrete fasteners or assembled fasteners.

Point-based fasteners and assembled fasteners make use of position points to create the fasteners. Abaqus automatically creates the fastening points by projecting the positioning point onto the fastened surfaces. The main difference between point-based fasteners and assembled fasteners is that the former creates individual fastener objects which can be viewed and manipulated while working in Abaqus/CAE, while the latter are used to efficiently replicate complex fastener-like behaviour in several places by creating a template model which is mapped to the corresponding locations in the main model. Assembled fasteners can be produced only by direct coding into the input file.

Discrete fasteners are similar to point-based fasteners in the sense that they also create individual fastener objects and can be modelled using connector elements or beam MPCs. However, discrete fasteners make use of attachment lines to create the mesh-independent fasteners. The process of creating an attachment line is similar to the process of creating point-based fasteners. The first point of the attachment line (or the first fastening point in a point-based fastener) is generated by either projecting the positioning point onto the closest surface along a normal to the surface or along a specified projection direction, as shown in Figure 2.9. The location of the second point of the attachment line (or fastening point) is determined by projecting the first fastening point onto the other surface along the fastener normal direction, which generally coincides with the normal of the closest surface. The main advantage of discrete fasteners over point-based fasteners and assembled fasteners is that when discrete fasteners are modelled using connectors they allow for connector loads and connector boundary conditions to be applied individually to their available components of relative motion. In addition to that, discrete fasteners can be viewed with their connectors and couplings outside the Visualization module.

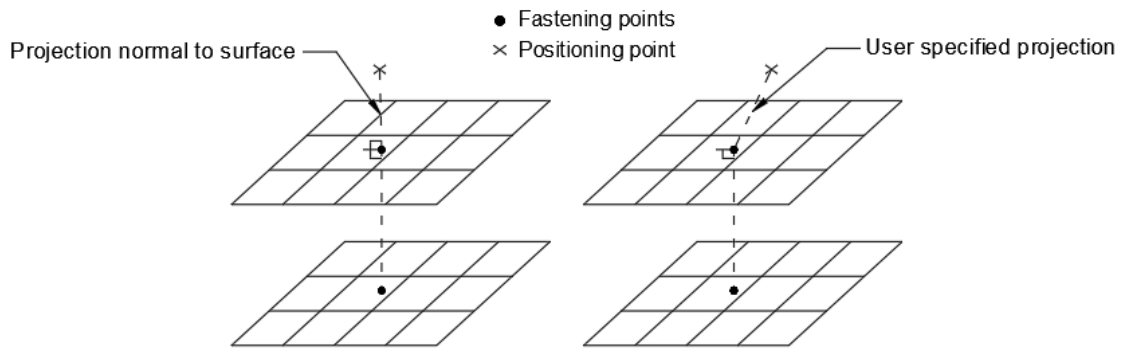


Figure 2.9: Methods used to locate the fastening points with a point-based or a discrete fastener

2.8.5.2 Coupling methods

Abaqus/Standard offers two different ways to couple the motion of the fastening point to the motion of the neighbouring nodes on the fastened surface: the continuum coupling method and the structural coupling method.

By default, Abaqus/Standard uses the continuum coupling method to attach the fastening points to the connected surfaces. In the continuum method, the translational and rotational degrees of freedom of the fastening point are coupled to the average translational degrees of freedom of the neighbouring coupling nodes on each of the fastened surfaces. Therefore, forces and moments at the fastening point are distributed only as coupling forces to the coupling nodes. The advantage of the continuum coupling method is that it can be used with any type of shell element. However, in some situations, when the fastened surfaces are close to one another, this method may provide unrealistic contact interaction.

The structural coupling method couples the translational and rotational degrees of freedom of the fastening point to both the average translational and rotational degrees of freedom of the neighbouring coupling nodes on each of the fastened surfaces, rather than to the translational degrees only. The constraint distributes forces and moments at the fastening point as coupling node forces and moments. This coupling method is particularly suited for bending-like applications of shells when the coupling constraint only spans a small patch of nodes. However, in order to be applicable, all the rotational degrees of freedom at the coupling nodes must be active and constrained. Therefore, the structural coupling method cannot be used with shell elements which only have two rotational degrees of freedom such as S4R5 or S9R5 elements.

2.8.6 Fastener coordinate system

Fasteners are formulated in a local coordinate system which rotates with the motion of the reference node (first fastening point). If point-based fasteners are used, Abaqus, by default defines the local coordinate system of the fastener by projecting the global coordinate system

onto the surface containing the first fastening point, so that the z-axis of the fastener local coordinate system is normal to this surface. On the other hand, if the connectors are modelled with discrete fasteners, the orientation of the local coordinate system of the fastener, by default, coincides with that of the global coordinate system. A schematic representation of the fastener coordinate system which is by default created by Abaqus when using point-based and discrete fasteners is illustrated in Figure 2.10.

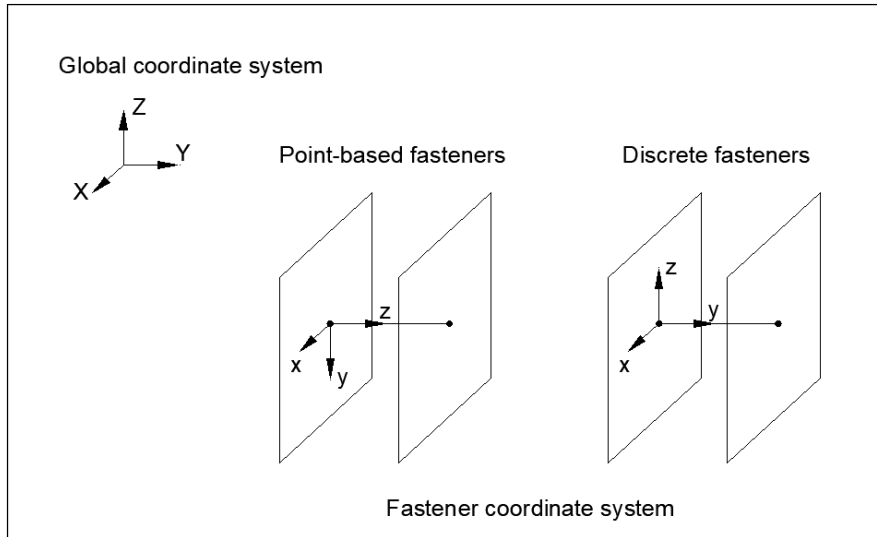


Figure 2.10: Global and fastener coordinate systems

If the fastener is defined using a connector element, it may be necessary to specify its orientation to ensure that the components of relative motion of the connector act in the desired directions. This is achieved by defining a local coordinate system for the connector ($T_{connector}$), relative to the local coordinate system for the fastener ($T_{fastener}$). Assuming that $T_{connector}$ and $T_{fastener}$ are orthogonal rotation matrices with the local x , y and z -axis corresponding to the first, second and third rows, respectively, the orientation of the connector relative to the local coordinate system of the fastener ($T_{conn.orientation}$) is given by:

$$T_{conn.orientation} = T_{connector} \cdot T_{fastener} \quad (2.28)$$

As an example, if two parallel surfaces have to be connected in such a way that they can only rotate about the axis of the fastener normal to the surfaces, the fastener can be modelled using a HINGE connector. However, since the only available component of relative motion of this connector is a rotation about its x -axis, if the default local coordinate system is used for the fastener (with the z -axis normal to the surfaces), the connector has to be orientated using a $T_{connector}$ matrix in which the x -axis is set to $(0., 0., 1.)$.

Chapter 3

Experimental Study of Cold-Formed Steel Built-up Stub Columns

3.1. Introduction

The experimental programme described in this chapter intended to investigate the cross-sectional compressive behaviour and capacity of four different built-up geometries. Particular attention was devoted to the way the individual components within the cross-section interact with each other and affect each other's stability. Furthermore, the experiments sought to quantitatively study the effects of the connector type and the longitudinal connector spacing on the cross-sectional stability and the ultimate capacity of the built-up specimens. A total of 20 stub columns were tested. The entire experimental programme was carried out in the Heavy Structures Laboratory at The University of Sheffield.

Figure 3.1 illustrates the four cross-sectional geometries included in the tests. Cross-sectional geometries 1 and 2 were assembled using commercially available cold-formed steel sections, supplied by BW Industries and selected from their catalogue of standard sections. The sections were manufactured from pre-galvanized steel plates with a guaranteed yield stress of 450 MPa and a nominal 0.04 mm thick Z275 zinc coating. They were connected using M6 bolts, tightened with a torque of 10 Nm. This torque did not result in any substantial clamping force on the connected plates. Rather it is more representative of hand-tightened bolts. A wrench with measured torque was used, however, for reasons of consistency. The bolts used to assemble built-up geometries 1 and 2 are shown in Figure 3.2a. Built-up geometry 1 was formed by connecting the flanges of two plain channel sections with a nominal depth of 154 mm and thickness of 1.4 mm to flat plate sections with a nominal width of 200 mm and thickness of 2.4 mm. In built-up geometry 2 the plate sections were replaced by plain channels with a nominal depth of 154 mm and thickness of 1.4 mm, connected to the flanges of two plain channels with a nominal depth of 79 mm and thickness of 1.2 mm.

Cross-sectional geometries 3 and 4 were assembled using bespoke plain and lipped channel sections with nominal depths of 120 mm and 110 mm, respectively, and thicknesses of 1.2 mm, brake-pressed by an external specialist fabricator. The sections were fabricated from hot-dip zinc coated steel sheet with material characteristics adherent to the CEN (1995) standard. The plain and lipped channels had a guaranteed yield stress of at least 260 MPa. No information about the zinc coating could be obtained from the manufacturer. Therefore, the coating thicknesses was determined by measuring the total thickness at each end of the plain and lipped channels before and after removing the coating. An average coating thickness of 0.03 mm was obtained. The plain and lipped channels used to construct both built-up geometries 3 and 4 had identical nominal cross-sectional dimensions and were joined together using M5.5 self-drilling sheet metal screws (Figure 3.2b). Built-up geometry 3 resembled a box section in which two lipped channels were connected through their flanges to the webs of two plain channels. Built-up geometry 4 could be interpreted as an I-shaped section with double webs and stiffened flanges, as illustrated in Figure 3.1.

All columns were loaded in uniform compression between fixed supports. For cross-sectional geometries 1 and 2 three different connector spacings were considered, while for the other two geometries two different connector spacings were investigated. Each test was repeated in order to account for statistical variability in the results.

Prior to testing the columns, their geometric imperfections were measured by moving a laser sensor along different lines on each face of the built-up columns. Tensile coupons were also extracted from the corner regions and the flat portions of each type of component in order to determine their material properties.

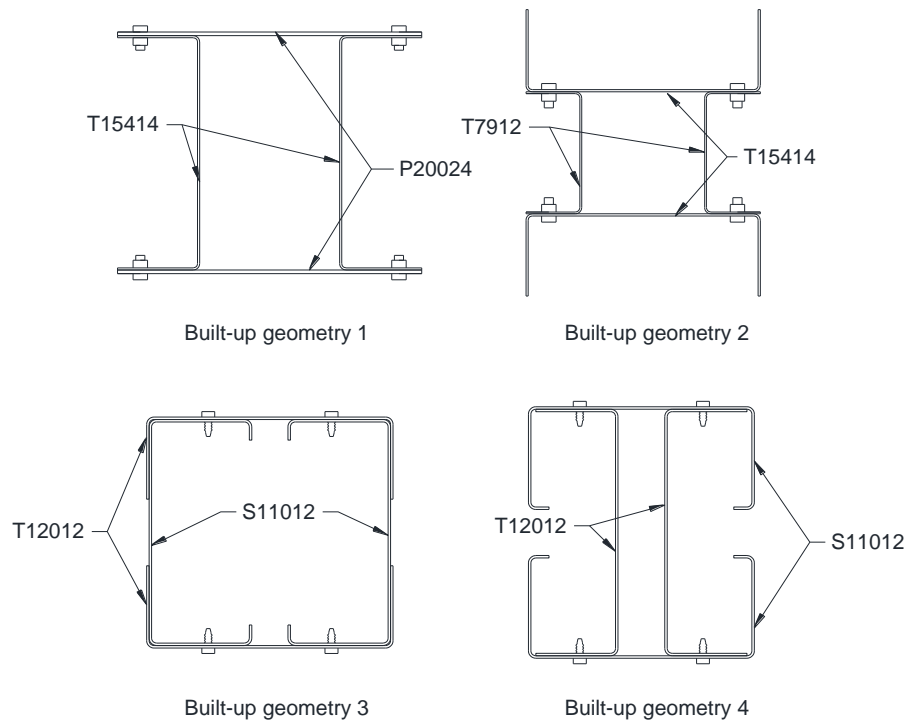


Figure 3.1: Built-up cross sections

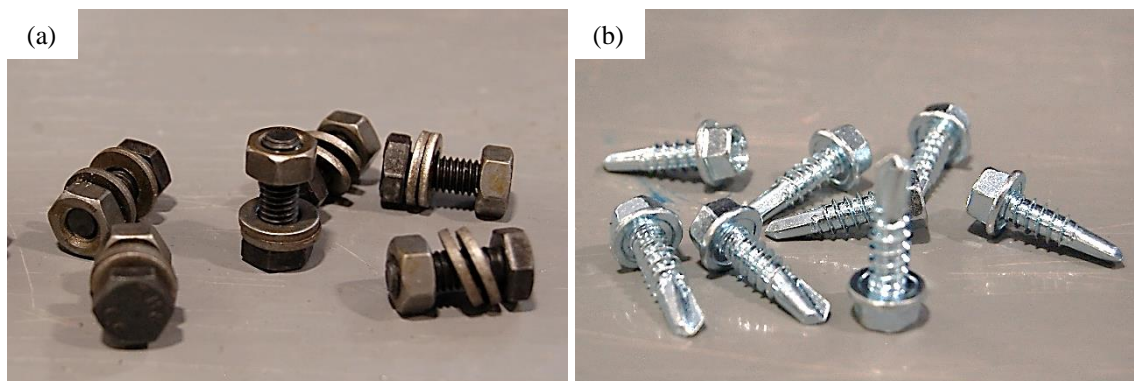


Figure 3.2: a) M6 bolts, b) M5.5 self-drilling screws

3.2. Labelling

The cross-sectional components (i.e. the constituent channels and flat plates) were given a specific label, as were the completed built-up test specimens. Plain channels and lipped channels were labelled using the letter ‘*T*’ or ‘*S*’, respectively, followed by the nominal width of their web in mm and the nominal wall thickness in mm multiplied by 10. To refer to the plate sections, the letter ‘*P*’ was chosen, followed by the width of the plate and its thickness multiplied by 10.

To refer to each built-up specimen, a label was used consisting of the letters ‘*SC*’ to indicate that the specimen was a stub column, followed by a number ranging from 1 to 4 to indicate its cross-sectional geometry (with reference to Figure 3.1). Next, following a hyphen, the number of

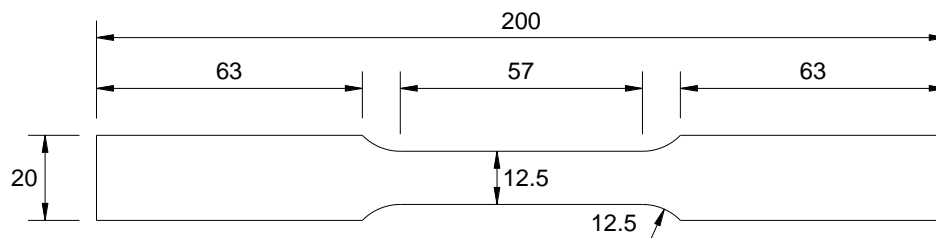
rows of intermediate connectors (i.e. not counting the connectors in the end sections) in the built-up column was provided. Finally, as each test was repeated, the letters ‘*a*’ and ‘*b*’ were used to indicate whether the specimen was the first or the second of twin columns tested. As an example, the label ‘*SCI-2a*’ referred to the first stub column tested with cross-section geometry 1, which contained two intermediate rows of connectors between the end connectors.

3.3. Material Properties

The material properties of the test specimens were obtained by carrying out a series of tensile coupon tests. The coupons were cut from spare sections belonging to the same batch as those used in the test and were taken in the longitudinal (rolling) direction of the specimen. Two flat coupons were taken along the centre line of the web of each type of channel section and along the centre line of the plate section. In addition, two corner coupons were also cut from the web-flange junction of each type of channel section. Therefore, ten coupons were tested in total. The dimensions of all coupons adhered to the specifications provided in (CEN, 2009b).

3.3.1 Flat coupons

All flat coupons had a nominal width of 12.5 mm. Figure 3.3 shows the nominal dimensions of the flat coupons and Figure 3.4a shows all of the flat coupons before testing.



Dimensions in mm

Figure 3.3: Flat coupon dimensions

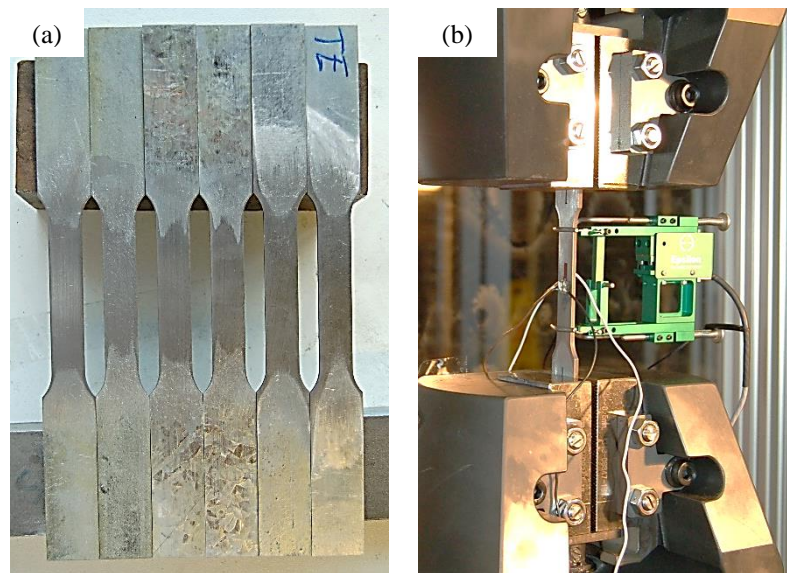


Figure 3.4: a) Flat coupons before testing, b) Flat coupon during testing

Each coupon was instrumented with an extensometer with 50 mm gauge length and one linear 5 mm strain gauge on each side of the coupon, as depicted in Figure 3.4b. In order to effectively attach the strain gauges to the coupons, the zinc coating of the coupons was removed using an emery cloth. After removing the coating, the width and thickness of each coupon were measured using a digital Vernier caliper with a precision of ± 0.03 mm. The measured values are listed in Table 3.1, where the letters ‘*a*’ and ‘*b*’ were used to differentiate between twin coupons.

Table 3.1: Measured dimensions of flat coupons

Component section	Coupon	b_c (mm)	t (mm)	A (mm ²)
P20024	a	12.48	2.44	30.4512
P20024	b	12.48	2.34	29.2032
T15414	a	12.49	1.39	17.3611
T15414	b	12.48	1.39	17.3472
T7912	a	12.48	1.09	13.6032
T7912	b	12.48	1.09	13.6032
T12012	a	12.53	1.09	13.6299
T12012	b	12.53	1.09	13.6161
S11012	a	12.53	1.07	13.3799
S11012	b	12.52	1.07	13.4080

Readings from the extensometer were used to obtain the stress-strain curve of the coupons over a wider strain range than the strain gauges allowed, whereas the average readings from the strain gauges were used to obtain a more accurate measurement of the Young’s modulus.

3.3.2 Corner coupons

Corner coupons with two different dimensions were used, as illustrated in

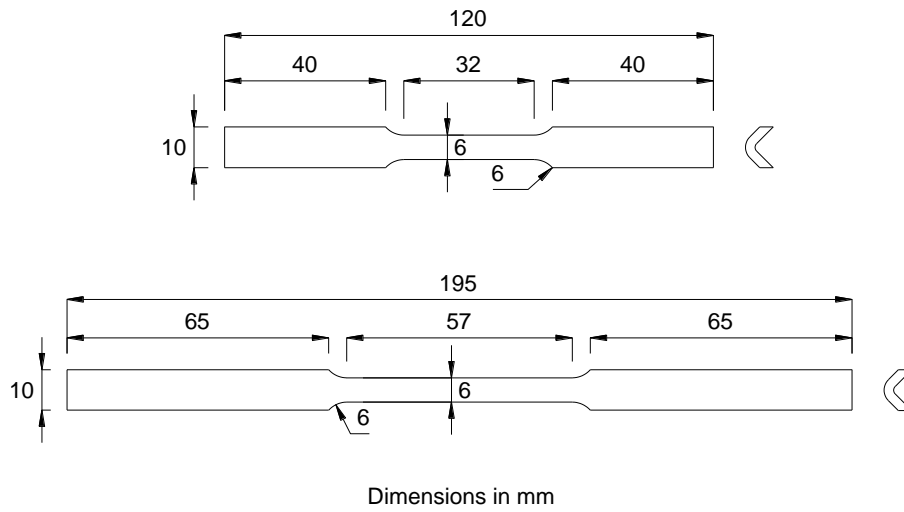


Figure 3.5. All corner coupons had the same nominal width of 6 mm, but differed in gauge length and grip length. The corner coupons taken from the components of built-up geometries 1 and 2 had a gauge length of 25 mm. This gauge length was found to be too short to allow for an easy installation of the instrumentation onto the coupon, and therefore the coupons taken from the components of built-up geometries 3 and 4 were cut with a gauge length of 50 mm.

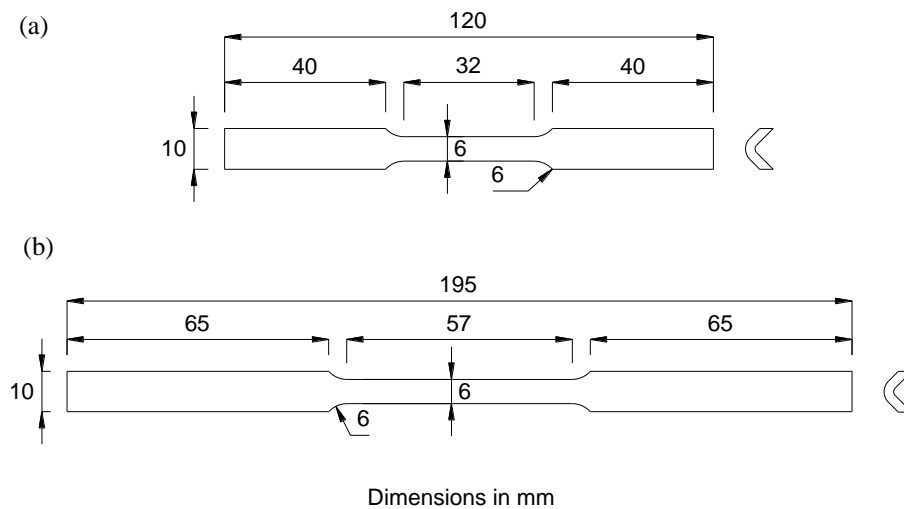


Figure 3.5: Corner coupon dimensions

The corner coupons were tested in pairs in order to avoid the introduction of unwanted bending resulting from flattening the gripped ends. Two coupons extracted from the same type of channel were tested together, with a square bar in between the gripped ends of the coupons. The square bar had two opposite corners machined in order to improve contact with the inner side of the coupons. Figure 3.6 illustrates the arrangement. Each pair of corner coupons was instrumented with an extensometer of either 25 mm gauge length or 50 mm gauge length,

depending on the dimensions of the coupons. In addition, a 5 mm strain gauge was fitted on the outer side of each coupon. Figure 3.7 shows the corner coupons before and during testing.

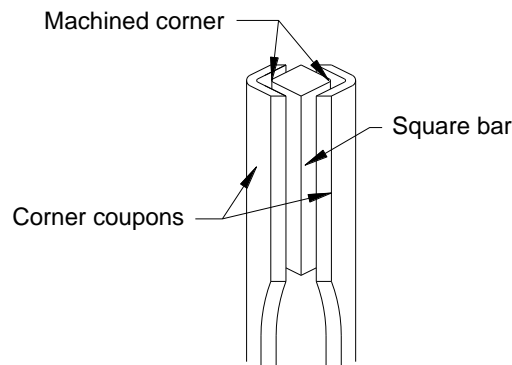


Figure 3.6: Corner coupons and square block arrangement

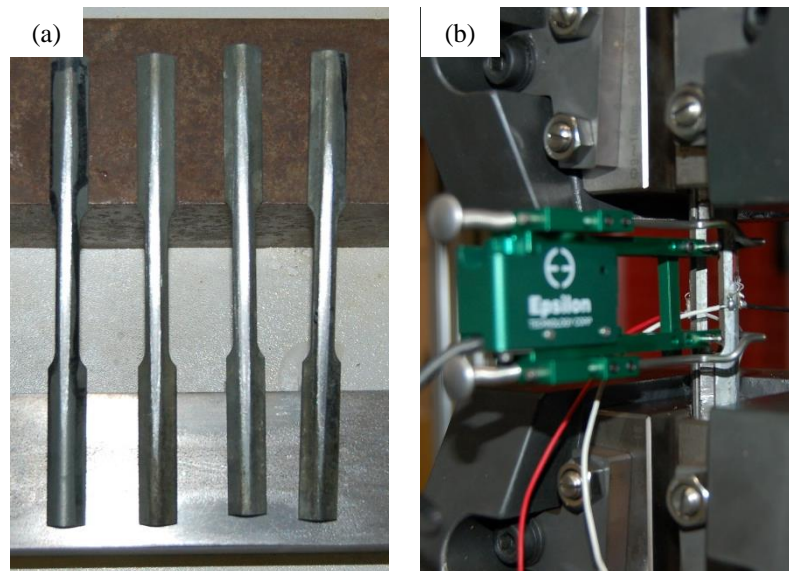


Figure 3.7: a) Corner coupons before testing, b) Pair of corner coupons during testing

To determine the cross-sectional area of the corner coupons, it was assumed that the sides of the coupon were parallel along the gauge length, an assumption which agreed with observation. The width of the coupon at the grip end and along the gauge length was measured with a micrometre with a precision of ± 0.002 mm. The end section of the coupon was then photographed using the reverse lens technique, whereby special care was taken to place the coupon as perpendicular to the camera as possible to avoid distortion of the cross-section. Next, the photograph was imported into AutoCAD® software and scaled using the measurement taken at the grip end of the coupon, as illustrated in Figure 3.8. Finally, using the width of the cross-section measured along the gauge length of the coupon, the cross-section of the coupon was drawn on the photograph and the area was calculated automatically by the software. The process was repeated with pictures taken from the opposite end of the coupon and the average calculated area was

used. Differences of less than 1.46 %, 2.92 %, 2.86 % and 1.10 % were observed in the calculated areas of coupons T15414, T7912, T12012 and S11012, respectively, when using photographs from opposite ends. Table 3.2 lists the measured area obtained for each corner coupon.

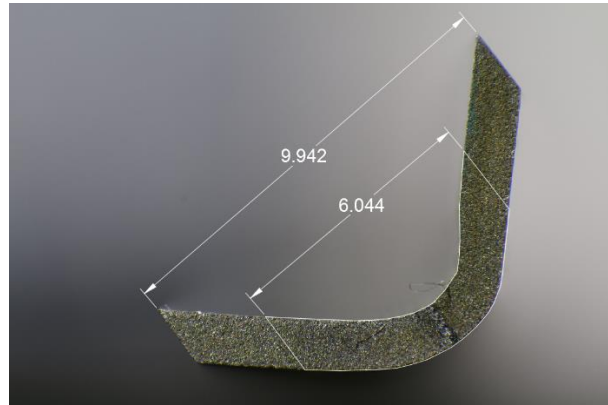


Figure 3.8: Photograph of the cross-section of corner coupon T10412-a

Table 3.2: Measured area of corner coupons

Component section	Coupon	A (mm ²)
T15414	a	10.6978
T15414	b	10.6546
T7912	a	8.7997
T7912	b	8.7777
T12012	a	7.7140
T12012	b	7.5662
S11012	a	7.6751
S11012	b	7.6263

Readings from the extensometer were used to obtain the average stress-strain curve of each pair of coupons, whereas the readings from the strain gauges were used to calculate the Young's modulus.

3.3.3 Coupon test procedure and results

All coupons were tested following the specifications given in the standard (CEN, 2009b). The tests were performed in a 300 kN Shimadzu AGS-X universal testing machine employed in displacement control mode. A displacement rate of 2 mm/min was used for the tensile coupons extracted from sections P20024, T15414 and T7912, while for the tensile coupons extracted from sections T12012 and S11012 the displacement rate was reduced to 1 mm/min.

Each test was halted for 2 min at regular intervals, with the first pause imposed when yielding was first observed in the coupon. This allowed the load to settle down to 'static' values and eliminated strain rate effects. The 'dynamic' stress-strain curve obtained from the readings,

together with the magnitude of the drop in stress when halting the test, were then used to generate a *static* stress-strain curve, from which the material properties were derived. It is worth noting that the stresses and strains obtained from the tests correspond to ‘*engineering*’ values. Unlike the **true** stress and **true** strain values, they did not consider the reduction of the cross-section as the coupons were strained and its effect on the stress, while strains were calculated based on the original undeformed gauge length. Figure 3.9 shows the stress-strain curve of one of the flat coupons taken from channel T15414. The figure also includes the *static true* stress-strain curve, which was used to define the material properties in a numerical Abaqus model. The stress-strain curves of all coupons are included in Appendix A.

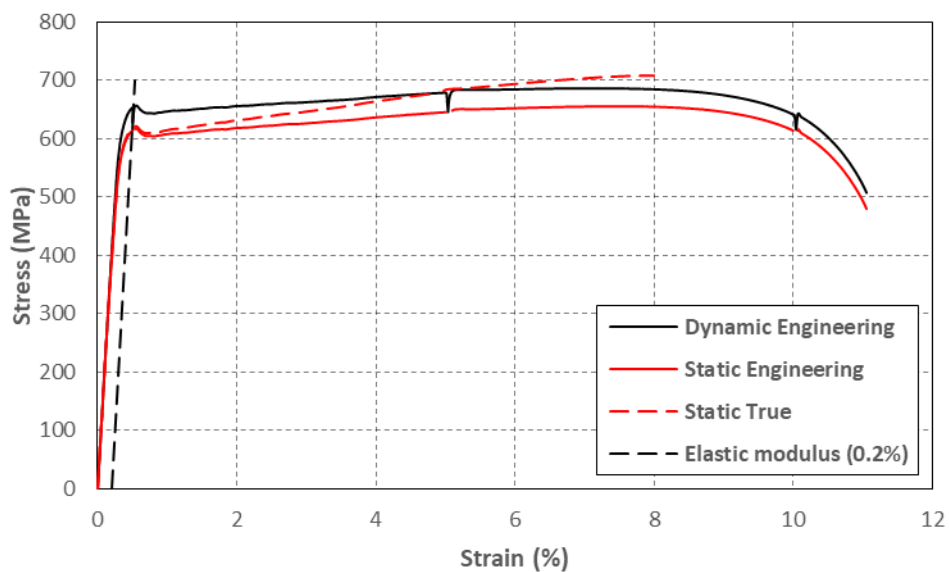


Figure 3.9: T15414-a Flat coupon test results

Table 3.3 lists the engineering (static) values of the 0.2 % proof stress ($\sigma_{0.2\%}$), the ultimate tensile strength (σ_u) and the elongation after fracture (ϵ_f) obtained for each coupon, as well as the average values over twin coupons. For the corner coupons extracted from sections P20024, T15414 and T7912 the elongation at fracture was based on a gauge length of 25 mm, while for the rest of corner coupons and all of the flat coupons this was based on a gauge length of 50 mm.

Table 3.3: Material properties of tensile coupons

Type	Section	Coupon	E (GPa)		$\sigma_{0.2\%}$ (MPa)		σ_u (MPa)		ϵ_f (%)	
			Ind.	Avg.	Ind.	Avg.	Ind.	Avg.	Ind.	Avg.
Flat	P20024	a	203	197	425	428	464	465	-	17
Flat	P20024	b	191		430		466			
Flat	T15414	a	213	214	617	604	656	647	11	12
Flat	T15414	b	215		591		637			
Flat	T7912	a	200	198	430	411	480	483	14	15
Flat	T7912	b	195		391		485			
Flat	T12012	a	190	192	244	242	319	320	30	31
Flat	T12012	b	194		240		321			
Flat	S11012	a	197	198	275	277	356	357	28	28
Flat	S11012	b	198		279		357			
Corner	T15414	a	214	222	-	604	-	676	-	11
Corner	T15414	b	230		-		-			
Corner	T7912	a	192	199	-	462	-	522	-	18
Corner	T7912	b	206		-		-			
Corner	T12012	a	237	235	-	309	-	353	-	16
Corner	T12012	b	234		-		-			
Corner	S11012	a	276	258	-	344	-	384	-	12
Corner	S11012	b	239		-		-			

The table shows that for the coupons taken from sections P20024, T15414 and T7912, the grade of steel used to fabricate the sections was at least S450, as specified by the supplier. In the case of sections T15414, the 0.2 % proof stress was found to be considerably larger than the minimum specified, with an average 0.2 % proof stress of over 600 MPa for the flat coupons. For the coupons belonging to sections T12012 and S11012, it was concluded that the sections were most likely fabricated using steel grades DX52D and DX53D, with nominal yield strengths of 300 MPa and 260 MPa, respectively, as specified by (CEN, 1995). It is important to note that although the values of the 0.2 % proof stresses listed in the table are in some cases lower than the nominally specified values, the values listed in the table correspond to the *static*, not the *dynamic*, 0.2 % proof stresses. The dynamic values (with strain rates within the limits set by the standards) are the ones routinely used and reported in practice as the nominal values.

The results obtained from the tensile coupons also showed the effect of cold-working on the mechanical properties of the coupons. As an example, Figure 3.10 shows the stress-strain curve obtained from the flat and corner coupons extracted from section T12012. The figure shows that the corner coupon displayed increases in the yield stress and the ultimate strength of 28 % and 10 %, respectively, and a reduction of the ductility by almost half with respect to the average flat coupon. Although the reduction in ductility due to cold-working is not evident in the coupons extracted from sections T15414 and T7912, this is only due to the fact that the gauge length over which the strains were recorded in the corner coupons was only half of the one used in the flat coupons. Increments in the yield stress and the ultimate strength due to cold-working similar to those presented for coupons T12012 were also observed in all the other coupons.

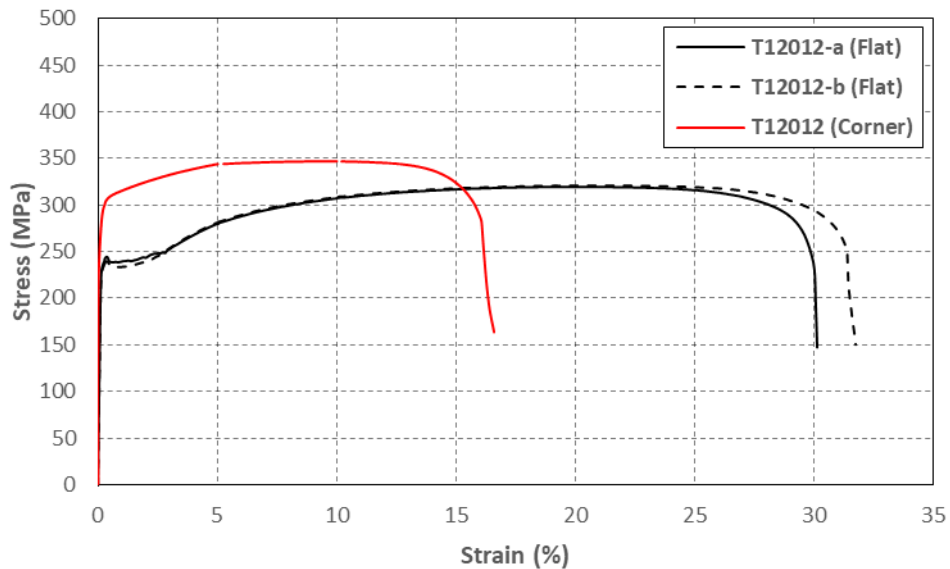


Figure 3.10: Stress-strain curve of flat and corner coupons belonging to section T12012

It is worth pointing out that the Young's modulus obtained for the corner coupons was up to 38 % larger than the expected value of 200 GPa. This was due to some minor amount of bending deformations experienced by the coupons (see Figure 3.11), which resulted from the offset between the centroid of the gripped section and that of the reduced section along the gauge length. Consequently, additional compressive bending strains were introduced into the strain gauges attached on the outer surface of the coupons. These additional strains may have slightly affected the 0.2 % proof strength reported.

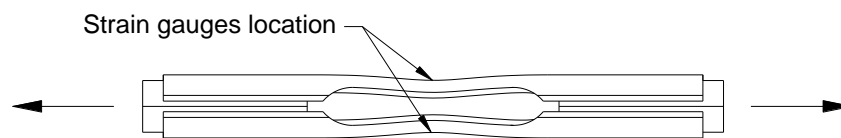


Figure 3.11: Bending deformations in corner coupons

3.4. Section design and geometry

This paragraph serves to explain the design process which led to the development of the geometries of the test specimens pictured in Figure 3.1. Four different built-up cross-sections were designed. Two of them were designed with three different connector spacings, while the other two were designed with two. Two identical columns were fabricated for each built-up geometry and connector spacing in order to increase confidence in the results obtained from the tests. All of the stub columns were designed to fail by cross-sectional instability, buckling of the

individual components between connectors, or a combination of both, but without influence of global instabilities.

Built-up geometries 1 and 2 were designed using standard sections taken from the catalogue of BW Industries, a UK cold-formed steel manufacturer, in order to improve the immediate practicality of the solution.

Built-up geometries 3 and 4 were both designed using T12012 and S11012 components. Both geometries had identical nominal material properties, as well as the same connector type and spacing, but the components were arranged in different configurations. This allowed for a more direct comparison between the two different built-up geometries. Custom brake-pressed sections were used. However, the cross-sectional dimensions of the components fell within the range of geometries allowed by (CEN, 2006), in particular with respect to their width-to-thickness ratios.

The nominal cross-sectional dimensions of the components used to assemble each built-up geometry are listed in Table 3.4. The relevant symbols are illustrated in Figure 3.12.

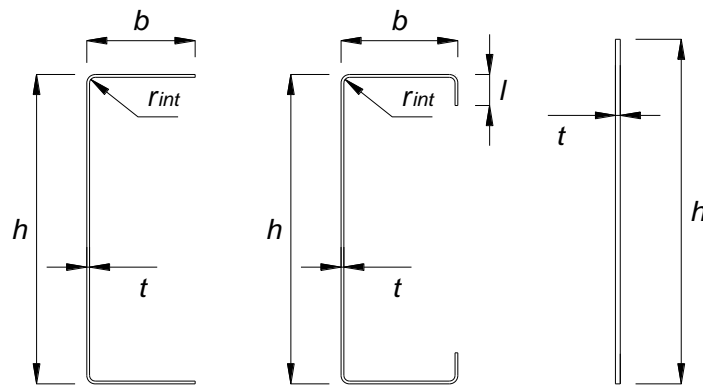


Figure 3.12: Nomenclature used to refer to the dimensions of the component sections

Table 3.4: Nominal dimensions of the component sections

Column	section	h (mm)	b (mm)	l (mm)	t (mm)	r_{int} (mm)
SC1	T15414	154	54	-	1.4	2.8
	P20024	200	-	-	2.4	-
SC2	T15414	154	54	-	1.4	2.8
	T7912	79	36	-	1.2	2.4
SC3/SC4	T12012	120	40	-	1.2	2.4
	S11012	110	50	10	1.2	2.4

The design process of the test specimens was facilitated by an elastic stability analysis of the individual components which made up the cross-section. The elastic critical buckling stress of each individual section was obtained using the CUFSM 4.05 software (Schafer, 2006), which uses the finite strip method to calculate the critical buckling stresses at different half-wave lengths. The lengths of the stub columns were chosen following the specifications given by the ‘Column Research Council’, which state that the length of the column should be larger than

three times the largest dimension of the cross-section and smaller than 20 times the least radius of gyration (Ziemian, 2010). As a result, the length chosen for columns 1, 3 and 4 was 1100 mm and the length of column 2 was 800 mm. At these lengths, all columns were expected to buckle with at least three half-waves along their length. This resulted in at least one buckling wave (in the middle) where the influence of the boundary conditions was minimal.

During the preliminary design stage, some simplifying assumptions were made. In particular, it was assumed that the individual components in the cross-section buckle independently from each other and that no interaction occurs through contact between surfaces. Furthermore, it was assumed that the connectors remain in their original position during buckling, without translating or rotating.

Built-up column 1 was designed with 2, 3 and 5 equally spaced connectors, built-up column 2 was designed with 2, 4 and 6 equally spaced connectors, and built-up columns 3 and 4 were designed with 2 and 5 equally spaced connectors.

3.4.1 Design of built-up column 1

Figure 3.13 shows the critical buckling stress vs. the buckle half-wave length (the so-called ‘signature curve’) of the components used in built-up column 1. The red curve represents local buckling of the T15414 channels, whereas the black curve represents the stresses at which the P20024 plate sections fail in global flexural buckling about their minor axis. Both the channel and the plate sections are assumed to buckle with a half-wave length equal to half the distance between connectors. For the plates, this is justified by the fact that the plates can only physically buckle outwards due to the presence of the channel webs. For the channels, on the other hand, local buckling at the connector points is restrained by the need for transverse bending in the plates. The resulting half-wave lengths are indicated by the dashed lines in Figure 3.13 for the three connector configurations.

From Figure 3.13 it can be seen that in the column with two connectors, global buckling of the plate is expected to occur at a stress lower than the local buckling stress of the channel, whereas in the column with five connectors local buckling of the channel occurs before the plate buckles. The column with three connectors was designed to trigger buckling of the channel and the plate sections at approximately the same stress level and to encourage interactive buckling effects.

The critical buckling stress of the channel is expected to be approximately the same for the columns with two and three connectors and very close to the minimum buckling stress of 63 MPa in the signature curve. In the column with five connectors, as the spacing between connectors (and consequently the buckle half-wave length) is reduced, the buckling stress of the channel is expected to increase to 95 MPa.

The critical stress of the plate is expected to increase from 38 MPa to 153 MPa as the number of connectors is increased from two to five and the spacing between connectors is reduced. The predicted buckling stresses of the components of built-up column 1 are summarized in Table 3.5.

Table 3.5: Predicted buckling stress of built-up column 1

Column	Predicted buckling stress (MPa)	
	Channel	Plate
SC1-2	63	41
SC1-3	63	73
SC1-5	95	165

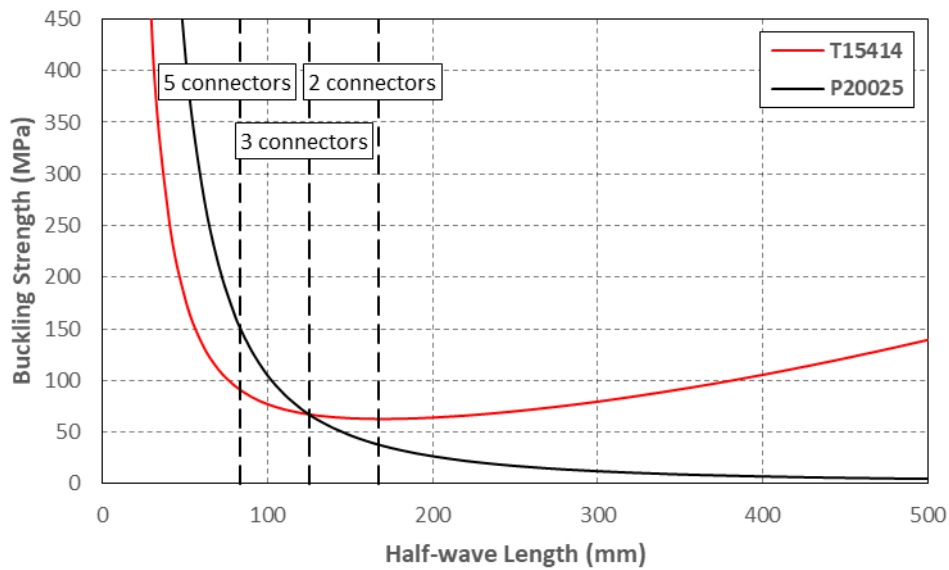


Figure 3.13: Signature curve of the components of built-up column 1

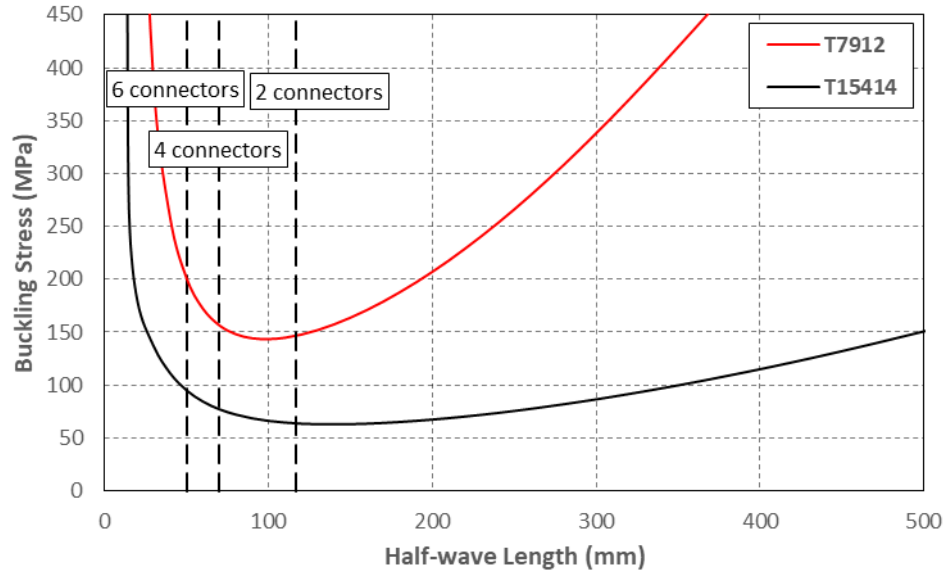
3.4.2 Design of built-up column 2

Figure 3.14 shows the signature curves of the individual components that form built-up column 2. In this case, both curves represent local buckling modes. The red curve represents the stress at which local buckling occurs in the inner channels (T7912), whereas the black curve represents the stress at which the outer channels (T15414) buckle locally. The three dashed vertical lines represent the buckling half-wave lengths of the individual components when they buckle between connectors (i.e. half of the connector spacing). This assumption is again motivated by the fact that the webs of the outer channels prevent the flanges of the inner channels from buckling outwards.

In Figure 3.14 it is seen that local buckling of the outer channels is critical over local buckling of the inner channels in all columns. The local buckling stress is expected to increase in both the inner and the outer channels as the connector spacing is decreased. Table 3.6 summarizes the predicted buckling stresses of all of the components of built-up column 2.

Table 3.6: Predicted buckling stress of built-up column 2

Column	Predicted buckling stress (MPa)	
	Int. Channel	Ext. Channel
SC2-2a	146	71
SC2-4a	156	112
SC2-6a	201	180

**Figure 3.14: Signature curve of the components of built-up column 2**

3.4.3 Design of built-up columns 3 and 4

For built-up columns 3 and 4, the signature curves of the individual components are illustrated in Figure 3.15. The red curve represents the stresses at which the lipped channels (S11012) buckle. For these channels, buckles with half-wave lengths up to 200 mm are mainly composed of the local mode, while buckles with half-wave lengths of more than 250 mm are predominantly distortional. The black curve shows the stresses at which the plain channel (T12012) buckles in a local mode.

From the figure it can be seen that the plain channels buckle before the lipped channels. For the columns with five connectors, still assuming that the connectors do not translate or rotate, both the lipped channels and the plain channels buckle with a (local) buckling pattern that accommodates one buckle (with a full wave-length) between the connectors. This buckling pattern corresponds to a buckling stress of 82 MPa in the plain channels and 125 MPa in the lipped channels. For the columns with two internal connectors, due to the increased spacing the lipped channel can accommodate two buckles between connectors, while the plain channels (possessing a longer local buckle half-wave length) still buckle with only one, as this requires the lowest stress. The predicted local buckling stresses of each component in built-up columns 3 and 4 are listed in Table 3.7.

It is also noted from Figure 3.15 that the individual lipped channels possess a distortional mode with a half-wave length of approximately 370 mm and a critical stress of 187 MPa.

Table 3.7: Predicted buckling stress of built-up columns 3 and 4

Column	Predicted buckling stress (MPa)	
	Lipped Channel	Plain Channel
SC3-2/SC4-2	125	82
SC3-5/SC4-5	125	91

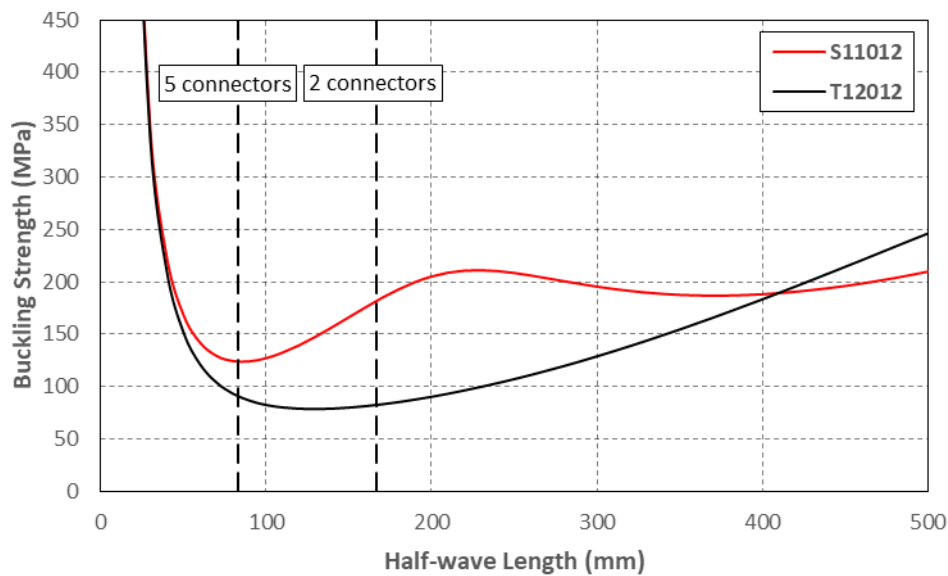


Figure 3.15: Signature curve of the components of built-up columns 3 and 4

3.5. Cross-section assembly and specimen preparation

The sections used for the tests were supplied by an external fabricator, cut to the right length with a tolerance of 2 mm and unperforated. Sections P20024, T15414 and T7912 had a zinc coating with a total nominal thickness of 0.04 mm, while for sections T12012 and S11012 the coating thickness was not specified by the manufacturer, but was determined to be 0.03 mm by measuring the thickness of the sections at each end before and after removing the zinc coating with hydrochloric acid. The preparation and assembly of the test specimens were carried out in the Heavy Structures Laboratory at The University of Sheffield, using the process described in this paragraph.

First, the cross-sectional dimensions of all individual sections were measured prior to assembly. The thickness of the sections was measured using a digital micrometre with a precision of ± 0.002 mm, while the rest of measurements were carried out using a digital Vernier caliper with a precision of ± 0.03 mm. All measurements were of the outside dimensions, as illustrated in

Figure 3.12. The measured cross-sectional dimensions of the specimens belonging to geometries 1, 2, 3 and 4 are listed in Table 3.8, Table 3.9, Table 3.10 and Table 3.11, respectively. Each listed value is the average result of several measurements taken at different locations. For the components used in built-up geometries 1 and 2 the listed values were obtained after deducting the nominal 0.04 mm zinc coating thickness, while for the components used in built-up geometries 3 and 4 they were obtained after deducting the 0.03 mm zinc coating, assuming that the coating was equally distributed on each side of the cross-sections.

Table 3.8: Measured dimensions of built-up column 1

Column	Channel				Plate		
	section	h (mm)	b (mm)	t (mm)	section	h (mm)	t (mm)
SC1-2a	T15414-1	153.96	53.90	1.452	P20024-1	199.83	2.476
	T15414-2	154.19	53.60	1.440	P20024-2	199.73	2.466
SC1-2b	T15414-3	154.09	53.83	1.444	P20024-3	199.67	2.474
	T15414-4	154.09	53.43	1.435	P20024-4	199.83	2.472
SC1-3a	T15414-5	154.19	53.73	1.441	P20024-5	199.53	2.493
	T15414-6	154.06	53.65	1.441	P20024-6	199.27	2.486
SC1-3b	T15414-7	154.13	53.41	1.429	P20024-7	199.43	2.482
	T15414-8	154.06	53.73	1.445	P20024-8	200.40	2.481
SC1-5a	T15414-9	154.13	53.58	1.437	P20024-9	200.10	2.478
	T15414-10	154.13	53.61	1.429	P20024-10	199.47	2.477
SC1-5b	T15414-11	154.09	53.35	1.417	P20024-11	198.93	2.472
	T15414-12	154.19	53.60	1.425	P20024-12	198.73	2.487
Average		154.11	53.62	1.436		199.58	2.479
St. Dev.		0.067	0.166	0.010		0.465	0.008

Table 3.9: Measured dimensions of built-up column 2

Column	Channel				Channel			
	section	h (mm)	b (mm)	t (mm)	section	h (mm)	b (mm)	t (mm)
SC2-2a	T15414-1	154.03	53.43	1.426	T7912-1	78.93	36.26	1.147
	T15414-2	154.06	53.28	1.416	T7912-2	78.99	36.25	1.172
SC2-2b	T15414-3	153.96	53.46	1.428	T7912-3	78.83	36.40	1.142
	T15414-4	153.96	53.40	1.407	T7912-4	79.13	36.30	1.176
SC2-4a	T15414-5	154.03	53.58	1.43	T7912-5	79.16	36.40	1.145
	T15414-6	153.96	53.26	1.438	T7912-6	79.09	36.46	1.169
SC2-4b	T15414-7	154.03	53.70	1.434	T7912-7	79.06	36.50	1.128
	T15414-8	154.13	53.51	1.436	T7912-8	79.13	36.46	1.166
SC2-6a	T15414-9	154.03	53.51	1.422	T7912-9	79.03	36.51	1.143
	T15414-10	154.29	53.35	1.417	T7912-10	79.06	36.41	1.172
SC2-6b	T15414-11	154.16	53.73	1.433	T7912-11	79.03	36.16	1.141
	T15414-12	154.23	53.68	1.431	T7912-12	78.99	36.30	1.171
Average		154.07	53.49	1.427		79.04	36.37	1.156
St. Dev.		0.108	0.158	0.009		0.093	0.111	0.016

Table 3.10: Measured dimensions of built-up column 3

Column	Channel				section	Channel			
	section	h (mm)	b (mm)	t (mm)		h (mm)	b (mm)	l (mm)	t (mm)
SC3-2a	T12012-1	119.61	39.97	1.117	S11012-1	110.46	49.83	9.83	1.109
	T12012-2	119.97	40.01	1.090	S11012-2	111.07	49.93	9.87	1.095
SC3-2b	T12012-3	119.82	40.07	1.102	S11012-3	110.75	49.79	9.83	1.107
	T12012-4	119.84	39.99	1.097	S11012-4	110.91	49.92	9.88	1.090
SC3-5a	T12012-5	119.96	40.03	1.118	S11012-5	110.80	49.97	9.79	1.098
	T12012-6	119.81	40.01	1.127	S11012-6	110.44	49.93	9.89	1.119
SC3-5b	T12012-7	119.59	39.99	1.124	S11012-7	110.07	49.90	9.87	1.120
	T12012-8	119.72	39.95	1.095	S11012-8	110.85	49.82	9.85	1.098
Average		119.79	40.00	1.109		110.67	49.88	9.85	1.104
St. Dev.		0.144	0.035	0.014		0.325	0.064	0.033	0.011

Table 3.11: Measured dimensions of built-up column 4

Column	Channel				section	Channel			
	section	h (mm)	b (mm)	t (mm)		h (mm)	b (mm)	l (mm)	t (mm)
SC4-2a	T12012-9	119.70	39.94	1.101	S11012-9	111.07	49.98	9.76	1.094
	T12012-10	119.90	39.98	1.089	S11012-10	111.13	49.91	9.86	1.088
SC4-2b	T12012-11	119.90	39.97	1.085	S11012-11	111.08	49.88	9.83	1.086
	T12012-12	119.83	39.97	1.096	S11012-12	110.89	49.83	9.87	1.097
SC4-5a	T12012-13	119.71	40.01	1.096	S11012-13	110.15	49.89	9.88	1.120
	T12012-14	119.89	39.98	1.096	S11012-14	111.11	49.86	9.88	1.103
SC4-5b	T12012-15	119.77	40.00	1.118	S11012-15	110.79	49.82	9.78	1.115
	T12012-16	119.67	40.05	1.120	S11012-16	110.87	49.92	9.84	1.092
Average		119.80	39.99	1.100		110.89	49.89	9.84	1.099
St. Dev.		0.097	0.034	0.013		0.325	0.050	0.046	0.012

As a next step in the preparation of the specimens, the zinc coating was removed at the ends of the specimens in order to improve the bond of the resin used to attach the endplates to the columns. For the specimens with geometries 1 and 2, this was achieved by grinding the surface of the sections over a length of 30 mm at both ends. However, since this process was time consuming and due to the difficulty in removing the zinc with the grinder in certain regions, such as the web-flange junction on the interior side of the channels, it was decided for the specimens with geometries 3 and 4 to remove the zinc using hydrochloric acid instead.

The specimens were built up using two different types of connectors. Geometries 1 and 2 were assembled using M6 bolts, while geometries 3 and 4 were assembled using M5.5 self-drilling sheet metal screws. In order to assemble geometries 1 and 2, bolt holes with a diameter of 6.25 mm were drilled in the appropriate locations. In the columns of geometry 1, the holes were first marked and drilled in the flat plate sections at the locations shown in Figure 3.16a. For the columns of geometry 2, the holes were first marked and drilled in the outer channels at the locations illustrated in Figure 3.16b. These sections were then used as templates to drill the holes in the rest of the sections after positioning all sections in their built-up configurations and securing them with clamps. With the clamps still in place, the sections were bolted together

using a torque wrench, applying a torque of 10 Nm. This permitted an accurate assembly of the sections, avoiding any major misalignment of the individual components at the end sections. Finally, the clamps were removed.

A similar procedure was followed in order to assemble the specimens with geometries 3 and 4. First, the locations of the screws were marked in one of the connecting components and small diameter holes were drilled in order to facilitate the installation of the screws and improve accuracy. Next, the sections were positioned in their built-up configuration and secured with clamps. Finally, the sections were screwed together and the clamps were removed. The locations of the screws are illustrated in Figure 3.18a and Figure 3.18b for geometries 3 and 4, respectively.

Figure 3.17a-d show some of the specimens with geometries 1 and 2 during and after the assembly process, while Figure 3.19a-c show the specimens with geometries 3 and 4.

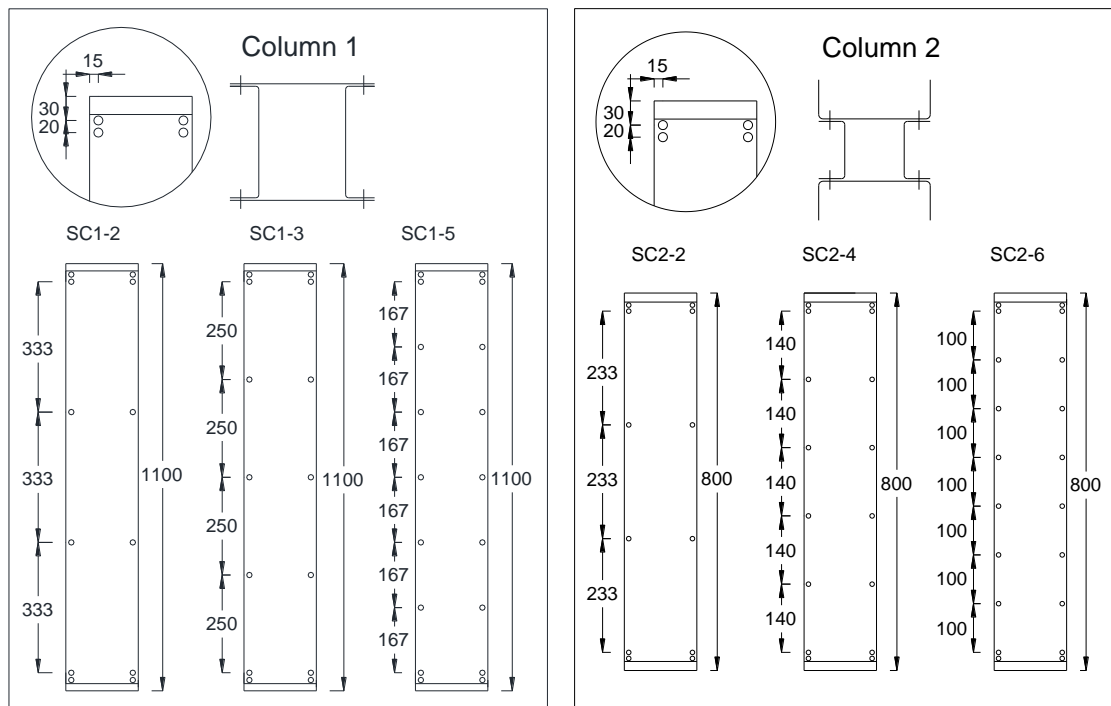


Figure 3.16: Location of connectors in a) geometry 1 and b) geometry 2



Figure 3.17: Images of built-up columns 1 and 2 during and after assembly

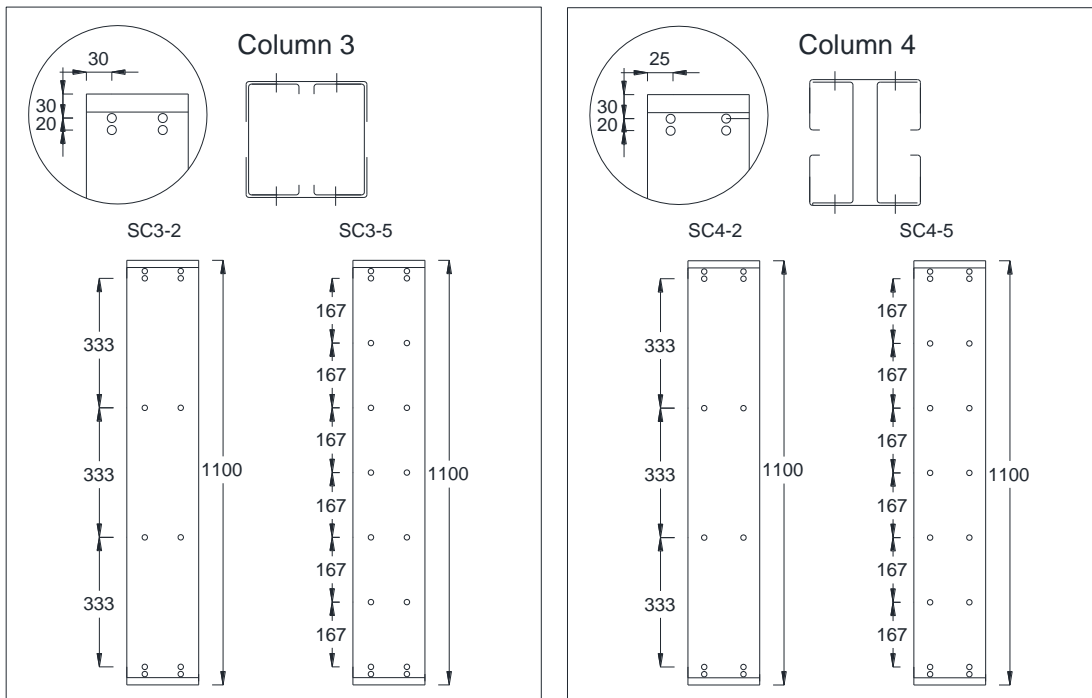


Figure 3.18: Location of connectors in a) geometry 3 and b) geometry 4



Figure 3.19: Images of built-up columns 3 and 4 during and after assembly

Once the assembly process was completed, both ends of each column were manually filed to correct the difference in length of the individual components. Much care was put into this process to ensure that a completely flush bearing surface was obtained between the specimen ends and the end plates.

Endplates with dimensions of $250 \times 300 \text{ mm}^2$ and a thickness of 20 mm were attached to both ends of the built-up columns with geometries 1 and 2, while endplates with dimensions of $200 \times 200 \text{ mm}^2$ and a thickness of 20 mm were attached to the ends of the built-up columns with geometries 3 and 4. It was decided not to weld the endplates to the columns because of the limited wall thickness of the sections and the concern that the welding process would introduce considerable distortions into the sections. Instead, a Sikadur 31 FC Normal 2-part thixotropic epoxy resin was used to attach the endplates to the columns, which in addition to a double row of connectors placed at each end of the columns and manually filing the ends, provided an extra means to ensure a uniform introduction of the load into all components. In order to reduce the amount of resin used for each column, a mould following the shape of the cross-section was prepared on the surface of the endplates using modelling clay and strips of cardboard, as depicted in Figure 3.20. The mould was then filled with the epoxy resin and the columns were placed into the mould. The height of the epoxy layer was 20 mm. Based on the specifications provided by the manufacturer (in particular, a bond strength of 18 MPa and an elastic modulus of 6.6 GPa), this was sufficient to transfer a load of 350 kN in shear through the interface with

the steel column. The resin was left to set for three days while applying a load on the column of 100 N before repeating the same process at the other end of the column.

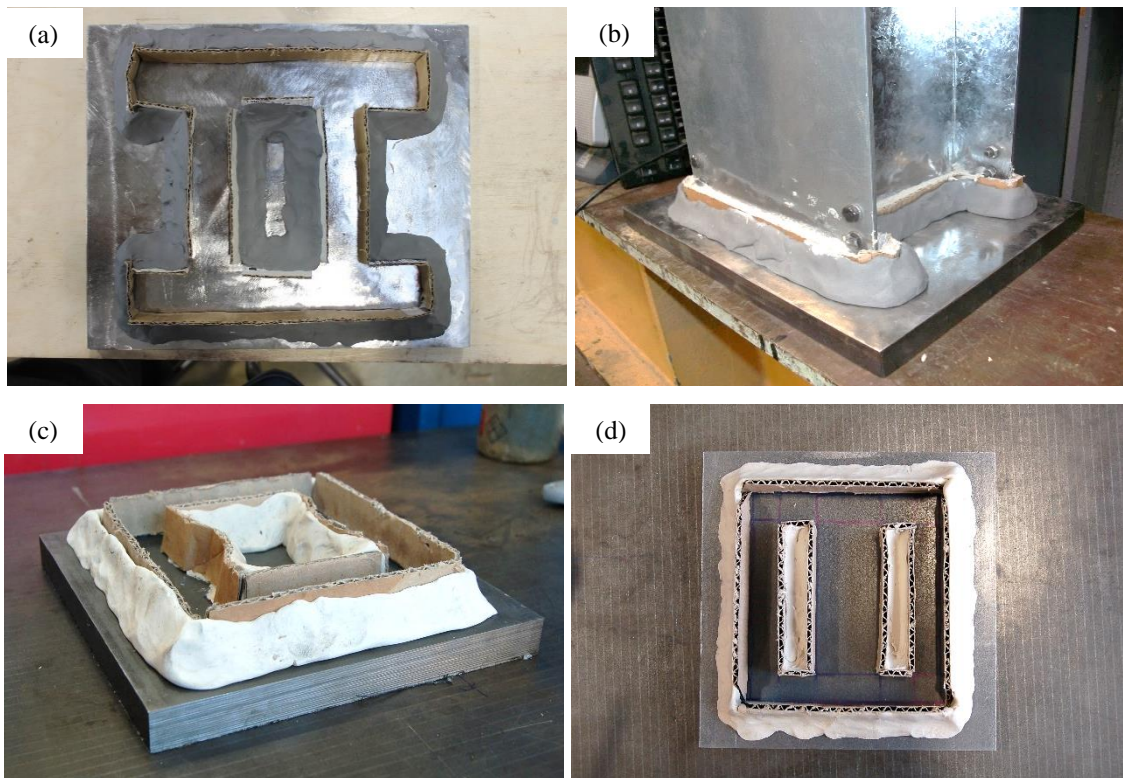


Figure 3.20: a), c) and d) Mould made with modelling clay and cardboard, b) Column set in resin

3.6. Imperfection Measurements

Imperfections may have a significant influence on the stability of thin-walled structural members, particularly when coupled instabilities are involved. The imperfections of all test specimens were therefore recorded before testing. The measurements were performed after the built-up columns were assembled into their final configurations, as joining the single sections together might somewhat modify their geometric imperfections.

3.6.1 Imperfection measuring rig

The imperfections were measured by moving a laser displacement sensor along different longitudinal lines on each face of the built-up column. The equipment used to carry out the measurements consisted of a steel table with a very high degree of flatness, a traverse system powered by electric motors travelling at a pre-determined constant speed and a laser displacement sensor.

The flat table was made of cast iron with dimensions of 1500x920 mm² and was considered to be grade 3 according to (BSI, 2008), meaning that it provided a flat surface with a deviation

from flatness of less than 0.06 mm. A traverse system consisting of an aluminium frame with a trolley, high-precision guiding bars and two electric motors was placed on top of the flat table as illustrated in Figure 3.21a and Figure 3.21b. The frame had dimensions of 2400x600 mm² and rested on four supports, adjustable in height by tightening or loosening a screw in each support. The two electric motors allowed movement of the laser sensor, attached to a trolley, along two orthogonal axes. Movement in the vertical direction was controlled manually by turning a crank handle located on the trolley (Figure 3.21c). This permitted the laser sensor to be positioned within measuring range from the surface.

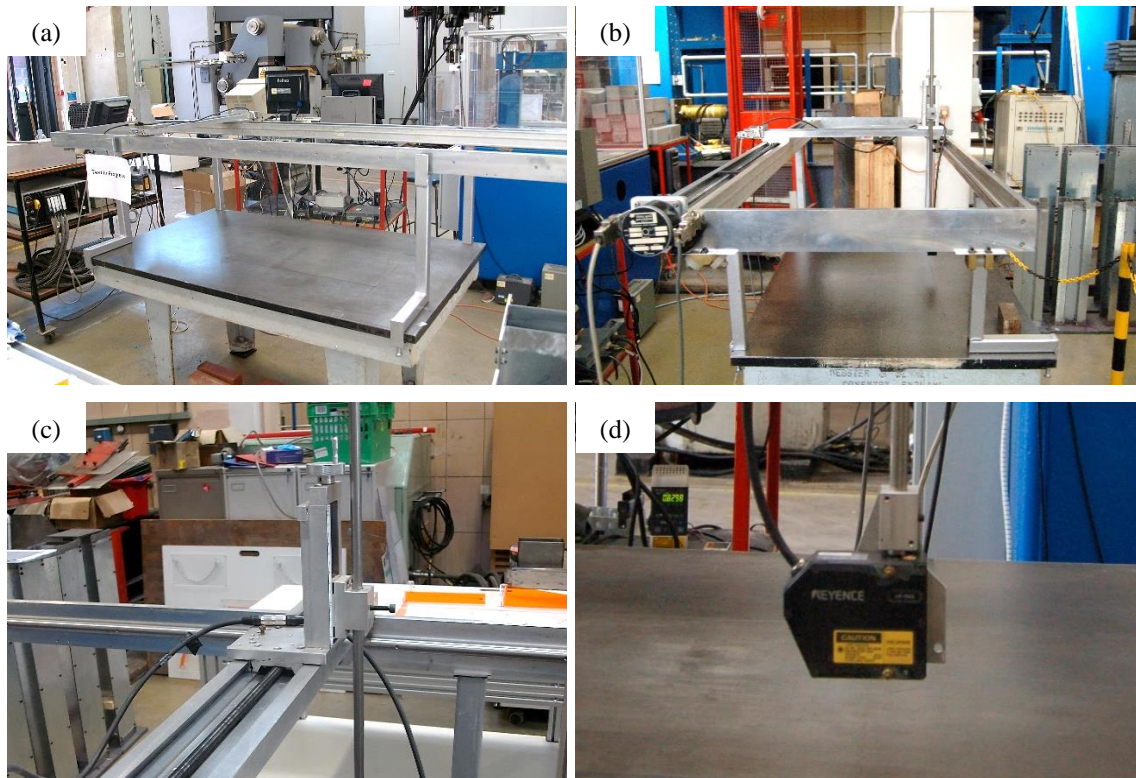


Figure 3.21: a) and b) Traverse system for measuring imperfections, c) Trolley, d) Laser sensor

The laser displacement sensor used for the measurement of the geometric imperfections was a Keyence LK-G82 sensor with a beam spot diameter of 70 μm , a measurement range between 65 and 95 mm and an accuracy of ± 0.0075 mm. This type of sensor uses triangulation, in which the distance to the target surface is measured by projecting the laser beam onto the surface and determining the position of the beam which is reflected back into the laser sensor. A picture of the laser sensor is shown in Figure 3.21d.

3.6.2 Measuring process

The out-of-plane imperfection measurements were used to determine representative imperfections of the components. For both the plain and the lipped channels, the imperfections of interest included the out-of-plane imperfections along the web (δ_{web}) and the out-of-plane

imperfections along the flange edge (the ‘flange edge’ either indicates the free edge in the case of a plain channel or the flange-lip junction in the case of a lipped channel). In addition, for lipped channels the out-of-plane imperfections along the centre line of the flange ($\delta_{flanges,L}$) were also considered.

The imperfections of the columns with geometry 1 were measured along three longitudinal lines on each face of the column, as illustrated in Figure 3.22. The readings along lines 2 and 5, as well as 8 and 11 were taken along the centre lines of the plates and the webs of the channels, respectively. The readings along lines 7, 9, 10 and 12 were taken 12 mm away from the inner flange surface of the channels, while the readings along lines 1, 3, 4 and 6 were taken 6 mm away from the edges of the plates. The flat plate sections in built-up column 1 were expected to buckle in a global flexural mode between connectors and the corresponding imperfections were captured by readings along lines 1, 2 and 3, and 4, 5 and 6. A representative magnitude of the imperfections of each plate section of the built-up geometry was computed using Eq. (3.1) and Eq. (3.2).

$$\delta_{plate}(x) = (Line_1 + Line_2 + Line_3) / 3 \quad (3.1)$$

$$\delta_{plate}(x) = (Line_4 + Line_5 + Line_6) / 3 \quad (3.2)$$

Local buckling of the channel sections was expected to be mainly affected by imperfections in the web, as this constituted the most slender part of the cross-section. Readings along lines 7, 8 and 9, as well as lines 10, 11 and 12 were therefore taken to capture the local imperfections of the two channels using Eq. (3.3) and Eq. (3.4).

$$\delta_{web}(x) = Line_8 - (Line_7 + Line_9) / 2 \quad (3.3)$$

$$\delta_{web}(x) = Line_11 - (Line_10 + Line_12) / 2 \quad (3.4)$$

The imperfections of the flanges, however, were not measured as there was not enough space within the channels to place the laser sensor at an appropriate distance from the flanges. The process of measuring the imperfections of the columns with geometry 1 is illustrated in Figure 3.23.

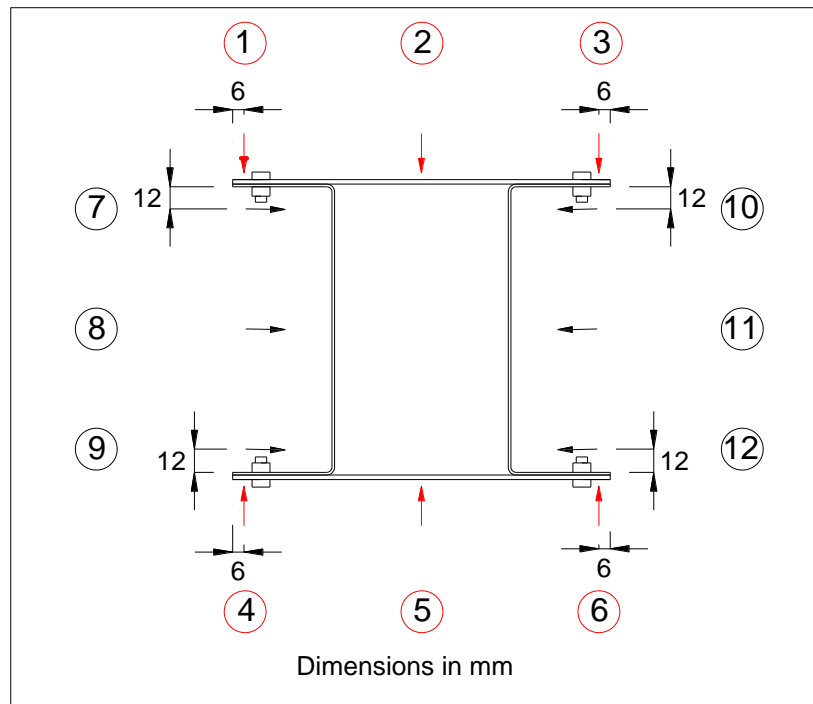


Figure 3.22: Location of the imperfection measurements in built-up column 1



Figure 3.23: Measurement of the imperfections of built-up column 1

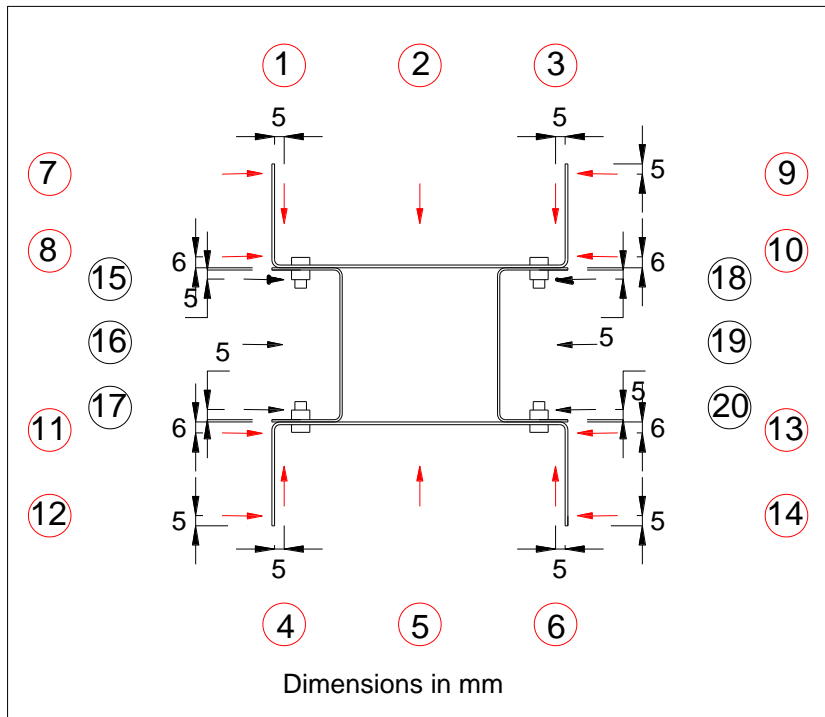


Figure 3.24: Location of the imperfection measurements in built-up column 2



Figure 3.25: Measurement of the imperfections of built-up column 2

In the columns with geometry 2, the imperfections were measured along twenty different longitudinal lines, as illustrated in Figure 3.24. The imperfections of the web of each channel were measured along three lines, with lines 2, 5, 16 and 19 located at the centre of the web and lines 1, 3, 4 and 6, as well as 15, 17, 18 and 20 located 5 mm away from the inner flange surfaces. These readings were used to compute δ_{web} for each component of built-up geometry 2 using Eqs. (3.5)-(3.8).

$$\delta_{web}(x) = Line_2 - (Line_1 + Line_3) / 2 \tag{3.5}$$

$$\delta_{web}(x) = Line_5 - (Line_4 + Line_6) / 2 \quad (3.6)$$

$$\delta_{web}(x) = Line_16 - (Line_15 + Line_17) / 2 \quad (3.7)$$

$$\delta_{web}(x) = Line_19 - (Line_18 + Line_20) / 2 \quad (3.8)$$

The imperfections of the flanges of the outer channels were also measured along two lines. The readings along lines 7, 9, 12 and 14 were located 5 mm away from the flange tips, while the readings along lines 8, 10, 11 and 13 were located 6 mm away from the outside surface of the web. The readings were mainly intended to capture imperfections in the shape of the local buckling pattern, and they were used to compute $\delta_{flanges}$ in the outer channels using Eqs. (3.9)-(3.12).

$$\delta_{flanges}(x) = Line_7 - Line_8 \quad (3.9)$$

$$\delta_{flanges}(x) = Line_9 - Line_10 \quad (3.10)$$

$$\delta_{flanges}(x) = Line_12 - Line_11 \quad (3.11)$$

$$\delta_{flanges}(x) = Line_14 - Line_13 \quad (3.12)$$

Readings of the flange imperfections of the inner channels were not taken because of access restrictions for the sensor. Figure 3.25 illustrates the imperfection measurement process for columns with geometry 2.

The imperfections in columns with geometry 3 were recorded along fourteen different longitudinal lines after the specimens were assembled. The readings along lines 2 and 5 were recorded along the centre lines of the plain channel webs, while the readings along lines 1, 3, 4 and 6, as well as lines 7, 9, 12 and 14 were recorded 6 mm away from the outer surfaces. The readings along lines 8, 10, 11 and 13 were taken 5 mm away from the tips of the plain channels. For the plain channels δ_{web} and $\delta_{flanges}$ were calculated using Eqs. (3.13)-(3.18).

$$\delta_{web}(x) = Line_2 - (Line_1 + Line_3) / 2 \quad (3.13)$$

$$\delta_{web}(x) = Line_5 - (Line_4 + Line_6) / 2 \quad (3.14)$$

$$\delta_{flanges}(x) = Line_8 - Line_7 \quad (3.15)$$

$$\delta_{flanges}(x) = Line_10 - Line_9 \quad (3.16)$$

$$\delta_{flanges}(x) = Line_11 - Line_12 \quad (3.17)$$

$$\delta_{flanges}(x) = Line_13 - Line_14 \quad (3.18)$$

Due to the closed configuration of the sections, the imperfections in the lipped channels could not be measured after the specimens were assembled. Therefore, they were recorded prior to assembly. Only the web imperfections of the lipped channels were considered to be important, as the web was the most slender part of the channel, and readings were taken at the same locations as for the plain channel webs, as illustrated in Figure 3.27. For these channels, δ_{web} was calculated as:

$$\delta_{web}(x) = Line_16 - (Line_15 + Line_17) / 2 \tag{3.19}$$

Figure 3.28 illustrates the process of measuring the imperfections of columns with geometry 3.

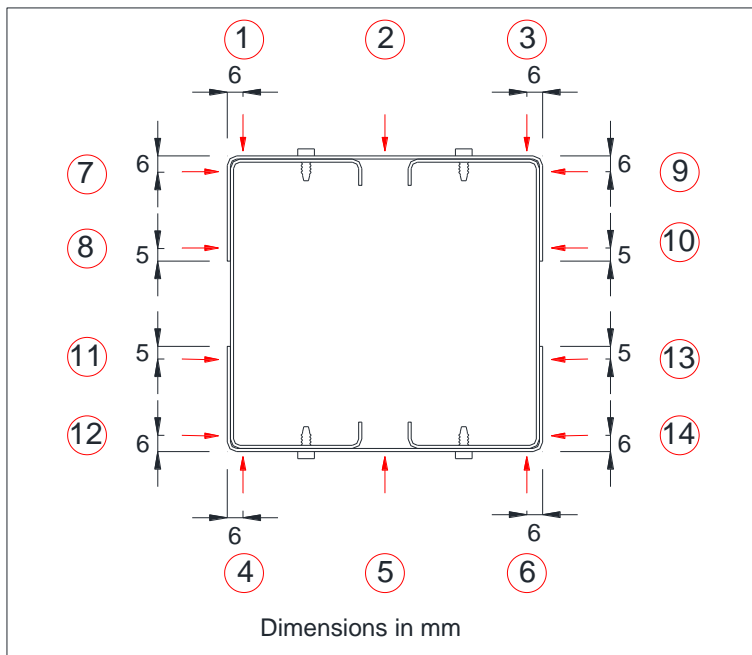


Figure 3.26: Location of the imperfection measurements in built-up column 3

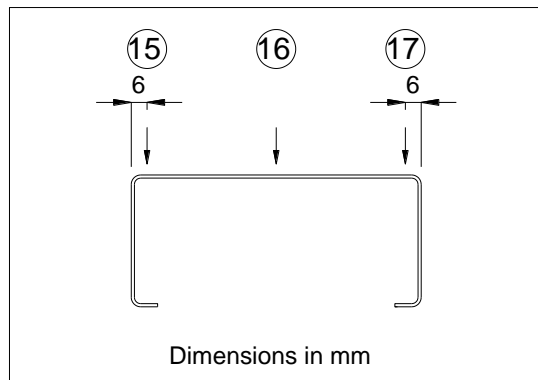


Figure 3.27: Location of the imperfection measurements in the lipped channels of built-up column 3

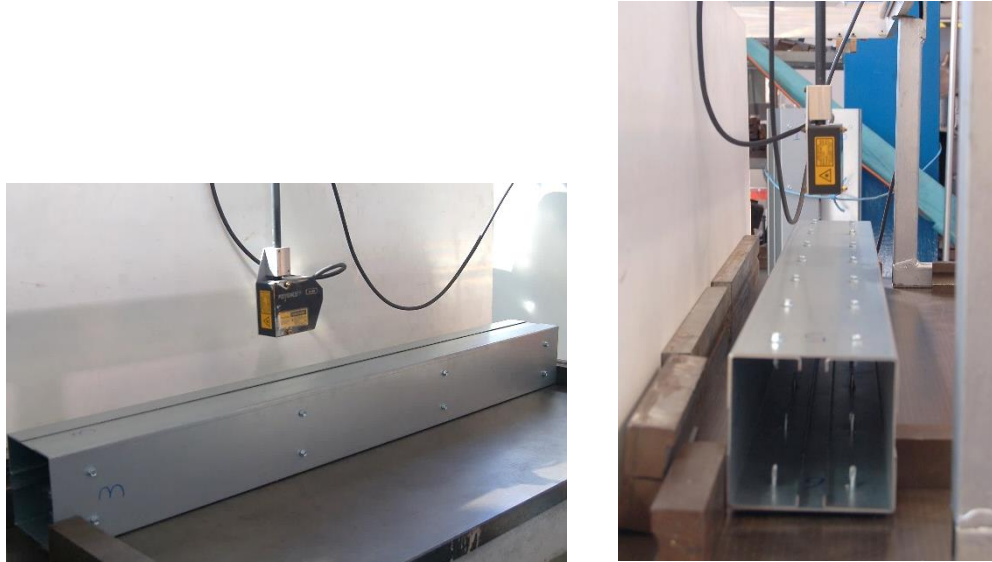


Figure 3.28: Measurement of the imperfections of built-up column 3

In the columns with geometry 4 the imperfections were recorded along three different lines on the webs and the flanges of the lipped channels, as illustrated in Figure 3.29. The readings aimed to capture the imperfections relevant to local and distortional buckling of these channels. Readings along lines 2 and 5, as well as 8, 11, 14 and 17 were recorded along the centre lines of the web and the flanges of the lipped channels, respectively, while the rest of readings were taken 6 mm away from the outer surface of the adjacent plate element. For the lipped channels, readings along lines 1-6, were used to calculate δ_{web} using Eq. (3.20) and Eq. (3.21), while readings along lines 7-18 were used to calculate $\delta_{flanges}$ using Eq. (3.22)-(3.25). In addition, readings along lines 7-18 were also used to calculate representative local imperfections in the flanges of the lipped channels ($\delta_{flanges,L}$) using Eqs. (3.26)-(3.29).

$$\delta_{web}(x) = Line_2 - (Line_1 + Line_3) / 2 \quad (3.20)$$

$$\delta_{web}(x) = Line_5 - (Line_4 + Line_6) / 2 \quad (3.21)$$

$$\delta_{flanges}(x) = Line_8 - Line_7 \quad (3.22)$$

$$\delta_{flanges}(x) = Line_10 - Line_9 \quad (3.23)$$

$$\delta_{flanges}(x) = Line_11 - Line_12 \quad (3.24)$$

$$\delta_{flanges}(x) = Line_13 - Line_14 \quad (3.25)$$

$$\delta_{web}(x) = Line_8 - (Line_7 + Line_9) / 2 \quad (3.26)$$

$$\delta_{web}(x) = Line_11 - (Line_10 + Line_12) / 2 \quad (3.27)$$

$$\delta_{web}(x) = Line_14 - (Line_13 + Line_15) / 2 \quad (3.28)$$

$$\delta_{web}(x) = Line_17 - (Line_16 + Line_18) / 2 \quad (3.29)$$

The imperfections of the plain channels could again not be recorded after the specimens were assembled and were therefore recorded before assembly. Only the web imperfections of the plain channels were measured (Figure 3.30), as the web constituted the most slender element, and the readings were taken at the same locations as for the lipped channels webs. For these components, δ_{web} was calculated as:

$$\delta_{web}(x) = Line_20 - (Line_19 + Line_21) / 2 \quad (3.30)$$

The process of measuring the imperfections of the columns with geometry 4 is illustrated in Figure 3.31.

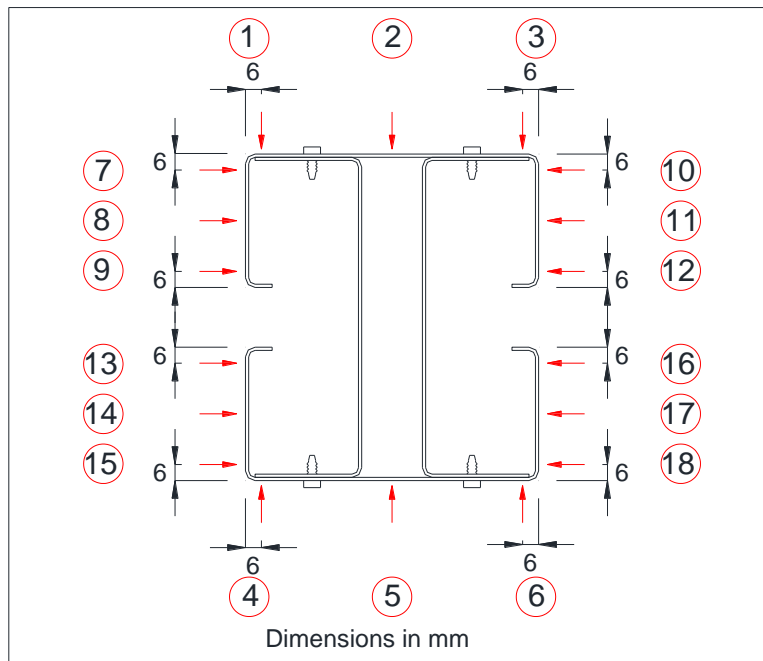


Figure 3.29: Location of the imperfection measurements in built-up column 4

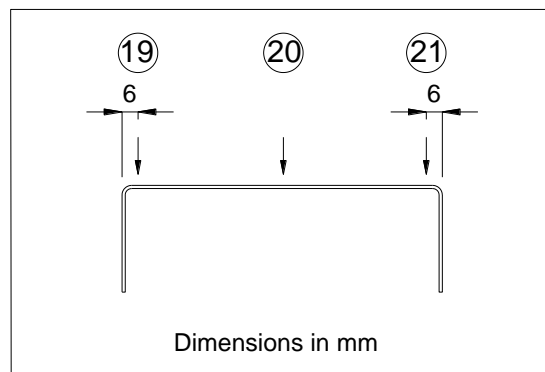


Figure 3.30: Location of the imperfection measurements in the plain channels of built-up column 4

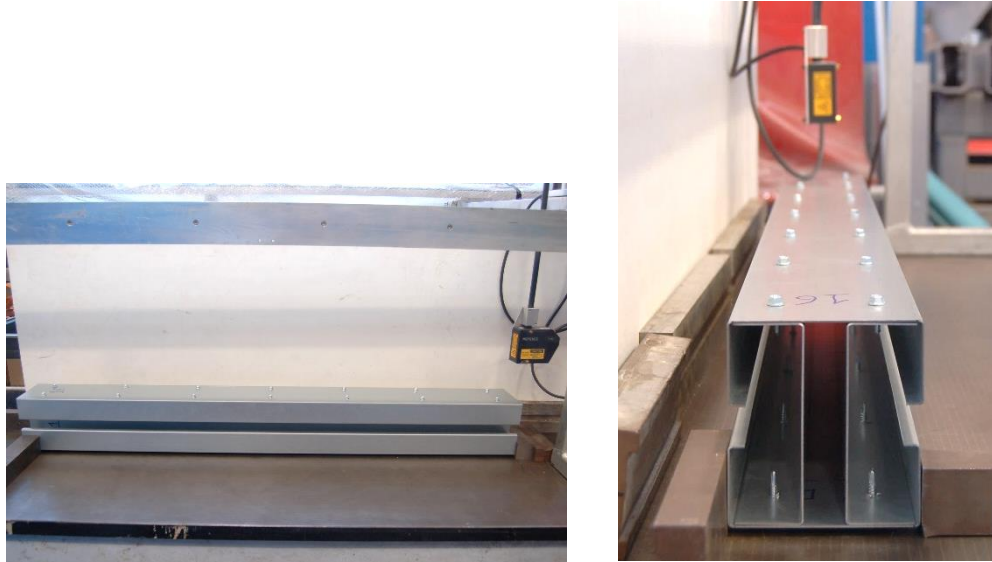


Figure 3.31: Measurement of the imperfections of built-up column 4

In order to measure the imperfections, the electric motors moved the laser sensor along longitudinal lines at a constant speed of 5 mm/s, while readings were taken with a sampling rate of 50 Hz for built-up columns 1 and 2, resulting in a reading every 0.1 mm. It was subsequently concluded that taking readings at such short intervals was not strictly necessary to obtain a representative imperfection profile of the sections. Therefore, for built-up columns 3 and 4 the sampling rate was reduced to 5 Hz, resulting in readings every 1 mm. Readings were continued for approximately 100 mm before and after the laser beam made contact with the surface to be measured. When the laser beam was not in contact with the surface of the columns, its readings indicated 'out of range'. This made it possible to identify the end points of the column in the output and consequently the location of each reading along the column length. Measurements of the nominally flat table, without a test specimen present, were used to correct for the out-of-straightness of the guiding bars along which the laser sensor was moved. Therefore, the accuracy of the measurements was determined by the flatness of the table and of the order of 0.06 mm.

Once the imperfections were recorded, the readings over the last 20 mm at each end of the column were discarded as these corresponded to the areas where the resin was applied. For each measured plate element (web, flange, etc.), the recorded imperfections were adjusted so that at the four corners of each plate element the value of the imperfection was zero. This was achieved by presenting the imperfections relative to an ideal plane which intersected the measured plate element at three of the corners, and forcing the imperfection at the fourth corner to be zero by applying a slight twist to the reference plane. While this process eliminated the global twist imperfection in each plate, this imperfection was not thought to be critical in stub columns failing by local/distortional instability. An assumption also had to be made on how to assemble the data measured on each plate individually into a complete 3D picture of the specimen

imperfections. It was therefore assumed that at each end of the specimen the respective plate elements in the built-up cross-section were perfectly orthogonal to each other.

3.6.3 Imperfection measurement results

Figures 3.32-3.34 show typical out-of-plane imperfections recorded from the components of the test specimens (after the measurements were adjusted using the process described above). In the figures, the coordinate along the length of the column is normalized by dividing it by the length of the column (after deducting the 20 mm at each end of the column), while the vertical dashed black lines indicate the location of the connectors along the columns. Figure 3.32 shows the imperfections of the web of channel T15414-2 of specimen SC1-2a, which was connected to the adjacent components through its flanges. Figure 3.33, on the other hand, shows the imperfections recorded along the web of channel S11012-9 of specimen SC4-2a, which was connected to the adjacent components directly through the web. In this channel, the location of the connectors is clearly evidenced by the imperfection shape. Figure 3.34 also illustrates the imperfections of one of the flanges of channel T15414-2 of specimen SC2. It is worth noting that the imperfections measured along the corner (Line 11) are smaller than the ones measured along the free end (Line 12), as expected. The imperfection profile in Figure 3.34 is very typical for those observed in the flanges of all the outer channels. The reader is reminded that positive readings indicate imperfections in the direction away from the centroid of the column. The imperfection data of all specimens are included in Appendix B.

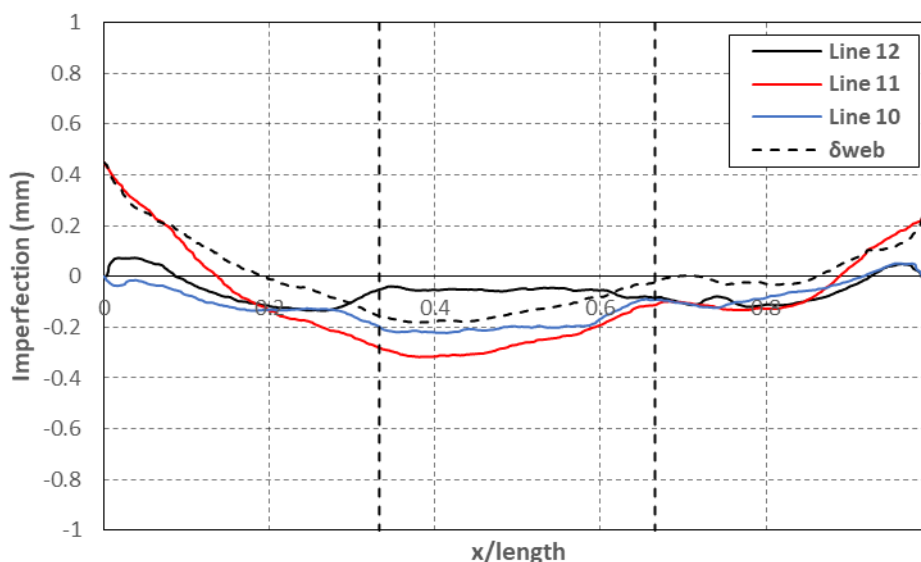


Figure 3.32: Typical web imperfections of channel T15414-2 in built-up column 1

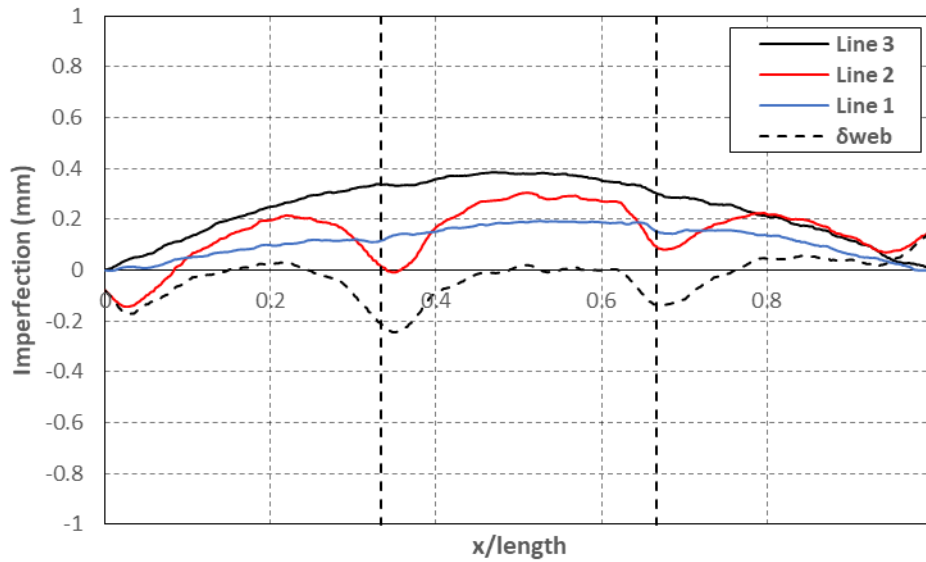


Figure 3.33: Typical web imperfections of channel S11012-9 in built-up column 4

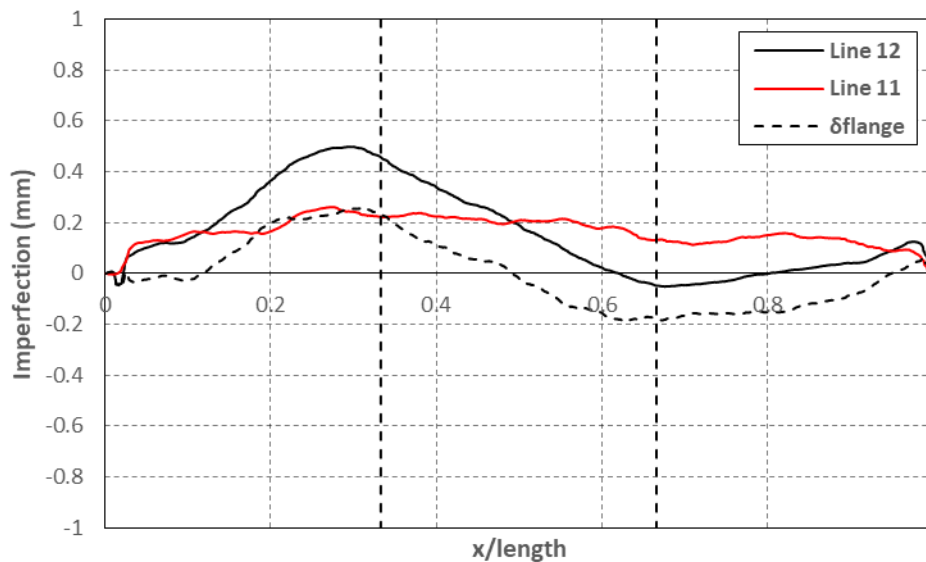


Figure 3.34: Typical flange imperfections of channel T15414-2 in built-up column 2

Table 3.12 lists, for each built-up geometry, the maximum and the average out-of-plane imperfections recorded on the individual components. For the imperfections recorded along the flanges of the channels, the maximum out-of-plane deviation of the flange edge would only coincide with the maximum δ_{flange} recorded if the web and the flanges of the channels were perfectly orthogonal at each end of the column. Since the angles between the web and the flanges of the channels were not measured, it was deemed most representative to report δ_{flange} relative to the average value along the flange of the channel.

Table 3.12: Maximum and averaged imperfection measurement

Specimen	Section	Imperfection (mm)		
			Max.	Avg.
SC1	P20024	δ_{plate}	0.60	0.21
	T15414	δ_{web}	0.64	0.13
SC2	T7912	δ_{web}	0.36	0.14
	T15414	δ_{web}	0.69	0.15
		δ_{flange}	0.47	-
SC3	T12012	δ_{web}	1.04	0.20
		δ_{flange}	0.58	-
	S11012*	δ_{web}	0.49	0.08
SC4	S11012	δ_{web}	0.39	0.09
		δ_{flange}	0.57	-
		$\delta_{flange,L}$	0.06	0.01
	T12012*	δ_{web}	0.26	0.11

*Imperfections recorded before the sections were assembled

The table shows that the maximum recorded imperfections were generally smaller than 1 mm in all the measured components. Only channel T12012 in the built-up columns with geometry 3 showed a maximum out-of-plane imperfection in the web larger than 1 mm. However, this relatively large imperfection was only recorded in one channel. The rest of the T12012 channels had a maximum imperfection less than 0.57 mm. In all the measured components the average recorded imperfection was below 0.21 mm. It is worth pointing out that the maximum and average imperfections $\delta_{flange,L}$ in the S11012 lipped channels were smaller than the accuracy of the measuring frame. Nonetheless, the imperfections are reported in the table to show how small they are.

3.7. Test Set up

3.7.1 Introduction

All specimens were tested between fixed end supports in an ESH universal testing machine with 1000 kN capacity. Any horizontal misalignment between the platens of the testing machine and the end plates of the columns was corrected by placing a plastic bag with plaster between the surfaces, as illustrated in Figure 3.35. The plaster was left to set under a preload which was progressively increased up to 10 kN. This ensured uniform contact between the platen of the testing machine and the end plate of the columns so that no additional moments were introduced.



Figure 3.35: Plaster used to correct misalignment between the platen of the machine and the column end plate

3.7.2 Instrumentation

3.7.2.1 Strain gauges

To monitor whether the load was transmitted uniformly to each component of the column, four columns –one of each geometry– were instrumented with strain gauges at mid-height. One strain gauge was placed on each individual component of the built-up columns. In the case of the channels, the strain gauges were installed at the centre line of the web, whereas for the flat plate sections the strain gauges were located at mid-width, as illustrated in Figure 3.36. For each geometry, one of the columns with the least amount of connectors was chosen to be instrumented. This choice was made because, in case the load was not being transmitted evenly through the endplate and the resin, these columns had fewer connectors available to transmit the load from one component to the other and the effects of uneven participation of the various components would have been most pronounced.

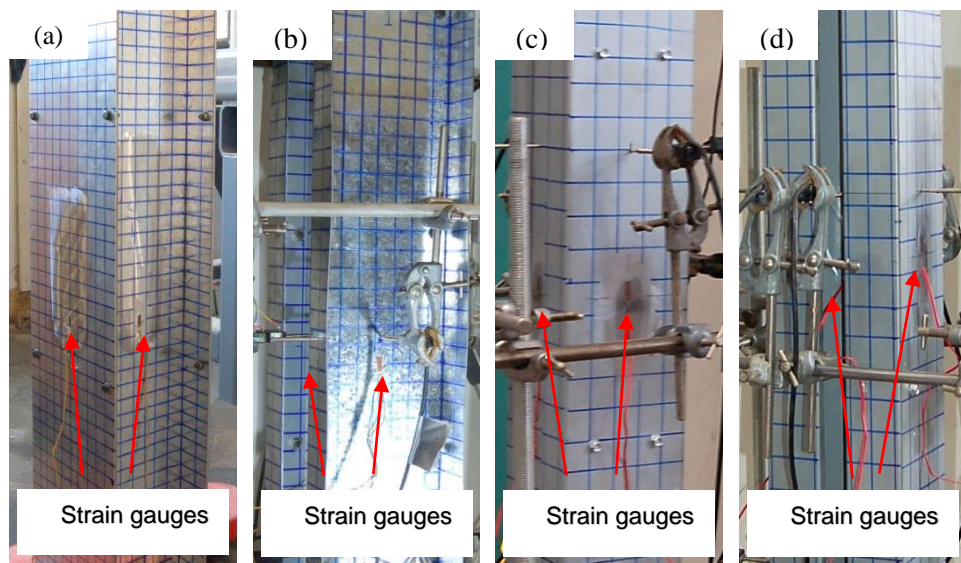


Figure 3.36: Location of strain gauges in a) SC1, b) SC2, c) SC3 and d) column 4

3.7.2.2 Transducers

Two potentiometers, with one placed on each side of the column as illustrated in Figure 3.37, were used to record the axial shortening of the specimens and monitor that no rotation occurred at the top end of the specimen. The readings obtained from these two potentiometers were in close agreement for all specimens, indicating that fixed support conditions were successfully achieved and that no end rotation took place during the test.

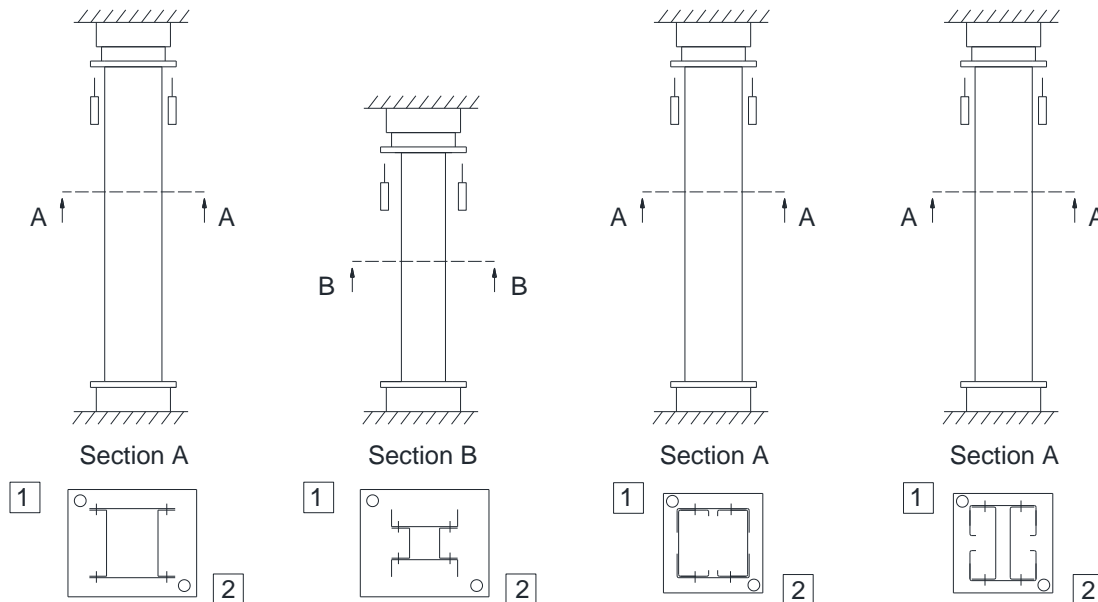


Figure 3.37: Arrangement of LVDTs to measure axial deformation

In addition, for specimens with built-up geometries 1 and 2 another twelve potentiometers with a stroke of 25 mm were divided over two cross-sections and placed at mid-distance between connectors. They were used to measure the out-of-plane deformations of the components and capture the onset of local buckling. Similarly, for specimens with built-up geometries 3 and 4 eight and ten potentiometers, respectively, were placed at two different heights in order to capture the onset of cross-sectional buckling. For these columns, the potentiometers were placed at the same relative location in all columns of a certain geometry. This resulted in columns SC3-2 and SC4-2 having both sets of four potentiometers located between connectors, while columns SC3-5 had one set of potentiometers located at mid-distance between connectors and the other set of potentiometers located at a cross-section containing connectors (Figure 3.38). Columns SC4-5 had both set of potentiometers located within a cross-section containing connectors.

The potentiometers were mounted on a frame which allowed adjustment of their position, as illustrated in Figure 3.38. The typical layout of the potentiometers for columns SC1 and SC2 is illustrated in Figure 3.39, while the layout for columns SC3 and SC4 is shown in Figure 3.40. The figures also show the potentiometer serial number enclosed in a square and the component number in a circle. At the bottom right of each figure, the vertical position of the potentiometers along the length of the columns is also indicated. In each pair of numbers associated with one

potentiometer in plan view, the lower number corresponds to the lower cross-section along the column height. For instance, potentiometer 6 was located in the lower part of column 1 whereas potentiometer 12 was located at mid height (see Figure 3.40a). The layout of the potentiometers for the other columns is included in Appendix C.

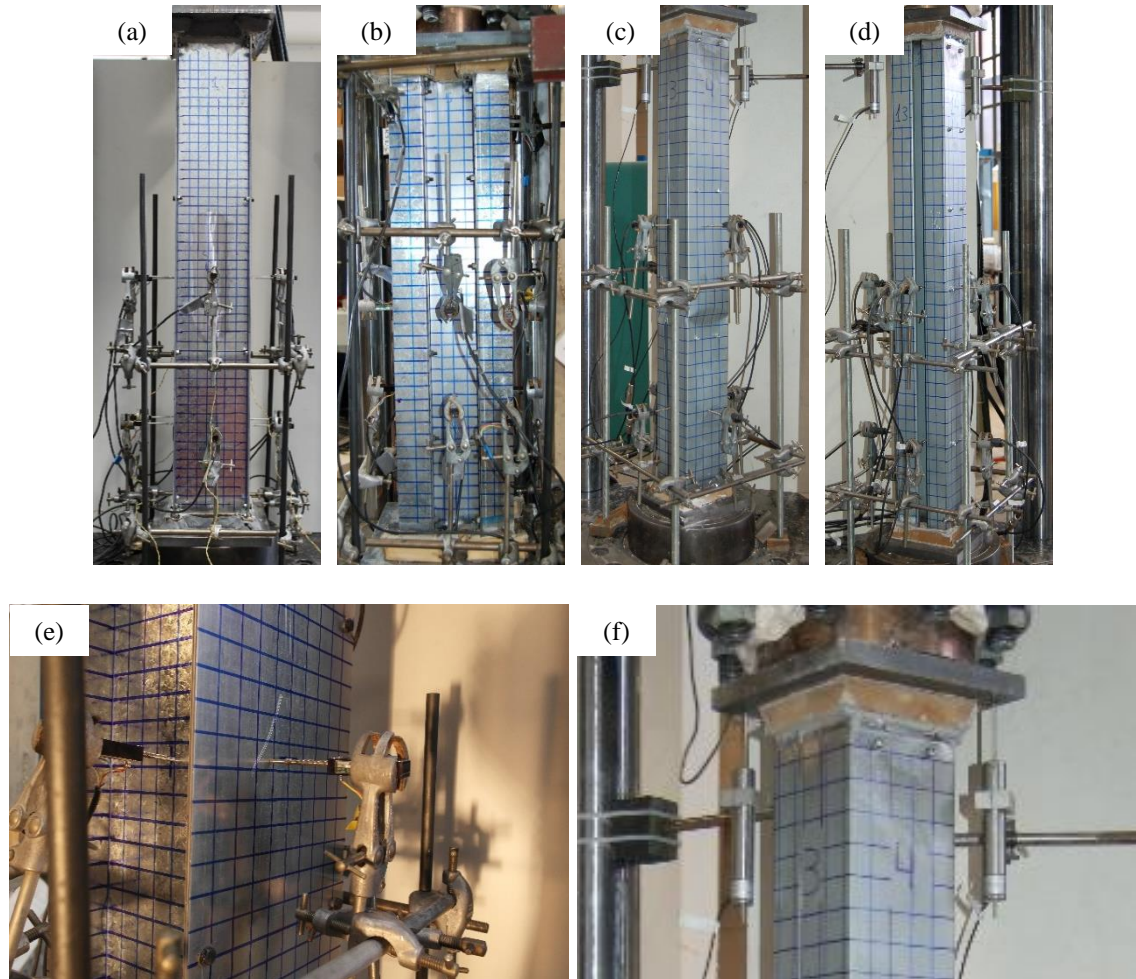


Figure 3.38: a), b), c) and d): Potentiometer frame, e) Potentiometer used to record out-of-plane deformations, f) LVDTs used to record axial deformation of the column

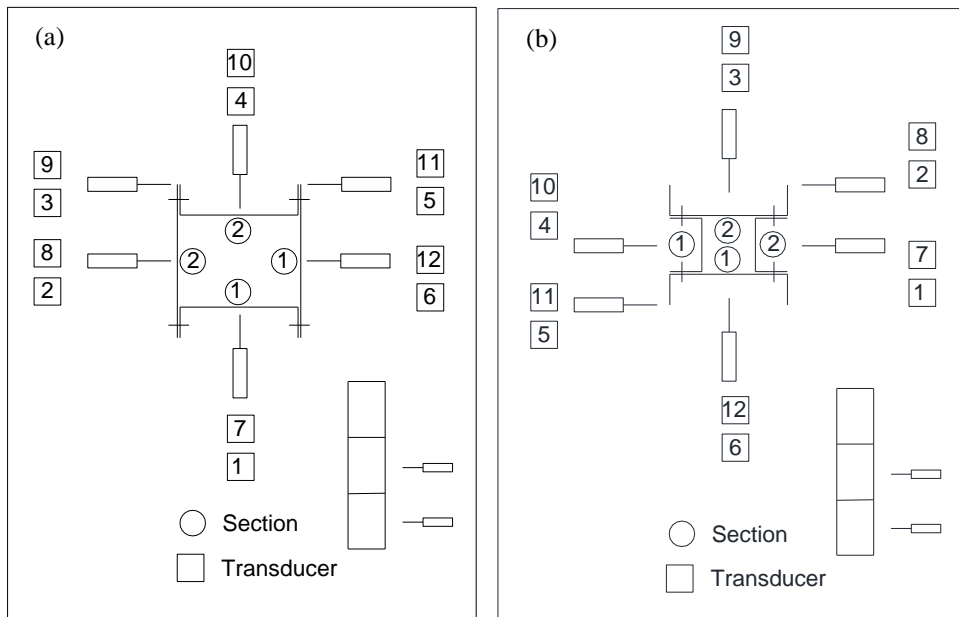


Figure 3.39: Potentiometer arrangement for a) column 1, b) column 2

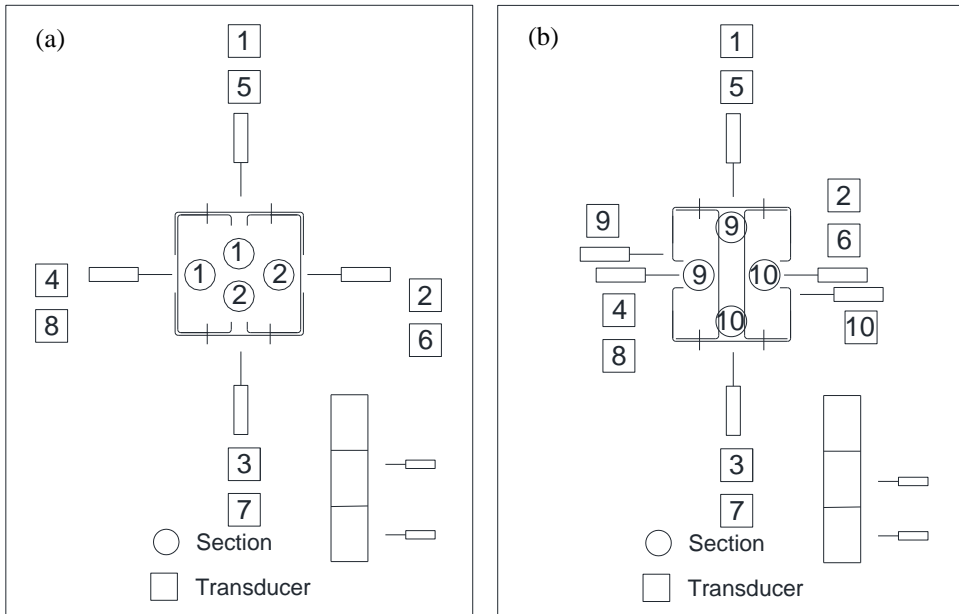


Figure 3.40: Potentiometer arrangement for a) column 3, b) column 4

3.7.3 Test procedure

The specimens were tested in an ESH universal testing machine with a capacity of 1000 kN. A consistent strain rate of 1.7×10^{-6} /s was applied to all the specimens. This corresponded to a displacement rate of 0.112 mm/min for geometries 1, 3 and 4 (with a length of 1100 mm), and 0.082 mm/min for geometry 2 (with a length of 800 mm). The columns with geometries 1 and 2 were compressed up to a deformation of 10 mm while the columns with geometries 3 and 4 were deformed up to 3.5 mm. This was sufficient to observe a significant drop in the load after the peak load. Each test was halted for 3 min when approaching the peak load in order to determine the lower bound ‘static’ value of the load without strain rate dependent effects.

The data acquisition system was controlled by a LabView script, which imposed a sampling rate of 1 Hz.

3.8. Test results

3.8.1 Strain gauge readings

Figure 3.41, Figure 3.42, Figure 3.43 and Figure 3.44 show the readings of the strain gauges over the course of the test for a column with geometry 1, 2, 3 and 4, respectively, with compressive strains taken as positive.

For built-up column 1, Figure 3.41 shows that the strains in the channel sections and the flat plate sections were in good agreement until buckling occurred at a load of 60 kN. Below this load, the strain in the flat plate sections differed by at most 12 % from the column average, while this number is 11 % for the channel sections. The readings also show that, typically, the plates carried slightly less strain compared to the channels for a given load. This may be due to the initial imperfections present in the plate sections and their relatively low flexural stiffness. This is also evidenced by Figure 3.55, which shows that the plate sections started to undergo small out-of-plane deformations from a very early stage (approximately at a load of 10 kN). These out-of-plane deformations introduced additional flexural tensile strains in the strain gauges, thus reducing the overall compressive strain.

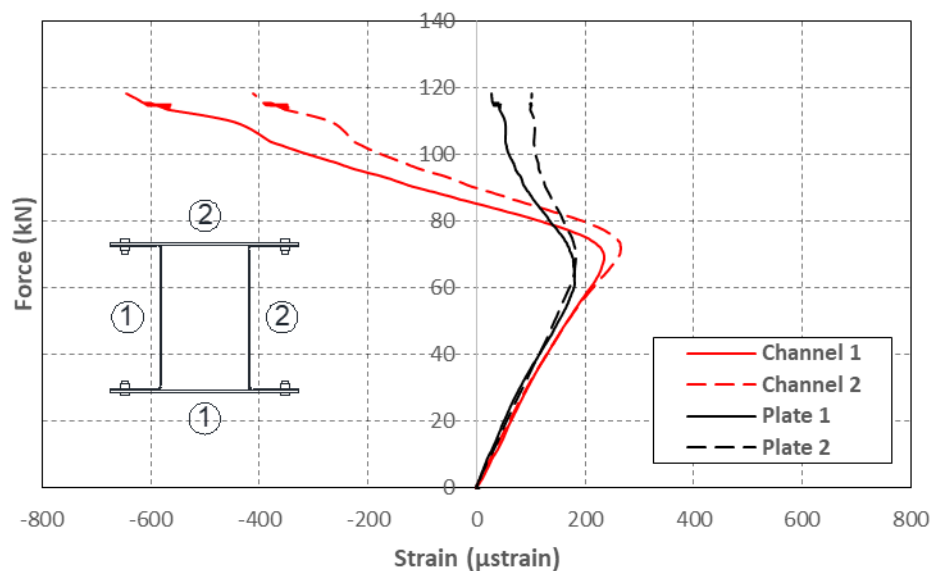


Figure 3.41: Axial load vs compressive strain in column SC1-2a

With respect to built-up column 2, Figure 3.42 shows a very similar strain response for all channel sections, with the slight exception of inner channel 1. This channel underwent larger strains than the other components for a given load, suggesting that it attracted slightly more

load. The maximum difference in strains between this channel and the other components was approximately 12 % with respect to their average at a load of 70 kN.

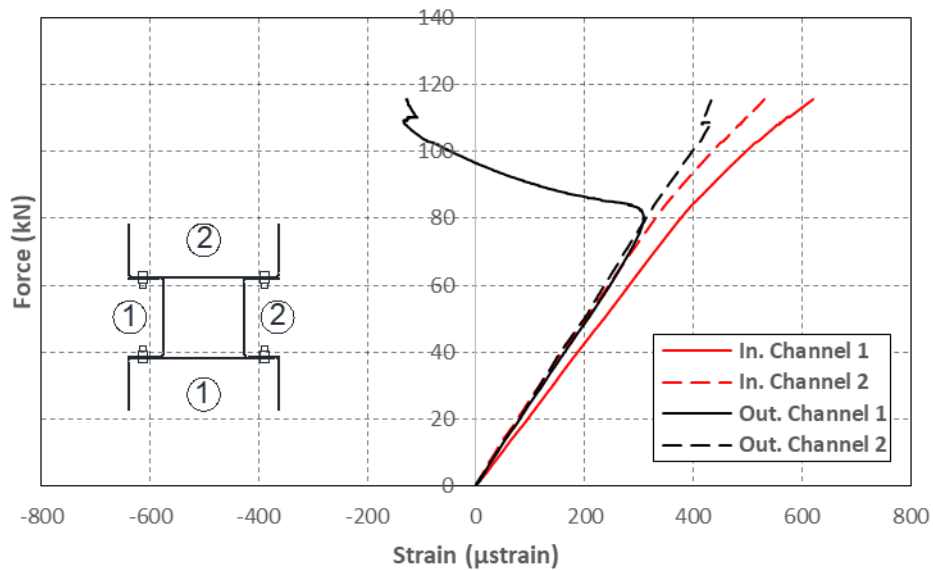


Figure 3.42: Axial load vs compressive strain in column SC2-2a

For built-up column 3, Figure 3.43 shows very good agreement between the strains experienced by the different components. At a load of 80 kN the maximum difference in strain between the components was approximately 10 %.

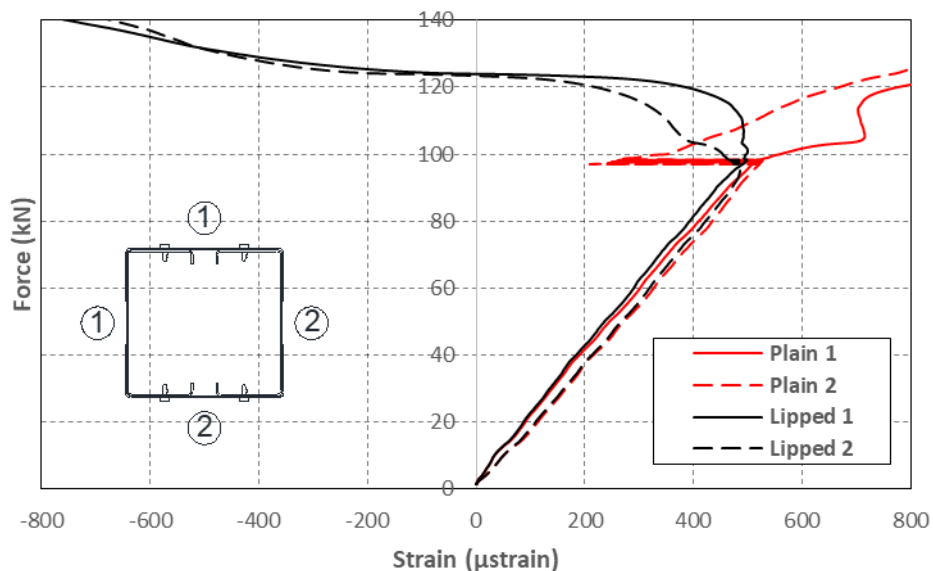


Figure 3.43: Axial load vs compressive strain in column SC3-2a

An even better agreement was achieved between the strains in the components of built-up column 4, as is seen in Figure 3.44. The maximum difference between the strains in each component was approximately 5 % at a load of 70 kN.

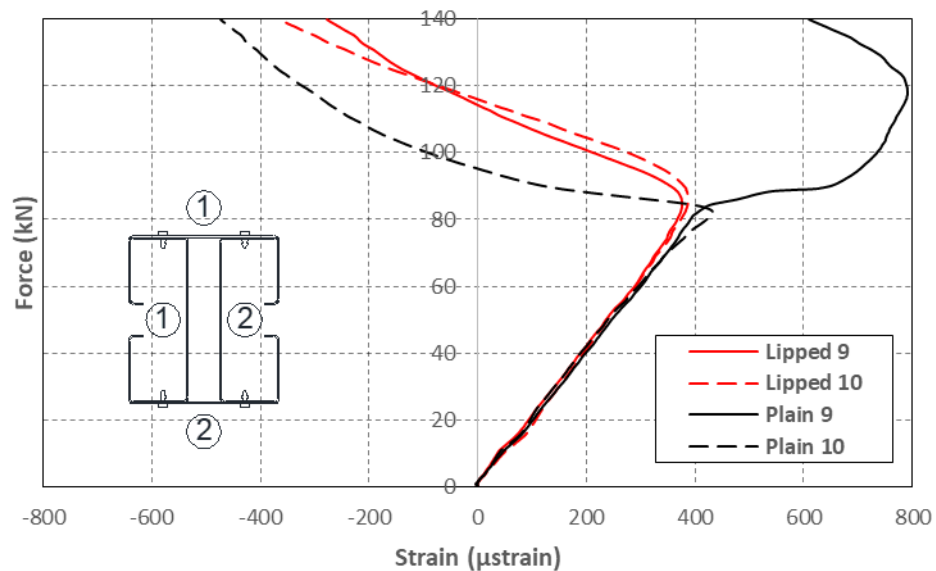


Figure 3.44: Axial load vs compressive strain in column SC4-2a

Based on these results, it was concluded that the load was being transmitted with a sufficient degree of uniformity to all components of the built-up columns. Therefore, the rest of the columns were tested without strain gauges.

3.8.2 Deformed shape

3.8.2.1 Built-up column 1

All columns with geometry 1 failed by interaction of global buckling of the plate sections between connectors and local buckling of the channels. Typically, multiple buckling half-waves were observed along the column in both the plates and the channels. An exception to this occurred in columns SC1-2, where the plate sections buckled only in the central field in between the inner sets of connectors and remained straight in the other fields. Every pair of twin columns showed the same initial buckled shape, although localization of the buckling pattern often occurred in different locations upon approaching the peak load. Eventually, yield lines started to appear in both the plates and the channels. Figure 3.45 illustrates the deformed shapes of the columns just before the peak load was reached. The deformed shape of the columns after the yield lines were formed are shown in Figure 3.46.

In columns SC1-2, containing the smallest amount of connectors, the observed buckling pattern most closely reflected the assumptions previously made in section 3.4.1 (Figure 3.45). The flat plate sections buckled in between connector points with a half-wave length approximately equal to half the connector spacing. However, the observation that the plate deformations were concentrated in the central field of the column, with the adjacent fields remaining straight was unanticipated. Seen the regularity of the buckling pattern in the adjacent channels, it is clear that a certain amount of bolt slip necessarily occurred in order to make this possible. The channel

components maintained deformational compatibility with the unbuckled plate sections in the end fields by the flanges buckling inwards over the whole length of the column with a half-wave length equal to half of the connector spacing. It is seen from Figure 3.13 that the signature curve for (unrestrained) local buckling of the channels displays a fairly flat minimum for half-wave lengths between 140-200 mm. The connector spacing of columns SC1-2, on the other hand, was 333 mm. While it is expected that the fact that the channel flanges are forced to buckle inwards slightly extended the natural half-wave length due to the extra bending necessary in the web, it can be understood from these numbers why the channels adopted a full wave-length in between connector points. In the post-peak range the channel deformations localized in the central field, with the buckling pattern largely disappearing in the end fields (Figure 3.46).

In columns SC1-3, the channel components buckled in a similar way with the flanges bending inwards. It was clear from the observed deformation pattern, however, that the channels preferred to adopt a half-wave length slightly beyond half the connector spacing. As shown in Figure 3.13, the connector spacing in columns SC1-3 stood at 250 mm and, consequently, the natural local buckle half-wave length of the channels exceeded half the connector spacing by a noteworthy amount. This extended half-wave length was particularly evident in the two central fields of the column and was made possible by localized deformations around the connectors. The flat plate sections buckled outwards in two of the fields with a half wave-length sympathetic to the one observed in the channels, while they remained largely straight in the other two fields, prevented from buckling inwards by the presence of the channel webs. In the latter two fields, the potentiometer readings confirmed negligible out-of-plane deformations. Similar to columns SC1-2 the post-peak deformations localized in a field where the plates buckled outwards.

Columns SC1-5 featured a connector spacing of 167 mm, which was approximately equal to the natural local buckling half-wave length of the channel components. The channels in these columns were observed to buckle in a completely different way from those in columns SC1-2 and SC1-3. They buckled with a half-wave length equal to the distance between the connectors, with the flanges alternately moving inwards and outwards in successive fields, much like the unrestrained local buckling pattern. The connector locations corresponded to the nodal lines of the buckling pattern, implying that they did not undergo any out-of-plane translation, but did accommodate the plate rotations. The flat plate sections buckled in a shape which completely followed the flange tips in the fields where those moved outwards, while they remained straight in the fields where the flange tips moved inwards, prevented from maintaining complete uniformity by the presence of the channel webs. The readings from the potentiometers again confirmed that the plates underwent negligible out-of-plane deformations in the regions where they were visually observed to remain straight. This buckling pattern in the plate sections

required some localized bending near the connectors. Post-peak localization of the buckled shape occurred in the central field, where the plate sections initially moved outwards.

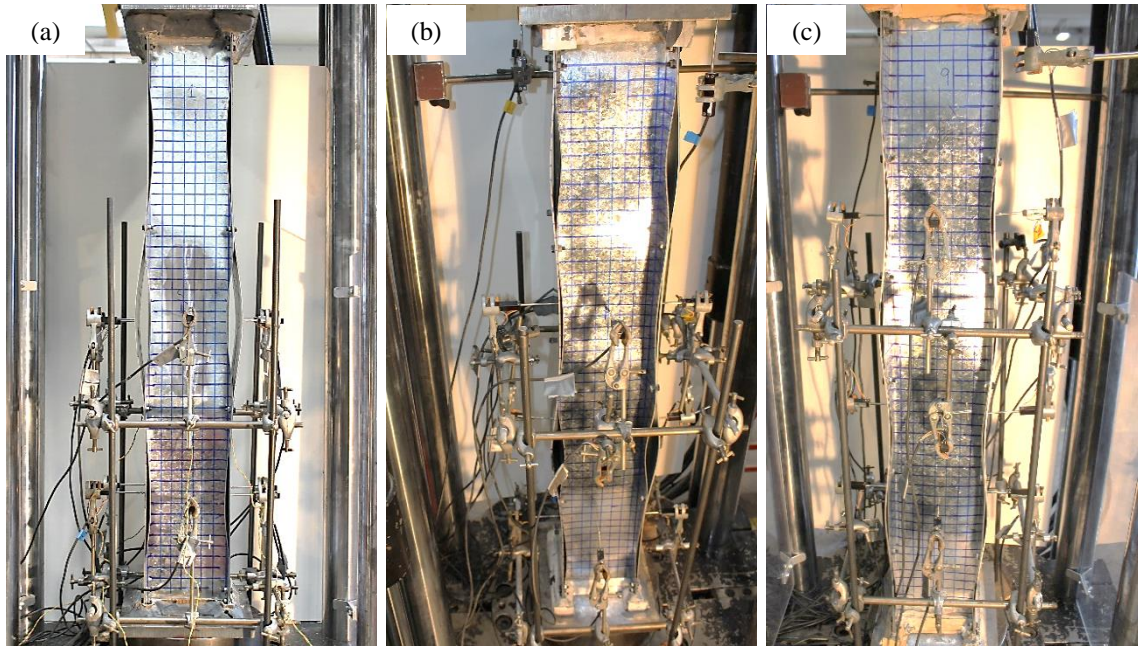


Figure 3.45: Deformed shape approaching ultimate load in a) SC1-2a, b) SC1-3a, c) SC1-5a

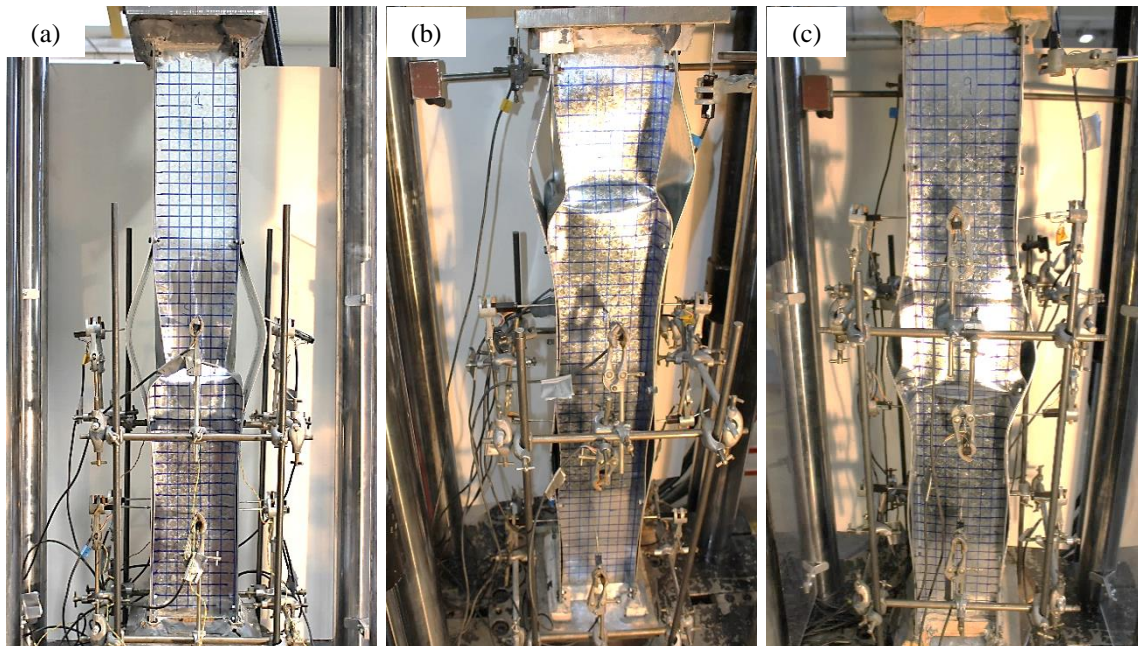


Figure 3.46: Final deformed shape at end of test in a) SC1-2a, b) SC1-3a, c) SC1-5a

It can be concluded from the above that the buckling pattern in these built-up columns is highly dependent on the connector spacing.

3.8.2.2 Built-up column 2

Unlike in the columns with geometry 1, where global buckling of one of the components in between connector points was prevalent, the relevant buckling modes of the components of

geometry 2 were all local. Geometry 2 aimed to study the interaction between the local buckling patterns in the inner and outer channels as a result of the presence of the connectors and contact between surfaces.

Multiple regular buckles were observed along the length of all columns, indicating that the chosen length of the stub columns was appropriate. Each pair of twin columns showed an identical buckling pattern. In the vicinity of the ultimate load, the buckling pattern started to localize and in the post-peak range a yield line mechanism was formed. Figure 3.47 illustrates the deformed shapes of the columns just before the peak load was reached, while the eventual yield line patterns are shown in Figure 3.48.

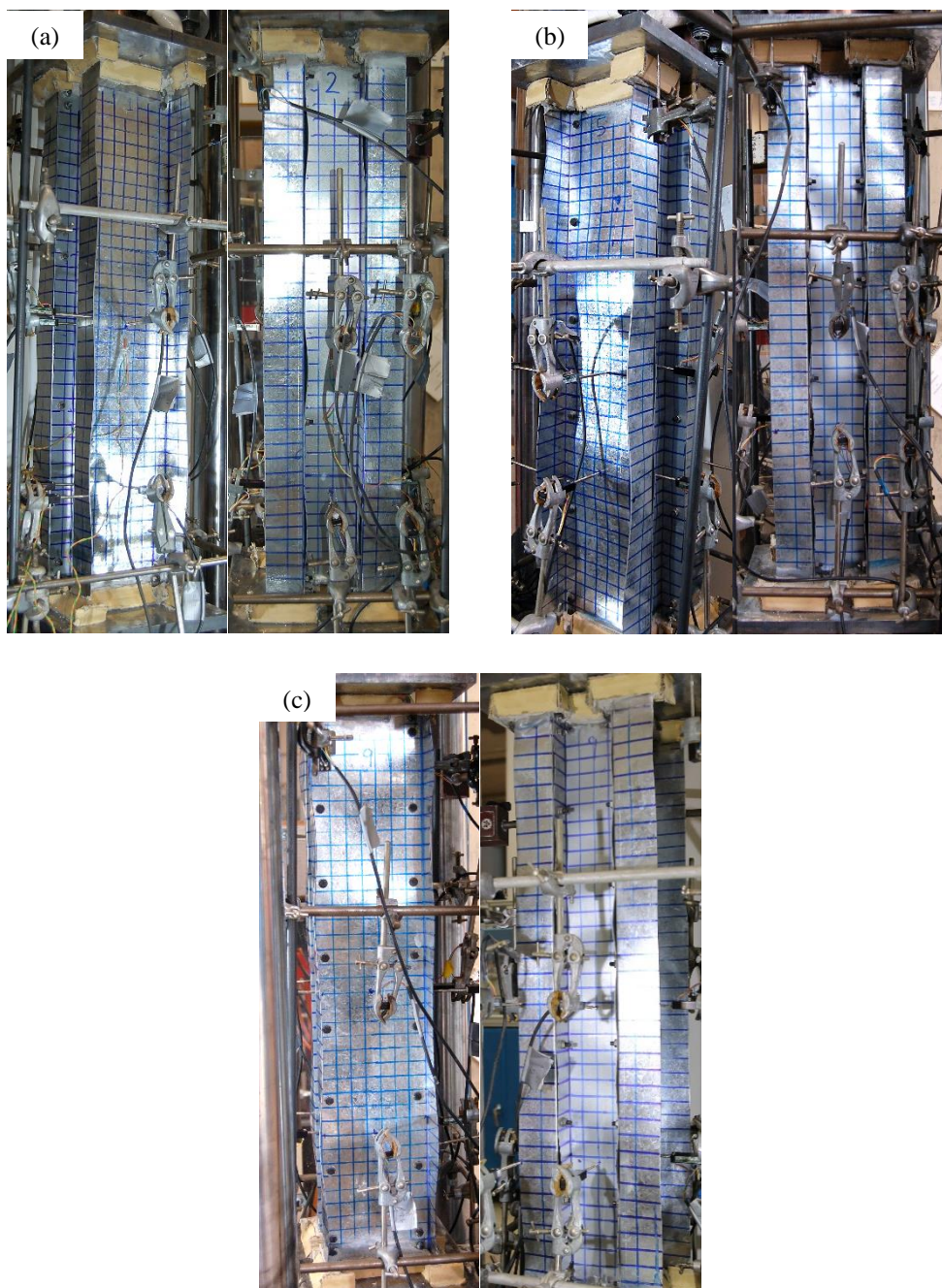


Figure 3.47: Deformed shape approaching ultimate load in a) SC2-2a, b) SC2-4a, c) SC2-6a

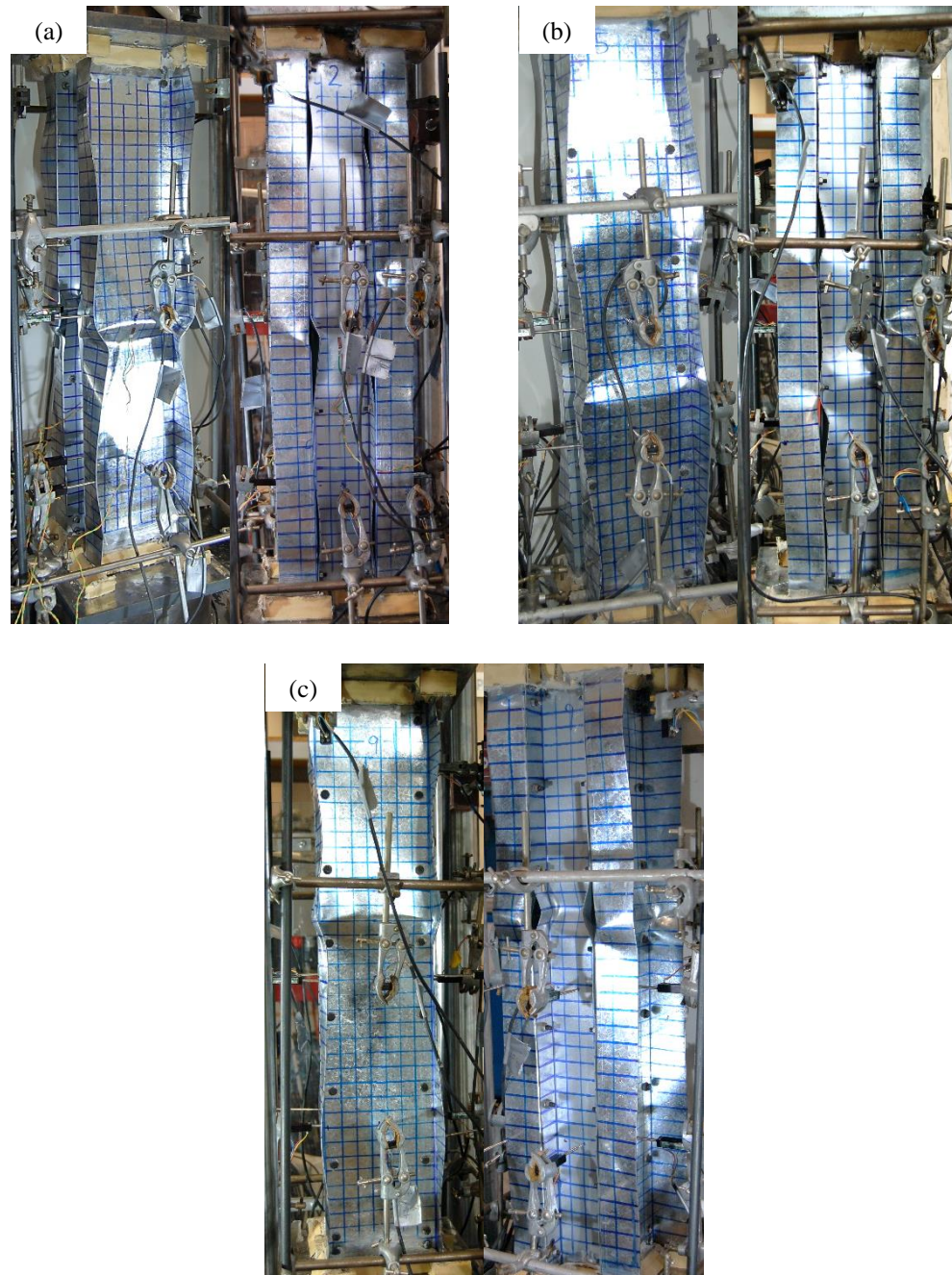


Figure 3.48: Final deformed shape at end of test in a) SC2-2a, b) SC2-4a, c) SC2-6a

In the columns with only two rows of intermediate connectors (SC2-2) the buckling half-wave length of the outer channels coincided with half the distance between the connectors. Due to the presence of the inner channels, the webs of the outer channels were forced to buckle outwards (away from the centre of the column). The buckled shape is shown in Figure 3.47a. This deformation pattern could be expected in the outer channels, as their natural half-wave length was calculated to be 170 mm, while the connector spacing was 233 mm.

In columns SC2-4 the outer channels buckled with a half-wave length equal to the distance between the connectors. This buckling pattern is shown in Figure 3.47b. It can easily be

explained when considering the results of a buckling analysis of an unrestrained channel. The critical stress associated with a half-wave length equal to the distance between connectors is 72 MPa, whereas generating buckles half that length would require a stress level of 124 MPa.

In columns SC2-6 the outer channels were observed to buckle with a varying half-wavelength along the column. Along part of the specimen height the outer channels buckled with a half-wave length very close to the distance between connectors. However, this pattern switched to one in which the outer channels generated a half-wave which spanned almost two fields over an intermediate connector. This is illustrated in Figure 3.47c. This buckling pattern of the outer channels can be explained by the fact that neither generating buckles with a half-wave length equal to the distance between connectors (100 mm) nor buckling with a half-wave length twice as large resulted in the lowest buckling stresses, as shown from the signature curve of the channel in Figure 3.14. Instead, the outer channels preferred to buckle with half-wave lengths slightly larger than 100 mm, while for compatibility that also meant that one of the buckles had to have a half-wave length slightly shorter than 200 mm. Figure 3.14 shows that this two half-wave lengths require very similar buckling stresses, and that these buckling stresses are lower than those required to generate a half-wave length of 100 mm or 200 mm.

In all specimens with geometry 2 the inner channel sections buckled with a half-wave length equal to half the distance between the connectors. Due to the presence of the outer channel webs, the flanges of the inner channels were forced to deform towards the inside of the channels. This pattern occurred in all columns despite the wide range of connector spacings and, consequently, the wide range of local buckle half-wave lengths in the inner channels, indicating a high degree of constraint on the inner channels.

3.8.2.3 Built-up column 3

All columns with geometry 3 failed by local buckling, displaying significant interaction between the individual components. In all cases multiple half-waves were observed along the column height. In the post-peak range the plastic deformations localized around mid-height in between two connector rows in all components simultaneously. The only exception to this occurred in column SC3-2a, where the plastic deformations of one of the plain channels localized near the bottom of the column at mid-distance between connector rows, while they localized at mid-height in the rest of components. Figure 3.49 and Figure 3.50 show the deformed shapes of the columns right before and well after the peak load was reached, respectively.

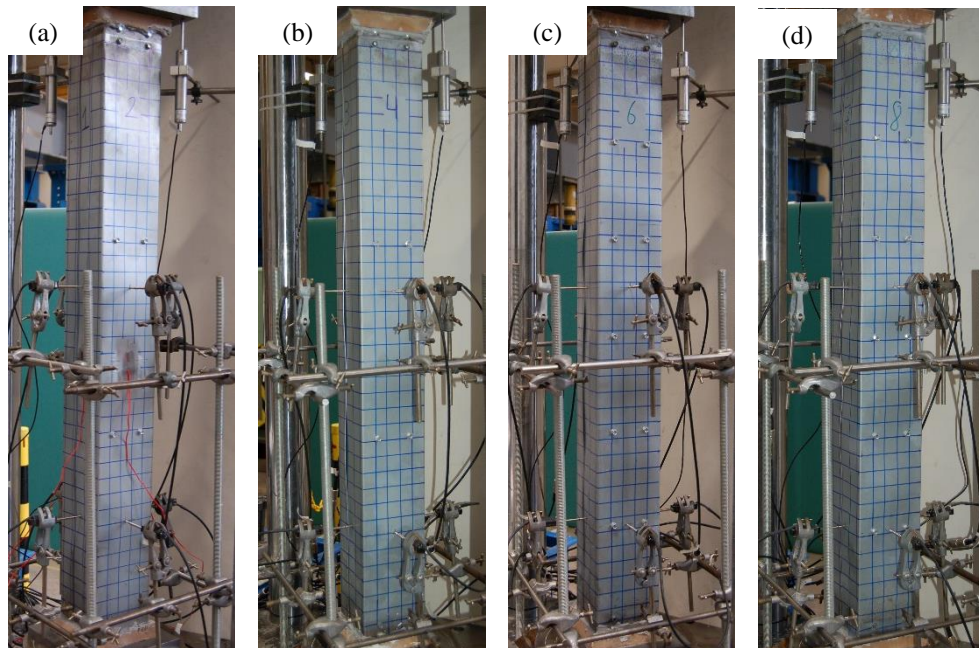


Figure 3.49: Deformed shape approaching ultimate load in a) SC3-2a, b) SC3-2b, c) SC3-5a, d) SC3-5b

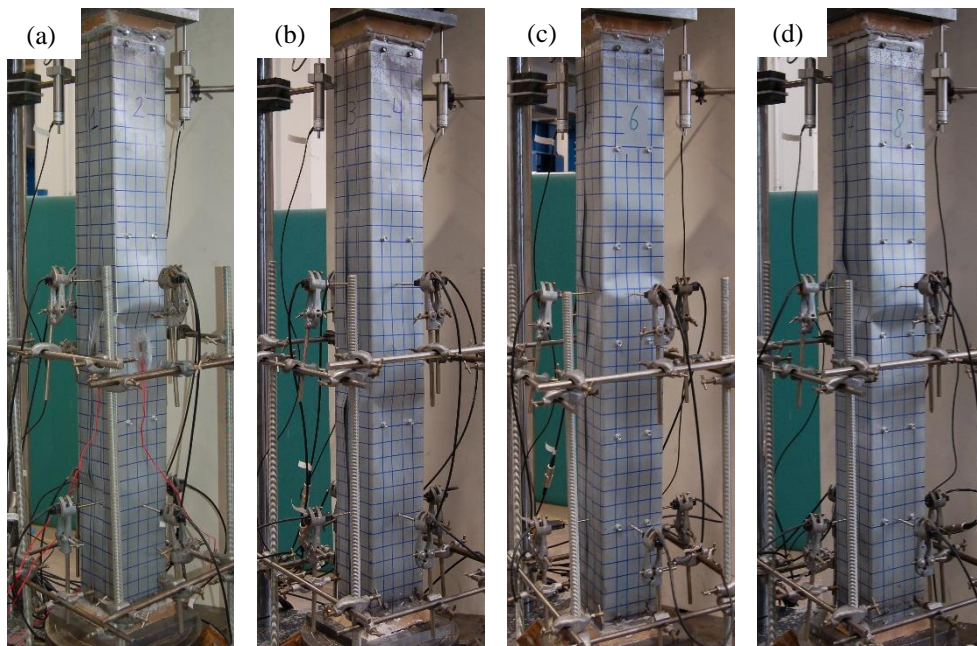


Figure 3.50: Final deformed shape at end of test in a) SC3-2a, b) SC3-2b, c) SC3-5a, d) SC3-5b

In all columns the lipped (inner) channels buckled with a half-wave length of approximately 83 mm, corresponding to four and two half-waves between connectors for columns SC3-2 and SC3-5, respectively. In comparison, the natural local buckling half-wave length of the unrestrained lipped channel associated with the minimum critical stress is 90 mm.

In columns SC3-2 the plain channels buckled generating between two and four half-waves between connectors. The cross-sections containing connectors thereby corresponded with the minima of the out-of-plane displacement pattern, so that no rotations or out-of-plane displacements of the connectors were necessary, suggesting no distortional buckling of the inner

channels. In column SC3-2a the flanges of the outer channels were seen to follow the half-wave length of the buckles in the web of the inner channels almost perfectly, despite the occurrence of some irregular buckles in the web of the inner and outer channels (Figure 3.49a). In twin specimen SC3-2b the flanges of the outer channels did not follow the half-wave length of the web of the inner channels, causing a more pronounced gap between the inner and outer channels, as is visible in Figure 3.49b. In this respect, it is also worth noting that the natural local buckling half-wave length of the plain channels was 130 mm, which was associated with a critical stress of 64 MPa. Half-wave lengths of 83 mm and 167 mm corresponded to buckling stresses of 74 MPa and 67 MPa on the local buckling curve, respectively.

A more regular buckling pattern was observed in the plain channels of the columns with five rows of intermediate connectors. In all columns the web of the plain channels buckled with a half-wave length equal to half the distance between connectors (83 mm). This occurred despite the slightly larger buckling stress associated with this wave length in comparison to a wave length twice as long, and is illustrative of the amount of restraint received by the outer channels. The plain and lipped channels buckled in near complete sympathy, especially in column SC3-5b, in which virtually no gap was formed between the flanges of the plain channels and the web of the lipped channels (Figure 3.49d). In column SC3-5a, on the other hand, the flanges of the plain channel, being less restrained by the connectors, were displaying a half-wave length closer to their natural half-wave length, resulting in the formation of some gaps between them and the web of the lipped channels (Figure 3.49c).

3.8.2.4 Built-up column 4

All columns with built-up geometry 4 failed predominantly by local buckling with some minor participation of distortional buckling of the lipped channels. Again, multiple local buckling half-waves were observed along the specimens, indicating that the length of the stub columns was appropriately chosen. The potentiometer readings indicated that in columns SC4-2a, SC4-2b and SC4-5a, distortional buckling originated in one of the lipped channels just before the peak load was reached, while for column SC4-5b distortional buckling originated in both lipped channels simultaneously. Figure 3.51 illustrates the deformed shape of the columns shortly before the peak load was reached, while Figure 3.52 shows the failed shapes after localization of the buckling pattern.

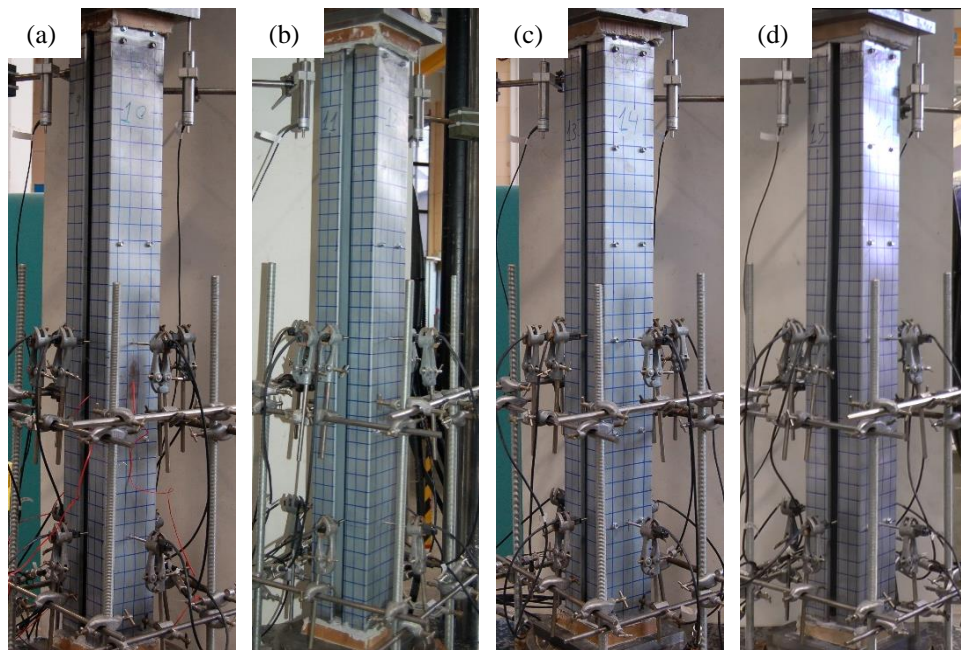


Figure 3.51: Deformed shape approaching ultimate load in a) SC4-2a, b) SC4-2b, c) SC4-5a, d) SC4-5b

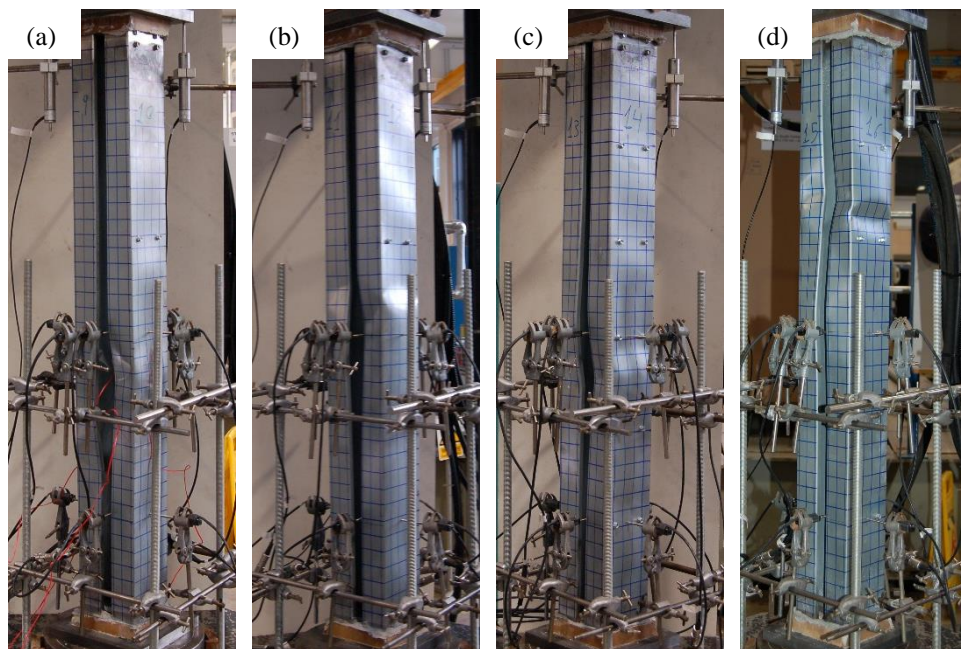


Figure 3.52: Final deformed shape at end of test in a) SC4-2a, b) SC4-2b, c) SC4-5a, d) SC4-5b

The reader is reminded that geometry 4 contains the same component sections as geometry 3, but arranged in a different configuration.

In all columns, the lipped channels first buckled in a local mode with a half-wave length of approximately 83 mm, corresponding to a quarter and half of the connector spacing in specimens SC4-2 and SC4-5, respectively. As the webs of the plain channels prevented the webs of the lipped channels from buckling towards the inside of the column, the flanges of the lipped channels were forced to buckle inwards.

Due to the geometric arrangement of the component sections, direct observation of the buckling pattern in the plain (inner) sections was difficult. The potentiometers placed on the plain channels still provided information, however, and their readings will be discussed as part of the next section.

3.8.3 Critical buckling stresses

This section explains how an estimate of the critical buckling stresses of the various components was obtained from the potentiometers readings during the test. The potentiometer readings as a function of the load applied on the column are included in Appendix C for all tests.

As indicated by the strain gauge readings (previously discussed in Section 3.8.1) the load can be considered in very good approximation to be uniformly transmitted to the component sections up to the point of first buckling. The loads at which the various channel sections buckled was determined by assuming that the stress, when plotted against the initial post-buckling out-of-plane displacements, follows a parabolic trend, as shown in Figure 3.53a. This has been confirmed by a perturbation analysis in classical plate theory (Bulson, 1970). The buckling load was thus found by determining the intersection point of this parabola and the vertical load axis

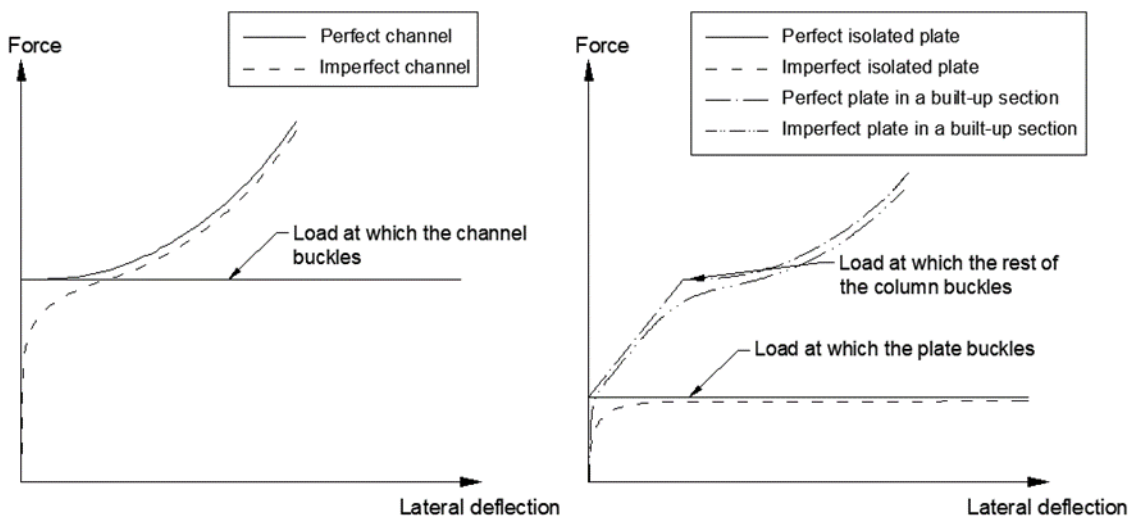


Figure 3.53: Force against lateral deflection curve for: a) a channel; b) a plate

It is worth pointing out that this parabolic post-buckling trend can be expected to occur only if the channel is unrestrained while undergoing local buckling. In a built-up column, on the other hand, the adjacent components of the built-up geometry may prevent the buckles of the channel from freely developing, and therefore determination of the critical buckling stress of the channel may become a subjective task. As an example, Figure 3.55 shows the out-of-plane deformations obtained for column SC1-2a. The load in the column at which the channels sections buckled

was found to be 76 kN. This value is in good agreement with the value obtained from the strain gauge readings shown in Figure 3.41 using the strain reversal method (Venkataramaiah and Roorda, 1982), which is 71 kN. Similar agreements were also obtained for the critical buckling loads calculated for the channels in the rest of the columns instrumented with strain gauges.

For a plate section, the critical buckling stress due to flexural buckling can be determined using Euler's equation for an isolated perfectly flat plate, which is represented by a solid line in Figure 3.53b. If the plate forms part of a built-up specimen, such as in columns LC1, once the plate buckles the unbuckled components of the cross-section are able to prevent the plate from collapsing. Therefore, the built-up specimen is able to continue resisting increments of load, although its axial stiffness is reduced by a certain amount after buckling of the plates. The out-of-plane deformations of the buckled plate then gradually increase as the rest of the column deforms axially. The dash-dotted lines in Figure 3.53b show the relationship between the total load applied to the column and the out-of-plane deformations of the plate, both for the case where geometric imperfections are included and for the case where they are not. As the figure shows, the load at which the plate buckles can approximately be determined by projecting a straight line onto the vertical load axis tangent to the portion of the load vs. lateral deformation curve in which the rest of the column remains unbuckled. When applying this technique to Figure 3.55 (corresponding to column SC1-2a), the critical buckling load of the plates is estimated to be 48 kN. This result does not agree well with the prediction given by the strain reversal method, which predicts a value of 66 kN. However, this is because the strain reversal method overestimates the critical buckling load of the plates due to the fact that after the plates buckle, their out-of-plane deformations are limited by the support provided by the rest of the column. Consequently, the tensile strains on the surface of the plates due to out-of-plane bending are relatively small. Figure 3.54 shows the strain gauges readings in column SC1-2a against the applied load. The figure shows a change in the axial stiffness of the column (highlighted by the dashed lines) at a load of around 47 kN, which agrees very well with the predictions of the potentiometers. It is worth noting that the change in stiffness is more obvious from the readings of the strain gauges attached to the channel sections than from those attached to the plates. This is due to the introduction of out-of-plane (tensile) bending strains in the strain gauges attached to the plates which, despite being relatively small, are opposite to the additional compressive strains resulting from the loss of axial stiffness in the column.

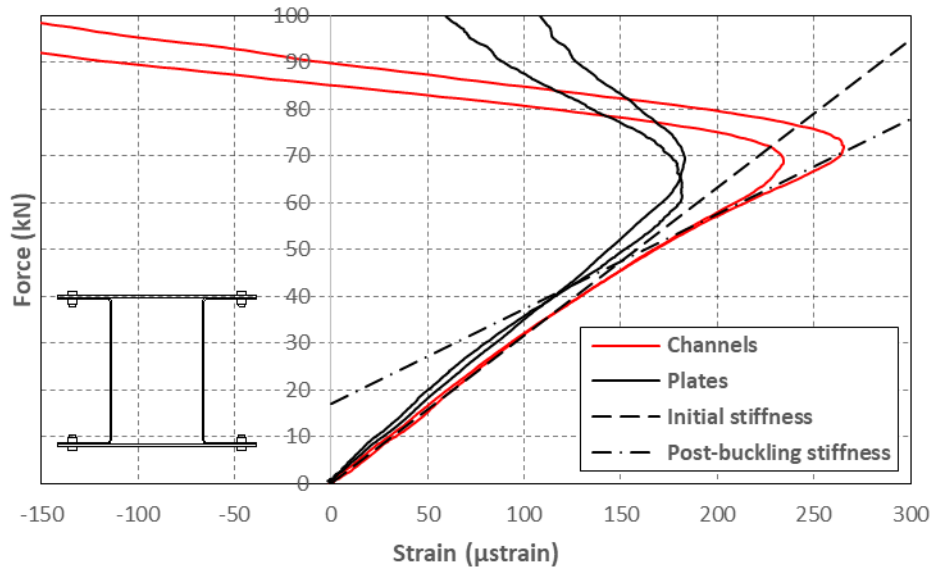


Figure 3.54: Post-buckling change of stiffness in column SC1-2a recorded with strain gauges

The overall column loads at buckling obtained from the potentiometer readings were then used to calculate the critical buckling stresses of each component sections by adopting the assumptions described in Sections 3.8.3.1-3.8.3.4 below for each geometry.

The experimental buckling stresses were compared to the theoretical buckling stresses calculated based on the measured cross-sectional dimensions (averaged over the two components in the cross-section) and using the Young's modulus obtained from the flat tensile coupons. The theoretical buckling stresses were obtained while considering the individual components in isolation, without any interaction with the rest of the cross-section, and whenever possible adopting the buckle half-wave length observed during the test, which was estimated based on the number of half-waves counted between connectors. For the plain and lipped channel sections, the theoretical critical buckling stresses were obtained using the CUFSM 4.05 software (Schafer, 2006), while for the plate sections in columns SC1, the critical buckling stresses were determined using Euler's equation:

$$\sigma_{cr} = \frac{\pi^2 E t^2}{12 L_p^2} \quad (3.31)$$

In the above Eq. (3.31), E is the Young's modulus, t is the averaged measured thickness of the two plate sections in the column and L_p is the buckle half-wave length.

3.8.3.1 Built-up column 1

In built-up columns SC1-2 and SC1-3, the plate sections buckled in a flexural mode before buckling of the channel sections occurred, while simultaneous buckling of the channel and plate sections was observed in columns SC1-5. The buckling stress of the plate sections was thus obtained by dividing the column load over the total area of the built-up section. As the plates

buckled in a global mode, it is a reasonable assumption due to the lack of post-buckling capacity in the global flexural mode, that after buckling of the plates any increase in load would be resisted entirely by the channels. Consequently, this allowed an estimate of the buckling stress of the channels based on the total column load.

In Figure 3.55 the readings from the potentiometers show that, due to the effect of initial imperfections, a gradual increase of the out-of-plane deformation occurred from the onset of loading (as opposed to sudden bifurcation of the equilibrium path in a perfectly flat plate). The effect of initial imperfections was generally more significant in the plate sections than in the channel sections. This can be attributed to the low flexural rigidity of the plate sections.

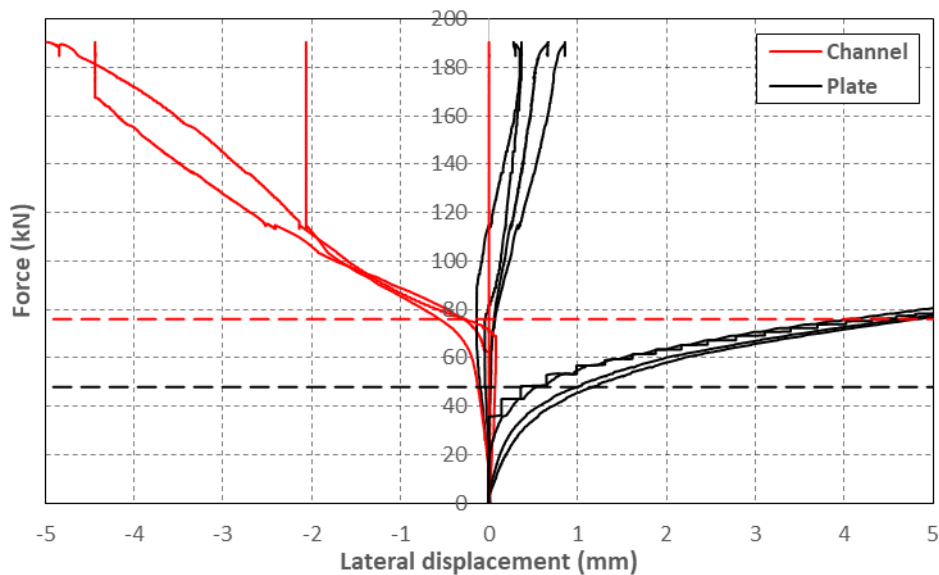


Figure 3.55: Axial load vs lateral displacements in SC1-2a

Table 3.13 shows the theoretical critical buckling stresses of the channels and the plates, and compares them to the ones obtained from the tests. An upper and a lower bound were defined for the theoretical buckling stresses of the plate sections. The upper bound corresponds to a half-wave length (effective length) equal to half the spacing between connectors, whereas the lower bound corresponds to a half-wave length equal to the distance between connectors.

Table 3.13: Buckling stresses of the components of geometry 1

Column	Theoretical buckling stress (MPa)			Buckling stress from test (MPa)	
	Channel	Plate		Channel	Plate
		Lower	Upper		
SC1-2a	71	9	35	65	28
SC1-2b	71	9	36	72	19
SC1-3a	76	16	64	70	46
SC1-3b	75	16	64	69	45
SC1-5a	70	36	144	69	69
SC1-5b	69	36	145	67	67

The table shows that for columns SC1-2 the plate sections buckled before the channels and their experimental buckling stresses were intermediate between the theoretical lower and upper bounds. This agrees with the experimentally observed buckled shape, in which the plates were forced by the channels web to buckle outwards. The channels, on the other hand, buckled at a stress very close to the theoretically predicted value (and which was around 4 % lower). This suggests that the channels were not significantly affected by any restraint provided by the buckled plates.

In columns SC1-3 the plates also buckled before the channels, which differed from the theoretical prediction that the plates would buckle at the same time as the channels. This can be explained by the experimental observation (Figure 3.45c) that the plates buckled with a half-wave length larger than half the connector spacing, contrary to what was initially assumed. The experimentally derived plate buckling stresses agreed with this observation, showing that the plates buckled at a stress which was around 29 % below the theoretical upper bound. The experimentally derived buckling stress of the channels was around 15 % lower than the theoretically predicted value, which was calculated for a half-wave length equal to half the connector spacing. This may be attributed to the fact that the channels buckled with a slightly larger half-wave length, as described in Section 3.8.2.1.

In columns SC1-5, the channels and the plates were observed to buckle simultaneously in the experiment. The plate sections buckled at a stress well below the theoretical upper bound value (around 53 % lower), but almost twice as high as the theoretical lower bound. Neither theoretical assumption bore much resemblance to the actual deformed shape, where the plates buckled outwards with a half-wave length roughly equal to the connector spacing, but were restrained from buckling inwards, resulting in localized bending around the connectors. The experimentally obtained buckling stress of the channels was approximately the same as the theoretical value, indicating that the channel sections were not significantly affected by the plate sections while trying to buckle in the observed pattern.

3.8.3.2 Built-up column 2

All components of built-up column 2 failed by local buckling. The local mode has significant post-buckling load-bearing capacity, however at the cost of a significantly reduced axial stiffness. Consequently, the relative distribution of the additional load over the column components after the first component buckles becomes a non-trivial problem. Therefore, only the critical buckling stress of the outer channels was determined from the experimental results (as they were the first components to buckle in all the columns) and was obtained by dividing the column load at which buckling was observed by the total cross-sectional area of the column.

In all but one column local buckling was observed nearly simultaneously in both outer channels. In column SC2-2a, however, the two outer channels buckled at slightly different loads, as shown in Figure 3.56. Both channel sections also initiated buckling in different locations along the height: one channel buckled first between the connectors at mid-height of the column, followed by buckling near the bottom, whereas the other channel buckled first near the bottom of the column and then at mid-height. This might have been due to the effect of imperfections or the effect of contact between the components. In column SC2-4a one of the outer channels was recorded to buckle slightly before the other, as shown in Figure 3.57. For both columns, both buckling stresses are listed in Table 3.14.

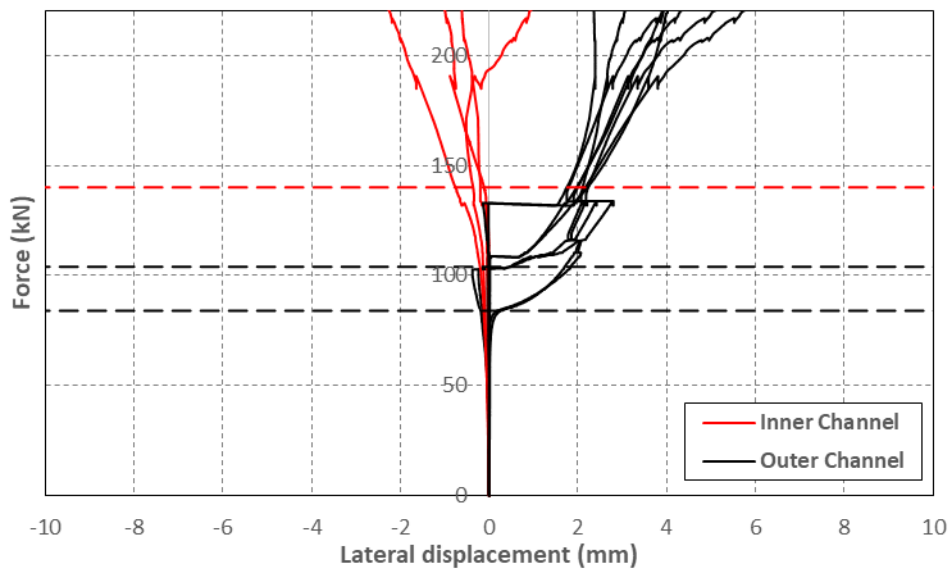


Figure 3.56: Axial load vs lateral displacements in SC2-2a

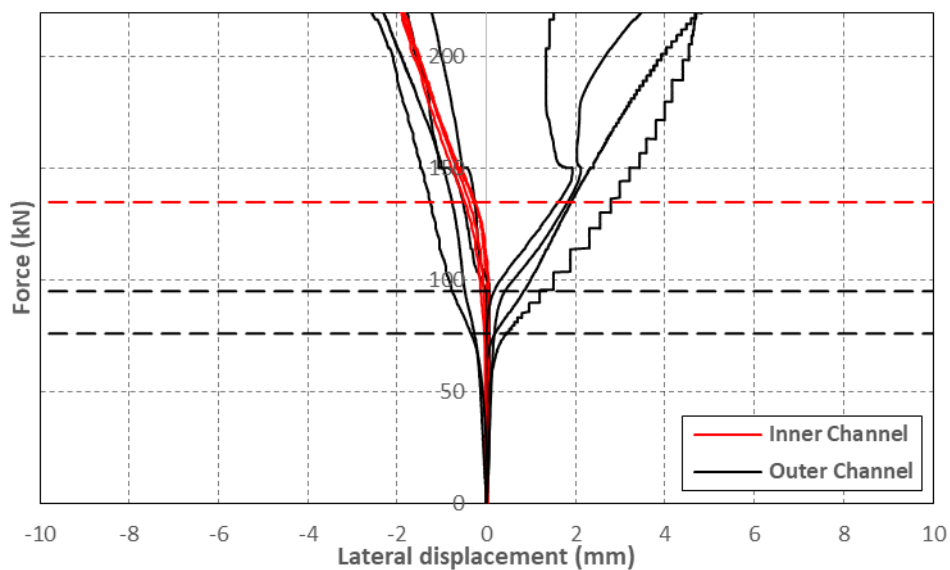


Figure 3.57 Axial load vs lateral displacements in SC2-4a

Table 3.14 shows the theoretical critical buckling stresses of the inner and outer channels, as well as the buckling stresses obtained from the tests for the outer channels. For columns SC2-2 and SC2-4, the buckling stresses of the outer channels obtained from the test are slightly larger than the predicted values, particularly in columns SC2-4. Nevertheless, a reasonably good agreement was obtained with an average error of 11 %. For columns SC2-6, the difference between the experimentally derived buckling stresses of the outer channels and the predicted values is more noticeable, with the buckling stresses obtained from the test being around 35 % larger than the theoretical ones. This indicates a significant amount of restraint exerted by the inner channels onto the outer channels as the connector spacing decreases.

Table 3.14: Buckling stresses of the components of geometry 2

Column	Theoretical buckling stress (MPa)		Buckling stress from test (MPa)	
	Inner Channel	Outer Channel	Inner Channel	Outer Channel
SC2-2a	132	76	-	77-95
SC2-2b	132	76	-	79
SC2-4a	140	72	-	69-86
SC2-4b	139	72	-	86
SC2-6a	180	70-84	-	105
SC2-6b	181	71-86	-	105

3.8.3.3 Built-up column 3

The plain and lipped channels buckled approximately at the same time in all columns with geometry 3. The critical buckling stress of the components was thus determined by dividing the load at which the components buckled over the total cross-sectional area of the column.

The theoretical and experimental critical buckling stresses of the components are listed in Table 3.15. The theoretical critical stresses were calculated at the buckle half-wave lengths observed during the test. In those columns in which the plain channels were seen to buckle in a mixed pattern with two different buckle half-wave lengths, the stresses associated with each half-wave length are included in the table.

Table 3.15: Buckling stresses of the different components of geometry 3

Column	Theoretical buckling stress (MPa)		Buckling stress from test (MPa)	
	Plain Channel	Lipped Channel	Plain Channel	Lipped Channel
SC3-2a	67-74	103	103	103
SC3-2b	67-74	102	84-96	96
SC3-5a	70-77	104	-	96-117
SC3-5b	75	104	108	108

In column SC3-2a the channels were observed to buckle at a stress level of approximately 103 MPa. This stress is very close to the theoretically predicted buckling stress of the lipped channel, while it is around 39 % higher than the highest theoretical buckling stress predicted for the plain channel. This indicates that the plain channels clearly benefited from the restraint provided by the lipped channels. A similar conclusion can be drawn for the twin specimen SC3-2b, although in this case one of the potentiometers placed near the bottom of the column detected the onset of local buckling in one of the plain channels at a slightly lower stress level. The rest of potentiometers, however, detected local buckling of the components at a stress level of 96 MPa, which was around 30 % higher than the stress predicted for the plain channels and 6% lower than the stress predicted for the lipped channels.

In column SC3-5b local buckling occurred at a stress level very close to the predicted value for the lipped channels, and around 44 % larger than the predicted value for the plain channels. In column SC3-5a local buckling was first detected in the lipped channels by the potentiometers at mid-height of the column at a stress level of 96 MPa and subsequently by the potentiometers near the bottom at a stress level of 117 MPa (Figure 3.58). These stresses are relatively close to the predicted buckling stress of the lipped channels. However, compared to its twin specimen an anomaly was observed in that the plain channels (which have the lower theoretical buckling stress) remained unbuckled up to a stress level of 117 MPa. However, as soon as the plain channels buckled, the lipped channels were forced to adjust and reverse the initial directions of some of their out-of-plane deformations in order to accommodate local buckling of the plain channels (Figure 3.58).

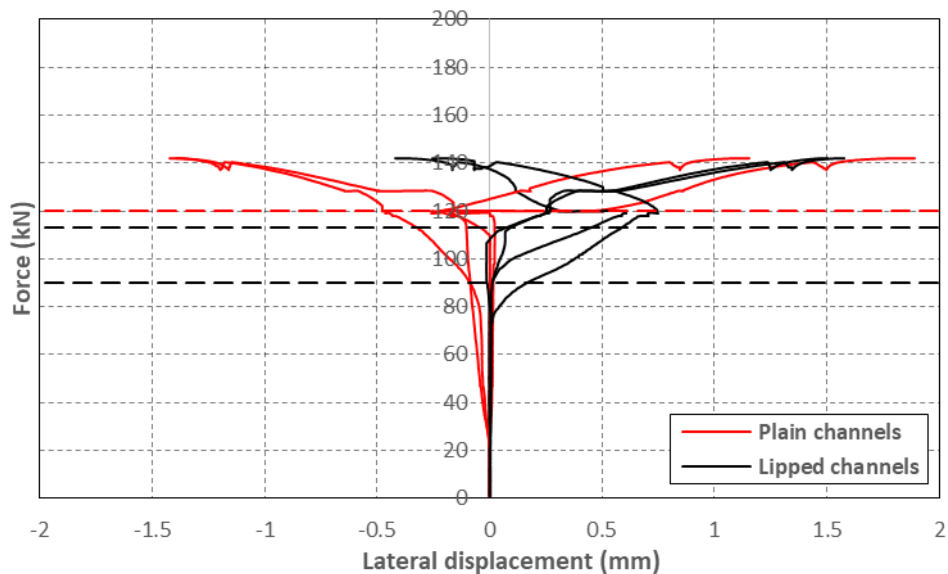


Figure 3.58: Axial load vs lateral displacements in SC3-5a

3.8.3.4 Built-up column 4

In columns SC4-2, the plain channels buckled before the lipped channels, while in columns SC4-5 all the components buckled at approximately the same time. Consequently, the experimental buckling stresses of the lipped channels of columns SC4-5, as well as the experimental buckling stresses of the plain channels of all columns were determined by dividing the load at which the components buckled over the total area of the cross-section.

Table 3.16 lists the theoretical and experimental buckling stresses of the different components of the columns with geometry 4. As the buckle half-wave length of the plain channels could not be directly observed during the tests due to the geometric arrangement, theoretical buckling stresses associated with buckle half-wave lengths of 167 mm and 83 mm were included in the table. These values correspond to the plain channels generating two and four half-waves between connectors in columns SC4-2, respectively, or one and two half-waves between connectors in columns SC4-5. These assumed values are close to the natural local buckle half-wave length of 130 mm, and consistent with the observations in the (geometrically identical) plain channels of columns SC3.

Table 3.16: Buckling stresses of the different components of geometry 4

Column	Theoretical buckling stress (MPa)		Buckling stress from test (MPa)	
	Plain Channel	Lipped Channel	Plain Channel	Lipped Channel
SC4-2a	66-73	100	87	-
SC4-2b	66-72	100	88	-
SC4-5a	66-73	105	73-91	91
SC4-5b	69-76	103	93-104	104

For specimens SC4-2, Table 3.16 shows that the plain channels buckled at a stress level which is around 21 % higher than the highest predicted value for the assumed buckle half-wave lengths. This is due to the restraint exerted by the lipped channels, which force the flanges of the plain channels to buckle inwards.

For specimens SC4-5, the plain and lipped channels buckled, in general, at approximately the same stress level. However, it should be noted that some potentiometers recorded buckling in the plain channels at slightly lower stresses compared to the lipped channels, as shown in Figure 3.59 for column SC4-5b. This does not alter the overall conclusion, however, that the plain channels buckled at stresses which were around 25 % higher than the predicted ones, while the lipped channels buckled at stresses which were up to 13 % lower than the predicted ones. This again illustrates that the plain channels benefited from the restraint provided by the lipped channels, while the plain channels as a result of their buckling deformations played a role in initiating buckling in the lipped channels.

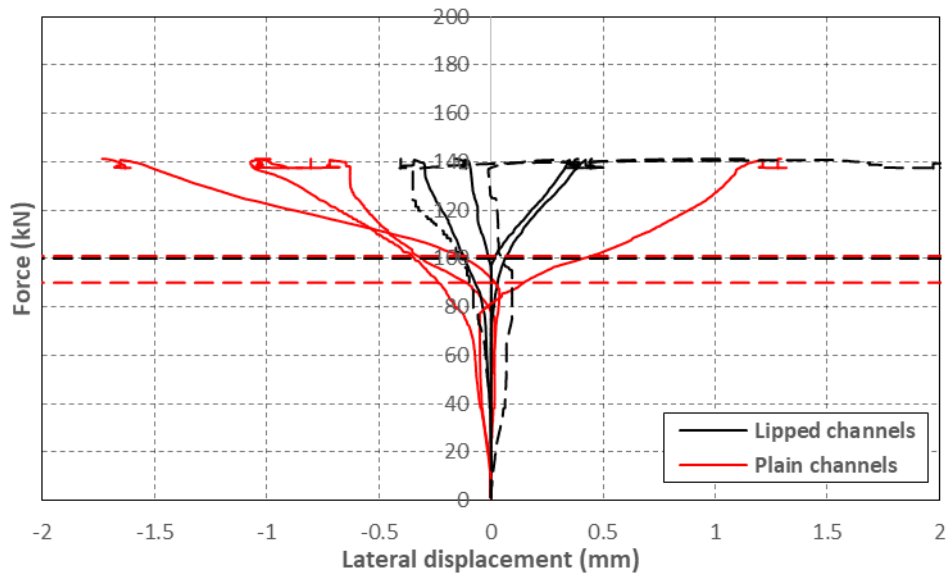


Figure 3.59: Axial load vs lateral displacements in SC4-5b

3.8.4 Ultimate load

Figure 3.60 shows a typical load-axial shortening curve (SC2-4a). The figure also shows (in red) the equivalent ‘static’ curve, obtained by eliminating strain rate dependent effects. The red curve was obtained by scaling down the load values outside the elastic range using the observed settlement in the load after halting the test close to the ultimate load.

Figure 3.61, Figure 3.62, Figure 3.63 and Figure 3.64 plot the (static) load vs. axial displacement curves of all columns with geometries SC1, SC2, SC3 and SC4, respectively. It is worth pointing out the marked decrease in the stiffness of the columns SC1 after first buckling of one of their components takes place, compared to the more gradual decrease in stiffness observed in the columns with geometries SC2, SC3 and SC4. This decrease in stiffness experienced by columns SC1 can be explained by the fact that the cross-sectional area of the plate sections contributed 57 % to the total cross-sectional area of the built-up column while, after buckling in a global flexural mode, these sections were unable to contribute in resisting a further increase in load.

The ultimate loads obtained for all the columns with geometries SC1, SC2, SC3 and SC4 are listed in Table 3.17, Table 3.18, Table 3.19 and Table 3.20, respectively. The tables include both the ‘dynamic’ and the ‘static’ ultimate loads, together with the averaged values for each set of twin columns.

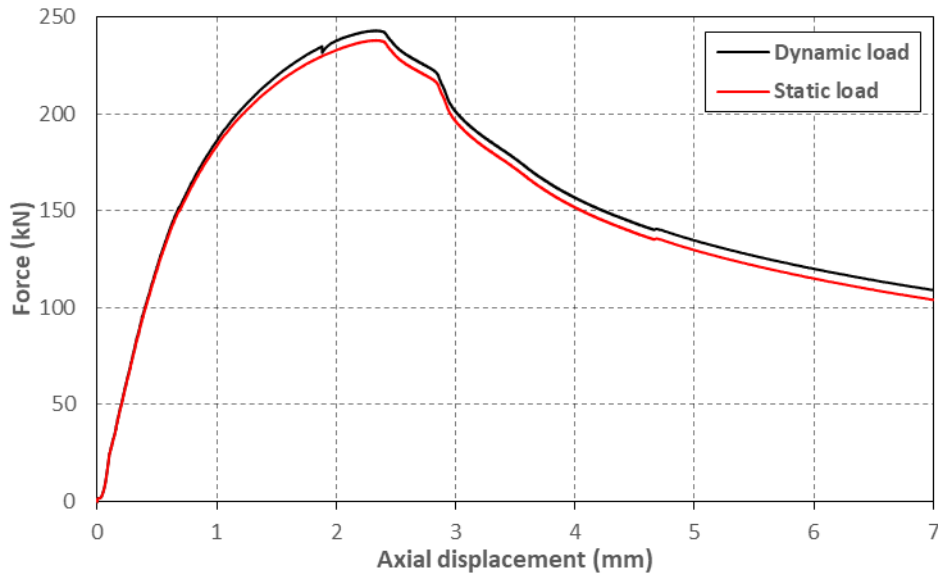


Figure 3.60: Axial load vs axial displacements in SC2-4a

3.8.4.1 Built-up column 1

Table 3.17 shows that for the columns with geometry 1, the difference in the (static) ultimate load achieved in twin specimens was 9 % for columns SC1-2, 4 % for columns SC1-3 and 7 % for columns SC1-5. The tests also showed a moderate increase in ultimate load as the spacing between connectors was reduced. More specifically, halving the spacing between connectors from 333 mm to 167 mm produced an increase in the average ultimate load of 11 %.

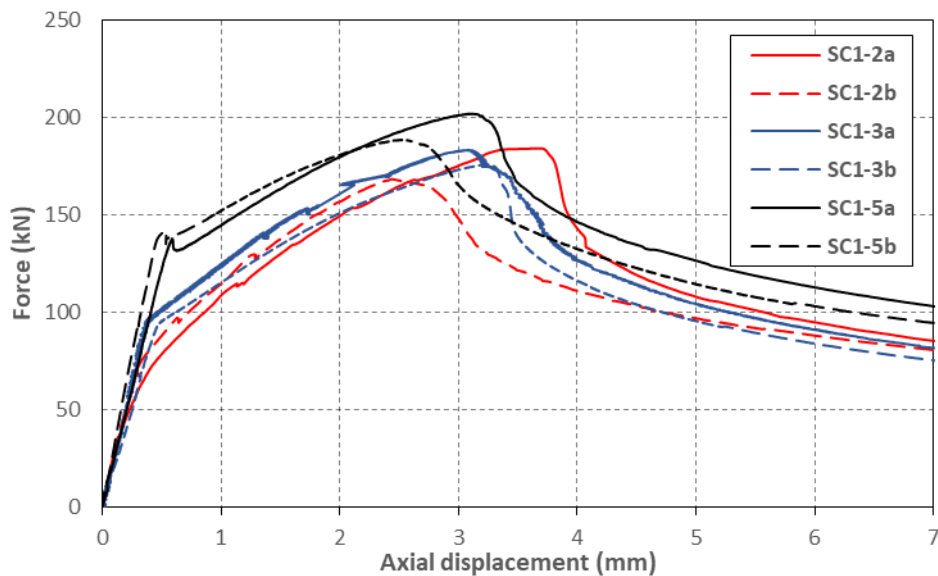


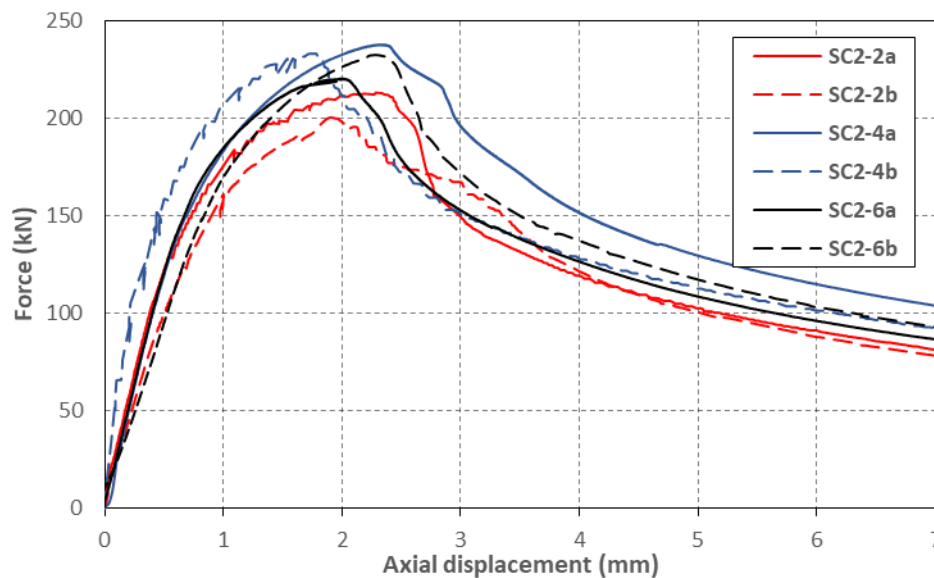
Figure 3.61: Axial load vs. deformation curves: geometry 1

Table 3.17: Ultimate loads: geometry 1

Column	Ultimate load (kN)		Averaged Ultimate load (kN)	
	Dynamic	Static	Dynamic	Static
SC1-2a	190.47	183.97	181.56	176.07
SC1-2b	172.65	168.17		
SC1-3a	193.01	183.01	189.44	179.44
SC1-3b	185.86	175.86		
SC1-5a	208.60	201.72	201.94	195.11
SC1-5b	195.28	188.50		

3.8.4.2 Built-up column 2

In the columns with geometry 2 good agreement was again obtained between the results of twin specimens, as shown in Table 3.18. The difference in ultimate load was 6 % for columns SC2-2, 2 % for columns SC2-4 and 5 % for columns SC2-6. In this case the tests showed that reducing the spacing between connectors did not necessarily result in a noticeable increase in ultimate load. For example, the columns with a connector spacing of 140 mm (columns SC2-4) showed marginally higher ultimate loads than columns with connectors spaced every 100 mm (columns SC2-6). However, the largest connector spacing (233 mm) did result in an evidently lower ultimate load, which was on average 9 % below that of the SC2-6 columns.

**Figure 3.62: Axial load vs. deformation curves: geometry 2****Table 3.18: Ultimate loads: geometry 2**

Column	Ultimate load (kN)		Averaged Ultimate load (kN)	
	Dynamic	Static	Dynamic	Static
SC2-2a	227.46	213.32	220.97	206.83
SC2-2b	214.47	200.34		
SC2-4a	243.00	238.00	241.20	235.70
SC2-4b	239.39	233.39		
SC2-6a	226.24	220.54	232.18	226.58
SC2-6b	238.12	232.62		

3.8.4.3 Built-up column 3

Table 3.19 shows that the difference in ultimate load between twin specimens was 3 % for columns SC3-5 and just 1 % for columns SC3-2. The results also show that halving the connector spacing from 333 mm to 167 mm only resulted in a negligible increase in ultimate capacity of 2 %.

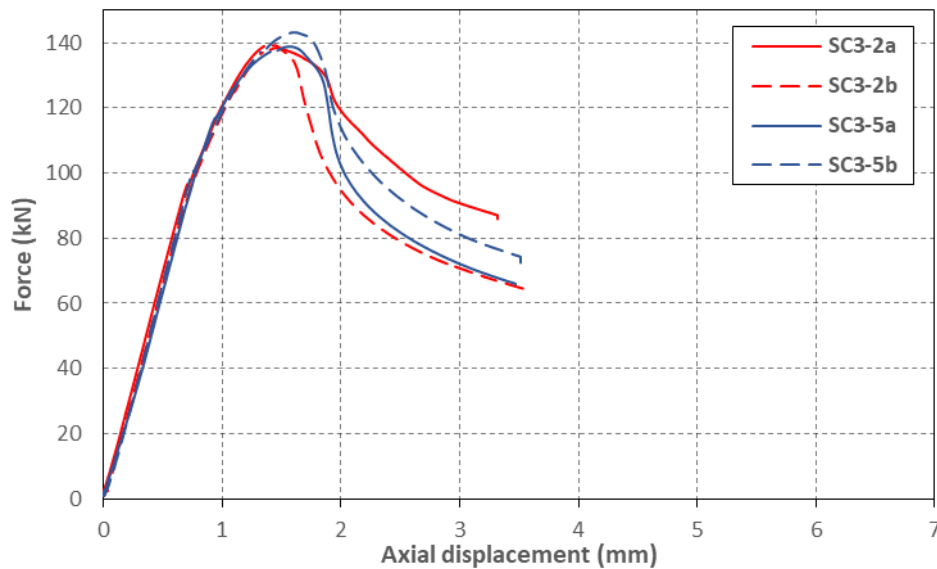


Figure 3.63: Axial load vs. deformation curves: geometry 3

Table 3.19: Ultimate loads: geometry 3

Column	Ultimate load (kN)		Averaged Ultimate load (kN)	
	Dynamic	Static	Dynamic	Static
SC3-2a	142.90	139.30	142.32	138.92
SC3-2b	141.73	138.53		
SC3-5a	142.07	138.77	144.03	141.08
SC3-5b	146.00	143.40		

3.8.4.4 Built-up column 4

With respect to columns SC4, Table 3.20 shows that the difference in ultimate load between twin specimens was 3 % for columns SC4-5 and 0.7 % for columns SC4-2. In this case, reducing the connector spacing actually resulted in a slight reduction in the ultimate capacity. More specifically, halving the connector spacing from 333 mm to 167 mm caused a reduction in the ultimate capacity of 6 %. The difference is quite marginal and might be due to the statistical variation of the relevant parameters (imperfections, geometry, material properties, etc.). Whether this is the case or not will be further investigated using detailed finite element models in following chapters.

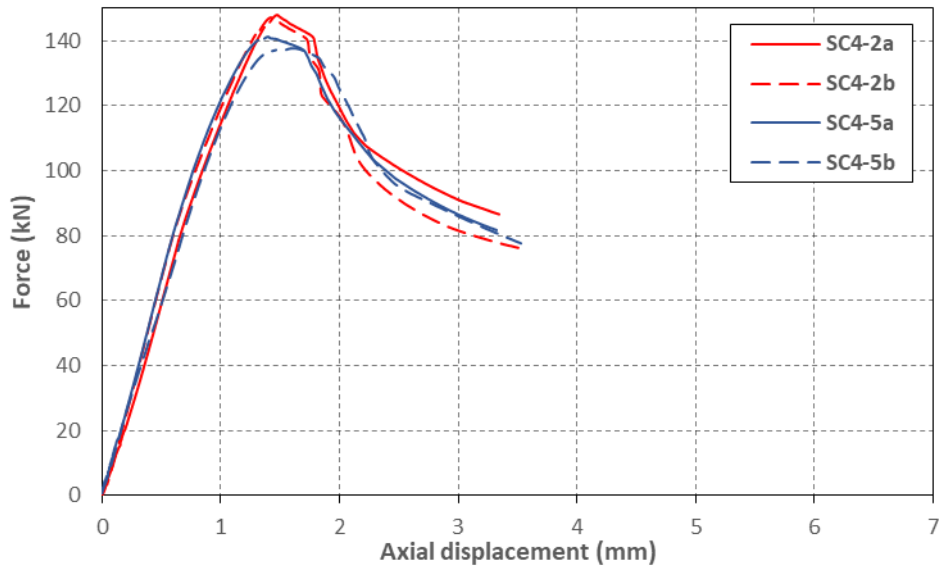


Figure 3.64: Axial load vs. deformation curves: geometry 4

Table 3.20: Ultimate loads: geometry 4

Column	Ultimate load (kN)		Averaged Ultimate load (kN)	
	Dynamic	Static	Dynamic	Static
SC4-2a	150.29	148.09	149.61	147.56
SC4-2b	148.93	147.03		
SC4-5a	144.13	141.23	142.69	139.49
SC4-5b	141.24	137.74		

3.9. Summary and conclusions

An experimental program was carried out consisting of 20 built-up thin-walled stub columns with four different cross-sectional geometries. The cross-sections were assembled from flat plate, plain channels and lipped channels with nominal thicknesses ranging from 1.2 mm to 2.4 mm. Two of the cross-sectional geometries (SC1 and SC2) were assembled using M6 bolts, while the other two (SC3 and SC4) were assembled using M5.5 self-drilling sheet metal screws. The connector spacing was varied among specimens of the same cross-sectional geometry.

The experimental investigation included tensile coupon tests to determine the material properties of the flat portions and the corner regions of the different components. Accurate measurements of the out-of-plane geometric imperfections of the specimens were also carried out using a laser sensor.

The columns were compressed between fixed supports in a displacement controlled regime. Strain gauge readings obtained from a select number of specimens confirmed a uniform introduction of the load into all components of the cross-sections. This was achieved thanks to

hand-filing the end sections, placing a double row of connectors at the specimen ends and epoxy-gluing the end plates to the specimens.

The out-of-plane deformations of each column component were recorded during the test using potentiometers. This allowed, in most cases, a determination of the stress at which buckling occurred in the components. These values were compared to theoretical predictions which considered the individual components in isolation without any interaction with the rest of the cross-section, but used the experimentally observed wave-lengths.

The following conclusions could be drawn from the experimental investigation:

- It was clear from the observations of the deformed column shapes that the buckling patterns of the individual components within the columns were subject to considerable restraint. This restraint manifested itself in two different ways: (1) a change in the natural local buckle half-wave length to accommodate the presence of the connectors, and (2) contact between adjacent surfaces forcing the buckling out-of-plane displacements to occur in a certain direction.
- Substantially different buckling patterns were generally observed in columns with the same cross-sectional geometry, but different connector spacing.
- Out of all the possible buckling patterns allowed by the constraints imposed by the connectors and contact with the rest of the column, the components choose the one which required the lowest buckling stresses. This resulted in some cases in a buckling pattern with a varying half-wave length along the member, as was observed in the outer channels of columns SC2-6, or in a buckling pattern isolated in one field, as seen in the plate sections of columns SC1-2 and SC1-3. The latter was only possible after some slip between the components at the connector points.
- By comparing the theoretical predictions of the buckling stresses to the experimentally measured values it was observed that the buckling stress of the most slender components was increased by up to 44 % as a result of the restraint provided by the remainder of the cross-section. The amount of restraint was seen to be dependent on the connector spacing. The less slender components, on the other hand, generally showed buckling stresses which ranged from being 30 % lower than the predicted values to being very close to the theoretical value.
- Although the buckling deformations and the buckling stresses of the component sections showed considerable dependence on the connector spacing, the ultimate capacity showed much less sensitivity:
 - Columns SC1 exhibited a modest increase in the ultimate strength of around 11 % when halving the connector spacing. This gain was mainly a result of the

increase in the global flexural buckling capacity of the plate sections in between connectors.

- When the critical buckling modes of the individual components were all local, the difference was even smaller. Only the SC2-2 columns showed 11 % less capacity than the SC2-4 and SC2-6 columns, which had similar capacities. For geometries 3 and 4, the effect of the connector spacing was negligible or non-existent.
- Geometries 3 and 4, which were assembled from individual components with identical nominal dimensions using the same connector type and spacing, allowed a direct comparison with respect to the effect of their relative arrangement. However, both geometries achieved similar capacities. For the specimens with two intermediate connectors, columns SC3 showed an ultimate capacity which was on average 6 % lower than the one achieved by columns SC4, while for the specimens with five intermediate connectors the ultimate capacities were within 1 % of each other.

Chapter 4

Experimental Study of Cold-Formed Steel Built-up Beams

4.1. Introduction

The experimental programme described in this chapter intended to investigate the cross-sectional bending moment capacity of two different built-up thin-walled beams. Particular attention was devoted to the way in which the individual components of the cross-section interacted with each other as they underwent local buckling. The specimens were tested in a 4-point bending configuration, with point loads applied 1600 mm apart. This length was long enough to allow the component sections to generate several buckles along the constant moment span. Lateral-torsional buckling was excluded as a failure mode by means of lateral supports. All specimen preparation, assembly and testing was carried out in the Heavy Structures Laboratory at The University of Sheffield.

The test specimens were assembled using commercially available cold-formed steel sections, supplied by BW Industries. All sections were manufactured from pre-galvanized steel plates with a nominal 0.04 mm Z275 zinc coating and a guaranteed yield strength of at least 450 MPa. The two built-up cross-sectional geometries are illustrated in Figure 4.1. The first built-up section consisted of two channels with a nominal depth of 129 mm and thickness of 1.5 mm, which were connected back-to-back, and two extra channels with a nominal depth of 104 mm and thickness of 1.2 mm, which were attached to the flanges of the back-to-back channels. The second built-up geometry was assembled using three channels. Two channels with a nominal depth of 129 mm and thickness of 1.5 mm were connected back-to-back and a channel with a nominal depth of 104 mm and 1.2 mm thickness was attached to the top flanges of the back-to-back channels with its flanges facing upward. Grade 8.8 M6 bolts were used to join the individual sections together in both geometries. Each built-up geometry was tested with three different connector spacings and each test was repeated, accounting for a total of 12 tests. The geometric imperfections of all specimens were recorded prior to the test. Coupon tests were also

extracted from the flat portions and the corners regions of each different components in order to determine their material properties.

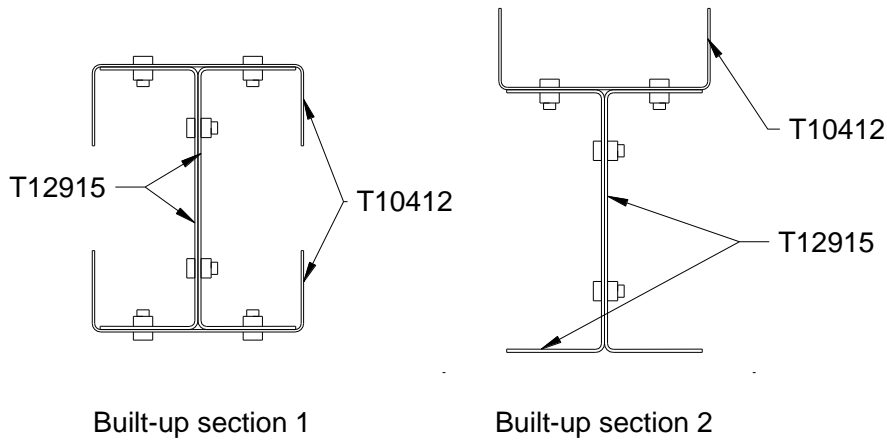


Figure 4.1: Built-up cross-sections

4.2. Labelling

The labelling used to refer to the cross-sectional components is consistent with the one used for the stub columns: the channel sections are identified using the letter ‘*T*’ followed by the nominal width of their web in mm and their nominal thickness in mm multiplied by 10.

The built-up specimens are labelled using the letter ‘*B*’ followed by the number 1 or 2, indicating the geometry with reference to Figure 4.1. Then, following a hyphen, the number of intermediate rows of connectors between the loading points is indicated. Finally, since each test was repeated, the letter ‘*a*’ and ‘*b*’ are used to differentiate between twin test specimens. As an example, the label ‘*B1-2a*’ refers to the first beam tested with cross-sectional geometry 1 which has connectors at two intermediate cross-sections along the constant moment span.

4.3. Material Properties

A series of coupon tests were carried out in order to determine the material properties of the beams. The coupons were cut along the rolling direction (i.e. the longitudinal direction of the beams) near the end section of one of the test specimens after testing. This location was chosen since the material had not been subject to significant stress during the test. For each type of channel section, two flat coupons were cut along the centre line of the web and two corner coupons were taken from the web-flange junction. Therefore, eight coupons were tested in total. The dimensions of all coupons follow the specifications set in CEN (2009).

4.3.1 Flat coupons

The flat coupons had the same nominal dimensions as those used to determine the material properties of the stub columns, and they were measured and instrumented in the same way, as described in Section 3.3.1 of Chapter 3. Figure 4.2 shows a flat coupon during testing, while Table 4.1 lists the measured width and thickness of the coupons. The letters ‘*a*’ and ‘*b*’ are used to differentiate between twin coupons.

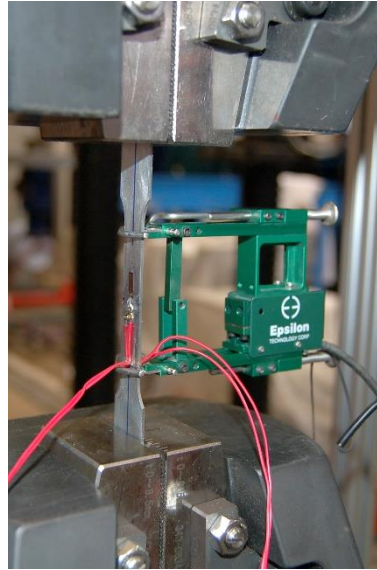


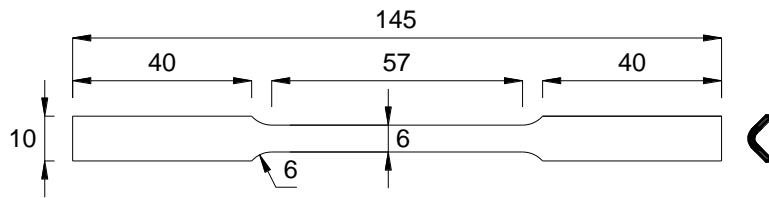
Figure 4.2: Flat coupon during testing

Table 4.1: Measured dimensions of flat coupons

Component section	Coupon	b_c (mm)	t (mm)	A (mm ²)
T10412	a	12.484	1.141	14.2962
T10412	b	12.480	1.146	14.3325
T12915	a	12.482	1.501	18.7355
T12915	b	12.481	1.484	18.5218

4.3.2 Corner coupons

The corner coupons had a nominal width of 6 mm. The nominal dimensions of the coupons are illustrated in Figure 4.3. They were instrumented in the same way as the corner coupons taken from the stub columns and were tested using the same arrangement, as described in Section 3.3.2. Figure 4.4 shows the corner coupons during testing.



Dimensions in mm

Figure 4.3: Corner coupon dimensions

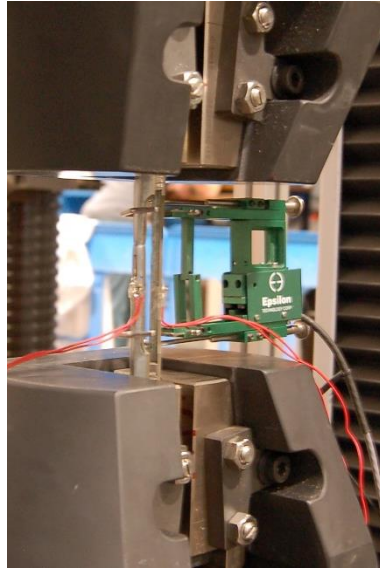


Figure 4.4: Pair of corner coupons during testing

The cross-sectional area of the corner coupons along the gauge length was determined by following the technique previously described in Section 3.3.2 of Chapter 3, which involves taking a macro-photograph of the coupon cross-section from each end. The photographs taken from each end of the coupon provided two cross-sectional areas per coupon, which were averaged. Differences of less than 1.42 % and 1.08 % were observed between the calculated areas obtained from each end of coupons T10412 and T12915, respectively. Table 4.2 lists the area obtained for each corner coupon after accounting for the (nominal) thickness of the zinc coating.

Table 4.2: Measured area of corner coupons

Component section	Coupon number	A (mm ²)
T10412	a	7.9821
T10412	b	7.9549
T12915	a	10.4495
T12915	b	10.4286

As in the flat coupons, the readings from the extensometer were used to obtain the average stress-strain curve of each pair of coupons, while the readings from the strain gauges were used to calculate the Young's modulus.

4.3.3 Coupon testing and results

The tensile coupons were tested in a 300 kN Shimadzu AGS-X universal testing machine controlled in displacement mode. A displacement rate of 2 mm/min was used for all coupon tests.

Each test was halted for 2 minutes at regular intervals in order to allow the load to settle down to 'static' values and eliminate strain rate effects. The 'dynamic' stress-strain curve obtained from the test was then used to generate a *static* stress-strain curve from which the material properties were derived. As an example, Figure 4.5 shows the stress-strain curve of the pair of corner coupons cut from channel T12915. The figure also includes the *static true* stress-strain curve, which was used to define the material properties in a numerical Abaqus model. The stress-strain curves of all the tested coupons are included in Appendix D.

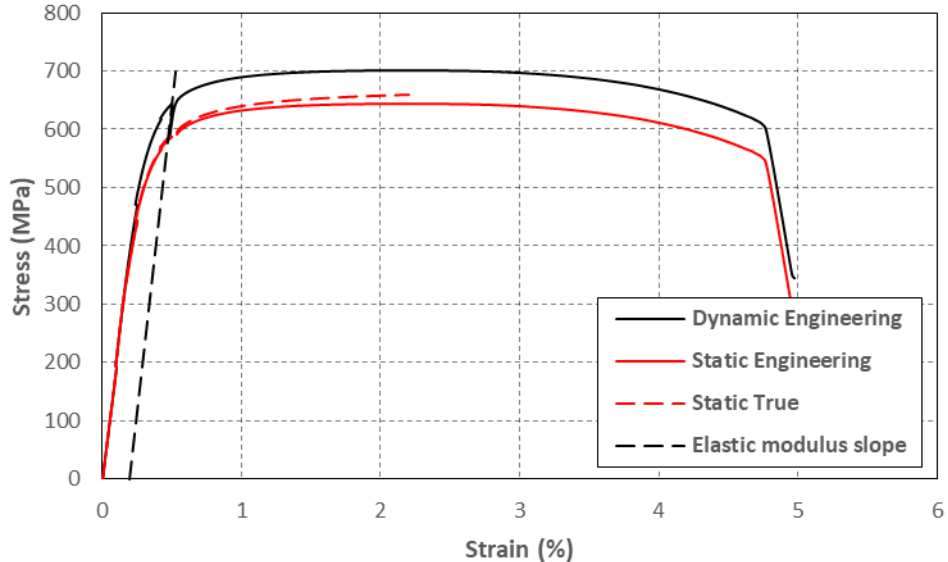


Figure 4.5: T12915 Corner coupon test results

Table 4.3 illustrates the (static) engineering values of the material properties obtained for each coupon, as well as the averaged values. In the table, ($\sigma_{0.2\%}$) corresponds to the 0.2% proof stress, (σ_u) is the ultimate tensile strength and (ϵ_f) is the elongation after fracture measured over a gauge length of 50 mm.

Table 4.3: Material properties of tensile coupons

Type	Section	E (GPa)		$\sigma_{0.2\%}$ (MPa)		σ_u (MPa)		ϵ_f (%)	
		Ind.	Avg.	Ind.	Avg.	Ind.	Avg.	Ind.	Avg.
Flat	T10412-a	212	208	432	426	471	466	14	14
Flat	T10412-b	204		419		461		14	
Flat	T12915-a	201	204	544	531	628	619	13	13
Flat	T12915-b	207		518		610		12	
Corner	T10412-a	193	198	-	460	-	479	-	3
Corner	T10412-b	202		-		-			
Corner	T12915-a	211	218	-	585	-	645	-	5
Corner	T12915-b	225		-		-			

The results confirmed that the steel grade used to fabricate the channels was at least S450, as specified by the manufacturer. Although the values of the 0.2 % proof stress listed in the table for the flat coupons taken from sections T10412 are smaller than 450 MPa, this can be attributed to the fact that these values correspond to the *static* 0.2 % proof stress, and not the *dynamic* 0.2 % proof stress, which is normally used to determine the grade of the steel. The *dynamic* values of the 0.2 % stress obtained from all the tensile coupons were larger than 450 MPa.

It is also important to mention that the steel grade of section T12915 is considerably larger than the minimum specified by the manufacturer, with the flat coupons extracted from these sections showing an averaged *static* 0.2 % proof stress of 531 MPa.

4.4. Section Design and geometry

Two different built-up cross-sectional geometries were chosen for testing, as illustrated in Figure 4.1. The first geometry was chosen because it resembles the traditional I-shaped cross-section widely used for beams in construction. In addition to the traditional back-to-back channel arrangement this built-up geometry included two additional channels to increase the flange area and provide increased bending capacity. The second built-up geometry was selected in consultation with cold-formed steel manufacturers/contractors, who indicated that this built-up geometry is regularly used as a solution to bridge large openings in structural framing systems made of cold-formed steel. The back-to-back channels thereby work as a lintel, while the top channel is used as a track to receive the studs of the wall above the opening. Due to lack of design guidance, however, only the capacity of the back-to-back channels is currently counted on in practice.

In addition to the connectors placed in the cross-sections under the loading points, specimens were designed with zero, two and three equally spaced connectors within the constant moment span. Two identical beams were fabricated for each configuration in order to gain increased confidence in the results. All beams were designed to fail by local buckling of the individual components, without any influence of global instability of the beam. The shear span length was

chosen as 700 mm. This was determined to be long enough to avoid premature shear failure in the webs of the built-up specimens. The component sections were bolted together in this region with a connector spacing of 100 mm to encourage even load sharing and as an extra safety measure against shear buckling in the webs of the built-up specimens, as shown in Figure 4.10 and Figure 4.11 for specimens with built-up geometry 1 and 2, respectively. The nominal dimensions of the cross-sections are listed in Table 4.4. The symbols in the table refer to the dimensions of the individual channels, as clarified in Figure 4.6.

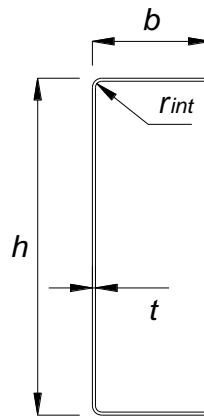


Figure 4.6: Nomenclature used to refer to the dimensions of the component sections

Table 4.4: Nominal dimensions of the component sections

Beam	Section	h (mm)	b (mm)	t (mm)	r_{int} (mm)
B1	T12915	129	48	1.5	3.0
	T10412	104	42	1.2	2.4
B2	T12915	129	48	1.5	3.0
	T10412	104	42	1.2	2.4

The built-up specimens were designed with the help of an elastic stability analysis using the CUFSM 4.05 software (Schafer, 2006). Each component was analysed individually (without interaction with the other components), but under a linear stress gradient consistent with the assumption that the whole cross-section remained plane under pure bending (no slip in the connectors). Figure 4.7 illustrates the stress distribution used as input in CUFSM 4.05 for each component. In addition, the connectors were assumed not to translate or rotate while the component sections buckled. Therefore, the individual components were only allowed to rotate with respect to each other at the connector location about an axis aligned with the connector axis.

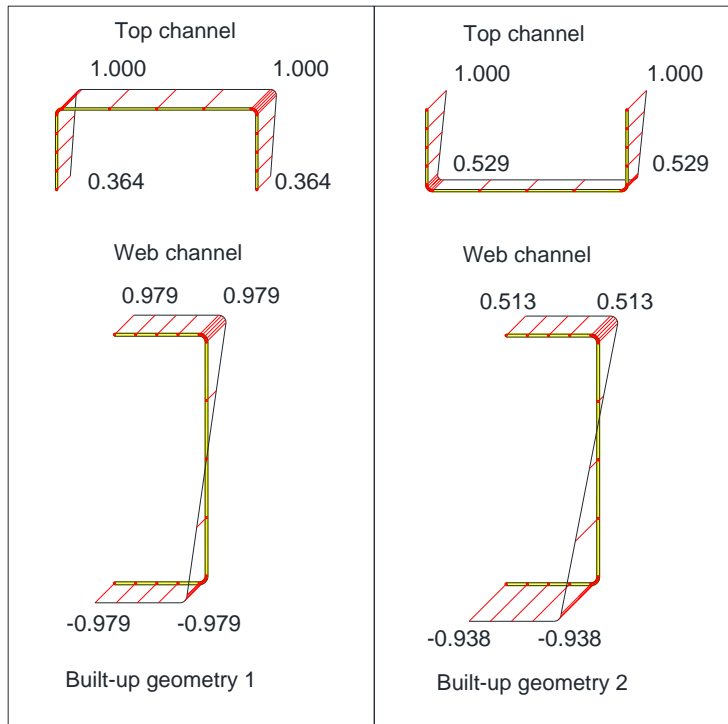


Figure 4.7: Stress distribution within component sections for elastic stability analysis

Figure 4.8 and Figure 4.9 show the critical buckling stress vs. the buckle half-wave length of the components of geometries 1 and 2, respectively. The critical stresses in these diagrams represent the maximum compressive stresses in the full cross-section, in order to allow a fairer comparison and evaluate which component of the built-up cross-section is likely to buckle first. Thus, in Figure 4.8, the vertical axis represents the stress in the web of the channel which forms the top flange of geometry 1 (T10412), whereas in Figure 4.9 it is the stress at the tip of the flanges of the top channel in geometry 2. Figure 4.8 shows that the critical local buckle half-wave length of both types of channels in geometry 1 is 110 mm. Figure 4.9, on the other hand, shows that in geometry 2 the critical half-wave lengths are 120 mm for the top channel and 110 mm for the web channels.

Based on the assumption that the connectors do not translate or rotate as the components buckle, an expected buckle half-wave length can be determined depending on the number of buckles that can geometrically fit between connectors. Of all possible solutions, the one that corresponds to the lowest buckling stress in the signature curve is the most likely to occur. For instance, in the beams with 3 rows of intermediate connectors (corresponding to a connector spacing of 375 mm), the lowest critical buckling stress is achieved if four half-waves with a length of 94 mm occur between connectors. This conclusion applies equally to all component channels of geometries 1 and 2. Similarly, in the beams with 2 rows of intermediate connectors, four half-waves of 125 mm are expected. In the beams without intermediate connectors, 14 half-waves are anticipated in the components of geometry 1, while in geometry 2 the top channel and the

web channels are expected to display 12 and 14 half-waves between the loading points, respectively.

The elastic stability analysis also indicated that interaction between local and global buckling of the top channel might occur in both geometries with zero intermediate connectors provided that the global buckling stress of the locally buckled section falls below the point at which the ultimate capacity of the beam is reached. The critical global buckling mode thereby corresponding to a flexural-torsional mode with a buckling half-wave length of 750 mm.

Table 4.5 and Table 4.6 show the predicted buckling stresses of the individual components of geometries 1 and 2, respectively. It is seen that the top channel is the critical component and is expected to buckle first in all beams, irrespective of the geometry.

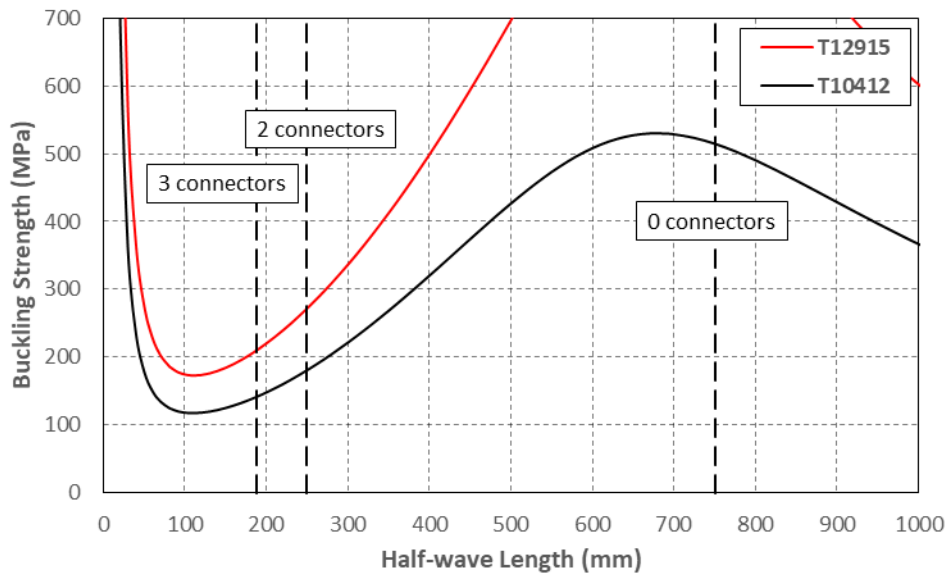


Figure 4.8: Signature curve of the components of geometry 1

Table 4.5: Predicted buckling stresses of the components of geometry 1

Beam	Predicted buckling stress (MPa)		Number of half-waves between connectors	
	T12915	T10412	T12915	T10412
B1-0	173	118	14	14
B1-2	174	119	4	4
B1-3	176	120	4	4

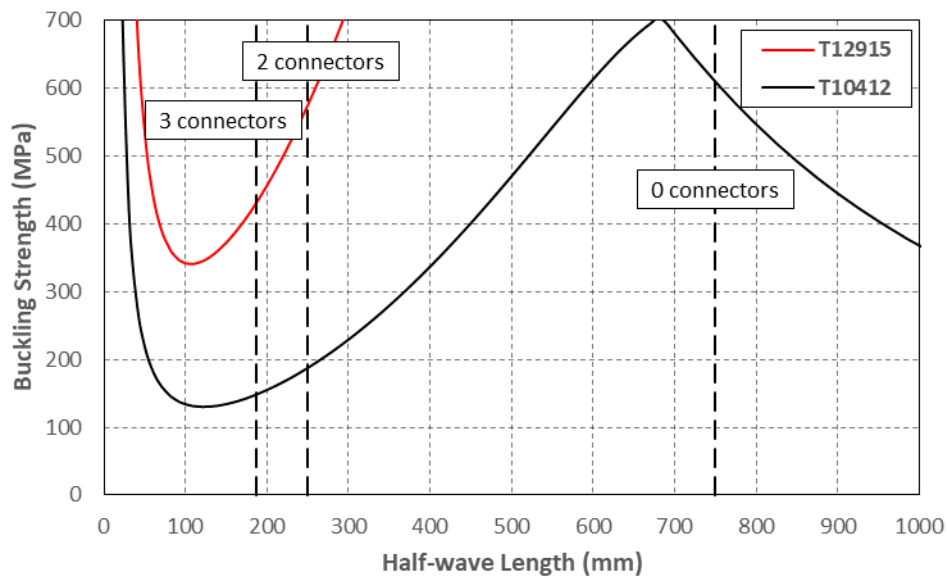


Figure 4.9: Signature curve of the components of geometry 2

Table 4.6: Predicted buckling stresses of the components of geometry 2

Beam	Predicted buckling stress (MPa)		Number of half-waves between connectors	
	T12915	T10412	T12915	T10412
B2-0	340	130	14	12
B2-2	348	130	4	4
B2-3	344	136	4	4

4.5. Cross-section assembly and specimen preparation

The assembly of the built-up beams was carried out in the Heavy Structures Laboratory at The University of Sheffield.

The cross-sectional dimensions of each component were measured at several locations along its length before assembly. The dimensions of the web and the flanges were measured using a digital Vernier caliper with a precision of 0.03 mm. All measurements were taken of the outside dimensions. The thickness of the cross-section was measured with a micrometre with a precision of ± 0.002 mm. The measured cross-sectional dimensions are listed in Table 4.7 and Table 4.8 for all the specimens belonging to geometry 1 and 2, respectively. Each listed value represents the average of several measurements. The values reported in the tables were obtained after accounting for the 0.04 mm nominal thickness of the zinc coating.

Table 4.7: Measured dimensions of geometry 1 specimens

Beam	Web channels				Flange channels			
	section	Web (mm)	Flange (mm)	Thickness (mm)	section	Web (mm)	Flange (mm)	Thickness (mm)
B1-0a	T12915-1	129.36	43.38	1.493	T10412-1	104.35	39.82	1.141
	T12915-2	129.15	43.49	1.487	T10412-2	104.10	39.92	1.139
B1-0b	T12915-3	129.31	43.48	1.495	T10412-3	104.24	39.95	1.136
	T12915-4	129.20	43.45	1.493	T10412-4	104.05	39.72	1.137
B1-2a	T12915-5	129.26	43.45	1.489	T10412-5	103.95	39.94	1.137
	T12915-6	129.13	43.53	1.496	T10412-6	104.06	40.04	1.139
B1-2b	T12915-7	128.95	43.78	1.501	T10412-7	104.04	39.99	1.139
	T12915-8	129.02	43.66	1.496	T10412-8	104.01	39.97	1.144
B1-3a	T12915-9	128.93	43.74	1.498	T10412-9	103.95	39.98	1.141
	T12915-10	128.90	43.69	1.501	T10412-10	104.18	39.97	1.140
B1-3b	T12915-11	128.83	43.70	1.506	T10412-11	104.22	39.86	1.147
	T12915-12	128.87	43.69	1.497	T10412-12	103.96	39.93	1.146
Average		129.08	43.59	1.496		104.09	39.92	1.141
St. Dev.		0.183	0.136	0.005		0.129	0.087	0.004

Table 4.8: Measured dimensions of geometry 2 specimens

Beam	Web channels				Flange channels			
	section	Web (mm)	Flange (mm)	Thickness (mm)	section	Web (mm)	Flange (mm)	Thickness (mm)
B2-0a	T12915-1	129.28	43.42	1.486	T10412-1	104.11	39.71	1.141
	T12915-2	129.25	43.45	1.487	-			
B2-0b	T12915-3	129.41	43.40	1.489	T10412-2	104.04	39.92	1.136
	T12915-4	129.13	43.44	1.490	-			
B2-2a	T12915-5	129.05	43.65	1.495	T10412-3	103.99	39.71	1.137
	T12915-6	129.14	43.49	1.494	-			
B2-2b	T12915-7	128.80	43.69	1.495	T10412-4	103.89	39.76	1.137
	T12915-8	128.84	43.72	1.495	-			
B2-3a	T12915-9	129.02	43.69	1.507	T10412-5	103.98	39.78	1.133
	T12915-10	128.85	43.62	1.504	-			
B2-3b	T12915-11	128.91	43.63	1.506	T10412-6	103.95	39.70	1.134
	T12915-12	129.07	43.61	1.508	-			
Average		129.06	43.57	1.496		103.99	39.76	1.136
St. Dev.		0.201	0.123	0.007		0.076	0.083	0.003

In order to assemble the specimens, holes with a nominal diameter of 6.25 mm were first drilled in one of the components at the appropriate locations. Figure 4.10 and Figure 4.11 illustrate the locations of the holes in built-up beam 1 and built-up beam 2, respectively. The components were then positioned in their built-up configuration and secured with clamps. The first component (containing the holes) was used as a template to drill the holes in the components that were in contact with them. This allowed for an easy assembly, avoiding any mismatch of the holes. Finally, the components were bolted together with M6 bolts, and the clamps were removed. All bolts were tightened with a controlled torque of 10 Nm. This is representative of the torque exerted by a spanner when hand-tightening the bolts and did not introduce any significant pre-tensioning in the bolts. Figure 4.12 shows some of the specimens during and after the assembly process.

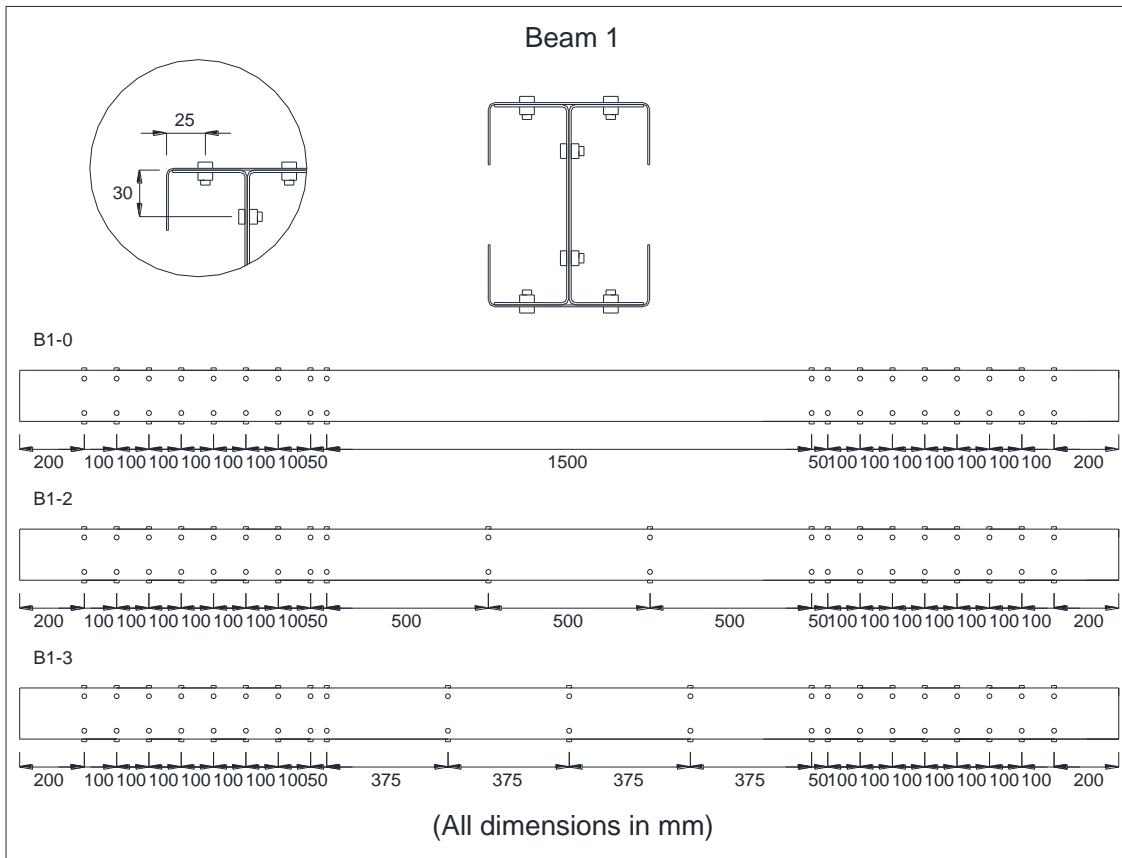


Figure 4.10: Location of connectors in geometry 1 beams

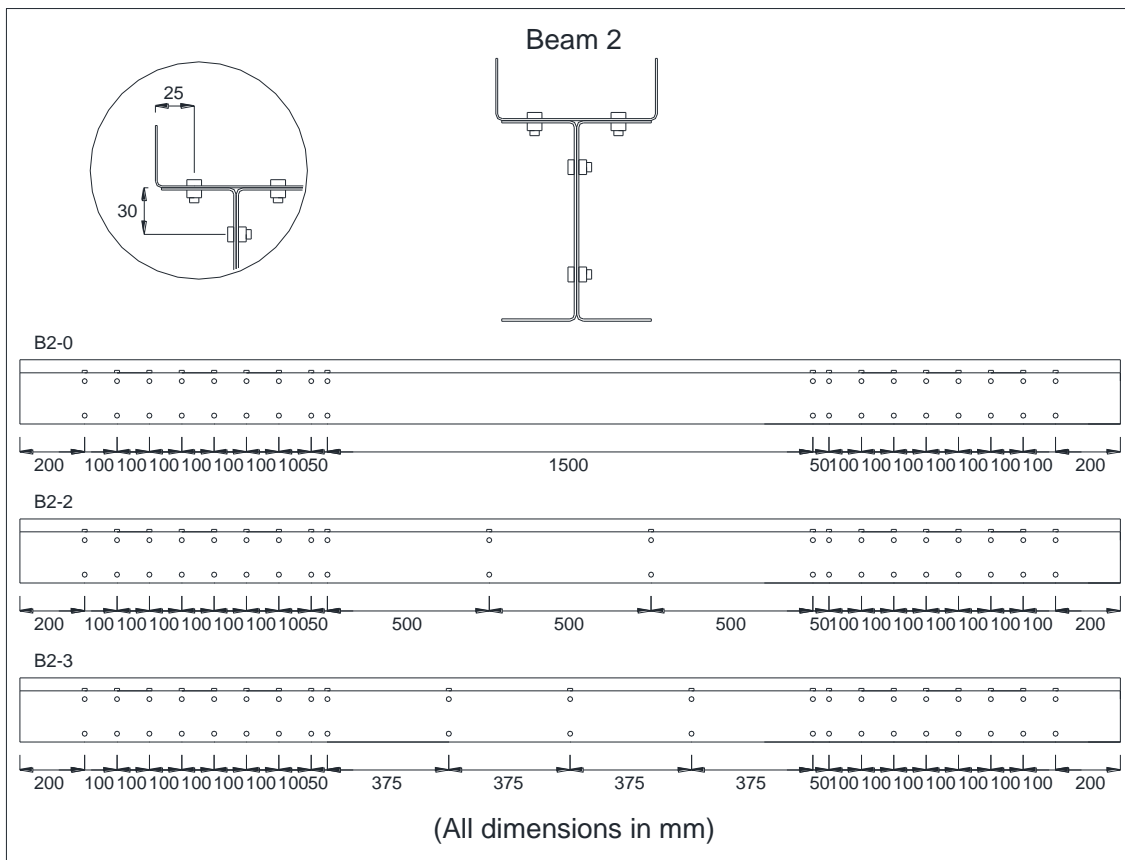


Figure 4.11: Location of connectors in geometry 2 beams

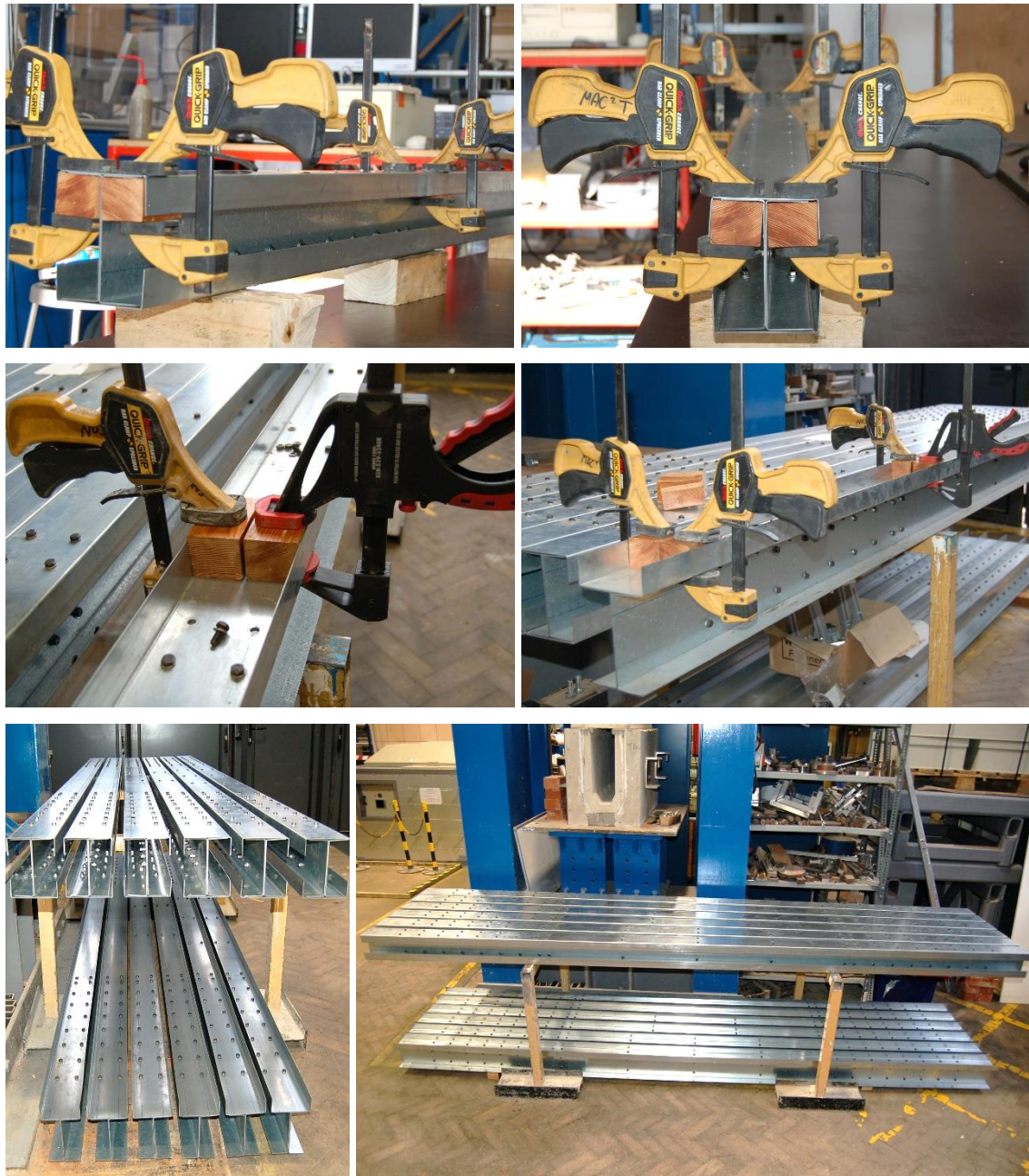


Figure 4.12: Built-up beams during and after assembly

4.6. Imperfection Measurements

The imperfections of all test specimens were measured before testing. The measurement set-up consisted of a nominally flat steel table and a traverse system powered by two electric motors which allowed the movement of a laser displacement sensor in two orthogonal directions (as previously described in Section 3.6.1 of Chapter 3). Since the specimens were expected to buckle in a local mode in the constant moment span between the applied loads, the imperfections were only recorded in this zone, which occupied a length of 1500 mm in the central part of the beams. The set-up was estimated to provide readings with an accuracy of less than 0.06 mm, as this was the guaranteed flatness of the table.

As the beams underwent bending in the test, only their top flange and the upper portion of the webs were subject to compression and were at risk of buckling. For this reason, imperfections were recorded in the webs and the top flanges of the built-up specimens only. It should be noted that in geometry 1 the channel which formed the bottom flange of the built-up beam was also observed to undergo local buckling of its flanges in the test, since the neutral axis of the built-up cross-section shifted downward by a sufficient amount due to buckling in the upper part of the cross-section. However, this did not occur until far into the post-peak range and did not have any effect on the ultimate capacity of the built-up specimen. Therefore, the imperfections of the bottom channel were not recorded.

The geometric imperfections of the specimens were recorded after assembling the individual components as much as possible. Exceptions were made for the imperfections in the webs of the built-up specimens, which were recorded before assembling the channels that form the flanges of geometry 1, and before assembling the top channel in geometry 2. This was due to the fact that for the specimens with geometry 1, the channels which comprise the flanges of the built-up specimens would have interfered with the laser beam when measuring the imperfections of the webs, while for the specimens with geometry 2, the bolts connecting the top channel to the web channels would have partially blocked the laser beam when measuring the imperfections of the webs along the adjacent edge. The locations where the imperfections were recorded in geometries 1 and 2 are illustrated in Figure 4.13 and Figure 4.15, respectively.

In both geometries the imperfections were recorded along three longitudinal lines on the webs of the channels and along two longitudinal lines on the flanges of the top channel. These imperfection readings permitted the determination of the out-of-plane imperfections in the channels related to local buckling of the web (δ_{web}) and local buckling of the flanges ($\delta_{flanges}$).

The exact angles between the web and the flanges of the channels were not measured, and it was assumed that at each end of the constant moment span the flanges were perfectly orthogonal to the web. The imperfections recorded on the web and the flanges of the channels were adjusted so that the imperfection value at each corner of the plate element was zero. This imposition inevitably resulted in the elimination of the twist imperfection in each plate. However, eliminating this imperfection component can be expected to have little effect on the capacity of beams failing due to cross-sectional instabilities.

For geometry 1 the readings along lines 3, 5, 8, 10, 11 and 13 were taken 6 mm away from the flange outer surface, while the readings along lines 4, 9 and 12 were taken along the centre line of the channels web. The readings along lines 2 and 6 were taken 6 mm away from the outer surface of the web of the top channel and the readings along lines 1 and 7 were taken 4 mm away from the flange tips.

For geometry 2 the imperfection readings along lines 3 and 5 were taken 4 mm away from the inner surface of the flanges, while the readings along lines 8, 10, 11 and 13 were taken 6 mm away from the outer surface of the flanges. The readings along lines 4, 9 and 12 were taken along the centre line of the web. In the flanges of the top channel lines 2 and 6 were located 6 mm away from the outer surface of the web, while lines 1 and 7 were located 4 mm away from the flange tips.

For both geometries, the imperfections recorded along the different lines were used to compute δ_{web} and $\delta_{flanges}$ using Eqs. (3.5)-(4.5). Figure 4.14 and Figure 4.16 illustrate the process of measuring the imperfections in geometries 1 and 2, respectively.

$$\delta_{web}(x) = Line_4 - (Line_3 + Line_5) / 2 \quad (4.1)$$

$$\delta_{web}(x) = Line_9 - (Line_8 + Line_{10}) / 2 \quad (4.2)$$

$$\delta_{web}(x) = Line_{12} - (Line_{11} + Line_{13}) / 2 \quad (4.3)$$

$$\delta_{flange}(x) = Line_1 - Line_2 \quad (4.4)$$

$$\delta_{flange}(x) = Line_7 - Line_6 \quad (4.5)$$

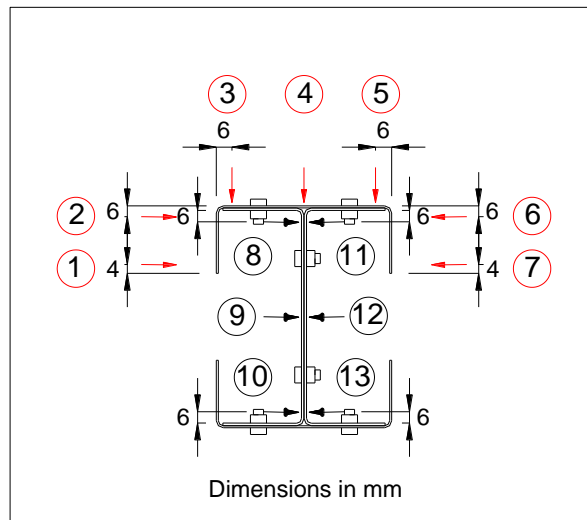


Figure 4.13: Locations of the imperfection measurements in geometry 1

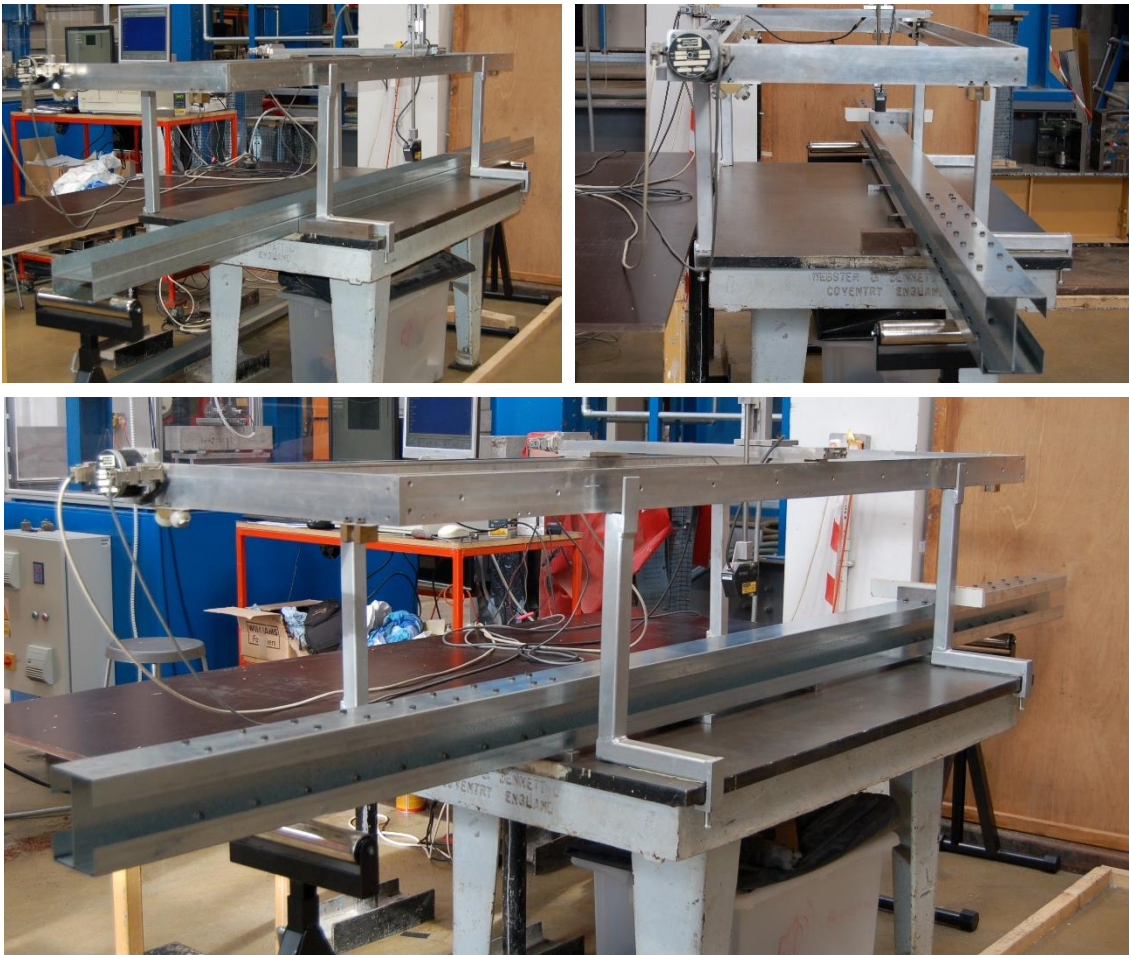


Figure 4.14: Measurement of the imperfections in geometry 1

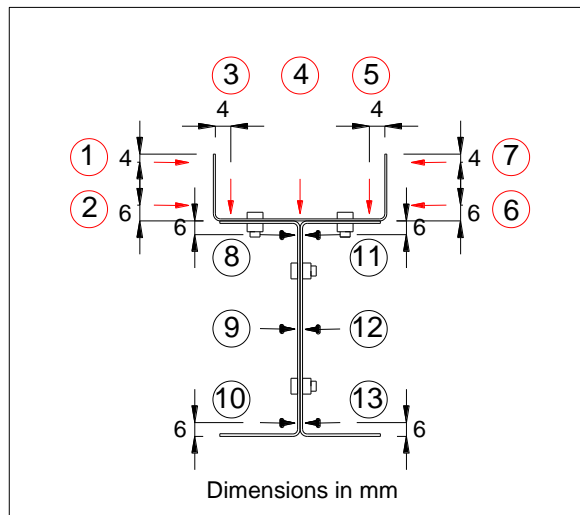


Figure 4.15: Locations of the imperfection measurements in geometry 2



Figure 4.16: Measurement of the imperfections in geometry 2

The maximum and the average out-of-plane imperfections recorded in the individual components of each built-up geometry are listed in Table 4.9. Since the exact angles between the web and the flanges of the top channel were not measured, it was deemed most representative to report δ_{flange} relative to the average value along the flange of the channel.

Table 4.9: Maximum and averaged imperfection measurement

Specimen	Section	Imperfection (mm)		
			Max.	Avg.
B1	T12915	δ_{web}	0.24	0.07
	T10412	δ_{web}	0.25	0.07
		δ_{flange}	0.49	-
B2	T12915	δ_{web}	0.24	0.07
	T10412	δ_{web}	0.35	0.11
		δ_{flange}	0.51	-

As Table 4.9 shows, the maximum and average out-of-plane imperfections in the web of channels T12915 were virtually the same for both built-up geometries. This can be explained by the fact that in both geometries these channels were connected back-to-back with the same number of connectors along the constant moment span, and that their imperfections were recorded at the stage when only the web channels were connected, without the presence of the

flange channels. On the other hand, the web of channels T10412, which in geometry 1 were assembled with the flanges facing down and in geometry 2 with the flanges facing upwards, showed the largest differences in the maximum and average imperfections.

Providing examples of the measurements, Figure 4.17 shows the out-of-plane imperfections recorded in the web of one of the web channels of beam B1-2a, while Figure 4.18 shows the imperfections recorded in one of the flanges of the top channel of beam B2-0a. The vertical dashed lines in Figure 4.17 indicate the location of the connectors (the specimen in Figure 4.18 was tested without connectors in the constant moment span). In both figures, the length coordinate along the constant moment span is normalized with respect to the total constant moment span length. Positive readings indicate imperfections in the direction away from the centroid of the built-up cross-section. The imperfection data of all specimens are included in Appendix E.

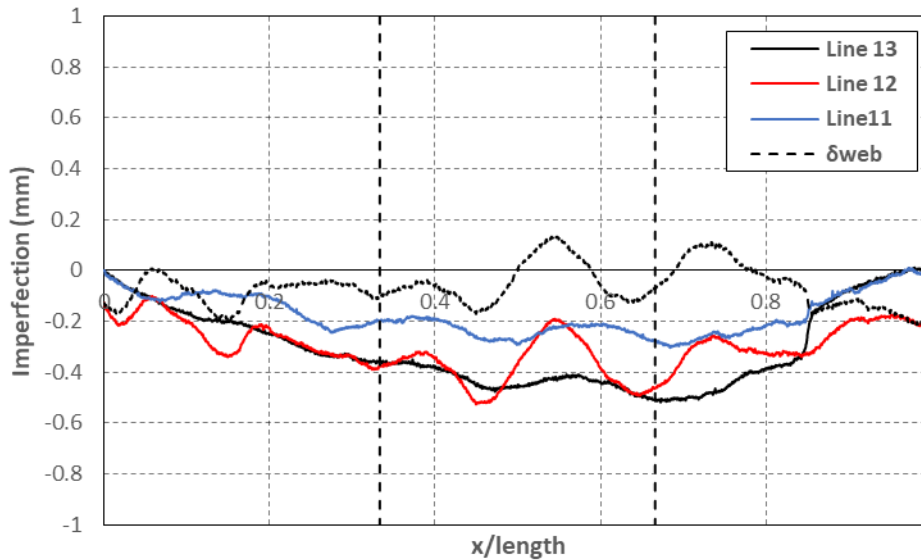


Figure 4.17: Imperfections in the web of channel T12915-6 (geometry 1)

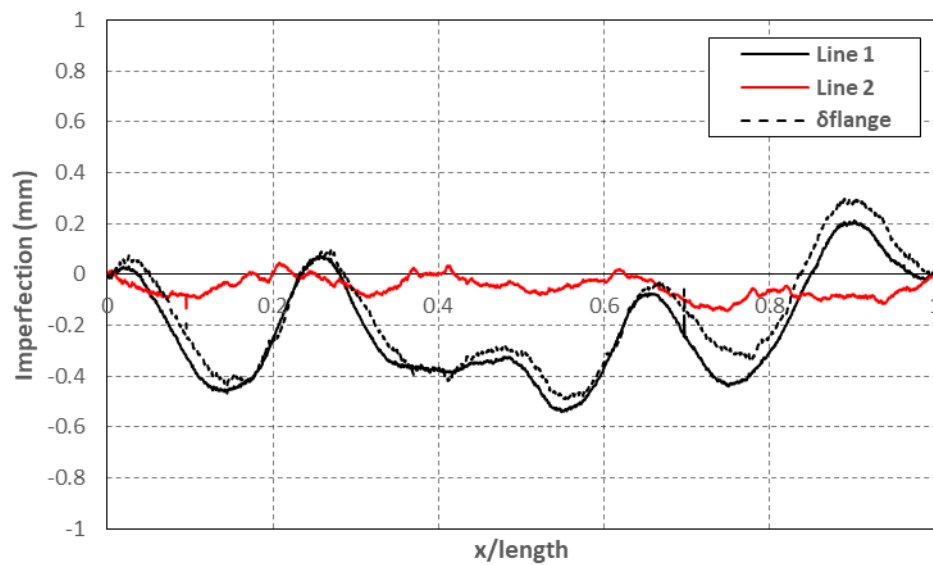


Figure 4.18: Imperfections of a flange of channel T10412-1 (geometry 2)

4.7. Test Set up

4.7.1 Introduction

All specimens were tested adopting a 4-point bending configuration. The specimens were bent about their major axis, with lateral restraint provided at the loading points. The rig used in the tests is illustrated in Figure 4.19.

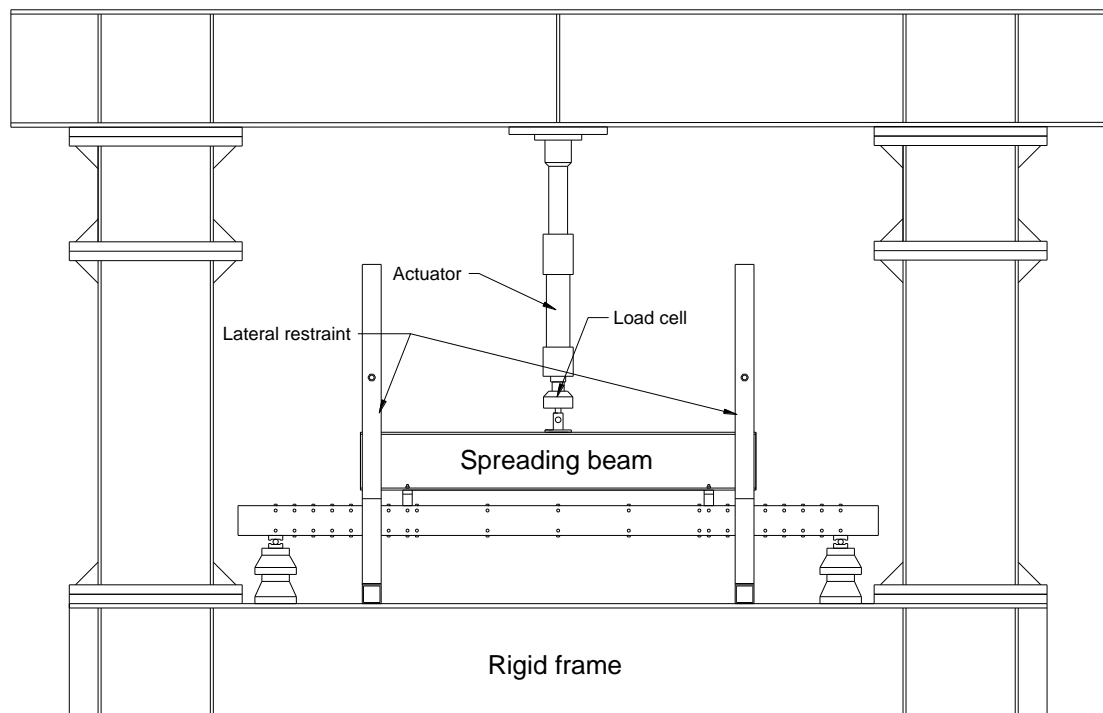


Figure 4.19: 4-point bending test rig

4.7.2 Boundary conditions

4.7.2.1 Roller supports

The test specimens were simply supported at their ends on rollers located 3000 mm apart. These supports allowed rotations about the major axis and axial shortening, while preventing vertical displacement and twist. The out-of-plane forces at the beam ends resulting from the tendency of the beam to fail in lateral-torsional buckling were small enough to be restrained by friction between the rollers and the bottom surface of the test specimens.

4.7.2.2 Lateral uprights

The specimens were loaded through a spreader beam, which applied concentrated loads at points 1600 mm apart. The spreader beam was restrained near its ends against any out-of-plane movement by the assemblies shown in Figure 4.20. These consisted of adjustable upright supports made of 6 mm thick square hollow sections, which were bolted to the reaction frame. Steel plates of 6 mm thickness were welded to the flanges of the spreader beam and had nylon blocks bolted to them. The nylon blocks worked as linear bearing pads which increased contact surface and reduced friction between the spreader beam and the uprights. The uprights were adjusted to ensure full contact with the nylon blocks by tightening or loosening the top and bottom threaded rods shown in Figure 4.20. Friction between the uprights and the spreader beam was estimated to be around 50 N at the beginning of the test.

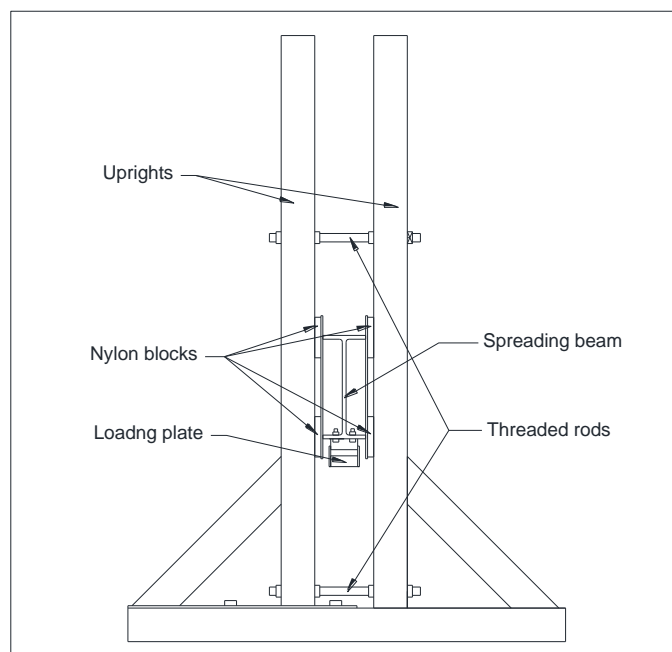


Figure 4.20: Laterally restraining assembly

4.7.2.3 Loading points

Special devices, which are illustrated in Figure 4.21, were built to transmit the vertical load from the spreader beam to the test specimens. They consisted of a bottom half with a steel cylinder which either tightly fitted in a rounded recess or was free to roll over a rectangular area, and a matching top half. High strength steel flanges were bolted to both sides of the bottom halves in order to prevent out-of-plane displacements of the test specimens at the loading points. The one device emulated a pin connection, allowing only rotations in the plane of loading between the spreader beam and the test specimen. The other one emulated a roller connection, which allowed rotations in the plane of loading, as well as axial displacements. The top and bottom halves of each device were bolted to the spreader beam and the test specimens, respectively. Sufficient clearance was provided in the holes drilled in the spreader beam to allow tight alignment between the top and bottom halves.

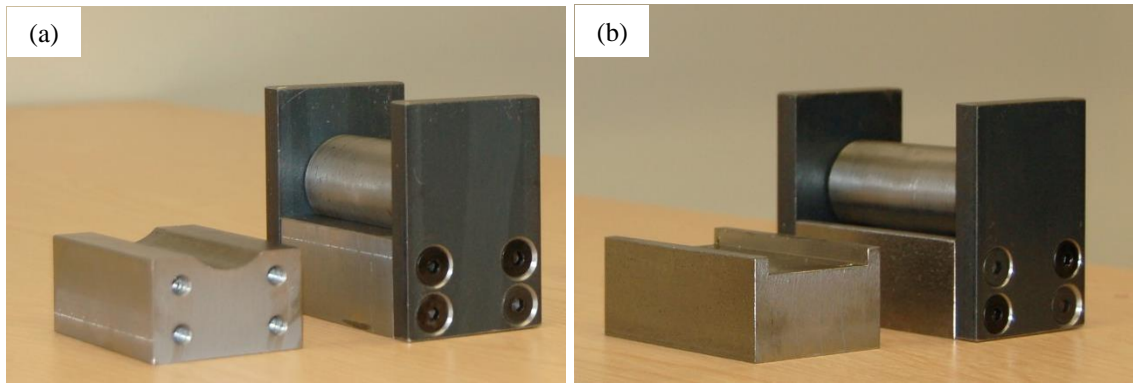


Figure 4.21: Loading devices: a) Pin support, b) Roller support

4.7.2.4 Wooden blocking

The end sections of the built-up specimens above the supports were packed with wooden blocks which tightly fitted within the web and flanges. While this also prevented possible bearing failure, the main reason was to prevent a distortion of the cross-section caused by a lateral displacement of the compression flange combined with bending of the web about a horizontal axis in its plane. The lateral bending of the compression flange originated from a tendency of the beam to fail in lateral-torsional buckling in between the loading points as the built-up specimens approached their maximum moment capacity, but after local buckling of the component sections was observed. Neither the devices at the loading points nor the lateral restraint assemblies were thereby able to completely eliminate rotations of the beam about the vertical axis. This phenomenon was observed in built-up beam B1-0a, which was tested without wooden blocks and resulted in the built-up beam being unable to reach the load attained by its twin specimen.

4.7.3 Instrumentation

4.7.3.1 LVDTs

Three LVDTs with a stroke of 50 mm were used to record the deflections of the beams. The LVDTs were placed underneath the specimens, vertically aligned with the centroid of the built-up cross-section, at the loading points and at mid-span, as illustrated in Figure 4.22. Steel plates were bolted to the bottom flanges of the channels which formed the web of geometry 2 in order to provide a smooth surface for the LVDTs to bear on, as illustrated in Figure 4.23.

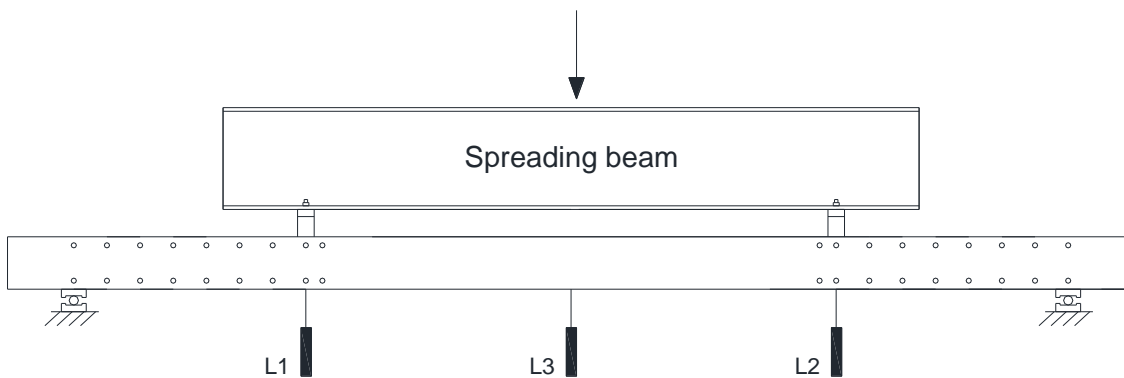


Figure 4.22: Distribution of the LVDTs along the test specimen

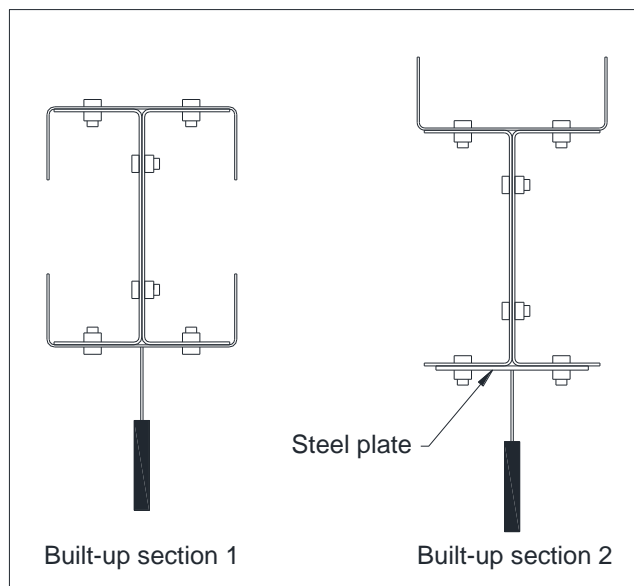


Figure 4.23: Location of the LVDTs within the cross-section

4.7.3.2 Potentiometers

Eight potentiometers with a stroke of 25 mm were used to measure the buckling deformations of the component sections. The potentiometers were mounted on two identical yokes, which were attached to the bottom flange of the built-up cross-sections, as illustrated in Figure 4.24. As the

test specimens underwent overall bending, the bottom flange of the built-up cross-section experienced tension and was not at risk of local buckling, while the yokes were able to move with the cross-section as a whole. Thus, the potentiometers were able to record the out-of-plane deformations of the web and the top flange of the built-up cross-sections due to local buckling.

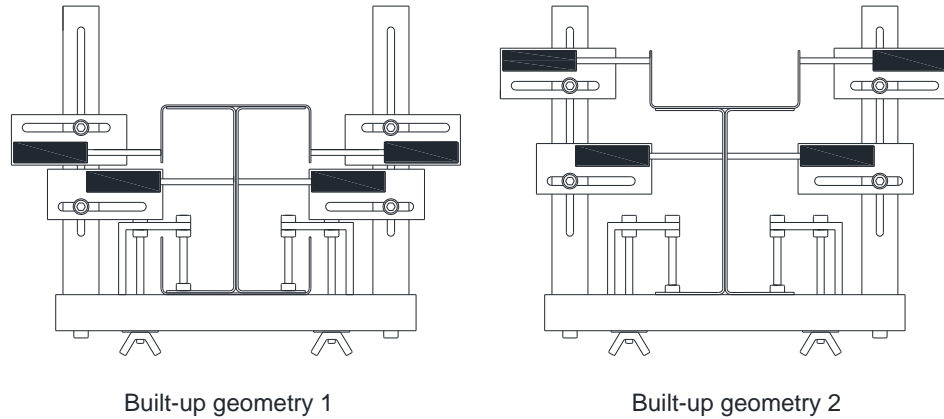


Figure 4.24: Potentiometer lay-out within the cross-sections

Figure 4.25 illustrates the locations at which the yokes were placed for each test specimen of geometry 1 and 2. For the specimens without intermediate connectors in between the loading points, yoke *Y1* was placed 200 mm to the left of the mid-span and yoke *Y2* 300 mm to the right. These locations were chosen while considering the buckling half-wave length of the different components, so that if one of the yokes happened to coincide with the inflection point of the local buckling pattern in one of the components, the other yoke would still be able to record its buckling deformations. For the specimens with two and three intermediate connectors, the potentiometers were placed at mid-distance between the connectors.

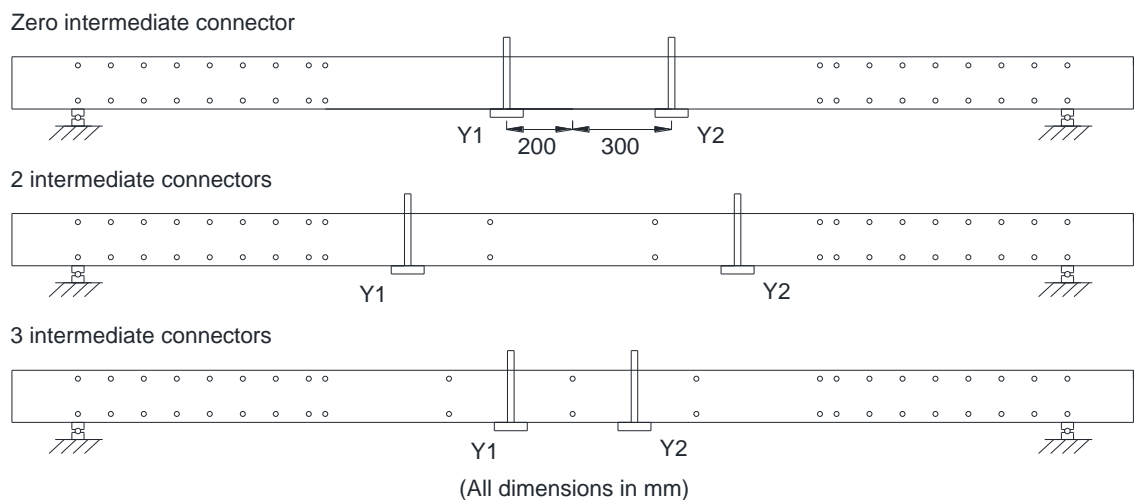


Figure 4.25: Location of the potentiometers along the test specimens

4.7.4 Test procedure

The specimens were tested in a reaction frame using an actuator with a maximum capacity of 160 kN and a 50 kN load cell. The actuator was steered using a Cubus controller, operated in displacement mode. The load was applied using a displacement rate of 1 mm/min and the test was halted for 4 min slightly before the peak load was reached in order to determine the lower bound 'static' value of the load. The specimens were deformed well beyond the peak load in order to identify the location at which the plastic deformations localized.

The data was also collected using the Cubus system, using a sampling rate of 1 Hz.

4.8. Test results

4.8.1 Deformed shape

4.8.1.1 Geometry 1

All test specimens with geometry 1 failed by local buckling in the constant moment region, with significant interaction taking place between the top channel and the channels comprising the web of the built-up cross-section. Multiple buckling half-waves were observed along the constant moment span. The top channel buckled before buckling was observed in the channels comprising the webs of the built-up cross-section in all beams.

In beams B1-0 and B1-2, the top channel buckled in a pattern containing 15 or 16 half-waves with approximately the same half-wave length along the constant moment span. These buckles were estimated to have an average half-wave length of around 100 mm. In the case of beams B1-2, one intermediate set of connectors coincided with an inflection point in the local buckling pattern, where the web of the top channel neither buckled outward nor inward. Consequently, these connectors underwent a rotation about an axis perpendicular to the plane of loading. The other set of connectors, on the other hand, coincided with a cross-section in which the flanges of the top channel buckled outward and the web buckled inward. Consequently, these connectors rotated about an axis parallel to the plane of loading.

For beams B1-3, buckles with a similar half-wave length to the one reported for beams B1-0 and B1-2 were observed. However, in these beams the flanges of the top channel buckled outward in the cross-sections containing connectors. This resulted in the top channel buckling with 17 half-wave buckles along the constant moment span, with two of the buckles being smaller than the others, as shown in Figure 4.26.

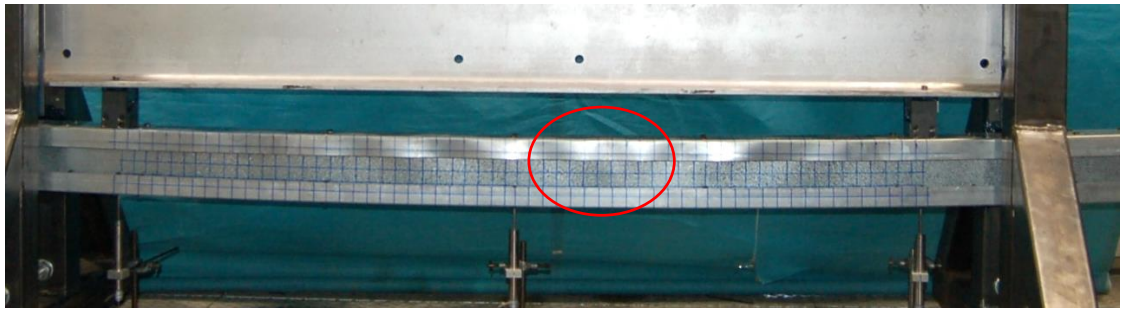


Figure 4.26: Top channel in specimen B1-3b displaying buckles with different half-wave lengths

It is important to note that the half-wave length of the buckles displayed by the top channel in all beams was very close to its natural (calculated) local buckle half-wave length of 110 mm. The web channels had a similar natural local buckle half-wave length of 100 mm, however the number of buckles generated in the web channels and the associated wave length could not be determined as the magnitude of these buckles was not large enough to allow accurate measurements.

Despite the similarity in the initial buckling pattern observed for each pair of twin specimens, the plastic deformations generally localized around the peak load in different locations. Figures 4.27-4.32 illustrate the deformed shape before and after the peak load for all beams with geometry 1.

As Figure 4.27 shows, beam B1-0a was tested without packing the end sections with wooden blocks. This caused the built-up cross-section to experience significant lateral distortion at the end sections, accompanied by in-plane bending of the top flange and resulted in a slightly lower ultimate load compared to the twin specimen. To avoid this in subsequent tests, the remaining built-up specimens were tested with wooden blocking at each end.

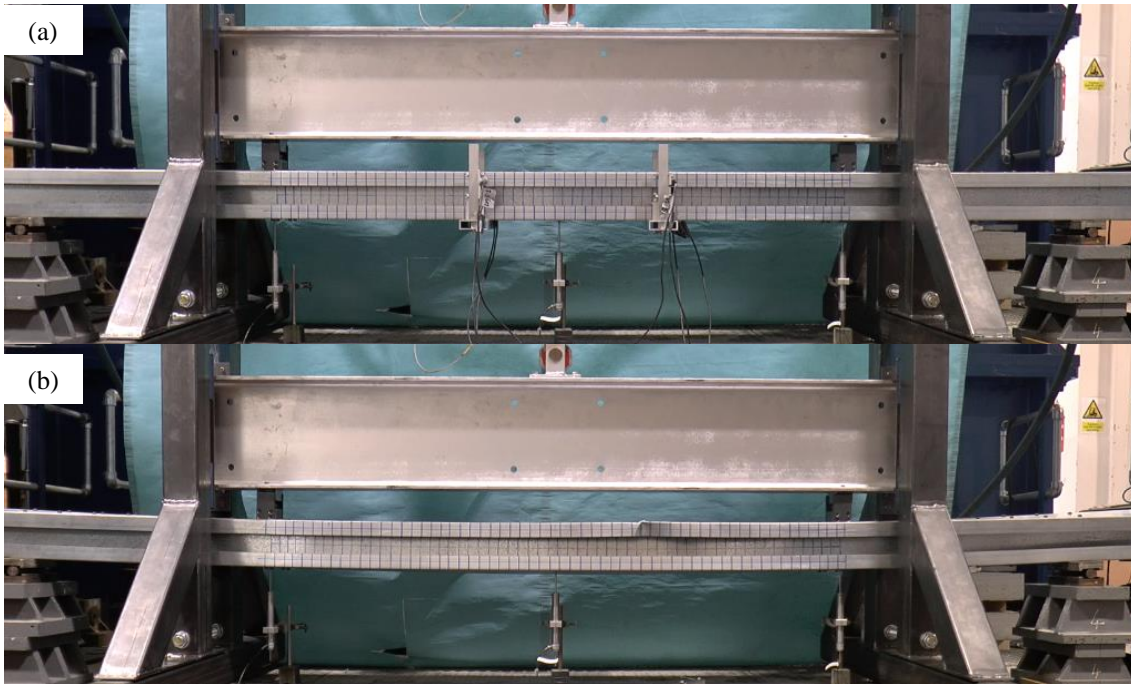


Figure 4.27: Deformed shape of specimen B1-0a: a) before peak load, b) after peak load

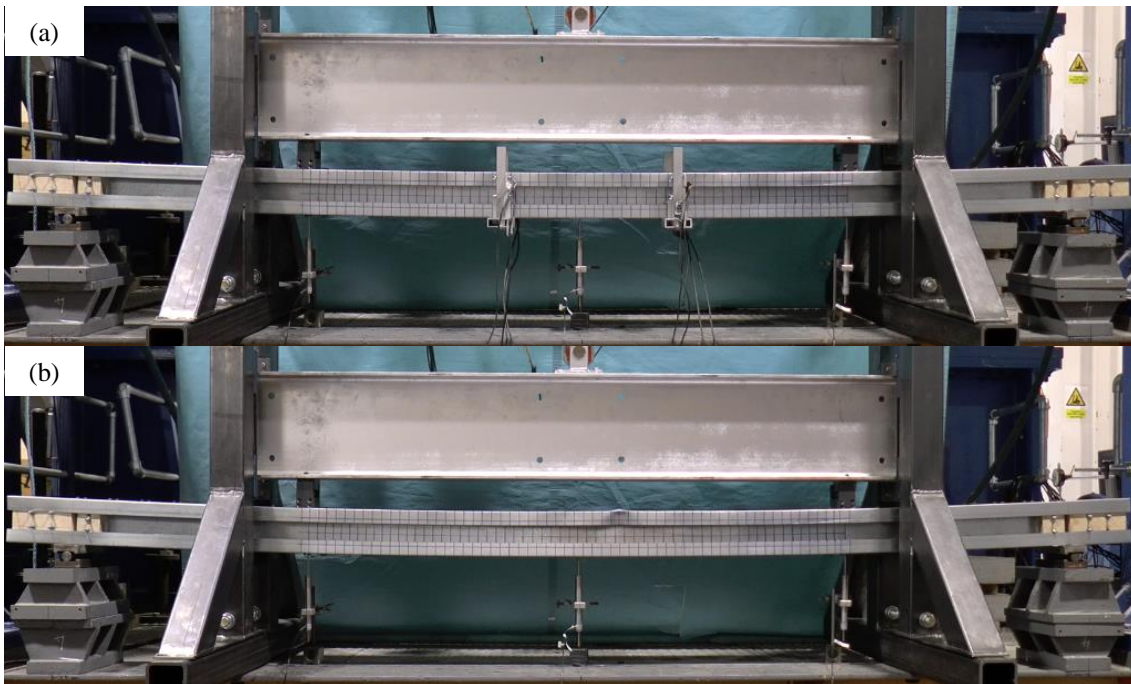


Figure 4.28: Deformed shape of specimen B1-0b: a) before peak load, b) after peak load

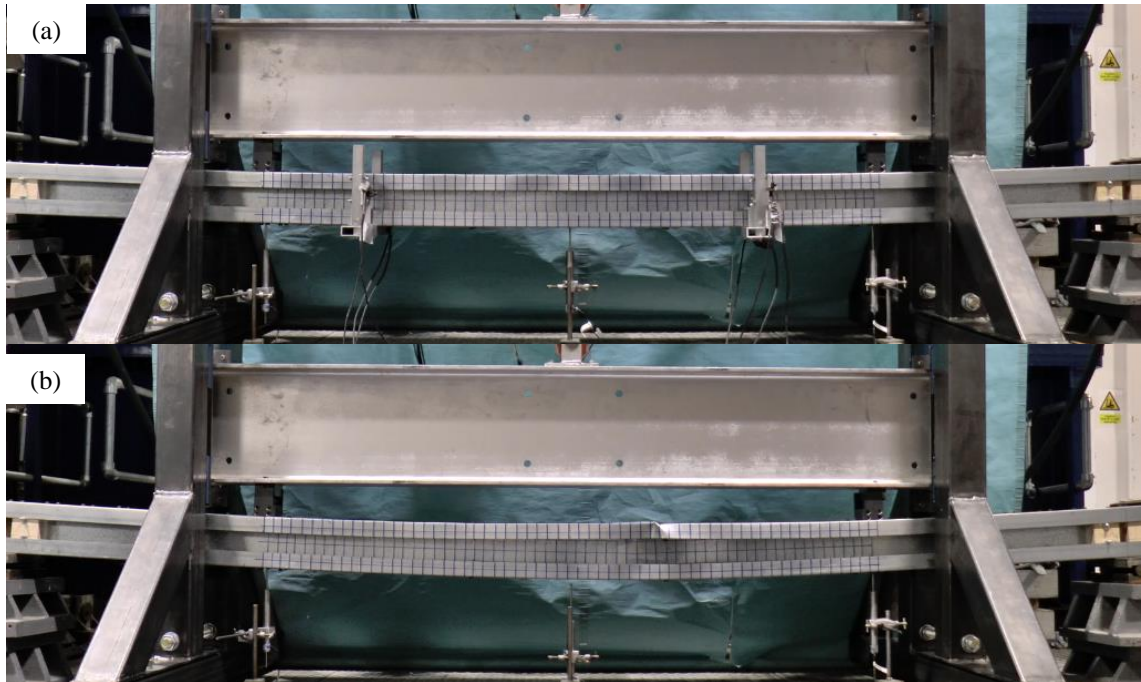


Figure 4.29: Deformed shape of specimen B1-2a: a) before peak load, b) after peak load

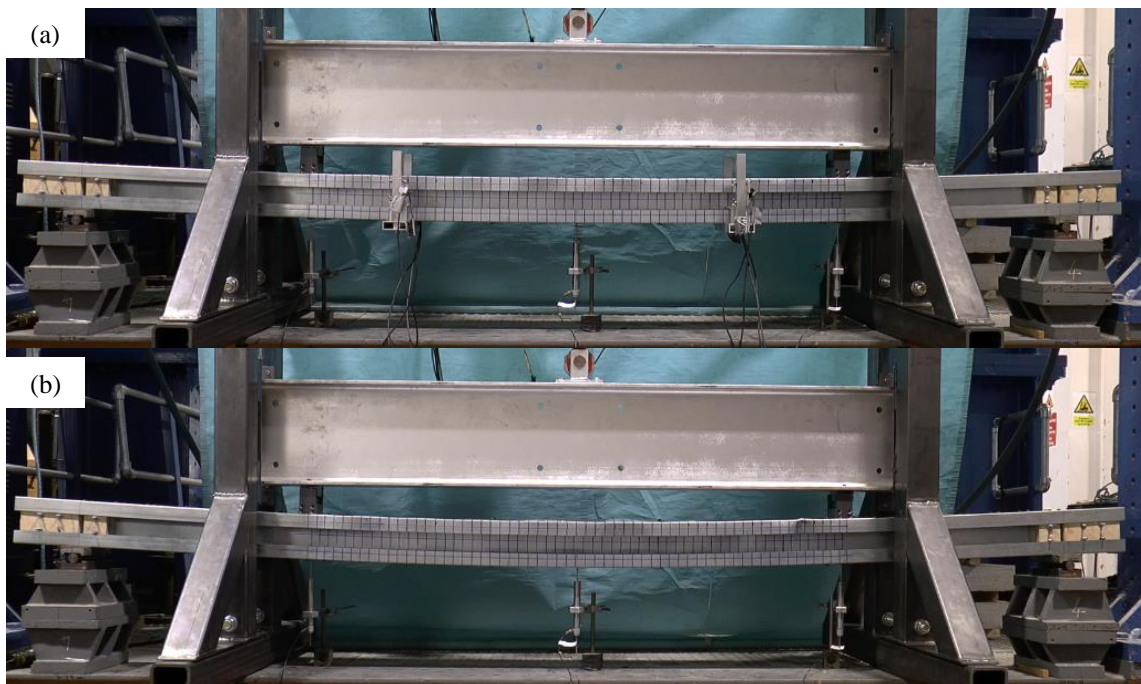


Figure 4.30: Deformed shape of specimen B1-2b: a) before peak load, b) after peak load

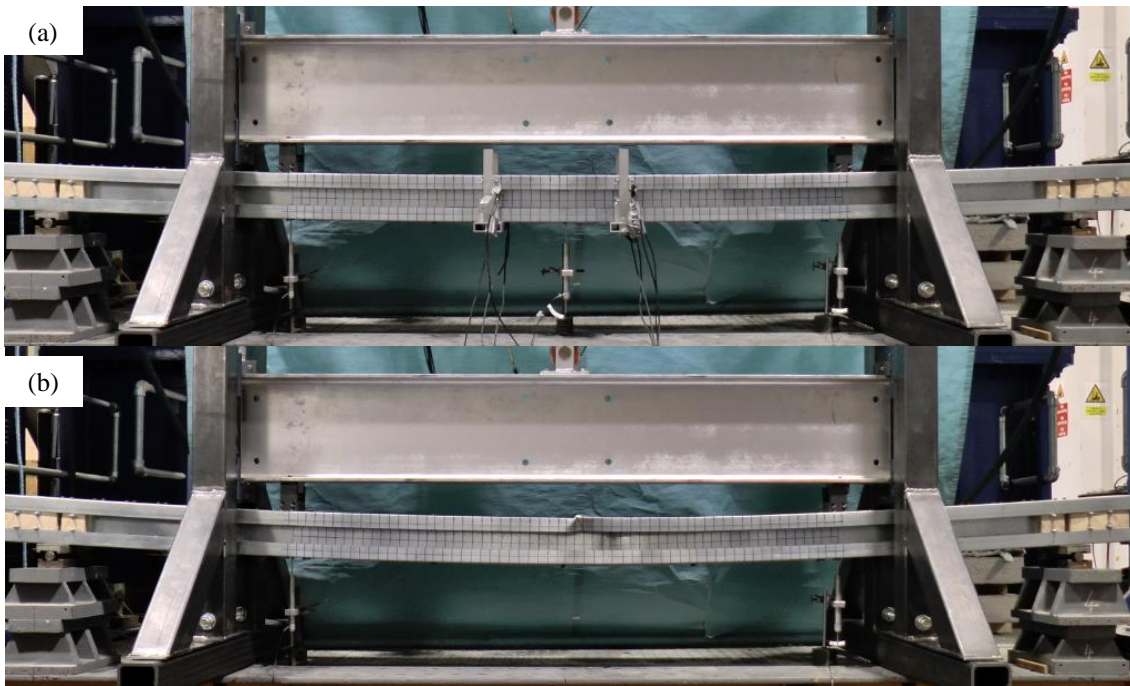


Figure 4.31: Deformed shape of specimen B1-3a: a) before peak load, b) after peak load

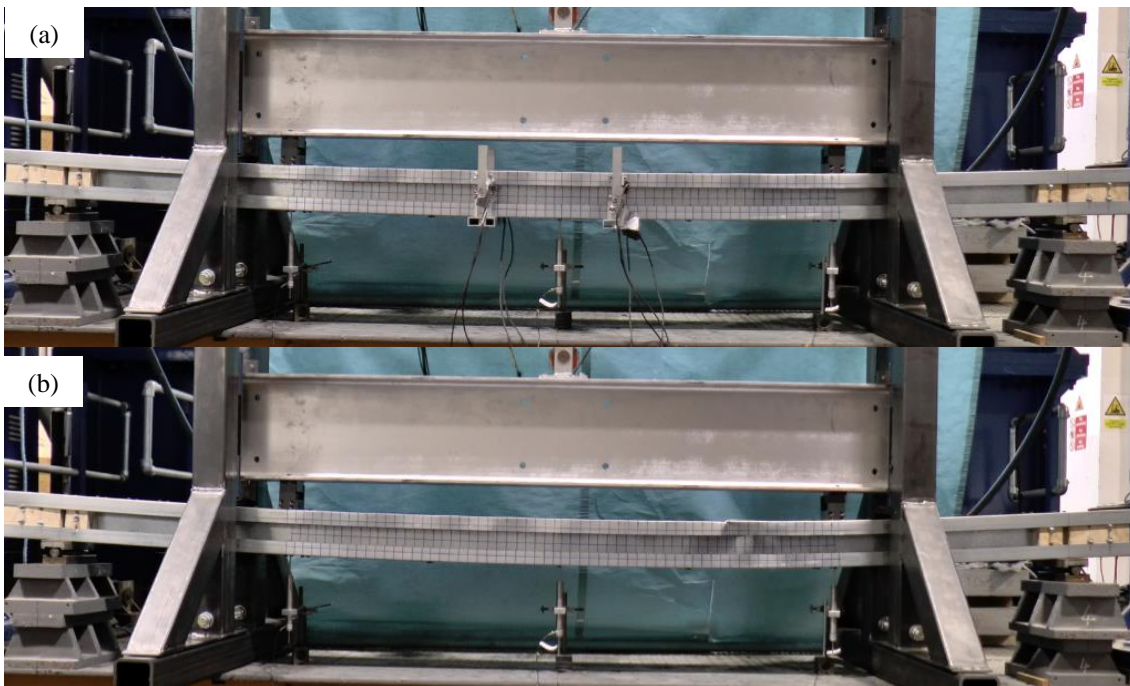


Figure 4.32: Deformed shape of specimen B1-3b: a) before peak load, b) after peak load

For most of the test specimens, a yield line pattern developed at one specific location along the constant moment span, resulting in a hinge-like behaviour. Yield lines simultaneously developed in the top channel and in the web and the top flange of the channels comprising the web of the built-up specimens. In general, the pattern in the top channel was symmetric with respect to the plane of bending, while that in the web of the web channels was anti-symmetric, as shown in Figure 4.33. An exception to this occurred in specimens B1-0b and B1-2b, in which the top channel developed an asymmetric yield line pattern near mid-span. This was

accompanied by the top flange undergoing some out-of-plane deformations combined with twisting of the cross-section along the constant moment span, while a second ‘hinge’ appeared near one of the loading supports, as shown in Figure 4.34. As a result, lateral forces were induced at the end supports which eventually underwent some lateral slip. However, the out-of-plane displacements of the beam did not occur until after the peak load was reached and therefore, all beams could be considered fully laterally restrained until the test specimens reached their ultimate capacity.

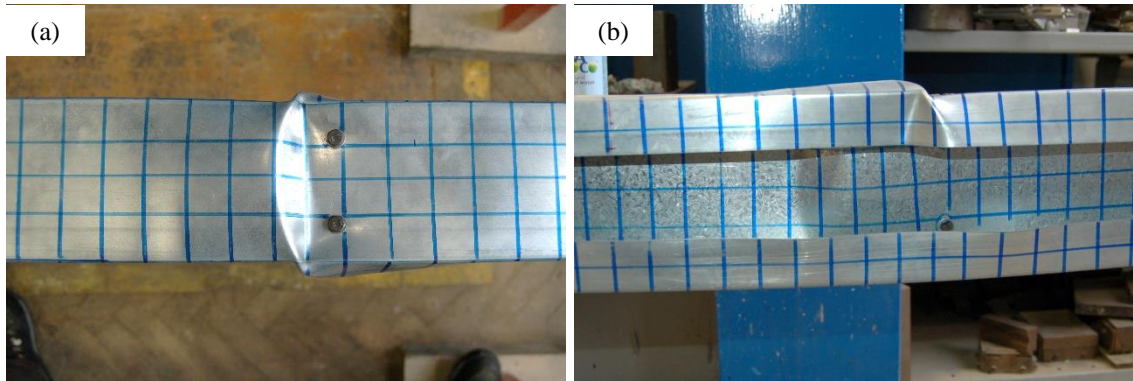


Figure 4.33: Plastic hinge in B1-2a: a) Top channel b) Channels comprising the web

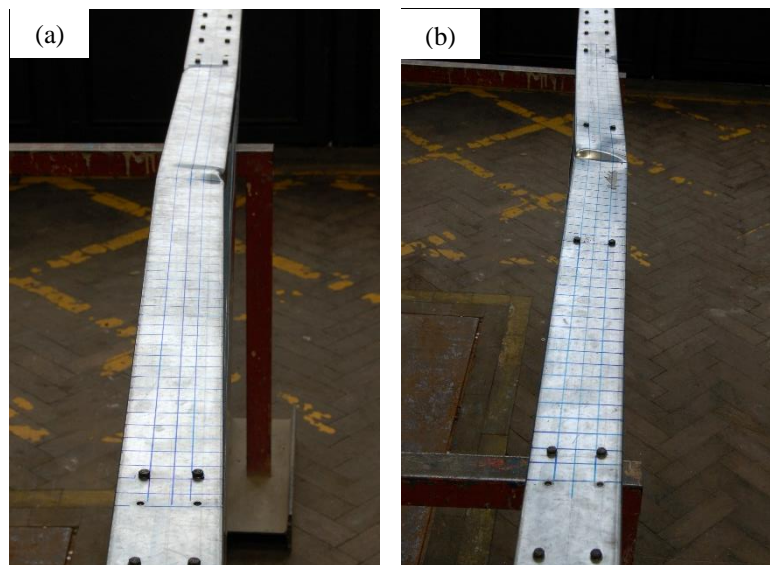


Figure 4.34: Asymmetric plastic hinge in built-up specimens a) B1-0b b) B1-2b

Regarding the initial buckling deformations, the potentiometers mounted on the yokes recorded a locally buckled shape in the top channel which was symmetric about the plane of bending in all beams with both flanges buckling either inward or outward. The web channels were recorded to buckle in a symmetric shape with respect to the plane of bending in those specimens without any connectors in the constant moment span (B1-0), while in the remaining specimens the buckling pattern was anti-symmetric. The symmetric buckling pattern of the web channels in beams B1-0 can be attributed to the fact that the channels were able to buckle largely

independently from each other, without any connectors in the constant moment span forcing them to remain in contact. On the other hand, a connector spacing of 500 mm, as encountered in beams B1-2, was short enough to force the web channels to buckle in a synchronous manner. This is illustrated in Figure 4.35, which shows the out-of-plane deformations of the components of beam B1-2a against the applied load. In the figure, the solid and dashed lines represent the readings obtained from the sets of potentiometers placed on each of the two yokes. Positive values indicate deformations towards the potentiometer (outward) while negative values indicate deformations away from the potentiometers (inward).

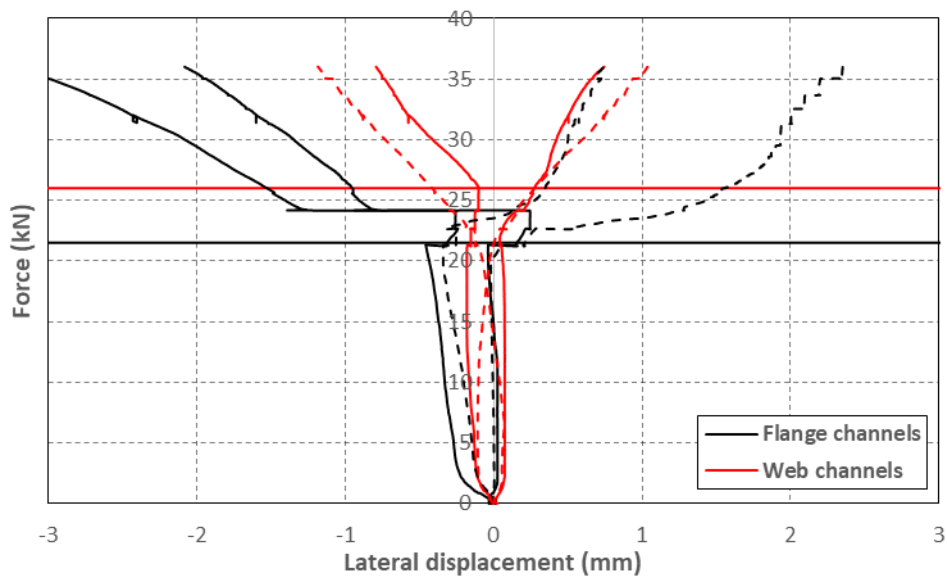


Figure 4.35: Axial load vs lateral displacements (B1-2a)

In the specimens with two and three sets of intermediate connectors along the constant moment span, the buckling pattern of the top channel was seen to be affected by subsequent buckling of the web channels. More specifically, in beam B1-2a one set of potentiometers recorded the flanges of the top channel changing the initial direction of their buckles when the web channels started buckling, as shown in Figure 4.35, while in beam B1-2b the potentiometers only recorded the flanges of the top channels adjusting the amplitude of their buckles. In beams B1-3 this interaction was even more pronounced. In beam B1-3a, all four potentiometers at the top channel recorded the flanges changing the direction of their buckles when the web channels started buckling, as illustrated in Figure 4.36. A similar behaviour was also observed in the twin specimen (B1-3b). These observations can be interpreted as an attempt of the top channel to accommodate the buckling deformed shape of the web channels by modifying the wavelength of its buckles. The closer the connector spacing, the more pronounced this effect becomes.

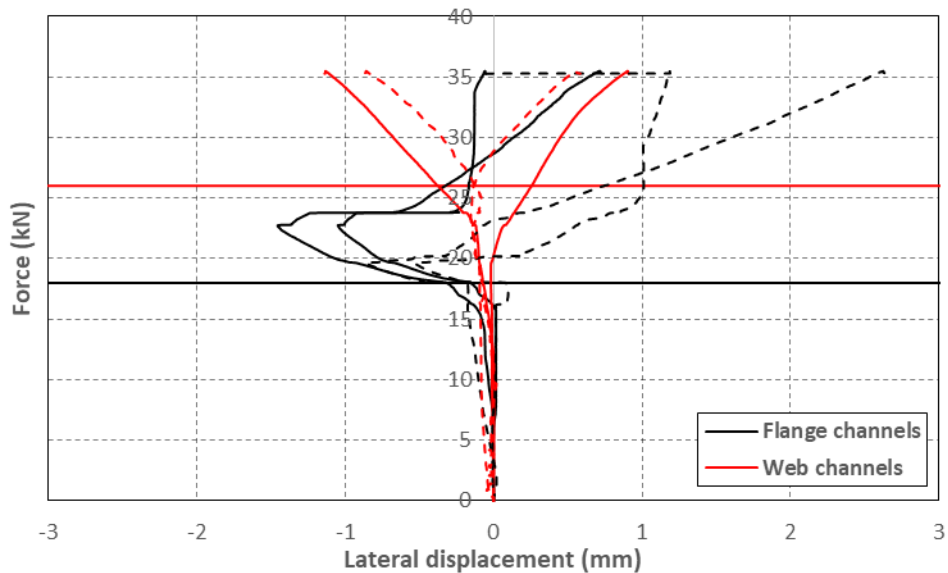


Figure 4.36: Axial load vs lateral displacements (B1-3a)

4.8.1.2 Geometry 2

In general, the specimens with geometry 2 failed predominantly by local buckling, characterized by significant interaction between the buckling patterns in the top channel and the web channels. Figures 4.37-4.42 show the deformed shapes of all test specimens before and after the peak load. In the beams without intermediate connectors (B2-0), global twisting of the top channel was observed to interact with local buckling near the peak load. In the case of beam B2-0a this occurred shortly after the local buckling deformations in the top channel localized near mid-span, resulting in a localized twisting, as illustrated in Figure 4.37b. However, in specimen B2-0b the interaction between local buckling and flexural-torsional buckling of the top channel was more significant, causing the top channel to twist with a half wave-length of approximately 750 mm before the built-up specimen reached its ultimate capacity, as shown in Figure 4.38b.

In all test specimens, the top channel buckled locally before the web channels, and the amplitude of its buckles was significantly larger. The top channel buckled while displaying 14 or 16 half-waves along the constant moment span with approximately the same half-wave length. The number of half-waves generated in the web channels was not easily appreciated due to their small amplitude. However, it was estimated to also be approximately 14 or 16 along the constant moment span. This resulted in half-wave lengths in the top channel and the web channels ranging from approximately 94 mm to 107 mm. These half-wave lengths were very close to the natural local buckling half-wave lengths of the top channel and the web channels, which are 120 mm and 100 mm, respectively.

In the beams without intermediate connectors (B2-0), a gap developed along the constant moment span between the top channel and the web channels as the specimens deformed. This gap was more pronounced around mid-span, allowing a larger amplitude of the buckles in the

top flange of the web channels to develop in this region. On the other hand, towards the ends of the constant moment span, where the components were in closer contact with each other, the amplitude of the buckles in the top flange of the web channels was considerably smaller, to the point that it was difficult to observe them. In the B2-0 specimens, the top channels buckled while displaying 14 or 15 half-waves along the constant moment span.

In beams B2-2, the top channel also tended to separate from the web channels, especially at mid-span. However, the intermediate connectors opposed this separation, thereby pulling the flanges of the web channel upward. This resulted in the connectors between the top channel and the web channels undergoing a slight translation in the vertical direction and a rotation about an axis parallel to the length of the beam. In addition, due to the presence of the connectors one of the buckles in the web channels (at mid-span) had a half-wave length which was almost twice as large as the others. This half-wave tried to divide into two half-waves as the specimens continued to deform. In the B2-2 specimens, 15 half-waves were counted in the top channel along the constant moment span, while between 14 and 16 half-waves were counted in the top flange of the web channels.

In beams B2-3, no gap originated between the top channel and the web channels and the locations of the intermediate connectors coincided with the cross-sections in which the top channel buckled with its flanges moving inward. In these specimens the top channels displayed four buckling half-waves between connectors resulting in 16 half-waves along the constant moment span.

Although the buckling pattern observed for twin specimens was, in general, similar until the ultimate capacity was reached, localization of the plastic failure often occurred at different locations along the constant moment region. As the built-up specimens deformed beyond their ultimate capacity, yield lines started to develop in the top channel and in the top flange of the web channels.

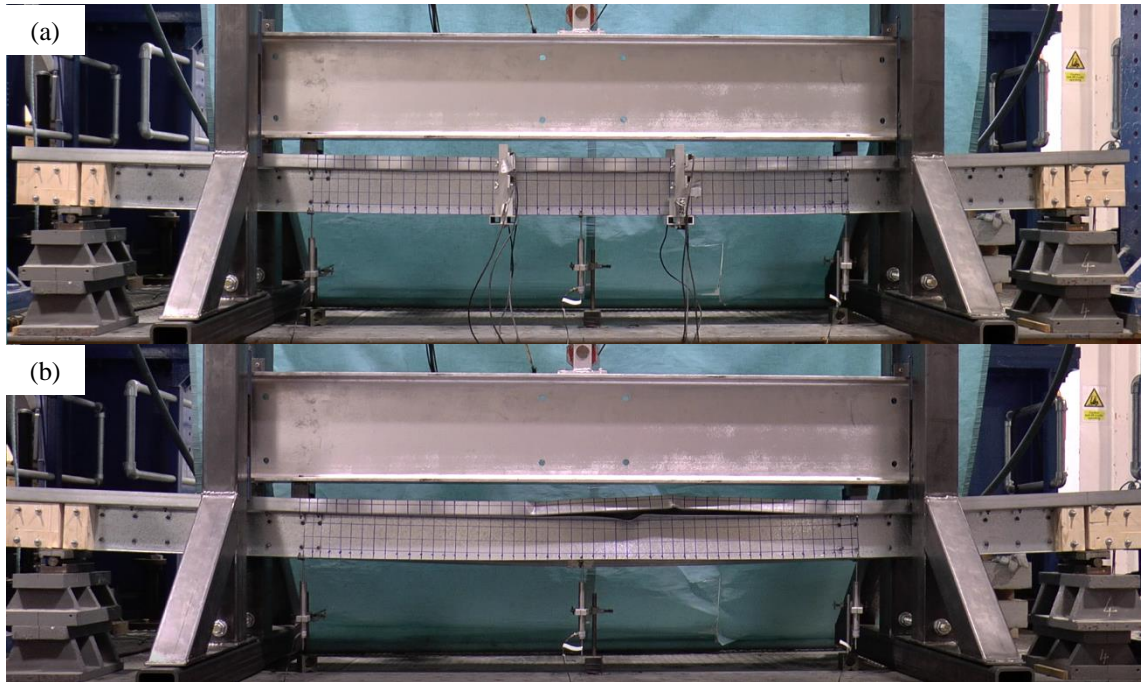


Figure 4.37: Deformed shape of specimen B2-0a: a) before peak load, b) after peak load

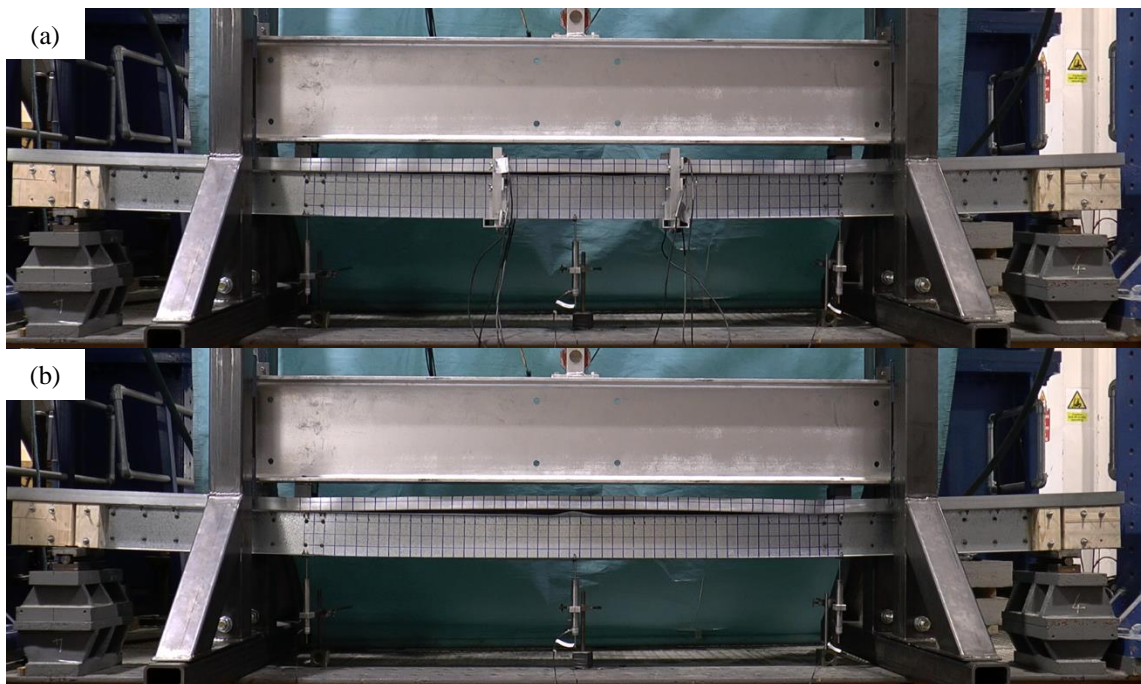


Figure 4.38: Deformed shape of specimen B2-0b: a) before peak load, b) after peak load

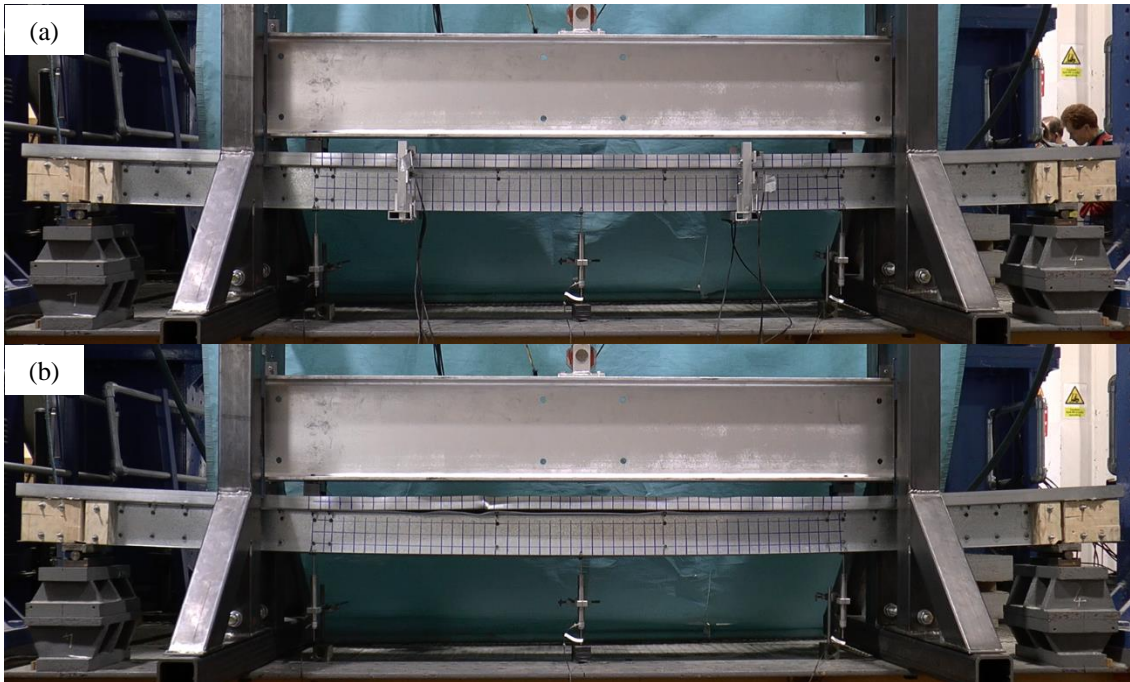


Figure 4.39: Deformed shape of specimen B2-2a: a) before peak load, b) after peak load

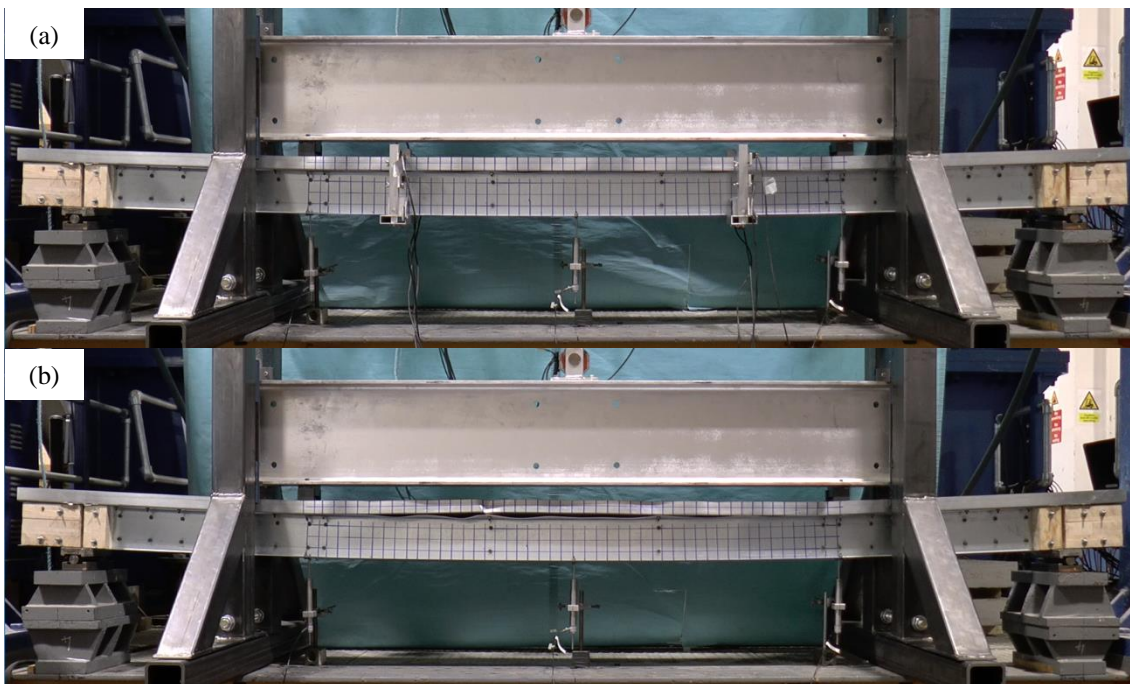


Figure 4.40: Deformed shape of specimen 2-2b: a) before peak load, b) after peak load

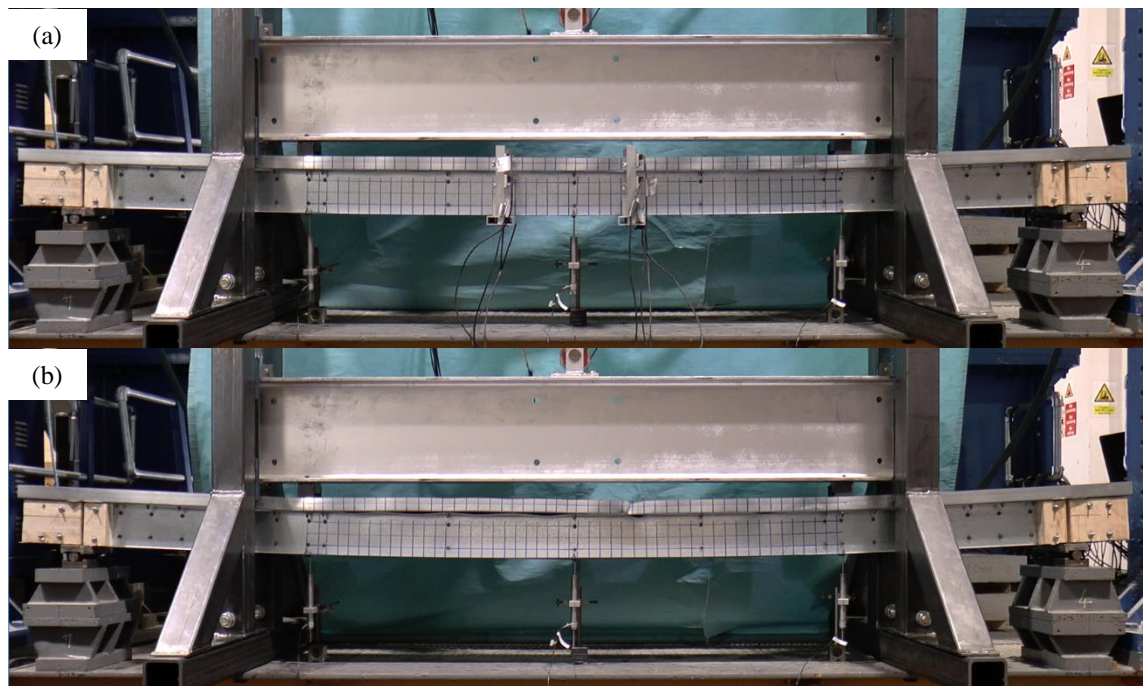


Figure 4.41: Deformed shape of specimen B2-3a: a) before peak load, b) after peak load

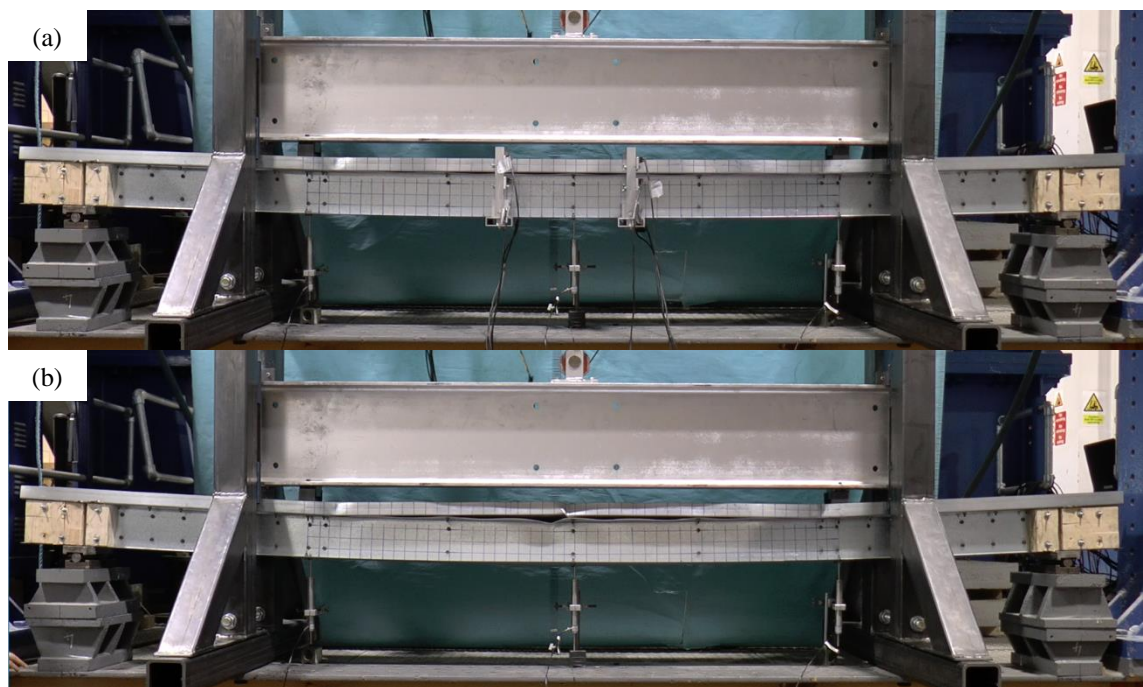


Figure 4.42: Deformed shape of specimen B2-3b: a) before peak load, b) after peak load

As the yield line mechanism developed, the specimens generally experienced some twisting and lateral displacement in the neighbourhood of the resulting hinge. These deformations gradually spread over the whole constant moment span as the specimen continued to deflect. Figure 4.43 shows the hinge which developed in the top channel and the top flange of the web channels of a typical specimen. The twisting and lateral deformations along the constant moment span finally resulted in lateral slip at the end supports. These end supports were not designed to restrain lateral displacement, except for the friction generated between their mechanical components.

However, this lateral displacement consistently occurred in the decreasing part of the load-deflection curve, after the peak load was reached, and it is therefore reasonable to consider the lateral displacement at the end supports as restrained until the test specimens reached their ultimate capacity.

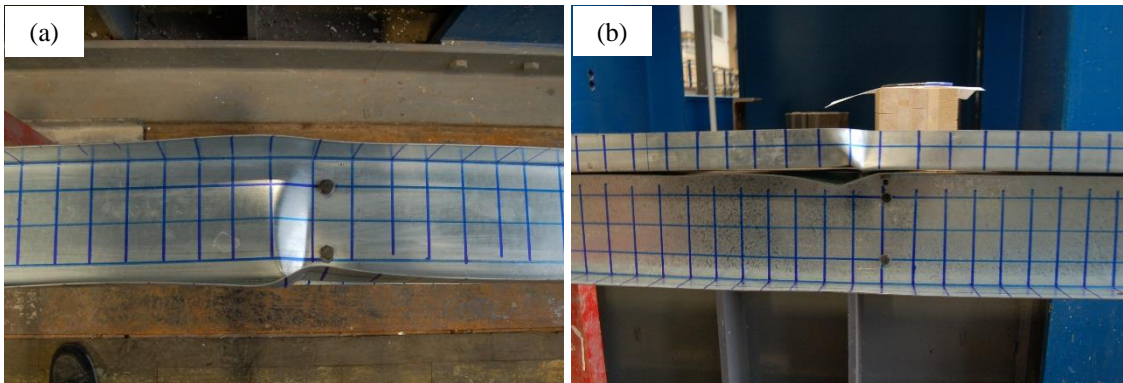


Figure 4.43: Yield line mechanism in B2-2a: a) Top channel, b) Channels comprising the web

Regarding the initial buckling deformations, the potentiometers recorded the top channels buckling with a symmetric buckling pattern with respect to the plane of bending along the constant moment span in all test specimens, while the web channels were recorded to buckle in an anti-symmetric shape. As an example, Figure 4.44 shows the out-of-plane deformations of the components of beam B2-0a. The potentiometers mounted on the yoke located 200 mm to the left of mid-span recorded both flanges of the top channel to buckle outward (solid black line), while the potentiometer mounted on the yoke located 300 mm to the right of mid-span recorded the flanges of this channel to buckle inward (dashed black line). Among the potentiometers which were used to measure the out-of-plane deformation of the web channels (red lines), in both yokes one of the potentiometers recorded an inward deformation, while the other potentiometer recorded an outward deformation.

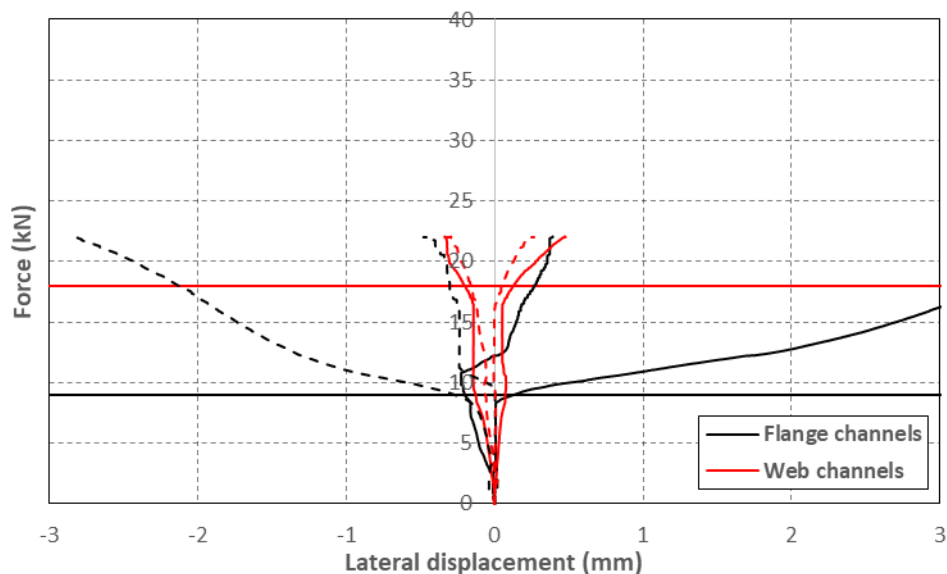


Figure 4.44: Axial load vs lateral displacements of B2-0a

In general, readings from the potentiometers did not record the buckling pattern of the top channels to be affected by subsequent buckling of the web channels to the same degree as in the specimens with geometry 1. Only beam B2-3b showed a noticeable interaction between the components, as illustrated by Figure 4.45, which shows that the magnitude of the buckles in the flanges of the top channel was altered when the web channels started to buckle.

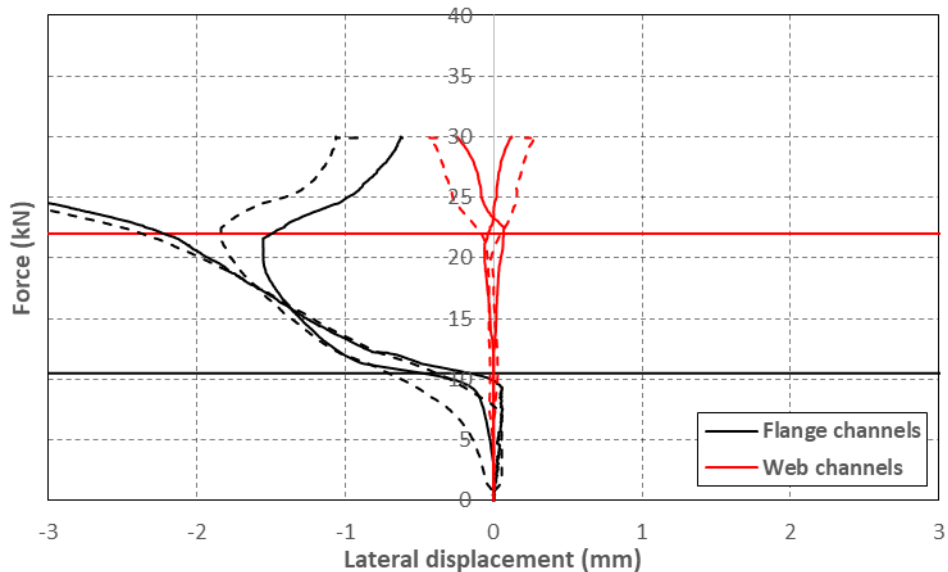


Figure 4.45: Axial load vs lateral displacements of B2-3b

4.8.2 Critical buckling stress and shear force at the connectors

The load at which the individual cross-sectional components buckled was determined from the readings of the potentiometers. Graphs showing the potentiometer readings against the applied load are included in Appendix F for all beams. The load at which the top channels buckled was determined based on the prediction by classical (perturbation) theory that, after local buckling occurs, the initial post-buckling deformations, when plotted against the load, follow a parabolic shape (Venkataramaiah and Roorda, 1982). This parabolic relationship between the load and the initial post-buckling deformations can be expected to appear when the section is free to develop its local buckles. This may not be strictly the case in a built-up member due to contact between the components. Nonetheless, this principle is expected to give a reasonable estimation of the load at which local buckling takes place.

An example of a typical load vs lateral deformation curves is illustrated in Figure 4.45 for beam B2-3b. Since the top channel was the first component to buckle in all of the test specimens, its critical buckling stress could be estimated from the recorded bending moment, assuming that no

slip occurred at the connectors prior to buckling, so that plane sections remained plane. Based on these assumptions, the critical stress in the top channel was obtained from the moment:

$$M = \frac{F \cdot s_{span}}{2} \quad (4.6)$$

where F is the critical load obtained from the load vs. lateral displacement curve, s_{span} is the length of the shear span and M is the moment in the constant moment zone. The stress (σ) in the top channel at a vertical distance y from the centroid of the built-up cross-section is then given by:

$$\sigma = \frac{M \cdot y}{I_{built-up,xx}} \quad (4.7)$$

where $I_{built-up,xx}$ is the second moment of area of the built-up cross-section about the horizontal axis through its centroid. The stress given by Eq. (4.7) provides an upper bound to the actual stress because connector behaviour is not accounted for. Since the web channels consistently buckled *after* the top channel, the critical buckling stress of these channels could not be determined.

For each beam the experimentally derived buckling stress of the top channel was compared with the theoretical buckling stress obtained from an elastic stability analysis carried out using CUFSM 4.05 (Schafer, 2006), in which the buckling stresses were determined based on the average measured cross-sectional dimensions and the Young's modulus obtained from the flat tensile coupons. The theoretical buckling stresses were obtained while considering the top channel in isolation, without any interaction with the rest of the cross-section, but under a stress gradient consistent with the plane section assumption, and using the buckle half-wave length observed during the test.

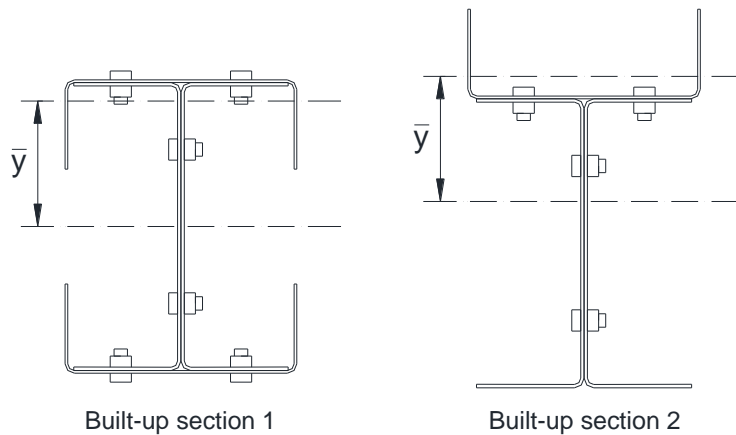


Figure 4.46: Distance between the centroid of the top channel and the centroid of the built-up cross-section 1

In order to confirm that no slip occurred prior to buckling, the shear force in the connectors located between the top channel and the web channels along the shear span was derived at the buckling load. This force was calculated using the same assumption previously employed to determine the critical buckling stresses in the top channel. Thus, knowing that the vertical shear force (V) in the shear span is constant and equal to half of the total force (F) applied to the beam, the shear force to which each connector was subjected when the top channel buckled (V_{con}) was obtained from:

$$V_{con} = \frac{V \cdot A_{topch} \cdot \bar{y}}{16I_{xx,built-up}} \cdot s_{span} \quad (4.8)$$

In the above equation A_{topch} is the area of the top channel, \bar{y} is the distance from the centroid of the top channel to the centroid of the built-up cross-section, as illustrated in Figure 4.46 for both geometries, and s_{span} is the length of the shear span. The resulting force was compared to the slip force of the connectors, which was determined from single lap shear tests aimed at determining the full shear behaviour of the connectors of the tested built-up beams. A detail description of these tests is included in Chapter 6.

4.8.2.1 Geometry 1

Table 4.10 shows that the slip force exceeded the experimentally derived shear force in each tested beam with geometry 1, indicating that no slip occurred in the connectors before the top channel started buckling. This result supports the initial assumption that plane sections remained plane at least up to the moment at which the top channel started buckling.

Table 4.10: Shear force in shear span connectors of specimens with geometry 1

Specimen	V_{con} (N)	V_{slip} (N)	V_{slip}/V_{con} (-)
B1-0a	1528	2600	1.702
B1-0b	1881	2600	1.382
B1-2a	2010	2600	1.294
B1-2b	1836	2600	1.416
B1-3a	1573	2600	1.653
B1-3b	1490	2600	1.745

Table 4.11 shows the theoretical critical buckling stress of the top channel for each test specimen and compares this value to the one derived from the test.

Table 4.11: Buckling stresses of the top channel of specimens with geometry 1

Specimen	Component section	Theoretical buckling stress (MPa)	Buckling stress from test (MPa)	Buckling stress from test /Theoretical buckling stress
B1-0a	T10412-1	107	138	1.29
B1-0b	T10412-3	111	170	1.53
B1-2a	T10412-5	106	170	1.60
B1-2b	T10412-7	109	154-166	1.41-1.52
B1-3a	T10412-9	107	142	1.33
B1-3b	T10412-11	108	126-134	1.17-1.24

The potentiometers located on the two different yokes captured the onset of local buckling in the top channel at consistent stress levels in each specimen, with the marginal exception of specimens B1-2b and B1-3b, for which the two slightly different readings are listed in Table 4.11. Comparing the critical buckling stresses obtained from the tests with the ones obtained from the analysis, it is seen that the former are, on average, 40 % higher than the latter. This can be attributed to the fact that the top channel benefited from the constraint provided by the unbuckled web channels.

The relatively high value of the buckling stress reported in Table 4.11 for built-up beam B1-2a was due to the fact that, in this specimen, the buckling pattern was initially localized in between the two sets of connectors located near mid-span. As the load increased, the buckling pattern gradually spread out over the whole constant-moment span. Consequently, the potentiometers, which were located outside the central set of connectors, were not able to record the initial buckling deformations. In the twin specimen (B1-2b), the buckles were observed to appear simultaneously over the whole constant-moment span, although they were noticeably more pronounced near mid-span.

While no slip occurred in the connectors before first buckling, once the specimens deformed beyond their ultimate capacity, some slip was typically noticed at one end of the built-up beams. This is illustrated in Figure 4.47, where the relative movement between the components has been exaggerated for clarity. The observed slip measured between 1 and 2 mm at the end of the test.

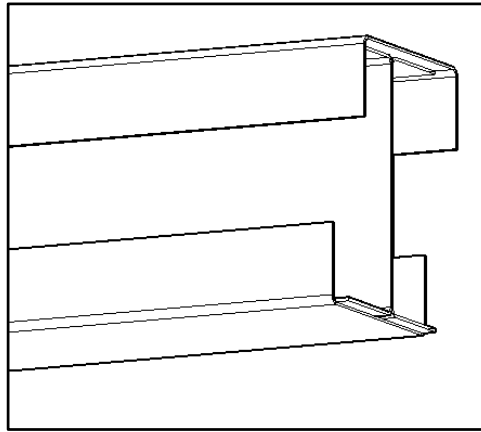


Figure 4.47: Slip at specimen end between the components of built-up beam 1

4.8.2.2 Geometry 2

Table 4.12 shows that in all tested beams with geometry 2, the slip force of the connectors was more than twice the estimated shear force in the connectors located between the top channel and the web channels in the shear span at the moment when the top channel buckled. Therefore, it is reasonable to conclude that no slip had occurred up to that point, and that the initial assumptions used to calculate the theoretical and experimental buckling stresses of the top channel were valid.

Table 4.12: Shear force in shear span connectors of specimens with geometry 2

Specimen	V_{con} (N)	V_{slip} (N)	V_{slip}/V_{con} (-)
B2-0a	1044	2600	2.490
B2-0b	954	2600	2.725
B2-2a	1091	2600	2.383
B2-2b	1041	2600	2.498
B2-3a	1087	2600	2.392
B2-3b	1035	2600	2.512

Table 4.13 lists the theoretical critical buckling stress of the top channel, and compares this value to the one obtained from the test.

Table 4.13: Buckling stresses of the top channel of specimens with geometry 2

Specimen	Component section	Theoretical buckling stress (MPa)	Buckling stress from test (MPa)	Buckling stress from test / Theoretical buckling stress
B2-0a	T10412-1	126	127	1.01
B2-0b	T10412-2	126	120-142	0.95-1.13
B2-2a	T10412-3	127	133-152	1.05-1.20
B2-2b	T10412-4	127	121-136	0.95-1.07
B2-3a	T10412-5	128	133	1.04
B2-3b	T10412-6	128	128	1.00

Table 4.13 shows that, in some specimens, the two sets of potentiometers captured the onset of local buckling in the top channel at a slightly different stress level. This was the case, for example, in beams B2-0b and B2-2a. It is also noted that in beam B2-2b only one of the potentiometers recorded the flange of the top channel buckling at a stress level of 121 MPa, while all the other recorded the top channel buckling at a stress level of 136 MPa. The table also shows that, in general, the experimentally derived buckling stresses were only marginally higher than the theoretical ones, indicating that in the specimens with geometry 2 the top channel did not noticeably benefit from any restraint provided by the unbuckled web channels.

While no slip between the components occurred before first buckling, after the specimens deformed beyond the peak load some slip was typically noticed at one specimen end. However, the exact moment at which slip occurred could not be determined. Figure 4.48 illustrates the relative movement observed between the components of the specimens with geometry 2. As for the beams with geometry 1, the observed slip measured between 1 and 2 mm at the end of the test.

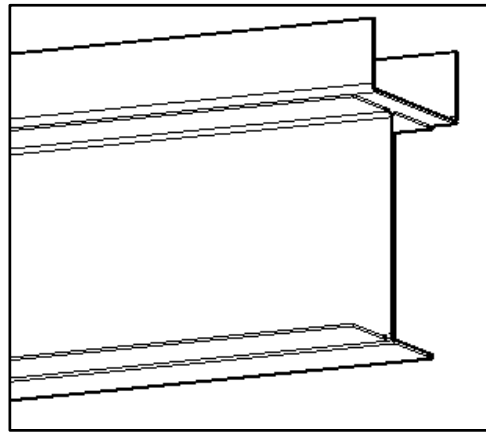


Figure 4.48: Slip at specimen end between the components of built-up beam 2

4.8.3 Ultimate capacity

The load-deflection behaviour of a representative test specimen (B1-2a) is illustrated in Figure 4.49. The vertical axis represents the bending moment in the constant moment zone, obtained using Eq. (4.6), while the horizontal axis shows the deflection at mid-span measured relative to the deflections of the beam at the loading points:

$$\delta_{r,mid} = \frac{(L3 - L1) + (L3 - L2)}{2} \quad (4.9)$$

In the above equation $\delta_{r,mid}$ is the relative deflection at mid-span and $L1$, $L2$ and $L3$ are the readings given by the LVDTs shown in Figure 4.22. The LVDT readings were considered positive when they recorded a downward displacement of the beam.

The black curve in Figure 4.49 corresponds to the ‘dynamic’ (measured) moment, while the red curve corresponds to the ‘static’ moment, which was obtained by deducting the decrease in moment observed when halting the test for 4 min shortly before the ultimate capacity of the specimen was reached from the dynamic moment in the inelastic range.

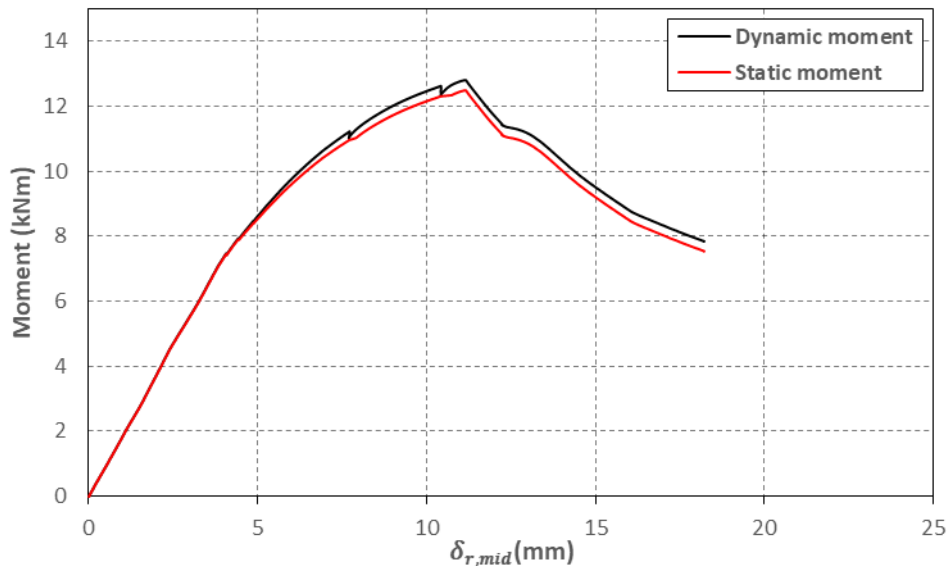


Figure 4.49: Moment vs relative deflection at mid-span (B1-2a)

4.8.3.1 Geometry 1

In Figure 4.50 the static moment is plotted against the relative deflection at mid-span for all specimens with geometry 1, while the static ultimate capacities are plotted against the connector spacing in Figure 4.51.

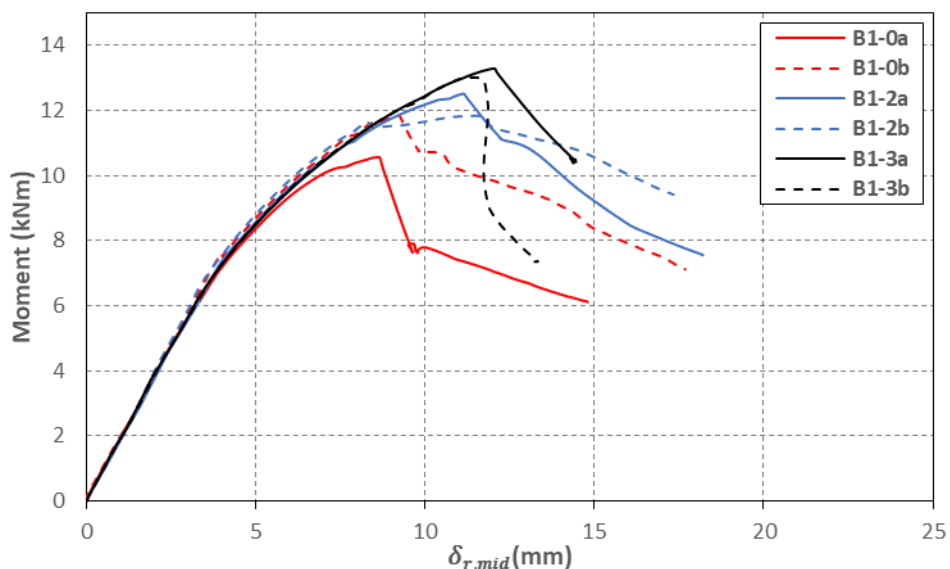


Figure 4.50: Moment vs relative deflection at mid-span of specimens with geometry 1

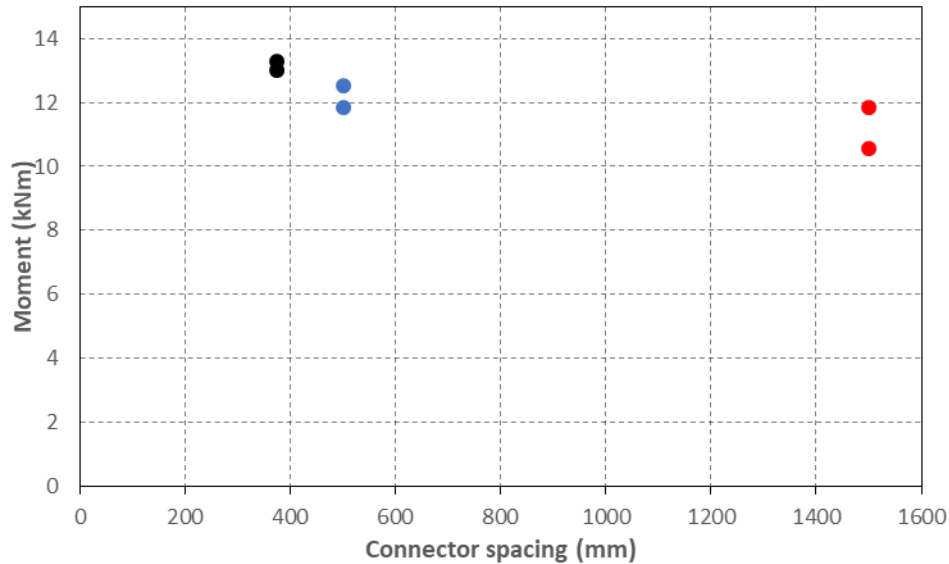


Figure 4.51: Ultimate capacity vs connector spacing of specimens with geometry 1

The ultimate moments obtained for all beams with geometry 1 are listed in Table 4.14. The table includes the dynamic and static moments, as well as the average values of the ultimate moments for each set of twin specimens.

Table 4.14: Ultimate capacity of built-up beam 1

Beam	Ultimate Moment (kNm)		Average Ultimate Moment (kNm)	
	Dynamic	Static	Dynamic	Static
B1-0a	(10.79)	(10.56)	12.06	11.84
B1-0b	12.06	11.84		
B1-2a	12.79	12.51	12.43	12.17
B1-2b	12.07	11.83		
B1-3a	13.51	13.28	13.38	13.14
B1-3b	13.25	13.01		

In general, good agreement in the ultimate capacity was achieved between each pair of twin specimens. Only the B1-0 pair showed a relatively large discrepancy in the ultimate capacity (11 %). This can be attributed to the fact that beam B1-0a was tested without wooden blocking in the end sections, causing the specimen to fail with significant distortion of the end sections accompanied by in-plane bending of the top flange. This resulted in the beam failing with a slightly lower ultimate load and, therefore, the results of this test were discarded. For beams B1-2 and B1-3, the twin specimens showed differences in the (static) ultimate capacity of 6 % and 2 %, respectively.

According to the test results, reducing the connector spacing in the constant moment span resulted in a modest increase in the ultimate capacity of the built-up specimens. The beams with two rows of connectors experienced an average increase in the (static) ultimate capacity of 3 %

relative to the beam without connectors, while the specimens with three rows of connectors exhibited an average increase of 11 %.

4.8.3.2 Geometry 2

Figure 4.52 plots the (static) moment against the relative deflection at mid-span for all beams with geometry 2, while Figure 4.53 plots the ultimate (static) moment against the connector spacing.

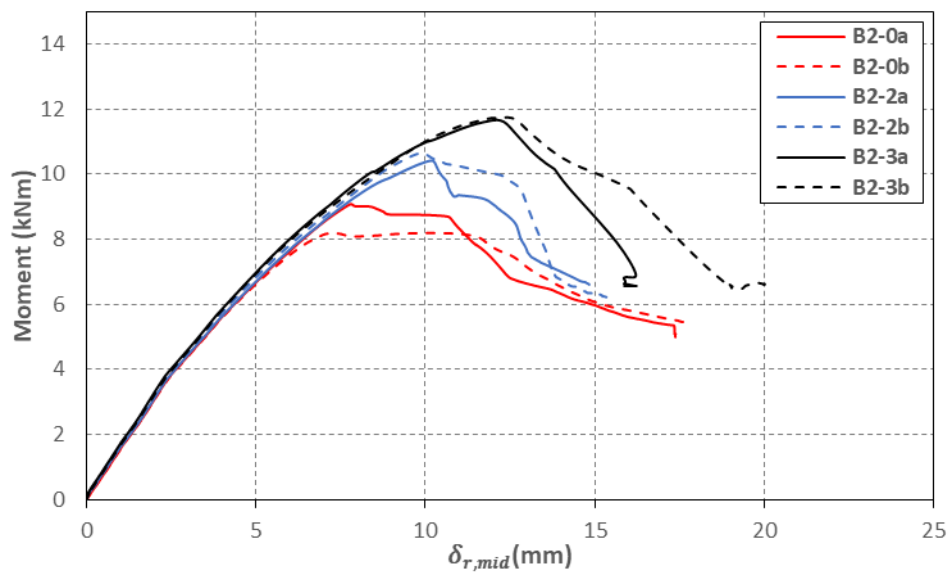


Figure 4.52: Moment vs relative deflection at mid-span of specimens with geometry 2

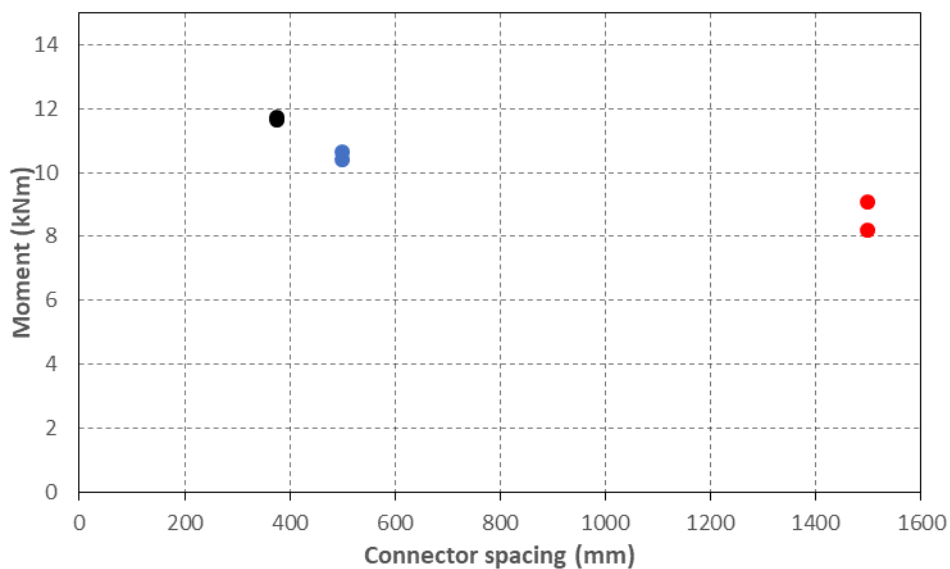


Figure 4.53: Ultimate capacity vs connector spacing of specimens with geometry 2

Table 4.15 lists the ultimate (static and dynamic) moments for all test specimens with geometry 2, together with the average value for each set of twin specimens.

Table 4.15: Ultimate capacity of built-up beam 2

Beam	Ultimate Moment (kNm)		Average Ultimate Moment (kNm)	
	Dynamic	Static	Dynamic	Static
B2-0a	9.23	9.08	8.78	8.63
B2-0b	8.33	8.19		
B2-2a	10.59	10.41	10.71	10.53
B2-2b	10.82	10.64		
B2-3a	11.83	11.66	11.90	11.70
B2-3b	11.97	11.74		

It is seen that twin specimens B2-0 showed the maximum difference in ultimate capacity, which was 11 %. This can be attributed to the fact that in beam B2-0b global flexural-torsional buckling of the top channel was observed before the specimen reached its ultimate capacity, while in beam B2-0a the top channel developed a yield line mechanism at mid-span due to local buckling before displaying flexural-torsional buckling. In beams B2-2 and B2-3, the difference in ultimate capacity between twin specimens was 2 % and 1 %, respectively.

Compared to geometry 1 the tests showed a more substantial increase in ultimate capacity when the spacing between connectors was reduced. The beams with two intermediate rows of connectors along the constant moment span experienced an average increase in ultimate capacity of 22 % relative to the beams without intermediate connectors, while the beams with three rows of intermediate connectors displayed an average increase of 36 %.

4.9. Summary and conclusions

A detailed experimental program including 12 built-up CFS beams with two different cross-sectional geometries, tested in a four-point bending configuration, was carried out. Lateral restraints were provided at the loading points in order to avoid global instability. The built-up specimens were composed of 104 mm to 129 mm deep plain channel sections with nominal thicknesses between 1.2 mm and 1.5 mm, which were joined together using M6 bolts. The beams were designed to fail within the constant moment span by local buckling of the component sections. The connector spacing within the constant moment span was varied among specimens of the same cross-sectional geometry in order to study its effect. In one of the geometries, strut buckling of the channel comprising the top flange in between connector points was observed in addition to local buckling.

As part of the experimental program, the out-of-plane geometric imperfections of the test specimens were measured using a laser sensor prior to testing. In addition, the material properties of the constituent channels were determined by testing a series of tensile coupons which were extracted from the flat parts and rounded corner zones of the channels.

The deflections of the beams were recorded during the test using three LVDTs located at mid-span and at the loading points. In addition, potentiometers recorded the out-of-plane deformations of each component in order to determine the onset of local buckling. The experimentally determined buckling stresses were compared to theoretical predictions which considered the individual components in isolation, without any interaction with the rest of the cross-section.

The following conclusions were drawn from the experimental program:

- The deformed shapes of the beams after buckling revealed an adjustment in the buckling patterns of the component sections relative to their preferred pattern as individual sections as a result of being part of the built-up cross-section. This adjustment manifested itself both as a reduction in the amplitude of the buckles due to contact between the components and an adjustment of the half-wave length of the buckles due to the constraints provided by the connectors. However, the latter effect was relatively minor and the individual components buckled with half-wave lengths close to the ones associated with their minimum buckling stress. Specimens with built-up geometry 1 showed a more significant interaction between their components than specimens with built-up geometry 2, and this interaction was more pronounced in the specimens with the largest number of intermediate connectors within the constant moment span.
- The connectors were observed to rotate and/or translate in order to accommodate the buckling pattern and could not be considered as fixed points in space. No slip occurred in the shear span connectors before buckling, but some slip was noticed in all beams at the end of the test.
- The potentiometer readings showed that the top channel was the first component to buckle in all beams. By comparing the experimentally derived critical buckling stress of this component with the theoretical prediction obtained from an elastic analysis, it was concluded that in the specimens with geometry 1 the top channel significantly benefitted from the restraint provided by the unbuckled web channels. In the specimens with geometry 2, on the other hand, the top channel did not benefit to the same degree from the restraint provided by the web channels.
- The tests showed a relatively modest increase in the ultimate capacity when reducing the connector spacing in the specimens with geometry 1, while the ultimate capacity of the specimens with geometry 2 was more significantly affected by the connector spacing. More specifically, reducing the connector spacing from 1500 mm to 375 mm resulted in increases in the ultimate capacity of 11 % and 36 % for the specimens with geometries 1 and 2, respectively.

Chapter 5

Experimental Study of Long Cold-Formed Steel Built-up Columns

5.1. Introduction

The experimental programme described in this chapter intended to investigate the behaviour and capacity of long built-up columns, paying special attention to the interaction between buckling of the individual components between connector points, cross-sectional instabilities and global buckling of the built-up member. The experiments also sought to study the effects of the connector spacing on these buckling interactions and the ultimate capacity. A total of 24 long column tests were completed. All the specimen preparation, assembly and testing was carried out in the Heavy Structures Laboratory at The University of Sheffield.

Four different cross-sectional geometries, each assembled from four individual sections, were tested, as shown in Figure 5.1. Geometries 1 and 2 were assembled with M6 bolts, tightened with a torque of 10 Nm, representative of hand-tightened ‘snug’ conditions. These geometries are nearly identical to those used in the stub column tests presented in Chapter 3. However, the precise cross-sectional dimensions and the material properties of their components differed. Built-up geometry 1 was constructed using two plain channels with a nominal depth of 130 mm and a thickness of 1.4 mm, and two flat plate sections with a nominal width of 150 mm and a thickness of 2.0 mm. All columns had a nominal length of 3000 mm. In built-up geometry 2 the two inner channels had a nominal depth of 79 mm and a thickness of 1.4 mm, while the two outer channels had a nominal depth of 154 mm and a thickness of 1.4 mm. The nominal length of these columns ranged from 1800 mm to 2500 mm. Geometries 3 and 4 were constructed using plain and lipped channels with identical nominal cross-sectional dimensions, but assembled into different configurations using M5.5 self-drilling sheet metal screws. The plain and lipped channel sections had nominal depths of 120 mm and 110 mm, respectively, a thickness of 1.2 mm and a nominal length of 3000 mm. The cross-sectional dimensions of these

columns were nominally identical to those of the stub columns with geometries 3 and 4 presented in Chapter 3 and their components were fabricated from steel sheets belonging to the same batch. The components of all the built-up geometries considered in this chapter were guaranteed to have a yield stress of at least 260 MPa. However, no information about their zinc coating could be obtained from the manufacturer.

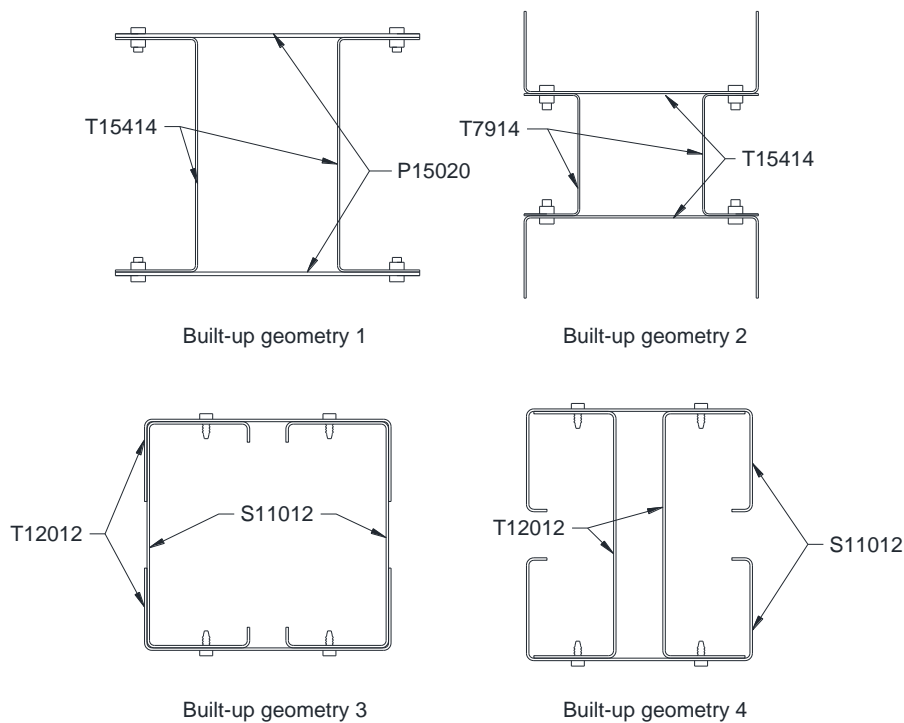


Figure 5.1: Built-up cross sections

All columns were subjected to compression between pin-ended boundary conditions, while applying the load with eccentricities of $L/1000$ or $L/1500$. Three different connector spacings were investigated for each built-up geometry and eccentricity. In order to verify the eccentricity, half of the test specimens were instrumented with strain gauges at mid-height.

It is acknowledged that relative slip between the components at the column ends may play an important role both in the buckling behaviour and the capacity of built-up columns, especially when global instabilities are present. This effect was deemed likely to overshadow the potentially more modest effects of other factors involved, such as the connector spacing. In addition, potential small differences in length between the components would have made it difficult to determine the load attracted by each component of the built-up geometry, making it more difficult to study and evaluate the interaction between the various instabilities in the member. For this reason, it was decided to spot weld the different components of the built-up geometries together at each end, while also welding endplates to the column ends. This also facilitated positioning the columns relative to the pin supports.

In addition, coupon tests were extracted from the flat portions and corner regions of each different component in order to determine their material properties. Detailed measurements of the geometric imperfections were also carried out on the components before and after they were assembled into their final configuration to study the effect of the assembly process on the amplitude and shape of the imperfections. An imperfection measuring rig incorporating a laser displacement sensor and a traverse system, able to perform measurements over a length of 3000 mm, was specifically designed for this purpose. A simple and inexpensive calibration technique, which was developed to achieve imperfection measurements with sufficient accuracy to capture both the global and cross-sectional imperfections of the specimens, is also presented and assessed.

5.2. Labelling

The labelling system used to refer to the cross-sectional components of the long columns is consistent with the one used for the cross-sectional components of the stub columns in Chapter 3. Plain channels and lipped channels are identified by the letter '*T*' or '*S*', respectively, followed by the nominal width of the web in mm and the nominal wall thickness in mm multiplied by 10. The flat plate sections were identified by the letter '*P*' followed by the width of the plate and its thickness multiplied by 10.

The labelling used to refer to each built-up specimen consists of the letters '*LC*', followed by a number ranging from 1 to 4 to indicate its cross-sectional geometry (with reference to Figure 5.1), a hyphen and the number of intermediate rows of connectors (i.e. not counting the connectors in the end sections). Since each test was repeated, the letter '*a*' and '*b*' are used to differentiate between twin test specimens. As an example, the label '*LC1-2a*' refers to the first column tested with cross-sectional geometry 1 which contained two intermediate rows of connectors in addition to the end connectors.

5.3. Material Properties

A total of 26 tensile coupons were tested in order to quantify the material properties of the test specimens. The coupons were cut along the rolling direction of spare specimens belonging to the same batch as those used in the test. For each type of channel section, two flat coupons were taken along the centre line of the web and two corner coupons were cut from the web-flange junction, while for the plate sections two flat coupons were cut along the centre line of the plate.

It is worth mentioning that the coupon results for sections T12012 and S11012 have already been presented in Section 3.3 of Chapter 3 discussing the stub columns, as sections with identical cross-sectional dimensions fabricated from steel sheet belonging to the same batch were used to fabricate some of the stub columns. Those coupon tests results are here repeated for completeness.

Also, channels T15414, which were used to assemble the columns with geometry 2, were supplied in two different lengths. It was noted that the pattern of the zinc coating of the shorter channels differed from the coating pattern of the longer ones. In addition, although all channels labelled as T15414 had the same nominal dimensions, the measured thickness of the shorter channels was noted to be slightly smaller than that of their longer counterparts. This is evidenced in Table 5.10, which lists the measured dimensions of the different components of all columns with geometry 2. It was thus suspected that channels T15414 were fabricated from two different steel sheets and, therefore, two flat and two corner coupons were cut for each batch.

The dimensions of all the tensile coupons adhered to the specifications provided in (CEN, 2009b).

5.3.1 Flat coupons

The nominal dimensions, preparation and instrumentation of the flat coupons are described in Section 3.3.1 of Chapter 3. Figure 5.2 shows the flat coupons before and during testing. The averaged measured width and thickness of the coupons are listed in Table 5.1, where the letters 'a' and 'b' were used to differentiate between twin coupons, and the letters 'l' and 's' following the label 'T15414' were used to differentiate between the coupons taken from the longest T15414 channels and the ones taken from the shortest, respectively.

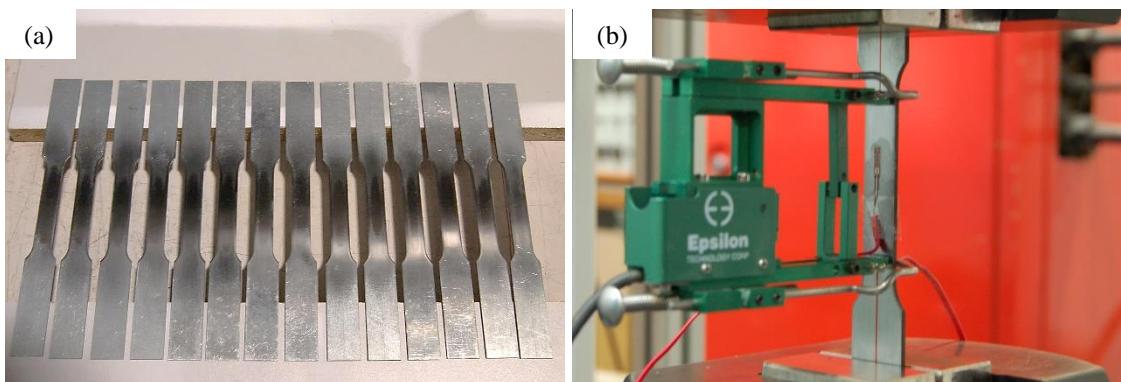


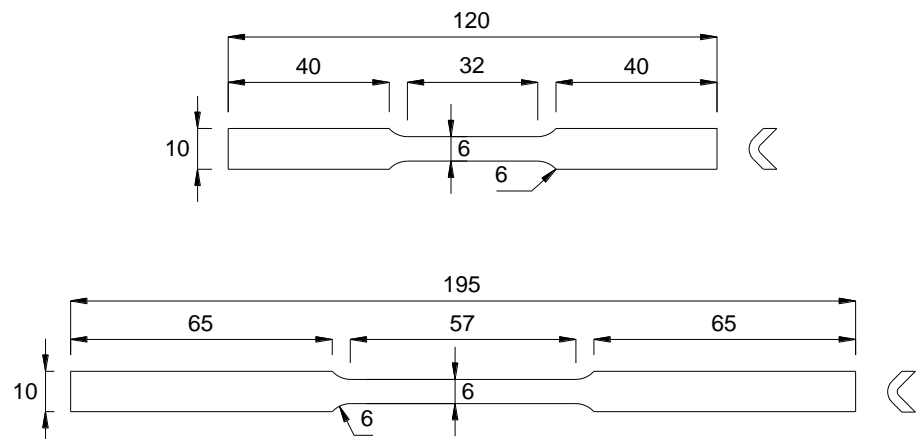
Figure 5.2: a) Flat coupons before testing, b) Flat coupon during testing

Table 5.1: Measured dimensions of flat coupons

Component section	Coupon	b_c (mm)	t (mm)	A (mm ²)
P15020	a	12.525	1.935	24.235
P15020	b	12.528	1.936	24.254
T13014	a	12.532	1.368	17.143
T13014	b	12.527	1.376	17.241
T15414 (l)	a	12.525	1.403	17.577
T15414 (l)	b	12.525	1.401	17.548
T15414 (s)	a	12.532	1.373	17.202
T15414 (s)	b	12.527	1.362	17.058
T7914	a	12.533	1.376	17.245
T7914	b	12.532	1.385	17.353
T12012	a	12.531	1.088	13.630
T12012	b	12.526	1.087	13.616
S11012	a	12.528	1.068	13.380
S11012	b	12.523	1.071	13.408

5.3.2 Corner coupons

The corner coupons had a nominal width of 6 mm. The nominal dimensions of the coupons are



Dimensions in mm

illustrated in

Figure 3.5b. Information about the instrumentation and the test arrangement used for the corner coupons is included in Section 3.3.2 of Chapter 3.

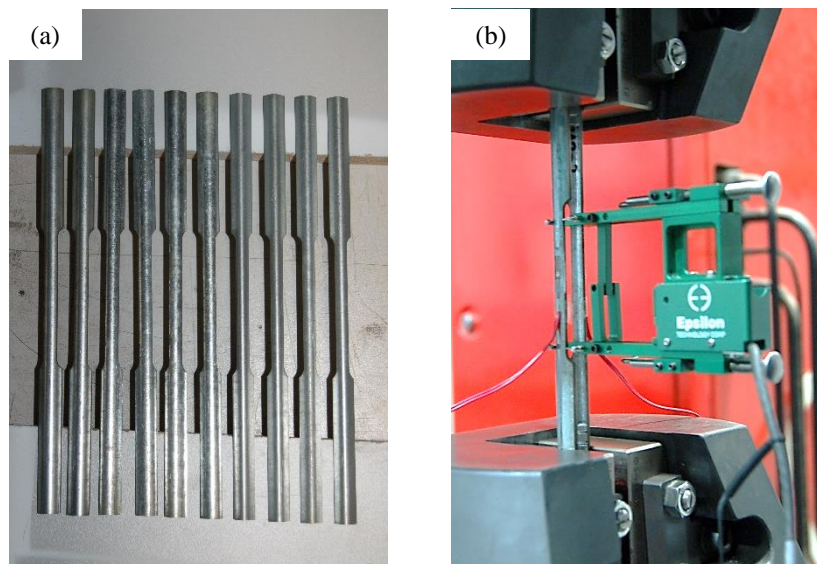


Figure 5.3: a) Corner coupons before testing, b) Pair of corner coupons during testing

The cross-sectional area along the gauge length of each corner coupon was determined by following the same procedure described in Section 3.3.2 of Chapter 3, which involves taking a macro-photograph of the cross-section from each end of the coupon using the reversed lens technique. The photographs taken from each end of the coupon provided two cross-sectional areas per coupon, which were averaged. Differences of less than 1.28 %, 1.59 %, 2.12 %, 2.21 %, 2.88 % and 1.10 % were observed between the calculated areas obtained from each end of coupons T13014, T15414(l), T15414(s), T7914, T12012 and S11012, respectively. Table 5.2 lists the area obtained for each corner coupon after accounting for the thickness of the zinc coating.

Table 5.2: Measured area of corner coupons

Component section	Coupon	A (mm ²)
T13014	a	9.155
T13014	b	9.307
T15414(l)	a	9.745
T15414(l)	b	9.771
T15414(s)	a	9.235
T15414(s)	b	9.096
T7914	a	9.164
T7914	b	9.224
T12012	a	7.595
T12012	b	7.447
S11012	a	7.551
S11012	b	7.503

5.3.3 Coupon testing and results

All coupons were tested following the specification given in the standard (CEN, 2009b). The tensile tests were carried out in a 300 kN Shimadzu AGS-X universal testing machine at a displacement rate of 1 mm/min. Each test was halted for 2 min at regular intervals in order to eliminate strain rate effects and determine the ‘static’ material properties of the coupons. The stress-strain curves of all the tested coupons are included in Appendix G.

The (static) engineering values of the material properties, reported as individual as well as averaged values for each set of coupons, are listed in Table 5.3. In this table ($\sigma_{0.2\%}$) corresponds to the 0.2% proof stress, (σ_u) is the ultimate tensile strength and (ε_f) is the elongation after fracture measured over a gauge length of 50 mm.

Table 5.3: Material properties of tensile coupons

Type	Section	E (GPa)		$\sigma_{0.2\%}$ (MPa)		σ_u (MPa)		ε_f (%)	
		Ind.	Avg.	Ind.	Avg.	Ind.	Avg.	Ind.	Avg.
Flat	P15020-a	202	206	257	260	355	357	25	26
Flat	P15020-b	209		262		358		26	
Flat	T13014-a	199	199	280	279	340	340	35	35
Flat	T13014-b	199		277		339		34	
Flat	T15414(l)-a	206	207	322	325	385	388	27	27
Flat	T15414(l)-b	207		327		390		27	
Flat	T15414(s)-a	198	198	280	280	341	341	35	34
Flat	T15414(s)-b	198		279		340		32	
Flat	T7914-a	200	203	278	281	339	339	34	35
Flat	T7914-b	206		283		338		36	
Flat	T12012-a	190	192	244	242	319	320	30	31
Flat	T12012-b	194		240		321		31	
Flat	S11012-a	197	198	275	277	356	357	28	28
Flat	S11012-b	198		279		357		27	
Corner	T13014-a	221	212	-	347	-	379	-	12
Corner	T13014-b	204		-		-		-	
Corner	T15414(l)-a	215	220	-	409	-	429	-	(6)
Corner	T15414(l)-b	226		-		-		-	
Corner	T15414(s)-a	236	231	-	361	-	395	-	12
Corner	T15414(s)-b	226		-		-		-	
Corner	T7914-a	241	227	-	342	-	383	-	13
Corner	T7914-b	212		-		-		-	
Corner	T12012-a	237	235	-	309	-	353	-	16
Corner	T12012-b	234		-		-		-	

Corner	S11012-a	276	258	-	344	-	384	-	12
Corner	S11012-b	239		-		-			

The results obtained from the tensile coupons show that the sections used in this experimental programme were fabricated from three different steel grades. Sections P15120 and T12012 were most likely fabricated using steel grade DX53D, with a nominal yield strength of 260 MPa, while sections T13014, T15414(s), T7914 and S11012 were most likely fabricated using steel grade DX52D, with a nominal yield strength of 300 MPa, as specified by CEN (1995). Interestingly, the flat coupons belonging to sections T15414(l) showed that these sections were fabricated with steel grade DX51D, which, as suspected, was different from the steel grade used to fabricate sections T15414(s). The difference can be appreciated from Figure 5.4. The average 0.2 % proof strength of 325 MPa obtained from the flat coupons extracted from sections T15414(l) was 16 % larger than the average proof stress obtained from the coupons extracted from sections T15414(s).

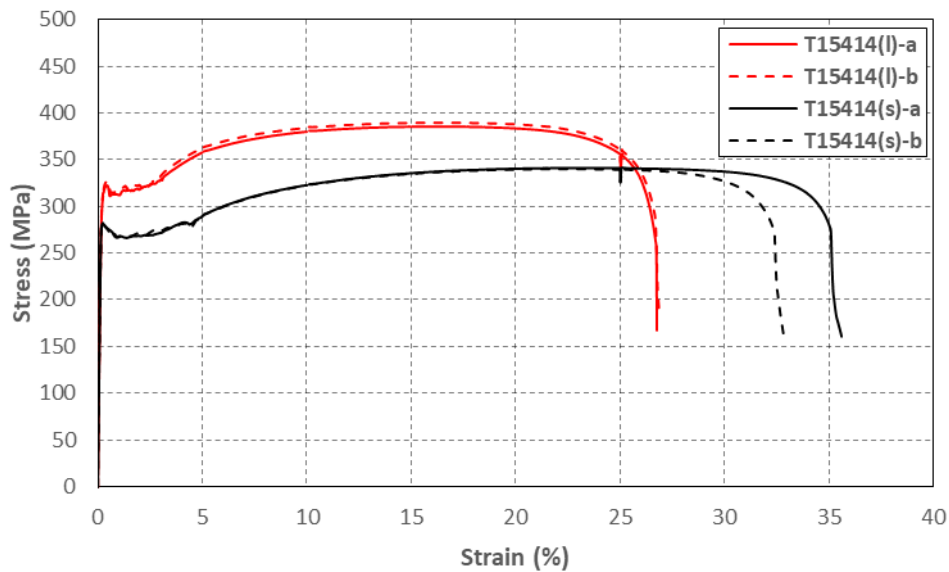


Figure 5.4: static stress–strain curve for flat coupons T15414(l) and T15414(s)

It is worth mentioning that, while all flat coupons failed at a cross-section around the middle of the gauge length, the corner coupons tended to fail towards one end of the gauge length. Although in nearly all of the corner coupons failure occurred at a sufficient distance from the grips of the extensometer to allow for all the localized plastic deformations (necking) to be fully contained within the gauge length, in the pair of corner coupons extracted from sections T15414(l) failure occurred right next to one of the grips of the extensometer, with a large portion of the localized plastic deformation falling outside the measured gauge length. Therefore, the elongation after fracture obtained for this pair of corner coupons should be disregarded.

An explanation for the relatively large Young's modulus obtained for the corner coupons is included in Section 3.3.3 of Chapter 3.

5.4. Section design and geometry

Four different built-up cross-sectional geometries were designed, as shown in Figure 5.1. The specimens were designed to fail by interaction between cross-sectional instability, possible global-type buckling of individual components between connectors and global flexural buckling of the whole column. Each built-up geometry was designed with three different connector spacings. Built-up columns 1 and 2 were assembled using M6 bolts, while built-up columns 3 and 4 were assembled with M5.5 self-drilling screws. Two identical columns were fabricated for each geometry and connector spacing. However, they were tested while applying the load with different eccentricities.

All cross-sectional dimensions of the components fell within the range of geometries allowed by CEN (2006), in particular with respect to their width-to-thickness ratios. The nominal cross-sectional dimensions of the components used to assemble each built-up geometry are listed in Table 5.4. The relevant symbols are illustrated in Figure 5.5.

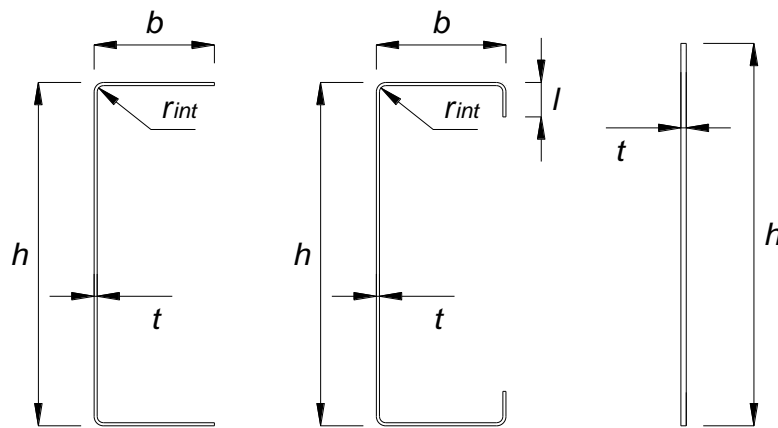


Figure 5.5: Nomenclature used to refer to the dimensions of the component sections

Table 5.4: Nominal dimensions of the component sections

Column	section	h (mm)	b (mm)	L (mm)	t (mm)	r_{int} (mm)
LC1	T13014	130	35	-	1.4	2.8
	P15020	150	-	-	2.0	-
LC2	T15414	154	54	-	1.4	2.8
	T7914	79	36	-	1.4	2.8
LC3/LC4	T12012	120	40	-	1.2	2.4
	S11012	110	50	10	1.2	2.4

The built-up specimens were designed with the help of the CUFSM 4.05 software (Schafer, 2006) which was used to carry out an elastic stability analysis of the individual components which made up the cross-section, as well as of the built-up cross-section as a whole. When analysing the individual components of the cross-section, it was assumed that they buckled independently from one another, without experiencing any contact interaction. However, it was also assumed that the connectors remained in their original position during buckling, without translating or rotating, and that the individual components were only allowed to rotate at the connector point in a plane perpendicular to the axis of the connector. This assumption was inspired by the observation that for the geometries illustrated in Figure 5.1 local/distortional buckling of the components in one direction (either inward or outward) is restrained by adjacent components. Similarly, when analysing the cross-section as a whole, no contact interaction was considered between the components. However, the discrete connector points in the built-up cross-section were modelled by defining coupling constraints between all the available degrees of freedom of the pair of nodes at the locations of the connectors, which were smeared along the column length. As a rough but representative estimate, global elastic buckling of the built-up cross-sections can be assumed to occur at a stress level about 60 % below to that given by the signature curve of the built-up cross-section, based on the reduction in flexural stiffness experienced by the theoretical van der Neut column after local buckling of its flanges take place (Van der Neut, 1969).

5.4.1 Design of built-up column 1

Built-up column 1 was designed with a nominal length of 3000 mm and 2, 3 or 8 equally spaced connectors.

Figure 5.6 shows the signature curve of the individual components used to assemble geometry 1, as well as the signature curve of the whole built-up cross-section. The black curve represents the stresses at which the P15020 plates buckle in a global flexural mode about their minor axis, while the red curve represents the stresses at which the T13014 channels buckle. For these channels, buckles with half-wave lengths of up to 600 mm are mainly composed of the local mode, while buckles with half-wave lengths exceeding 800 mm are predominantly associated with global flexural buckling. The blue curve shows the stresses at which the built-up cross-section buckles as a whole. Only the descending part of this curve, which represents the stresses at which the built-up member buckles in a global flexural mode about its major axis, is of current interest.

Based on the assumption that the connectors do not translate or rotate as the components buckle, an expected buckle half-wave length can be determined depending on the number of buckles that can geometrically fit between connectors. Of all possible solutions, the one that corresponds

to the lowest buckling stress in the signature curve is the most likely to occur. For instance, the plates can only physically buckle outwards between connector points due to the presence of the channel webs, so they are expected to buckle with a half-wave length equal to half the distance between connectors for any connector configuration. In the case of the channels, on the other hand, if they try to buckle in a local mode, they will be restrained at the connector points by the need for transverse bending of the plates. Therefore, in the columns with 8 internal connectors the lowest critical buckling stress will be achieved if the channels buckle with two half-waves which lengths are equal to half the connector spacing, while in the columns with 3 and 2 internal connectors the channels are anticipated to buckle with six and eight half-waves between connectors, respectively. In addition, in the columns with 2 internal connectors, minor axis global flexural buckling of the channels between connectors is also anticipated since at a half-wave length of 960 mm (the connector spacing) the critical buckling stress of this buckling mode is 200 MPa, which is lower than the stress at which the whole built-up specimen is expected to buckle in a global flexural mode, as indicated by the red dashed vertical line and the blue dashed horizontal line in Figure 5.6. For this type of buckling mode, the half-wave length is assumed to coincide with the connector spacing because the channels are not prevented from rotating at the connector points in the plane orthogonal to the connector axis.

Figure 5.6 also shows that global buckling of the plates is critical over local buckling of the channels in all the columns, and their critical buckling stress is expected to increase from 3 MPa to 26 MPa as the number of connectors is increased from two to five and the spacing between connectors is reduced. The critical buckling stress of the channels, on the other hand, is expected to be approximately the same in all the columns and very close to the minimum buckling stress of 97 MPa in the signature curve. The predicted buckling stresses of the components of built-up column 1, as well as the predicted global flexural buckling stress of the whole built-up cross-section reduced by 60 % to approximately account for the reduction of flexural stiffness of the built-up column after local buckling are listed in Table 5.5.

Table 5.5: Predicted buckling stress of built-up column 1

Column	Predicted buckling stress (MPa)			
	Channel		Plate	Built-up section
	Local	Global	Global	Global
LC1-2	98	200	3	254
LC1-3	98	-	5	254
LC1-8	100	-	26	254

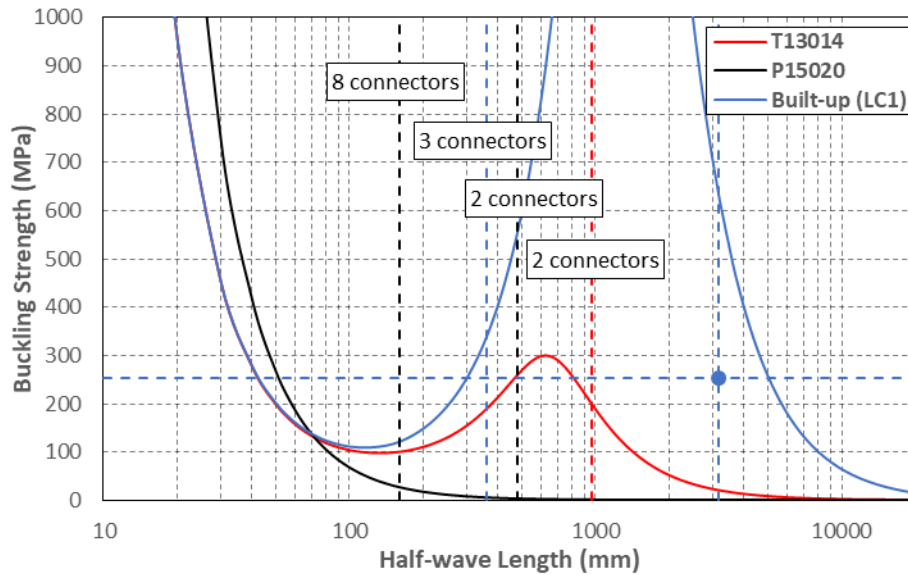


Figure 5.6: Signature curve of the components of built-up column 1

5.4.2 Design of built-up column 2

Built-up column 2 was designed with nominal lengths of 1800 mm and 4 equally spaced connectors, and 2500 mm and 2 and 6 equally spaced connectors. Although, columns LC2-4 and LC2-6 have different lengths and number of internal connectors, their connector spacing was approximately the same, 336 mm and 340 mm, respectively.

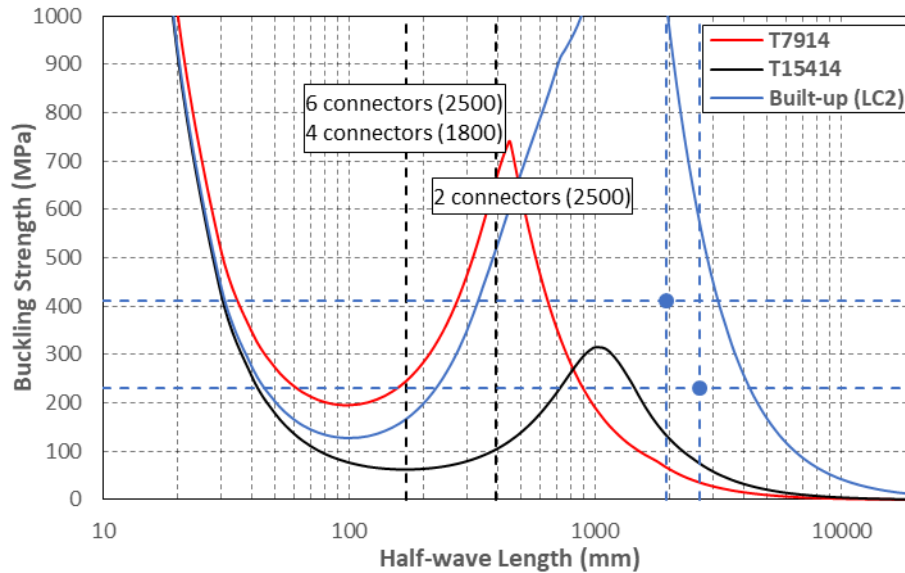
Figure 5.7 shows the signature curves of the individual components that form built-up column 2, as well as of the whole built-up cross-section. In the figure, the red and black curves represent the stress at which the inner channels (T7912) and the outer channels (T15414) buckle, while the blue curve shows the stresses at which the built-up cross-section buckles as a whole. The descending part of the blue curve corresponds to the built-up cross-section buckling in a global flexural mode about its mayor axis.

In Figure 5.7, it is seen that if the connectors are to remain in their original position, the lowest critical stress due to local buckling in the outer channels is achieved in the columns with 4 and 6 internal connectors if these channels buckle with a half-wave length equal to half the distance between connectors, while in the columns with 2 internal connectors this occurs if the outer channels buckle with four half-waves between connectors. Likewise, the inner channels are expected to buckle in a local mode generating eight half-waves between connectors in columns LC2-2, and four half-waves in columns LC2-6 and LC2-4.

Table 5.6 summarizes the predicted bucking stresses of all of the components of built-up column 2, as well as of the whole built-up cross-section reduced by 60 %.

Table 5.6: Predicted buckling stress of built-up column 2

Column	Predicted buckling stress (MPa)		
	Int. Channel	Ext. Channel	Built-up section
	Local	Local	Global
LC2-2	196	64	232
LC2-6	199	63	232
LC2-4	199	63	411

**Figure 5.7: Signature curve of the components of built-up column 2**

5.4.3 Design of built-up columns 3 and 4

Built-up columns 3 and 4 were designed with a nominal length of 3000 mm and 2, 3 and 8 equally spaced connectors. Both built-up geometries were designed using T12012 and S11012 components, but the components were arranged in different configurations. This allowed for a more direct comparison between the two different built-up geometries.

The signature curves of the individual components, as well as of the whole built-up cross-section are illustrated in Figure 5.8 and Figure 5.9 for built-up column 3 and 4, respectively. In both figures, the black and red curves show the stresses at which the plain channel (T12012) and the lipped channels (S11012) buckle, respectively, while the blue curves represent the stresses at which the built-up cross-sections buckle as a whole, with the descending part of these curves corresponding to global flexural buckling of the built-up cross-sections about their mayor axis. The black and red curves are the same in both figures, since the built-up geometries were assembled using the same type of components. For the plain channels, the black curves show that buckling half-waves lengths up to 300 mm are predominantly associated with the local buckling mode. Likewise, for the lipped channels, the red curves, show that buckles with half-wave lengths up to 200 mm are mainly composed of the local mode, while buckles with half-wave lengths between 250 mm and 850 mm are predominantly distortional.

From the figures, it can also be seen that local buckling of the plain channels occurs before local buckling of the lipped channels. Assuming that the connectors do not translate or rotate, the plain channels are anticipated to buckle in a local mode generating 8, 6 and 2 half-waves buckles between connectors in the columns with 2, 3 and 8 internal connectors, respectively, since this requires the lowest buckling stresses. Likewise, for the columns with 2, 3 and 8 internal connectors, the lipped channels are expected to buckle in a local mode generating 12, 8 and 4 half-waves between connectors.

It is also noted from Figure 5.8 and Figure 5.9 that the lipped channels may also buckle in a distortional mode with a half-wave length of approximately 370 mm and a critical stress of 187 MPa., since the critical buckling stress of the distortional mode in the lipped channels is very close to the critical buckling stress that triggers global flexural buckling of the whole cross-section in columns with geometry 3 and 4.

The predicted buckling stresses of each component, as well as of the whole built-up cross-section are listed in Table 5.7 and Table 5.8 for built-up columns 3 and 4, respectively. In the tables, the global flexural buckling stresses predicted by CUFSM were reduced 60 % to approximately account for the reduction in the flexural stiffness of the columns as a result of local buckling.

Table 5.7: Predicted buckling stress of built-up columns 3

Column	Predicted buckling stress (MPa)		
	Lipped Channel	Plain Channel	Built-up section
	Local	Local	Global
LC3-2	125	79	164
LC3-3	125	79	164
LC3-8	125	81	164

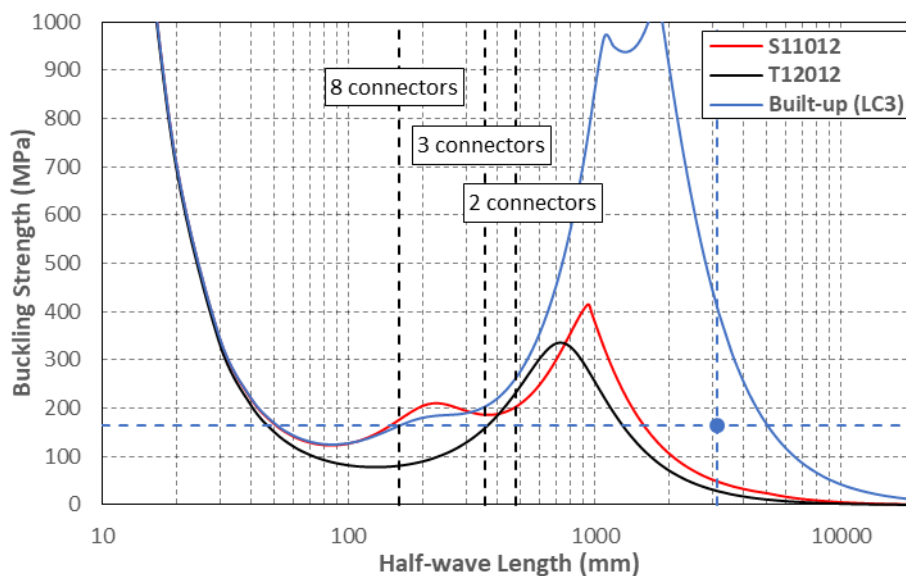
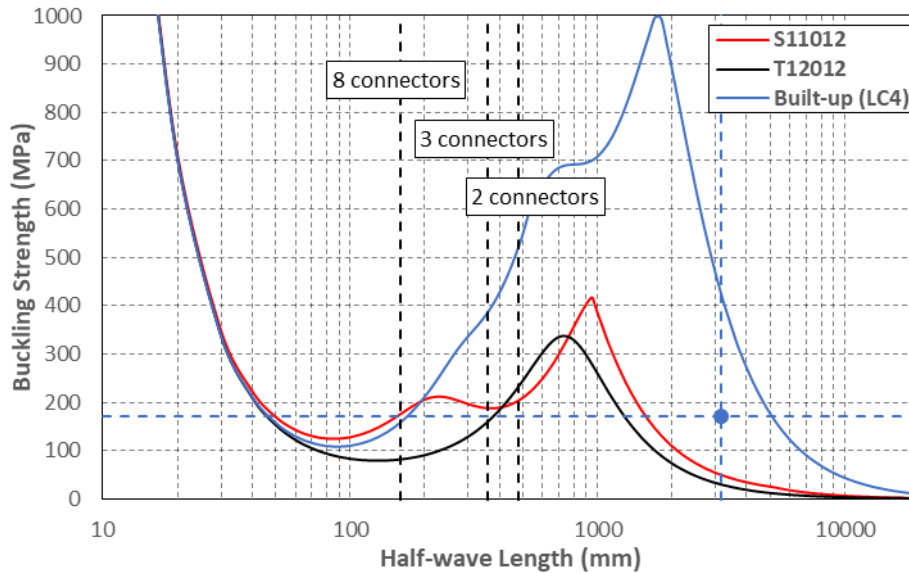


Figure 5.8: Signature curve of the components of built-up columns 3

Table 5.8: Predicted buckling stress of built-up columns 4

Column	Predicted buckling stress (MPa)		
	Lipped Channel	Plain Channel	Built-up section
	Local	Local	Global
LC4-2	125	79	170
LC4-3	125	79	170
LC4-8	125	81	170

**Figure 5.9: Signature curve of the components of built-up columns 4**

5.5. Cross-section assembly and specimen preparation

All columns were assembled and prepared for testing in the Heavy Structures Laboratory at The University of Sheffield.

Prior to assembly, the cross-sectional dimensions of each component were measured at three locations along its length. The widths of the web and the flanges of the channels, as well as the width of the plate sections, were measured using a digital Vernier caliper with a precision of ± 0.03 mm, while the thicknesses of the sections were measured with a digital micrometre with a precision of ± 0.002 mm. Table 5.9, Table 5.10, Table 5.11 and Table 5.12 list the averaged measured cross-sectional dimensions of the components belonging to geometries 1, 2, 3 and 4, respectively, using the nomenclature established in Figure 5.10. The values reported in the tables were obtained after deducting the thickness of the coating from the measured dimensions. An average coating thickness was determined for each type of channel by measuring the thickness of each channel at both ends before and after removing the zinc coating with hydrochloric acid. In addition, as the sections T15414 with lengths of 1800 mm and 2500 mm were fabricated from two different types of steel sheets, the average thickness of the zinc coating was determined for each length. The measurements are listed in Table 5.13 for each component type.

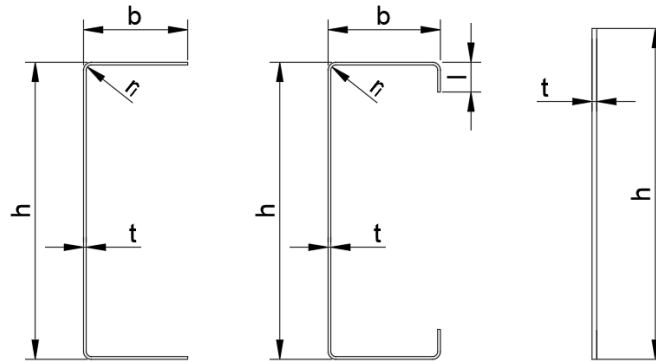


Figure 5.10: Nomenclature used to refer to the dimensions of the component sections

Table 5.9: Measured dimensions of built-up column 1

Column	Channels				Plates		
	component	h (mm)	b (mm)	t (mm)	component	h (mm)	t (mm)
LC1-2a	T13014-1	129.64	35.85	1.381	P15020-1	149.91	1.962
	T13014-2	129.70	35.91	1.382	P15020-2	149.87	1.929
LC1-2b	T13014-3	129.87	35.79	1.375	P15020-3	150.18	1.964
	T13014-4	130.11	35.81	1.368	P15020-4	149.86	1.959
LC1-3a	T13014-5	129.92	35.97	1.377	P15020-5	150.01	1.957
	T13014-6	129.92	35.88	1.380	P15020-6	149.82	1.962
LC1-3b	T13014-7	129.87	35.89	1.373	P15020-7	150.02	1.956
	T13014-8	129.96	35.86	1.370	P15020-8	149.75	1.928
LC1-8a	T13014-9	129.75	35.99	1.388	P15020-9	150.02	1.963
	T13014-10	129.86	35.96	1.386	P15020-10	149.85	1.955
LC1-8b	T13014-11	129.93	35.89	1.373	P15020-11	149.97	1.949
	T13014-12	129.84	35.94	1.382	P15020-12	149.94	1.948
Average	T13014	129.87	35.90	1.378	P15020	149.93	1.953
St. Dev.	T13014	0.124	0.062	0.006	P15020	0.115	0.012

Table 5.10: Measured dimensions of built-up column 2

Column	Outer channels				Inner channels			
	component	h (mm)	b (mm)	t (mm)	component	h (mm)	b (mm)	t (mm)
LC2-2a	T15414(l)-1	153.72	54.43	1.403	T7914-1	78.93	36.87	1.373
	T15414(l)-2	153.86	54.37	1.386	T7914-2	79.00	36.88	1.368
LC2-2b	T15414(l)-3	153.88	54.37	1.381	T7914-3	79.09	36.83	1.459
	T15414(l)-4	153.67	54.43	1.404	T7914-4	79.05	36.88	1.375
LC2-6a	T15414(l)-5	153.79	54.28	1.399	T7914-5	79.02	36.91	1.375
	T15414(l)-6	153.71	54.34	1.399	T7914-6	78.73	36.90	1.373
LC2-6b	T15414(l)-7	153.91	54.40	1.393	T7914-7	78.87	36.68	1.360
	T15414(l)-8	153.86	54.41	1.378	T7914-8	78.95	36.83	1.369
LC2-4a	T15414(s)-9	153.77	54.13	1.368	T7914-9	79.63	36.31	1.366
	T15414(s)-10	153.84	54.09	1.377	T7914-10	79.12	36.71	1.372
LC2-4b	T15414(s)-11	153.73	54.31	1.381	T7914-11	79.20	36.81	1.371
	T15414(s)-12	153.73	54.21	1.383	T7914-12	79.26	36.79	1.364
Average	T15414(l)	153.80	54.38	1.393	T7914	79.07	36.78	1.377
	T15414(s)	153.77	54.19	1.377				
St. Dev.	T15414(l)	0.090	0.051	0.010	T7914	0.227	0.165	0.026
	T15414(s)	0.052	0.097	0.007				

Table 5.11: Measured dimensions of built-up column 3

Column	Plain channels				Lipped channels				
	component	h (mm)	b (mm)	t (mm)	component	h (mm)	b (mm)	l (mm)	t (mm)
LC3-2a	T12012-1	119.67	39.92	1.101	S11012-1	108.98	49.50	9.62	1.100
	T12012-2	119.21	39.86	1.103	S11012-2	109.21	49.50	9.62	1.096

LC3-2b	T12012-3	119.39	39.91	1.107	S11012-3	109.54	49.61	9.70	1.108
	T12012-4	119.57	40.05	1.109	S11012-4	108.99	49.75	9.71	1.102
LC3-3a	T12012-5	119.61	40.03	1.104	S11012-5	110.14	49.71	9.73	1.093
	T12012-6	119.62	40.10	1.110	S11012-6	109.27	49.76	9.75	1.103
LC3-3b	T12012-7	119.65	40.06	1.107	S11012-7	109.18	49.55	9.80	1.104
	T12012-8	119.62	40.04	1.112	S11012-8	109.66	49.74	9.86	1.104
LC3-8a	T12012-9	119.60	40.00	1.104	S11012-9	109.32	50.04	9.96	1.102
	T12012-10	119.62	40.03	1.109	S11012-10	109.71	50.06	9.98	1.100
LC3-8b	T12012-11	119.23	39.83	1.112	S11012-11	109.65	49.97	10.03	1.105
	T12012-12	119.19	39.73	1.115	S11012-12	109.78	49.85	9.97	1.104
Average	T12012	119.50	39.96	1.108	S11012	109.45	49.75	9.81	1.102
St. Dev.	T12012	0.188	0.113	0.004	S11012	0.351	0.198	0.145	0.004

Table 5.12: Measured dimensions of built-up column 4

Column	Plain channels				Lipped channels				
	component	h (mm)	b (mm)	t (mm)	component	h (mm)	b (mm)	l (mm)	t (mm)
LC4-2a	T12012-13	119.15	39.72	1.113	S11012-13	109.89	49.85	9.97	1.097
	T12012-14	119.19	39.78	1.107	S11012-14	109.37	49.84	9.88	1.107
LC4-2b	T12012-15	119.29	39.73	1.102	S11012-15	109.24	49.75	9.96	1.108
	T12012-16	119.29	39.75	1.103	S11012-16	110.86	49.77	9.22	1.110
LC4-3a	T12012-17	119.12	39.69	1.100	S11012-17	109.47	49.80	9.80	1.108
	T12012-18	119.17	39.74	1.102	S11012-18	109.17	49.77	9.82	1.107
LC4-3b	T12012-19	119.17	39.80	1.110	S11012-19	109.88	49.79	9.81	1.091
	T12012-20	119.24	39.69	1.108	S11012-20	109.27	49.93	9.75	1.104
LC4-8a	T12012-21	119.18	39.67	1.108	S11012-21	109.66	49.82	9.82	1.096
	T12012-22	119.29	39.62	1.108	S11012-22	110.21	49.71	9.70	1.097
LC4-8b	T12012-23	119.29	39.60	1.102	S11012-23	109.06	49.78	9.88	1.102
	T12012-24	119.11	39.71	1.110	S11012-24	108.93	49.98	9.83	1.106
Average	T12012	119.21	39.71	1.106	S11012	109.58	49.82	9.79	1.103
St. Dev.	T12012	0.070	0.060	0.004	S11012	0.553	0.077	0.194	0.006

Table 5.13: Average thickness of zinc coating

Section	Measured thickness (mm)	
	Average	Standard Deviation
P15020	0.039	0.006
T13014	0.019	0.008
T15414(l)	0.054	0.006
T15414(s)	0.025	0.004
T7914	0.031	0.016
T12012	0.031	0.006
S11012	0.031	0.010

In order to accurately position the specimens relative to the axis of the pin supports, the location of the major axis of the built-up cross-section was scribed onto the channel webs at each end before the components were assembled into their final configuration. Due to the symmetry of the built-up geometries, the scribed lines coincided with the centre line of the channel webs.

The specimens were assembled using the same types of connectors used to assemble their stub column counterparts described in Chapter 3. In particular, geometries 1 and 2 were assembled using M6 bolts, while geometries 3 and 4 were assembled using M5.5 sheet metal screws. The

procedure followed to assemble the columns was similar to the one used for the stub columns. The locations of the connectors were first marked in one component of each pair to be connected and small diameter holes were drilled. The components were then positioned in their built-up configuration, secured with clamps and spot welded together at each end. Four spot welds were used at each end for each contact pair. The spot welds were designed to ensure a uniform distribution of the stresses between the different components of the built-up specimens upon loading. Finally, bolt holes with a diameter of 6.25 mm were drilled into the specimens with geometries 1 and 2, and the components were bolted together while applying a torque of 10 Nm, whereas the specimens with geometries 3 and 4 were screwed together using self-drilling screws. Due to the significant overall length of the columns, the components tended to separate when drilling or screwing the components together. In order to avoid this clamps were placed near the connectors whenever possible and the drilling/screwing sequence was started from the ends of the column (close to the spot welds), while moving towards the centre of the column.

The locations of the connectors, as well as the arrangement of the spot welds, are illustrated in Figure 5.11a, Figure 5.11b, Figure 5.13a and Figure 5.13b for geometries 1, 2, 3 and 4, respectively. Figure 5.12a-d shows some of the specimens with geometries 1 and 2 during and after the assembly process, while Figure 5.14a-c shows specimens with geometries 3 and 4.

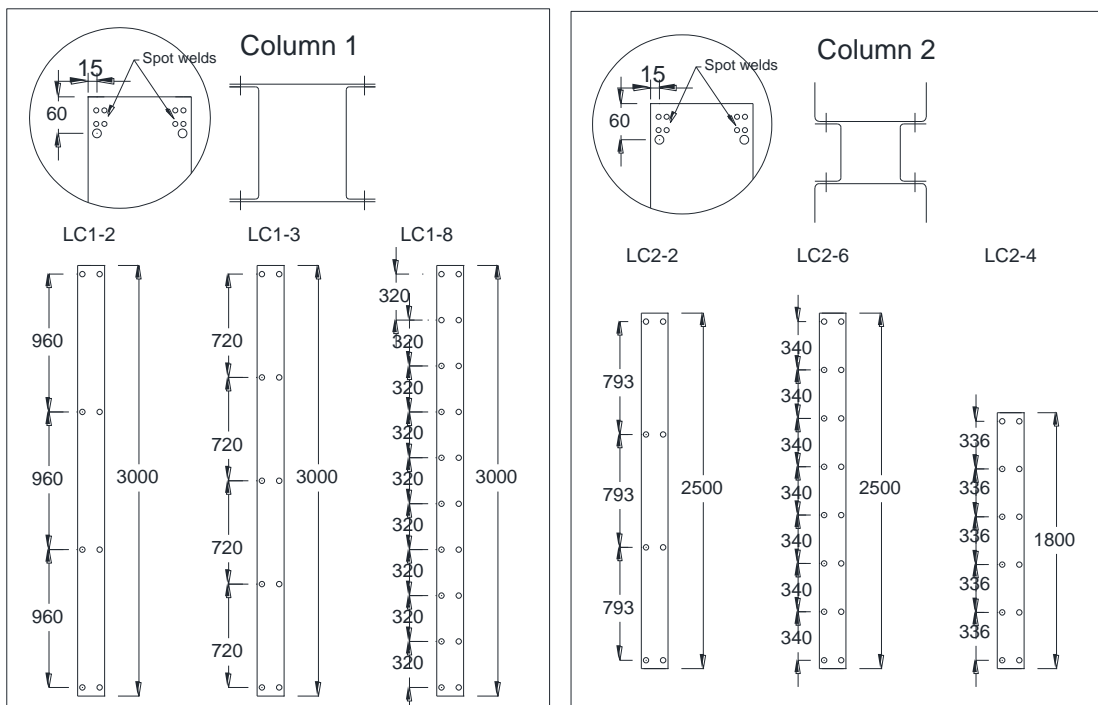


Figure 5.11: Location of connectors in a) geometry 1 and b) geometry 2

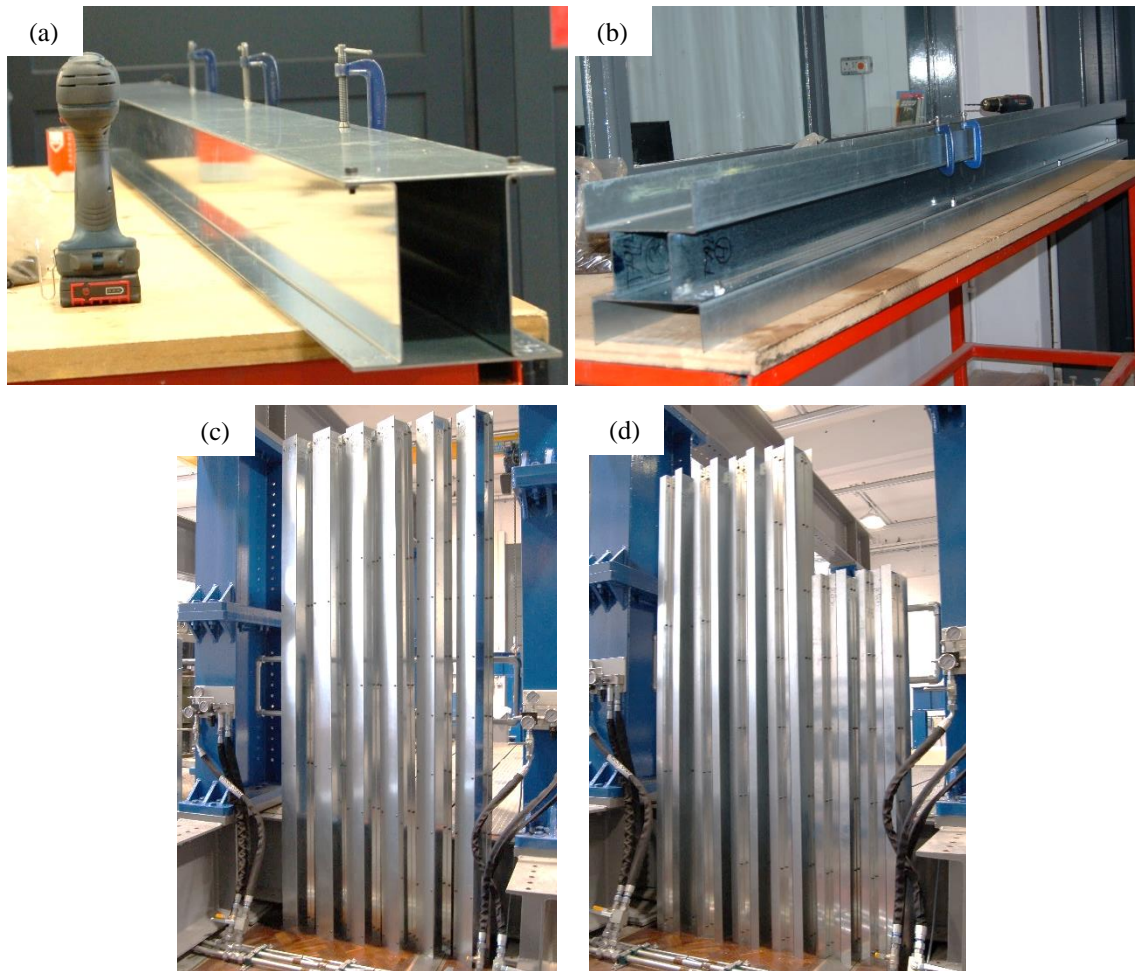


Figure 5.12: Built-up columns 1 and 2 during and after assembly

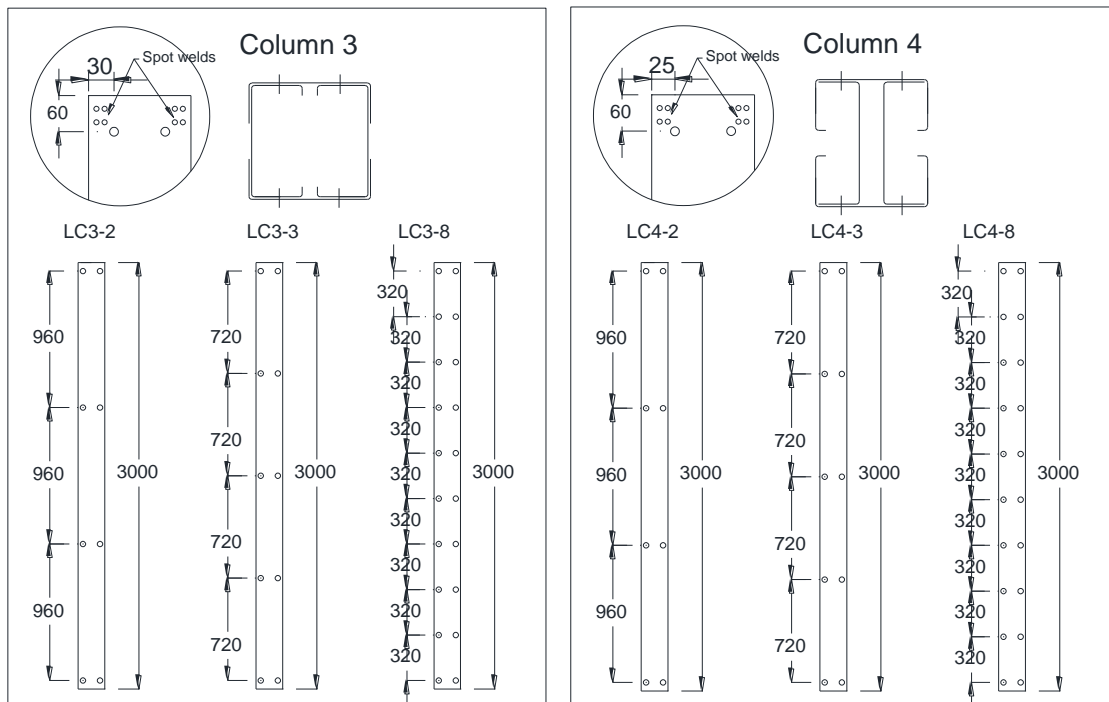


Figure 5.13: Location of connectors in a) geometry 3 and b) geometry 4

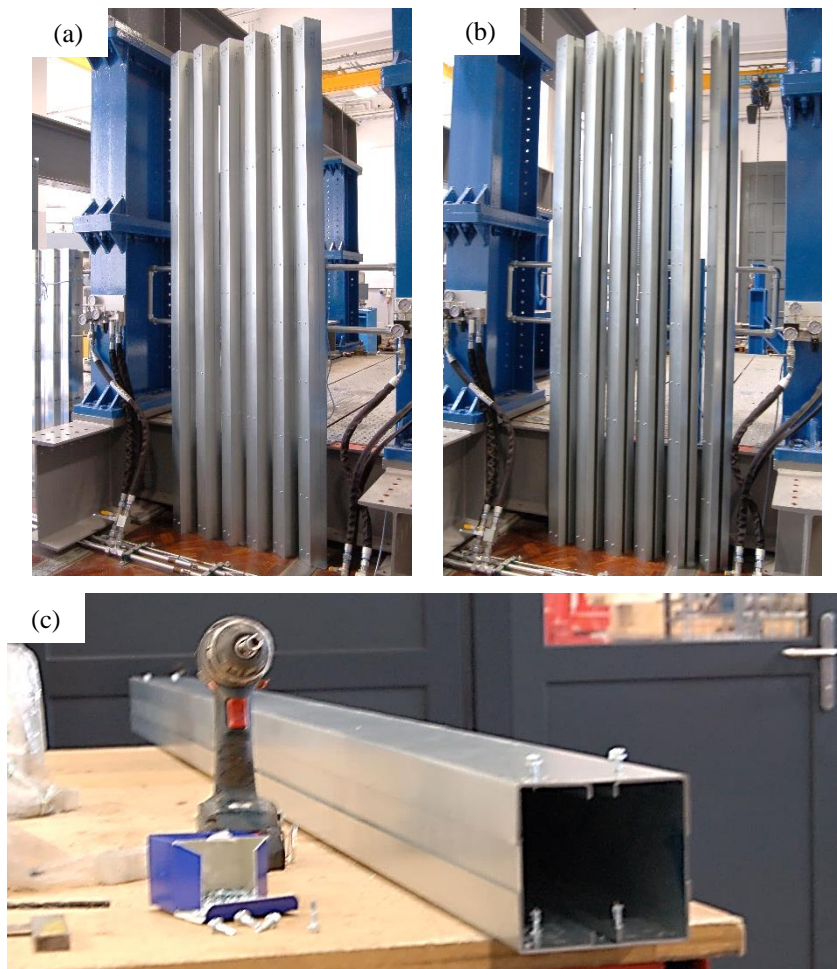


Figure 5.14: Built-up columns 3 and 4 during and after assembly

Endplates with dimensions of $250 \times 300 \text{ mm}^2$ and a thickness of 20 mm were marked with scribed lines along the centre line of their shorter edge and were welded to each end of the built-up specimens after aligning them with the scribed lines previously marked onto the latter, as illustrated in Figure 5.15. The endplates had slotted holes near each corner which allowed for around 10 mm of adjustment when bolting the endplates to the pin supports.

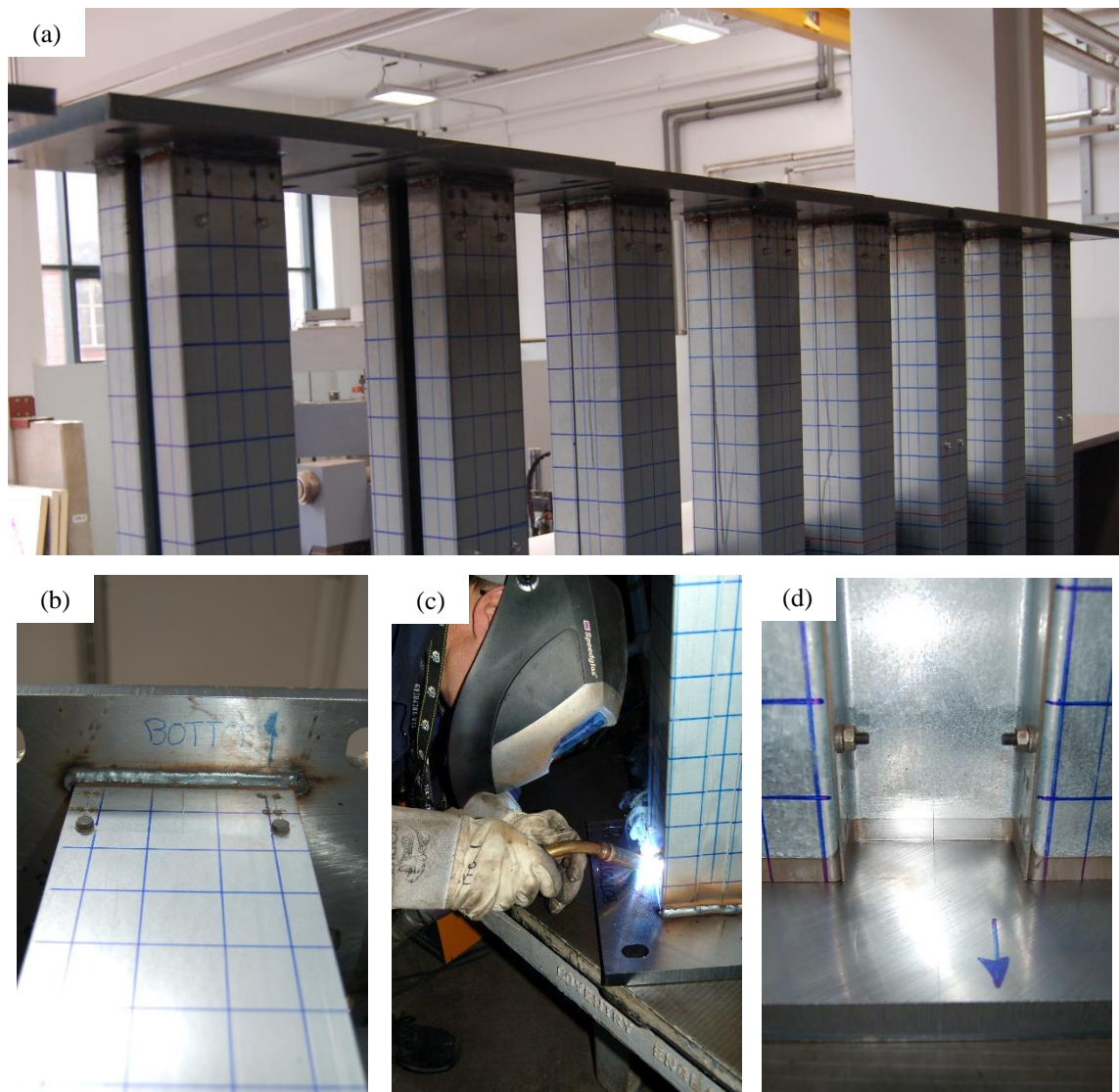


Figure 5.15: a) and b) Endplate welded to the columns; c) welding process d) scribed lines on specimen and endplate;

It is worth mentioning that, although the specimens with geometries 3 and 4 did not show any local end distortion after welding on the endplates, specimens with geometries 1 and 2 did show some local distortion. More specifically, in the specimens with geometry 1, the plate sections showed a small out-of-plane bending deformation immediately after welding on the endplates. This deformation was mainly noticeable in the specimens with 2 and 3 intermediate connectors and had mostly disappeared after the welding area had cooled down. It should also be noted that for geometry 1 the plate sections were up to 2 mm longer than the channels components, as opposed to the less than 1mm length difference observed between the components of the other built-up geometries. In the case of the specimens with geometry 2, the flange tips of channels T15414 bent out at each end of the column after welding on the endplates, as shown in Figure 5.16, and although this effect diminished when the welding area cooled down, it was still noticeable in the final state. The flange distortion was especially noticeable in specimens LC2-4, which had a length of 1800 mm.

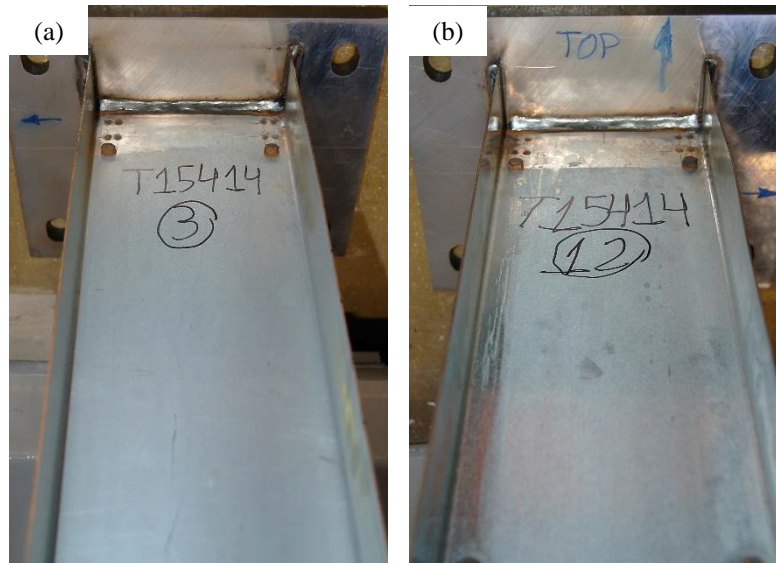


Figure 5.16: Typical flange distortion at the end of channel T15414 in specimens: a) LC2-2b; b) LC2-4b

5.6. Imperfection Measurements

Global buckling is known to be sensitive to initial geometric imperfections. This sensitivity is typically even more pronounced when the column fails by interaction of global and cross-sectional buckling. For this reason the geometric imperfections of all test specimens were measured before they were tested. The imperfections were measured before and after the individual components were assembled into their final configuration in order to assess the effect the assembly process may have had on their magnitude and shape.

5.6.1 Imperfection measuring rig

An imperfection measuring rig was specially designed to record the imperfections of the test specimens. The rig consisted of a traverse system with two electric motors which moved a laser sensor mounted on a trolley along high precision bars in two orthogonal directions. The measuring frame had dimensions of 3390x1250 mm² and was able to take measurements over a length of 3000 mm. The traverse system had six adjustable supports which were bolted on top of a rigid steel frame, as illustrated in Figure 5.17. The rigid frame, in turn, also had six adjustable supports which ensured that the entire rig was fully resting on the floor. The specimens to be measured were placed on two beams spanning across the rigid frame, of which both the position along the frame and the height could be adjusted.

The laser displacement sensor had an accuracy of ± 0.0075 mm and a measuring range between 65 and 95 mm. A crank handle on the trolley controlled the vertical position of the laser sensor. This permitted the laser sensor to be positioned within its measuring range relative to the surface to be measured.

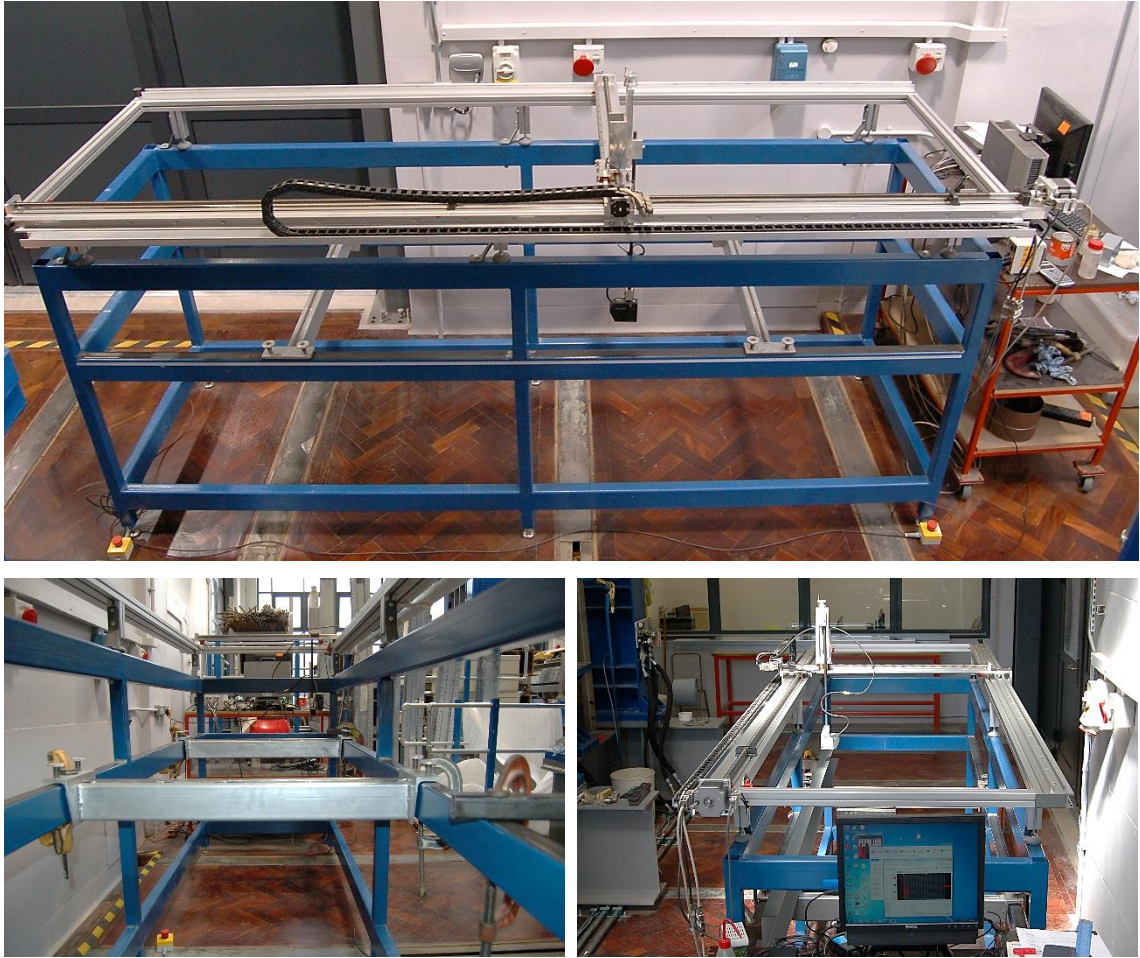


Figure 5.17: Imperfection measuring rig

5.6.2 Measuring process

The specimens were placed on the adjustable beams within the measuring rig. In order to minimise the deflections of the specimen due to its self-weight, the beams were positioned at a distance of $5/9L$ from each other, where L is the specimen length.

The imperfections were measured by moving the laser displacement sensor along different longitudinal lines on each plate element comprising the cross-section (web, flange, etc.). A more detailed description of the exact locations where the readings were taken for the individual channels as well as for the built-up specimens is included in section 5.6.2.1 and section 5.6.2.2, respectively. The laser sensor was moved at a constant speed of 20 mm/s, while readings were taken at a sampling rate of 20 Hz, resulting in one reading every millimetre. Readings were

continued slightly before and after the laser beam made contact with the surface to be measured and these ‘out of range’ readings permitted to identify the end points of the plate element and therefore the location of each reading along the specimen length. After the imperfections of all specimens were recorded, the out-of-straightness of the guiding bars along which the laser sensor was moved was accounted for by measuring a nominally flat surface and deducting these readings from the imperfections recorded for each specimen. Details on how the flat surface was generated and the obtained accuracy of the measurements is included in section 5.6.4.

Vibrations generated by the motors used to move the laser sensor were removed from the imperfection readings by post-processing the data using a Fourier filter to remove the high frequency components. In addition, the recorded imperfections of each plate element were adjusted so that the imperfection amplitudes at the four corners of the plate element were zero. This was achieved by calculating the imperfections relative to an imaginary plane which intersected the measured plate element at three of the corners, and then forcing the imperfection at the fourth corner to be zero by applying a linearly varying twist to the reference plane. Although this adjustment eliminated the global twist imperfection in each plate element, this particular imperfection was not deemed to have a significant effect on the buckling behaviour of the columns. However, this adjustment also implied that after combining the imperfections measured on each plate element, all plate elements in the cross-section were perfectly orthogonal to each other at each specimen end, making it easier to incorporate the geometric imperfections into the FE models.

The imperfection data were further used to determine the magnitudes of the cross-sectional out-of-plane imperfections, as well as the global imperfections, separately.

5.6.2.1 Individual components

The imperfections of the individual components were measured before they were assembled into their final configuration. For each channel, the imperfections were recorded along four equally spaced lines on the web and the flanges, while for the lipped channels the imperfections were additionally recorded along two lines on the lips, as illustrated in Figure 5.18. The figure also shows the sign convention used for the imperfection measurements. The process of measuring the imperfections of the individual channels is illustrated in Figure 5.19.

The imperfections recorded on each plate element of the channels were used to determine representative cross-sectional out-of-plane imperfections and representative global imperfections of the channels.

For both the plain and the lipped channels cross-sectional imperfections of interest include the out-of-plane imperfection along the web (δ_{web}) and the out-of-plane imperfection along the flange edge ($\delta_{flanges}$) (the ‘flange edge’ either indicates the free edge in the case of a plain

channel, or the flange-lip junction in the case of a lipped channel). Additionally, for lipped channels relevant cross-sectional imperfections also include the out-of-plane imperfection along the centre line of the flanges ($\delta_{flanges,L}$) and the out-of-plane imperfection along the free edge of the lips (δ_{lips}).

δ_{web} was calculated as the imperfection along the centre line of the web relative to the straight line connecting the corner lines of the web in each cross-section. Since no readings were taken along the centre line of the web, these imperfection values were determined using polynomial interpolation between the imperfections recorded along the four equally spaced lines in the web. δ_{web} was calculated according to Eq. (5.1):

$$\delta_{web}(x) = (-Line_1/16 + 9 \cdot Line_2/16 + 9 \cdot Line_3/16 - Line_4/16) - (Line_1 + Line_4)/2 \quad (5.1)$$

For the plain channels, $\delta_{flanges}$ is indicative of the imperfections relevant to local buckling, while for the lipped channels $\delta_{flanges}$ is connected to distortional buckling. For each flange $\delta_{flanges}$ was calculated as the difference between the flange edge readings and the readings along the flange-web junction:

$$\delta_{flange}(x) = Line_8 - Line_5 \quad (5.2)$$

$$\delta_{flange}(x) = Line_12 - Line_9 \quad (5.3)$$

For the lipped channels, $\delta_{flanges,L}$ is relevant to local buckling. However, these imperfections are expected to be significantly smaller than $\delta_{flanges}$, and for a typical lipped channel, their effect on the local buckling mode is expected to be of less significance than δ_{web} due to the relatively low plate slenderness of the flanges compared to the web. Even so, these imperfections were calculated for each flange of the lipped channels as follows:

$$\delta_{flange,L}(x) = (-Line_5/16 + 9 \cdot Line_6/16 + 9 \cdot Line_7/16 - Line_8/16) - (Line_5 + Line_8)/2 \quad (5.4)$$

$$\delta_{flange,L}(x) = (-Line_9/16 + 9 \cdot Line_10/16 + 9 \cdot Line_11/16 - Line_12/16) - (Line_9 + Line_12)/2 \quad (5.5)$$

In addition, for the lipped channels, δ_{lips} is relevant to local buckling, and for each lip in the channel δ_{lips} was calculated as the imperfection reading along the lip edge relative to the reading along the lip-flange junction:

$$\delta_{lip}(x) = Line_14 - Line_13 \quad (5.6)$$

$$\delta_{lip}(x) = Line_15 - Line_16 \quad (5.7)$$

The global imperfections calculated for the lipped and plain channels consisted of a minor axis flexural imperfection $\delta_{global,m}$ and a major axis flexural imperfection $\delta_{global,M}$.

$\delta_{global,m}$, was determined using Eq. (5.8) and Eq. (5.9) for the plain and the lipped channels, respectively, considering imperfections positive towards the centroid of the channel:

$$\delta_{global,m} = (Line_1 + Line_4) / 2 \quad (5.8)$$

$$\delta_{global,m} = (Line_13 + Line_16) / 4 + (Line_1 + Line_4) / 4 \quad (5.9)$$

For both types of channels $\delta_{global,M}$ was calculated using Eq. (5.10) :

$$\delta_{global,M} = (Line_9 - Line_5) / 2 \quad (5.10)$$

The geometric imperfections of the plate sections in built-up column 1 were not recorded prior to the assemblage since they were not able to sustain their self-weight without exhibiting deformations far greater than the out-of-plane deviations which could be attributed to geometric imperfections.

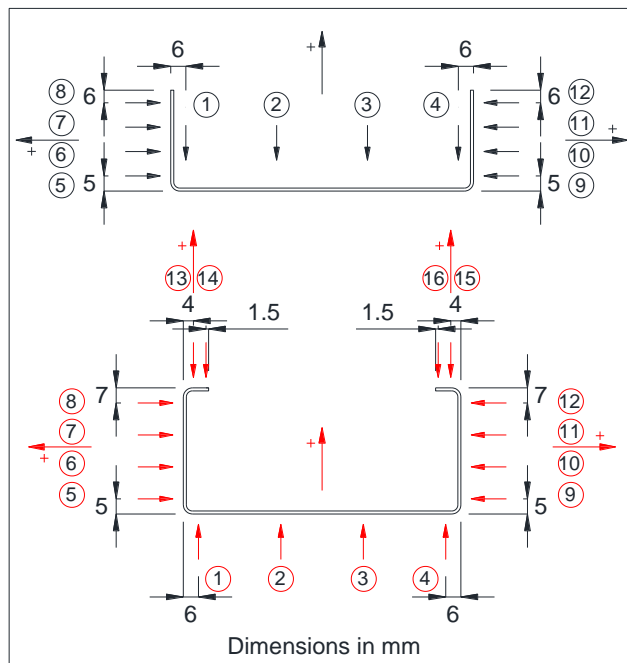


Figure 5.18: Imperfections measured in plain and lipped channels

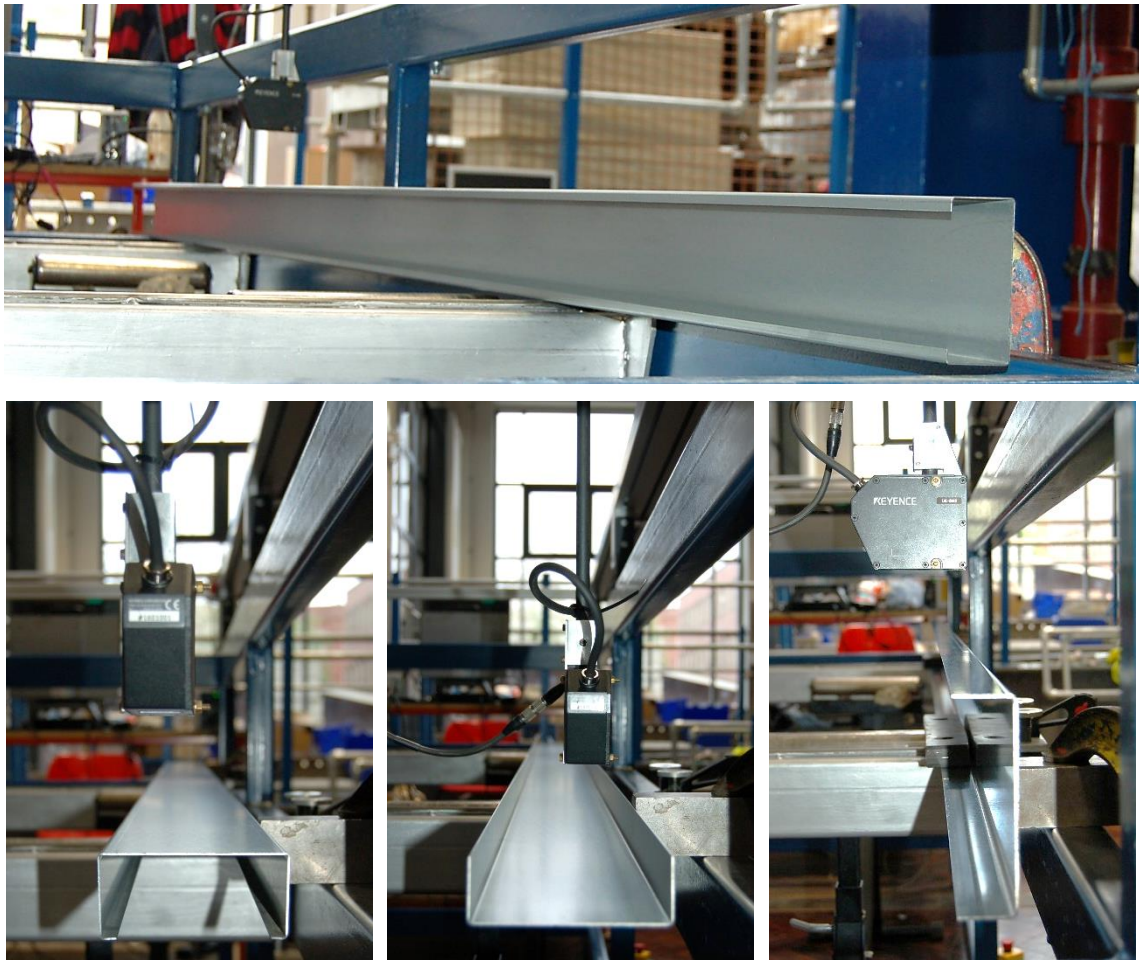


Figure 5.19: Impertion measurements on the individual channels

5.6.2.2 Built-up specimens

The geometric imperfections of the components were measured again after the different built-up geometries were assembled. The imperfections of each component were measured along the same lines as before the assemblage wherever the geometry permitted it.

In the specimens with built-up geometry 1, the geometric imperfections of the plates and the web of the channels were recorded along four equally spaced lines, as shown in Figure 5.20. The process of measuring the imperfections of the columns with geometry 1 is illustrated in Figure 5.21.

The magnitude of the imperfections recorded in the plate sections was not expected to provide an accurate representation of the initial state of the plate sections during the tests, since the low flexural rigidity of the plates resulted in these imperfections being significantly reduced due to the self-weight of the plates. The imperfections were nonetheless recorded in order to have an approximate imperfection profile which could be used in an FE model. Moreover, the out-of-plane imperfections of the plates were not expected to have a significant effect on the overall behaviour of the built-up specimens.

The geometric imperfections of the channels were only recorded along the web. The imperfections of the flanges were not recorded because after assembling the built-up geometry there was not enough space within the channels to place the laser sensor at an appropriate distance from the flanges. Therefore, for the channels used in built-up geometry 1 (T13014), only the out-of-plane imperfections δ_{web} were calculated using Eq. (5.11) and Eq. (5.12).

$$\delta_{web}(x) = (-Line_9/16 + 9 \cdot Line_10/16 + 9 \cdot Line_11/16 - Line_12/16) - (Line_9 + Line_12)/2 \quad (5.11)$$

$$\delta_{web}(x) = (-Line_13/16 + 9 \cdot Line_14/16 + 9 \cdot Line_15/16 - Line_16/16) - (Line_13 + Line_16)/2 \quad (5.12)$$

This information was considered sufficient to quantify the imperfections of the channels related to local buckling, since local buckling is expected to be primarily affected by the imperfections in the most slender part of the cross-section. The imperfections recorded along the web of the channels of built-up geometry 1 were also used to calculate $\delta_{global,m}$ after they were assembled into built-up geometry 1, using Eq. (5.13) and Eq. (5.14).

$$\delta_{global,m} = (Line_9 + Line_12)/2 \quad (5.13)$$

$$\delta_{global,m} = (Line_13 + Line_16)/2 \quad (5.14)$$

However, for these channels $\delta_{global,M}$ could not be calculated after the channels were assembled because the imperfections of the flanges could no longer be measured.

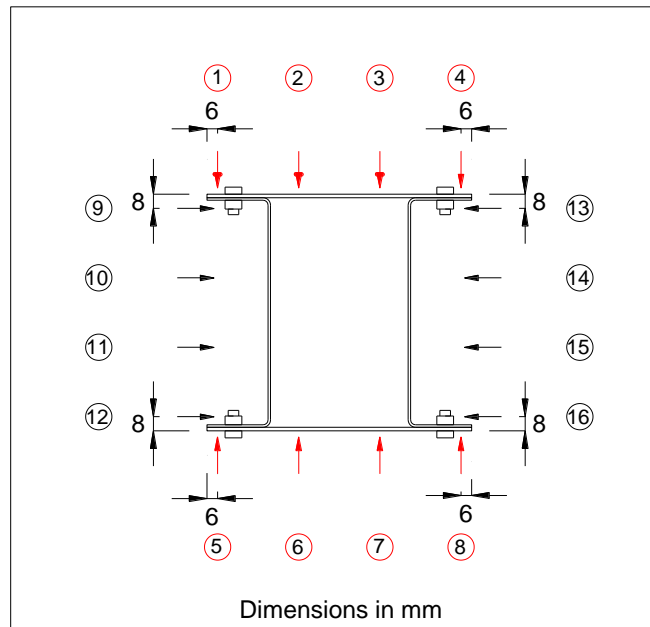


Figure 5.20: Location of the imperfection measurements in built-up column 1



Figure 5.21: Measurement of the imperfections of built-up column 1

In the specimens with geometry 2, the geometric imperfections were measured along four equally spaced lines on the web of the inner channels (T7914), as well as on the web and the flanges of the outer channels (T15414), as depicted in Figure 5.22. The process of measuring the imperfections of the columns with geometry 2 is illustrated in Figure 5.23.

The readings taken on the outer channels were used to calculate their cross-sectional out-of-plane imperfections δ_{web} and $\delta_{flanges}$, using Eq. (5.15)-(5.19), which are relevant to the local buckling mode.

$$\delta_{web}(x) = (-Line_1/16 + 9 \cdot Line_2/16 + 9 \cdot Line_3/16 - Line_4/16) - (Line_1 + Line_4)/2 \quad (5.15)$$

$$\delta_{web}(x) = (-Line_5/16 + 9 \cdot Line_6/16 + 9 \cdot Line_7/16 - Line_8/16) - (Line_5 + Line_8)/2 \quad (5.16)$$

$$\delta_{flange}(x) = Line_9 - Line_12 \quad (5.17)$$

$$\delta_{flange}(x) = Line_13 - Line_16 \quad (5.19)$$

$$\delta_{flange}(x) = Line_20 - Line_17 \quad (5.18)$$

$$\delta_{flange}(x) = Line_24 - Line_21 \quad (5.19)$$

The global buckling imperfections $\delta_{global,m}$ and $\delta_{global,M}$ were also calculated for these channels using Eq (5.20)-(5.23).

$$\delta_{global,m} = (Line_1 + Line_4) / 2 \quad (5.20)$$

$$\delta_{global,m} = (Line_5 + Line_8) / 2 \quad (5.21)$$

$$\delta_{global,M} = (Line_16 - Line_12) / 2 \quad (5.22)$$

$$\delta_{global,M} = (Line_17 + Line_21) / 2 \quad (5.23)$$

For the inner channels, readings of the flange imperfections were not taken because of access restrictions for the laser sensor. However, the imperfections recorded along the web were used to calculate δ_{web} and $\delta_{global,m}$ using Eq. (5.24)-(5.27).

$$\delta_{web}(x) = (-Line_25/16 + 9 \cdot Line_26/16 + 9 \cdot Line_27/16 - Line_28/16) - (Line_25 + Line_28)/2 \quad (5.24)$$

$$\delta_{web}(x) = (-Line_29/16 + 9 \cdot Line_30/16 + 9 \cdot Line_31/16 - Line_32/16) - (Line_29 + Line_32)/2 \quad (5.25)$$

$$\delta_{global,m} = (Line_25 + Line_28)/2 \quad (5.26)$$

$$\delta_{global,m} = (Line_29 + Line_32)/2 \quad (5.27)$$

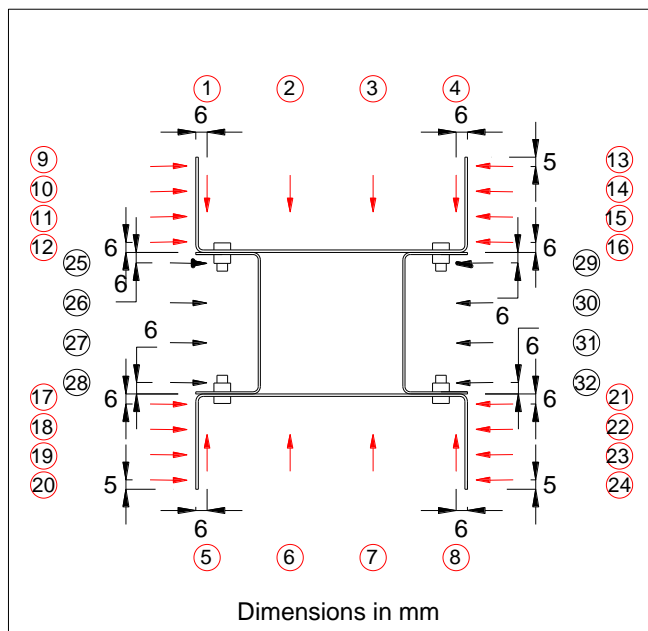


Figure 5.22: Location of the imperfection measurements in built-up column 2

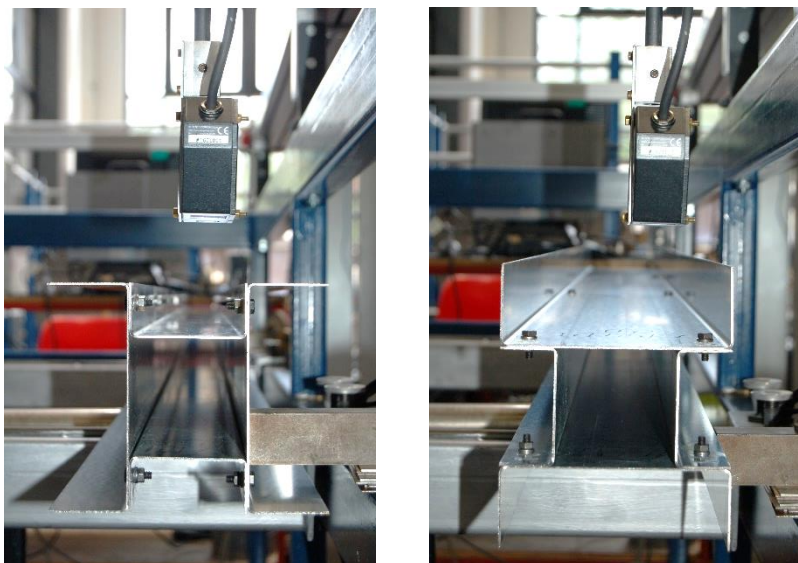


Figure 5.23: Measurement of the imperfections of built-up column 2

After the specimens with geometry 3 were assembled, only the geometric imperfections of the plain channels (T12012) could be measured. The imperfections of these channels were recorded along four equally spaced lines on the web and the flanges, as shown in Figure 5.24. These readings were used to calculate δ_{web} , $\delta_{flanges}$, $\delta_{global,m}$ and $\delta_{global,M}$, using Eq. (5.28)-(5.37). Figure 5.25 illustrates the imperfection measurement process for columns with geometry 3.

$$\delta_{web}(x) = (Line_1/16 - 9 \cdot Line_2/16 - 9 \cdot Line_3/16 + Line_4/16) + (Line_1 + Line_4) / 2 \quad (5.28)$$

$$\delta_{web}(x) = (Line_5/16 - 9 \cdot Line_6/16 - 9 \cdot Line_7/16 + Line_8/16) + (Line_5 + Line_8) / 2 \quad (5.29)$$

$$\delta_{flange}(x) = Line_12 - Line_9 \quad (5.30)$$

$$\delta_{flange}(x) = Line_16 - Line_13 \quad (5.31)$$

$$\delta_{flange}(x) = Line_17 - Line_20 \quad (5.32)$$

$$\delta_{flange}(x) = Line_21 - Line_24 \quad (5.33)$$

$$\delta_{global,m} = -(Line_1 + Line_4) / 2 \quad (5.34)$$

$$\delta_{global,m} = -(Line_5 + Line_8) / 2 \quad (5.35)$$

$$\delta_{global,M} = (Line_9 - Line_13) / 2 \quad (5.36)$$

$$\delta_{global,M} = (Line_24 + Line_20) / 2 \quad (5.37)$$

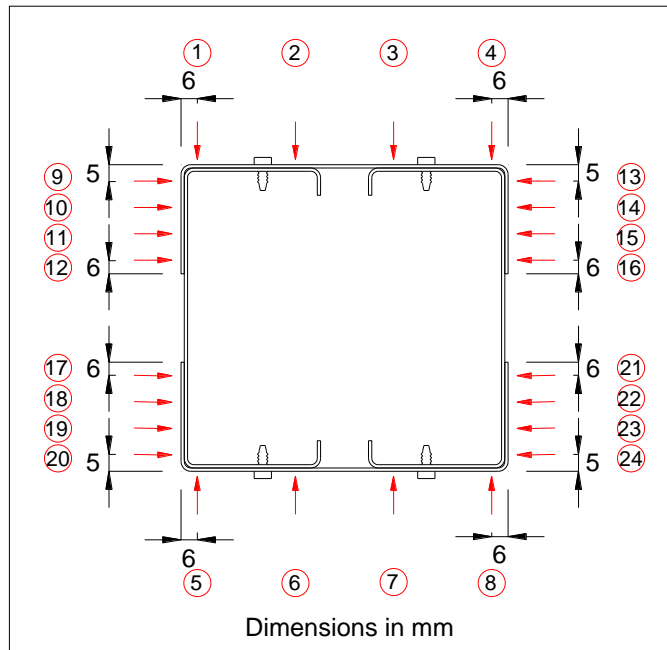


Figure 5.24: Location of the imperfection measurements in built-up column 3

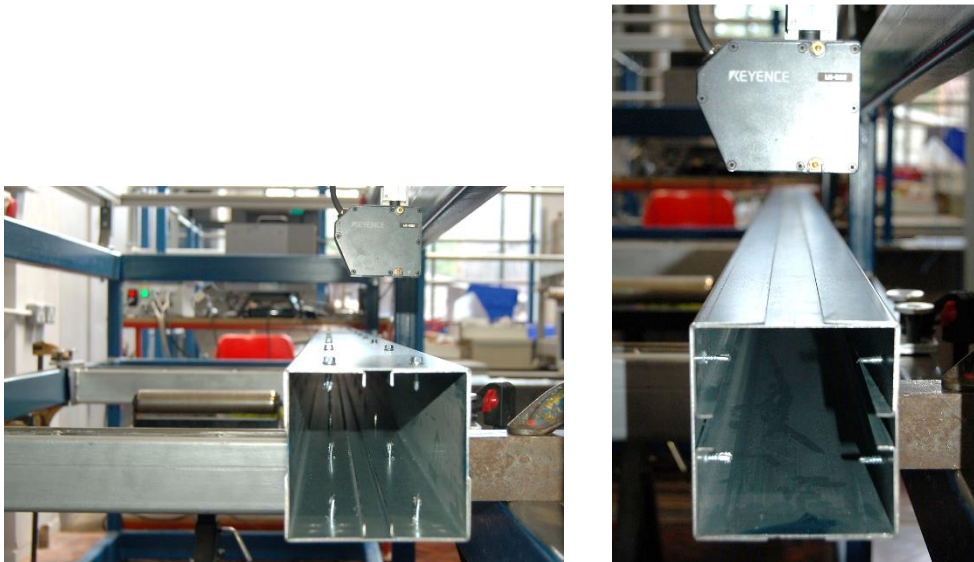


Figure 5.25: Measurement of the imperfections of built-up column 3

In the specimens with geometry 4, the imperfections could only be recorded in the lipped channels (S11012) due to the impossibility of accessing the plain channels with the laser sensor after the specimens were assembled. The imperfections were recorded along four equally spaced lines on the web and the flanges of the lipped channels, as shown in Figure 5.26. These imperfections readings were used to determine δ_{web} , $\delta_{flanges}$, $\delta_{global,m}$ and $\delta_{global,L}$, using Eq. (5.28)-(5.37). In addition, Eq. (5.38)-(5.41) were used to calculate $\delta_{flanges,L}$.

$$\delta_{flange,L}(x) = (-Line_9/16 + 9 \cdot Line_10/16 + 9 \cdot Line_11/16 - Line_12/16) - (Line_9 + Line_12)/2 \quad (5.38)$$

$$\delta_{flange,L}(x) = (-Line_13/16 + 9 \cdot Line_14/16 + 9 \cdot Line_15/16 - Line_16/16) - (Line_13 + Line_16)/2 \quad (5.39)$$

$$\delta_{flange,L}(x) = (-Line_{17}/16 + 9 \cdot Line_{18}/16 + 9 \cdot Line_{19}/16 - Line_{20}/16) - (Line_{17} + Line_{20})/2 \quad (5.40)$$

$$\delta_{flange,L}(x) = (-Line_{21}/16 + 9 \cdot Line_{22}/16 + 9 \cdot Line_{23}/16 - Line_{24}/16) - (Line_{21} + Line_{24})/2 \quad (5.41)$$

Figure 5.27 illustrates the process of measuring the imperfections of the columns with geometry 4.

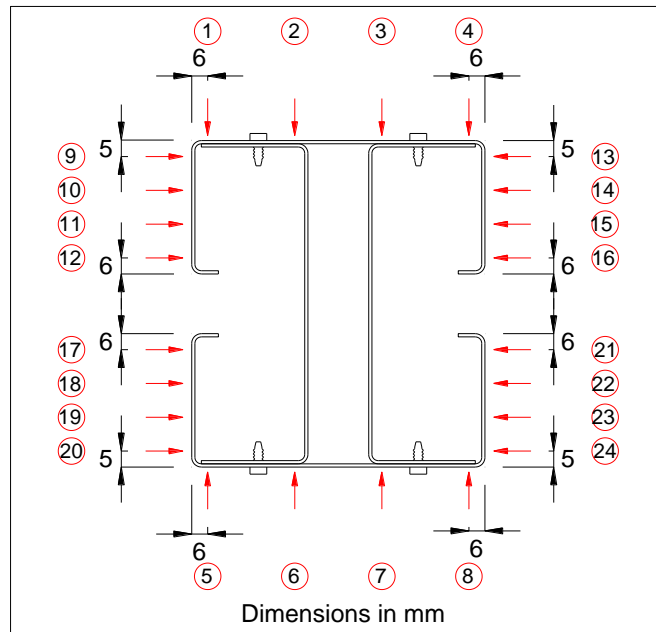


Figure 5.26: Location of the imperfection measurements in built-up column 4



Figure 5.27: Measurement of the imperfections of built-up column 4

5.6.3 Imperfection measurement results

The imperfections recorded on the individual channels and the built-up specimens were classified into out-of-plane imperfections and global imperfections. The following sections

discuss the main observations extracted from the experimental results, while the detailed imperfection data of the channels, measured before and after they were assembled, are included in Appendix H and I, respectively. In addition, Appendix J present a comparison between the cross-sectional imperfections of the channels before and after they were assembled.

5.6.3.1 Cross-sectional imperfections

Before assembling the channels

Before the individual channels were assembled, each type of channel revealed a similar out-of-plane imperfection profile along their web, flanges and lips, respectively. This consistency in the imperfection shape can be attributed to the fact that each type of channel section was presumably fabricated from the same steel coil and followed the same type of cold-forming process and handling.

The out-of-plane imperfections recorded along the web (δ_{web}) were very small in all channels, with typical maximum amplitudes of 0.14 mm for the S11012 channels, 0.13 mm for the T12012 channels, 0.16 mm for the T13014 channels, 0.31 mm for the T15414 channels and 0.06 mm for the T7914 channels. In the lipped channels (S11012), the out-of-plane imperfection profile along the web consisted mainly of one undulating component A_{und} with a half-wave length of around 600 mm and a constant component A_{cons} of similar magnitude, while in the plain channels the web out-of-plane imperfection consisted of several undulating components of varying wavelength, in addition to the constant imperfection component A_{cons} , as presented in Figure 5.28 and Figure 5.29 for channel S11012-7 and T13014-2, respectively. A_{cons} was calculated as the average out-of-plane imperfection in the measured plate element, while A_{und} was taken as the difference between the extremities of the imperfection profile. When computing A_{cons} and A_{und} the localised out-of-plane deformations at the support locations (which resulted from direct bearing of the channels onto the support beams) were first removed from the imperfection profile. A further discussion of these bearing deformations is included in section 5.6.4.

The ratio between the constant imperfection component (A_{cons}) and the undulating imperfection component (A_{und}) varied significantly among channels of identical nominal cross-sectional dimensions, as well as among different types of channels. This ratio was particularly large (more than 2 on average) in channels T15414 with a length of 2500 mm. This reveals a great deal of conservatism in the common practice to use the maximum out-of-plane imperfection measurement to characterise the imperfections related to local or distortional buckling, given that the constant imperfection component does not contribute to the onset of these types of buckling modes. Moreover, using the maximum undulating imperfection component A_{und} is also expected to result in a conservative characterisation of the out-of-plane imperfections since the profile of the undulating component will not necessarily resemble the longitudinal shape of the

cross-sectional critical buckling mode of the channel. However, using the maximum undulating imperfection component is a simple way to characterise the measured out-of-plane imperfections and provides more meaningful information about the measured imperfections than simply reporting the maximum value.

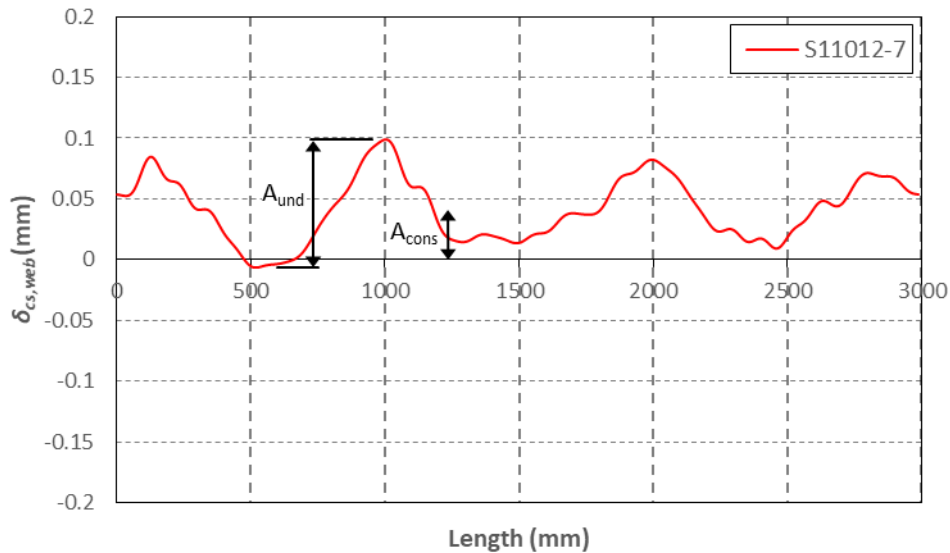


Figure 5.28: Imperfection components and bearing deformations along the web of channel S11012-7

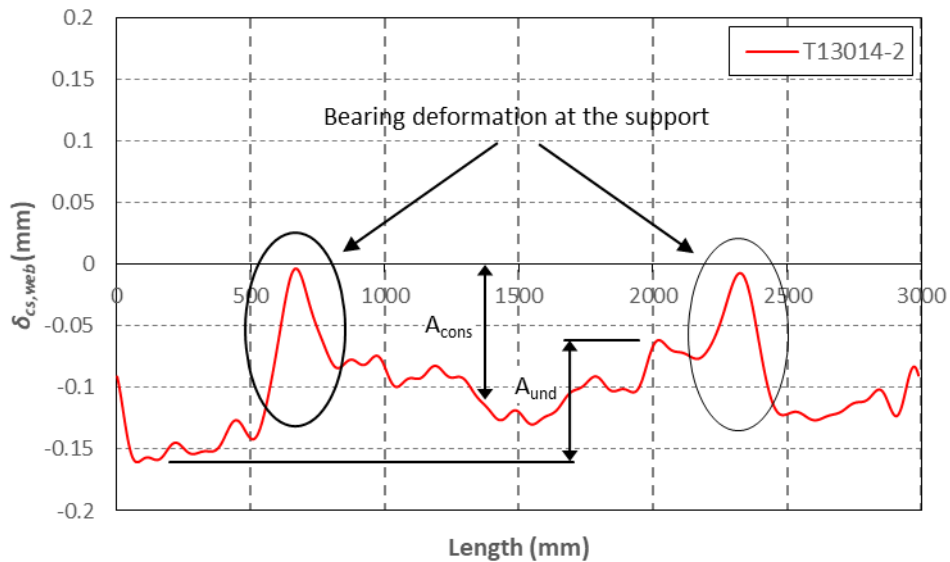


Figure 5.29: Imperfection components and bearing deformations along the web of channel T13014-2

Regarding the imperfections recorded along the edge of the channel flanges (δ_{flange}), it was observed that these out-of-plane imperfections were mainly dominated by one undulating component A_{und} , as illustrated in Figure 5.30 for a sample channel S11012-2. It is important to note that, since the imperfections δ_{flange} were measured with respect to only one reference line

(the web-flange junction), and since the angles between the flanges and the web of the channels were not measured in this study, it was not possible to determine the constant imperfection component of the flange imperfection δ_{flange} . However, as mentioned before, this constant component is not expected to have a significant effect on the buckling behaviour.

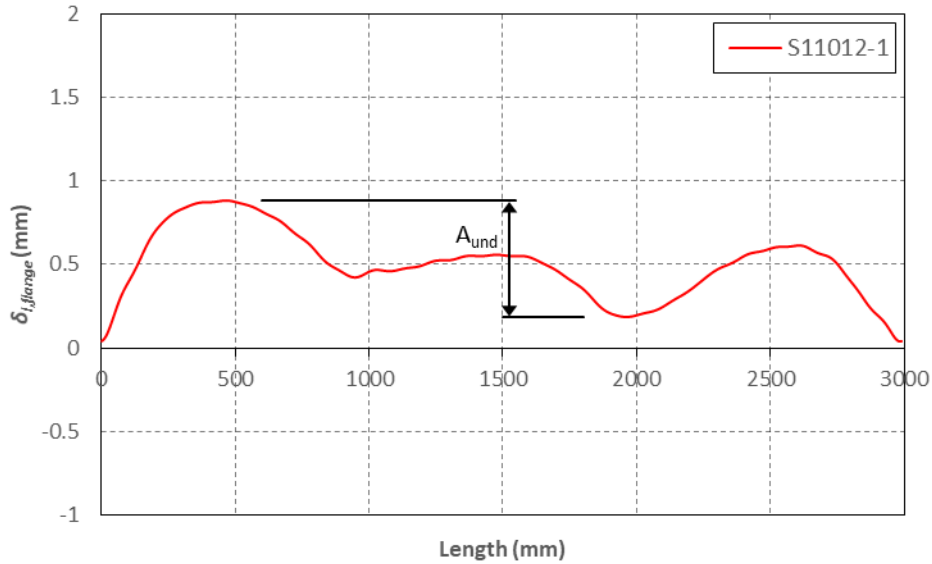


Figure 5.30: Undulating imperfection component along the left flange of channel S11012-2

All the measured channels displayed a similar imperfection profile along their flanges, with a half-wave length of the undulating component A_{und} ranging from 600 mm to 800 mm. Figure 5.31 shows the out-of-plane imperfections δ_{flange} recorded along the left flange of one channel of each type and length.

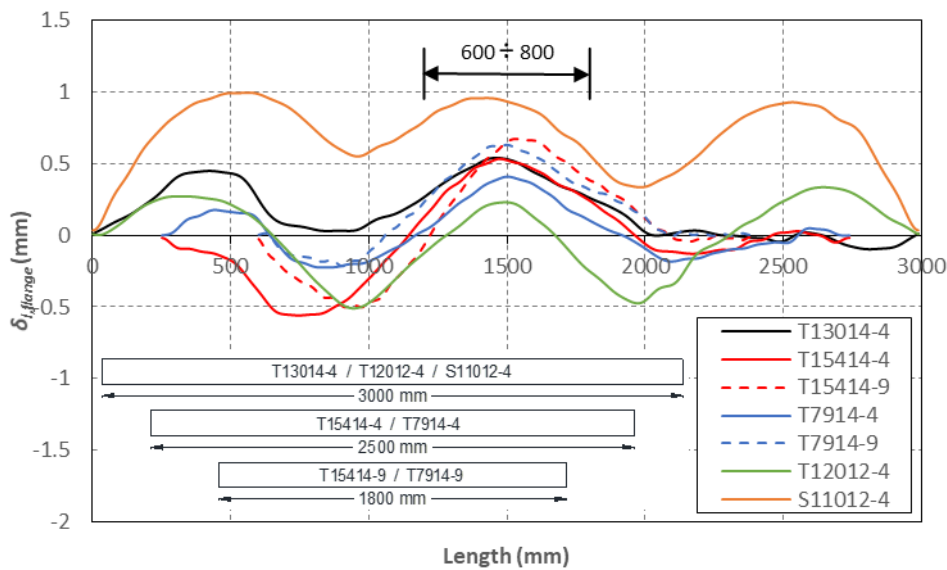


Figure 5.31: Imperfection profile recorded along the left flange of specimens of each type of channel

The out-of-plane imperfections recorded along the flange tips of channels T12012 had an almost symmetric profile, while in channels T13014, T15414, T7914 and S11012 this symmetry was not as evident. However, in the less symmetric imperfection profiles, it was noticed that the imperfection shape on one flange was nearly the mirror image (with respect to mid-length) of the shape on the other flange, as illustrated in Figure 5.32. The figure also shows, a symmetric imperfection profile obtained for the flanges of a representative channel belonging to series T13014. These observations clearly suggest that the $\delta_{i,flange}$ imperfection profile is largely a result of the ‘imprint’ left by the brake-press and the need to turn the specimen over 180° about mid-length in order to press the second flange. This is in agreement with observations by Schafer (1997), who suggested that these imperfections are largely determined by the manufacturing process and not by the slenderness of the element.

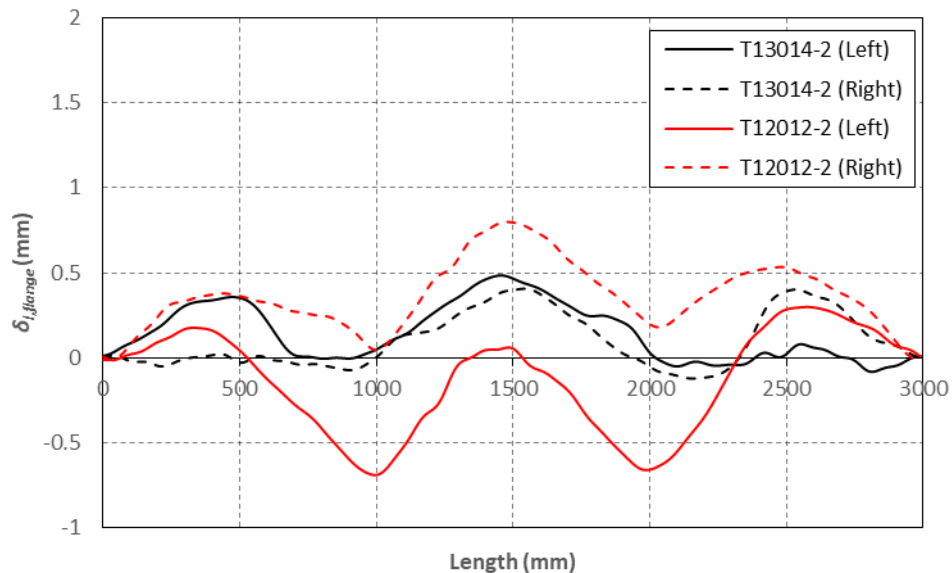


Figure 5.32: Imperfection profile along the flanges of channels T13014-2 and T12012-2

In the lipped channels (S11012), the out-of-plane imperfections recorded along the web, the flange edges and the free edges of the lips approximately followed the same profile, as shown in Figure 5.33 for channel S11012-3. It is noted that, in this figure, the imperfection profile along the web of the channel is inverted with respect to the ones along the flanges and lips due to the sign convention used when recording the imperfections. The imperfections in the web were considered to be positive towards the interior of the channel, while the opposite convention was adopted for the imperfections in the flanges and the lips.

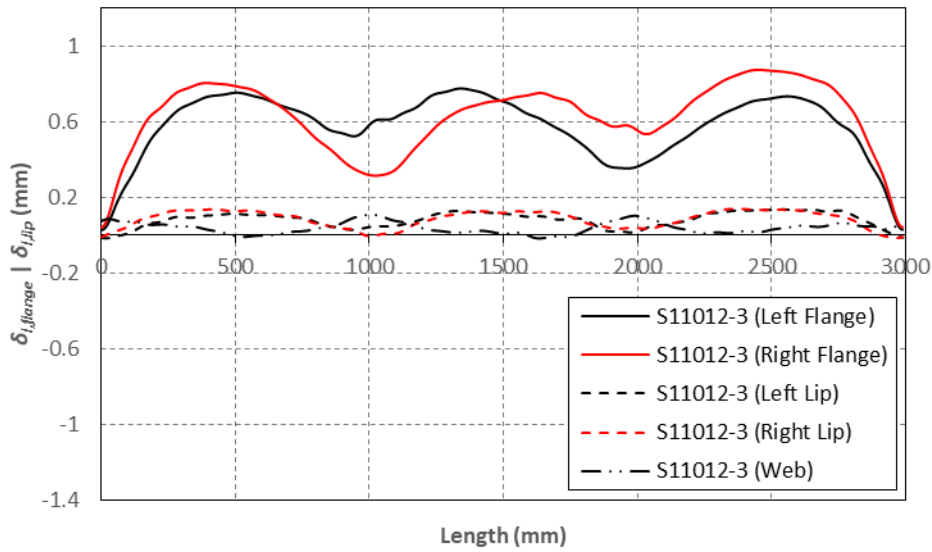


Figure 5.33: Imperfection profile along the web, flanges and lips of channel S11012-3

The out-of-plane imperfections recorded along the centre line of the flanges of channels S11012 relative to the line connecting the edges ($\delta_{flange.L}$) were significantly smaller than the rest of the imperfections recorded in the lipped channels, with a maximum amplitude of the undulating and the constant components of less than 0.1 mm and 0.03 mm, respectively.

Table 5.14 lists the 25%, 50%, 75%, 95% and 99% percentiles of the amplitudes of the constant and undulating imperfection components, as well as the maximum imperfection, obtained for δ_{web} , $\delta_{flanges}$, $\delta_{flanges.L}$ and δ_{lips} based on the measurements before the components were assembled. The table also includes the mean and the standard deviation of the reported imperfections. Since the exact angles between the web and the flanges of the channels were not measured, a representative maximum value of $\delta_{flanges}$ was computed as the maximum $\delta_{flanges}$ imperfection measured relative to the average $\delta_{flanges}$ imperfection.

The table shows that the maximum δ_{web} imperfections recorded in the web of the channels are, on average, 47 % larger than the undulating imperfection components. However, they can be up to 183 % larger than the undulating component, as shown for the T15414 channels with a length of 2500 mm.

Table 5.14: Statistical values of the out-of-plane imperfection of the channels before the assemblage

Section	Length (mm)	Imp.	Imp. Comp.	P($\Delta < \delta$)					Mean	St. dev.
				0.25	0.50	0.75	0.95	0.99		
T13014	3000	δ_{web}	A_{und}	0.07	0.08	0.08	0.10	0.10	0.08	0.012
			A_{cons}	0.02	0.10	0.16	0.17	0.17	0.10	0.062
			Max.	0.09	0.15	0.20	0.22	0.23	0.16	0.058
		$\delta_{flanges}$	A_{und}	0.55	0.57	0.58	0.62	0.64	0.57	0.029
			Max.	0.34	0.35	0.37	0.39	0.34	0.35	0.025
T15414	2500	δ_{web}	A_{und}	0.11	0.11	0.12	0.14	0.14	0.12	0.015
			A_{cons}	0.25	0.26	0.31	0.34	0.34	0.28	0.041
			Max.	0.30	0.34	0.38	0.40	0.40	0.34	0.045
		$\delta_{flanges}$	A_{und}	0.87	0.95	1.02	1.09	1.11	0.95	0.100
			Max.	0.46	0.50	0.53	0.57	0.59	0.48	0.129
	1800	δ_{web}	A_{und}	0.15	0.15	0.16	0.19	0.19	0.16	0.018
			A_{cons}	0.01	0.05	0.16	0.23	0.23	0.11	0.099
			Max.	0.13	0.15	0.27	0.32	0.32	0.21	0.090
		$\delta_{flanges}$	A_{und}	1.06	1.17	1.33	1.44	1.44	1.21	0.162
			Max.	0.57	0.61	0.69	0.75	0.75	0.63	0.083
T7914	2500	δ_{web}	A_{und}	0.04	0.05	0.05	0.06	0.06	0.05	0.006
			A_{cons}	0.01	0.02	0.04	0.05	0.05	0.02	0.017
			Max.	0.05	0.05	0.06	0.09	0.09	0.06	0.014
		$\delta_{flanges}$	A_{und}	0.63	0.65	0.69	0.72	0.77	0.66	0.041
			Max.	0.37	0.39	0.39	0.43	0.45	0.39	0.021
	1800	δ_{web}	A_{und}	0.04	0.05	0.05	0.05	0.05	0.05	0.005
			A_{cons}	0.01	0.02	0.02	0.03	0.03	0.02	0.009
			Max.	0.05	0.05	0.05	0.06	0.06	0.05	0.005
		$\delta_{flanges}$	A_{und}	0.84	0.87	0.88	0.92	0.92	0.87	0.038
			Max.	0.42	0.45	0.47	0.50	0.50	0.41	0.161
T12012	3000	δ_{web}	A_{und}	0.10	0.11	0.13	0.18	0.23	0.12	0.031
			A_{cons}	0.01	0.03	0.06	0.12	0.12	0.04	0.040
			Max.	0.07	0.09	0.16	0.28	0.35	0.13	0.074
		$\delta_{flanges}$	A_{und}	0.84	0.89	0.93	1.03	1.26	0.90	0.125
			Max.	0.46	0.50	0.55	0.63	0.72	0.52	0.109
S11012	3000	δ_{web}	A_{und}	0.12	0.14	0.18	0.21	0.41	0.16	0.062
			A_{cons}	0.01	0.04	0.05	0.08	0.09	0.04	0.024
			Max.	0.11	0.13	0.15	0.18	0.41	0.14	0.063
		$\delta_{flanges.L}$	A_{und}	0.03	0.03	0.04	0.07	0.09	0.04	0.016
			A_{cons}	0.00	0.00	0.01	0.02	0.03	0.01	0.006
			Max.	0.03	0.04	0.05	0.10	0.14	0.04	0.025
		$\delta_{flanges}$	A_{und}	0.53	0.60	0.69	1.22	1.34	0.65	0.204
			Max.	0.48	0.57	0.63	0.73	1.11	0.58	0.128
		δ_{lips}	A_{und}	0.14	0.14	0.17	0.21	0.23	0.15	0.027
			Max.	0.11	0.11	0.12	0.14	0.17	0.12	0.015

After assembling the channels

After the individual channels were assembled into their final configuration, similarity of the out-of-plane imperfection magnitude and shape along the web and flanges of each type of channel was still evident in those channels with the same connector distribution along their length.

Channels T13014 and T7914 were used to assemble the specimens with built-up geometry 1 and built-up geometry 2, respectively, by connecting them through their flanges to the adjacent components, as shown in Figure 5.1. In these channels, the magnitude of the undulating

component of the out-of-plane imperfections along the centre line of the web (δ_{web}) had clearly increased after the channels were assembled, with the largest amplitude of the undulations being displayed around mid-length, as illustrated in Figure 5.34 for channels T13014. This can be explained by the fact that, before the channels were assembled, the flanges consistently exhibited an outward imperfection at mid-length with a large undulation, as shown in Figure 5.32 for channel T12012-2. Therefore, as contact between the different components of the built-up specimens was enforced by the connectors, the flanges of channels T13014 and T7914 had to rotate inward to accommodate the adjacent components, with the rotation being more pronounced at mid-length due to the larger outward imperfection of the flanges. Due to the continuity of the cross-section the rotation of the flanges caused an increased out-of-plane imperfection in the web. The particularly marked out-of-plane imperfection at mid-length shown in Figure 5.34 for the channels with three intermediate connectors is attributed to the fact that in these specimens the connectors were sparsely distributed along the column (with a connector spacing of 720 mm) and the cross-section at mid-length coincided with one of the cross-sections containing connectors.

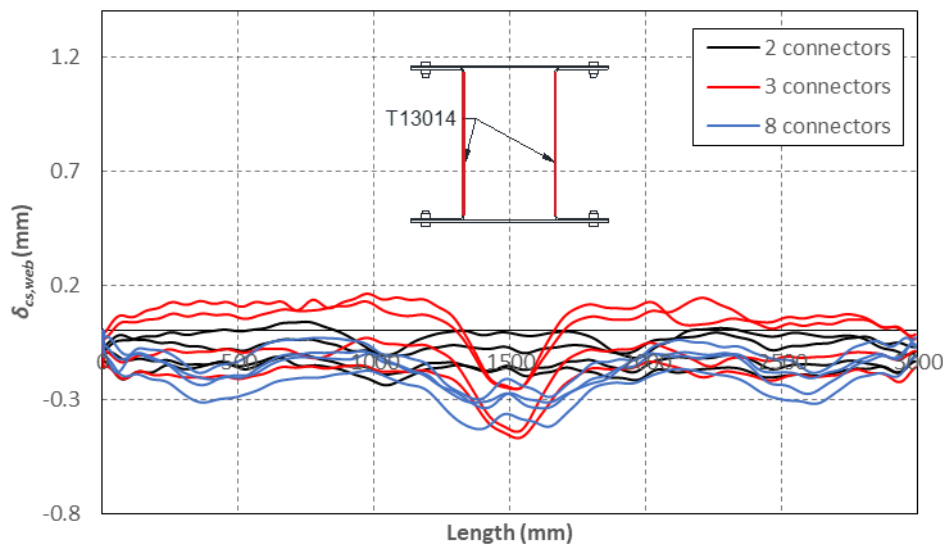


Figure 5.34: Imperfection distribution along the web of channels T13014 after assembly

On the other hand, channels T15414, T12012 and S11012, which were used to assemble geometries 2, 3 and 4, respectively, were connected to their adjacent components through their webs, as shown in Figure 5.1. In these channels the assembly process affected the out-of-plane imperfection profile along the web of the channel (δ_{web}) significantly more than in the channels connected through their flanges. The connectors created localised out-of-plane imperfections along the web, which resulted in an imperfection profile with repetitive ‘bumps’, as shown in Figure 5.35 and Figure 5.36 for channels T15414 and channels S11012, respectively.

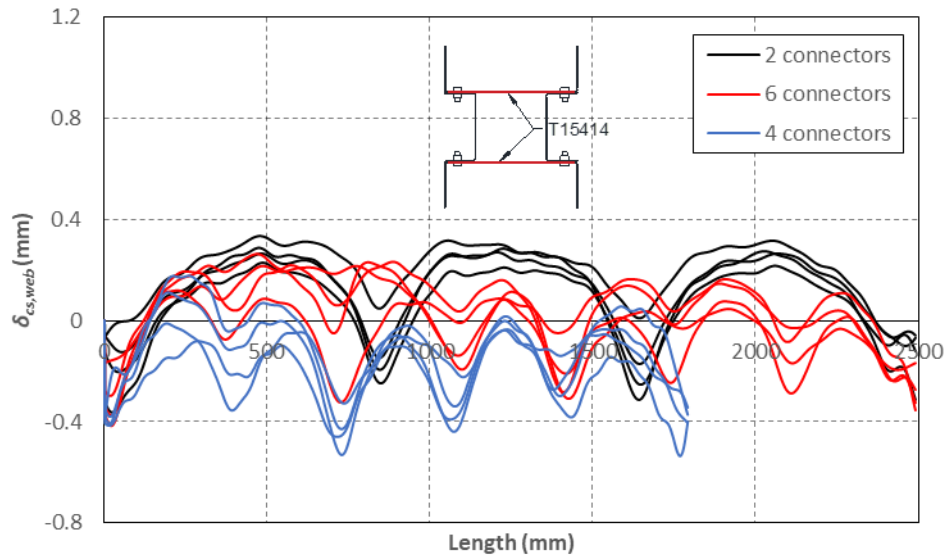


Figure 5.35: Imperfection profile along the web of channels T15414 after assembly

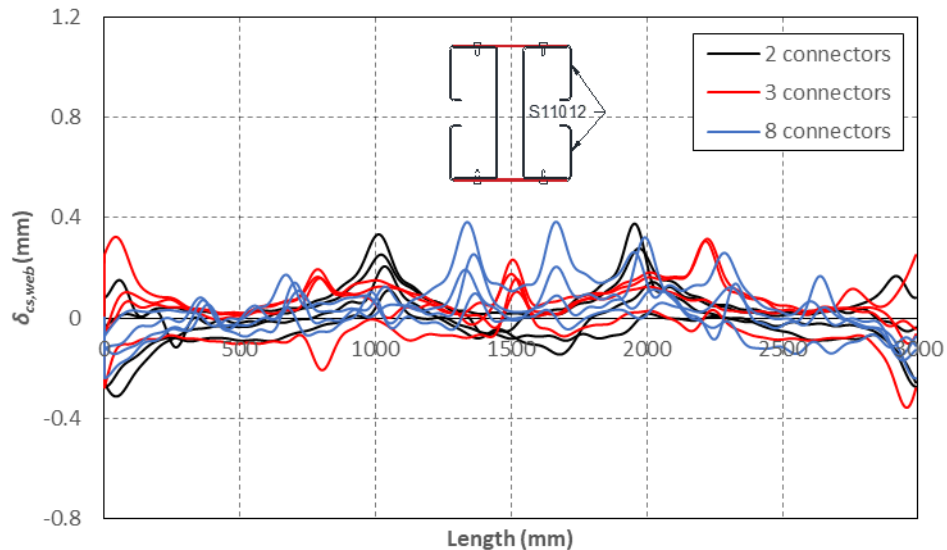


Figure 5.36: Imperfection profile along the web of channels S11012 after assembly

The flanges of channels T15414, T12012 and S11012 were affected by the assembly process to a lesser degree than the webs. In most of these channels the out-of-plane imperfection profile along the flange edges remained almost unaltered after the channel was assembled into its built-up configuration, with only a slight increase or decrease in the magnitude of the undulating component. However, in the case of channels T15414, which were connected to the adjacent components of geometry 2 with connectors spaced at around 340 mm along the channel web (i.e. channels with a length of 2500 mm and 6 intermediate connectors and channels with a length of 1800 mm and 4 intermediate connectors), the presence of the connectors introduced an undulating out-of-plane imperfection component in the flanges with a half-wave length equal to the distance between connectors. This is illustrated in Figure 5.37 for the left flange of channels T15414-1, T15414-5 and T15414-9 before and after they were assembled using 2, 6 and 4 equally spaced intermediate connectors along the length of the channel, respectively.

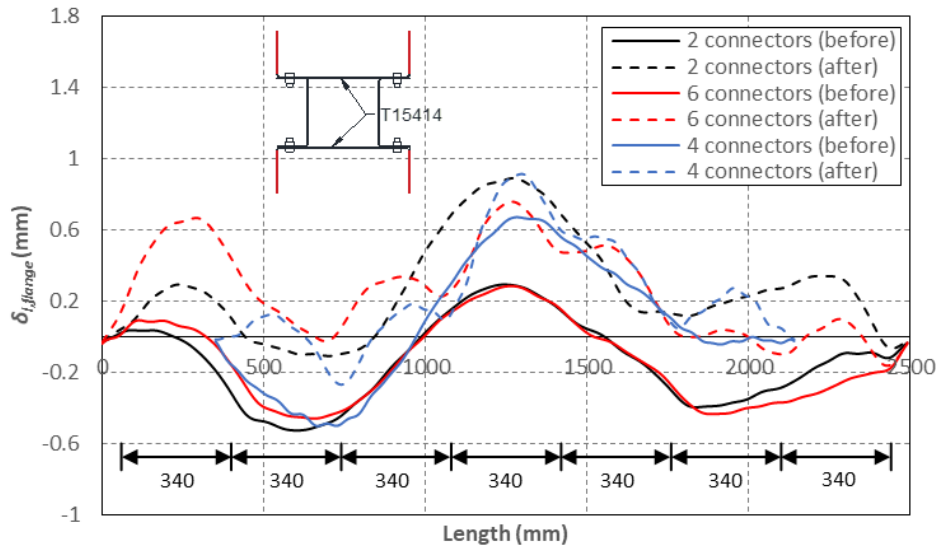


Figure 5.37: Imperfection profile along one of the flanges of channels T15414-1, T15414-5 and T15414-9 after the assemblage

Table 5.15 lists the 25%, 50%, 75%, 95% and 99% percentiles, as well as the mean and the standard deviation of the out-of-plane imperfections of each type of channel after they were assembled into their final configuration, including their maximum values.

Table 5.15: Statistical values of the out-of-plane imperfections of the channels after the assemblage

Section	Length (mm)	Imp.	Imp. Comp.	P($\Delta < \delta$)					Mean	St. dev.
				0.25	0.50	0.75	0.95	0.99		
T13014	3000	δ_{web}	A_{und}	0.12	0.25	0.33	0.41	0.42	0.26	0.119
			A_{cons}	0.06	0.13	0.18	0.21	0.26	0.13	0.073
			Max.	0.20	0.27	0.35	0.45	0.48	0.30	0.117
T15414	2500	δ_{web}	A_{und}	0.44	0.48	0.52	0.60	0.60	0.48	0.080
			A_{cons}	0.05	0.06	0.10	0.20	0.20	0.08	0.059
			Max.	0.28	0.34	0.42	0.50	0.50	0.36	0.083
	$\delta_{flanges}$	A_{und}	1.00	1.12	1.17	1.24	1.26	1.10	0.110	
		Max.	0.62	0.66	0.72	0.78	0.80	0.67	0.075	
		A_{und}	0.41	0.43	0.62	0.64	0.64	0.52	0.124	
1800	δ_{web}	A_{cons}	0.11	0.15	0.17	0.17	0.17	0.15	0.026	
		Max.	0.40	0.47	0.54	0.57	0.57	0.49	0.076	
		A_{und}	1.12	1.18	1.41	1.67	1.67	1.30	0.221	
$\delta_{flanges}$	Max.	0.62	0.65	0.80	0.96	0.96	0.73	0.132		
	2500	δ_{web}	A_{und}	0.13	0.15	0.18	0.25	0.25	0.17	0.047
			A_{cons}	0.00	0.01	0.02	0.04	0.04	0.02	0.014
Max.			0.09	0.11	0.16	0.59	0.59	0.23	0.222	
1800	δ_{web}	A_{und}	0.17	0.19	0.19	0.20	0.20	0.19	0.013	
		A_{cons}	0.01	0.04	0.07	0.07	0.07	0.05	0.029	
		Max.	0.13	0.16	0.19	0.19	0.19	0.17	0.029	
T12012	3000	δ_{web}	A_{und}	0.24	0.29	0.38	0.41	0.61	0.33	0.116
			A_{cons}	0.01	0.02	0.03	0.13	0.14	0.04	0.046
			Max.	0.36	0.44	0.45	0.58	0.61	0.44	0.088
		$\delta_{flanges}$	A_{und}	0.78	0.86	0.98	1.06	1.07	0.87	0.133
Max.	0.44		0.47	0.56	0.64	0.65	0.50	0.087		
S11012	3000	δ_{web}	A_{und}	0.24	0.35	0.39	0.45	0.46	0.34	0.088
			A_{cons}	0.02	0.06	0.07	0.07	0.09	0.05	0.027
			Max.	0.30	0.34	0.35	0.39	0.41	0.33	0.052
		$\delta_{flanges.L}$	A_{und}	0.03	0.04	0.05	0.09	0.12	0.05	0.021
			A_{cons}	0.00	0.01	0.01	0.03	0.07	0.01	0.015
			Max.	0.03	0.04	0.04	0.07	0.15	0.04	0.026
		$\delta_{flanges}$	A_{und}	0.45	0.60	0.69	0.96	1.13	0.61	0.195
			Max.	0.46	0.64	0.84	1.05	1.12	0.67	0.232

Comparison of the out-of-plane imperfections based on Power Spectral Densities

In order to study the effect of the assembly process on the magnitude and shape of the out-of-plane imperfections, the power spectral density (PSD) function was computed for the imperfections recorded along the web and flanges of each channel, before and after they were assembled. The PSD represents the spatial frequency response of the sinusoidal components into which the imperfection signal can be decomposed. For the purpose of this study, the PSD plotted the imperfection magnitude of each sinusoidal component against its half-wave length.

Figures 5.38-5.46 compare the PSD functions of the imperfections recorded along the web and flanges of each type of channel, before and after they were assembled. The channels were grouped according to the number of connectors used to assemble them. The solid lines correspond to the PSD of the imperfections before the channels were assembled and the dashed lines correspond to the PSD of the imperfections after the channels were assembled. The figures also show three vertical lines which represent half of the distance between the connectors.

The PSDs reveal that, in general, before the channels were assembled the out-of-plane imperfection profile along the web of the channels was mainly composed of imperfection components with half-wave lengths larger than 500 mm, as illustrated in Figure 5.38, Figure 5.39, Figure 5.40, Figure 5.41 and Figure 5.46 for channels T13014, T15414, T7914, T12012 and S11012, respectively.

For the flanges of the plain channels, on the other hand, the out-of-plane imperfection profile was mainly composed of one component with a half-wave length which ranged from around 600 mm for channels T12012 to 800 mm for channels T15414, as illustrated in Figure 5.45 and Figure 5.44, respectively. For the lipped channels, two imperfection components of similar magnitude were seen to dominate the out-of-plane imperfection profile along the flanges, with half-wave lengths of around 600 mm and 1000 mm, as shown in Figure 5.46.

After the channels were assembled into their final configuration, the PSDs show the web imperfection components were amplified over a relatively wide range of half-wave lengths. Channels T13014 and T7914 were both connected through their flanges to the adjacent components of the built-up geometry. For channels T13014 the half-wave-lengths of the amplified components ranged from 250 mm to around 1100 mm, with an average maximum amplification at a half-wave length of around 600 mm, while for channels T7914, mainly components with half-wave lengths larger than 500 mm were amplified, as shown in Figure 5.38 and Figure 5.40, respectively. This might be indicative of the fact that the imperfections induced by the connectors do not have an exact sinusoidal shape (but look more like the 'bumps' previously described), so that a range of frequencies (or half-wave lengths) is needed to mathematically describe them.

Similar observations were made for channels T12012, S11012 and T15414, where the connectors were located in the web of the channels. For channels T12012 and S11012 the assembly process mainly affected components with a half-wave length larger than 100 mm, as shown in Figure 5.41 and Figure 5.43, respectively. In the case of channels T12012 the connectors mainly amplified components with a half-wave length close to the connector spacing. In addition, imperfection components of around 500 mm and 1000 mm were also amplified irrespective of the number of connectors used along the channel, with the amplification being more pronounced in the channels with the largest number of connectors. This may be attributed to the fact that the web of these channels was connected to the flanges of the S11012 lipped channels, which before the assembly had undulating imperfection components close to these half-wave lengths, as shown in Figure 5.42. For channels T15414, on the other hand, after the channels were assembled the connectors clearly amplified the imperfection components with a half-wave length equal to half the distance between connectors in all channels, as shown in Figure 5.39.

It is important to note that for the channels studied, the local buckling half-wave lengths ranged from 100 mm to 400 mm, while the distortional half-wave lengths of the lipped channels reached up to 800 mm. This was precisely the range of half-wave lengths which were most affected by the assembly process.

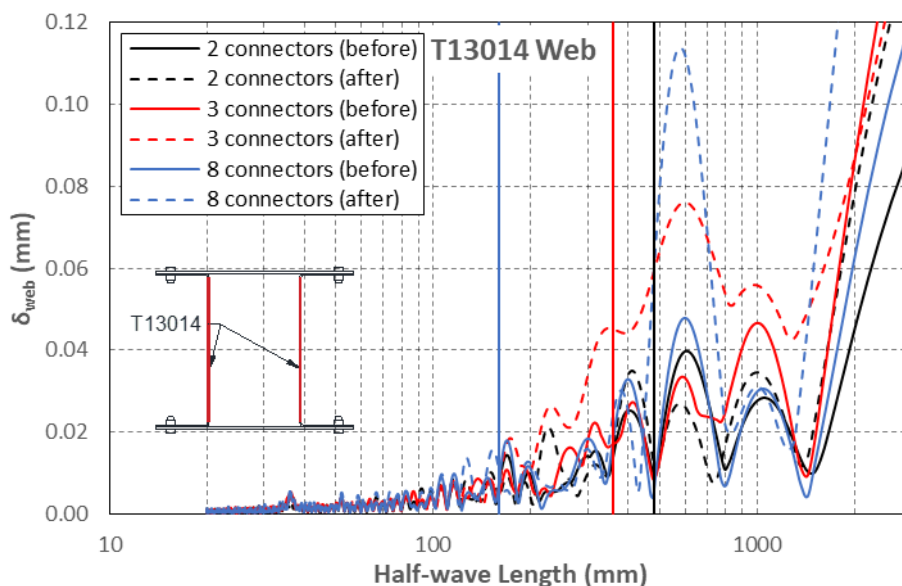


Figure 5.38: Average PSD of the web imperfections of channels T13014 before and after the assemblage

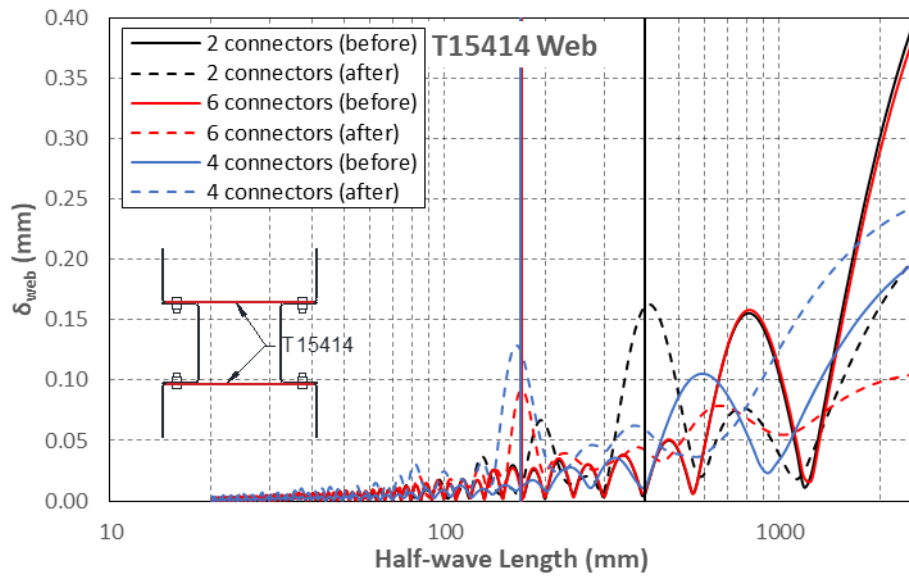


Figure 5.39: Average PSD of the web imperfections of channels T15414 before and after the assemblage

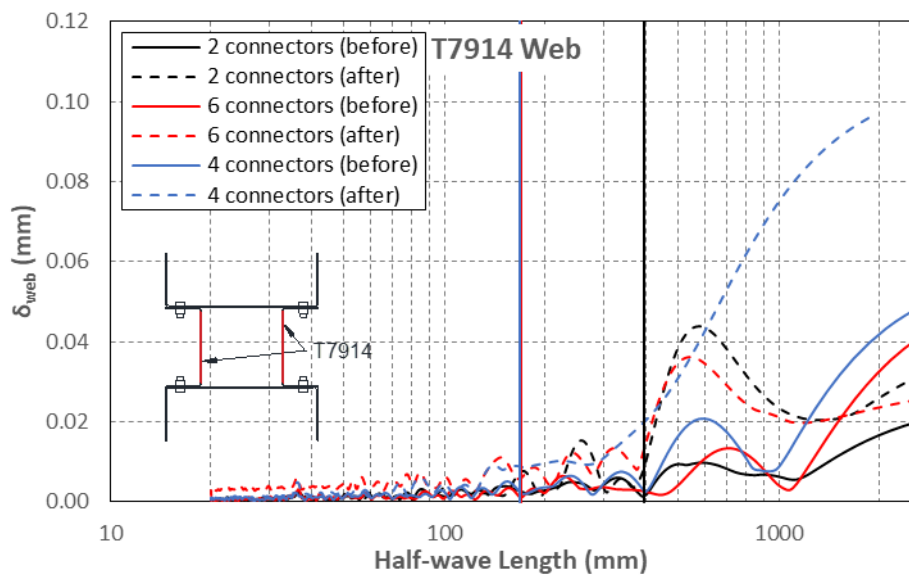


Figure 5.40: Average PSD of the web imperfections of channels T7914 before and after the assemblage

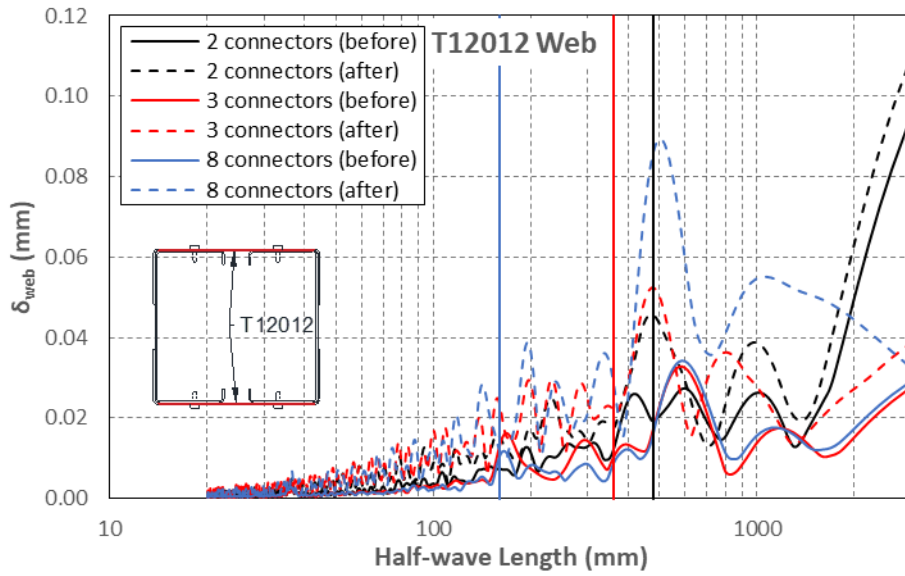


Figure 5.41: Average PSD of the web imperfections of channels T12012 before and after the assemblage

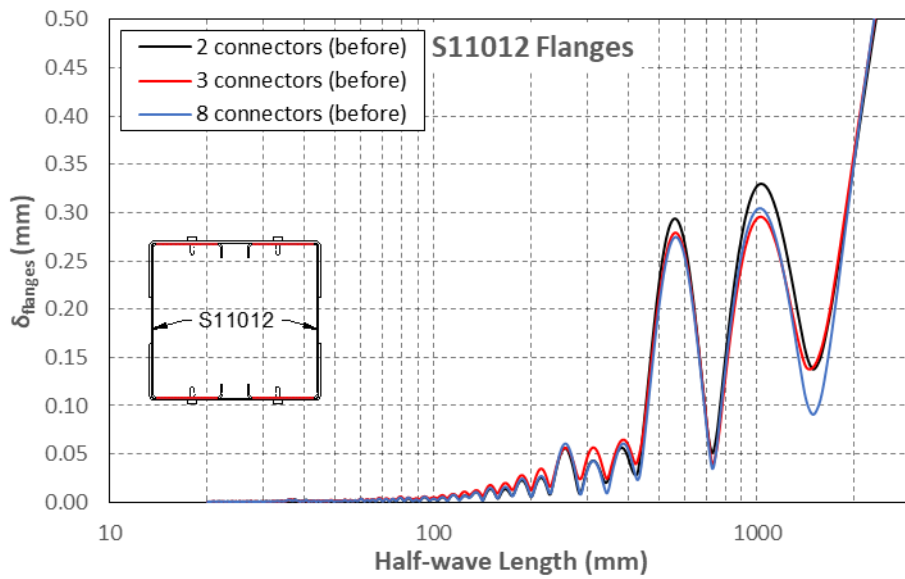


Figure 5.42: Average PSD of the flange imperfections of channels S11012 before the assemblage

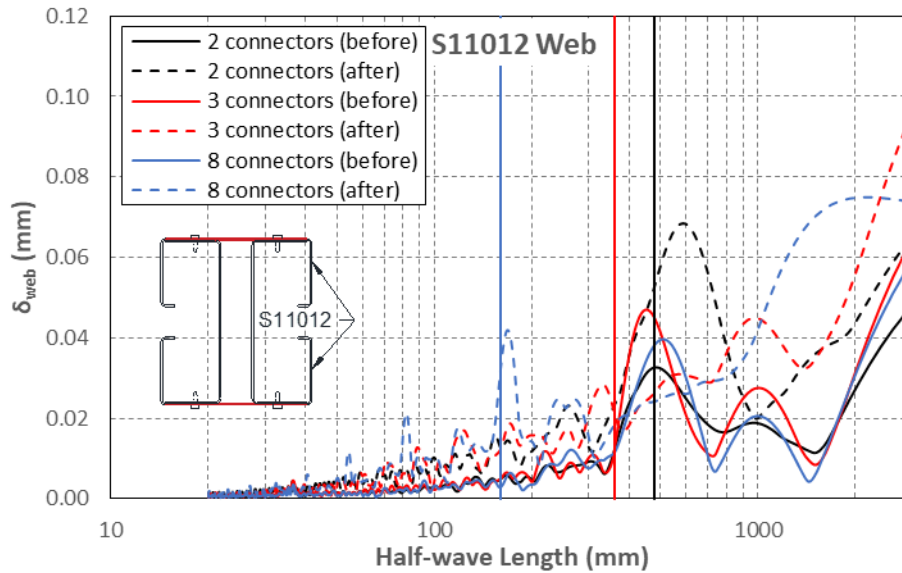


Figure 5.43: Average PSD of the web imperfections of channels S11012 before and after the assemblage

Regarding the out-of-plane imperfections along the flanges of the channels, Figure 5.44, Figure 5.45 and Figure 5.46 compare the PSD functions of channels T15414, T12012 and S11012 before and after they were assembled. The figures show that in channels T12012 and S11012 the assembly process did not significantly affect the imperfection profile. However, in channels T15414, the assembly process tended to reduce the half-wave length of the main component. For the channels with a connector spacing of around 430 mm, it also introduced an additional imperfection component with a half-wave length equal to half the distance between connectors, as previously revealed in Figure 5.37.

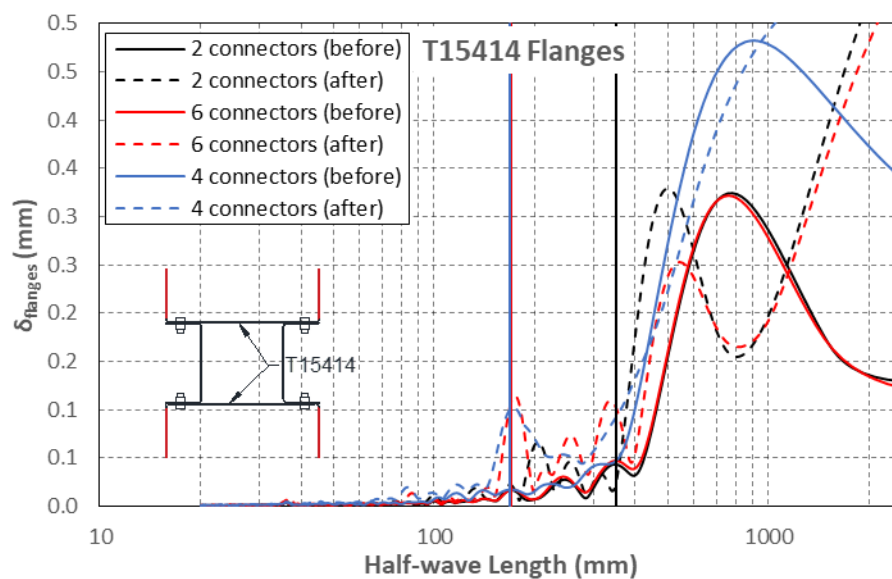


Figure 5.44: Average PSD of the flange imperfections of channels T15414 before and after the assemblage

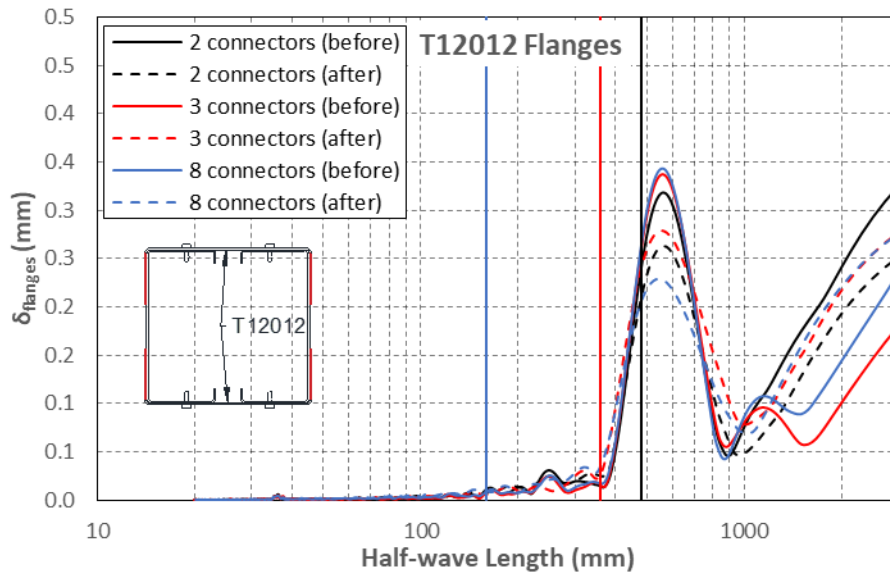


Figure 5.45: Average PSD of the flange imperfections of channels T12012 before and after the assemblage

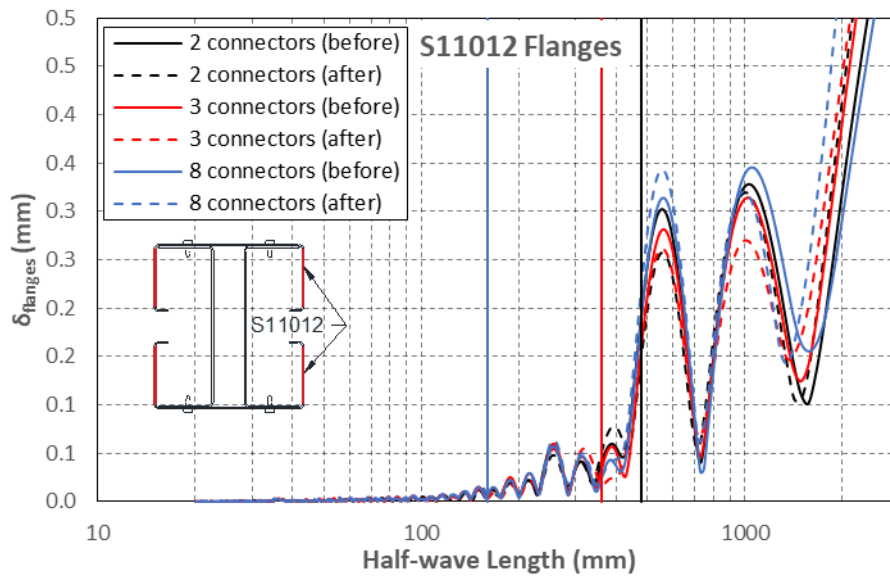


Figure 5.46: Average PSD of the flange imperfections of channels S11012 before and after the assemblage

5.6.3.2 Global imperfections

Before assembling the channels

All measured channels displayed a global flexural imperfection about the minor axis $\delta_{global,m}$ with a profile closely resembling a ‘Bow imperfection’ (i.e. a half-sinusoidal wave equal to the channel length) with a maximum imperfection amplitude around mid-length. Figure 5.47 shows the average bow imperfection recorded for a representative channel of each type and length. The direction of the Bow imperfection was consistently towards the web in all channels, irrespective of their cross-sectional dimensions or whether they were stiffened with a lip. This bias in the imperfection is attributed to the details of the fabrication process (Zeinoddini and Schafer,

2011), in particular whether the steel sheet used to fabricate the channels was fed into the forming machine with a concave or convex residual curvature as a result of the coiling-uncoiling stage.

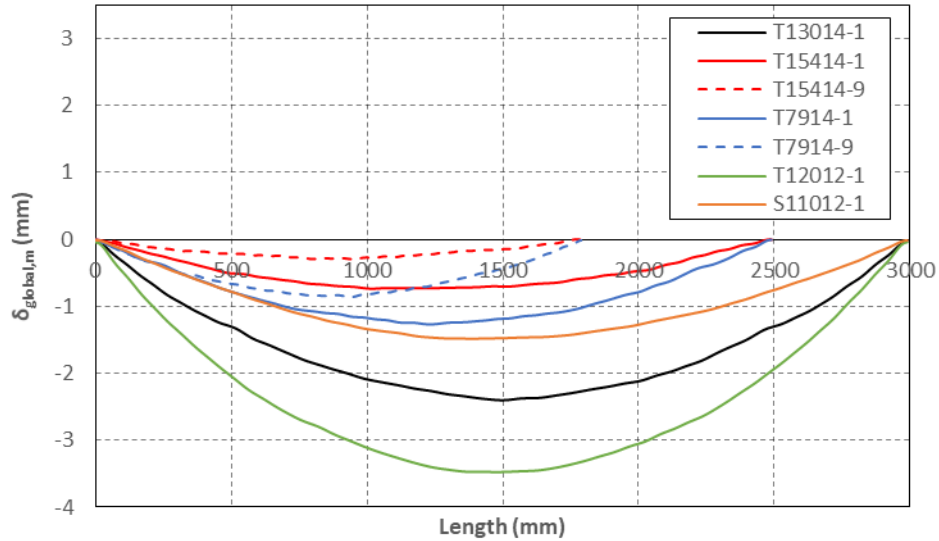


Figure 5.47: Minor axis global imperfection of a representative specimen of each type of channel before the assemblage

A large scatter in the magnitude of the bow imperfection was observed, even among channels with the same nominal cross-sectional dimensions and length. As an example, Figure 5.48 shows the bow imperfections measured in all T12012 channels, with a length of 3 m. This large variability in the magnitude of the bow imperfection may be attributed to the differences in the radial location within the coil of the steel sheet used to fabricate the channels. As indicated by Moen et al. (2008) and Quach et al. (2004), this position introduces longitudinal residual stresses and strains which are locked into the member as it is cold-formed into its structural shape.

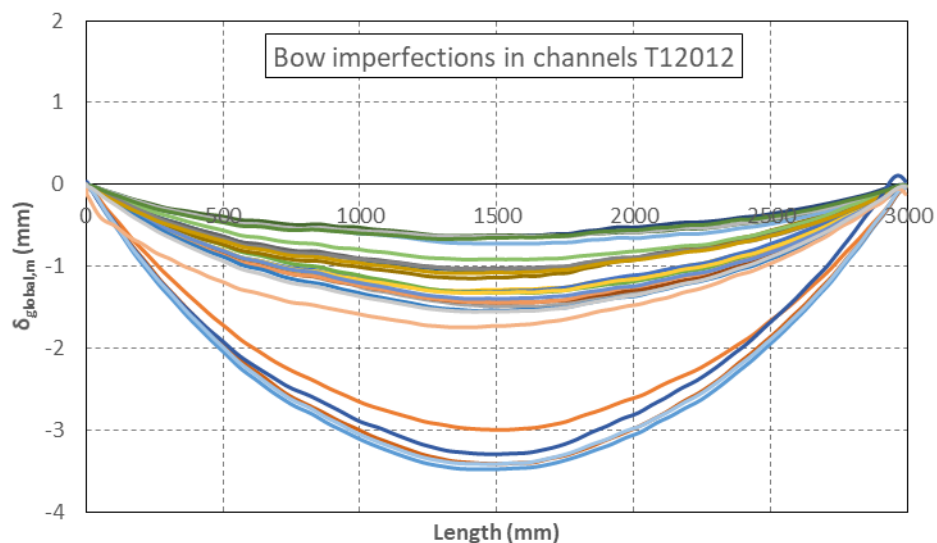


Figure 5.48: Minor axis global imperfections of channels T12012 before the assemblage

In all channels the global flexural imperfections about the major axis ($\delta_{global,M}$) were significantly smaller than those recorded about the minor axis, and their profile could be less accurately approximated by a ‘Camber imperfection’ (i.e. a half-sinusoidal wave equal to the channel length). In most cases the maximum amplitude was recorded away from the mid-length of the channel, as illustrated in Figure 5.49 for one specimen of each type of channel. Similarly to the minor axis bow imperfections, a large scatter was observed in the magnitude of the major axis global imperfections, even for channels with the same nominal dimensions.

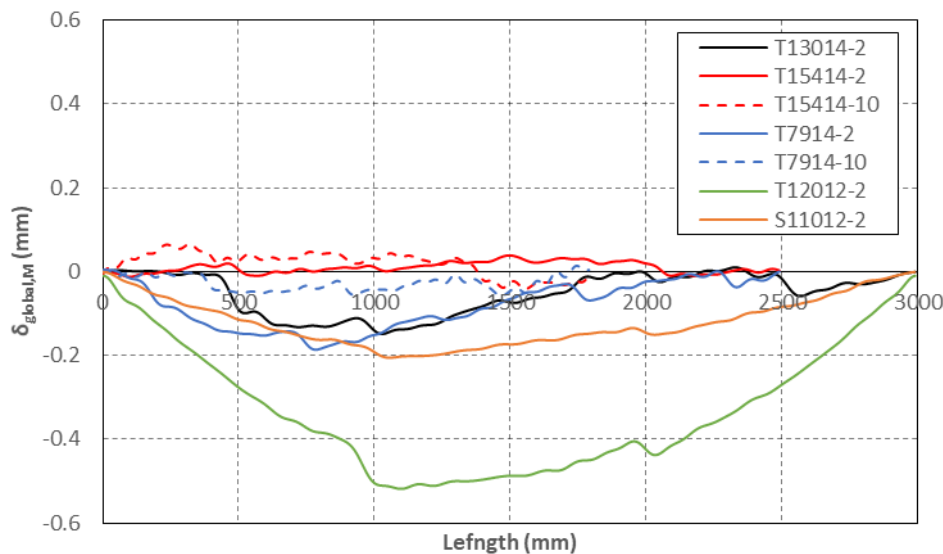


Figure 5.49: Major axis global imperfections of a representative specimen of each type of channel before the assemblage

Table 5.16 lists the 25%, 50%, 75%, 95% and 99% percentiles, as well as the mean and the standard deviation of the minor and major axis global flexural imperfections at mid-length, obtained for each type of channel section and length. The table also includes the statistical results obtained when combining the measurements of all channels.

The table shows that the mean bow imperfection recorded at mid-length was $L/2218$, while 95% of the bow imperfections were smaller than $L/1000$, which is commonly adopted in the numerical analysis of cold-formed steel members as a conservative value. The major axis global imperfection at mid-length, on the other hand, was found to be, on average, more than ten times smaller than the minor axis global imperfection, with an average magnitude at mid-length of $L/24275$ and a maximum value of $L/5345$ (which was encountered in channels T12012).

These results justify the use of a maximum out-of-straightness of $L/1000$ to model the bow imperfection of single CFS channel members. However, this imperfection magnitude seems

excessively conservative when modelling the global flexural imperfection about the major axis of CFS channels.

Table 5.16: Statistical values of the global imperfection of the channels before the assemblage

Section	Length (mm)	Imp.	$P(\Delta < \delta)$					Mean	St. dev.
			0.25	0.50	0.75	0.95	0.99		
T13014	3000	$\delta_{global,m}$	L/1556	L/1398	L/1295	L/1249	L/1228	L/1440	L/7809
		$\delta_{global,M}$	L/149033	L/39033	L/28525	L/22647	L/18821	L/38359	L/56765
15414	2500	$\delta_{global,m}$	L/6743	L/3594	L/3284	L/2711	L/2711	L/3860	L/11860
		$\delta_{global,M}$	L/208978	L/124932	L/77356	L/42265	L/42265	L/99130	L/82258
	1800	$\delta_{global,m}$	L/6369	L/4866	L/4818	L/4546	L/4546	L/5063	L/36046
		$\delta_{global,M}$	L/398624	L/258842	L/59233	L/25420	L/25420	L/63904	L/49335
T7914	2500	$\delta_{global,m}$	L/2203	L/2099	L/2033	L/1972	L/1972	L/2197	L/12246
		$\delta_{global,M}$	L/85251	L/43027	L/22360	L/16749	L/16749	L/34561	L/28054
	1800	$\delta_{global,m}$	L/3023	L/2976	L/2556	L/2157	L/2157	L/2629	L/16188
		$\delta_{global,M}$	L/91002	L/54995	L/44130	L/30280	L/30280	L/47138	L/108393
T12012	3000	$\delta_{global,m}$	L/3288	L/2293	L/2015	L/880	L/879	L/1935	L/3219
		$\delta_{global,M}$	L/75442	L/28205	L/13110	L/6159	L/5345	L/18362	L/13241
S11012	3000	$\delta_{global,m}$	L/4166	L/2501	L/2194	L/1527	L/1498	L/2651	L/7271
		$\delta_{global,M}$	L/27972	L/17160	L/14038	L/10016	L/9248	L/17758	L/15450
All sections	-	$\delta_{global,m}$	L/3431	L/2379	L/2015	L/1002	L/879	L/2218	L/4305
		$\delta_{global,M}$	L/85251	L/30865	L/17084	L/9248	L/6159	L/24275	L/26483

After assembling the channels

The assembly process significantly affected the weak axis flexural imperfection $\delta_{global,m}$ of the individual channels. In general, after the channels were assembled the shape of the minor axis global imperfections resembled less of a sinusoidal bow imperfection. This was particularly the case for channels T12012, which were used to assemble geometry 3, as illustrated in Figure 5.50. This can be attributed to the fact that in this built-up geometry, the relatively large flexural rigidity of the stiffened flanges of the lipped channels, to which channels T12012 were attached, resulted in large pulling forces at the connector locations which significantly affected the minor axis global flexural imperfection profile of these channels.

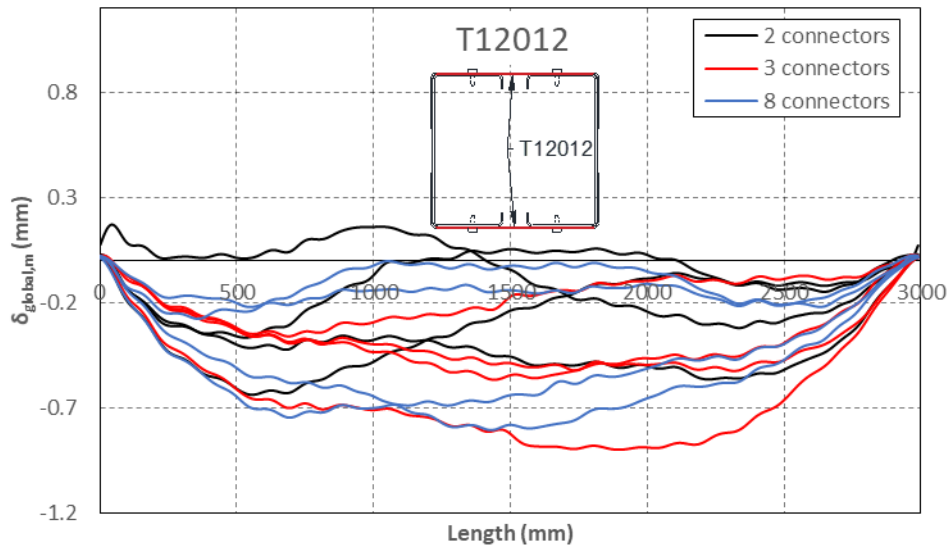


Figure 5.50: Minor axis global imperfections of channels T12012 after the assemblage

On the other hand, for channels T15414, T7914 and S11012, the minor axis flexural imperfection profile was still reasonably close to the initial bow imperfection present in the channels before they were assembled, as illustrated in Figure 5.51 for channels S11012. However, in all the channels belonging to series T15414 and T7914, which were used to assemble geometry 2, the direction of the bow imperfection was reversed after the channels were connected, as illustrated in Figure 5.52 and Figure 5.53 for channels T7914 and T15414, respectively. A similar situation was observed in some of the T13014 channels, which were connected to plate sections in geometry 1, where two channels experienced a reverse in the direction of their bow imperfection.

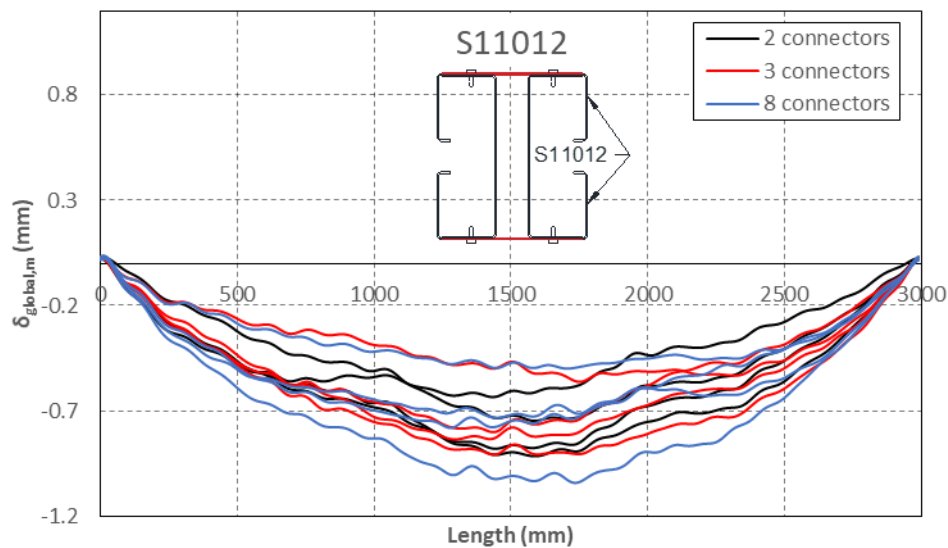


Figure 5.51: Minor axis global imperfections of channels S11012 after the assemblage

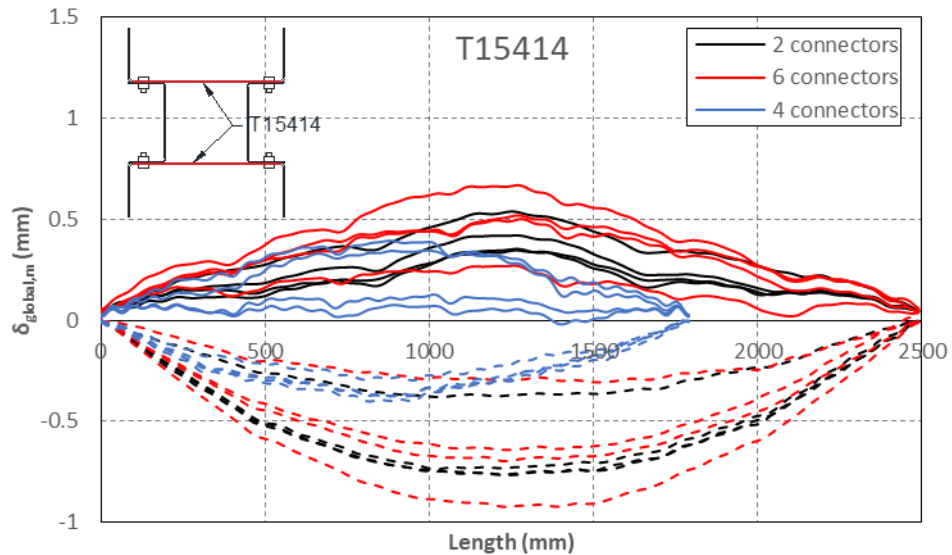


Figure 5.52: Minor axis global imperfections of channels T15414 after the assemblage

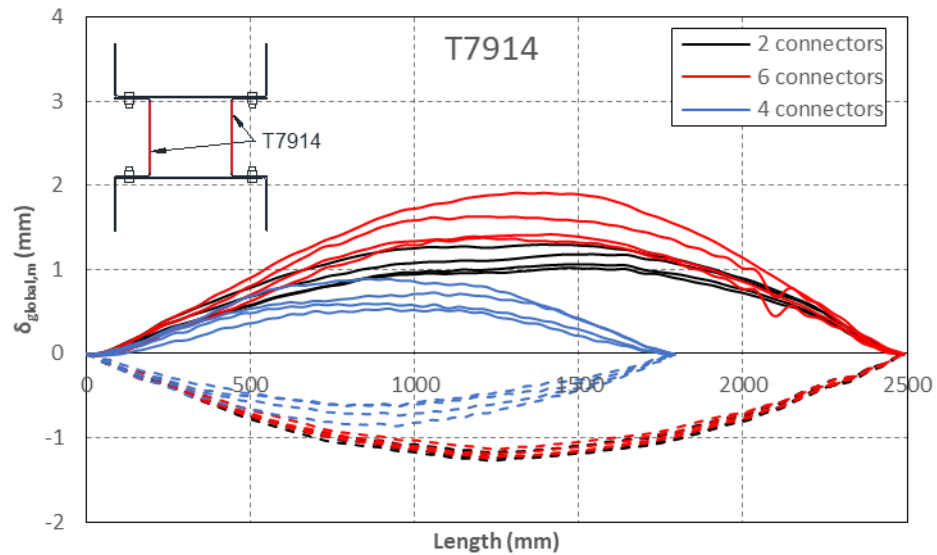


Figure 5.53: Minor axis global imperfections of channels T7914 after the assemblage

Figure 5.54-1.59 compare the minor axis imperfection at mid-length for channels T13014, T15414, T7914, T12012 and S11012, respectively, before and after they were assembled. In addition, Figure 5.55, Figure 5.57 and Figure 5.58 also include a comparison of the major axis imperfection at mid-length for channels T15414, T12012 and S11012, respectively.

The figures show that the assembly process affected the major axis imperfections of channels T15414, T12012 and S11012 in different ways. In particular, after the channels T15414 were assembled the major axis imperfections remained almost unaltered, as shown in Figure 5.55, while for the channels T12012 and S11012, in some cases the assembly process increased the major axis imperfections, while in other cases it reduced them or even inverted the direction of the imperfections, as shown in Figure 5.57 and Figure 5.58, respectively.

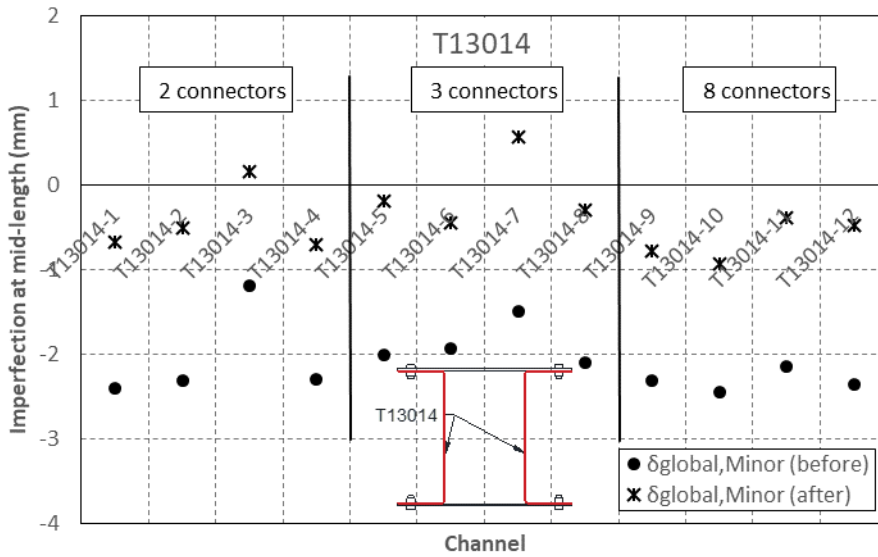


Figure 5.54: Global imperfection of channels T13014 before and after the assemblage

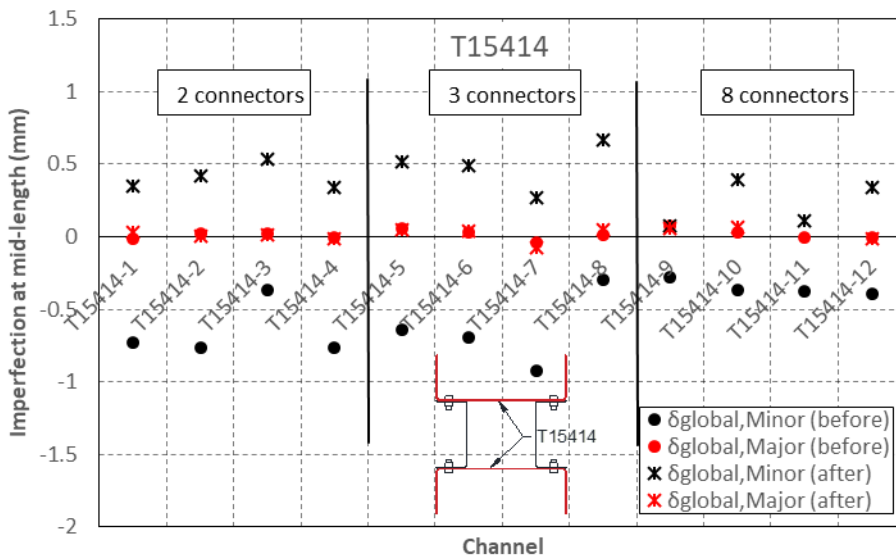


Figure 5.55: Global imperfection of channels T15414 before and after the assemblage

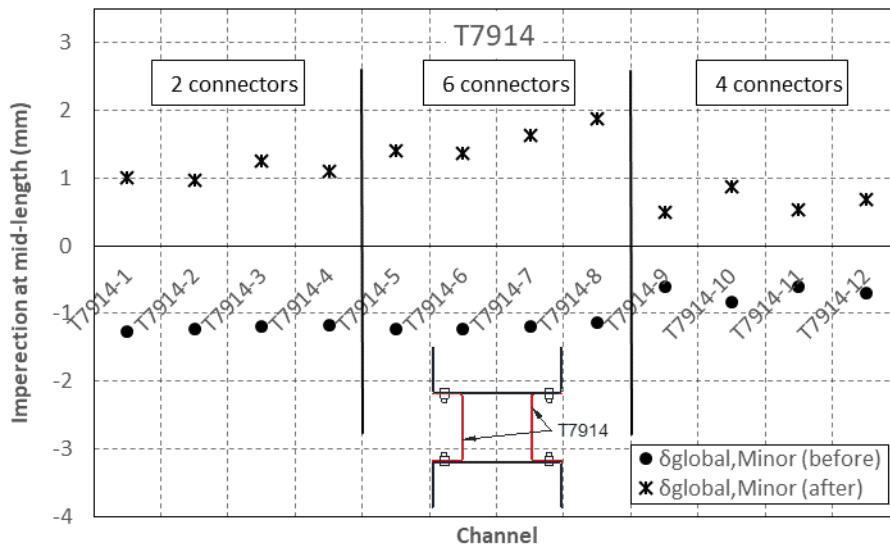


Figure 5.56: Global imperfection of channels T7914 before and after the assemblage

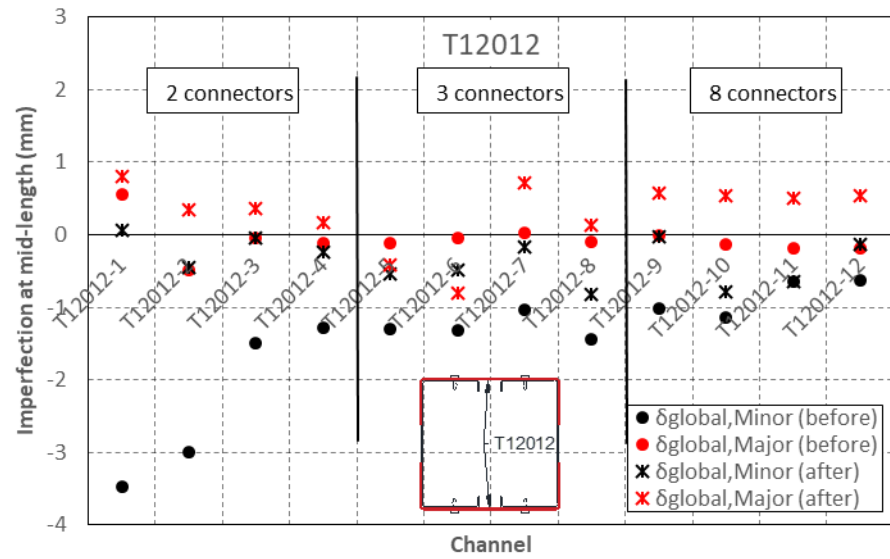


Figure 5.57: Global imperfection of channels T12012 before and after the assemblage

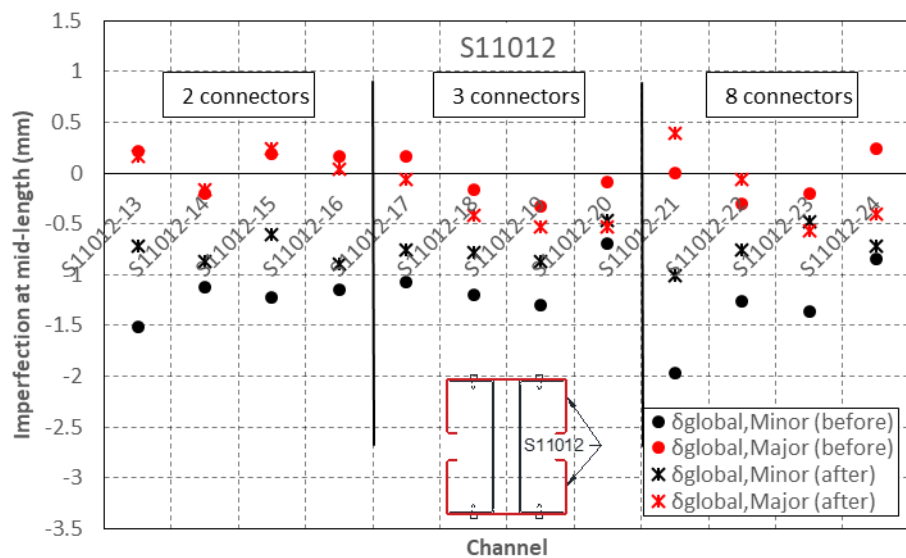


Figure 5.58: Global imperfection of channels S11012 before and after the assemblage

The 25%, 50%, 75%, 95% and 99% percentiles of the minor and major axis global imperfections, measured at mid-length after assembly, are listed in Table 5.17 for each type of channel. The table also includes the mean and the standard deviation obtained for each type of channel and length.

When comparing the results listed in Table 5.16 and Table 5.17 it can be seen that, on average, after the channels were assembled the mean minor axis global imperfection at mid-length was reduced by 48%, from $L/2218$ to $L/4255$, while the maximum imperfection amplitude was reduced from $L/879$ to $L/1326$. The major axis global imperfection at mid-length, on the other hand, was still found to be, on average, smaller than the minor axis one, with an average

amplitude at mid-length of $L/10465$ and a maximum amplitude of $L/3710$ (which occurred in channels T12012).

Table 5.17: Statistical values of the global imperfection of the channels after the assemblage

Section	Length (mm)	Imp.	$P(\Delta < \delta)$					Mean	St. dev.
			0.25	0.50	0.75	0.95	0.99		
T13014	3000	$\delta_{global,m}$	L/9998	L/6372	L/4414	L/3852	L/3229	L/5885	L/7182
		$\delta_{global,M}$	-	-	-	-	-	-	-
15414	2500	$\delta_{global,m}$	L/7269	L/5956	L/4868	L/3764	L/3764	L/5568	L/19612
		$\delta_{global,M}$	L/271243	L/71717	L/55655	L/34861	L/34861	L/75286	L/63055
	1800	$\delta_{global,m}$	L/23564	L/16384	L/5240	L/4594	L/4594	L/7813	L/11229
		$\delta_{global,M}$	0	L/135950	L/135950	L/33086	L/33086	L/52853	L/41165
T7914	2500	$\delta_{global,m}$	L/2495	L/1983	L/1791	L/1326	L/1326	L/1887	L/7930
		$\delta_{global,M}$	-	-	-	-	-	-	-
	1800	$\delta_{global,m}$	L/3643	L/3441	L/2650	L/2048	L/2048	L/2796	L/10197
		$\delta_{global,M}$	-	-	-	-	-	-	-
T12012	3000	$\delta_{global,m}$	L/54042	L/12546	L/5501	L/3845	L/3667	L/8191	L/9903
		$\delta_{global,M}$	L/8588	L/5922	L/5226	L/3753	L/3710	L/6104	L/6385
S11012	3000	$\delta_{global,m}$	L/4930	L/3994	L/3466	L/3340	L/2966	L/4032	L/18335
		$\delta_{global,M}$	L/45213	L/12432	L/7144	L/5630	L/5277	L/10028	L/9091
All sections	-	$\delta_{global,m}$	L/7124	L/4691	L/3466	L/1834	L/1541	L/4255	L/6451
		$\delta_{global,M}$	L/54293	L/17480	L/5922	L/4206	L/3710	L/10465	L/12099

5.6.4 Measuring rig accuracy

The accuracy of the measuring rig is largely dependent on the straightness of the high precision bars along which the laser sensor is moved. However, imperfection measurements with a higher accuracy than the one provided by the guiding bars can be achieved by measuring the out-of-flatness of a surface of which the tolerances are smaller than those of the guiding bars. This way, the out-of-straightness of the guiding bars can be measured against the surface and used to correct the imperfection measurements taken of the specimens. Obviously, the accuracy of the measurements then depends on the deviation from flatness of the surface. However, other sources of error, including the deformation of the specimen due to its self-weight, torsion of the specimen due to uneven support conditions and vibrations of the laser sensor and the specimen resulting from the propulsion mechanism will also limit the accuracy of the measurements.

In order to measure the out-of-straightness of the guiding bars, a flat surface was created by taking advantage of the fact that a liquid at rest with a low viscosity tends to form a flat surface. In this experimental study, the liquid chosen to generate the flat surface was milk, since its surface was reflective to the laser sensor and its low viscosity permitted to obtain a measuring surface which was virtually perfectly flat. In addition, milk has the advantage of being low-cost and easily obtainable and can easily be cleaned up.

In order to generate a milk surface that could be measured by the laser sensor, a sealed container for the milk was built and placed within the measuring rig, as illustrated in Figure 5.59. The

container was designed to be wide enough to ensure that all the measurements taken of the milk surface were sufficiently far away from the edges of the container in order to avoid introducing errors due to capillarity between the milk and the container. The container rested on two portable stands, which were independent from the measuring frame in order to avoid introducing vibrations originating from the stepper motors to the milk surface. Readings of the milk surface were taken along the same longitudinal lines as the imperfection measurements of the test specimens. This permitted to correct for the out-of-straightness of the longitudinal as well as the transverse guiding bars.



Figure 5.59: Calibration of the imperfection measuring rig

Figure 5.60 shows the imperfections of the guiding bars, as detected from measuring the milk surface along the same lines used to measure the imperfections of the web of channels T12012. It can be seen that the deviation from straightness of the longitudinal guiding bars is around 0.6 mm over a length of 3 m.

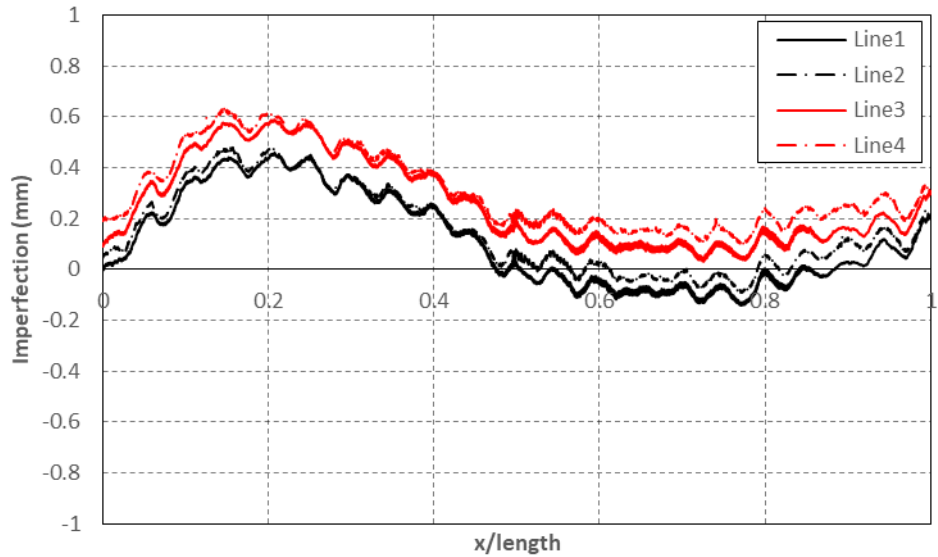


Figure 5.60: Imperfections of the guiding system along the measuring lines of the web of channels T12012

The measurements taken of the milk surface were then subtracted from the measurements of the imperfections recorded on each test specimen.

Assuming that the reference surface was perfectly flat, the remaining errors in the corrected measurements were mainly introduced by the deformations of the test specimen due to its self-weight, and to a lesser degree by vibrations induced into the specimen during the measurements by the movement of the laser sensor. The vibrations in the measurements had an amplitude of around 0.05 mm. However, they were mostly removed during the data post-processing. The self-weight deformations of the specimen can be decomposed into flexural deformations and a torsion induced due to uneven support conditions, as illustrated in Figure 5.61. The latter is composed of a point-symmetric component and a rigid body twist.

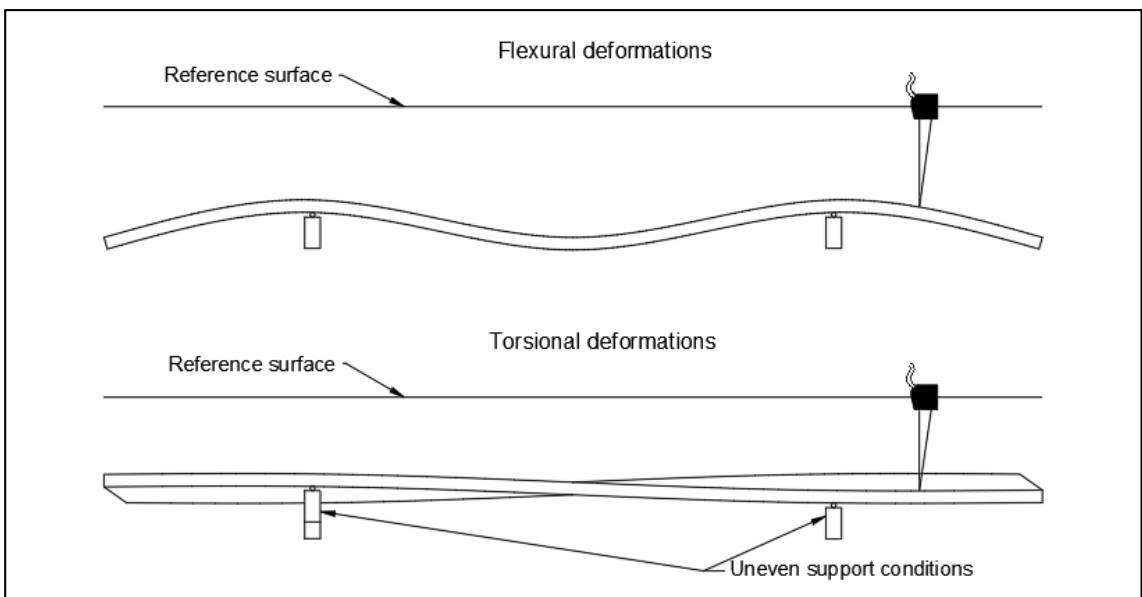


Figure 5.61: Flexural and torsional deformations due to self-weight

Errors due to flexural deformations of the specimen can be quantified by comparing the geometric imperfections of the same plate element measured before and after flipping the specimen so with each measurement the self-weight of the specimen causes it to deform in opposite directions relative to the geometric imperfections in the plate element.

For this reason, in order to check the accuracy obtained from the imperfection measurements, after accounting for the out-of-straightness of the guiding bars of the measuring rig, the web of three plain channels, two of them with a length of 3000 mm and a third one with a length of 2500 mm, were measured with the channel placed in the four positions relative to the measuring rig illustrated in Figure 5.62. The imperfections of the channels web were recorded along the same equally spaced four lines used to record the imperfections in the rest of plain channels.

If the thickness of each channel web is assumed to be constant over the entire web, by comparing the imperfections taken with the test specimen in positions 1 and 3, and 2 and 4, respectively, the error introduced into the measurements due to the flexural deformation of the specimen can be determined. It is important to note that by comparing the imperfection measurements with the channel placed in the aforementioned positions, it is not possible to detect errors introduced into the measurements related to the torsional deformation of the test specimen due to uneven support conditions. This error component is, however, of little interest for this experimental programme since the imperfection recorded from all the measured surfaces were adjusted to zero the imperfection values at the corners of the surface by applying a small twist to the reference surface from which the imperfections were taken, as described in section 5.6.2.

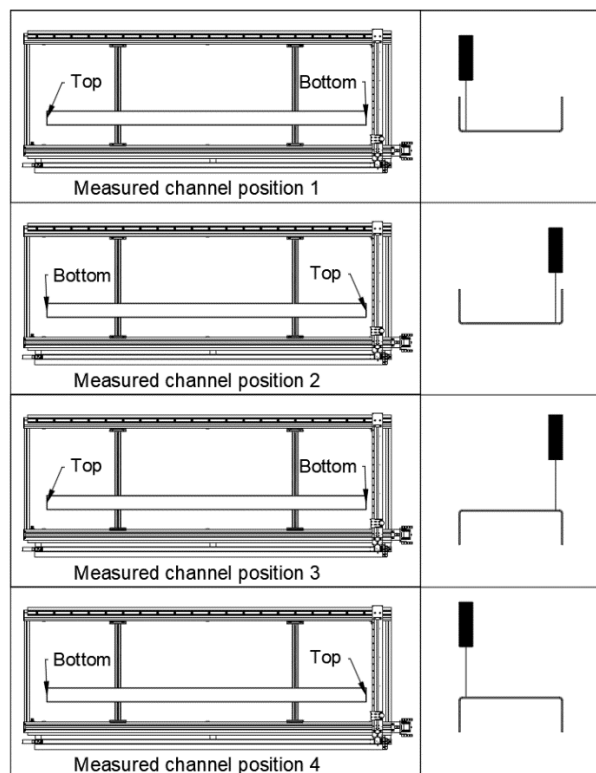


Figure 5.62: Measured channel positions to check accuracy of the measuring rig

Figure 5.63 shows the corrected imperfections readings obtained along each line measured on the web of channel T12012-26 before the flexural deformation of the specimen due to its self-weight was deducted, with the channel placed in the four aforementioned positions (Figure 5.62). In the figure, the solid lines show the measurements obtained with the channel placed in positions 1 and 2, while the dashed lines shows the measurements obtained with the channel in positions 3 and 4. The imperfections presented in the figure were obtained after processing the data as described in section 5.6.2. The sign of the imperfection measurements was adjusted so that positive values indicate imperfections towards the centroid of the cross-section.

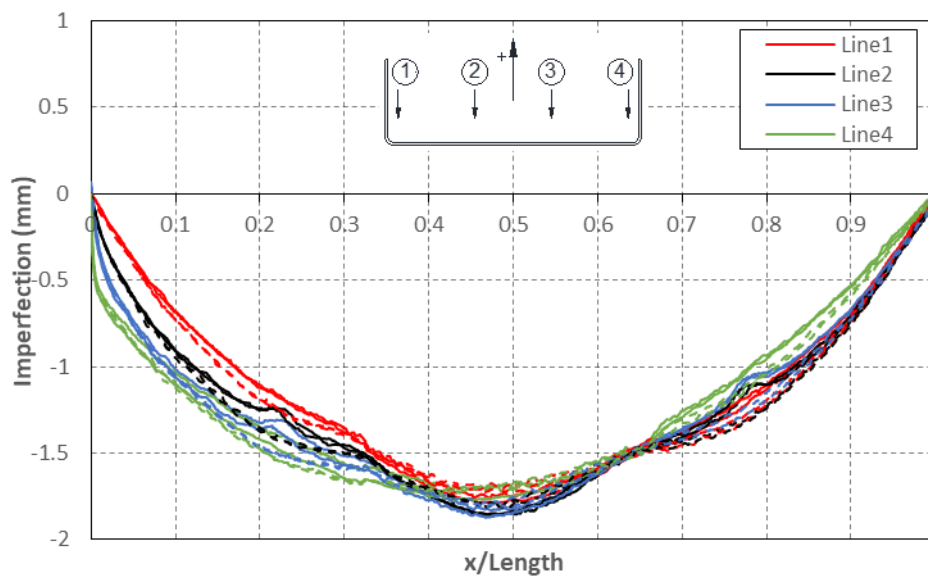


Figure 5.63: Imperfections of the web of channel T12012-26 measured in four different positions

The effect of the self-weight on the measurements taken along the web of channel T12012-26 is revealed in Figure 5.64, which shows, for each measured line, the imperfection difference $\Delta_{Imp,L_i}(x)$, calculated using Eq. (5.42):

$$\Delta_{Imp,L_i}(x) = \left(Line_i_{position_1}(x) + Line_i_{position_2}(x) \right) / 2 - \left(Line_i_{position_3}(x) + Line_i_{position_4}(x) \right) / 2 \quad (5.42)$$

$$\Delta_{Imp}(x) = \text{Max}(\Delta_{Imp,L_1}(x), \Delta_{Imp,L_2}(x), \Delta_{Imp,L_3}(x), \Delta_{Imp,L_4}(x)) \quad (5.43)$$

where $Line_i_{position_1}$, $Line_i_{position_2}$, $Line_i_{position_3}$ and $Line_i_{position_4}$ correspond to the imperfection taken along each of the lines measured in the web, with the channel in position 1, 2, 3 and 4, respectively. Eq. (5.42) gives the difference between the average imperfection obtained with the channel in positions 1 and 2, versus positions 3 and 4, while preserving the sign of the difference.

Likewise, the maximum difference for the minor axis global flexural imperfection measured at mid-length of the plain channel ($\Delta\delta_{global,m}$) can be calculated using Eq. (5.44)

$$\Delta\delta_{global,m} = \left(\delta_{global,m,position_1} + \delta_{global,m,position_2} \right) / 2 - \left(\delta_{global,m,position_3} + \delta_{global,m,position_4} \right) / 2 \quad (5.44)$$

where $\delta_{global,m,position_1}$, $\delta_{global,m,position_2}$, $\delta_{global,m,position_3}$ and $\delta_{global,m,position_4}$ are calculated using Eq. (5.8) with the channel in positions 1, 2, 3 and 4, respectively.

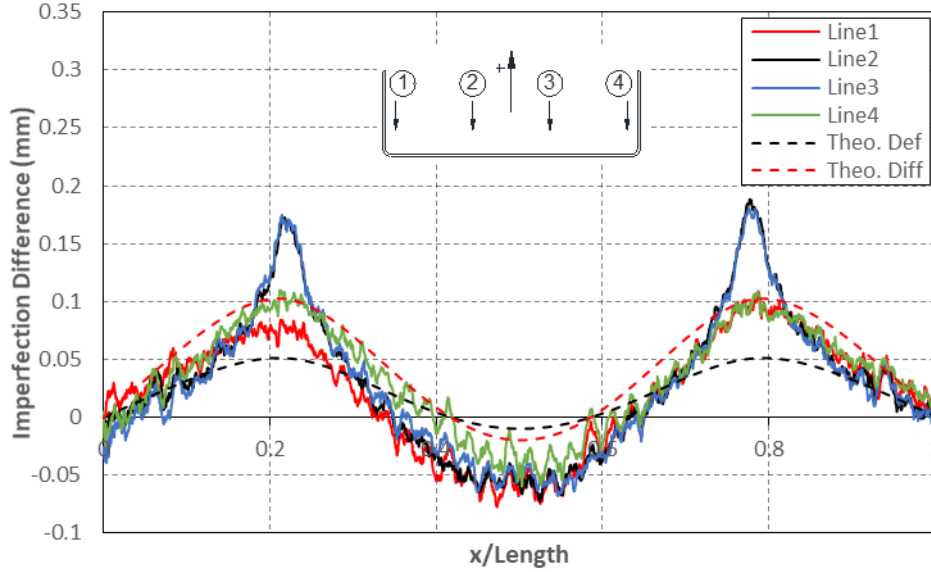


Figure 5.64: $\Delta_{Imp,L_i}(x)$ obtained in the web of channel T12012-26

It is important to note that, for each measured line, the true imperfection must lay at approximately mid-distance between the maximum and minimum value of the recorded imperfection. Therefore, the accuracy of the imperfection measurements (ξ) can be estimated as:

$$\xi = \pm \text{Max}(\Delta_{Imp}(x)) / 2 \quad (5.45)$$

$$\xi_{global,m} = \pm \Delta\delta_{global,m} / 2 \quad (5.46)$$

Figure 5.64 shows that, for each measured line, the shape of $\Delta_{Imp,L_i}(x)$ closely follows the expected flexural deformation of the channel due to its self-weight multiplied by two, as represented by the red dashed line. This reveals that at this state, the accuracy of the measurements is limited by the effect of the self-weight of the specimen to be measured. The fact that the difference of the measurements follows twice the deformed shape of the specimens can be expected since when the web of the channel was measured with the channel in positions 1 and 2, the deformation of the channel due to its self-weight reduced the imperfection of the channel web, while the opposite can be said when the channel was measured in positions 3 and 4. The sharp increase of the imperfection difference, in Figure 5.64, calculated along lines 2 and

3 at $x/length$ equal to 0.22 and 0.78 is due to the fact that when the channel was measured in positions 1 and 2 the channel was directly rested on its web, which experienced localised deformations at the supports location. This deformations, however, only covered a length of around 100 mm along the channel. Therefore, it is not expected to have a significant effect on the buckling behaviour of the built-up specimen. Similar imperfections measurements were recorded along the web of the rest of plain channels.

In order to reduce the error in the measurements, the deformations due to the self-weight of the channels were subtracted from the readings, assuming that, for a given cross-section along the channel length, each point within the cross-section deflected by the same amount. In addition, the calculation of the flexural deformations of the channel due to its self-weight was based on the nominal cross-sectional dimensions of the channel, a Young modulus of 203 GPa, a density of the steel of 7850 Kg/m³ and the measured distance between supports. Figure 5.65 shows $\Delta_{Imp,L,i}(x)$ for each measured line after removing the flexural deformations of the channel due to its self-weight, while Figure 5.66 shows the differences (in absolute value) between the imperfections recorded with the channel in positions 1, 2, 3 and 4, after removing the self-weight deformations of the channel. Figure 5.66 also includes the maximum and average imperfection differences, as well as the standard deviation. The effect of the localized bearing deformations at the support locations was not considered when calculating these statistical parameters.

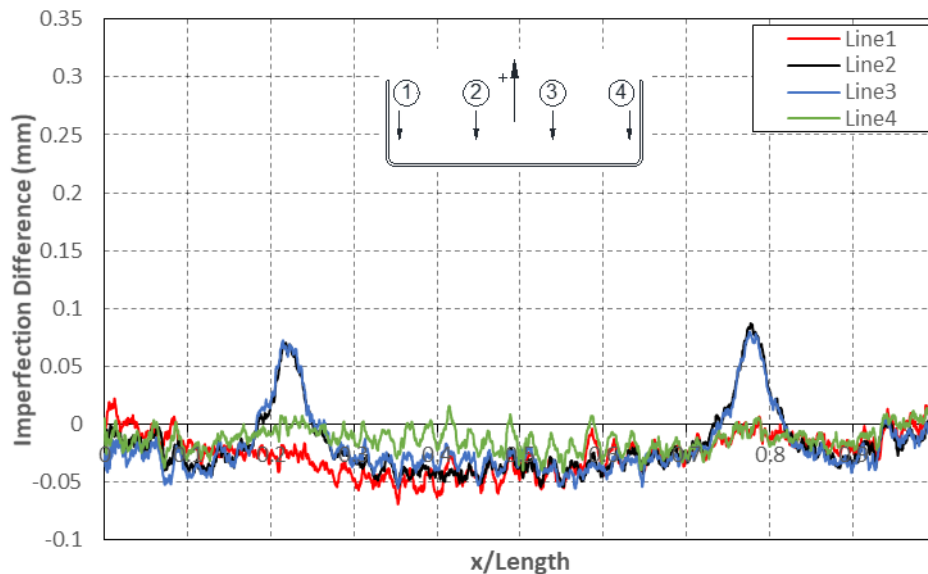


Figure 5.65: $\Delta_{Imp,L,i}$ obtained in the web of channel T12012-26 after removing the self-weight deflections

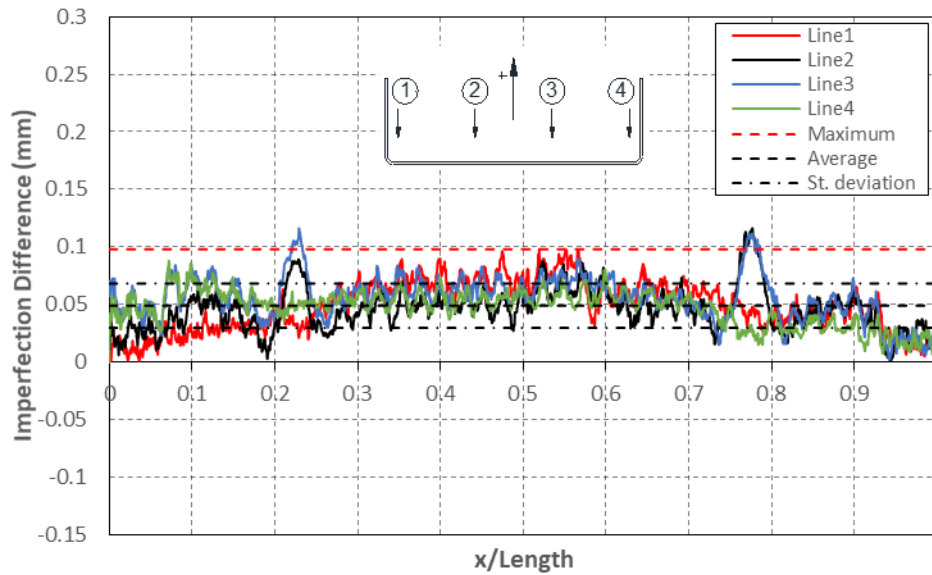


Figure 5.66: Maximum imperfection difference obtained in the web of channel T12012-26 after removing the self-weight deflections

Using Eq. (5.45) the accuracy of the imperfection measurements taken along the web of channel T12012-26 was estimated to be around ± 0.05 mm after the deflections of the channel were removed from the measurements, with an average error of ± 0.03 mm and a standard deviation of ± 0.01 mm. In addition, Eq. (5.46) was also used to estimate the accuracy of the global flexural buckling imperfection calculated at mid-length of channel T12012-26. In this case, the accuracy obtained was ± 0.03 mm after removing the effect of the self-weight of the channel from the measurements.

Similar results were also obtained when comparing the imperfection measurements taken on the web of channels T12012-25 and T7914-13. Figure 5.67 and Figure 5.68 show the differences (in absolute value) between the imperfections recorded when the channels were placed in positions 1, 2, 3 and 4, after removing the self-weight deformation of the channel, for channels T12012-25 and T7914-13, respectively. A summary of the accuracy obtained from the imperfection measurements and the global flexural imperfections carried out on the web of channels T12012-25, T12012-26 and T7914-13 is listed in Table 5.18 and Table 5.19, respectively.

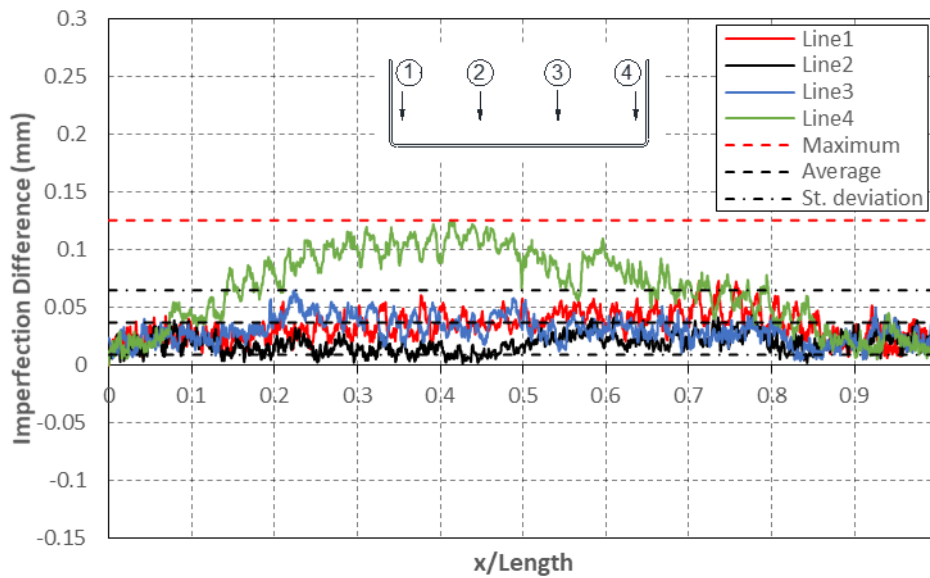


Figure 5.67: Maximum imperfection difference obtained in the web of channel T12012-25 after removing the self-weight deflections

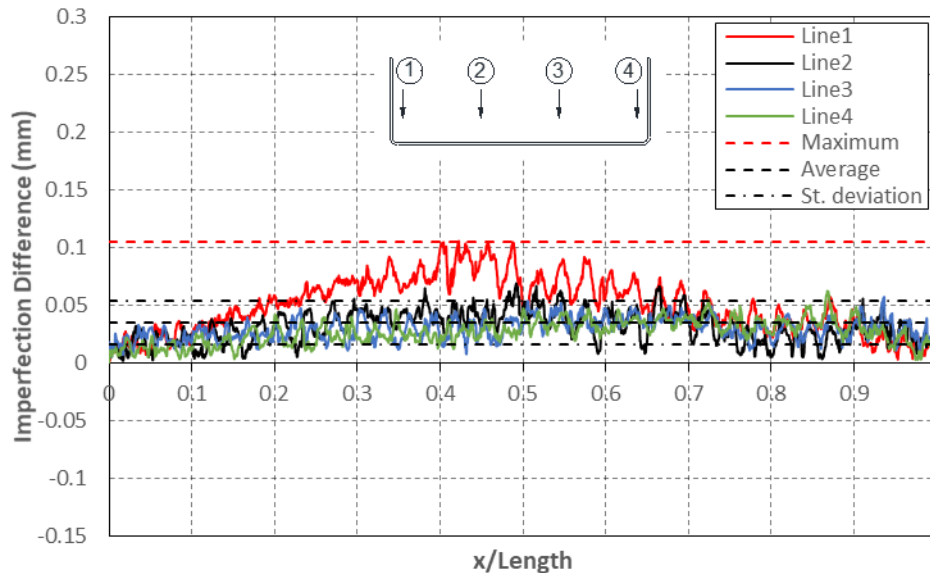


Figure 5.68: Maximum imperfection difference obtained in the web of channel T7914-13 after removing the self-weight deflections

From Table 5.18 it can be seen that the maximum imperfection in the web of the channels chosen to assess the accuracy of the measuring rig varied from 4.4 mm to 0.66 mm. The table also shows that, on average, after removing the effect of the self-weight of the channel, the maximum error in the imperfection measurements was reduced around 30%. Channels T12012 were also more affected by the effect of the self-weight than channel T7914. This could be expected since channels T12012 had a larger self-weight/inertia ratio and were longer than channel T7914. Therefore, they were expected to experience larger deformations under their self-weight. Table 5.18 also shows that the accuracy of the imperfection measurements obtained, after accounting for the self-weight, was virtually the same for all the channels, and below ± 0.063 mm, irrespective of the magnitude of the imperfection present in the channel.

Table 5.19, on the other hand, shows that the global flexural imperfection calculated at mid-length of the channels had an accuracy of less than ± 0.03 mm for all the channels after accounting for the effect of the self-weight on the imperfection measurements. However, in this case, removing the deformation of the channel due to its self-weight only resulted in an averaged increase of the measurements accuracy of around 9 %. This can be explained by the fact that the adjustable beams on which the channels were supported were positioned so as to minimize the deflection of the channels due to their self-weight, which occurs when the deflection at each end of the channel is the same as at mid-length. Therefore, since the imperfections of the channel web are presented respect to a plane that intersect the corners of the web, the deflection of the channel at the cross-section were the global flexural imperfection were calculated was almost null.

Table 5.18: Imperfection difference obtained in channels measured in positions 1, 2, 3 and 4

Section	Before removing the self-weight				After removing the self-weight			
	Max Imp (v)	Imperfection error (ξ)			Max Imp (v)	Imperfection error (ξ)		
		Max.	Avg.	St. dev.		Max.	Avg.	St. dev.
	(mm)	(mm)	(mm)	(mm)	(mm)	(mm)	(mm)	
T12012-25	4.446	± 0.104	± 0.038	± 0.023	4.446	± 0.063	± 0.018	± 0.014
T12012-26	1.838	± 0.077	± 0.033	± 0.015	1.839	± 0.049	± 0.025	± 0.009
T7914-13	0.657	± 0.057	± 0.019	\pm	0.657	± 0.053	± 0.017	± 0.009

Table 5.19: Global flexural imperfection difference in channels measured in positions 1, 2, 3 and 4

Section	Before removing the self-weight			After removing the self-weight		
	$\delta_{global,m}$	$\xi_{global,m}$	$\xi/\delta_{global,m}$	$\delta_{global,m}$	$\xi_{global,m}$	$\xi/\delta_{global,m}$
	(mm)	(mm)	(%)	(mm)	(mm)	(%)
T12012-25	-3.311	± 0.006	± 0.18	-3.311	± 0.015	± 0.45
T12012-26	-1.718	± 0.037	± 2.15	-1.718	± 0.024	± 1.40
T7914-13	-0.596	± 0.015	± 2.52	-0.596	± 0.014	± 2.35

5.7. Test Set up

5.7.1 Introduction

All long columns were tested in a 2000 kN AMSLER universal testing machine. The columns were subjected to compression between pin-ended boundary conditions, applying the load with nominal eccentricities of $L/1000$ and $L/1500$. The bottom end of the column was the active end accommodating the hydraulic actuator and a 300 kN load cell was mounted between the actuator and the bottom support. The test set-up is illustrated in Figure 5.69.

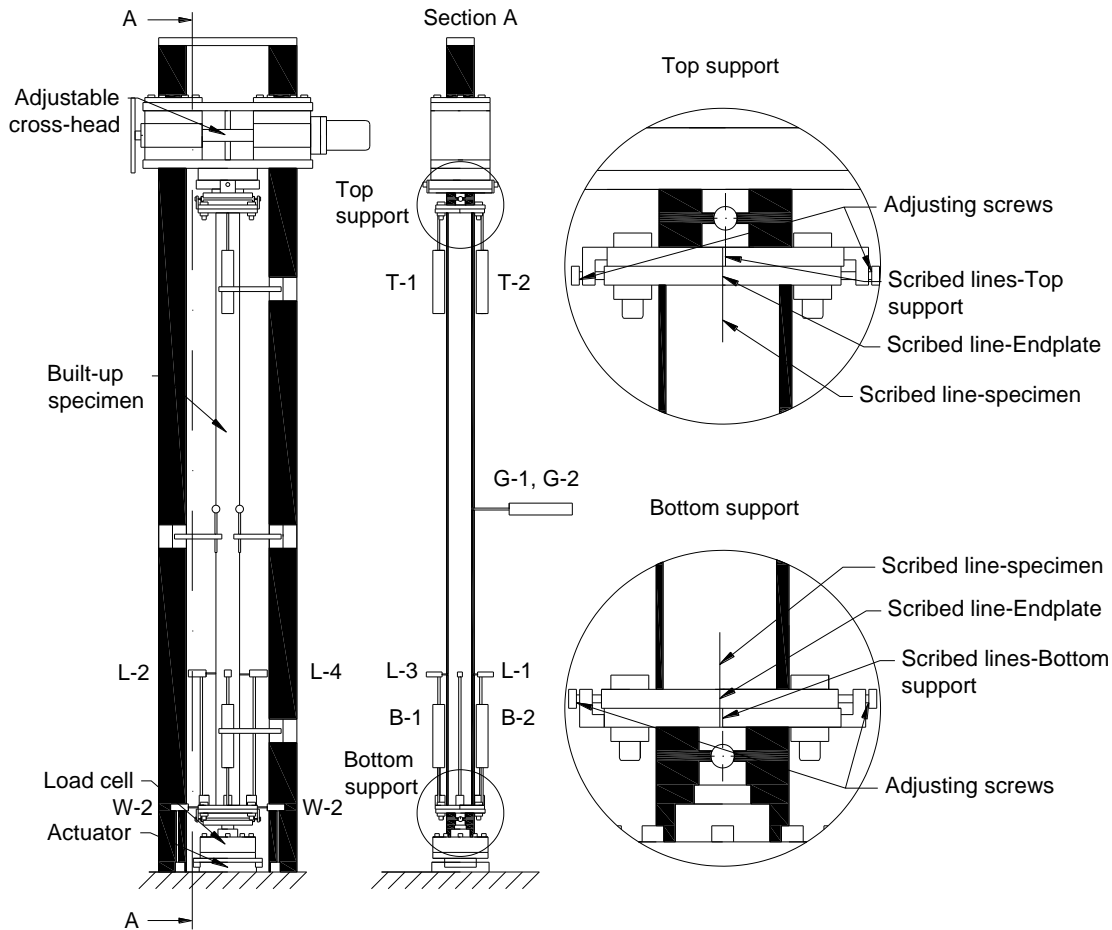


Figure 5.69: Test set-up

5.7.2 Pin-ended supports

The pin-ended supports were designed to allow rotations about the major axis, while restraining twisting and rotations about the minor axis. They consisted of hinge assemblies of which one side was fixed to the cross-head or the actuator of the testing machine, while the other side was welded to steel plates with dimensions of $250 \times 300 \text{ mm}^2$ and a thickness of 20 mm, and containing slotted holes of 22 mm width, as shown in Figure 5.70. Two scribed lines were marked on the sides of the steel plates. One of them was lined up with the axis of the pin, while the other one was parallel to it, indicating the eccentricity to be applied. The steel plates were bolted to the endplates of the column after aligning the centroid of the built-up specimens with the scribed line on the bearing plates which indicated the applied eccentricity. Fine adjustment between the specimens and the supports was achieved by means of four adjustable screws located on the bearing plates (Figure 5.71). The distance from the centre of the pin of the top support to the top end of the column was 75 mm, while the distance from the centre of the pin of the bottom support to the bottom end of the column was 72 mm. Therefore, the effective length of each specimen was calculated as:

$$L_e = L + 147 \quad (5.47)$$

where L_e and L are the effective length and the actual length of the specimen in mm.

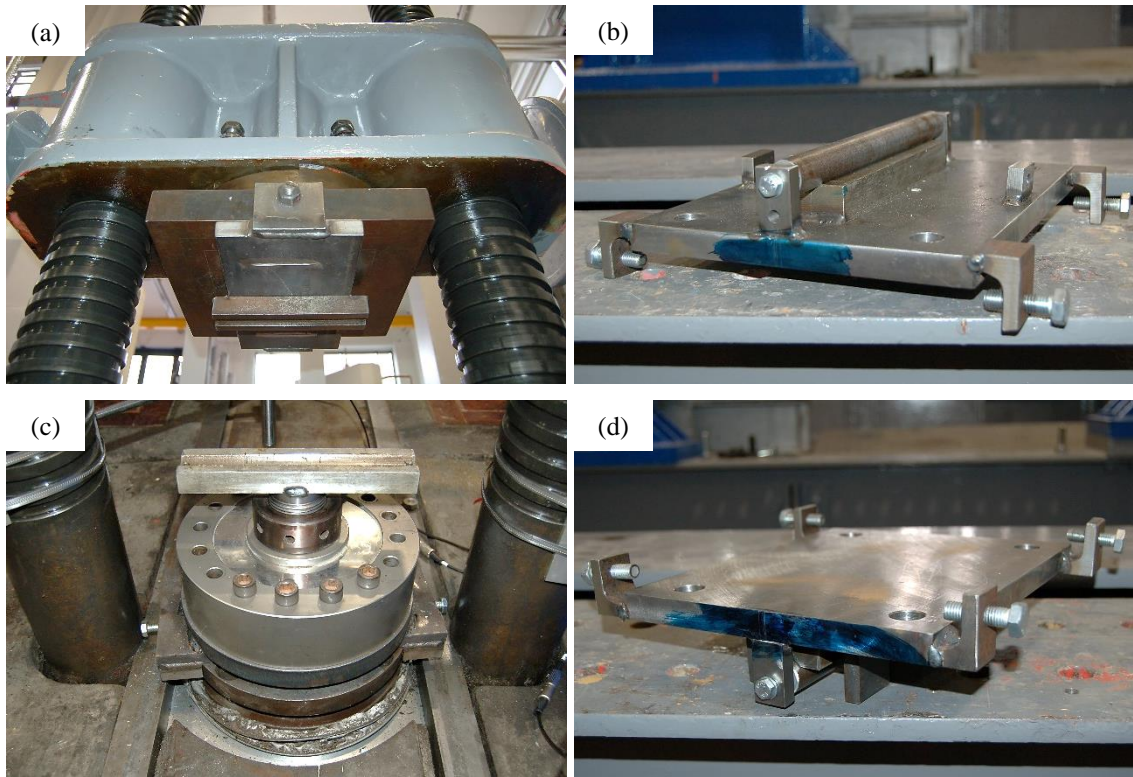


Figure 5.70: a) and b) components of top support; c) and d) components of bottom support

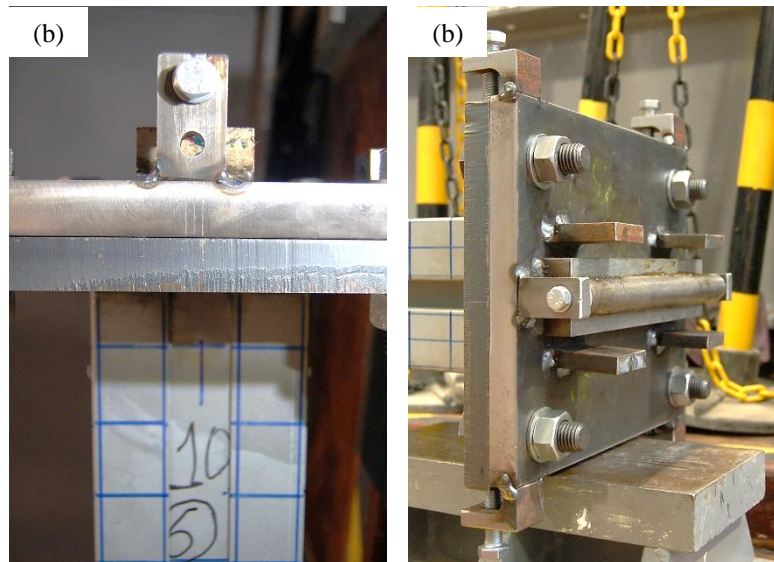


Figure 5.71: a) alignment between scribed lines; b) bottom support bolted to the specimen

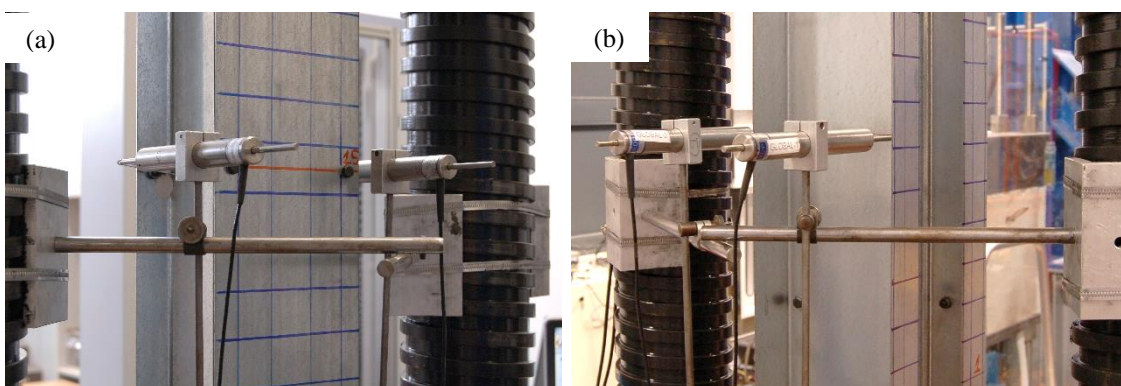
5.7.3 Instrumentation

The columns were instrumented with 6 LVDTs with a maximum stroke of 50 mm and six potentiometers with a maximum stroke of 25 mm. In addition, half of the specimens were also instrumented with four 10 mm strain gauges.

5.7.3.1 LVDTs

Figure 5.69 shows the overall layout of the LVDTs used in the tests. The LVDTs were clamped to the pillars of the testing machine. Four LVDTs were used to record the axial shortening of the columns as well as their end rotations. LVDTs *T1* and *T2*, and *B1* and *B2* were placed at a horizontal distance of 110 mm away from the pin axis of the top and bottom support, respectively.

The global flexural buckling deformations at mid-height were recorded with LVDTs *G1* and *G2*. The LVDTs were placed on the side of the specimen which experienced superimposed tensile stresses due to the flexural buckling deformations and which will herein be referred to as the ‘*tension side*’ of the specimen (in the appreciation that the total stress may still be compressive). The opposite side, where flexural buckling caused additional compressive stresses, will be referred to as the ‘*compression side*’. In geometries 2, 3 and 4, the LVDTs were placed at the corners of the web of the channel component, while in the case of geometry 1, as the plate sections were expected to buckle in a flexural mode between connectors before global flexural buckling of the column, the LVDTs were placed at the flange corner of the channels, as illustrated in Figure 5.72.



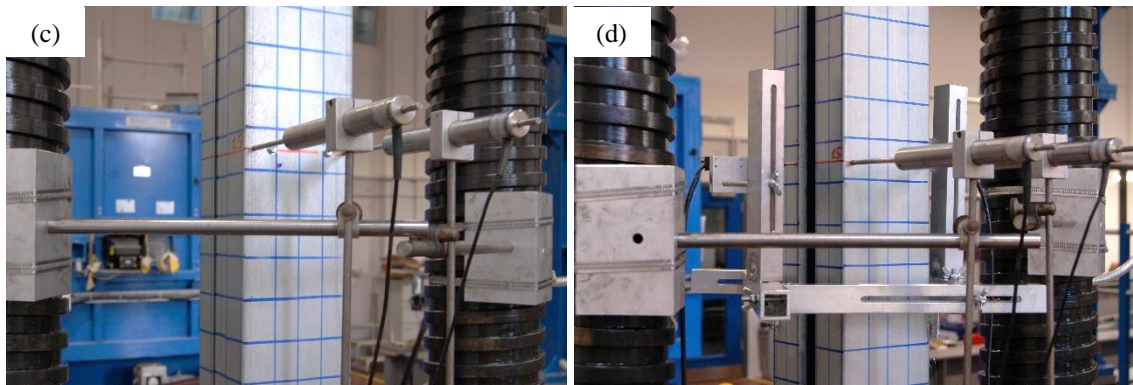


Figure 5.72: Location of LVDTs G1 and G2 for: a) LC1; b) LC2; c) LC3 and d) LC4

5.7.3.2 Potentiometers

The local buckling deformations of the component sections were recorded using potentiometers $L1$, $L2$, $L3$ and $L4$. The potentiometers were mounted on individual stands which were attached to the bottom endplate of the specimen with magnetic bases. The potentiometers were placed at the centre of the channels web or, in the case of geometry 1, at the centre of the flat plate sections, near the bottom of the column. For each set of twin specimens (i.e. specimens with the same built-up geometry and connector spacing), the location of the potentiometers relative to the bottom end of the column was chosen with the aim of capturing the maximum buckle amplitude based on the locally deformed shape of the components obtained from an FE model. Table 5.20 lists the vertical position of each potentiometer for each pair of twin specimens.

Table 5.20: Vertical location of potentiometers $L1$, $L2$, $L3$ and $L4$

Specimen	Vertical position (mm)			
	$L1$	$L2$	$L3$	$L4$
LC1-2	540	434	540	434
LC1-3	420	433	420	433
LC1-8	540	475	540	475
LC2-2	480	480	480	480
LC2-6	468	400	468	400
LC2-4	434	396	434	396
LC3-2	570	577	570	577
LC3-3	520	430	520	430
LC3-8	490	475	490	475
LC4-2	490	490	490	490
LC4-3	530	490	530	490
LC4-8	575	525	575	525

In addition, in the specimens with geometries 1, 2 and 3, potentiometers $W1$ and $W2$ were used to check for potential twisting of the specimen at the bottom end, as shown in Figure 5.73. The top end was not checked, as twisting of the top support was completely restrained by the cross-head of the testing machine. Readings from the potentiometers showed that no twisting occurred during the tests.

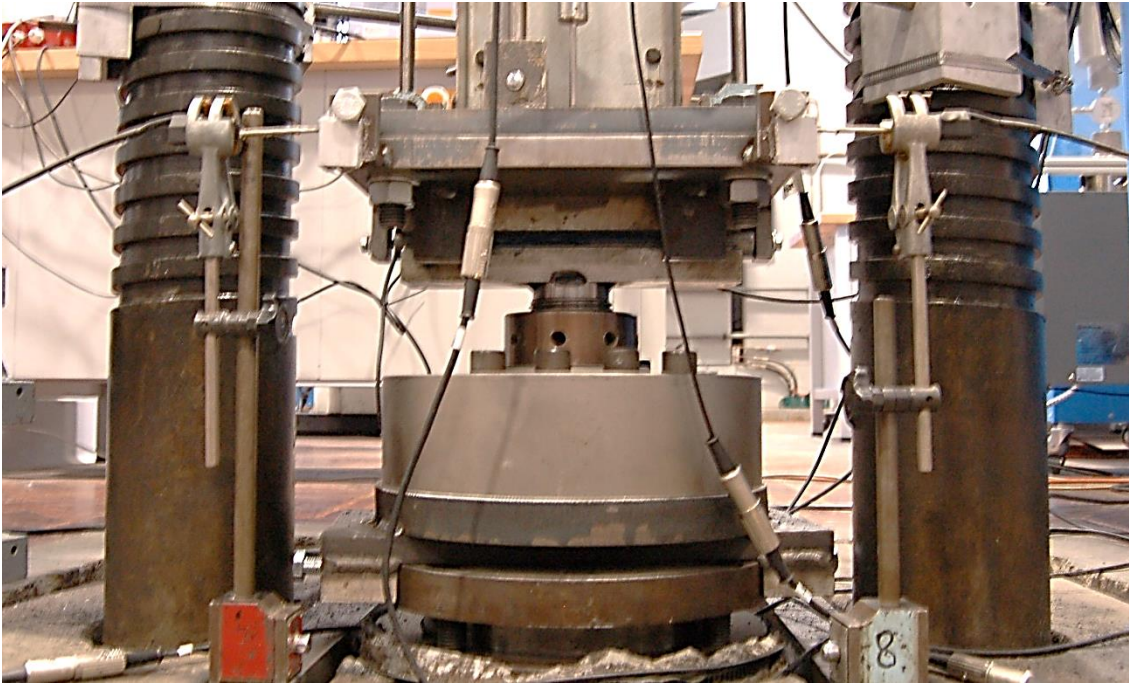


Figure 5.73: Location of potentiometers W-1 and W-2

Results obtained from FE models showed that the specimens with geometry 4 generated twisting forces at the supports of the same order of magnitude as the specimens with built-up geometry 3. Therefore, twisting deformations in these specimens were not measured. In geometry 4, the potentiometers were mounted on an aluminium frame, which was in contact with the cross-section at its four corners and rested on three supports which were glued to the corners of the cross-section, as illustrated in Figure 5.74. The frame was fixed to the supports by hand-tightening a screw at one of the supports. Therefore, the frame was able to remain in place when the specimens experienced cross-sectional deformations, while moving with the cross-section as a whole when global buckling occurred. The potentiometers were located at mid-height of the column. Potentiometer *D1* was used to record the deformations of one of the flanges of the lipped channel located on the tension side of the cross-section, while potentiometer *D2* was used to record the distortional buckling deformations of one of the flanges of the lipped channel located on the compression side. Figure 5.75 shows the aluminium frame with the potentiometers when mounted on specimen LC4-2b.

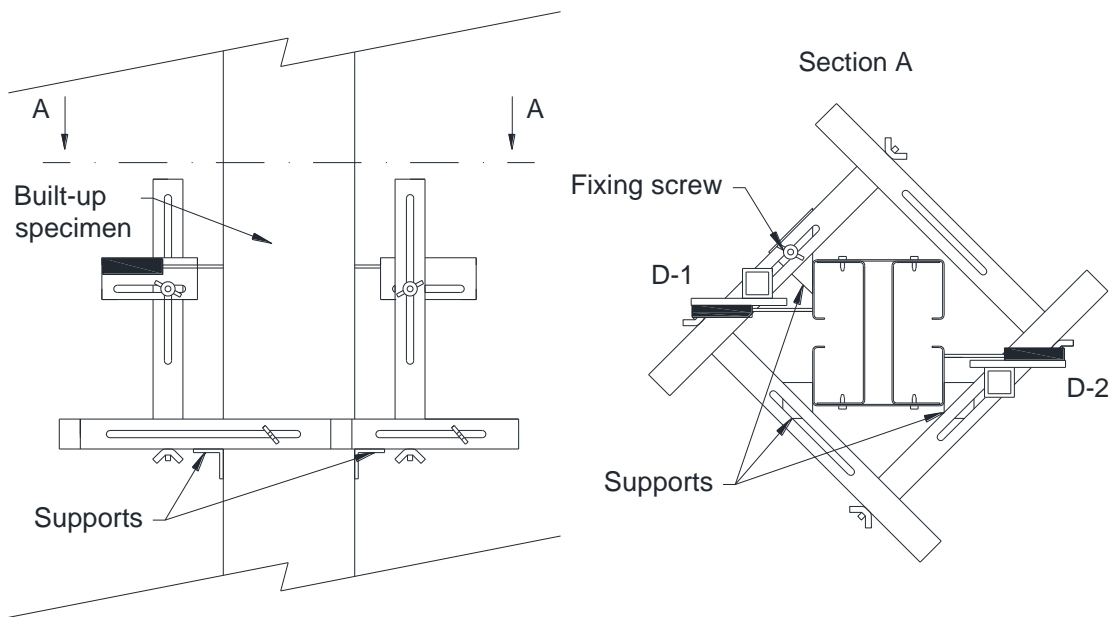


Figure 5.74: Schematic representation of the aluminium frame holding potentiometers *D1* and *D2*

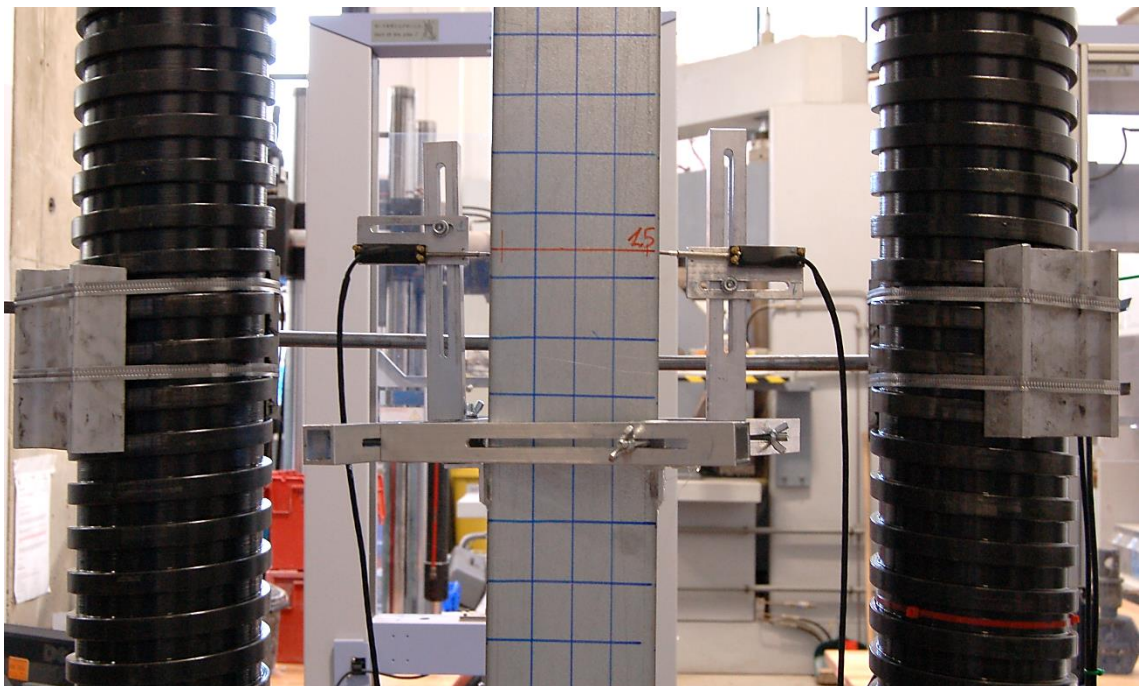


Figure 5.75: Aluminium frame attached to a specimen with geometry 4

5.7.3.3 Strain gauges

As global buckling and, in particular, the interaction of global and cross-sectional modes are sensitive to the presence of geometric imperfections and therefore also to the initial eccentricity of the applied load, all specimens tested with a load eccentricity of $L/1000$ were instrumented with four strain gauges at mid-height in order to verify the applied eccentricity, as illustrated in Figure 5.76. Figure 5.77 shows the strain gauge configuration used for each geometry. Strain gauges *SG1* and *SG2* were placed on the tension side of the cross-section, while strain gauges

SG3 and SG4 were located on the compression side. The strain gauge readings were also used to check whether the magnitude of the minor axis bending moments resulting from possible uneven contact along the supporting pin was small enough to be neglected.

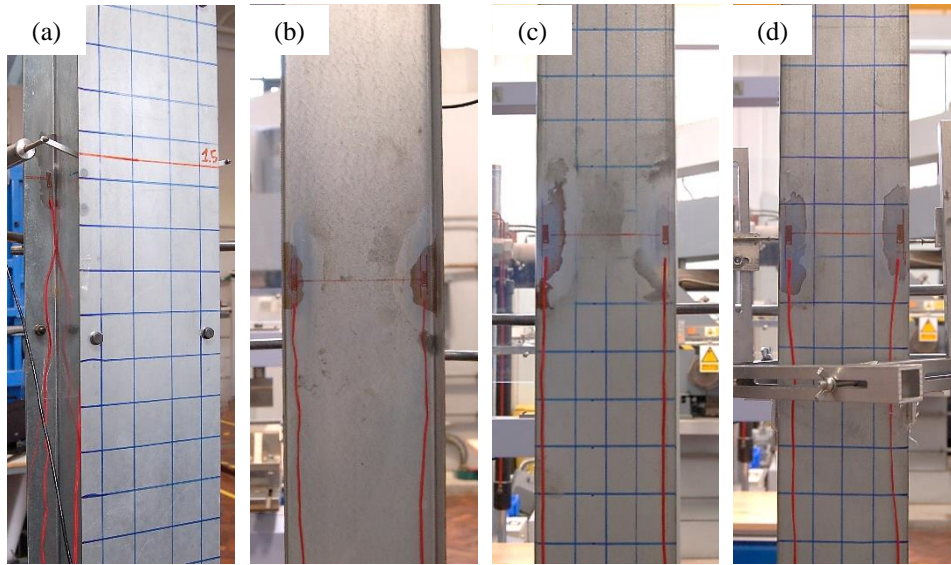


Figure 5.76: Location of strain gauges in a) LC1, b) LC2, c) LC3 and d) LC4

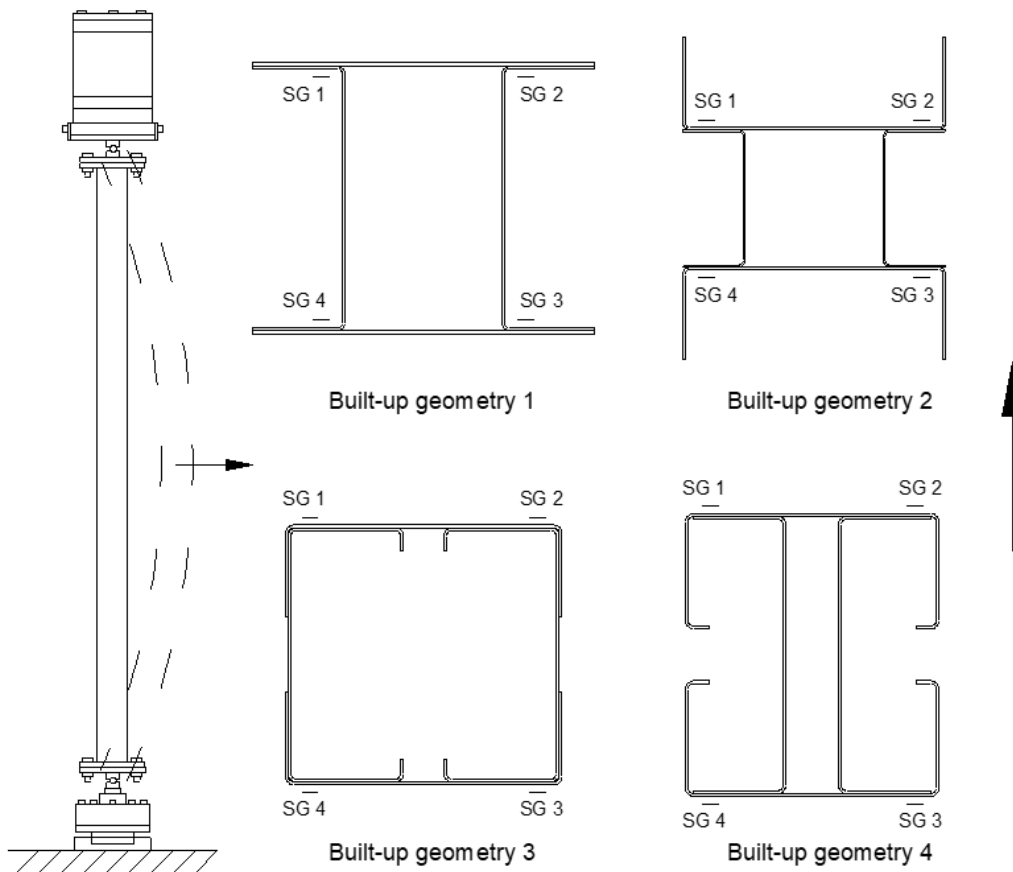


Figure 5.77: Strain gauge lay-out for each geometry

5.7.4 Test procedure

The specimens were tested while manually controlling the displacement rate at which the columns were compressed. The data were collected in a Cubus data acquisition system using a sampling rate of 1 Hz. The AMSLER testing machine used for the tests had a single piston actuator which was controlled by opening or closing two valves. In order to perform the test in a displacement controlled mode, a virtual channel was created in Cubus by differentiating the average readings obtained from LVDTs *B1* and *B2* with respect to the time to obtain the rate at which the specimen deformed axially. The valves controlling the actuator were then adjusted during the test to keep the displacement rate as close to 0.08 mm/min as possible. This resulted in approximate strain rates of 4.4×10^{-7} /s, 5.3×10^{-7} /s and 7.4×10^{-7} /s for the specimens with lengths of 3000 mm, 2500 mm and 1800 mm, respectively. In addition, the test was halted for 4 min slightly before the peak load was reached in order to eliminate strain rate dependent effects. After the peak load was reached, the displacement rate was increased. Figure 5.78 shows the displacement rate achieved for a representative test specimens.

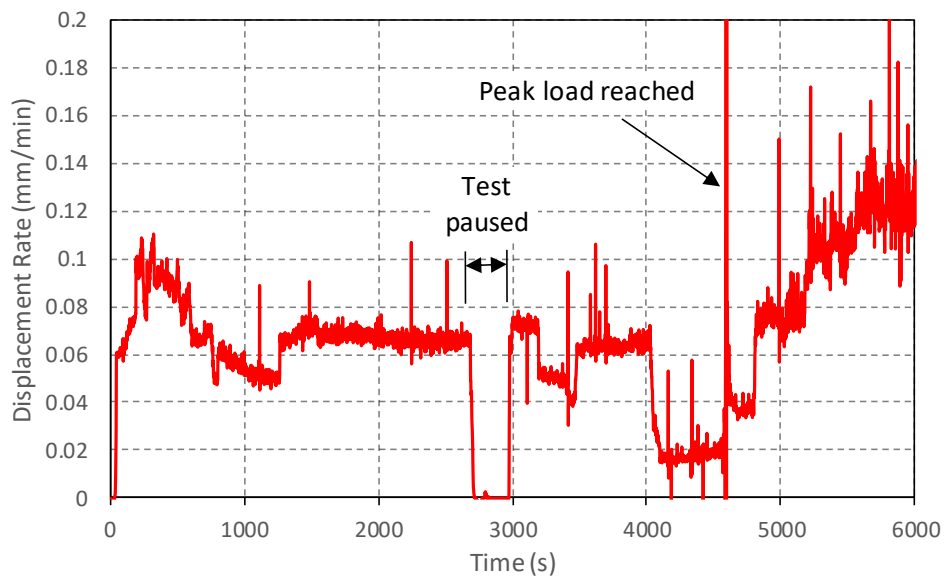


Figure 5.78: Displacement rate achieved in specimen LC1-8a

5.8. Test results

5.8.1 Strain gauge readings

Strain gauge readings obtained over the course of the test for representative columns with geometry 1, 2, 3 and 4 are shown in Figure 5.79, Figure 5.80, Figure 5.81 and Figure 5.82,

respectively. In these figures, compressive strains were taken as positive. All readings obtained from columns instrumented with strain gauges are included in Appendix K.

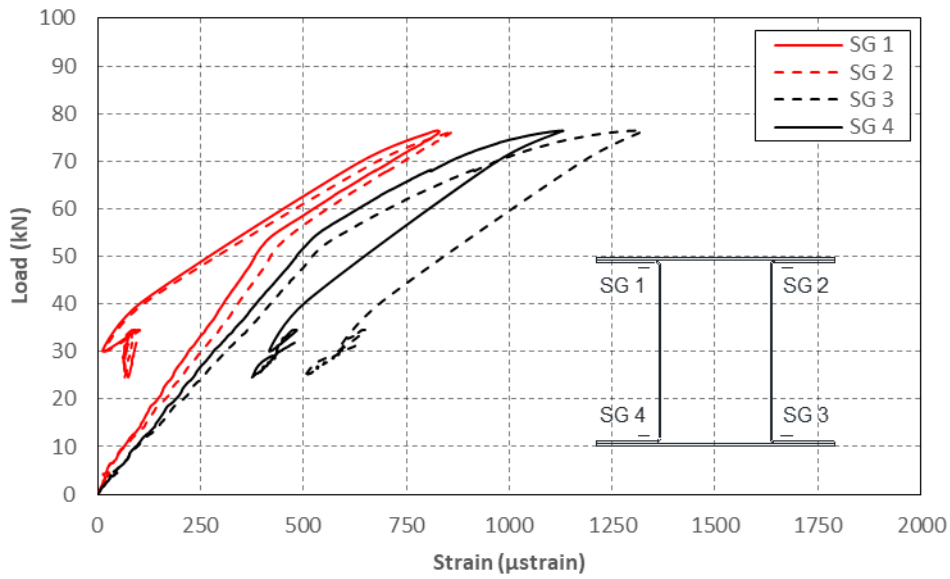


Figure 5.79: Axial load vs compressive strain in column LC1-2a

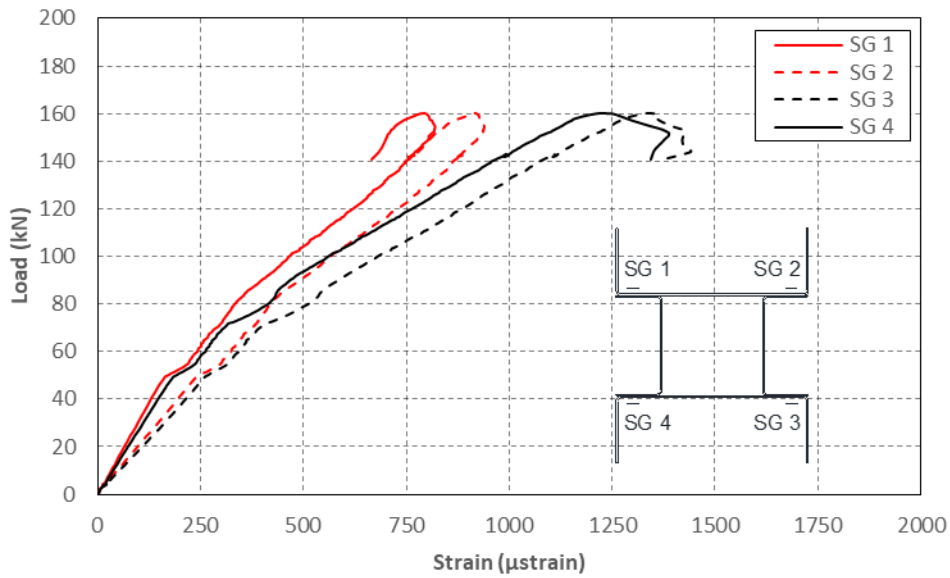


Figure 5.80: Axial load vs compressive strain in column LC2-2a

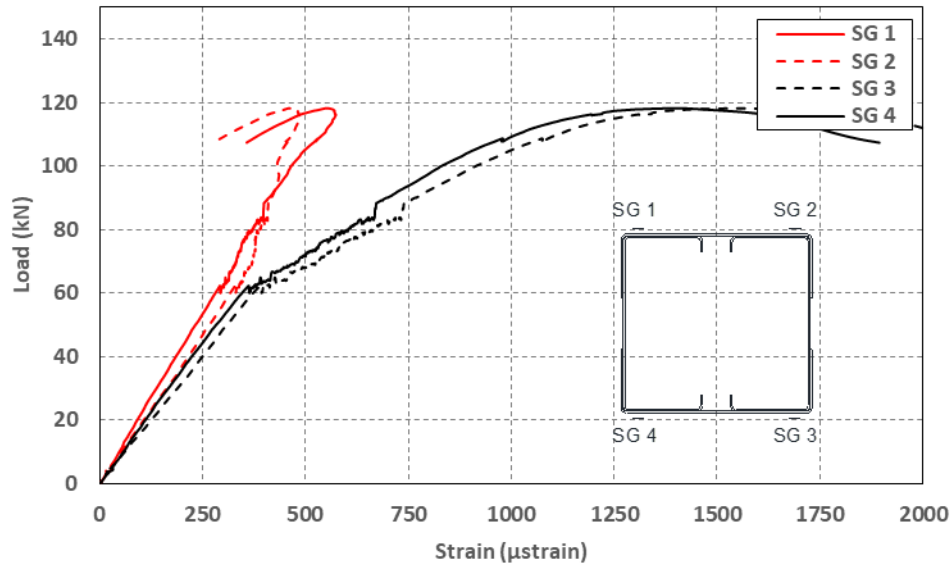


Figure 5.81: Axial load vs compressive strain in column LC3-2a

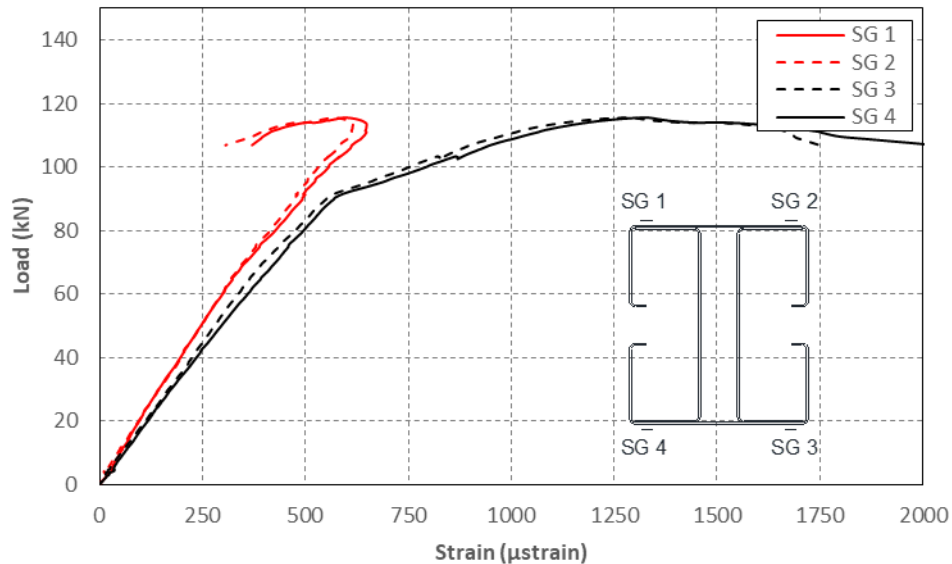


Figure 5.82: Axial load vs compressive strain in column LC4-2a

5.8.1.1 Minor axis bending

Due to possible uneven contact between the endplates of the columns and the platens of the testing machine, a small minor axis bending moment might have been introduced into the built-up specimens. Steel shims were placed between the column endplates and the hinge assemblies in order to reduce this unwanted bending moment. However, the introduction of a small bending moment during the test was deemed unavoidable.

In order to assess the effect of the minor axis bending moment on the stresses which developed in the components of the built-up geometry half of all columns were instrumented with strain gauges at mid-height. The stresses at the centre line of the webs of two channels located on opposite sides of the minor axis of the built-up geometries were calculated from the strain gauge

readings slightly before the channels started buckling in a local mode. In each built-up geometry the stresses at the centre line of the web of the channels located to the left and to the right of the minor axis (Figure 5.83) were determined using Eq. (5.48) and Eq. (5.49), respectively.

$$\sigma_{SG,ch,L} = E \left(\varepsilon_{avg} - \frac{(\varepsilon_R - \varepsilon_L) d_w}{2d_{SG,x}} \right) \quad (5.48)$$

$$\sigma_{SG,ch,R} = E \left(\varepsilon_{avg} + \frac{(\varepsilon_R - \varepsilon_L) d_w}{2d_{SG,x}} \right) \quad (5.49)$$

In the above equations E is the Young's modulus, taken as 203000 MPa, ε_L , ε_R and ε_{avg} are given by Eq. (5.50), Eq. (5.51) and Eq. (5.52), respectively, $d_{SG,x}$ is the distance between the centre lines of the strain gauges and d_w is the distance between the webs of the channels, as illustrated in Figure 5.83 for each geometry.

$$\varepsilon_L = \frac{(\varepsilon_{SG1} + \varepsilon_{SG4})}{2} \quad (5.50)$$

$$\varepsilon_R = \frac{(\varepsilon_{SG2} + \varepsilon_{SG3})}{2} \quad (5.51)$$

$$\varepsilon_{avg} = \frac{(\varepsilon_{SG1} + \varepsilon_{SG2} + \varepsilon_{SG3} + \varepsilon_{SG4})}{4} \quad (5.52)$$

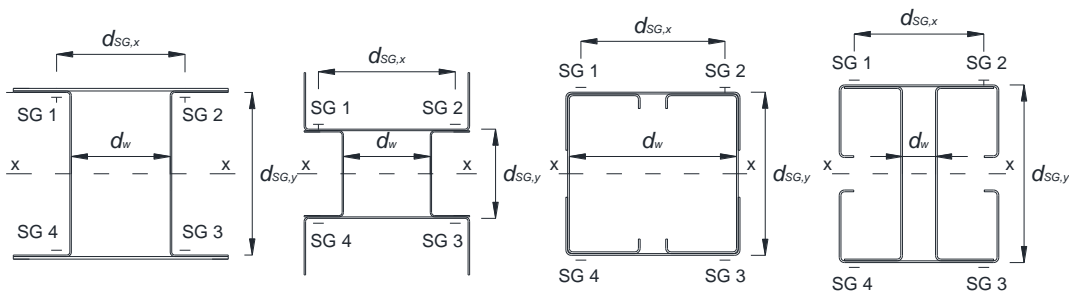


Figure 5.83: Strain gauge locations and distance between left and right channel webs

Table 5.21 lists the load at which the stresses were calculated, the average stress in the column obtained from the strain gauges readings ($\sigma_{SG,avg}$) and the average stress ($\sigma_{L,avg}$) obtained by dividing the column load over the measured cross-sectional area of the built-up column. The table also includes the stresses in the webs of the left channel ($\sigma_{SG,ch,L}$) and right channel ($\sigma_{SG,ch,R}$), their difference ($\Delta\sigma_{R-L}$), and an estimation of the importance of the minor axis bending stresses in the web of these channels, defined as:

$$\xi_{ch} = 100 \times \frac{|\sigma_{SG,ch} - \sigma_{SG,avg}|}{\sigma_{SG,avg}} \quad (5.53)$$

Table 5.21: Stress difference between left and right channel

Specimen	Load (kN)	$\sigma_{L,avg}$ (MPa)	$\sigma_{SG,avg}$ (MPa)	$\sigma_{SG,ch,L}$ (MPa)	$\sigma_{SG,ch,R}$ (MPa)	$\Delta\sigma_{R-L}$ (MPa)	ξ_{ch} (%)
LC1-2a	45	40	83	80	86	6	4
LC1-3a	45	40	75	73	77	3	2
LC1-8a	45	40	52	49	55	6	6
LC2-2a	75	67	78	72	83	11	7
LC2-6a	75	67	65	60	69	9	7
LC2-4a	75	68	69	64	74	10	7
LC3-2a	55	61	61	58	65	7	6
LC3-3a	55	61	64	60	67	8	6
LC3-8a	55	60	61	55	66	11	9
LC4-2a	55	60	60	60	59	1	0
LC4-3a	55	60	64	64	64	0	0
LC4-8a	55	60	61	60	61	1	1

Table 5.21 shows that, with the exception of columns LC1, good agreement was generally achieved between $\sigma_{L,avg}$ and $\sigma_{SG,avg}$. For columns LC2, the only exception occurred in column LC2-2a, for which a difference of 11 MPa was obtained between $\sigma_{L,avg}$ and $\sigma_{SG,avg}$. This larger discrepancy was preceded by a loss of linearity recorded by the strain gauges at a load of around 50 kN, as illustrated in Figure 5.80. However, up to this load the values obtained for $\sigma_{L,avg}$ and $\sigma_{SG,avg}$ agreed well and were 45 MPa and 44 MPa at a load of 50 kN, respectively. For columns LC3 and LC4, an almost perfect match between $\sigma_{L,avg}$ and $\sigma_{SG,avg}$ was obtained, with only columns LC3-3a and LC4-3a showing a slightly larger discrepancy. This slightly larger difference was believed to be due to stress concentrations captured by the strain gauges due to their close proximity to some of the connectors, which in these columns were located only a few millimetres away from the strain gauges.

Table 5.21 also shows that the difference between $\sigma_{SG,ch,L}$ and $\sigma_{SG,ch,R}$ was less than 11 MPa in all the columns instrumented with strain gauges, while the average difference between these stresses and the average stress in the built-up cross-section was around 5 %. This shows that the effect of the minor axis bending moment introduced into the test specimens was minor. However, the results listed in Table 5.21 should be taken into consideration when interpreting the readings obtained from the potentiometers, which were used to derive the critical buckling stresses in the components of the built-up specimens.

5.8.1.2 Eccentricity

Readings from the strain gauges were also used to assess the accuracy of the load eccentricity achieved by aligning the scribed lines on the supports and the endplates of the built-up columns, as described in Section 5.7.3.3.

Using the initial linear portion of the strain gauges readings, the initial eccentricity at mid-height ($e_{0,SG}$) was derived by computing the moment to axial load ratio in the cross-section at mid-height, while correcting for the lateral displacement experienced by the cross-section as loading progressed. This resulted in Eq. (5.54), which has been used in (Becque, 2008) for a similar purpose.

$$e_{0,SG} = \frac{2I_{built-up,xx} (\varepsilon_c - \varepsilon_t)}{A_{built-up} d_{SG,y} (\varepsilon_c + \varepsilon_t)} - \frac{G1 + G2}{2} \quad (5.54)$$

In the above equation $A_{built-up}$ and $I_{built-up,xx}$ are the cross-sectional area and the second moment of area about the major axis of the built-up geometry. $d_{SG,y}$ is the distance between the centrelines of the strain gauges, as indicated in Figure 5.83. $G1$ and $G2$ are the lateral deformations of the built-up specimen at mid-height given by LVDTs $G1$ and $G2$, and ε_c and ε_t are the average strains given by the strain gauges attached to the compression and tension side of the built-up geometry, calculated as:

$$\varepsilon_c = \frac{(\varepsilon_{SG3} + \varepsilon_{SG4})}{2} \quad (5.55)$$

$$\varepsilon_t = \frac{(\varepsilon_{SG1} + \varepsilon_{SG2})}{2} \quad (5.56)$$

In Eq. (5.54), $e_{0,SG}$ includes both the load eccentricity applied at the ends of the built-up column and the initial major axis global imperfection of the built-up specimen at mid-height $\delta_{global,M}$. Therefore, a direct assessment of the accuracy of the load eccentricity can be achieved by adding $\delta_{global,M}$ to the applied end eccentricity to obtain $e_{0,mid}$, and comparing it with $e_{0,SG}$. Figure 5.84 provides a graphical representation of this comparison for one of the specimens, while Table 5.22 compares $e_{0,mid}$ and $e_{0,SG}$ for all the specimens instrumented with strain gauges.

In Figure 5.84, after the specimen settles under the load, a region with a fairly constant eccentricity can be distinguished. The average eccentricity within this region was used to compute the values of $e_{0,SG}$ listed in Table 5.22.

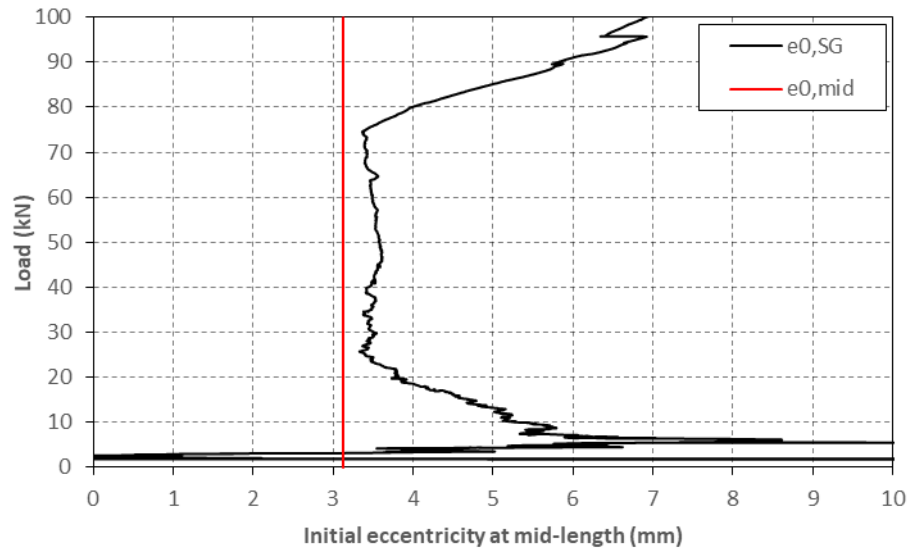


Figure 5.84: Axial load vs initial eccentricity at mid-height for column LC4-8a

Table 5.22: Accuracy assessment of load eccentricity

Specimens	$\delta_{global,M}$ (mm)	$e_{0,nom}$ (mm)	$e_{0,mid}$ (mm)	$e_{0,SG}$ (mm)	Difference (mm)
LC1-2a	-	3.0	-	-	-
LC1-3a	-	3.0	-	-	-
LC1-8a	-	3.0	-	3.13	-
LC2-2a	-0.03	2.5	2.47	3.01	0.54
LC2-6a	0.01	2.5	2.51	2.73	0.22
LC2-4a	-0.16	1.8	1.64	1.50	-0.14
LC3-2a	-0.26	3.0	2.75	3.08	0.33
LC3-3a	0.03	3.0	3.03	(2.02)	(-1.01)
LC3-8a	-0.38	3.0	2.62	2.85	0.23
LC4-2a	-0.07	3.0	2.93	3.01	0.08
LC4-3a	-0.02	3.0	2.99	(4.76)	(1.77)
LC4-8a	0.13	3.0	3.13	3.48	0.35

In Table 5.22, $\delta_{global,M}$ was calculated from the imperfections recorded along the top and bottom channels after they were assembled into their final configuration, as shown in Figure 5.83. For the specimens with built-up geometry 1, $e_{0,mid}$ was not calculated since the major axis global imperfection at mid-height of this specimens was not considered to be represented by the imperfections recorded along the plate sections due to their low flexural rigidity. Moreover, in columns LC1-2a and LC1-3a the plate sections displayed out-of-plane displacements between the connectors from the onset of loading.

Table 5.22 shows that in most cases a good agreement was achieved between the eccentricities calculated from the strain gauges readings and the ones obtained from adding the major axis global imperfection of the built-up specimen to the nominal eccentricity applied at the ends of the column. An exception occurred in specimens LC3-3a and LC4-3a, where a relatively large difference between $e_{0,SG}$ and $e_{0,mid}$ was obtained. As previously mentioned, the reason for these larger differences can be attributed to stress concentrations captured by the strain gauges due to their close proximity to a set of connectors which were also located at mid-height in these

specimens. With the exception of said specimens, the average difference between $e_{0,SG}$ and $e_{0,mid}$ was 0.27 mm, which proves the high accuracy of the procedure followed during this experimental programme when applying the load eccentricity to the test specimens.

5.8.2 Deformed shape

This section describes the way in which the different columns deformed during the test, with special emphasis on the different types of buckling modes observed in the components as well as in the built-up specimen as a whole.

In all columns, local buckling of the components was observed before the built-up specimen failed due to global flexural buckling. In column LC1 a global-type buckling of the plates in between connector points was also observed. As a result of the combined effects of the applied eccentricity and the initial imperfections lateral displacements of the column took place from the onset of loading. This introduced additional second order compressive stresses on one side of the column and superimposed tensile stresses on the opposite side (as stated before, here referred to as the '*compression*' and '*tension*' side of the built-up specimen, respectively). Consequently, in all tested columns, the magnitude of the buckles of the component located on the compression side of the built-up specimen was observed to be larger than the magnitude of the buckles formed in the symmetric component located on the tension side.

5.8.2.1 Built-up geometry 1

Columns with geometry 1 failed by global flexural buckling about the major axis of the built-up specimen which interacted with local buckling of the channels and a global-type buckling of the plate sections between connector points, while global flexural-torsional buckling of the channels between connectors was also observed in some columns. Columns with the same number of connectors exhibited the same initial buckled shape. However, development of the plastic yield line mechanism often occurred at different locations along the specimen. In all columns, yield lines formed in the web and the flange of the channels located on the compression side of the built-up specimen. The deformed shapes of all the columns with geometry 1, before and after yield line formation, are illustrated in Figure 5.85 and Figure 5.86, respectively.

In columns LC1-2 and LC1-3, the relatively large connector spacing caused the plate sections to buckle outward within each field between connectors in a global flexural mode with a half-wave length equal to half the distance between connectors. The channels, on the other hand, buckled in a local mode, generating 22 half-waves along the column, irrespective of the number of connectors.

In columns LC1-2, the distance between connectors was large enough (960 mm) to cause failure of the channels due to flexural-torsional buckling between connectors. In the lower field of the columns the channels rotated and translated towards the interior of the built-up cross-section, while in the central field the channels rotated and moved outwards. Flexural-torsional buckling of the channels prompted a sudden failure of the built-up specimen due to global flexural buckling. Upon localization of the deformation pattern the formation of yield lines symmetric with respect to the major axis of the column was observed.

In column LC1-3b, which was tested with a load eccentricity of $L/1500$ and had a connector spacing of 720 mm, the channels also failed by flexural-torsional buckling between connectors. However, in this case, both channels rotated and moved laterally in the same direction, while this direction alternated in successive fields. Upon failure of the channels, yield lines developed in the channels in the field where they moved towards the interior of the column. This meant that one of the channels developed its plastic mechanism in the field below the column mid-height, while in the other channel the plastic mechanism was formed in the field above mid-height. As the specimen continued deforming, a second plastic mechanism developed in each channel in the field where they moved outward. The tendency of the channels to twist and move laterally introduced some twisting into the already buckled plate sections, in the fields sharing the set of connectors located at mid-height (Figure 5.85d). However, the readings obtained from potentiometer $W1$ revealed no twisting of the built-up column as whole, with the specimen instead failing by global flexural buckling about the major axis. In column LC1-3a, which was tested with a larger load eccentricity ($L/1000$) than LC1-3b, but with an identical connector spacing, the channels only experienced local buckling, without any flexural-torsional deformations, as illustrated in Figure 5.85c. In this specimen the yield line mechanism, which developed slightly below mid-height, was perfectly symmetric about the major axis of the column. It is worth noting the difference in the plastic yield line mechanism which formed in the channels when they failed by interaction between local buckling and flexural-torsional buckling between connector points, as opposed to the one which formed when failure occurred due to interaction between local buckling of the channels and global flexural buckling of the built-up specimen. In the former, the plastic hinge mechanism developed mainly in the compression flange of the channels, as illustrated in Figure 5.87b for specimen LC1-3b, while in the latter, yield lines also spread across the web of the channels, as shown in Figure 5.87a for specimen LC1-3a

In columns LC1-8, the channels were also observed to initially buckle in a local mode with multiple half-wave lengths along the column. However, the precise number of buckles could not be determined. Due to the shorter distance between connectors in these columns the plate sections did not buckle with a half-wave length equal to half the distance between connectors. Rather the plate sections buckled outwards in every other field along the column and remained

almost straight in the adjacent fields, as the channels web prevented them from buckling inwards. The buckle half-wave length was longer than half the connector spacing, which required some localized deformations to take place around the connector points. It is also important to note that this discontinuous buckling pattern could only be possible if some slip between the plate and the channels occurred at the connector points. Interestingly, in both columns tested with eight intermediate connectors, the plate sections always remained straight in the top and bottom field, and consequently in the central field of the column. This is most likely due to a higher degree of fixity of the plates in the end fields with respect to their end rotations as a result of the fillet weld between the column and the endplates. In both columns, the post-peak deformations in the channels localized in fields where the plates initially buckled outward. In the case of column LC1-8a, the plastic deformations in each channel localized in different fields, namely in the field below the central field in one of the channels, and in the field above it in the other channel, as shown in Figure 5.85e. In column LC1-8b, on the other hand, a yield line mechanism symmetric with respect to the major axis of the column was formed, with the plastic mechanism in both channels developing in the second field from the bottom, as shown in Figure 5.85f.

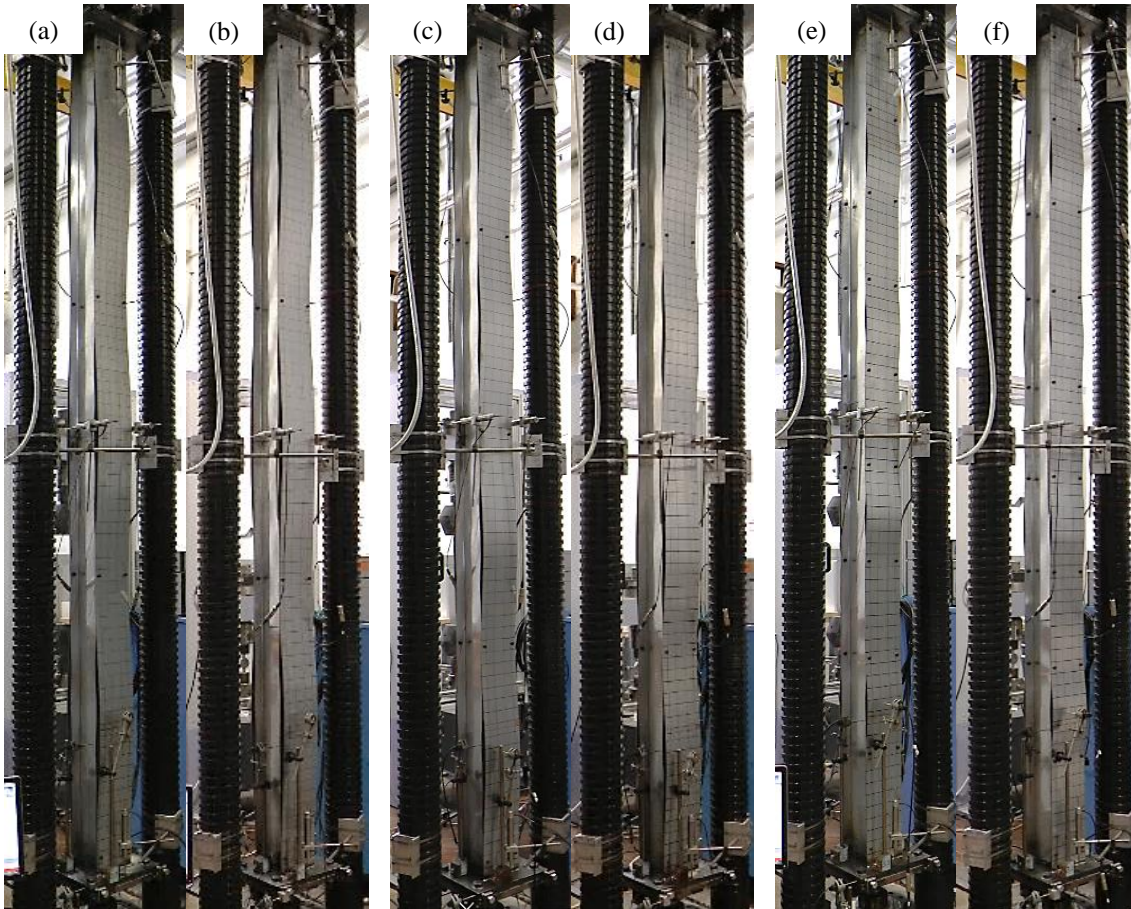


Figure 5.85: Deformed shape approaching ultimate load in a) LC1-2a, b) LC1-2b, c) LC1-3a, d) LC1-3b, e) LC1-8a, f) LC1-8b

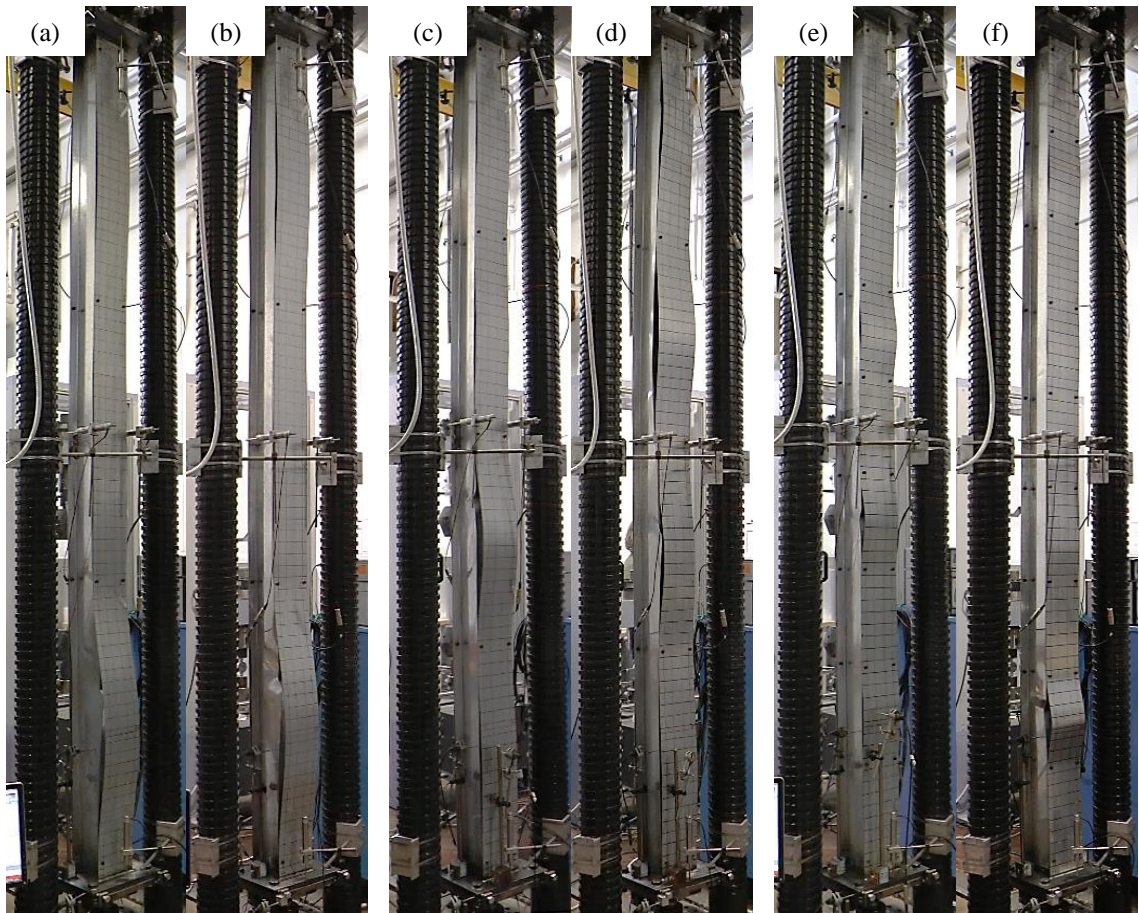


Figure 5.86: Final deformed shape at end of test in a) LC1-2a, b) LC1-2b, c) LC1-3a, d) LC1-3b, e) LC1-8a, f) LC1-8b

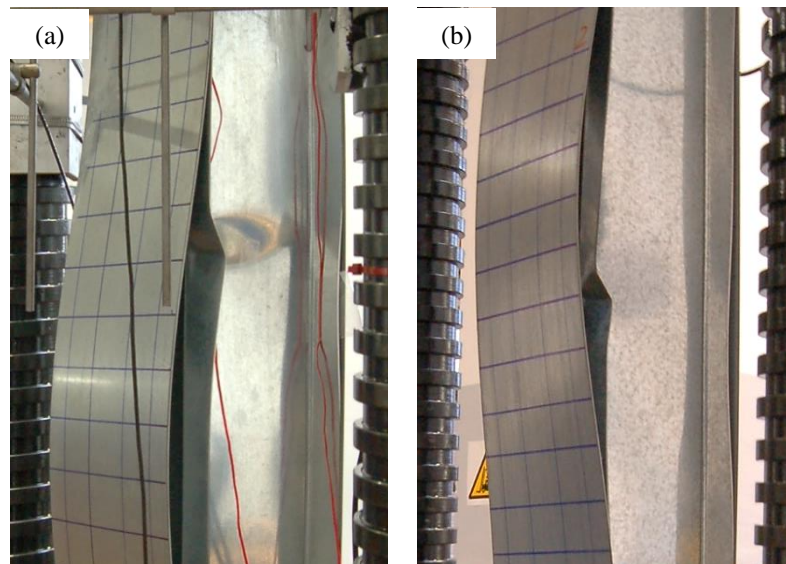


Figure 5.87: Plastic yield line mechanism in a) LC1-3a, b) LC1-3b

5.8.2.2 Built-up geometry 2

All columns with geometry 2 failed by interaction between global flexural buckling about the major axis of the built-up specimen and local buckling of the individual components. Multiple

regular local buckles were observed along the columns. A distortion of the outer channel flanges at each end of the column, caused by the localized temperature gradients during welding of the endplates (as described in Section 5.5), was noticeable before the test in all specimens of geometry 2 (Figure 5.16). These initial out-of-plane deformations were amplified as the specimens were loaded, even before the channels buckled locally. Also, in some columns, buckles with slightly larger amplitude were observed in the flanges of the outer channels on one side of the minor axis. This was attributed to the small, yet ineludible bending moments present about the minor axis of the built-up specimen.

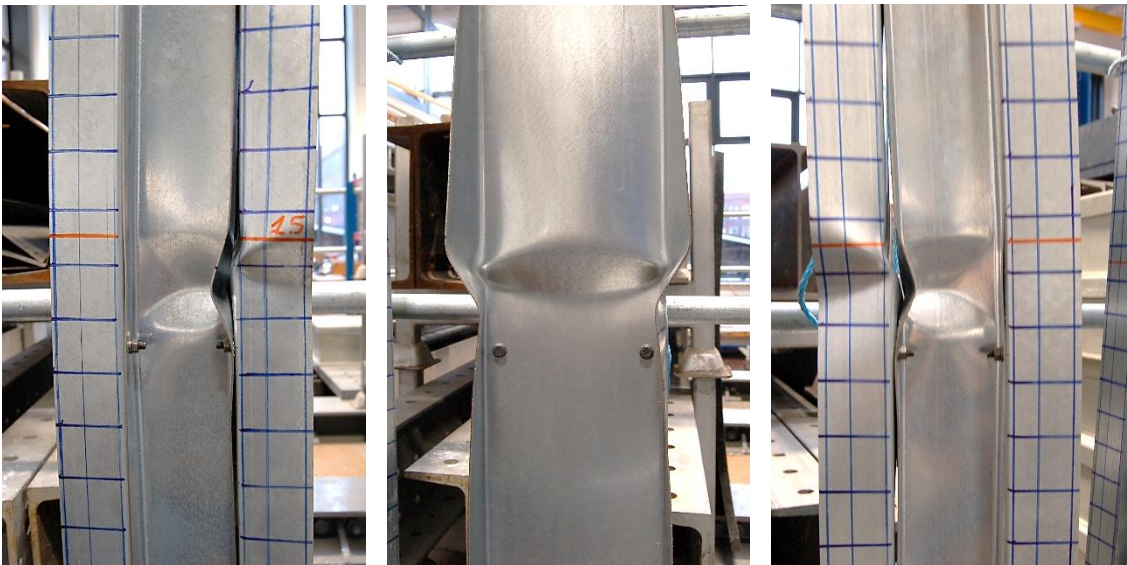


Figure 5.88: Plastic yield line mechanism in LC2-6b

In all columns yield lines formed in the outer channel located on the compression side of the built-up specimen, and in the web and the most compressed flange of the inner channels. This yield line mechanism was identical in most of the columns and is shown in Figure 5.88 for column LC2-6b after the load was removed. The deformed shapes before and after the ultimate capacity was reached are illustrated in Figure 5.89 and Figure 5.90, respectively, for all columns with built-up geometry 2.

In columns LC2-2, with two rows of intermediate connectors, the outer channels were forced to buckle mainly outwards due to the presence of the inner channels, displaying four half-waves between the connectors in the central field. This could be expected since the natural buckle half-wave length of the outer channels was calculated to be 170 mm, and this was close to the 200 mm resulting from fitting four half-waves between connector points. In the adjacent fields, on the other hand, the outer channels accommodated six half-waves, with the buckle closest to the end of the column being noticeably shorter than the others. This is attributed to the initial distortion of the outer channel flanges. The remaining buckles in the top and bottom fields had a

buckle half-wave length somewhere between 130 mm and 200 mm, which was still close to their natural buckle half-wave length. The inner channels in these columns did not buckle, as illustrated in Figure 5.89a and Figure 5.89b. After the ultimate capacity was reached, column LC2-2a formed a yield line mechanism in the vicinity of the upper set of connectors in the central field, as illustrated in Figure 5.90a. In column LC2-2b, a yield line mechanism was first formed in the outer channel around mid-height (Figure 5.90b) and in one of the inner channels close to the lower set of connectors in the central field. As the column was further compressed, a yield line mechanism also formed in the other inner channel, next to the plastic hinge previously formed in the outer channel. This sequential formation of yield lines in the built-up specimen was reflected in a loss of stiffness in the form of a descending step in the load-axial deformation curve (Figure 5.108).

Columns LC2-6 and LC2-4 had different column lengths, but similar connector spacings, namely 340 mm and 336 mm, respectively. Similarly to columns LC2-2, the inner channels forced the outer channels to buckle outwards. However, in columns LC2-4, some minor inwards out-of-plane displacements were recorded in the web of the outer channels by the potentiometers which were located around 40 mm above a cross-section containing connectors. This was attributed to a slight rotation of the flanges of the inner channels which were forced to open slightly in order to accommodate the inward buckles of the outer channels web. Due to the reduced connector spacing, the outer channels buckled with a half-wave length equal to half the distance between connectors, as shown in Figure 5.89c-f, which virtually coincided with their natural local buckle half-wave length.

In columns LC2-6, the initial distortion of the outer channel flanges resulted in the buckles in the top and bottom field having a slightly larger amplitude than the ones in the other fields. The amplitude of these initial imperfections was amplified from the beginning of the test. As a result of the reduced connector spacing in these columns, the interaction between the different components was more pronounced and triggered local buckling in the most compressed flange of the inner channels at around the point where the column reached its ultimate capacity, something which was not observed in the columns with larger connector spacing. The most compressed flange of these channels was forced to buckle towards the inside of the channel due to the presence of the outer channel webs and displayed four half-waves between connectors, as illustrated in Figure 5.89c and Figure 5.89d. After the ultimate capacity was reached, both columns developed a yield line mechanism around mid-height which was perfectly symmetric with respect to the major axis of the column, as shown in Figure 5.90c and Figure 5.90d, respectively.

In columns LC2-4, the initial distortion of the outer channel flanges was more pronounced than in columns LC2-6. As a result of this, the flanges of the outer channels buckled displaying four half-waves between connectors in one of the fields next to the column ends, while in all the

other fields only two half-waves were formed. In both columns, the plastic deformations localized in the end field located on the compression side of the built-up specimen where the four half-waves had previously formed, as shown in Figure 5.90e and Figure 5.90f. This resulted in premature failure, especially in column LC2-4a, where some twisting of the bottom endplate (by around 0.8°) was also recorded before the ultimate capacity of the specimen was reached. In this specimen, the plastic mechanism formed before the most compressed flange of the inner channels could buckle in a local mode, as illustrated in Figure 5.89e and Figure 5.90e. In column LC2-4b, on the other hand, the most compressed flange of the inner channels buckled just before the yield line mechanism localized at the top end of the column, as shown in Figure 5.89f and Figure 5.90f.

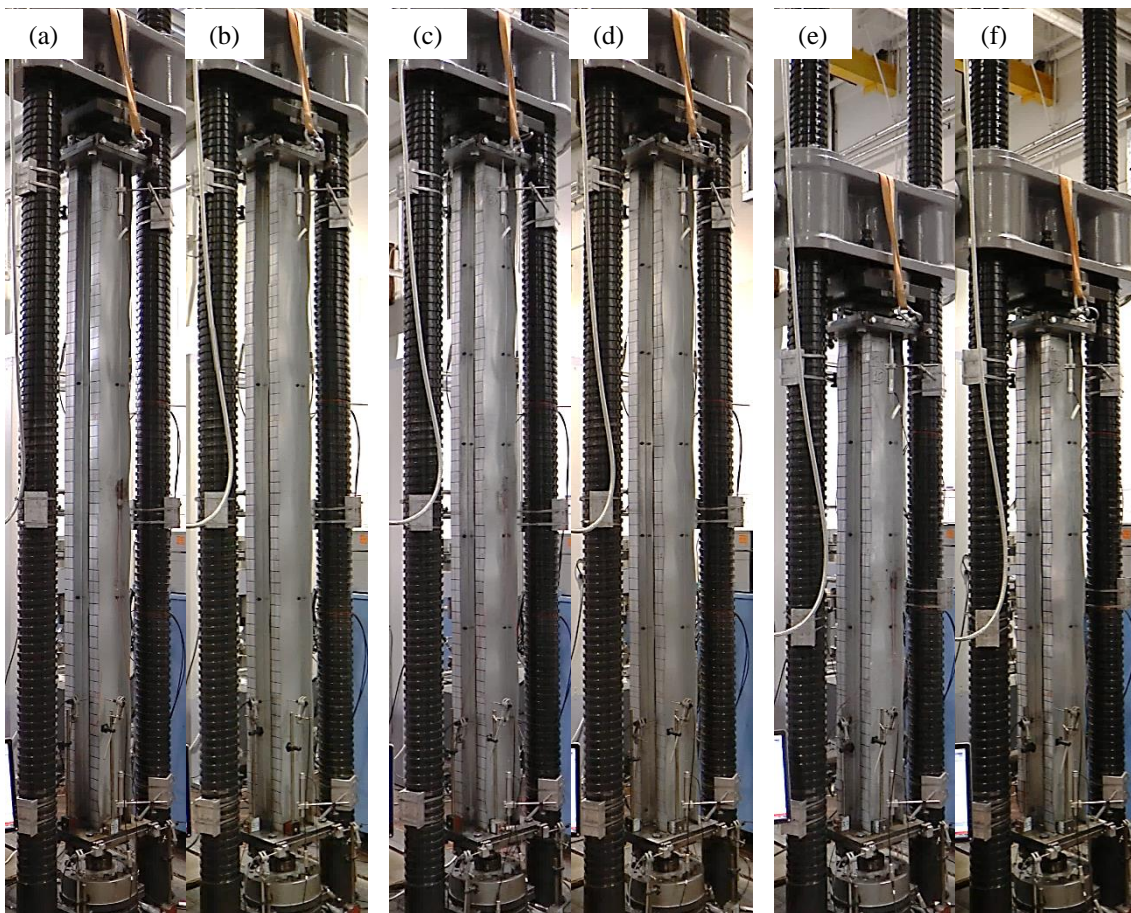


Figure 5.89: Deformed shape approaching ultimate load in a) LC2-2a, b) LC2-2b, c) LC2-6a, d) LC2-6b, e) LC2-4a, f) LC2-4b

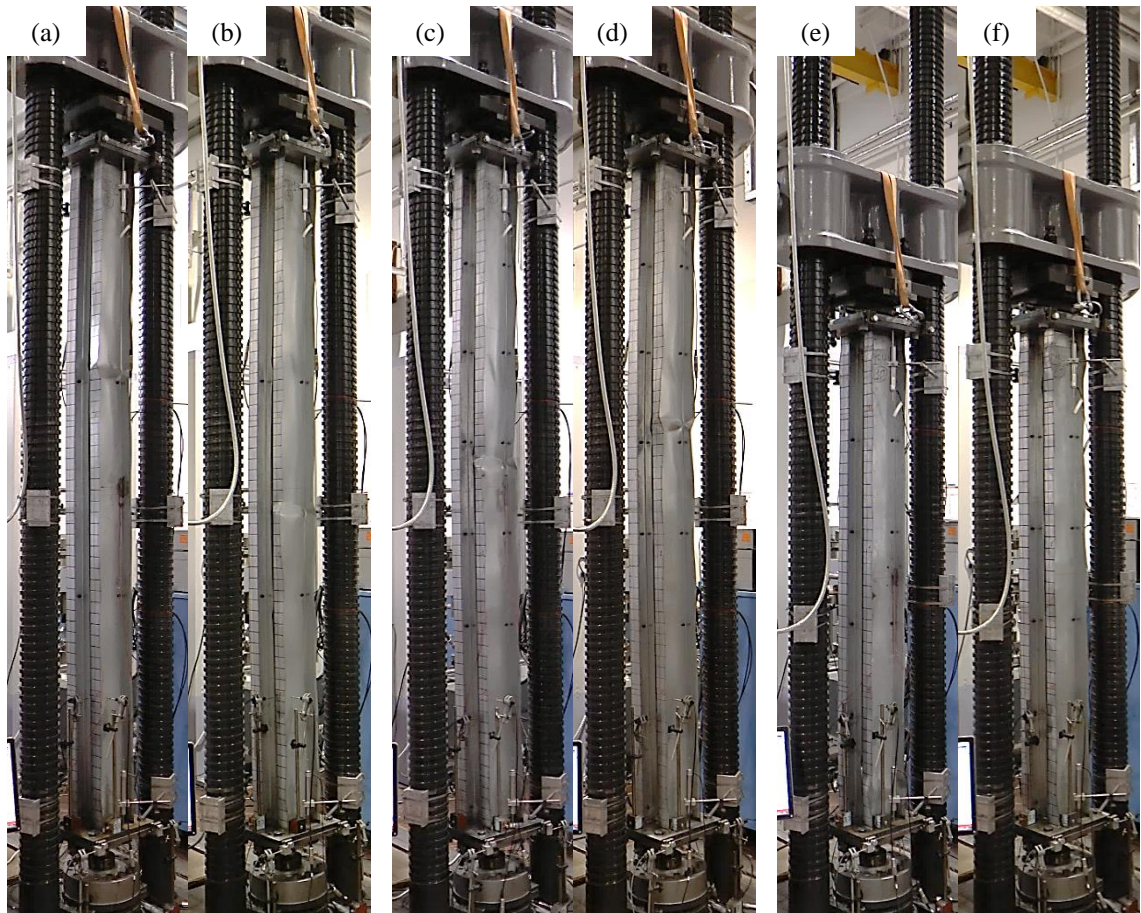


Figure 5.90: Final deformed shape at end of test in a) LC2-2a, b) LC2-2b, c) LC2-6a, d) LC2-6b, e) LC2-4a, f) LC2-4b

5.8.2.3 Built-up geometry 3

All columns with built-up geometry 3 failed by interaction between local buckling of the individual components and global flexural buckling about the major axis of the built-up specimen. Each component displayed multiple half-waves along the column height and for each pair of columns with the same number of intermediate connectors, a similar initial local buckling pattern was observed in each of the components, as illustrated in Figure 5.91. The plain channel located on the compression side of the built-up specimen always developed buckles of larger amplitude than the one located on the tension side. After reaching the ultimate capacity, a plastic yield line mechanism, almost perfectly symmetric with respect to the major axis of the specimen, was formed in each column, with yield lines appearing in the lipped channels, the plain channel located on the compression side of the built-up specimen and the flanges of the plain channel located on the tension side, as illustrated in Figure 5.92 for columns LC3-2b and LC3-8b. No yield lines were observed in the web of the plain channel located on the tension side of the built-up specimen. In most columns, the yield line mechanism was formed around mid-height. The only exception to this occurred in column LC3-3b, where the yield line mechanism formed near the top end of the column, as shown in Figure 5.93.

In columns LC3-2, with two intermediate sets of connectors, the lipped channels buckled with ten or twelve half-waves between connectors, with half-wave lengths ranging from 80 mm to 96 mm. The presence of the lipped channels forced the plain channels to buckle mainly outwards between connectors, with the cross-sections containing connectors always falling inside a concave buckle. Eight buckle half-waves were formed between connectors in the plain channels, with a half-wave length of around 120 mm. This buckling pattern could be expected, since the natural local buckle half-wave lengths of the lipped and plain channels were 90 mm and 130 mm, respectively.

In columns LC3-3, the connector spacing was reduced to 720 mm. In this case, the plain channels were again forced to buckle mostly outwards, generating six half-waves between connectors with a length of around 120 mm. The lipped channels typically buckled with eight half-waves between connectors, with a half-wave length equal to the natural local buckle half-wave length. However, in some regions of column LC3-3a, the lipped channels were seen to buckle sympathetically with the plain channels, generating only six half-waves between connectors.

In columns LC3-8, with a connector spacing of 320 mm, the plain and the lipped channels buckled generating either two or four half-waves between connectors. As in the columns with a larger connector spacing, the cross-sections containing connectors always fell within a concave buckle. However, as in some fields the plain channels were forced to accommodate two buckles between connectors, some of the concave buckles at the cross-sections containing connectors were slightly displaced, the cross-section with connectors thereby moving towards an inflection point in the local buckling pattern of the plain channels. Due to the different number of buckles accommodated between connectors, the plain and lipped channels generated buckles with half-wave lengths of either around 160 mm or around 80 mm. It is important to note that a half-wave length of 160 mm was preferable for the plain channels, since this is associated with a critical stress of 81 MPa, while buckles with a half-wave length of 80 mm are associated with a critical stress of 93 MPa. For the lipped channels on the other hand, buckles with a half-wave length of 80 mm were closer to their natural local buckle half-wave length of 90 mm. Although in some of the fields of column LC3-8a the lipped channels and plain channels buckled in sympathy, in other parts of the column this synchronisation was lost, as shown in Figure 5.94a. A more synchronous buckling pattern was observed in column LC3-8b, as illustrated in Figure 5.94b, where only a very small gap formed between the flanges of the plain channels and the web of the lipped channels as a result of local buckling of the components.

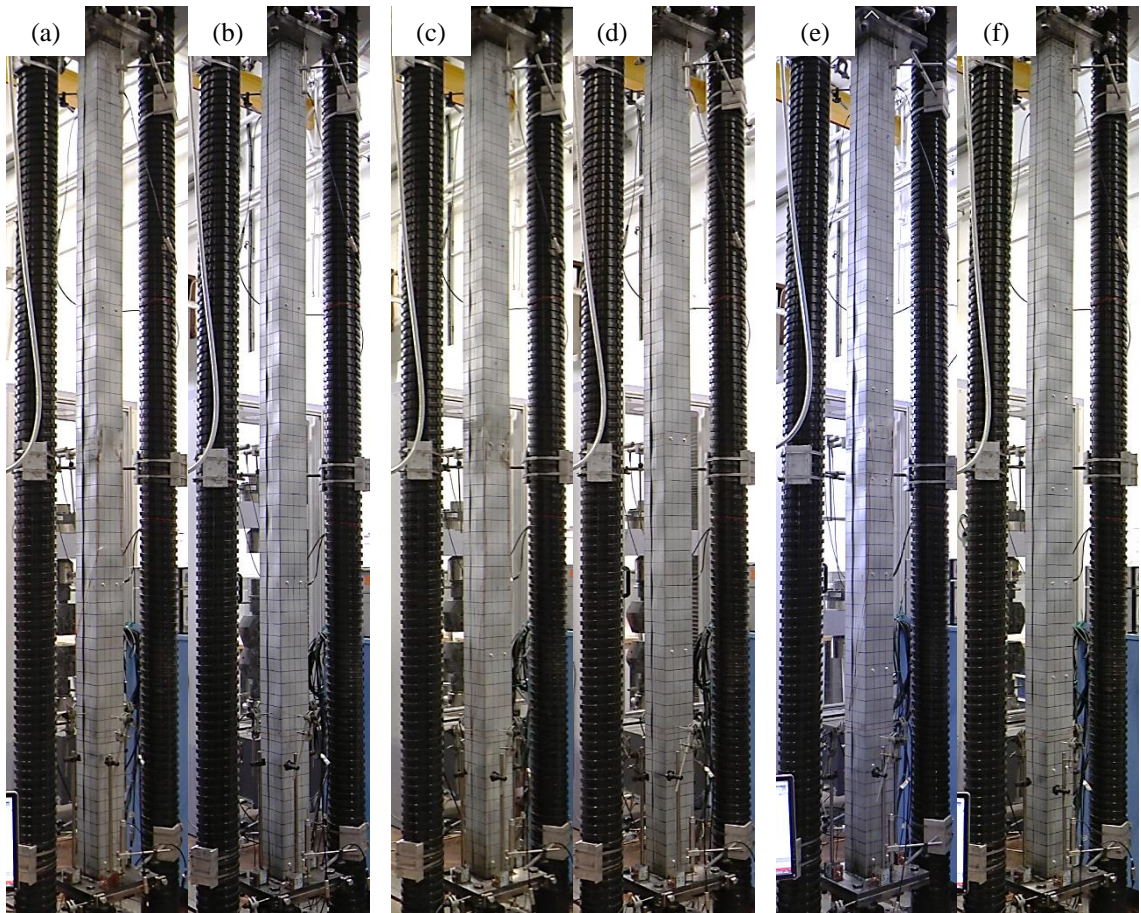


Figure 5.91: Deformed shape approaching ultimate load in a) LC3-2a, b) LC3-2b, c) LC3-3a, d) LC3-3b, e) LC3-8a, f) LC3-8b

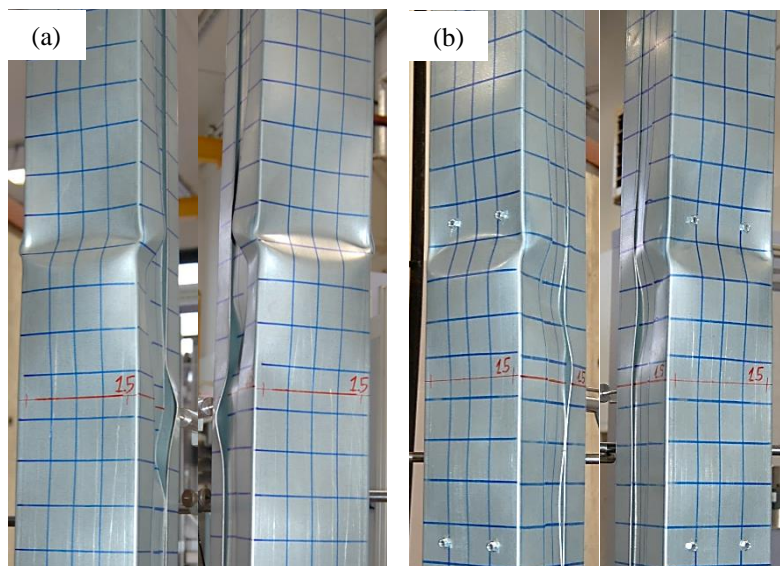


Figure 5.92: Yield line mechanism in a) LC3-2b, b) LC3-8b

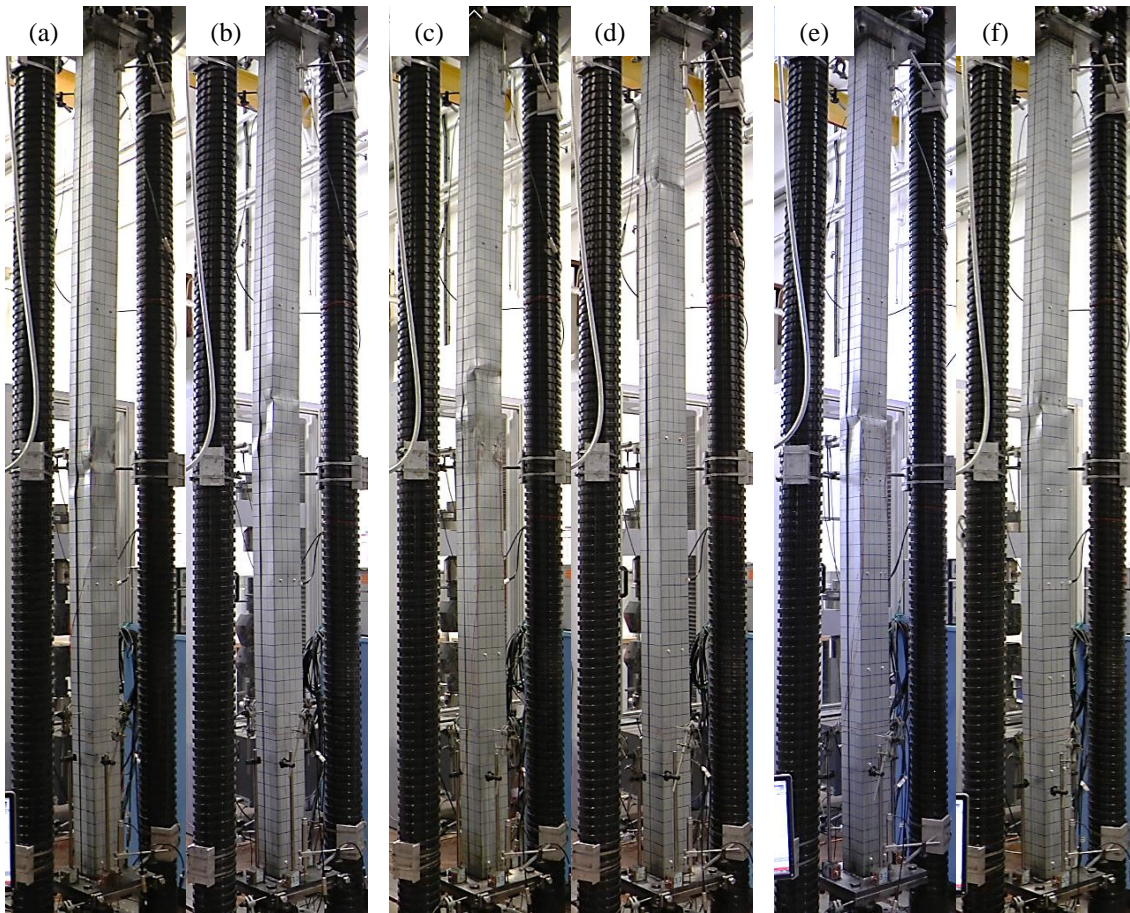


Figure 5.93: Final deformed shape at end of test in a) LC3-2a, b) LC3-2b, c) LC3-3a, d) LC3-3b, e) LC3-8a, f) LC3-8b

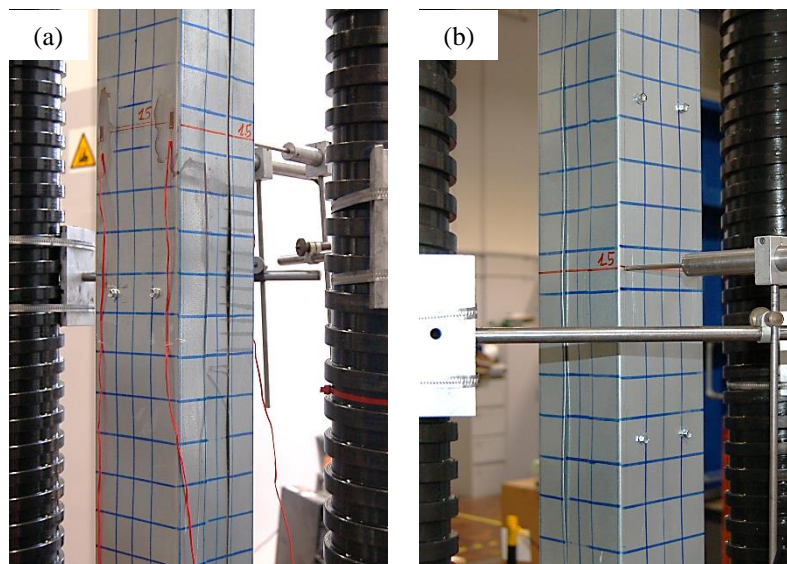


Figure 5.94: Synchronicity between the local buckling pattern of the lipped and plain channels in a) LC3-8a, b) LC3-8b

5.8.2.4 Built-up geometry 4

In all columns with geometry 4 the component sections buckled in a local mode before the column eventually failed by interaction of cross-sectional buckling and global flexural buckling

of the built-up specimen about the major axis. Columns with the same number of connectors showed an identical local buckling pattern in the lipped channels. The amplitude of the local buckling pattern was always more pronounced in the lipped channel located on the compression side of the built-up specimen and also developed with larger amplitude towards mid-height. The lipped channels were forced to buckle mostly outwards between connectors due to the presence of the plain channel webs. As a result, the cross-sections containing connectors always fell inside a concave buckle. The local buckle half-wave length in the lipped channels ranged from 80 mm to 90 mm in all columns. In columns LC4-2, this resulted in twelve half-waves between connectors in the central field and between ten and twelve in the adjacent fields, while in columns LC4-3 and LC4-8, the lipped channels generated eight and four half-waves between connectors, respectively.

Some minor interaction with the distortional mode could also be appreciated in the lipped channels of columns LC4-2 and LC4-3 before the peak load was reached. The distortional buckling pattern was again more visible in the lipped channel located on the compression side of the built-up specimen. Figure 5.95 shows the deformed shape of all columns with built-up geometry 4 just before the peak load was reached. Because the plain channels prevented the web of the lipped channels from buckling towards the inside of the column, the flanges of the lipped channels were forced to deform inwards when buckling distortionally. As the deformations localized and a yield line mechanism formed, the distortional buckling pattern became more evident. This was particularly the case in columns LC4-2b and LC4-3b, which were tested with a load eccentricity of $L/1500$, as illustrated in Figure 5.96a and Figure 5.96b, respectively.

Two distinctive yield line mechanisms were observed to form in the lipped channel located on the compression side of the column. The first yield line mechanism was dominated by the distortional mode and was spread over a much longer region along the channel, as illustrated in Figure 5.97a for column LC4-2b. The second mechanism was dominated by local buckling and resulted in a much more localized pattern, as shown in Figure 5.97b for columns LC4-8b. In both cases, due to the influence of global flexural buckling in the column the lipped channel located on the tension side of the built-up specimen did not form yield lines, while the plain channels only formed yield lines in the web and their most compressed flange. The yield line mechanism in one of the plain channels always formed at the same height as in the lipped channel. In the other plain channel it generally formed at a different location along the column, but always within a distance of less than 300 mm from the first one. In most columns the yield line mechanism which formed in the lipped channel located on the compression side was symmetric with respect to the major axis of the built-up specimen. The only exceptions to this occurred in columns LC4-2b and LC4-8a, where the mechanism was initially slightly more pronounced on one side of the column, as illustrated in Figure 5.97c for column LC4-8a. However, as the column continued to deform the yield line mechanisms became more

symmetric. The deformed shapes of all columns after the formation of the yield lines are shown in Figure 5.98.

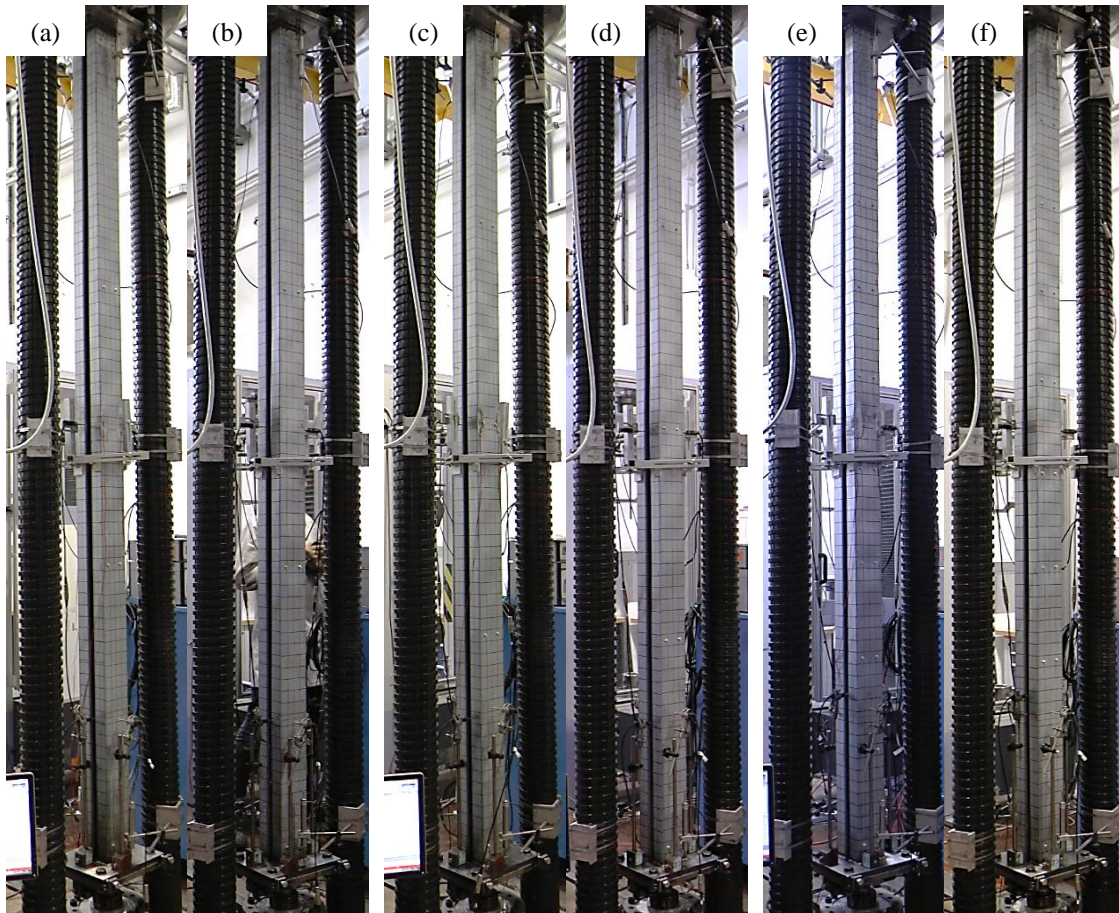


Figure 5.95: Deformed shape approaching ultimate load in a) LC4-2a, b) LC4-2b, c) LC4-3a, d) LC4-3b, e) LC4-8a, f) LC4-8b

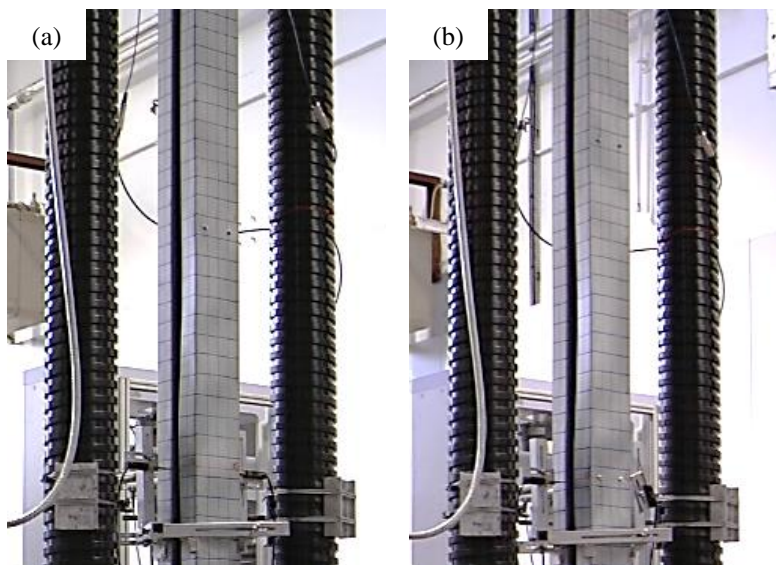


Figure 5.96: Distortional buckling in lipped channel on compression side as yield lines formed in a) LC4-2b, b) LC4-3b

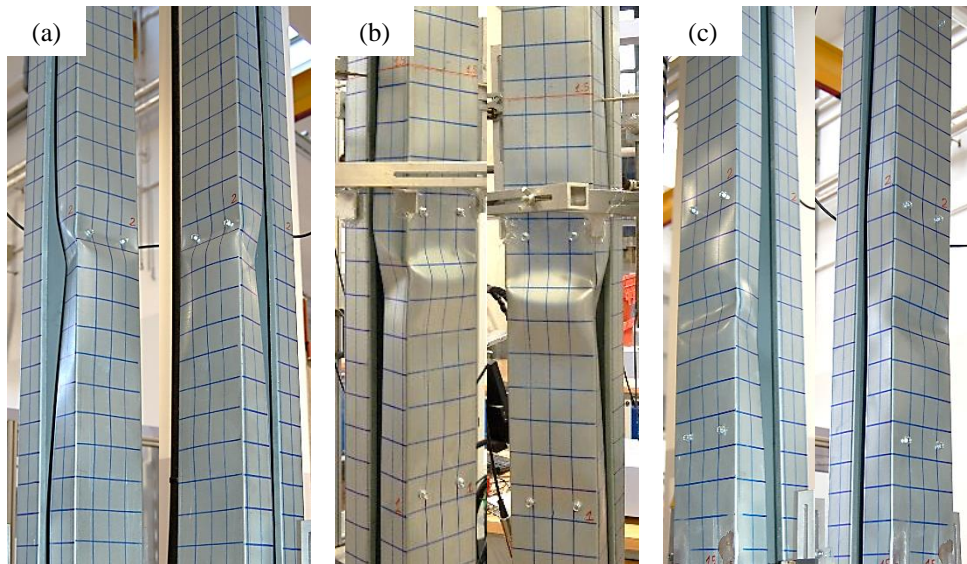


Figure 5.97: Yield line mechanism in column a) LC4-2b, b) LC4-8b, c) LC4-8a

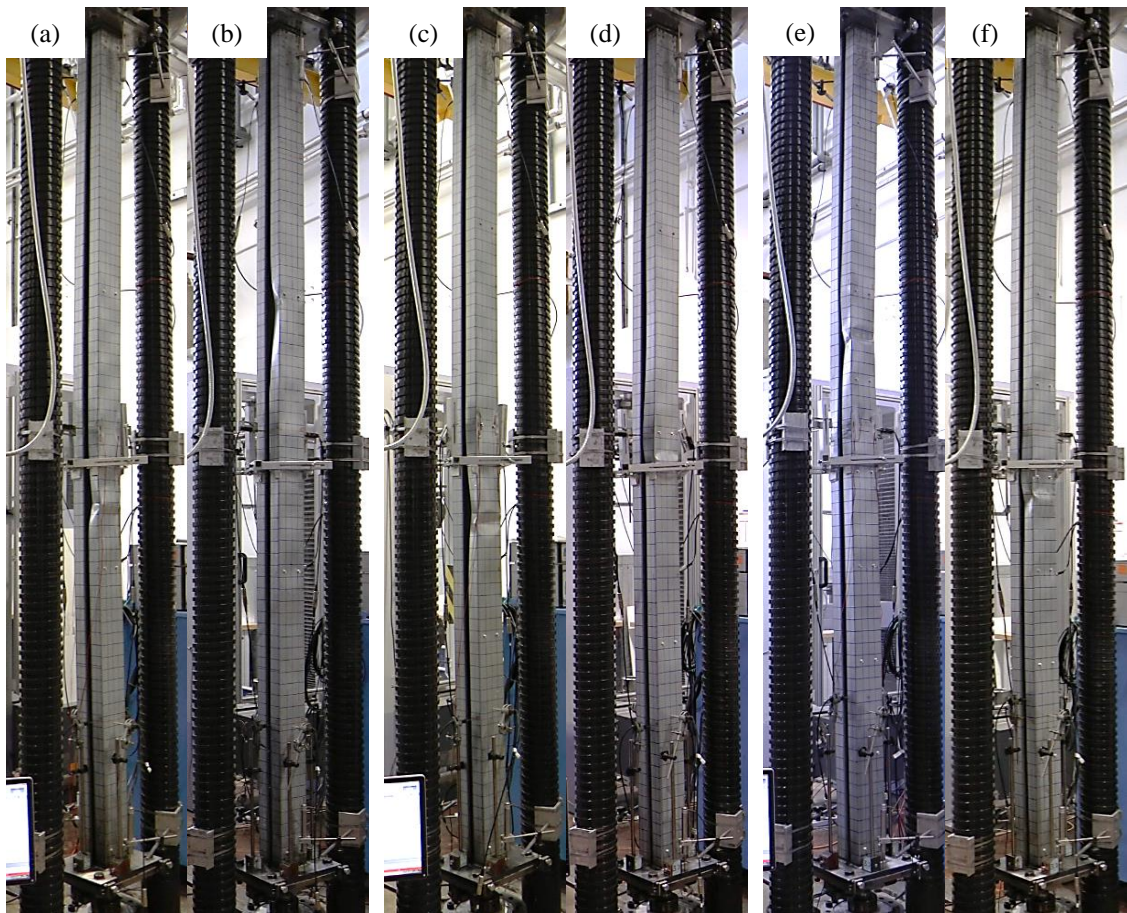


Figure 5.98: Final deformed shape at end of test in a) LC4-2a, b) LC4-2b, c) LC4-3a, d) LC4-3b, e) LC4-8a, f) LC4-8b

5.8.3 Critical buckling stresses

This section describes the way in which the critical buckling stresses of the various components of each built-up specimen were determined from the test results, and compares these buckling stresses against the theoretical predictions.

The experimentally derived buckling stresses were obtained while adopting certain assumptions, which are described in detail in Sections 3.8.3.1-3.8.3.4 for each geometry. The out-of-plane deformations of the components recorded by the potentiometers as a function of the load applied to the column are included in Appendix K for all columns.

The theoretical buckling stresses were calculated based on the measured cross-sectional dimensions (averaged over the two nominally identical components in the cross-section) and using the Young's modulus obtained from the flat tensile coupons. The individual components were considered in isolation and the buckle half-wave length observed during the test was adopted. The CUFSM 4.05 software (Schafer, 2006) was used to obtain the critical buckling stresses of the channels, while Eq. (5.57) was used to determine the critical buckling stresses of the plate sections in columns LC1.

$$\sigma_{cr} = \frac{\pi^2 E t^2}{12 L_p^2} \quad (5.57)$$

where E is the Young's modulus, t is the average measured thickness of the two plate sections in the column and L_p is the buckle half-wave length.

The experimentally derived and the theoretical buckling stresses of the component sections are listed in Table 5.23, Table 5.24, Table 5.25 and Table 5.26 for built-up geometries 1, 2, 3 and 4, respectively. For the sake of comparison, the tables also include the natural local buckling stress of the isolated channels, taken as the minimum in the signature curve corresponding to the local buckling mode.

5.8.3.1 Built-up geometry 1

In the columns with geometry 1 the plate sections buckled in a flexural mode between connectors before local buckling of the channels occurred. Under the assumption that the load was uniformly distributed over each component of the built-up cross-section, the buckling stress of the plate sections was thus obtained by dividing the column load over the total area of the built-up section. The buckling stress of the channels, on the other hand, was estimated from the recorded load by considering that the global flexural buckling mode does not have any post-buckling capacity and that the plate sections were therefore unable to carry any load increment after they buckled. This is described in more detail in Section 3.8.3 of Chapter 3.

The potentiometers consistently recorded that the plate sections located on the compression side of the built-up specimen buckled slightly before the plate sections located on the tension side, while the channels in most columns were recorded to buckle at the same time, as illustrated in Figure 5.99 for column LC1-2b. The critical buckling stress of the plate sections was taken as the average value of both plates.

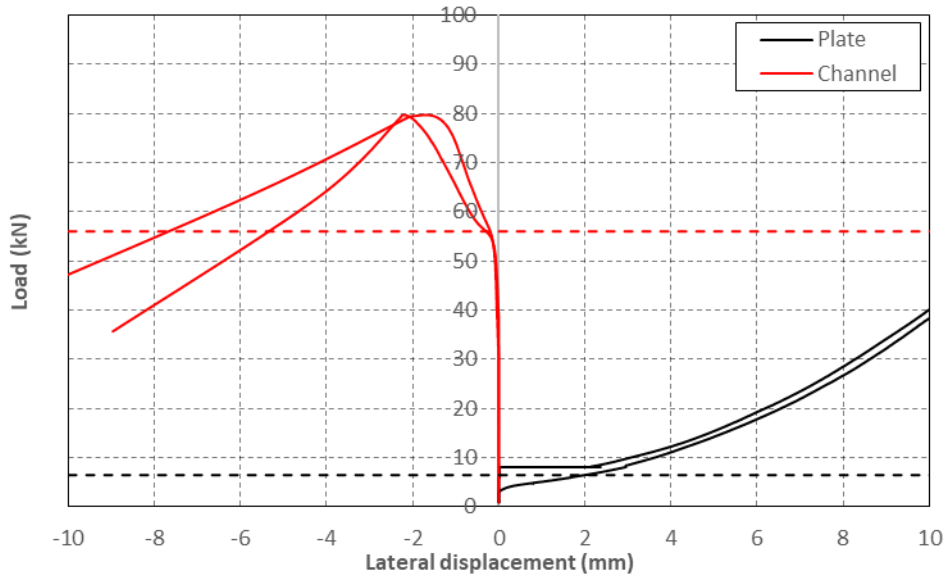


Figure 5.99: Axial load vs lateral displacements of LC1-2b

The theoretical and experimental buckling stresses of the plates and the channels are listed in Table 5.23, together with the buckling half-wave length observed during the test. Since the buckle half-wave length of the plate sections could not be accurately determined from the test, an upper and lower bound was defined. The upper bound corresponded to a half-wave length equal to half the distance between the connectors, and the lower bound corresponded to a half-wave length equal to the connector spacing.

In columns LC1-2 and LC1-3 the plate sections were seen to buckle outwards between connectors in each field along the column with a half-wave closer to the upper bound value. The plates were also seen to buckle in the top field first, where no potentiometer was present to record the out-of-plane deformations. This may explain why for these columns the experimentally derived buckling stresses of the plates were larger than the theoretical upper bound. In columns LC1-8, which had a connector spacing of 320 mm, the plate sections were seen to buckle in every other field with a buckle half-wave length slightly larger than half the distance between connectors. This was confirmed by the measured buckling stress of 23 MPa, which corresponds to a half-wave length of 170 mm (which is indeed slightly larger than half the distance between connectors).

The experimentally derived buckling stresses of the channels, on the other hand, were only around 8 % larger than the theoretically predicted values for columns LC1-2 and LC1-3, which virtually coincided with the natural local buckling stress of the channel, while for columns LC1-8 they were 11 % larger than the natural local buckling stress.

Table 5.23: Buckling stresses of the different components of geometry 1

Column	Min. theoretical buckling stress (MPa)	Half-wave length observed during tests (mm)			Theoretical buckling stress (MPa)			Buckling stress from test (MPa)	
		Channel	Channel	Plate		Channel	Plate		Channel
	Lower			Upper	Lower		Upper		
LC1-2a	93	131	960	480	93	1	3	99	6
LC1-2b	91	131	960	480	91	1	3	98	5
LC1-3a	92	131	720	360	92	1	5	97	8
LC1-3b	91	131	720	360	91	1	5	101	8
LC1-8a	93	-	320	160	-	6	25	100	23
LC1-8b	92	-	320	160	-	6	25	106	23

5.8.3.2 Built-up geometry 2

In the columns with built-up geometry 2 the outer channels buckled in a local mode before the inner channels. Since local buckling has a significant, yet not easily quantifiable, post-buckling load-bearing capacity, only the critical buckling stress of the outer channels was determined from the experimental results. This critical stress was obtained assuming that, prior to buckling, the load was uniformly distributed over the built-up cross-section. Thus, the load in the column at which buckling was observed was divided over the total cross-sectional area of the column.

In columns LC2-2 and LC2-6, with a length of 2.5 m, the outer channel located on the compression side of the built-up specimen was seen to buckle slightly before the outer channel located on the tension side, as shown in Figure 5.100 for column LC2-2a. Therefore, the critical buckling stress of these channels was taken as the average value of both channels. In columns LC2-4, with a shorter column length of 1.8 m, both outer channels buckled at approximately the same load, as shown in Figure 5.101 for columns LC2-4b.

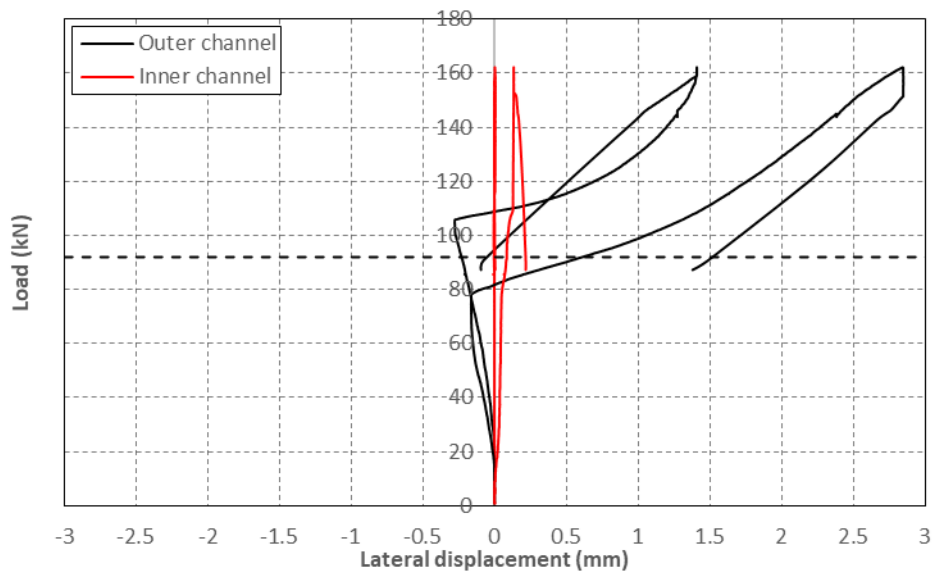


Figure 5.100: Axial load vs lateral displacements of LC2-2a

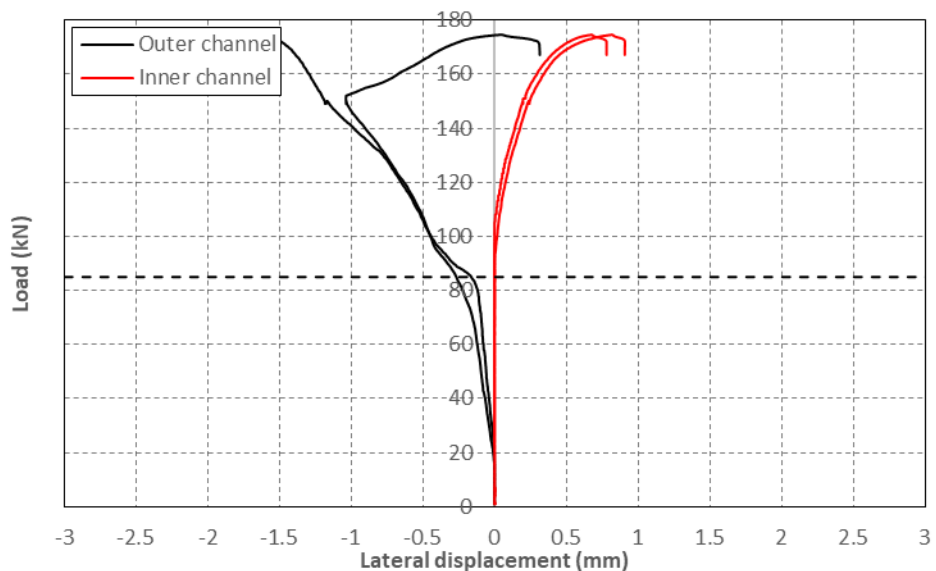


Figure 5.101: Axial load vs lateral displacements of LC2-4b

Table 5.24 shows the theoretical critical buckling stresses of the inner and outer channels, as well as their half-wave lengths observed from the tests and the buckling stresses of the outer channels obtained from the tests. The table shows that the buckling stresses of the outer channels obtained from the tests were larger than the theoretical predictions in all columns, with the difference being slightly affected by the connector spacing. In columns LC2-2 and LC2-6, with a column length of 2.5 m and connector spacings of 793 mm and 340 mm, respectively, the experimentally derived buckling stresses were around 20 % larger than the predicted values. In columns LC2-4, on the other hand, with a column length of 1.8 m and a connector spacing of 336 mm, a more significant difference of around 34 % was obtained. Table 5.24 also shows that, despite the fact that in most columns the outer channels buckled with a half-wave length equal to the natural local buckle half-wave length, the stress at which the outer channels buckled was, on average, around 26 % larger than the natural local buckling stress of the unrestrained

channel. This shows that the outer channels received a significant amount of restraint from the inner channels against local buckling.

Table 5.24: Buckling stresses of the different components of geometry 2

Column	Min. theoretical buckling stress (MPa)		Half-wave length observed in tests (mm)		Theoretical buckling stress (MPa)		Buckling stress from test (MPa) ²	
	Inner Channel	Outer Channel	Inner Channel	Outer Channel	Inner Channel	Outer Channel	Inner Channel	Outer Channel
LC2-2a	182	64	-	198	-	66	-	83
LC2-2b	182	64	-	198	-	66	-	77
LC2-6a	183	64	85	170	187	64	-	74
LC2-6b	181	63	85	170	185	63	-	78
LC2-4a	183	59	-	168	-	59	-	83
LC2-4b	181	60	84	168	185	60	-	76

5.8.3.3 Built-up geometry 3

In columns LC3-2 and LC3-3, the plain channels buckled before the lipped channels, while in columns LC3-8 the components buckled at approximately the same time, as shown in Figure 5.102 and Figure 5.103 for columns LC3-2b and LC3-8a, respectively. Under the assumption that the load was evenly distributed over the built-up cross-section before the components buckled, the experimental buckling stresses of the lipped channels in columns LC3-8, as well as the experimental buckling stress of the plain channels in all columns were determined by dividing the load at which the components buckled over the total area of the cross-section.

Table 5.25 lists the theoretical and experimental critical buckling stresses of the lipped and plain channels. The theoretical critical stresses were calculated at the buckle half-wave lengths observed during the test, which are also included in the table. In some columns the components were seen to buckle with two different half-wave lengths, as previously explained in Section 5.8.2.3, and the stresses associated with each half-wave length are included in the table. The table shows that the plain channels were expected to buckle before the lipped channels in all the columns, as their theoretical buckling stresses are almost 50 % lower than those of the lipped channels.

Table 5.25: Buckling stresses of the different components of geometry 3

Column	Min. theoretical buckling stress (MPa)		Half-wave length observed during tests (mm)		Theoretical buckling stress (MPa)		Buckling stress from test (MPa)	
	Plain Channel	Lipped Channel	Plain Channel	Lipped Channel	Plain Channel	Lipped Channel	Plain Channel	Lipped Channel
LC3-2a	63	103	120	80-96	63	103-105	82	-
LC3-2b	64	104	120	80-96	64	104-106	84	-
LC3-3a	64	102	120	90-120	64	102-115	77	-
LC3-3b	64	104	120	90	64	104	79	-
LC3-8a	63	103	80-160	80-160	75-66	103-148	82-105	99
LC3-8b	65	103	80-160	80-160	77-67	104-148	88-109	109

In columns LC3-2 and LC3-3, the plain channels were observed to buckle at a stress level in between the predicted values for the plain and lipped channels. In column LC3-2, with a connector spacing of 960 mm, the measured buckling stress in the plain channels was around 31 % higher than the theoretical prediction, while in column LC3-3, with a connector spacing of 720 mm, the measured buckling stress in the plain channels was around 22 % higher than the theoretically predicted value. This is indicative of the high level of restraint which the plain channels received from the lipped channels in these columns, despite the relatively large connector spacing.

Interaction between the different components was even more pronounced in columns LC3-8. In these columns, the plain channel located on the compression side of the built-up specimen first buckled at a stress level of around 85 MPa. However, as the load was further increased, the lipped channels and the plain channel located on the tension side of the built-up specimen buckled simultaneously at a stress level close to the theoretical value predicted for the lipped channels. The plain channel located on the compression side was then forced to reverse the initial direction of its out-of-plane deformations in order to accommodate the local buckling pattern of the adjacent components, as illustrated in Figure 5.103 for column LC3-8a.

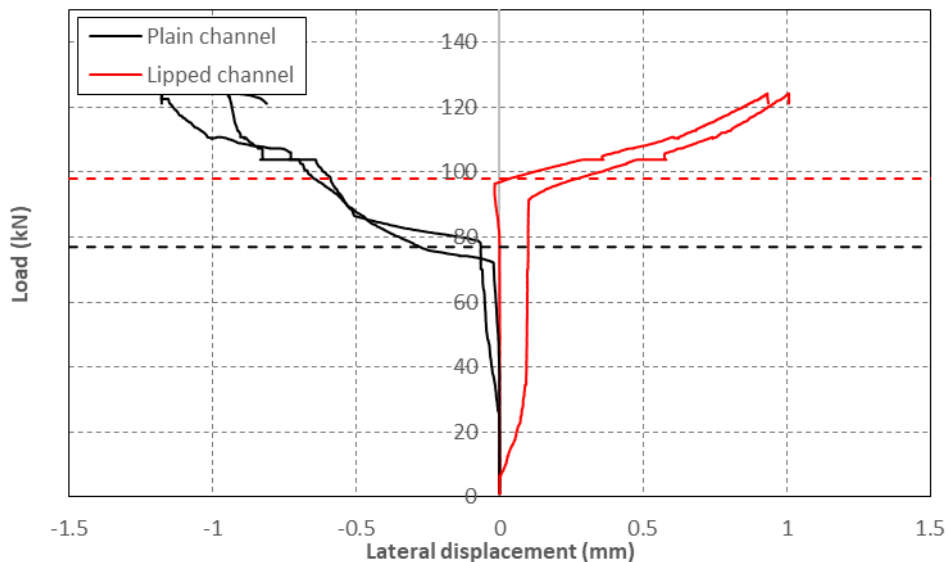


Figure 5.102: Axial load vs lateral displacements of LC3-2b

Table 5.25 also shows that in most cases the components buckled with a half-wave length very close to their natural half-wave length. Only in columns LC3-8, with the shortest connector spacing, the components showed some buckles along the column with a half-wave length which differed from the natural local buckle half-wave length. On average, the plain channels buckled at a stress around 34 % larger than their natural local buckling stress.

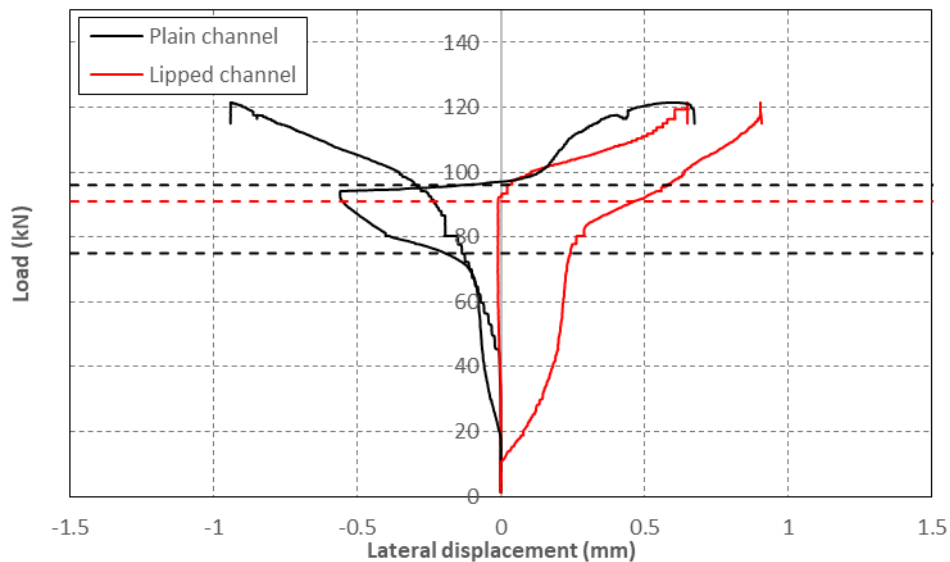


Figure 5.103: Axial load vs lateral displacements of LC3-8a

5.8.3.4 Built-up geometry 4

The plain channels buckled before the lipped channels in all columns with geometry 4. Therefore, only the critical buckling stress of the plain channels could be experimentally determined, under the assumption that the load was evenly distributed over the built-up cross-section prior to buckling. Thus, the critical buckling stresses of the plain channels were obtained by dividing the load at which the channel buckled over the total cross-sectional area of the column.

The theoretical and experimental buckling stresses of the different components are listed in Table 5.26, which also includes the buckle half-wave length observed in the lipped channels during the tests. Since the geometric arrangement of the components in the columns with built-up geometry 4 prevented direct observation of the buckle half-wave length of the plain channels during the tests, the theoretical buckling stresses included in the table for these channels are associated with the buckle half-wave lengths observed in the plain channels of columns LC3 (which had identical nominal dimensions).

Table 5.26: Buckling stresses of the different components of geometry 4

Column	Min. theoretical buckling stress (MPa)		Half-wave length observed during tests (mm)		Theoretical buckling stress (MPa)		Buckling stress from test (MPa)	
	Plain Channel	Lipped Channel	Plain Channel	Lipped Channel	Plain Channel	Lipped Channel	Plain Channel	Lipped Channel
LC4-2a	64	103	-	80-96	64	103-104	74	-
LC4-2b	64	103	-	80-96	64	104-105	63	-
LC4-3a	64	104	-	90	64	105	78	-
LC4-3b	64	102	-	90	65	102	73	-
LC4-8a	66	101	-	80	68-77	102	63-85	-
LC4-8b	64	104	-	80	66-76	105	67	-

The table shows that the critical buckling stresses of the plain channels measured during the tests were on average 7 % larger than the theoretical predictions using the assumed buckle half-wave length, while compared to the natural local buckling stress of the unrestrained channel, they were on average around 11 % larger. However, in columns LC4 the connector spacing did not seem to significantly affect the stress at which the plain channels buckled.

It may be worth noting that in columns LC4-2b and LC4-3b, the critical buckling stresses of the plain channels were slightly lower than those measured in the plain channels of columns LC4-2a and LC4-3a, respectively. This may be attributed to the fact that in columns LC4-2b and LC4-3b, distortional buckling of the lipped channels occurred at approximately the same time as local buckling in the plain channels, as illustrated by the black dashed curves in Figure 5.104 for column LC4-2b. In column LC4-2a, on the other hand, the potentiometers did not record any significant distortion of the lipped channels flanges, while in column LC4-3a distortional buckling of the lipped channels was recorded to occur after the plain channels buckled. No significant flange distortion was recorded in the lipped channels of columns LC4-8.

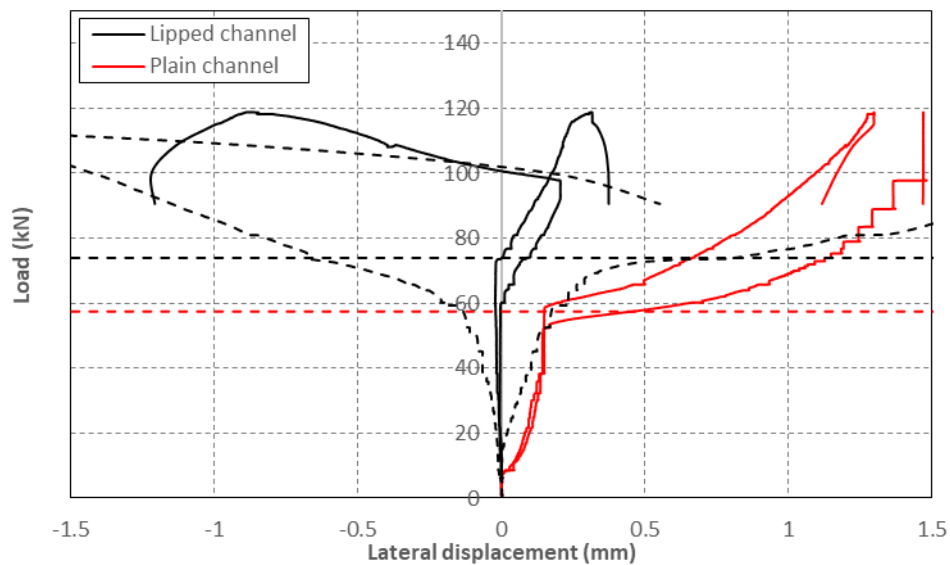


Figure 5.104: Axial load vs lateral displacements of LC4-2b

5.8.4 Ultimate load

All columns failed by interaction between cross-sectional buckling of the component sections and global flexural buckling about the major axis of the whole column, while in columns LC1 a global-type buckling of the components in between connector points was also observed. Figure 5.105 shows a typical load vs axial displacement curve, obtained for column LC3-2b, in which both the ‘dynamic’ load, as well as the ‘static’ load (obtained by accounting for the decrease in

the *dynamic* load observed after halting the test for 4 min shortly before the peak load was reached) are plotted. The figure reveals that there is little difference between the *dynamic* and *static* curves. The maximum difference observed at the peak load among all columns was 1.65 kN, obtained for column LC4-8a, while the average difference at the peak load was 0.72 kN. This small difference was due to the relatively slow targeted displacement rate of 0.08 mm/min employed during the tests.

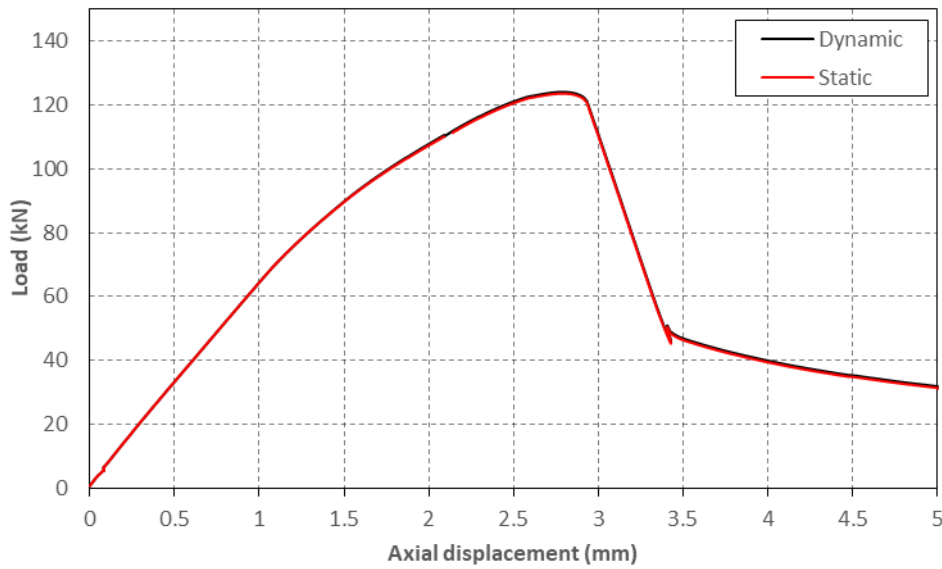


Figure 5.105: Axial load vs axial displacements of LC3-2b

The (static) load vs. axial displacement curves of all columns with geometries LC1, LC2, LC3 and LC4 are plotted in Figure 5.106, Figure 5.108, Figure 5.110 and Figure 5.112, respectively, while for the same columns, Figure 5.107, Figure 5.109, Figure 5.111 and Figure 5.113 plot the load against the average lateral deflections recorded at mid-height.

For columns LC1, three distinct areas can be distinguished in Figure 5.106, in terms of the stiffness of the columns before the ultimate load is reached. A first transition is characterised by a marked decrease in stiffness, which in the case of columns LC1-2 and LC1-3 occurs at a load of less than 10 kN, due to early buckling of the plate sections in a global flexural mode between connectors. In columns LC1-8, however, with a considerably smaller connector spacing, the first reduction of stiffness is delayed to a load just below 30 kN due to the postponement of global buckling of the plate sections between connectors. A second loss of stiffness in Figure 5.106 is attributed to the channels buckling in a local mode. This transition is characterised by a more gradual decrease in stiffness, and is similar to the one observed in columns LC2, LC3 and LC4.

In Figure 5.108 two different initial stiffness values can be distinguished for columns LC2. This geometry was tested with two different column lengths, the stiffer curves corresponding to the

shorter columns. Other than this, the columns showed an almost identical initial stiffness for each length.

The test results also show that the ultimate capacity of the columns loaded with an eccentricity of $L/1500$ (identified by the letter ‘*b*’ at the end of their label) was slightly larger than that of columns tested with a load eccentricity of $L/1000$ (identified by the letter ‘*a*’ at the end of the label). The only exception to this occurred in columns LC3-8, where the ultimate capacity of column LC3-8b was 0.6 % lower than that of column LC3-8a. This can likely be attributed to a loose wire in the cable acquiring the load data while testing column LC3-8a, which resulted in a noisy signal and a drop in the recorded load of around 5 kN just before the peak load was reached, as illustrated in Figure 5.110. Therefore, the peak load value for this column should be disregarded.

The *dynamic* and the *static* ultimate loads, as well as the average lateral deflection recorded at mid-height when the ultimate capacity was reached are listed in Table 5.27, Table 5.28, Table 5.29 and Table 5.30 for all the columns with geometries LC1, LC2, LC3 and LC4, respectively. The tables also include the squash load for each column, which was calculated based on the measured cross-sectional dimensions of the components and using the 0.2 % proof strength obtained from the flat coupons for the relevant type of component.

5.8.4.1 Built-up geometry 1

Regarding the columns with geometry 1, Table 5.27 shows that, on average, the ultimate capacity of the columns tested with a load eccentricity of $L/1500$ was marginally larger (by 1.8 %) than the ultimate capacity of the columns tested with a load eccentricity of $L/1000$ and the same connector spacing. In addition, as could be expected, most columns tested with a load eccentricity of $L/1000$ experienced a larger lateral deflection before failing than the columns tested with a load eccentricity of $L/1500$ and the same connector spacing. In particular, the maximum lateral deflections experienced by columns LC1-2a and LC1-8a were 12.8 % and 20.3 % larger than those experienced by columns LC1-2b and LC1-8b. The maximum lateral deflection of column LC1-3a, however, was 13.3 % lower than that of its twin counterpart, tested with a smaller load eccentricity (LC1-3b). This could likely be attributed to a larger global imperfection in column LC1-3b, which in combination with the load eccentricity applied at the ends of the column resulted in an eccentricity at mid-height larger than that of column LC1-3a.

Regarding the effect of the connector spacing, only columns LC1-8, with a connector spacing of 320 mm, showed a noticeable increase in the ultimate capacity (of 15.1 %) with respect to columns LC1-2, which had a connector spacing of 960 mm. The ultimate capacity of columns LC1-3, with a connector spacing of 720 mm, was only 2.7 % larger than that of columns LC1-2.

Table 5.27 also shows that the ultimate capacity of the columns constituted only around 27 % of the squash load. The reason for this rather low ratio is found in the low efficiency of the plate sections, which buckled in a global flexural mode between connectors at a very early stage during the test, becoming ineffective in resisting any further increase of the load.

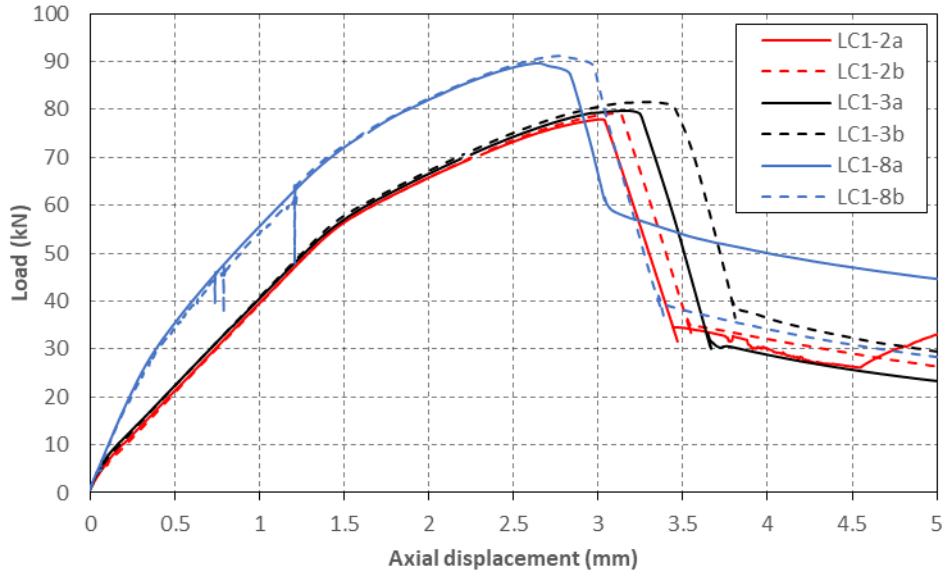


Figure 5.106: Axial load vs. axial deformation curves: geometry 1

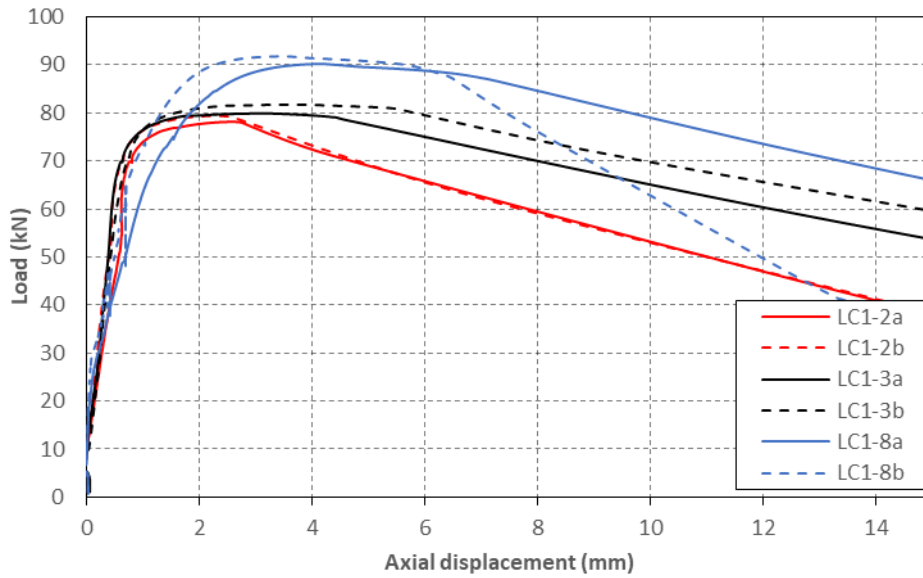


Figure 5.107: Axial load vs. lateral deflection curves: geometry 1

Table 5.27: Ultimate loads: geometry 1

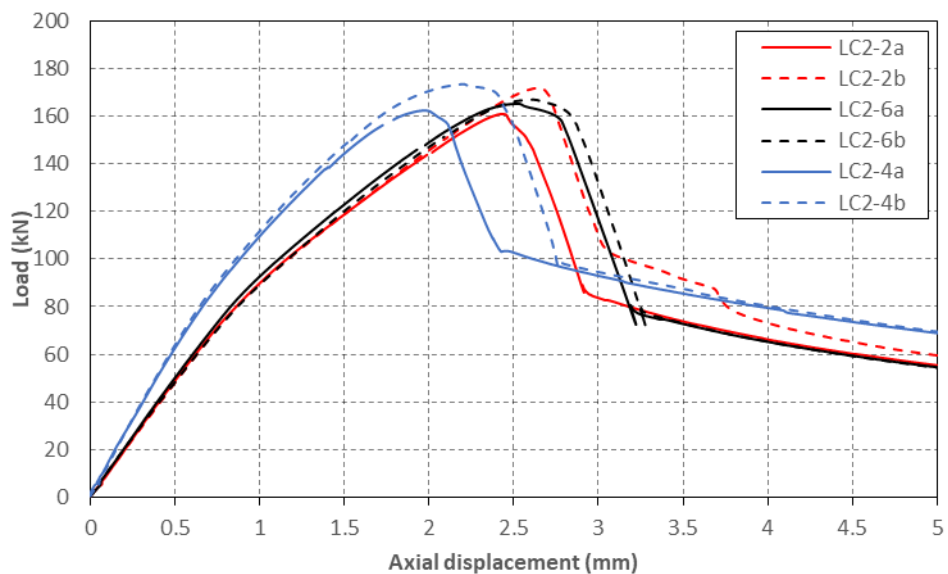
Column	Ultimate load (kN)		Deflection at peak load (mm)	Squash load (kN)	Static/Squash (-)
	Dynamic	Static			
LC1-2a	78.14	77.94	2.56	302.50	0.26
LC1-2b	79.38	79.18	2.27	302.92	0.26
LC1-3a	79.88	79.73	3.14	303.44	0.26
LC1-3b	81.72	81.57	3.62	301.35	0.27
LC1-8a	90.21	89.66	4.15	304.39	0.29
LC1-8b	91.77	91.17	3.45	302.61	0.30

5.8.4.2 Built-up geometry 2

The shortest columns with geometry 2 (LC2-4) were observed to fail while the plastic deformations localised close to one end of the column. Failure in these columns was thus deemed to be affected by the distortions and stress concentrations introduced into the flanges of the outer channels while welding the endplates to the ends of the columns. Therefore, the peak load values listed in Table 5.28 for columns LC2-4a and LC2-4b should be disregarded. For the rest of columns, however, Table 5.28 shows that reducing the connector spacing from 793 mm (LC2-2) to 340 mm (LC2-6) did not result in a noticeable increase in the ultimate capacity.

Regarding the effect of the load eccentricity, columns LC2-2b and LC2-6b, which were tested with a load eccentricity of $L/1500$, showed increases in their ultimate capacity of 6.56 % and 1.0 % and a reductions in the lateral deflection at the peak load of 16.9 % and 13.2 % with respect to columns LC2-2a and LC2-6a, respectively,

On average, the ultimate capacity of the columns with geometry 2 was around 48 % of the squash load.

**Figure 5.108: Axial load vs. axial deformation curves: geometry 2**

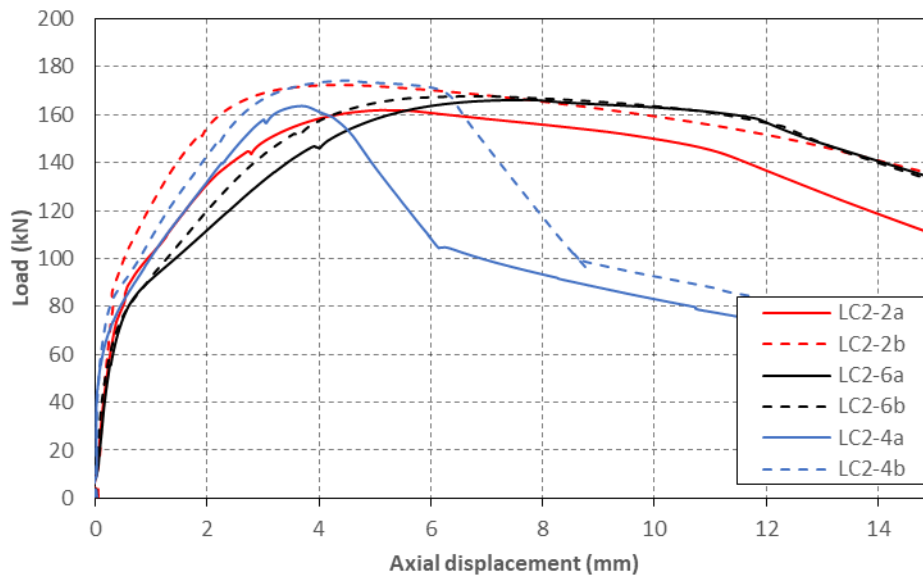


Figure 5.109: Axial load vs. lateral deflection curves: geometry 2

Table 5.28: Ultimate loads: geometry 2

Column	Ultimate load (kN)		Deflection at peak load (mm)	Squash load (kN)	Static/Squash (-)
	Dynamic	Static			
LC2-2a	161.90	160.90	5.13	345.89	0.47
LC2-2b	172.42	171.82	4.39	349.20	0.49
LC2-6a	166.15	165.15	7.71	346.73	0.48
LC2-6b	167.68	166.88	6.81	343.70	0.49
LC2-4a	(163.61)	(162.31)	(3.68)	309.72	(0.52)
LC2-4b	(174.27)	(173.37)	(4.53)	311.46	(0.56)

5.8.4.3 Built-up geometry 3

With respect to the columns with geometry 3, Table 5.29 shows that the ultimate capacity was slightly higher in the columns with the smaller load eccentricity. For example, the ultimate capacities of columns LC3-2b and LC3-3b, which were tested with a load eccentricity of $L/1500$, were on average 3.6 % larger than the ultimate capacities of columns LC3-2a and LC3-3a, which were tested with a load eccentricity of $L/1000$. In addition, columns LC3-2a and LC3-3a showed increases in the lateral deflection at the peak load of 35.7 % and 59.2 %, relative to the columns tested with a load eccentricity of $L/1500$ and the same connector spacing.

As for the effect of the connector spacing on the ultimate capacity of these columns, reducing the connector spacing resulted in a negligible increment in their ultimate capacity. For example, the increment in ultimate capacity obtained by reducing the connector spacing from 960 mm in column LC3-2a to 320 mm in column LC3-8a was only 0.5 %, while the ultimate capacity of columns LC3-3, with a connector spacing of 720 mm, was on average slightly lower than that of columns LC3-2 (by 0.1 %). All columns failed at a load which was around half of the squash load.

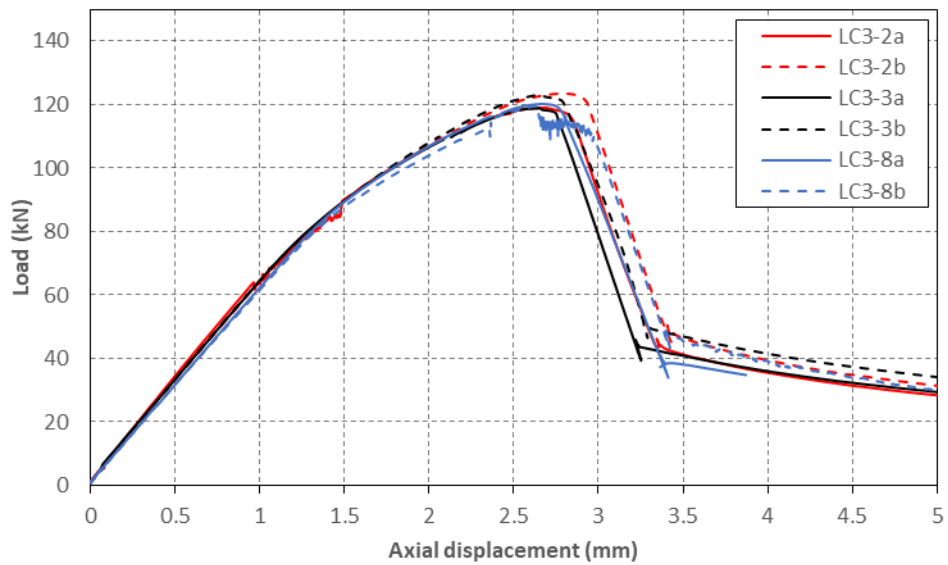


Figure 5.110: Axial load vs. axial deformation curves: geometry 3

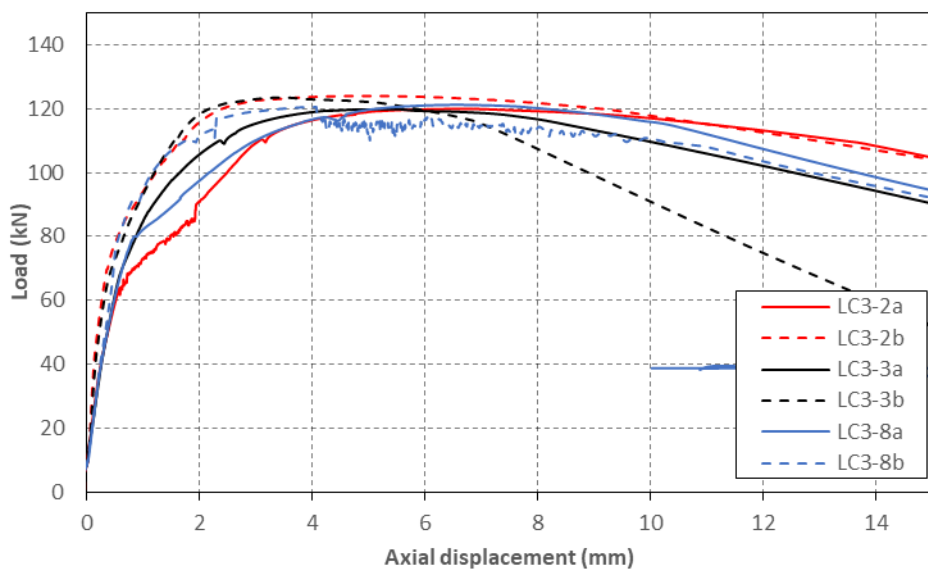


Figure 5.111: Axial load vs. lateral deflection curves: geometry 3

Table 5.29: Ultimate loads: geometry 3

Column	Ultimate load (kN)		Deflection at peak load (mm)	Squash load (kN)	Static/Squash (-)
	Dynamic	Static			
LC3-2a	119.94	119.04	6.62	236.50	0.50
LC3-2b	123.98	123.48	4.88	236.50	0.52
LC3-3a	119.88	118.88	5.43	238.01	0.50
LC3-3b	123.44	122.94	3.41	238.71	0.52
LC3-8a	121.22	120.22	6.60	238.78	0.50
LC3-8b	(120.54)	(119.54)	(4.07)	239.48	(0.50)

5.8.4.4 Built-up geometry 4

Regarding the columns with geometry 4, Table 5.30 shows that columns LC4-2b, LC4-3b and LC4-8b, which were tested with a load eccentricity of $L/1500$, achieved a peak load which was 1.2 %, 2.1 % and 9.7 % higher than the peak load achieved by columns LC4-2a, LC4-3a and LC4-8a, respectively, which were tested with a load eccentricity of $L/1000$. The relatively large difference in ultimate capacity obtained for the LC4-8 columns was due to the relatively low ultimate capacity achieved in column LC4-8a. This was most likely due to the relatively large global imperfection present in this column, which further increased the eccentricity at the column mid-height, as shown in Table 5.22. The increases in the lateral deflection at the peak load in the columns tested with a load eccentricity of $L/1000$, relative to those tested with a load eccentricity of $L/1500$, were 7.64 %, 42.1 % and 14.4 % for columns LC4-2, LC4-3 and LC4-8, respectively.

Regarding the effect of the connector spacing on the ultimate capacity, Table 5.30 shows that this was negligible, with a mere 0.7 % increase when reducing the connector spacing from 960 mm to 320 mm, and a 0.3 % increase when reducing the connector spacing from 960 mm to 720 mm. All columns failed at a load of less than 50 % of the calculated squash load.

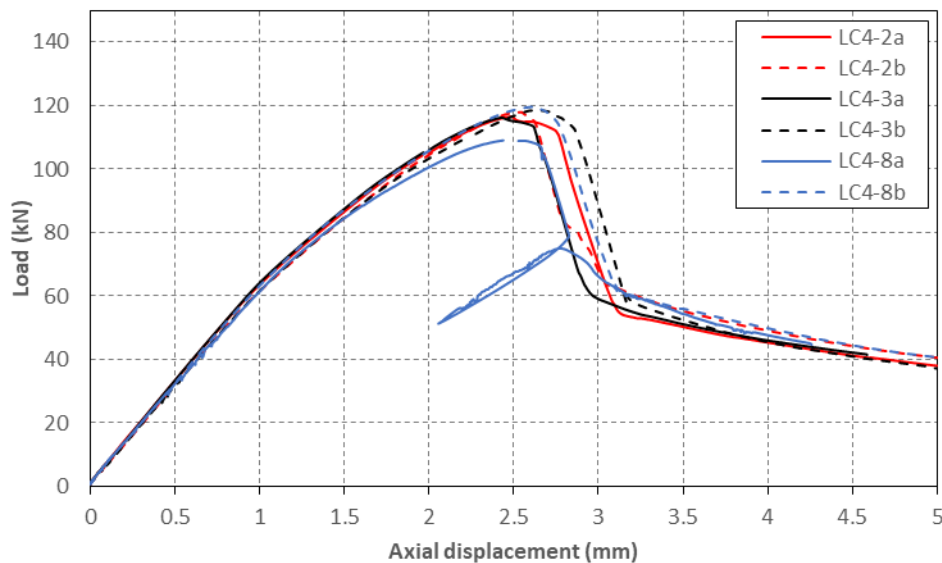


Figure 5.112: Axial load vs. axial deformation curves: geometry 4

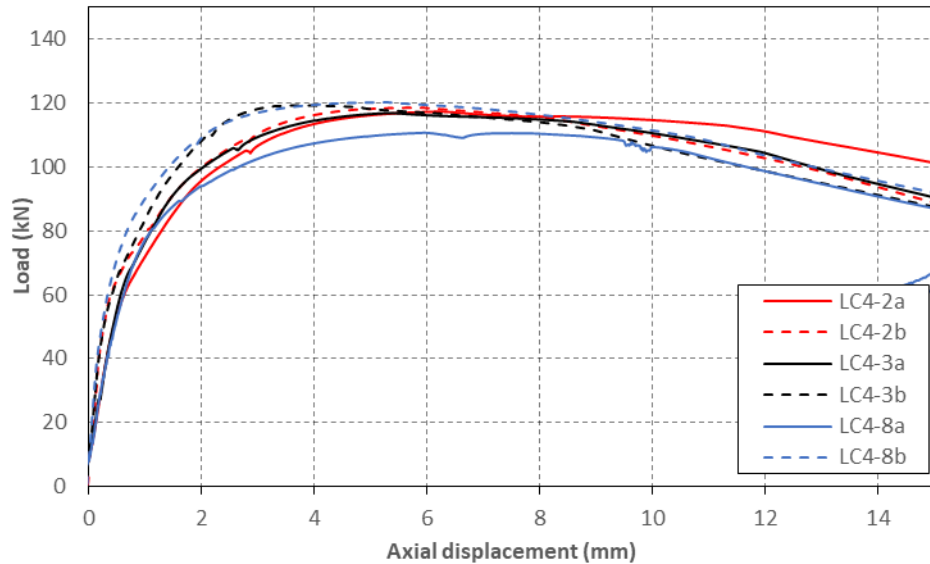


Figure 5.113: Axial load vs. lateral deflection curves: geometry 4

Table 5.30: Ultimate loads: geometry 4

Column	Ultimate load (kN)		Deflection at peak load (mm)	Squash load (kN)	Static/Squash (-)
	Dynamic	Static			
LC4-2a	117.33	116.53	6.20	238.48	0.49
LC4-2b	118.50	117.90	5.76	238.46	0.49
LC4-3a	116.84	116.19	5.30	237.81	0.49
LC4-3b	119.22	118.57	3.73	237.63	0.50
LC4-8a	110.71	109.06	5.96	238.55	0.46
LC4-8b	120.20	119.65	5.21	237.83	0.50

5.9. Summary and conclusions

A comprehensive experimental programme consisting of compression tests on 24 long built-up columns with four different cross-sectional geometries and lengths ranging from 1800 mm to 3000 mm is presented. The cross-sections were assembled from flat plates, plain channels and lipped channels with nominal depths ranging from 79 mm to 154 mm and thicknesses ranging from 1.2 to 2.0 mm. Two of the cross-sectional geometries (LC1 and LC2) were assembled using M6 bolts, while the other two (LC3 and LC4) were assembled using M5.5 self-drilling sheet metal screws.

The columns were subjected to compression between pin-ended boundary conditions, applying the load with eccentricities of $L/1000$ or $L/1500$, while varying the connector spacing among specimens with the same cross-sectional geometry. The different components of the built-up specimens were spot welded together at each end and endplates were welded to the column ends to ensure a controlled introduction of the load to each component, as well as to facilitate positioning the columns relative to the pin supports. In order to verify the eccentricity, half of

the test specimens were instrumented with strain gauges at mid-height. In addition, coupon tests were taken from the flat portions and corner regions of the components in order to determine their material properties, and detailed measurements of their geometric imperfections were performed before and after they were assembled into their final configuration, using a specially designed measuring rig which consisted of a laser sensor moving along high precision guiding bars.

The out-of-plane deformations of each column component were recorded during the test using potentiometers located near the bottom end of the column. This allowed, in most cases, a determination of the stress at which buckling occurred in the components. These values were compared to theoretical predictions, obtained from a finite strip analysis which considered the individual components in isolation without any interaction with the rest of the cross-section.

The main conclusions obtained from this experimental programme are listed below. They are divided into those related to the accuracy of the developed imperfection measuring rig and the study of the effect of the assembly process on the amplitude and shape of the imperfections, and those related to the results obtained from the column tests.

5.9.1 Conclusions regarding the imperfection measurements

- The accuracy of the readings taken with the measuring rig was found to be limited by the out-of-straightness of the guiding bars along which the laser sensor is moved. A technique was proposed to achieve a higher measurement accuracy, which consisted of using a reflective liquid, such as milk, to generate a virtually perfectly flat surface, which can then be used to measure the out-of-straightness of the guiding bars. After accounting for this out-of-straightness, the accuracy of the imperfection measurements was estimated to be ± 0.06 mm over the full 3 m length of the rig.
- The imperfections recorded on the components of the built-up geometries were classified into out-of-plane imperfections and global imperfections.

A similar out-of-plane imperfection profile was recorded for each type of channel along their respective web, flanges and lips before they were assembled into their built-up configuration. This consistency in the imperfection shape was attributed to the fact that each type of channel section was presumably fabricated from the same steel coil and followed the same cold-forming process and handling. The fabrication process was also deemed responsible for the consistency in the minor axis global flexural imperfection recorded in all channels before they were assembled, which closely resembled a 'Bow imperfection' towards the web of the channel. The global imperfection of the channels about the major axis, on the other hand, could be less accurately approximated by a

‘Chamber imperfection’, with the maximum imperfection magnitude typically occurring away from the mid-length of the channel.

- Characterising the imperfections related to local or distortional buckling using the maximum out-of-plane imperfection was found to yield exceedingly conservative imperfection values. This conclusion was reached after decomposing the out-of-plane imperfections recorded in the channels (before they were assembled) into a constant and an undulating component along the channel length and noting that the former, which does not contribute to the onset of these cross-sectional buckling modes, may be up to twice as large as the latter. Moreover, using the maximum undulating imperfection component can also be expected to result in a conservative characterisation of the out-of-plane imperfections, since the profile of the undulating component does not necessarily resemble the longitudinal shape of the critical cross-sectional buckling mode of the channel.
- Assembling the channels into their final configuration significantly altered the amplitude and shape of the out-of-plane imperfections of the channels. The imperfections along the web of the individual channels were affected (1) due to direct contact with the adjacent components of the built-up geometry and the presence of the connectors, or (2) due to rotational compatibility at the junction with the flanges, which were themselves in a situation described in (1). The former resulted in a greater modification of the out-of-plane imperfections, with the connectors creating localised out-of-plane imperfections along the web, resulting in an imperfection profile with repetitive ‘bumps’. The assembly process had a lesser effect on the out-of-plane imperfections along the flanges of the channels, which in most cases resulted from rotational compatibility with the web.
- The assembly process was also found to significantly affect the minor axis global flexural imperfection of the channels, reducing its amplitude at mid-length or even inverting it. The shape of these imperfections was also affected, resembling less of a sinusoidal bow imperfection. For most of the channels, the reduction in the magnitude of their minor axis global flexural imperfection can be explained by the fact that the major axis global flexural imperfection of all the channels was significantly smaller than the one about the minor axis, while their flexural rigidity in that direction is significantly higher. Therefore, the channels connected through their web were straightened by the adjacent channels, which were positioned orthogonally to them. It is worth pointing out that in built-up geometries assembled from two identical channels connected to each other facing in opposite directions and with the plane of contact parallel to their minor axis (as is the case in a back-to-back I-shaped built-up section or a toe-to-toe built-up box section), if the individual channels are fabricated following the

same procedure, their minor axis global flexural imperfection after the assembly can be expected to be smaller than the one prior the assembly, since the imperfections of each channel is somehow cancelled by the imperfections of the other channel and the enforcement of contact exerted by the fasteners.

5.9.2 Conclusions regarding the column tests results

- All columns failed by interaction between cross-sectional instability of the component sections and global flexural buckling about the major axis of the built-up column, while a global-type buckling of the components in between connector points was also observed in columns LC1.
- The connectors were seen to affect the buckling patterns of the components by forcing them to adjust their individually preferred buckling half-wave length to accommodate their presence. For the channel sections, this adjustment resulted in half-wave lengths which were still relatively close to the natural local buckle half-wave length of the individual channels. In addition, whether the buckles were enlarged or shortened depended on which half-wave length required the lowest critical buckling stress.
- The cross-sectional buckling patterns of the individual components within the columns were also seen to be affected by contact with the adjacent components, which often forced the buckling out-of-plane displacements to exclusively occur in one direction.
- Interaction between global buckling of the built-up specimen and cross-sectional buckling of the components was evidenced by a slight amplification of the amplitude of the buckles of the component located on the most compressed side of the built-up specimen. These components were also recorded to buckle slightly before those located on the opposite side.
- A comparison between the theoretical predictions of the buckling stresses and the experimentally derived ones showed that the buckling stress of the most slender components was increased by up to 34 % as a result of the restraint provided by the rest of the cross-section. In particular, in columns LC1, LC2, LC3 and LC4, the stress at which the most slender component buckled exceeded the natural local buckling stress of the component considered in isolation by 13 %, 26 %, 34 % and 11 %, respectively.
- The tests also showed that in those columns where the individual components only experienced cross-sectional instabilities (i.e. columns LC2, LC3 and LC4), the effect of the connector spacing on the ultimate capacity was negligible. For instance, reducing the connector spacing from 793 mm to 340 mm in columns LC2 resulted in a mere 0.3 % increase in the ultimate capacity, while for columns LC3 and LC4, reducing the

connector spacing from 960 mm to 320 mm resulted in an increase in the ultimate capacity of less than 1 %. Only columns LC1 showed a noticeable increase in the ultimate capacity of 15.1 % when reducing the connector spacing from 960 mm to 320 mm, which resulted from an increase in the global flexural buckling capacity of the plate sections between connectors.

Chapter 6

Experimental Study of the Fastener Behaviour in Built-up Specimens

6.1. Introduction

The buckling behaviour and capacity of CFS built-up members may be significantly affected by the shear and bearing deformations of the connectors between the components. This is expected to particularly be the case for long built-up columns and built-up beams, where relatively large shear forces may be introduced into the connectors as a result of the relative displacements of the components originating from global buckling in the former and lateral-torsional buckling and/or bending in the latter. The result is a reduction in capacity, which may also be interpreted as an increase in the effective global slenderness of the built-up member.

For the above reasons a series of single lap shear tests were carried out in order to study the behaviour of the connectors used in the built-up members discussed in Chapter 3, Chapter 4 and Chapter 5. Ten different types of connector test specimens were fabricated in order to fully cover the various combinations of plate thicknesses and fastener types encountered in the built-up specimens, as well as to compare the behaviour of different types of fasteners when connecting steel plates with a given thickness and mechanical properties. The results obtained from the single lap shear tests were then used in Chapter 7, Chapter 8 and Chapter 9 as input data in detailed FE models used in parametric studies after validation against the experiment.

The experimental programme presented in this chapter also sought to investigate the reliability of Digital Image Correlation (DIC) for these purposes. DIC is a relatively new non-contact measuring technique, which has great potential in situations where conventional measuring techniques cannot be used, such as tests under fire conditions. To this end the deformations of the connector test specimens were recorded using both LVDTs and DIC and the results were compared.

6.2. Labelling

The connector test specimens were labelled with the letters ‘*BCS*’ or ‘*SCS*’ to indicate that the specimen was assembled using bolts or self-drilling screws, respectively, followed by the thicknesses of both steel plates multiplied by 10 and separated by a hyphen. The first thickness in the label corresponded to the plate directly underneath the head of the connector. Finally, the letters ‘*a*’, ‘*b*’ and ‘*c*’ were used to differentiate between multiple connector specimens with the same combination of plate thicknesses and fastener type. For example, the label ‘*BCS24-14a*’ refers to a bolted specimen assembled with steel sheets with nominal thicknesses of 2.4 mm and 1.4 mm.

The labelling used to refer to the cross-sectional components is consistent with the one used in previous chapters. Plain channels and lipped channels were labelled using the letters ‘*T*’ or ‘*S*’, respectively, followed by the nominal width of the web in mm and the nominal wall thickness in mm multiplied by 10, while the plate sections were labelled using the letter ‘*P*’ followed by the width of the plate and its thickness multiplied by 10.

6.3. Specimen geometry and preparation

The connector specimens consisted of single lap joints connected with the same type of bolts or self-drilling screws used to assemble the built-up members. Since the connector behaviour was expected to be affected not just by the type of fastener used, but also by the mechanical properties of the fastened sections, each steel sheet in the single lap joint was cut from spare sections of the built-up specimens, and they were paired together to cover all the combinations of plate thicknesses and connector type encounter in the built-up beams and columns previously tested. In order to avoid excessive tilting of the fastener and out-of-plane curling of the steel plates prior to failure, the specimens were assembled with two fasteners in the direction of the applied load. Figure 6.1 shows the specimens fabricated for each built-up geometry.

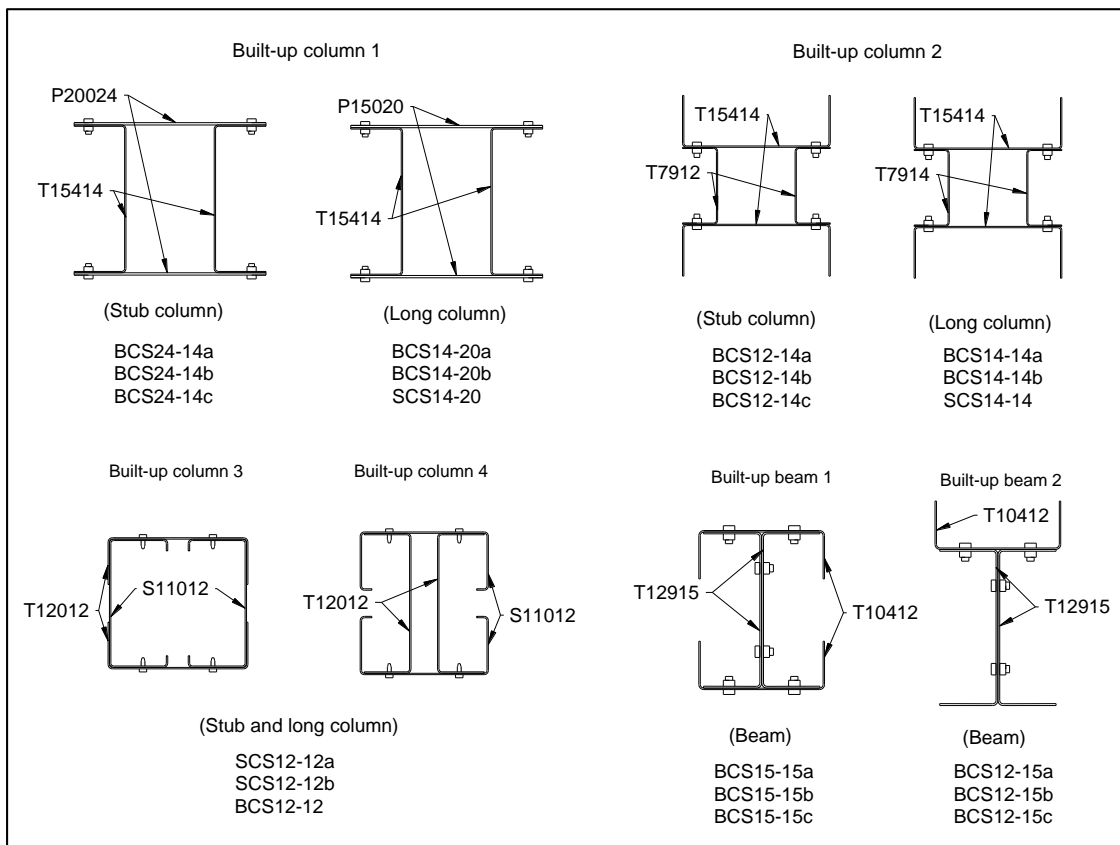


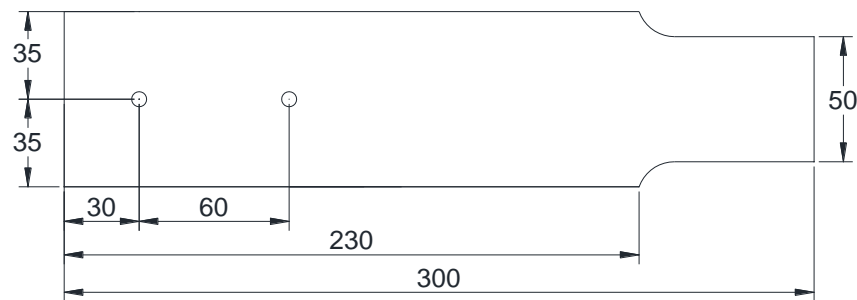
Figure 6.1: Connector specimens fabricated for each built-up geometry

The test programme was divided in two stages. During the first part, four different types of bolted specimens were fabricated to study the connector behaviour in geometries 1 and 2 of the built-up stub columns and beams (i.e. BCS24-14, BCS12-14, BCS15-15 and BCS12-15). The connector specimens belonging to the stub columns were fabricated after seeing clear evidence of slip between the components of geometry 1 during the stub column tests. Test specimens were also fabricated for the fasteners contained in the beams, so that the connector behaviour could be incorporated in FE models which did allow global instabilities of the built-up beams. Three identical test specimens were fabricated for each combination of plate thicknesses in order to assess the statistical variability of the results.

During the second part of the experimental programme, both bolted and screwed specimens were fabricated in order to study the connector response in the long built-up columns (i.e. BCS14-20, BCS14-14 and SCS12-12). It is worth noting that since the stub columns with geometries 3 and 4 were assembled from components with nominally identical thicknesses and material properties as those used to assemble the long columns, the test specimens fabricated to study the behaviour of the fasteners in the long columns with geometries 3 and 4 were also representative of the behaviour of the fasteners in the stub columns with geometries 3 and 4. Again three test specimens were fabricated for each combination of plate thicknesses. However, for each such combination one test specimen out of three was assembled using a different

fastener type (i.e. bolts or screws). This allowed for a direct comparison regarding the effect of the fastener type on the connection behaviour.

Figure 6.2 shows the nominal dimensions of the steel sheets used to construct the test specimens, as well as the location of the connectors. The steel sheets had a nominal width of 70 mm, which was reduced to 50 mm at one end in order to accommodate the specimen into the grips of the testing machine. The edge distance of the fasteners in the direction of the force and the distance between fasteners were chosen following the recommendations given by ECCS TC7 (2009), which ensured that the behaviour of the connector was not affected by its proximity to the edge.



(All dimensions in mm)

Figure 6.2: Nominal dimensions of steel plate

The thickness and the width of the steel sheets were measured prior to the assemblage. The thickness of the sheet was measured with a digital micrometre with a precision of ± 0.002 mm, while the width of the sheet was measured with a digital Vernier caliper with a precision of ± 0.03 mm. The measured dimensions of the steel sheets are listed in Table 6.1 for each specimen. They correspond to the averages of several measurements taken along the length of the sheet.

The bolted specimens were assembled using M6 bolts with M6 washers placed between the bolt head/nut and the steel sheets, replicating the same type of connection used to assemble the built-up specimens. It is worth mentioning that the bolts used during the first and second stage of the experimental programme were supplied by different manufacturers. However, all of them were grade 8.8. Holes with a nominal diameter of 6.25 mm were drilled into the connecting plates and the bolts were tightened with a torque of 10 Nm, identically to what was done for the actual built-up specimens.

The screwed specimens were assembled using the same M5.5 self-drilling sheet metal screws used to assemble the built-up specimens. In order to ensure the screws were aligned with the line of action of the applied force, small holes with a diameter of 3 mm were predrilled into the

steel sheets, which served as guidance for the screws. Once the steel sheets were positioned and secured with clamps, the screws were drilled applying the same torque as used to assemble the built-up specimens.

Table 6.1: Measured width and thickness of steel plates

Specimen	Section	Width (mm)	Thickness (mm)
BCS24-14a	P20024	69.73	2.530
	T15414	70.31	1.481
BCS24-14b	P20024	70.01	2.542
	T15414	70.34	1.479
BCS24-14c	P20024	70.40	2.546
	T15414	70.33	1.470
BCS12-14a	T7912	70.36	1.215
	T15414	70.33	1.475
BCS12-14b	T7912	63.96	1.186
	T15414	70.32	1.482
BCS12-14c	T10412	69.46	1.189
	T15414	70.34	1.473
BCS15-15a	T12915	70.40	1.528
	T12915	69.12	1.529
BCS15-15b	T12915	70.45	1.530
	T12915	70.76	1.544
BCS15-15c	T12915	70.40	1.542
	T12915	70.26	1.535
BCS12-15a	T10412	70.37	1.186
	T12915	70.14	1.540
BCS12-15b	T10412	70.41	1.197
	T12915	70.41	1.537
BCS12-15c	T10412	70.28	1.185
	T12915	70.28	1.532
BCS14-20a	T13014	69.94	1.398
	P15020	70.08	1.977
BCS14-20b	T13014	69.99	1.405
	P15020	70.09	1.976
SCS14-20	T13014	70.10	1.401
	P15020	70.12	1.973
BCS14-14a	T15414	70.11	1.447
	T7914	69.99	1.404
BCS14-14b	T15414	70.07	1.451
	T7914	70.24	1.406
SCS14-14	T15414	70.11	1.447
	T7914	69.89	1.400
SCS12-12a	T12012	70.11	1.137
	S11012	69.97	1.115
SCS12-12b	T12012	70.09	1.138
	S11012	70.19	1.112
BCS12-12	T12012	69.97	1.135
	S11012	70.00	1.112

6.4. Material Properties

Since the test specimens were fabricated from the flat portions of spare sections belonging to the same batch as those used to assemble the built-up specimens, the material properties of the steel sheets were the same as those of the sections used to assemble the built-up specimens. They can be found in Table 3.3 of Chapter 3 for connector specimens BCS24-14, BCS12-14, BCS12-12 and SCS12-12, Table 4.3 of Chapter 4 for connector specimens BCS15-15 and BCS12-15, and Table 5.3 of Chapter 5 for specimens BCS14-20, BCS14-14, SCS14-20 and SCS14-14.

6.5. Test Set-up

All specimens were tested in a 300 kN Shimadzu universal testing machine. The test set-up is illustrated in Figure 6.3. The specimens were loaded until failure at a constant displacement rate of 0.5 mm/min. Each steel sheet was packed at the end with a steel plate which had the same thickness as the adjacent steel sheet to ensure the load was being applied along the shear plane.

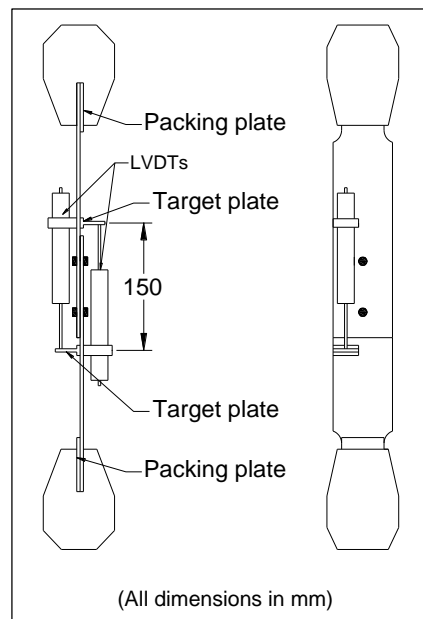


Figure 6.3: Single lap shear test set-up

The specimen deformations were recorded using two LVDTs, as well as with a DIC (digital image correlation) system. Representative bolted and screwed test specimens are shown in Figure 6.4a and Figure 6.4b, respectively, at the onset of testing.

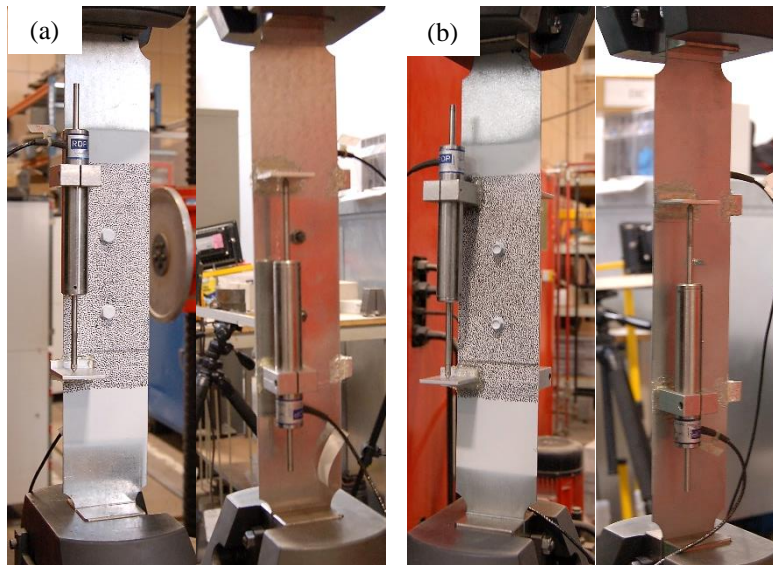


Figure 6.4: a) BCS14-14a and b) SCS12-12b

6.5.1 Transducers

Two LVDTs were glued to the steel sheets and spring-loaded against target plates, which were glued to the adjacent sheet a distance of 150 mm apart, as illustrated in Figure 6.3 and Figure 6.4. For specimens BCS12-14c, BCS12-15a, BCS15-15c and BCS24-14a, both LVDTs were attached on the same side of the specimen in order to keep the other side clear to carry out the DIC measurements. However, it was found that any initial curvature present in the specimens significantly affected the LVDT readings. Consequently, the remaining specimens were instrumented with one LVDT on each side of the specimen. This way, the effect of the initial curvature on one LVDT was compensated by the opposite effect on the LVDT placed on the other side of the specimen. The deformation of the specimen was then taken as the average reading obtained from both LVDTs.

6.5.2 Digital image correlation

DIC was explored as part of a more general initiative within the Cold-Formed Steel Research group at The University of Sheffield to develop alternative ways of measuring deformations in CFS members. In this test programme the DIC measurements were compared with the average measurements recorded by the LVDTs in order to assess the reliability of the DIC system.

In the DIC method a digital camera is used to take a series of pictures of the surface of an object as the object deforms. A software algorithm then tracks the changes in the grey value pattern between consecutive images. A grey value pattern can artificially be generated on the surface by printing or painting a randomly distributed speckle pattern onto it. DIC has the advantage of being a non-contact method which is able to provide full-field deformation measurements, as

opposed to the relative displacement measurements between two discrete points provided by more conventional measuring devices such as LVDTs or potentiometers.

In order to obtain the full deformation field around the fasteners a randomly distributed speckle pattern was created on one face of the specimens by first spray painting the specimens with Plasti-Kote Super Matt Spray White after they were assembled and then randomly generating the speckle pattern using a black marking pen. This method provided a pattern with high contrast and the density and size of the speckles could easily be controlled. This method can be recommended when covering small surfaces. Figure 6.4 shows the speckle patterns obtained for two representative connector specimens.

A direct comparison between the measurements obtained from the LVDTs and the ones obtained with DIC was achieved by marking horizontal scribed lines onto the connector specimen at the location where the LVDTs and the target plates were attached. The scribed lines were used to identify the pixels in the photographs which needed to be tracked.

The photographs were taken with a Canon EOS D70 DSLR camera, which was positioned 1 m away from the test specimens and was operated in manual focus mode with the autofocus feature deactivated, using an aperture of $f/7.1$, a shutter speed of $1/100$ sec and an ISO 200 setting. The camera was automatically triggered at regular intervals of 10 sec using a LabView script. Details about the technique used to synchronize the photographs with the acquisition of the load and the LVDTs readings are included in Section 6.6.3. Two 20 W LED floodlights were used to ensure that the specimens received sufficient light and that no shadows were projected onto the surface. The positioning arrangement of the camera and the lamps is illustrated in Figure 6.5.

Two different DIC software packages were used to obtain the deformations of the test specimens. During the first part of the experimental programme the Ncorr v1.2 software (Blaber et al., 2015) was used, while during the second part the DIC code developed by Jones (2015) was used. A more detailed description of the DIC process can be found in (Dai, 2017).



Figure 6.5: Camera and lamp arrangement for DIC

6.6. Test results

6.6.1 Ultimate capacity and failure mode

The load vs elongation curves are illustrated in Figures 6.6-6.12 for specimens assembled with various combinations of plate thicknesses. The load-elongation response of the individual fasteners was obtained by dividing the force applied to the specimen over the number of fasteners. All connector specimens with identical nominal dimensions and type of fasteners showed the same type of failure mode. In the bolted connector specimens the failure modes consisted of shear failure of the bolts, excessive bearing deformations of the thinnest steel plate and a combination of both, while all the screwed connector specimens failed by pull-out of the fastener as a result of tilting. In all the connector specimens the contributions of the elastic deformations of the plates to the measurements were estimated to be negligible (less than 0.1 mm at the peak load).

The load-elongation response of the bolted specimens was characterized by bolt slip of up to 1 mm at a load of around 3 kN. Although the bolts used to assemble the specimens were all grade 8.8., the bolts used during the later part of the programme (specimens BCS14-20, BCS14-14 and BCS12-12) seemed to be stronger than those used to assemble the specimens tested during the first part of the programme (specimens BCS24-14, BCS14-12, BCS15-15 and BCS12-15). The two sets of bolts were supplied by different manufacturers and as a result of the difference in strength, all specimens tested during the last part of the programme failed due to bearing of the steel plate, as opposed to those tested during the first part of the programme, which failed by bolt shear.

It is important to note that although the material properties of the bolts affected the failure mode of the specimens, this was not problematic since the main purpose of this experimental programme was to obtain the initial part of the load-elongation curve. Indeed, in the tested built-up members the relative deformation at the connector points was observed to be in all cases less than 2 mm before failure of the member occurred. Consequently, only the early part of the load-elongation curve was of interest. Nonetheless, a complete description of the connector behaviour, including the ultimate capacity and failure mode of each type of connector is included below.

With respect to the bolted specimens tested during the first part of the programme, the test results showed that, as the thickness of the steel plates decreased, the bearing deformations in front of the fastener became more pronounced, resulting in a more ductile type of failure. For example, specimens BCS24-14, assembled with steel plates of 2.4 mm and 1.4 mm thickness, failed by bolt shear with little bearing deformation of the steel plates, as shown in Figure 6.15a for specimen BCS24-14b. These specimens showed the least ductile behaviour, experiencing deformations of around 3 mm before failure (Figure 6.6). Similarly, specimens BCS15-15, assembled with steel plates of 1.5 mm thickness, also failed by bolt shear. However, in these specimens some bearing deformations developed in the steel plates before the bolts failed in shear (Figure 6.15b), which increase the deformation at failure to around 5 mm, as shown in Figure 6.7. In connector specimens BCS12-14 and BCS12-15, in which the thinnest steel plate had a thickness of 1.2 mm, the maximum deformations before shear failure of one of the bolts took place were around 6 mm (Figure 6.8) and 7 mm (Figure 6.9), respectively. In these specimens, the thinnest steel plate exhibited significant bearing deformations and out-of-plane curling, while the bolts exhibited a large amount of tilting, as illustrated in Figure 6.16a and Figure 6.16b for specimens BCS12-14c and BCS12-15a, respectively.

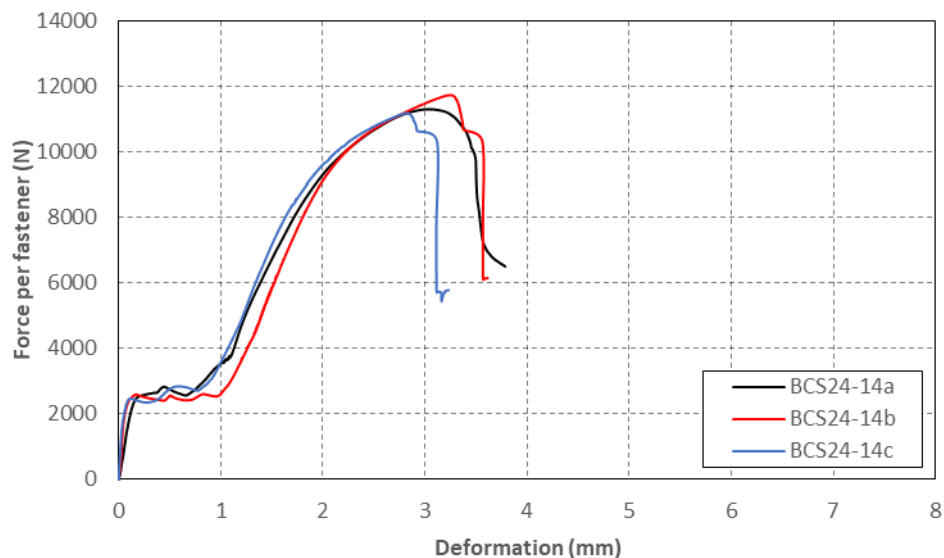


Figure 6.6: Load-elongation curve of specimens BCS24-14

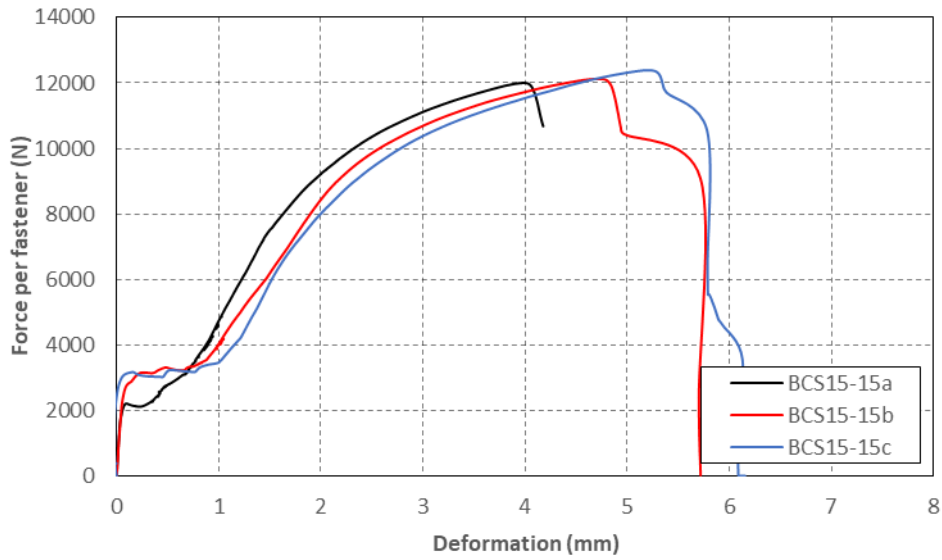


Figure 6.7: Load-elongation curve of specimens BCS15-15

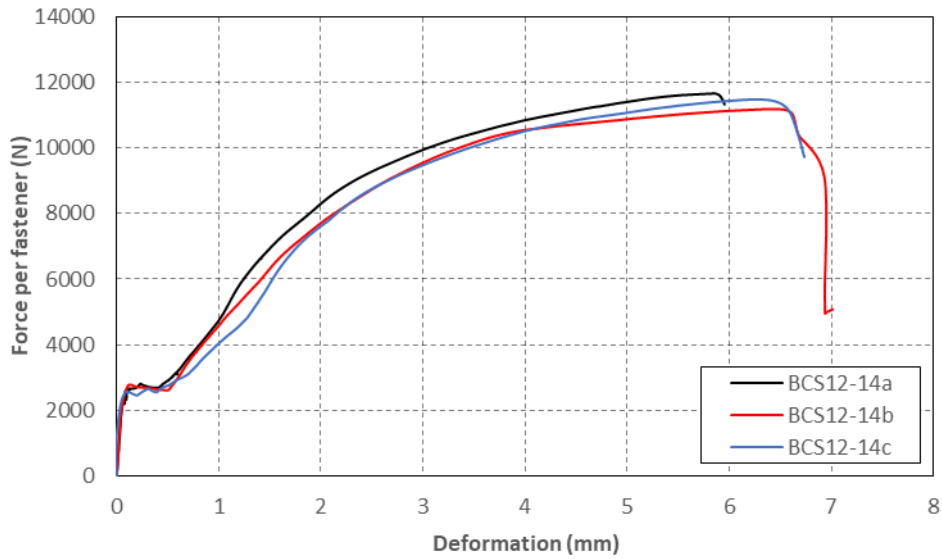


Figure 6.8: Load-elongation curve of specimens BCS14-12

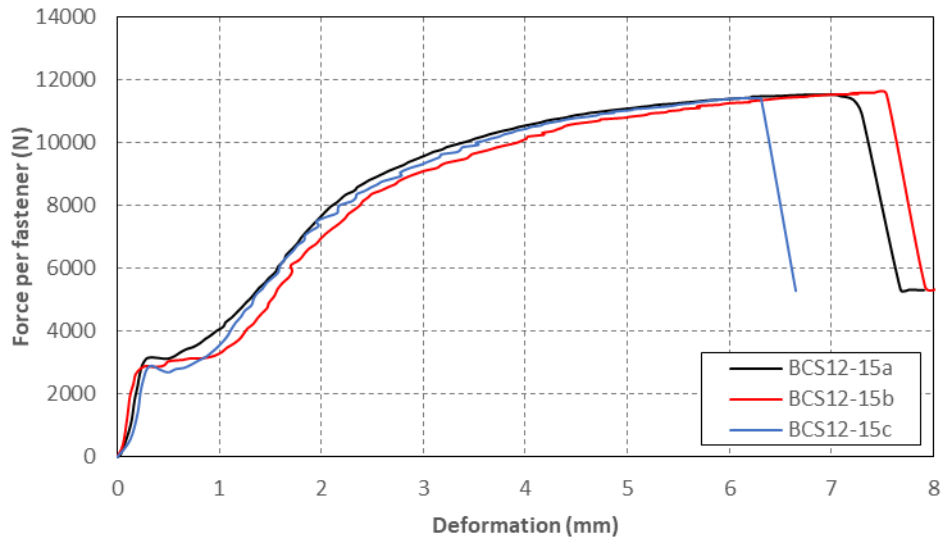


Figure 6.9: Load-elongation curve of specimens BCS15-12

All the bolted specimens tested in the second part of the experimental programme failed due to bearing failure in the thinnest steel plate. However, two distinctive types of failure could be distinguished depending on the amount of tilting of the fastener. In specimen BCS14-20b, for example, the thickest steel plate effectively limited the amount of tilting of the bolts, and although some tilting was noticeable (Figure 6.17a), most of the bearing in the steel plates resulted from direct contact between the bolt shaft and the edge of the hole. This resulted in a gradual loss of stiffness in the specimen towards the ultimate capacity, as illustrated in Figure 6.10. In specimens BCS14-14 and BCS12-12, on the other hand, the bolts experienced a larger amount of tilting due to the lower restraint provided by the steel plates, as illustrated in Figure 6.18a and Figure 6.19b for specimens BCS14-14b and BCS12-12c, respectively. As the bolts tilted, the load, which was initially transferred from the bolt shaft to the edge of the hole, started to mainly be transferred through the inner surface of the washer. This resulted in an increase of the bearing contact area and caused a slight increase in the stiffness of the specimen right before the ultimate capacity was reached, as shown in Figure 6.11 and Figure 6.12 for specimens BCS14-14 and BCS12-12, respectively.

Regarding the screwed specimens, all of them failed by pull-out of the screw. Consequently, the ultimate capacity of the screwed specimens was significantly lower than that of bolted specimens with the same combination of steel plates. Pull-out of the screw resulted in a load-elongation curve with a fluctuating stiffness in the later stages of deformation, as illustrated in Figure 6.10, Figure 6.11 and Figure 6.12 for specimens SCS14-20, SCS14-14 and SCS12-12, respectively.

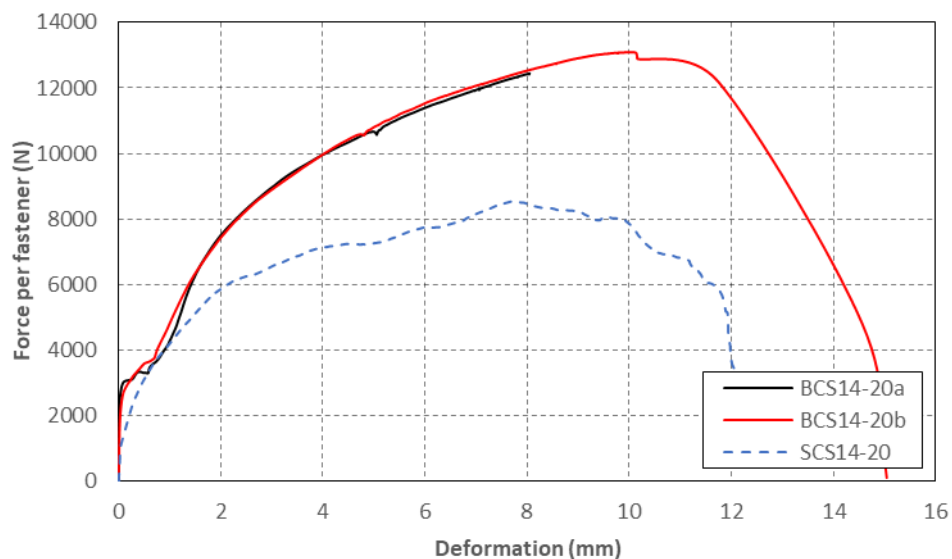


Figure 6.10: Load-elongation curve of specimens BCS14-20/SCS14-20

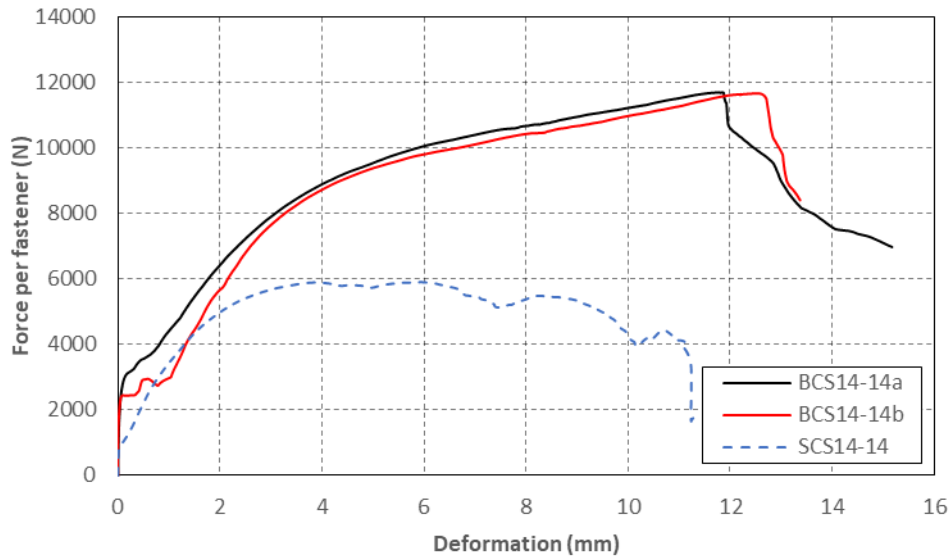


Figure 6.11: Load-elongation curve of specimens BCS14-14/SCS14-14

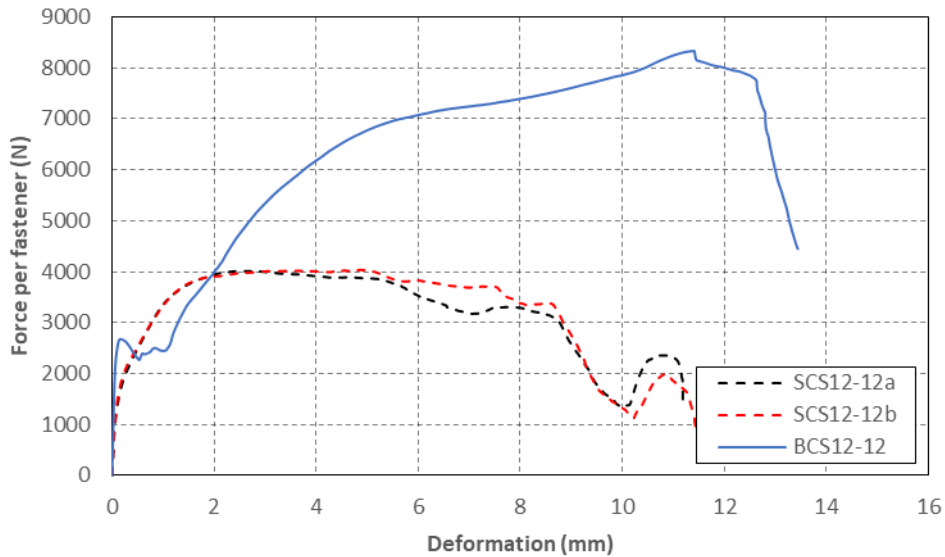


Figure 6.12: Load-elongation curve of specimens SCS12-12/BCS12-12

When comparing the results obtained for specimens with the same combination of plate thicknesses but a different type of fastener (Figure 6.10, Figure 6.11 and Figure 6.12), it is clear that the bolted specimens exhibited a stiffer response than the screwed specimens, at least until slip took place in the bolted connections. After slip, the bolted specimens were still able to provide an increasing bearing resistance, while the strength of the screwed specimens rapidly degraded. The reduced stiffness of the screwed specimens is mostly due to tilting of the fastener, which in the case of the bolted specimens is mostly prevented by the restraint provided by the washer and the nut. It is important to note that during the assembly of the bolted specimens the steel sheets were pressed against each other in the longitudinal direction in order to obtain maximum slip.

It is also worth mentioning that the response of the screwed specimens is highly dependent on how well the steel sheets are screwed together. For example, in specimen SCS14-14 the steel sheets separated while being screwed together, leaving a small gap, as illustrated in Figure 6.13. This resulted in a reduction in the stiffness of the connection, as shown in Figure 6.14, which compares the load-elongation curves obtained for all screwed specimens.



Figure 6.13: Small gap between steel sheets of specimen SCS14-14

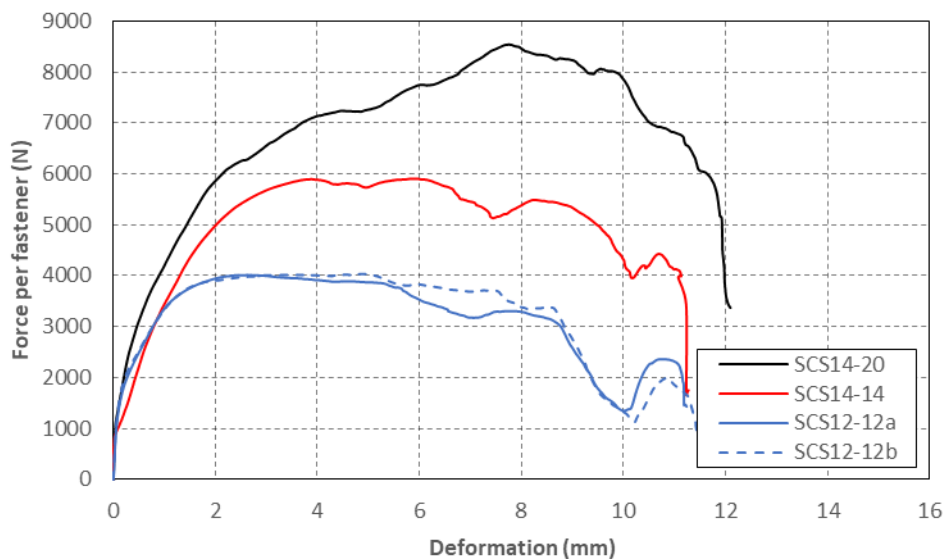


Figure 6.14: Load-elongation curve of all screwed specimens

Table 6.2 lists the ultimate load per fastener obtained for each specimen, and provides a brief description of the type of failure observed during the test. The table also lists the load in the fastener achieved at a deformation of 3 mm, as recommended by ECCS TC7 (2009). In general, good agreement was obtained between the ultimate capacities of twin specimens, with a maximum difference of less than 5 %. The only exception occurred for specimens BCS14-20, which showed a slightly larger difference. This was due to the fact that for specimen BCS14-20a the test was stopped before the specimen reached its ultimate capacity due to time

constraints in the lab. Therefore, the maximum load obtained for this specimen should be disregarded.

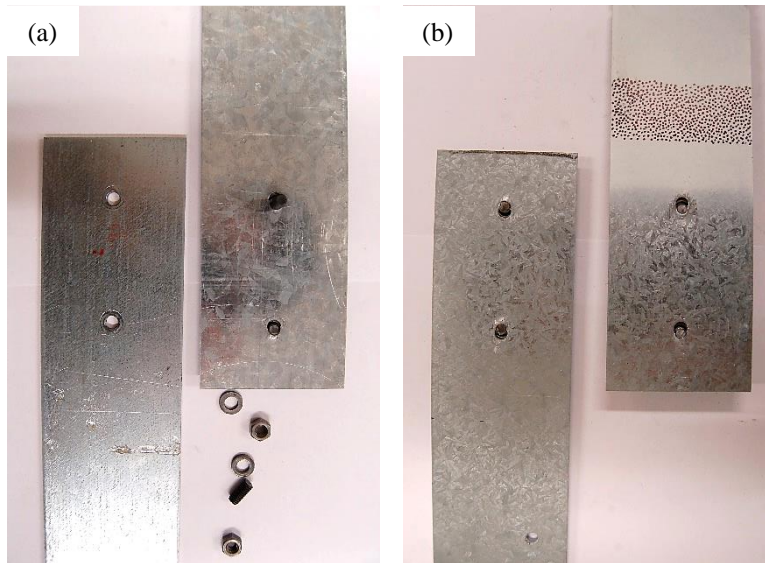


Figure 6.15: Deformed shape of a) BCS24-14b; b) BCS15-15c

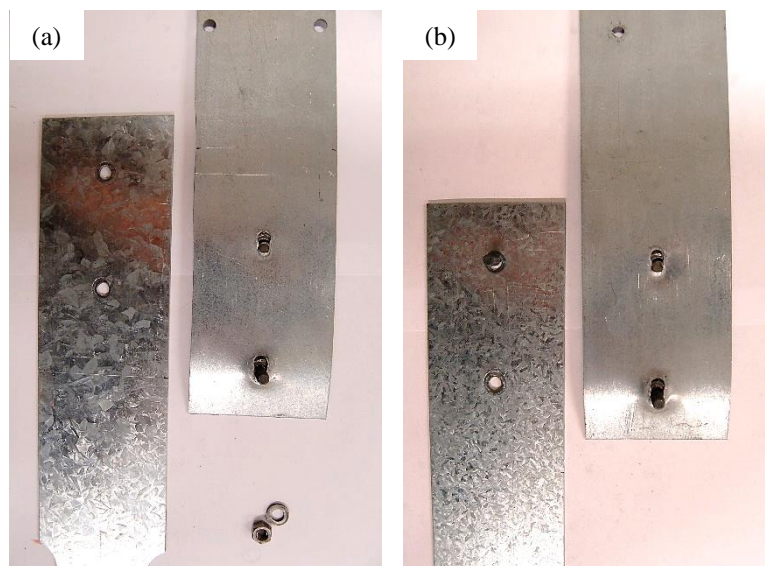


Figure 6.16: Deformed shape of a) BCS12-14c; b) BCS12-14a

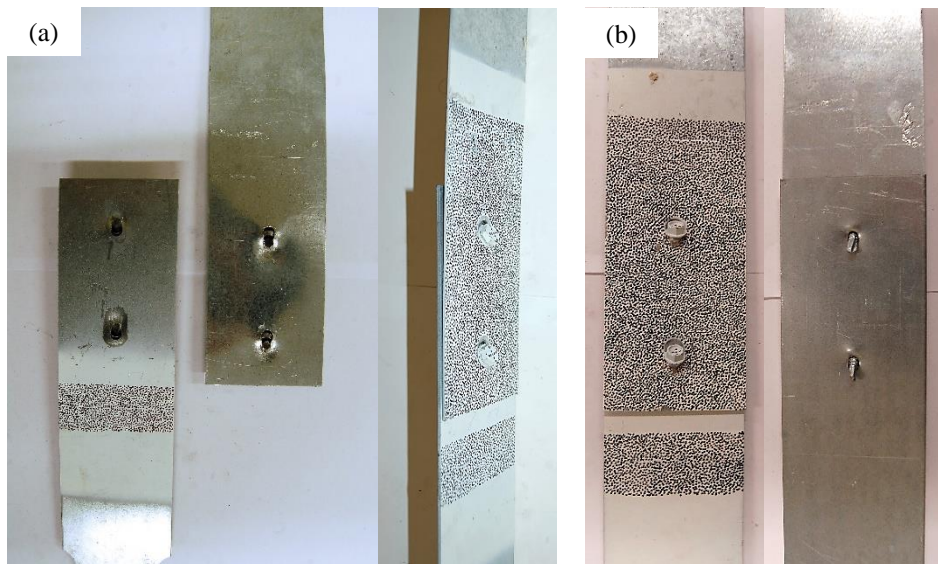


Figure 6.17: Deformed shape of a) BCS14-20b; b) SCS14-20c

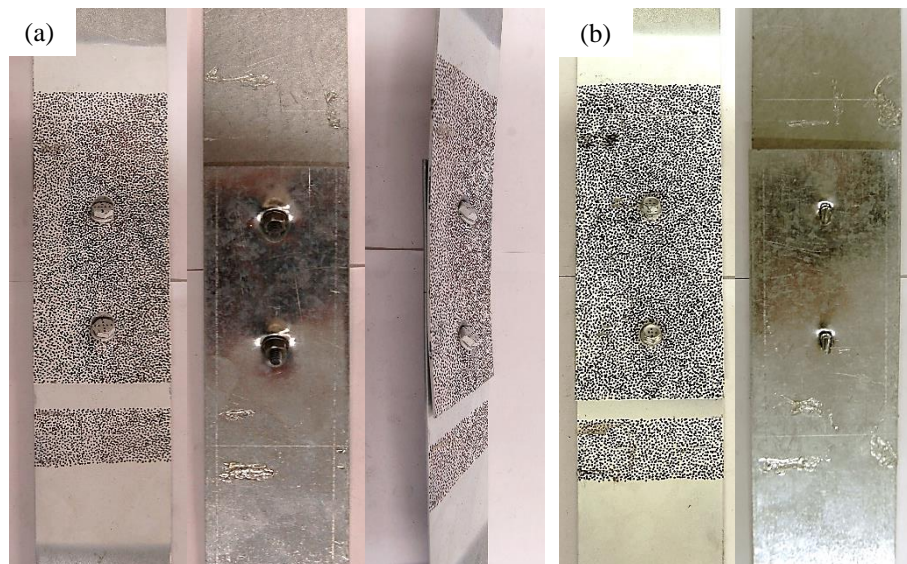


Figure 6.18: Deformed shape a) BCS14-14b; b) SCS14-14c

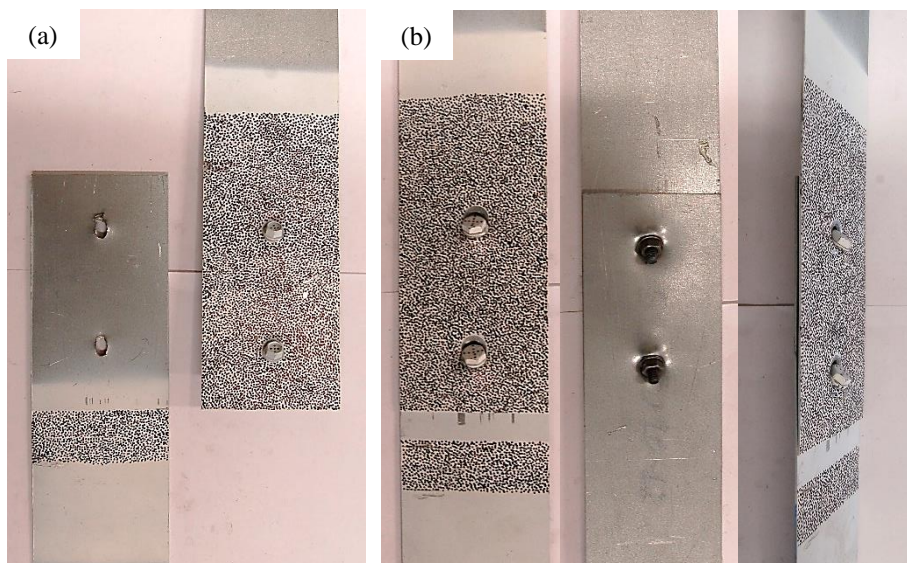


Figure 6.19: Deformed shape of a) SCS12-12a; b) BCS12-12c

Table 6.2: Ultimate capacity and failure mode of test specimens

Specimen	Ultimate load (N)		Type of failure
	P_{ult}	P_{ECCS}	
BCS24-14a	11304	11297	Shear failure of one of the bolts. Minor bearing deformations in the thinner plate. Almost no plate curling or bolt tilting.
BCS24-14b	11735	11481	
BCS24-14c	11179	10639	
BCS12-14a	11669	9951	Shear failure of one of the bolts with significant bearing deformations in the thinner plate. Curling of both plates, especially the thinner one.
BCS12-14b	11196	9558	
BCS12-14c	11487	9481	
BCS15-15a	12002	11118	Shear failure of the bolts. Bearing deformations equally distributed over both plates. Almost no plate curling or bolt tilting.
BCS15-15b	12127	10692	
BCS15-15c	12391	10382	
BCS12-15a	11506	10058	Shear failure of one of the bolts with significant bearing deformations in the thinner plate and some bearing deformations in the thicker plate. Curling of the thinner plate and slight tilting of the bolts.
BCS12-15b	11604	9320	
BCS12-15c	11419	9631	
BCS14-20a	(12444)	8960	Bearing failure of the thinner plate. Both plates showed significant bearing deformations. Noticeable tilting of the bolts.
BCS14-20b	13092	8895	
SCS14-20	8538	6552	Pull-out failure as a result of significant tilting of the screws. Noticeable bearing deformations, especially in the thinner plate.
BCS14-14a	11696	7898	Bearing failure in both plates with significant tilting of the bolts.
BCS14-14b	11663	7650	
SCS14-14	5904	5676	Pull-out failure as a result of significant tilting of the screws. Noticeable bearing deformations in both plates and some curling of the plate closest to the head of the screw.
SCS12-12a	4011	3994	Pull-out failure as a result of significant tilting of the screws. Noticeable bearing deformations in both plates.
SCS12-12b	4033	4007	
BCS12-12	8332	5341	Bearing failure in both plates with significant tilting of the bolts.

6.6.2 Comments on the LVDT arrangement

As a result of an initial curvature present in some of the specimens, the LVDTs located on opposite sides of the specimen recorded different deformations, as illustrated in Figure 6.20 for specimen BCS12-15c. This was due to the fact that the LVDTs recorded the deformations at a distance of 20 mm away from the surface of the specimen, as illustrated in Figure 6.21. As the specimen is loaded in tension (and tensile deformations are considered positive), the deformations recorded by each LVDT (δ_{LVDT_1} and δ_{LVDT_2}) are given by:

$$\delta_{LVDT_1} = \delta_v - x_1 - x_1' + x_2 \quad (6.1)$$

$$\delta_{LVDT_2} = \delta_v - x_2 - x_2' + x_1 \quad (6.2)$$

where δ_v is the actual elongation of the specimen over the gauge length, while x_1 , x_2 , x_1' and x_2' are deformations recorded by the transducers as a result of the flattening of the steel plates to which the LVDTs are attached, as illustrated in Figure 6.21 for one of the LVDTs. x_1 , x_2 , x_1' and x_2' can be determined using basic trigonometry, based on the measuring gauge length (150 mm), the distance from where the LVDT measurements were taken to the surface of the specimen (20 mm) and the initial inclination of the transducers and target plates, θ_1 and θ_2 , which resulted

from the initial curvature of the steel plates. It is worth noting that averaging the LVDT readings does not completely cancel out the effect of the initial curvature, as shown by Eq. (6.3).

$$\frac{\delta_{LVDT_1} + \delta_{LVDT_2}}{2} = \delta_v - \frac{(x_1' + x_2')}{2} \quad (6.3)$$

In fact, the average LVDT readings slightly underestimates the actual deformations by a factor of $(x_1' + x_2')/2$. However, the error is relatively small. For example, an average inclination of the LVDTs (θ_1 and θ_2) of 2° resulted in an error of around 0.2 mm. However, this is worth taking into account when comparing the deformations obtained using DIC with those obtained from the LVDTs.

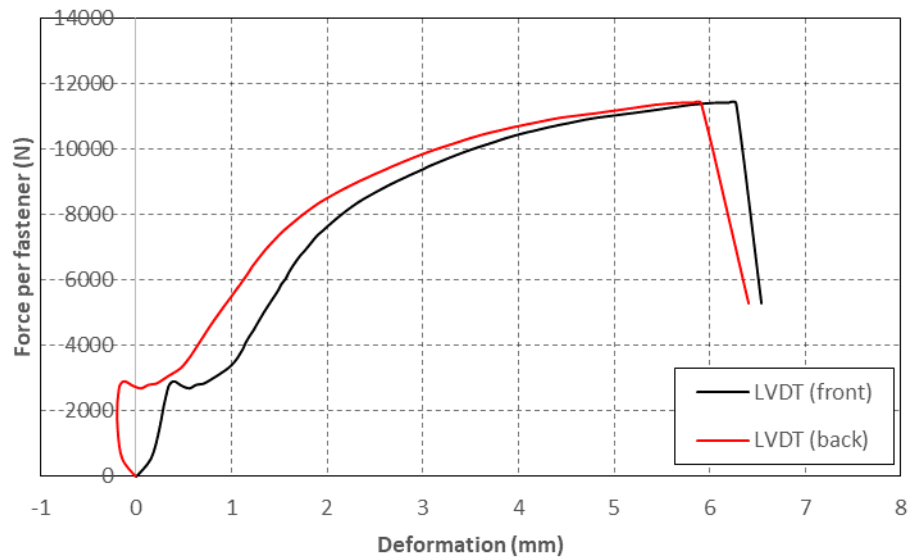
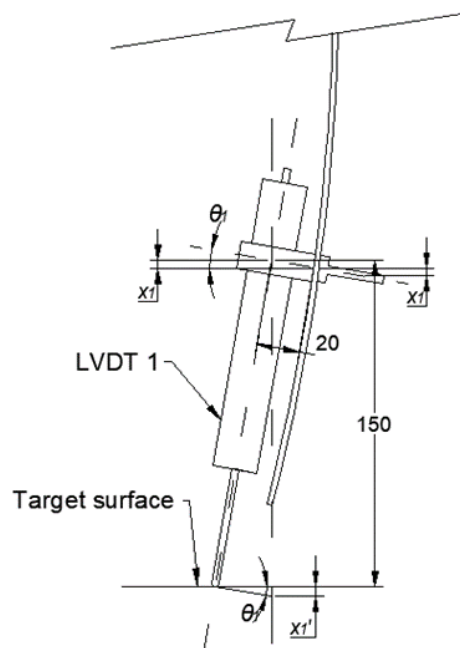


Figure 6.20: Force vs displacement curve of specimen BCS15-12c



All dimensions in mm

Figure 6.21: Source of error in LVDT readings

6.6.3 DIC accuracy

The accuracy of the DIC measurements was assessed by comparing the DIC results with the average deformations obtained from the LVDTs attached to the specimens. The accuracy of the readings given by the LVDTs was checked before and after testing the specimens and they were found to give readings with an accuracy of at least 0.08 mm for the range of deformations measured during the tests when verified against the stroke of a calibrated universal testing machine.

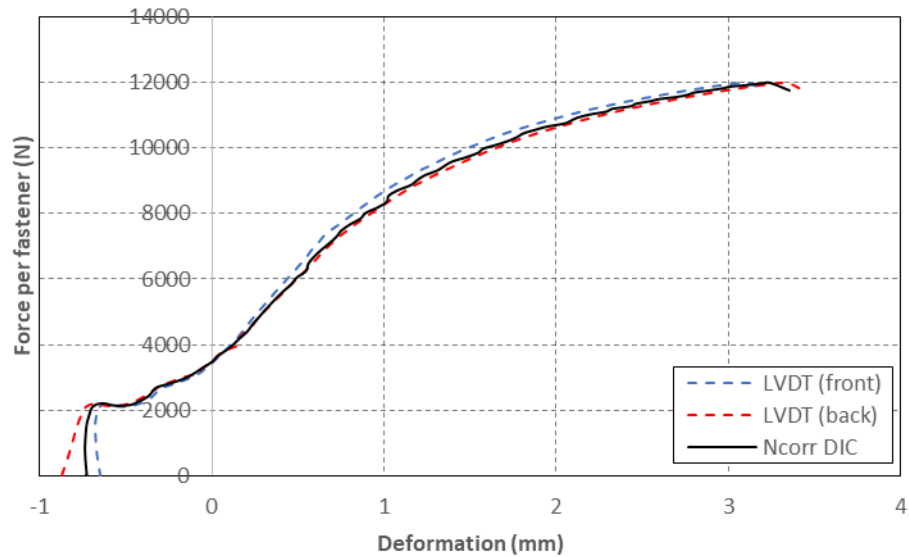
To ensure that the deformations measured with the DIC system and the LVDTs were synchronized in time, a computer monitor displaying the applied load and the LVDT readings was placed next to each specimen during the tests, so that this information was contained in the DIC pictures. This allowed for a direct comparison between the LVDT measurements and the DIC results. Only those specimens instrumented with LVDTs on both sides were used in the comparison. Table 6.3 lists the average and maximum differences between the deformations obtained using DIC and those obtained by averaging the readings provided by the LVDTs. The table also lists the average and maximum differences obtained between the deformations recorded with each LVDT. In addition, since the maximum deformation which was recorded varied significantly between different specimens (maximum deformations ranged from around 2 mm to 15 mm), the differences between the DIC and LVDT measurements are also presented as a fraction of the maximum recorded deformation. The deformations used to assess the accuracy of the DIC measurements were taken relative to a load level equal to 30 % of the ultimate capacity. This load level was chosen to avoid the initial loading range where possible straightening of the specimen took place.

Table 6.3 shows that the average difference between the deformations obtained with the Ncorr DIC code and the average deformations recorded with the LVDTs was 0.034 mm (or 0.92 % of the of the maximum displacement), which is less than the estimated error on the LVDT readings. The deformations obtained with Ncorr v1.2 differed by less than 0.142 mm from the average LVDT measurement in all specimens considered. It is important to note that in all of the specimens analysed with Ncorr v1.2, except specimen BCS12-14b, the average difference between the DIC and the LVDT measurements is less than half of the difference between the deformations recorded with the individual LVDTs. This indicates that the DIC measurements are situated in between the measurements recorded by each LVDT, as illustrated in Figure 6.22, which plots the load vs deformation curve obtained from the LVDT readings and from Ncorr v1.2 for a representative test specimen. Figure 6.23 shows the evolution of the difference between the LVDT and the Ncorr v1.2 measurements over the deformation history for different specimens. As the figure shows, the difference oscillates around zero without exhibiting any clear trend.

Table 6.3: Comparison between DIC and LVDTs

DIC Algorithm	Specimen	Difference between LVDTs		Difference between DIC and average LVDT (mm)			
		Avg. (mm)	Max. (mm)	Avg. (mm)	Max. (mm)	Avg. (% δ_{max})	Max. (% δ_{max})
Ncorr v1.2	BCS12-14a	0.193	0.621	0.046	0.142	1.32	4.02
	BCS12-14b	0.057	0.075	0.045	0.134	0.77	2.28
	BCS12-15b	0.195	0.518	0.042	0.136	0.60	1.96
	BCS12-15c	0.101	0.364	0.035	0.105	0.62	1.86
	BCS15-15a	0.136	0.229	0.026	0.066	0.77	1.97
	BCS15-15b	0.196	0.318	0.025	0.077	0.64	1.99
	BCS24-14b	0.047	0.075	0.015	0.047	0.63	1.95
	BCS24-14c	0.097	0.682	0.039	0.089	2.05	4.67
Jones DIC	SCS12-12a	0.135	0.290	0.178	0.299	1.66	2.80
	SCS12-12b	0.214	0.340	0.156	0.282	1.42	2.57
	BCS12-12	0.110	0.159	0.228	0.427	1.94	3.62
	BCS14-14a	0.257	0.348	0.114	0.248	0.79	1.72
	BCS14-14b	0.140	0.195	0.167	0.318	1.42	2.69
	SCS14-14c	0.431	0.594	0.123	0.216	1.17	2.06
	BCS14-20b	0.195	0.269	0.121	0.219	1.32	2.39
	SCS14-20	0.284	0.355	0.194	0.403	1.72	3.57
Ncorr v1.2	Avg.	0.128	0.360	0.034	0.100	0.92	2.59
	Max.	0.196	0.682	0.046	0.142	2.05	4.67
Jones DIC	Avg.	0.221	0.319	0.160	0.302	1.43	2.68
	Max.	0.431	0.594	0.228	0.427	1.94	3.62

Note: δ_{max} is the maximum recorded displacement

**Figure 6.22: Load vs deformation curve obtained from LVDTs and Ncorr v1.2 for specimen BCS15-15a**

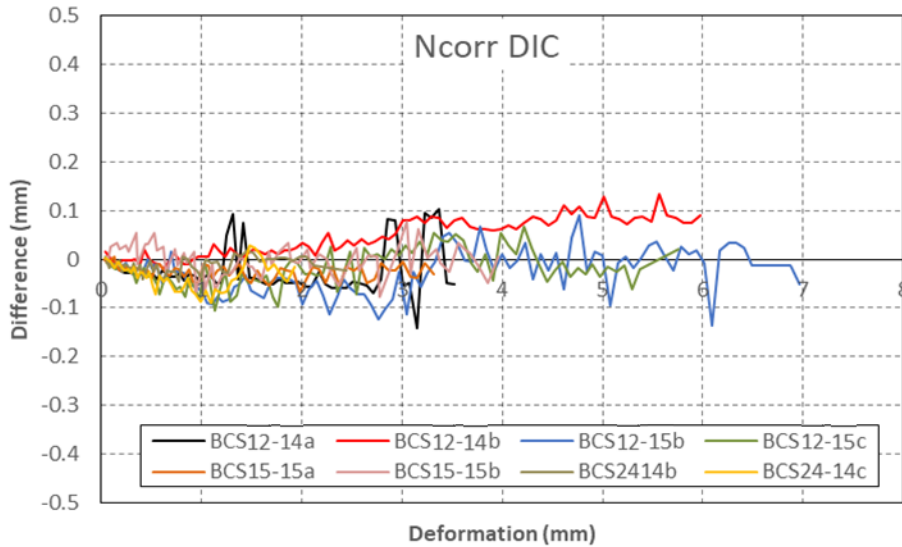


Figure 6.23: Difference between Ncorr v1.2 and average LVDT measurements

With respect to the difference between the deformations obtained using Jones’ DIC code and the average of the LVDTs readings, Table 6.3 shows that the average difference was 0.160 mm, or 1.43 % of the maximum deformation measured, while the maximum difference was 0.427 mm (for specimens BCS12-12 with a maximum deformation of around 12 mm). Figure 6.24 shows the difference obtained by deducting the DIC measurements from Jones’ algorithm from the average LVDT readings over the deformation history for different specimens. In this case a clear trend can be appreciated, whereby the deformations obtained with Jones’ DIC code were consistently smaller than those recorded by the LVDTs. The difference appeared proportional to the measured deformations and was roughly equal to 2.6 % of the recorded measurement.

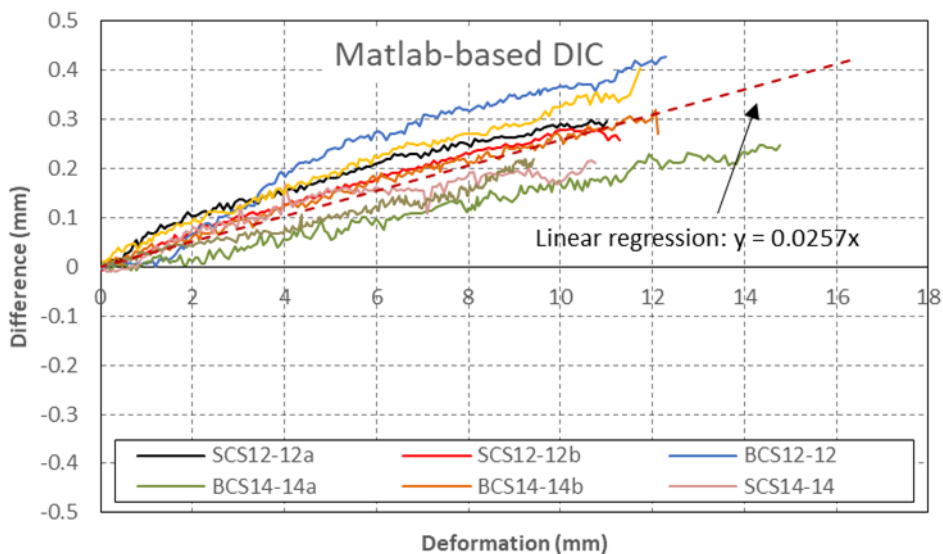


Figure 6.24: Difference between deformations obtained from Jones’ DIC and LVDTs

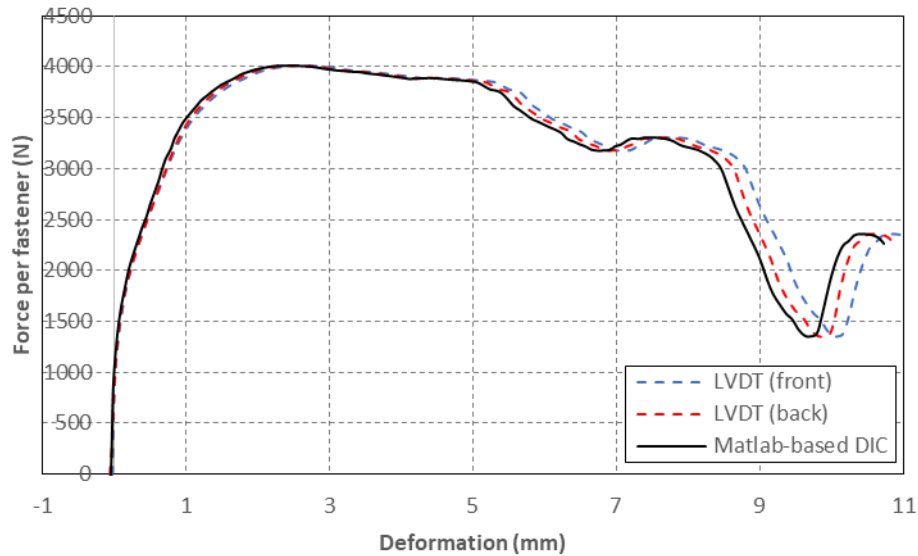


Figure 6.25: Load vs deformation curve obtained from LVDTs and Jones' DIC code for specimen SCS12-12a

6.7. Summary and conclusions

A series of single lap shear tests was carried out in order to determine the behaviour and capacity of the connectors used in the built-up members presented in Chapter 3, Chapter 4 and Chapter 5. The specimens were fabricated with the aim of replicating conditions in the actual built-up members as much as possible, in terms of dimensions, material properties, fabrication and torque.

The connector behaviour was recorded using LVDTs attached to the test specimens and also using Digital Image Correlation (DIC), an alternative, non-contact measuring technique of which the reliability was assessed by comparing the results with those obtained from the transducers.

The tests allowed to successfully obtain the load-deformation curves of the connectors, which were further used in the next chapters as input data in detailed FE models.

The assessment of the two DIC algorithms suggests that both algorithms can be successfully used to measure deformations in CFS sections, provided that the deformations are contained within a plane. Out of the two codes assessed, Ncorr v1.2 showed a significantly higher accuracy than Jones' DIC code. Moreover, the accuracy of the measurements obtained from Ncorr v1.2 was at least of the same order as the accuracy of the LVDTs. Therefore, in order to properly assess the accuracy of this DIC algorithm, the results would have to be compared to more precise measuring techniques. The measurements obtained from Jones' DIC code showed a systematic error of about 2.6 % when compared with the LVDTs readings. This shows that

DIC can be used as an alternative method to record deformations in CFS members. This might prove particularly useful in cases where conventional measuring techniques cannot be applied, such as in tests under fire conditions.

Chapter 7

Numerical Study of Cold-Formed Steel Built-up Stub Columns

7.1. Introduction

This chapter describes the development of detailed finite element (FE) models for the built-up stub columns presented in Chapter 3 using the software package Abaqus v.6.14 (Dassault Systemes, 2014). Figure 7.1 shows the cross-sectional geometry of the four different built-up columns modelled. Geometries 1 and 2 were assembled using M6 bolts, which were placed in holes with a slightly larger diameter, leading to the possibility of slip at the connector points during the deformation of the column. Geometries 3 and 4 were assembled using M5.5 self-drilling screws. In these columns relative deformations between the connected surfaces was only expected to originate from localized bearing deformations in the components and tilting of the connector.

The stub column models presented significant convergence issues which were addressed by modifying some of the solution control parameters which Abaqus/Standard uses when solving a non-linear problem, and by introducing artificial damping into the models. A stabilization analysis was carried out to ensure that the ultimate capacity predicted by the models was not significantly affected by the amount of damping introduced into the model.

The FE models were verified against the experimental data obtained from the stub column tests, which included the ultimate capacity of the column, their buckled shape and the critical buckling stresses obtained for some of their components. The validated models were further used to carry out parametric studies with the aim of investigating the way in which the connector modelling approach and connector spacing, as well as contact between the components affects the buckling response of the built-up stub columns.

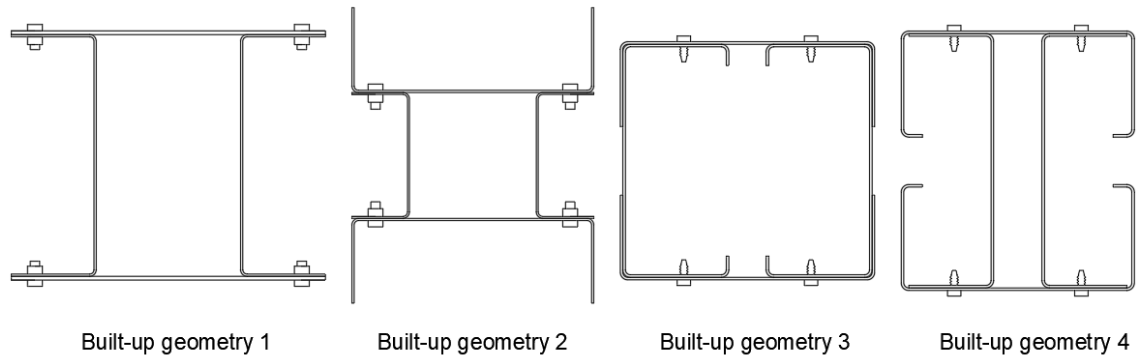


Figure 7.1: Built-up cross-sections

7.2. Details of the FE models

Detailed finite element models were developed of the built-up stub columns presented in Chapter 3 using the software package Abaqus v.6.14. The columns were discretized using structural shell elements with five integration points through the thickness and using Simpson's rule. The models were constructed based on the measured cross-sectional dimensions of the components. They included the initial geometric imperfections measured on the columns and material non-linearity obtained from tensile coupons. In addition, the connectors used to assemble the columns were modelled using mesh-independent fasteners which accounted for the connector properties obtained from single lap shear tests. All columns were modelled with fixed end conditions. The FE models were verified against the experimental data reported in Chapter 3, and were further used in parametric studies.

The numerical models were labelled following the same nomenclature used for the tested columns. The letters 'SC' were used to indicate that the model corresponded to a stub column, and the numbers 1 to 4 were used to indicate its cross-sectional geometry (with reference to Figure 7.1). The number after the hyphen was used to indicate the number of intermediate rows of connectors along the column. For example, the label 'SC1-2' refers to the FE model of a stub column with cross-sectional geometry 1 and two intermediate rows of connectors.

7.2.1 Boundary conditions

The test specimens were compressed between fix-ended boundary conditions under displacement control. The ends of the test specimens were attached to endplates using an epoxy resin which covered the specimens over a distance of 20 mm at each end. The FE models were developed assuming that the resin provided a mould rigid enough to prevent the enclosed ends of the specimens from rotating and deforming laterally. In order to simplify the FE models

neither the endplates nor the end portion of the column enclosed by the resin were included in the model.

In all of the FE models, the boundary conditions at the bottom end of the column were defined by constraining all translational and rotational degrees of freedom of the nodes in the end section. To define the boundary conditions at the top end of the column a reference point was created, coinciding with the centroid of the end section and all the rotational and translational degrees of freedom of the nodes in this cross-section were coupled to the degrees of freedom of the reference point using a BEAM MPC constraint. The boundary conditions were then applied to the reference point by constraining all its rotational and translational degrees of freedom, apart from the translational degree of freedom in the axial direction. The compressive force was applied to the column by imposing an axial displacement to the reference point.

7.2.2 Geometric imperfections

Initial geometric imperfections are unavoidable in cold-formed steel members, and since both their magnitude and shape may have a significant effect on the buckling behaviour of these members, they need to be appropriately incorporated in the FE models.

The initial geometric imperfections were recorded on the test specimens by moving a laser displacement sensor along several longitudinal lines, as shown in Figure 7.2. The procedure followed to record the imperfections of the stub columns is described in Section 3.6.2 of Chapter 3. These imperfections were incorporated into the FE model by modifying the coordinates of the nodes in the input file (*.inp) of a geometrically perfect FE model generated in Abaqus/Standard using a specially developed Matlab code.

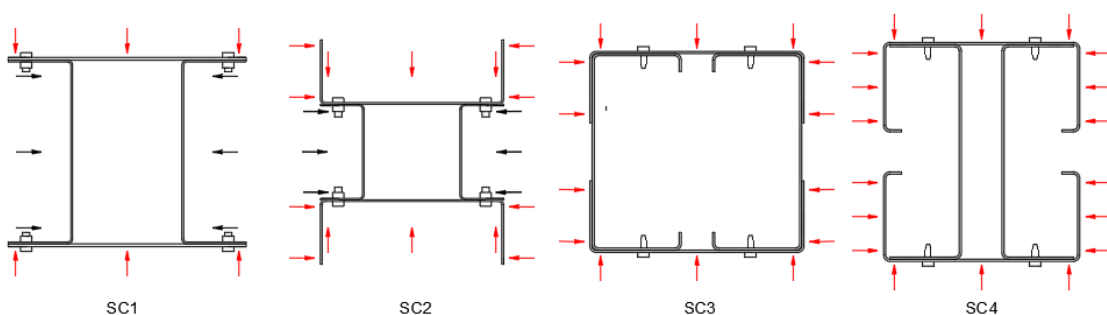


Figure 7.2: Location of measured imperfections in stub columns

The imperfections at the location of the nodes of the FE model were determined by interpolating the imperfection measurements taken on the test specimen. A quadratic interpolation was carried out to determine the nodal imperfections in the web of the channels and in the plate sections, while linear interpolation was used to determine the nodal imperfections in the flanges

of the channels, as illustrated in Figure 7.3. This technique was previously successfully employed in (Becque and Rasmussen, 2009a).

Figure 7.4 shows, as an example, FE models belonging to geometries SC1, SC2, SC3 and SC4 with amplified out-of-plane imperfections for clarity.

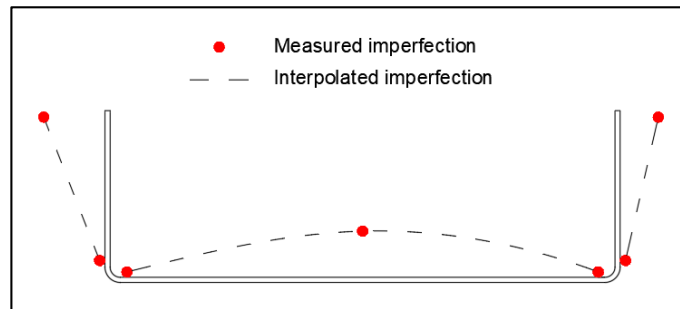


Figure 7.3: Interpolated imperfections

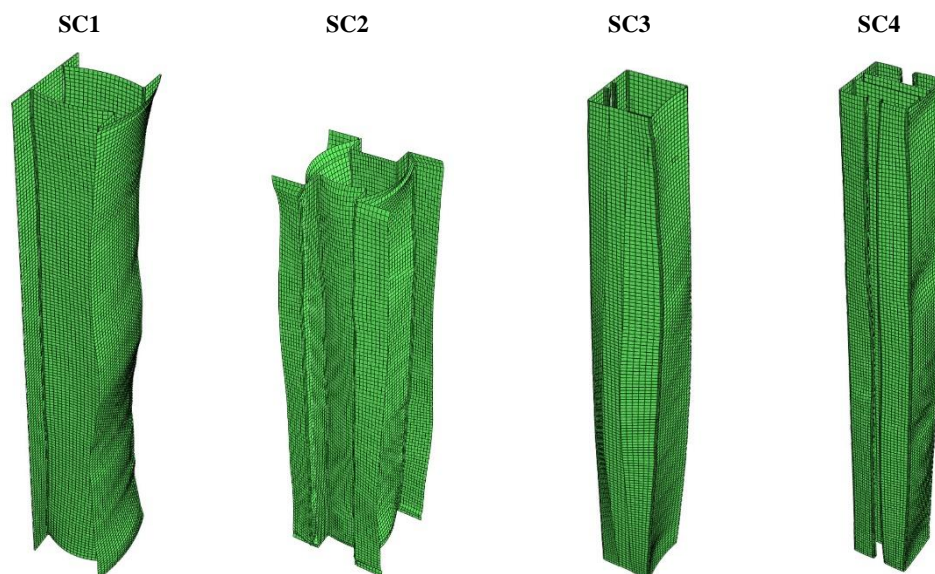


Figure 7.4: FE models including amplified out-of-plane imperfections

7.2.3 Material properties

The material properties of the components of the built-up columns were modelled as elastic-plastic using the isotropic linear elastic material model together with the metal plasticity model available in Abaqus/Standard. The data used in the FE models corresponded to the ‘static’ values of the material properties obtained from the flat and corner coupon tests, as described in Section 3.3.3 of Chapter 3. The elastic behaviour was defined using a Poisson’s ratio of 0.3 and the elastic modulus obtained from the tensile coupons, following the recommendations given by Huang and Young (2014). The metal plasticity behaviour was defined using the standard von

Mises yield surface with associated plastic flow and isotropic hardening. The start of the plastic range was taken as the last point on the stress-strain curve which was used to calculate the elastic modulus. Enough data points were taken from the stress-strain curve obtained from the tensile coupons in order to accurately replicate the inelastic behaviour of the material. Since Abaqus/Standard employs true stresses and true (logarithmic) plastic strains, the engineering values obtained from the coupons were converted into true values using the following relationship:

$$\sigma_T = \sigma(1 + \varepsilon) \quad (7.1)$$

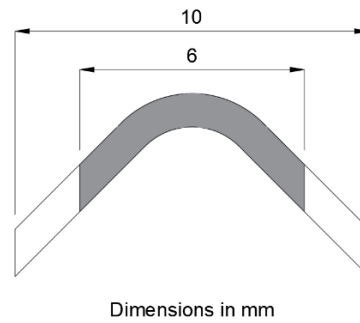
$$\varepsilon_T = \ln(1 + \varepsilon) \quad (7.2)$$

$$\varepsilon_T^{Pl} = \varepsilon_T - \sigma_T / E \quad (7.3)$$

where σ_T , ε_T and ε_T^{Pl} are the true stresses, the true strains and true plastic strains, respectively, and σ and ε are the engineering stresses and the engineering strains.

All the flat portions of a component section were considered to have the same material properties, regardless of the part of the section they belonged to (e.g. web, flanges or lips). This was considered to be a valid simplification, since it has been shown by Karren (1965) that similar cold-working effects are experienced by all the flat elements of the cross-section, irrespective of the forming-process used. In addition, since cold-working may significantly increase the yield stress of cold-formed steel sections, the enhancement of the mechanical properties in the corner regions of the individual channels was also included in the FE models. Karren, (1965) reported that the influence of cold-working may extend beyond the corner over a distance less than the sheet thickness. However, this influence decreases with the distance from the centre of the corner. The corner coupons tested in Chapter 3 had a width of 6 mm, as illustrated in Figure 7.5, covering, in general, a slightly larger portion than the actual corner of the cross-sections. However, since the values obtained from the tensile coupons corresponded to the average value of the material properties in this region, the corner regions in the FE models were defined based on the width of these coupons.

This approach to model the material properties in the FE models, which included an accurate representation of the stress-strain curve and the enhancement of the mechanical properties at the corner regions of the channels is further referred to as the ‘actual material’ modelling approach.



Dimensions in mm
Figure 7.5: Corner coupon width

7.2.3.1 Simplified approaches to model material properties

A material modelling study was carried out to investigate the degree to which the ultimate capacity of the built-up stub columns was affected by simplifications in modelling their material behaviour. The effects of two simplified material modelling approaches were investigated using a representative column of each built-up geometry, by comparing the ultimate load predictions obtained from the FE models incorporating these simplified material models with those obtained from the FE model including the actual material properties.

The first simplified material model approximated the stress-strain curve obtained from the tensile coupons by a bilinear curve. The elastic range was defined in the same way as in the actual material modelling approach described in the previous sub-section, while the plastic range was defined using the 0.2 % proof strength without any strain hardening, as shown in Figure 7.6. The enhancement of the mechanical properties in the corner regions was still included in this material modelling approach. The second simplified material modelling approach was identical to the actual material modelling approach, with the only exception that the enhancement of the mechanical properties in the corner regions was not considered.

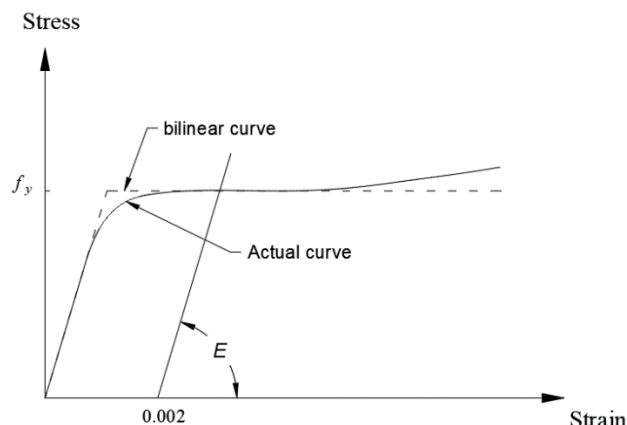


Figure 7.6: Bilinear and actual stress-strain curve

The load-axial deformation curves obtained using the three different material modelling approaches are illustrated in Figure 7.7 for a representative column belonging to each built-up geometry. As expected, the figure shows that, across all geometries, the post-buckling stiffness predicted by the FE model in which the material properties are approximated by a bilinear stress-strain curve remains higher (up to the peak load) than in the FE models including gradual yielding in the material behaviour, and the peak load is achieved at a smaller axial shortening of the column. The figure also shows that, across all geometries, the ultimate capacity obtained using the bilinear stress-strain curve is noticeably larger than the one obtained using the actual material modelling approach. On the other hand, ignoring the enhancement of the material properties in the corner regions resulted in slightly lower ultimate capacities with respect to the predictions given by the FE model including the actual material properties. Table 7.1 reports the differences in ultimate capacity obtained using the simplified material modelling approaches relative to the predictions obtained using the actual material properties for each geometry.

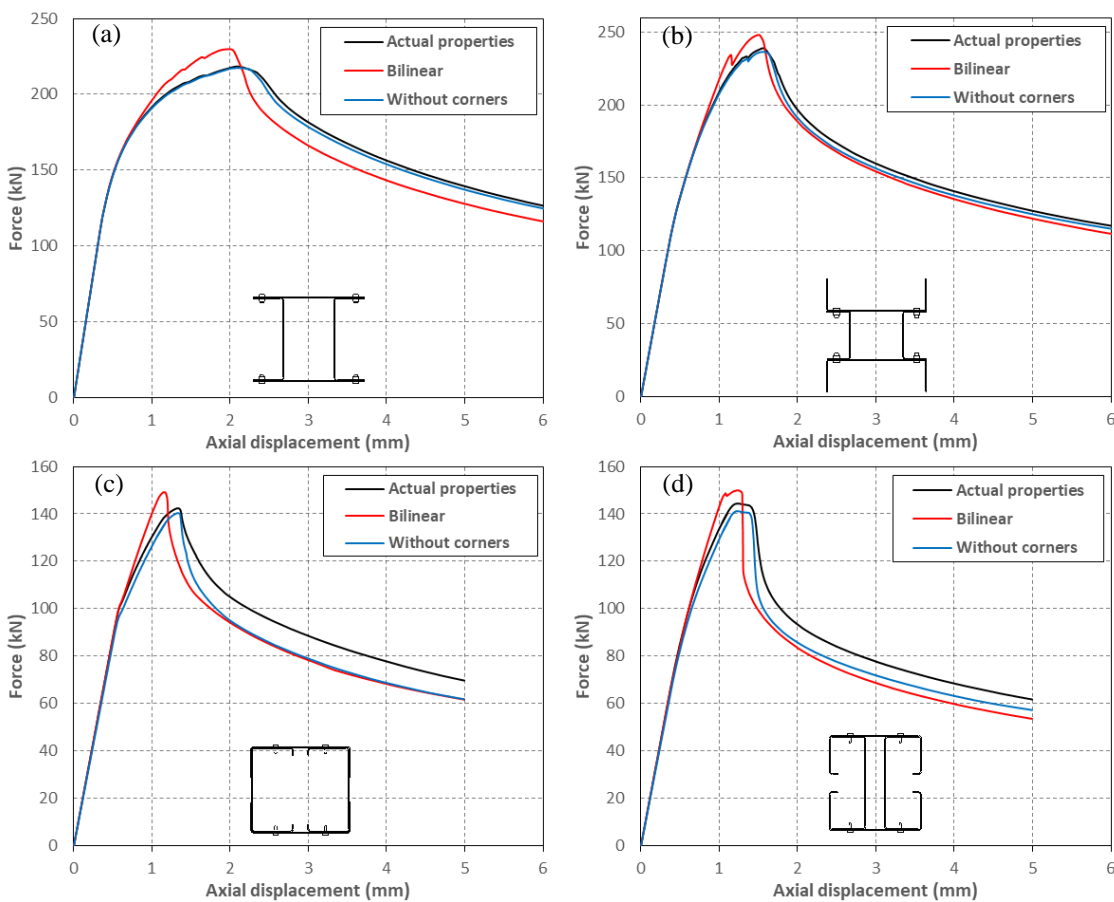


Figure 7.7: Effect of material modelling approach on predicted column response: a) SC1-5b; b) SC2-6a; c) SC3-5b; d) SC4-5a

Table 7.1 Difference in ultimate load relative to FE model with actual material properties

Column	Difference in ultimate load with respect to model with actual material properties (%)	
	Bilinear	Without corners
SC1-5a	5.0	-0.4
SC2-6a	4.0	-0.9
SC3-5b	4.6	-1.5
SC4-5a	4.0	-2.0

7.2.4 Contact interaction

In all numerical models contact was defined using the finite-sliding surface-to-surface contact formulation, in which the surfaces in contact are allowed to experience an arbitrarily large relative separation, sliding and rotation. The contact conditions are enforced in an average sense over regions nearby the slave nodes, avoiding large undetected penetration of the master nodes into the slave surface and improving contact pressure predictions. Since the components of the built-up geometries were modelled based on their mid-surface, the different components were positioned with respect to each other leaving a gap equal to their average thickness. The general contact formulation automatically accounts for the thickness associated with shell-like surfaces, defining contact on the outer faces. Interaction between the surfaces in contact was defined as ‘frictionless’ in the tangential direction, while a ‘hard’ pressure-overclosure relationship was approximated in the normal direction by using ‘Augmented Lagrange’ as the constraint enforcement method. This enforcement method reduces the amount of penetration of the slave nodes into the master surface, improving the accuracy of the ‘hard’ pressure-overclosure approximation.

In order to reduce the computational cost, contact was only activated between those surfaces of components which were likely to interact with each other during the analysis, as shown in Figure 7.8. For built-up column 1, these surfaces corresponded to the plate sections and the flanges of the channels, while for built-up column 2, these surfaces corresponded to the web of the outer channels and the flanges of the inner channels. For built-up column 3 contact was defined between the web of the lipped channels and the flanges of the plain channels, and also between the flanges of the lipped channels and the web of the plain channels. For built-up column 4 it was decided to only define contact between the flanges of the plain channels and the webs of the lipped channels. This contact definition for built-up column 4 implied that the edges of the flanges of the plain channels were allowed to penetrate into the flanges of the lipped channels. The additional edge-to-surface contact interaction resulted in significant convergence issues and therefore it was decided not to include it. This decision was supported by the fact that penetration of the edges of the plain channel flanges into the lipped channel flanges only occurred after the column reached its peak load. Therefore, not including edge-to-surface

contact between the flanges of the plain channels and those of the lipped channels was deemed not to affect the pre-peak behaviour and ultimate capacity of these columns.

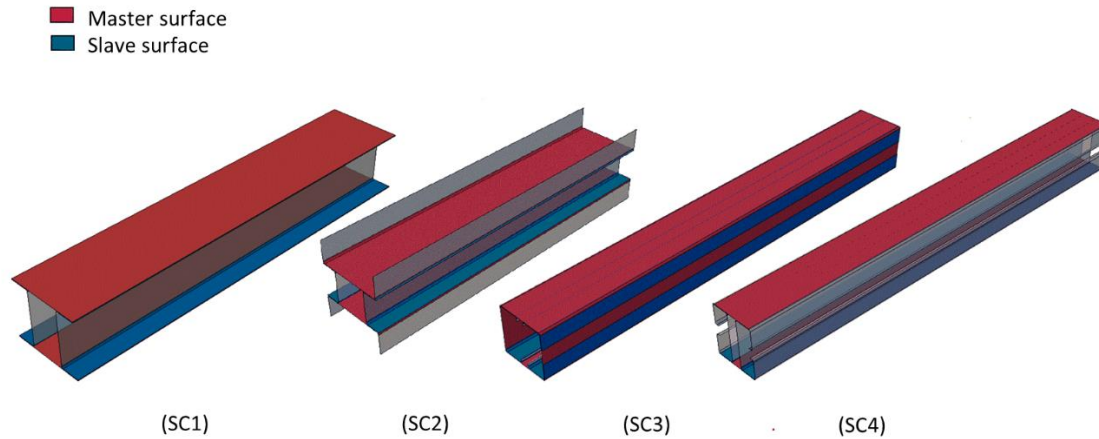


Figure 7.8: Master and slave role in contact interaction

Any possible initial overclosure between the slave and master surfaces in a contact interaction was eliminated at the beginning of each analysis using the strain-free adjustment method, which adjusts the positions of the penetrating slave nodes so they lie directly on their associated master surface. Initial overclosures were likely to occur due to the introduction of the initial geometric imperfections into the FE models. In addition, since the default strain-free adjustment available in Abaqus/Standard was designed to remove only small initial overclosures measuring up to the average thickness of the connected surfaces, the default search zone for the strain-free adjustment method was increased to 2 mm. Care was taken to ensure that the ‘master’ role in a contact interaction was assigned to a surface of which the nodes had previously been adjusted when introducing the geometric imperfections into the FE model. This warranted that the accurate modelling of the imperfection data was not lost due to the initial strain-free adjustment of the penetrating slave nodes.

7.2.5 Connector modelling

One of the main objectives during the development of the FE models was to determine the best way to model the two different types of connectors used to assemble the built-up columns, namely the bolts and the self-drilling screws. Built-up columns with geometry 1 and geometry 2 were connected using M6 bolts with a nominal diameter of 6 mm. To ease the assembly of the built-up specimens the holes were drilled with a nominal diameter of 6.25 mm. This resulted in a small clearance at the connectors which allowed a certain slip between the component sections. Built-up columns with geometry 3 and geometry 4 were assembled using M5.5 self-

drilling sheet metal screws. These type of fasteners are drilled into the metal sheets and do not result in any clearance.

In order to reduce the computational cost of the FE models, the body of the connectors was not explicitly modelled, but instead a discrete approach using mesh-independent fasteners was chosen. Mesh-independent fasteners create a point-to-point connection between two or more surfaces using fastening points, which are independent of the location of the nodes on each surface. The fastening point was connected to the neighbouring nodes on the surface using the structural coupling method, which couples the translational and rotational degrees of freedom of the fastening point to the average translational and rotational degrees of freedom of the neighbouring coupling nodes using a uniform weighting scheme. The radius of influence, which dictates the number of coupling nodes that are used to connect the fastening point to the surface, was not seen to affect the behaviour of the studied stub columns and this was set by defining a physical radius for the fastener of 5 mm in all numerical models.

The mesh-independent fasteners were modelled using discrete fasteners with PLANAR connector elements, which were orientated so that their rotational component of relative motion (CRM) was normal to the surfaces and the two translational CRMs were tangential to the plane of contact, as shown in Figure 7.9.

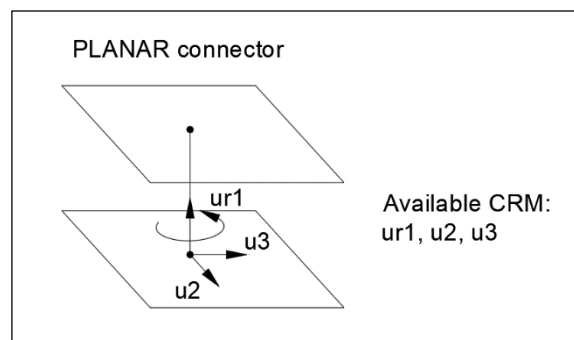


Figure 7.9: PLANAR connector element

In order to replicate the actual behaviour of the fasteners used to assemble the built-up stub columns, the elastic and plastic properties derived from the single lap shear tests carried out on the bolted and screwed connections were assigned to the two translational CRMs of the PLANAR connectors. This permitted to account in the FE model for the effect of the localized bearing deformations, possible tilting of the connector and, in the case of the bolted built-up columns, possible slip.

7.2.6 Type of analysis

A geometrically and material non-linear analysis of the stub columns was carried out using the General Static solver with the inclusion of artificial damping to stabilize the solution. This modelling approach has proved to be suitable for modelling the response of built-up specimens in which contact discontinuities may result in severe convergence errors. Abaqus/Standard automatically adjusted the time increments during the simulation using the automatic incrementation control algorithm.

7.2.7 Overcoming convergence issues in Abaqus/Standard

The numerical models of the built-up stub columns presented significant convergence issues. These issues arose mainly at the point when initial buckling took place and also when the columns reached their ultimate capacities. These events caused a sudden reduction in stiffness in certain areas of the built-up column. Moreover, contact between the components of the built-up column introduced significant discontinuities into the model, which further affected convergence.

In order to overcome these issues, the models were stabilized using either the automatic stabilization or the contact stabilization mechanisms available in Abaqus/Standard. Automatic stabilization and contact stabilization make use of artificial damping forces applied at the nodes to oppose their sudden movement. The main difference between these stabilization mechanisms is that automatic stabilization is designed to address convergence issues mainly related to geometric and material non-linearity. Therefore, the calculated viscous forces computed with this stabilization mechanism are applied to all the nodes of the model and their magnitude is proportional to the absolute velocity of each node. Contact stabilization, on the other hand, is only meant to smoothen contact discontinuities. In this case, the viscous forces are only applied to the slave nodes in a contact interaction and are proportional to the relative motion between the surfaces, as described in Section 2.8.3.2 of Chapter 2. Since both stabilization schemes help to achieve convergence by introducing artificial forces into the numerical model, it is important to ensure that these artificial forces are small enough so that they do not distort the solution. This can be achieved by performing a post-analysis check to ensure that the dissipated stabilization energy (ALLSD) is significantly smaller than the total strain energy of the system (ALLIE).

In addition to using the stabilization schemes available in Abaqus/Standard, convergence issues were significantly mitigated by modifying some of the default solution control parameters in the General Static solver. The solution control parameters which were modified were the displacement correction control parameter C_n^α and the time incrementation parameters I_0 and I_R .

In each increment Abaqus/Standard checks whether the force residuals at each node are within the tolerance limit (by default equal to 0.5 % of an average force in the structure, averaged over time). Subsequently it carries out an additional check to ensure that the maximum displacement correction c_{max}^{α} at each node is less than a fraction of the total incremental displacement of the node, as explained in Section 2.8.2 of Chapter 2. This fraction is given by C_n^{α} , which by default is set to 0.01. This additional check was found to create significant convergence issues in the column models due to the relatively large and sudden displacements and rotations the nodes in the model experience as a result of buckling, and also when the column is approaching its ultimate capacity and a yield line mechanism start to form. The check resulted in an unnecessary reduction of time increment sizes, despite the force residuals in the resulting equilibrium configuration being within the tolerance limits. Abaqus/Standard allows the user to remove this check by setting C_n^{α} to 1. This modification was found not to have any noticeable effect on the accuracy of the solution.

The time incrementation parameters I_0 and I_R are used to control the frequency with which Abaqus/Standard checks whether the solution converges monotonically and whether convergence is quadratic. The default values of these parameters (4 for I_0 and 8 for I_R) were increased to 8 and 10, respectively, as recommended in (Dassault Systemes, 2014) for severely discontinuous problems in order to avoid unnecessary cutbacks of the time increments. Also, the ‘line search algorithm’, which helps prevent divergence by applying a scale factor to the computed solution, was activated, allowing up to 40 line search iterations to calculate the scale factor and defining a tolerance for the change of the scale factor between successive iterations of 0.001. This permitted minimizing the amount of damping required to help Abaqus/Standard achieve convergence. It is important to note that, although these modified solution control parameters do not alter the accuracy of the solution, they require some additional computational time per increment. However, this additional computational cost was observed to be compensated by the smaller number of increments required to complete the simulation.

For all models presented in this chapter the strategy followed to achieve a converging solution consisted of running the model using the contact stabilization mechanism together with the non-default time incrementation control parameters previously described. If the simulation terminated before the ultimate capacity of the column was reached, an additional step was added to the simulation, in which the contact control scheme was removed and replaced with the automatic stabilization mechanism. Also, in this second step the maximum displacement correction check was removed by setting C_n^{α} to 1. The following sections describe a stabilization study which was carried out to ensure that the artificial viscous forces introduced through the contact stabilization and the automatic stabilization schemes were sufficiently low not to significantly alter the solution.

7.2.7.1 Contact stabilization

Contact stabilization was used through the *CONTACT CONTROL keyword while specifying a constant scale factor for the magnitude of the viscous forces normal to the surfaces in contact, which were automatically calculated by Abaqus/Standard. A suitable value for this scale factor which does not result in a significant distortion of the solution was determined by carrying out a series of numerical simulations for each built-up geometry, in which identical FE models were run while varying the scale factor from zero (no artificial damping added to the model) over 2×10^{-4} to 8×10^{-4} . No artificial damping was added to oppose the relative motion of the nodes in the tangential direction to the surfaces. This was achieved by setting the ‘tangent fraction’ parameter to zero. This option was chosen because the tangential viscous stresses are likely to absorb significant amounts of energy when there is slip between the contacting surfaces.

Table 7.2 lists the ultimate loads obtained for each built-up geometry and the corresponding values given to the scale factor. The table shows that column SC1 was the only geometry for which a converging solution could be achieved past the peak load by only adjusting the solution control parameters. Columns SC2 and SC3, on the other hand, were only able to converge after activating the contact control scheme, while for column SC4 a converging solution could not be achieved even after activating the contact control scheme. The ratio between the energy dissipated through artificial damping (ALLSD) and the total strain energy of the model (ALLIE) is illustrated in Figure 7.10a, Figure 7.11a and Figure 7.12a for columns SC1, SC2 and SC3, respectively. The vertical dashed line shows the approximate axial deformation at which the columns reached their ultimate capacity. The load-axial shortening curves of columns SC1, SC2 and SC3 are shown in Figure 7.10b, Figure 7.11b and Figure 7.12b, respectively.

Table 7.2: Ultimate load comparison with contact control schemes

Specimen	Stabilization scheme	Contact control	Ult. Load (kN)
SC1-2b	No stabilization	-	178.99
	cc 0.0002	2×10^{-4}	178.34
	cc 0.0005	5×10^{-4}	178.68
	cc 0.0008	8×10^{-4}	177.01
SC2-2b	No stabilization	-	Divergence
	cc 0.0002	2×10^{-4}	227.13
	cc 0.0005	5×10^{-4}	226.95
	cc 0.0008	8×10^{-4}	225.97
SC3-2a	No stabilization	-	Divergence
	cc 0.0002	2×10^{-4}	133.89
	cc 0.0005	5×10^{-4}	133.66
	cc 0.0008	8×10^{-4}	133.77
SC4-2a	No stabilization	-	Divergence
	cc 0.0002	2×10^{-4}	Divergence
	cc 0.0005	5×10^{-4}	Divergence
	cc 0.0008	8×10^{-4}	Divergence

Table 7.2 shows that the ultimate loads of columns SC1, SC2 and SC3 were not significantly affected by the contact stabilization scheme over the range of values selected for the scale factor. For column SC1, the difference in the ultimate load achieved with a scale factor equal to 2×10^{-4} was 0.36 % relative to the model in which no stabilization was used. For columns SC2 and SC3, the maximum variations in the ultimate load when varying the scale factor from 2×10^{-4} to 8×10^{-4} were only 0.51 % and 0.09 %, respectively. This small variation in the ultimate load can be attributed to the fact that in the contact stabilization scheme the viscous forces are only used to oppose the relative motion between the nodes involved in a contact interaction and they are only introduced into the model when the nodes are relatively close to each other. This occurs mainly when the components of the column start buckling, as shown in Figure 7.10a, Figure 7.11a and Figure 7.12a for columns SC1, SC2 and SC3, respectively. When the column is reaching its ultimate capacity, on the other hand, most of the contact or separation between the surfaces has already been established, and therefore the amount of artificial damping introduced at this point is significantly smaller.

Although the ultimate capacity of columns SC1 was not significantly affected by the artificial forces introduced through the contact stabilization scheme for the range of scale factors considered, the onset of global buckling of the plate sections between connector points was significantly delayed, as shown in Figure 7.13, which plots the load vs. lateral deformation curves of the plate sections at the column mid-height obtained for the different values given to the scale factor. However, once buckling of the plate sections was fully developed the load vs. lateral deformation curves of all FE models in which the contact stabilization scheme was activated converged to the curve obtained with the FE model in which no stabilization was used.

Based on this stabilization study it was decided not to use the contact stabilization scheme for the FE models with geometry SC1 in order to ensure an accurate prediction of the critical buckling stresses of the components of these columns. In addition, it was concluded that using a constant scale factor equal to 2×10^{-4} resulted in a negligible change in the ultimate capacity for the studied geometries and this value was used in all models in which the contact stabilization scheme was activated.

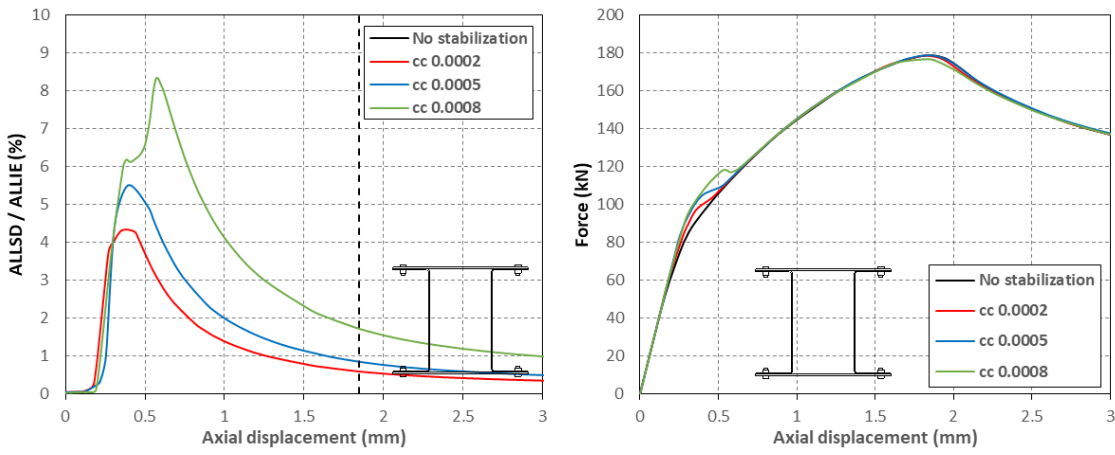


Figure 7.10: Contact stabilization in columns SC1-2b: a) Dissipated energy over total strain energy; b) Load-axial shortening curve

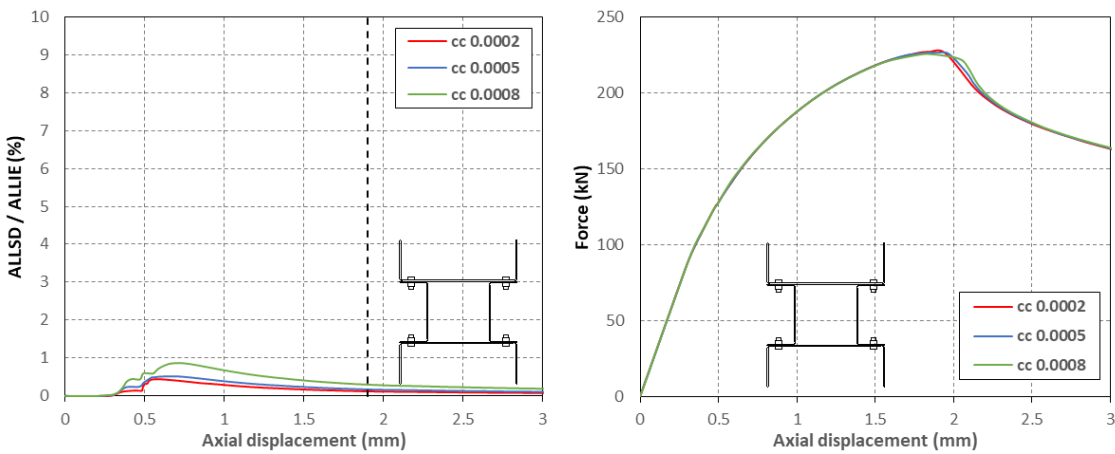


Figure 7.11: Contact stabilization in columns SC2-2b: a) Dissipated energy over total strain energy; b) Load-axial shortening curve

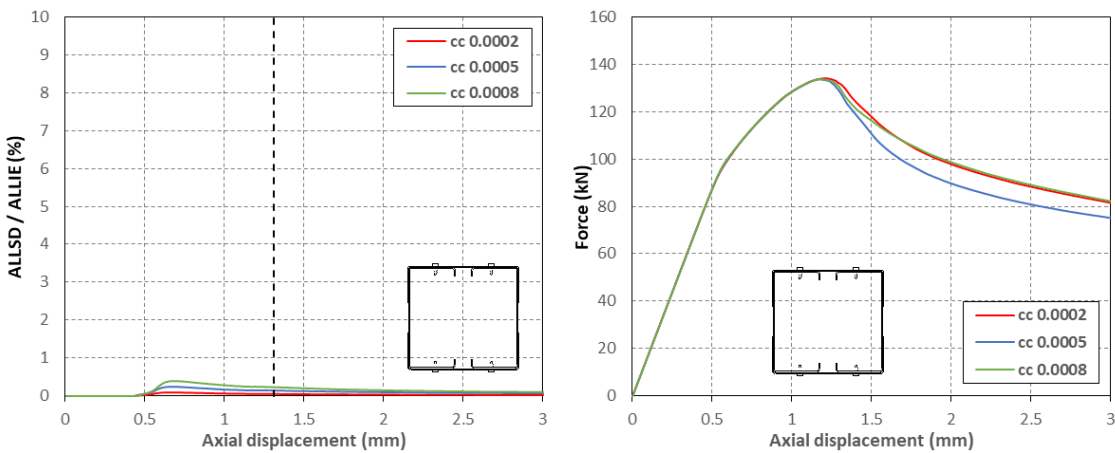


Figure 7.12: Contact stabilization in columns SC3-2a: a) Dissipated energy over total strain energy; b) Load-axial shortening curve

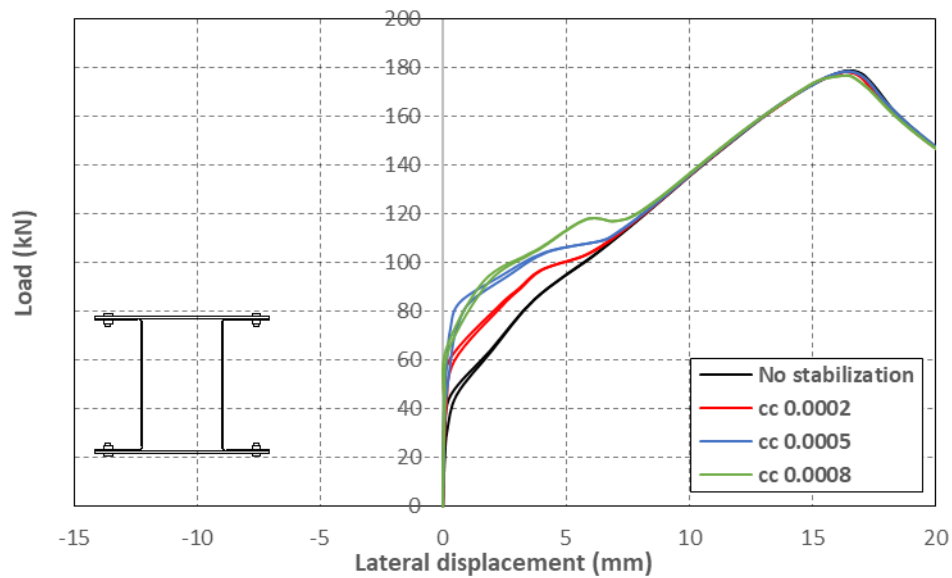


Figure 7.13: Load-lateral displacement curve of plate sections in column SC1-2b for different scale factors

7.2.7.2 Automatic stabilization

Automatic stabilization was used with the adaptive automatic stabilization scheme in order to minimize the effect of artificial damping on the calculated solution. In the adaptive stabilization scheme the amount of damping introduced into the model is calculated automatically by Abaqus/Standard for each node and increment. The initial damping factor is computed based on the ‘dissipated energy fraction’ (DEF), which is the ratio between the energy dissipated through artificial damping and the total strain energy in the first increment of the step. This factor is then adjusted throughout the step based on the convergence history and the accuracy tolerance (AT), which is used to limit the maximum amount of damping introduced per increment. To ensure that the solution predicted by the model is not significantly altered by the artificial damping forces introduced through the automatic stabilization scheme, a series of simulations were run for a representative column of each geometry, in which the DEF was set to 2×10^{-5} , while varying the AT from zero (no artificial damping added into the model) to 8×10^{-3} and the predicted ultimate capacities were compared.

Table 7.3 lists the ultimate loads obtained for each built-up geometry and the corresponding values given to the AT. The table shows that column SC1 was the only geometry which was able to reach convergence by only adjusting the solution control parameters. The ratio between the energy dissipated through artificial damping (ALLSD) and the total strain energy (ALLIE) is illustrated in Figure 7.14a, Figure 7.15a, Figure 7.16a and Figure 7.17a for columns SC1, SC2, SC3 and SC4, respectively. The vertical dashed line shows the approximate axial deformation at which the columns reached their ultimate capacity. The load-axial shortening curves of columns SC1, SC2, SC3 and SC4 are shown in Figure 7.14b, Figure 7.15b, Figure 7.16b and Figure 7.17b, respectively.

From the ALLSD/ALLIE ratios for each geometry it is seen that SC3 is the only geometry for which most of the artificial damping was introduced at the peak load. For this geometry, the peak load predicted by the FE model increased by 1.23 % when the AT was increased from 2×10^{-3} to 8×10^{-3} , while for columns SC2 and SC4 the increases in the ultimate load were only 0.20 % and 0.23 %, respectively. For columns SC1, on the other hand, the ultimate load showed a slight decrease as the AT was increased. In these columns, most of the artificial damping was introduced when the components started buckling.

For column SC1, the difference in the peak load predicted by the FE model in which the AT was set to 2×10^{-3} was only 0.06 % relative to the one in which no artificial damping was added, while the ALLSD/ALLIE ratio was around 0.1 % when the peak load was reached. Similar ALLSD/ALLIE ratios were obtained for the other geometries when the AT was set to 2×10^{-3} . More precisely, the ALLSD/ALLIE ratios were 0.12 %, 0.20 % and 0.07 % when the peak load was reached in the columns with geometries SC2, SC3 and SC4, respectively. Although no convergence could be reached in these geometries without damping, it seems reasonable to assume that the variation in the ultimate capacity in these columns as a result of the artificial damping forces is similar to the one observed in the column with geometry SC1. This variation in the ultimate capacity was considered to be negligible, and it was therefore decided to set the AT equal to 2×10^{-3} in all models in which automatic stabilization was activated.

Table 7.3: Ultimate load comparison with automatic stabilization schemes

Specimen	Stabilization scheme	DEF	AT	Ult. Load (kN)
SC1-2b	No stabilization	-	-	178.99
	sc 0.002	2×10^{-5}	2×10^{-3}	178.88
	sc 0.005	2×10^{-5}	5×10^{-3}	178.73
	sc 0.008	2×10^{-5}	8×10^{-3}	177.03
SC2-2b	No stabilization	-	-	Divergence
	sc 0.002	2×10^{-5}	2×10^{-3}	227.85
	sc 0.005	2×10^{-5}	5×10^{-3}	228.09
	sc 0.008	2×10^{-5}	8×10^{-3}	228.31
SC3-2a	No stabilization	-	-	Divergence
	sc 0.002	2×10^{-5}	2×10^{-3}	133.08
	sc 0.005	2×10^{-5}	5×10^{-3}	134.12
	sc 0.008	2×10^{-5}	8×10^{-3}	134.73
SC4-2a	No stabilization	-	-	Divergence
	sc 0.002	2×10^{-5}	2×10^{-3}	135.18
	sc 0.005	2×10^{-5}	5×10^{-3}	135.26
	sc 0.008	2×10^{-5}	8×10^{-3}	135.49

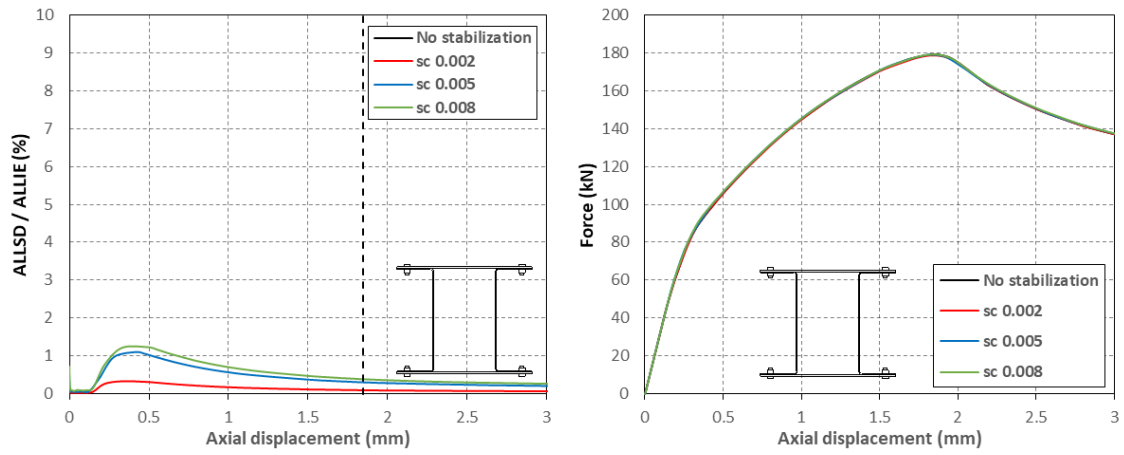


Figure 7.14: Automatic stabilization in columns SC1-2b: a) Dissipated energy over total strain energy; b) Load-axial shortening curve

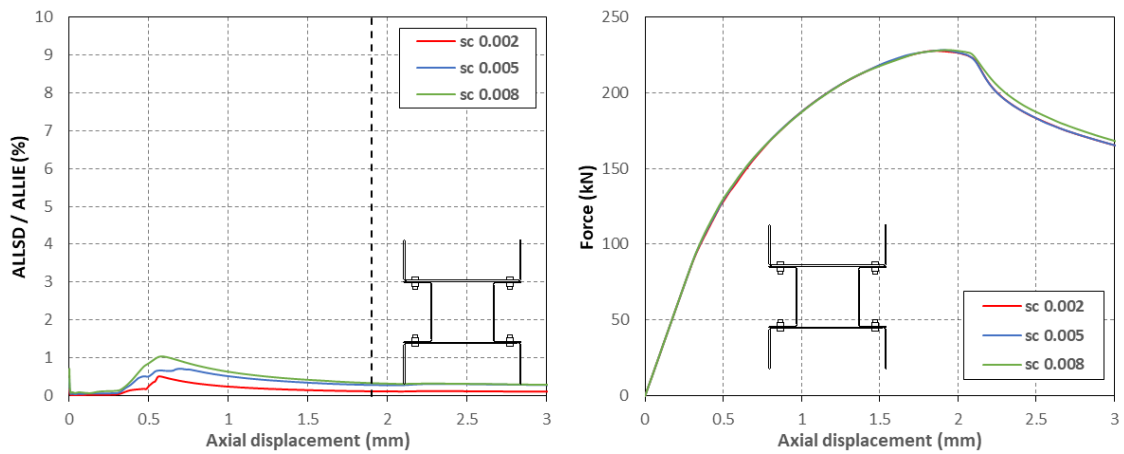


Figure 7.15: Automatic stabilization in columns SC2-2b: a) Dissipated energy over total strain energy; b) Load-axial shortening curve

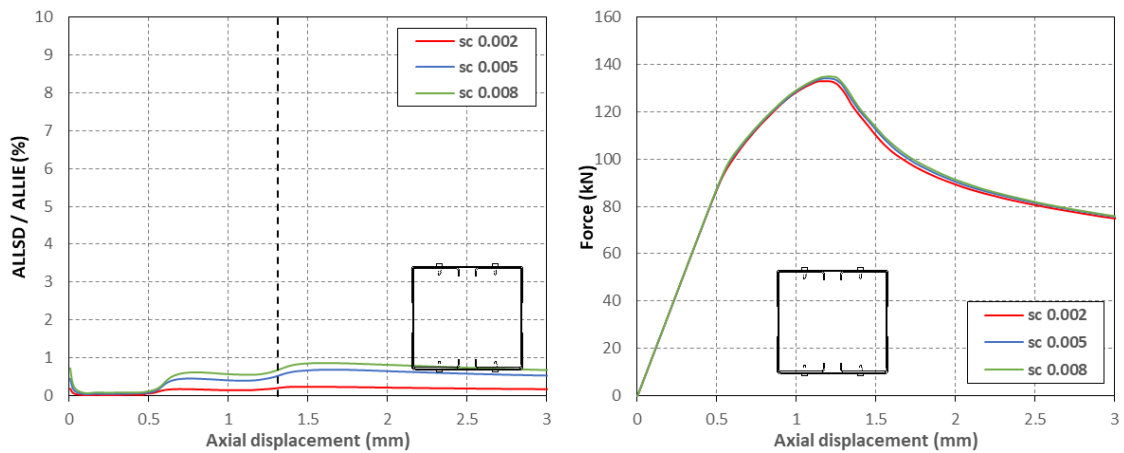


Figure 7.16: Automatic stabilization in columns SC3-2a: a) Dissipated energy over total strain energy; b) Load-axial shortening curve

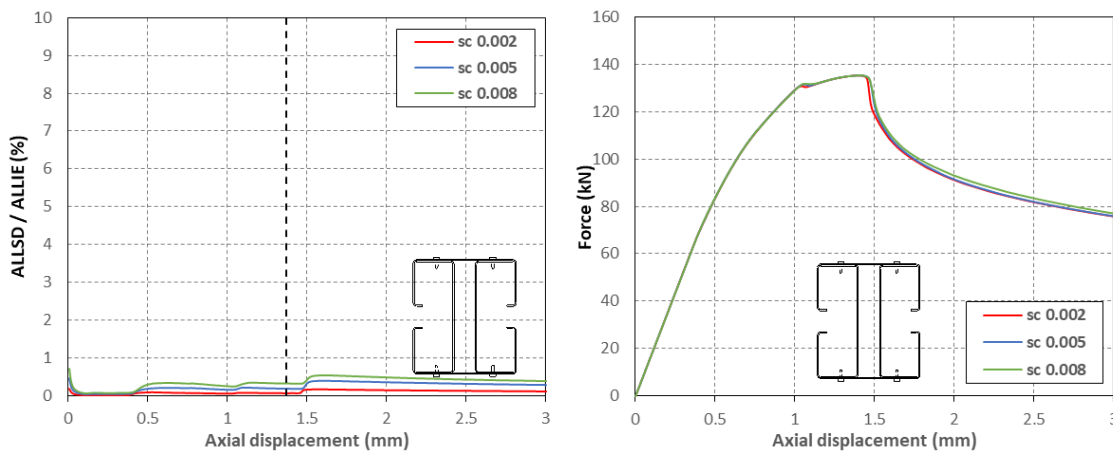


Figure 7.17: Automatic stabilization in columns SC4-2a: a) Dissipated energy over total strain energy; b) Load-axial shortening curve

7.2.8 Mesh analysis

A mesh analysis was carried out to establish the best suited element type to model the non-linear behaviour of CFS built-up stub columns and determine the effect of the mesh size on the accuracy of the model. The study was performed for representative columns of geometry SC1, SC2 and SC3, using five intermediate connectors for specimens SC1 and SC3 and six intermediate connectors for specimen SC2. The results obtained from the mesh analysis for columns SC3 were considered to also be applicable to columns SC4, since columns SC4 were assembled using component sections with the same nominal dimensions as those used to assemble the columns with geometry SC3. The specimens were modelled using the nominal dimensions of the component sections. The FE models included material non-linearity, which was obtained from coupon tests, and the recorded geometric imperfections of a representative test specimen of each geometry. The connectors were modelled using HINGE connector elements. Both the total CPU time required to run the analysis and the peak load were taken into account in the study.

7.2.8.1 Element type

The two element types chosen for the mesh analysis were the conventional shell elements S4 and S4R, available in Abaqus/Standard. These are general-purpose quadrilateral linear elements that have been widely used by other researchers to model the non-linear behaviour of cold-formed steel members (Becque and Rasmussen, 2009b; Jiahui, 2014; Li, Ádány, and Schafer, 2013; Yang and Hancock, 2006; Zhang and Young, 2015). These elements can be used to model thick and thin shell problems. They account for the transverse shear deformations present in thick shell elements. However, as the thickness of the shell decreases and the transverse shear deformations in the element become negligible, the elements follow discrete Kirchhoff theory, where plain sections normal to the mid-surface of the shell remain straight and normal

throughout the deformation of the mid-surface. The elements account for thickness changes as a result of in-plane deformations and they are not affected by transverse shear locking. These elements use finite membrane strain formulation, allowing for arbitrarily large deformations and rotations. Therefore, they are suitable for non-linear geometric analysis. S4 is a fully integrated shell element with three translational and three rotational degrees of freedom at each node. It has four integration points and does not have hourglass modes in either the membrane or bending response of the element. However, due to its number of integration points, this element is computationally more expensive, especially for large problems, than its counterpart S4R element with reduced integration points. S4R elements only use a single integration point to formulate the element stiffness. They can provide accurate results, although they are prone to hourglassing modes. However, in the problems under consideration hourglassing modes were not found to be an issue.

7.2.8.2 Mesh size

Five different mesh densities were used in the analysis. The size of the elements in the flanges and the web of the channels, as well as over the width of the plate sections, was chosen to be as similar as possible. The aspect ratio of these elements was kept below 2 as much as possible, following the recommendations given by Schafer (1997). The number of elements used across the corner regions of the channels was varied from two to six. Due to the limited area of the corners the aspect ratio of the elements in these regions was somewhat relaxed to be less than 4, in order to avoid an overly dense mesh. At least two elements were used across the lips of the lipped channels. Table 7.4, Table 7.6 and Table 7.8 show the number of elements and nodes used in the mesh analyses for columns SC1, SC2 and SC3, respectively, while Table 7.5, Table 7.7 and Table 7.9 report the aspect ratios of the studied meshes.

Table 7.4: Mesh configuration for built-up column 1

Mesh	N of elements					N of nodes	
	Channels			Plates	column		Total
	Flange	Web	Corner	Width	Length		
Mesh 1	2	6	2	8	76	3344	3696
Mesh 2	4	12	2	16	76	6080	6468
Mesh 3	6	18	4	24	152	18848	19584
Mesh 4	8	24	4	32	152	24320	25092
Mesh 5	10	30	6	40	228	46512	47632

Table 7.5: Mesh aspect ratios in built-up column 1

Mesh	Aspect ratio			
	Channels			Plates
	Flange	Web	Corner	Width
Mesh 1	0.569	0.581	4.000	0.558
Mesh 2	1.137	1.161	4.000	1.116
Mesh 3	0.853	0.871	4.000	0.837
Mesh 4	1.137	1.161	4.000	1.116
Mesh 5	0.948	0.968	4.000	0.930

Table 7.6: Mesh configuration for built-up column 2

Mesh	N of elements								N of nodes
	Inner Channels			Outer Channels			column	Total	
	Flange	Web	Corner	Flange	Web	Corner	Length		
Mesh 1	1	3	2	2	6	2	54	2484	2750
Mesh 2	3	6	2	4	12	2	54	4320	4620
Mesh 3	5	10	4	7	22	4	108	15552	16132
Mesh 4	7	15	4	10	30	4	108	20520	21146
Mesh 5	9	20	6	14	42	6	163	43032	43952

Table 7.7: Mesh aspect ratios in built-up column 2

Mesh	Aspect ratio					
	Inner Channels			Outer Channels		
	Flange	Web	Corner	Flange	Web	Corner
Mesh 1	0.452	0.609	4.000	0.574	0.586	4.000
Mesh 2	1.355	1.218	4.000	1.147	1.172	4.000
Mesh 3	1.129	1.015	4.000	1.004	1.074	4.000
Mesh 4	1.581	1.523	4.000	1.434	1.465	4.000
Mesh 5	1.347	1.345	4.000	1.331	1.359	4.000

Table 7.8: Mesh configuration for built-up column 3

Mesh	N of elements								N of nodes	
	Plain Channels			Lipped Channels				column		Total
	Flange	Web	Corner	Flange	Web	Lip	Corner	Length		
Mesh 1	2	4	2	2	4	2	2	74	4736	5100
Mesh 2	3	9	2	3	8	2	2	74	6660	7050
Mesh 3	4	13	4	5	12	2	4	148	21016	21754
Mesh 4	8	16	4	8	16	4	4	148	28416	29204
Mesh 5	10	20	6	10	20	6	6	220	56320	57460

Table 7.9: Mesh aspect ratios in built-up column 3

Mesh	Aspect ratio						
	Plain Channels			Lipped Channels			
	Flange	Web	Corner	Flange	Web	Lip	Corner
Mesh 1	0.814	0.519	4.000	0.711	0.571	5.552	4.000
Mesh 2	1.221	1.168	4.000	1.066	1.142	5.552	4.000
Mesh 3	0.814	0.843	4.000	0.888	0.857	2.776	4.000
Mesh 4	1.628	1.038	4.000	1.421	1.142	5.552	4.000
Mesh 5	1.369	0.873	4.000	1.195	0.961	5.603	4.000

7.2.8.3 Mesh analysis results

Table 7.10, Table 7.11 and Table 7.12 list the ultimate load and the total CPU time required to complete the simulations with different mesh densities and element types for columns SC1, SC2 and SC3, respectively. The tables also show the total number of increments in which the analyses were divided and the average CPU time required to solve each increment. The CPU times listed in brackets correspond to simulations in which, although the peak load was reached, the analysis was not completed.

Table 7.10: Effect of element type and mesh size on the ultimate load and total CPU time for columns SC1

Element type	Mesh	Ultimate Load (kN)	Total CPU time (s)	N of increments	CPU time per increment (s)
S4	Mesh 1	245.48	2315	210	11
	Mesh 2	231.19	2799	169	17
	Mesh 3	212.92	12555	198	63
	Mesh 4	215.90	10344	118	88
	Mesh 5	214.90	28816	155	186
S4R	Mesh 1	254.70	2884	283	10
	Mesh 2	234.77	(2472)	153	16
	Mesh 3	214.33	10715	189	57
	Mesh 4	216.59	10514	137	77
	Mesh 5	215.34	29301	177	166

Table 7.11: Effect of element type and mesh size on the ultimate load and total CPU time for columns SC2

Element type	Mesh	Ultimate Load (kN)	Total CPU time (s)	N of increments	CPU time per increment (s)
S4	Mesh 1	268.59	(1105)	132	8
	Mesh 2	261.08	1923	156	12
	Mesh 3	239.42	4741	104	46
	Mesh 4	239.25	7457	135	55
	Mesh 5	235.45	18012	137	131
S4R	Mesh 1	256.43	957	120	8
	Mesh 2	253.97	(1341)	113	12
	Mesh 3	238.94	4195	100	42
	Mesh 4	238.74	6669	126	53
	Mesh 5	235.35	14086	119	118

Table 7.12: Effect of element type and mesh size on the ultimate load and total CPU time for columns SC3

Element type	Mesh	Ultimate Load (kN)	Total CPU time (s)	N of increments	CPU time per increment (s)
S4	Mesh 1	175.96	946	48	20
	Mesh 2	163.48	1697	60	28
	Mesh 3	159.04	13464	113	119
	Mesh 4	158.20	14250	82	174
	Mesh 5	156.94	34124	81	421
S4R	Mesh 1	176.00	2095	99	21
	Mesh 2	162.65	2640	99	27
	Mesh 3	158.68	20334	164	124
	Mesh 4	157.94	16880	109	155
	Mesh 5	156.93	48466	122	397

From these tables it can be seen that the number of increments required to complete the simulations is not related to the mesh density of the model. For this reason, in order to better compare the computational efficiency of S4 and S4R elements Figure 7.18, Figure 7.19 and Figure 7.20 plot the ultimate load and the CPU time per increment obtained with these elements for the different mesh densities considered in this study.

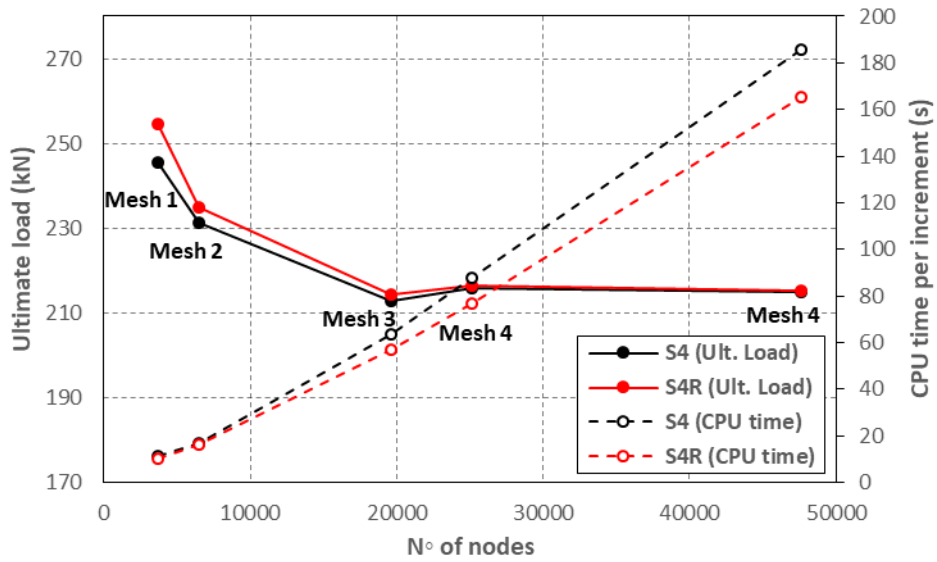


Figure 7.18: Effect of mesh size and element type on the ultimate load and total CPU time for columns SC1

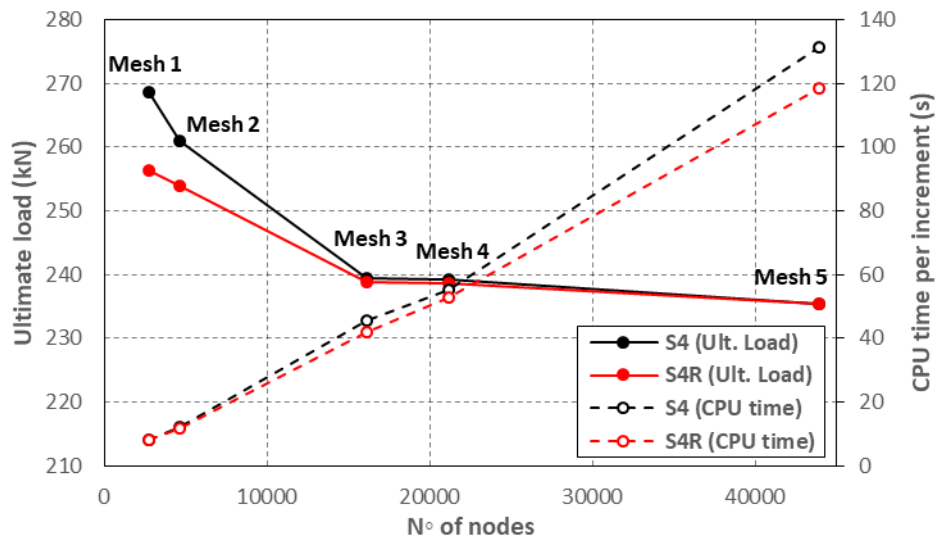


Figure 7.19: Effect of mesh size and element type on the ultimate load and total CPU time for columns SC2

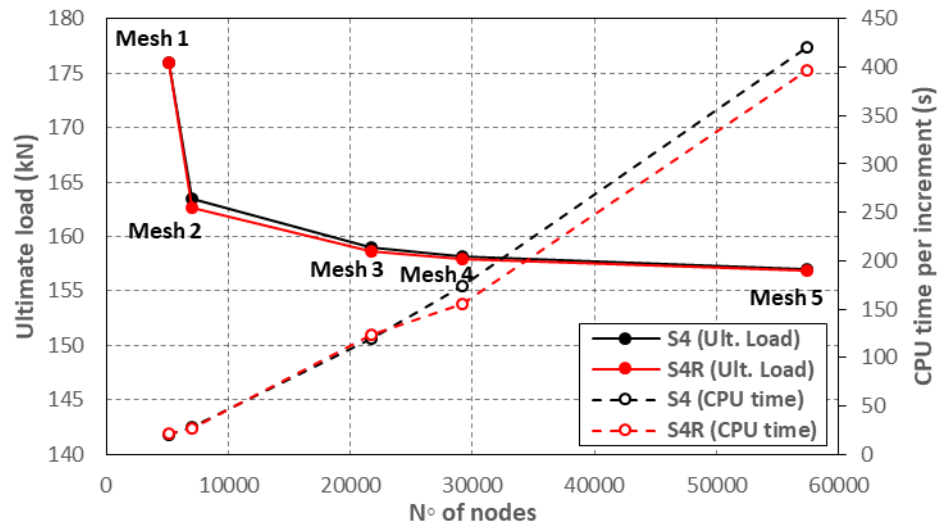


Figure 7.20: Effect of mesh size and element type on the ultimate load and total CPU time for columns SC3

The figures show that for columns SC1, SC2 and SC3, the ultimate capacities predicted by the FE models with both S4 and S4R elements converged asymptotically as the mesh size was reduced, and that both element types converged to virtually the same prediction. The CPU time per increment, on the other hand, increased more than linearly with the number of nodes in the model. The FE models with S4R elements required, on average, around 7 % less computational time per increment than the models built with S4 elements and the same mesh density across all the geometries, while the difference in the ultimate capacity predicted with the S4 and S4R elements was typically around 0.25 % for a given mesh density. For this reason, it was decided to use S4R elements to develop all the models presented in this thesis.

Regarding the mesh density, the differences in the ultimate capacities predicted with Mesh 3 and the finest mesh (Mesh 5) were 0.47 %, 1.53 % and 1.12 % for columns SC1, SC2 and SC3, respectively. This accuracy was considered to be satisfactory given the complexity of the models and therefore all models were meshed using a Mesh 3 configuration.

7.3. FE model verification

7.3.1 Ultimate load

Table 7.13, Table 7.14, Table 7.15 and Table 7.16 compare the FE predicted ultimate loads with the values obtained from the tests for the columns with geometry SC1, SC2, SC3 and SC4, respectively. The tables also include the stabilization settings used to help Abaqus/Standard achieve a converging solution. It is seen that the FE models were able to accurately predict the ultimate capacity of the tested columns across all studied geometries, with average errors of

2.88 % for columns SC1, 4.37 % for columns SC2, 2.52 % for columns SC3 and 5.02 % for columns SC4.

The load vs. axial shortening curves obtained from the FE models, as well as those obtained experimentally, are plotted in Figure 7.21, Figure 7.22, Figure 7.23 and Figure 7.24 for each test specimen belonging to geometry SC1, SC2, SC3 and SC4, respectively.

Table 7.13: Numerical and experimental ultimate loads of columns SC1

Specimen	Test ult. load (kN)	FEA ult. load (kN)	FEA/Test	Stabilization scheme	
				Step 1	Step 2
SC1-2a	183.97	179.55	0.976	No stabilization	-
SC1-2b	168.17	177.70	1.057	No stabilization	-
SC1-3a	183.01	182.50	0.997	No stabilization	sc 0.002
SC1-3b	175.86	182.50	1.038	No stabilization	sc 0.002
SC1-5a	201.72	194.51	0.964	No stabilization	-
SC1-5b	188.50	191.49	1.016	No stabilization	-
Avg.			1.008		
St. dev.			0.036		

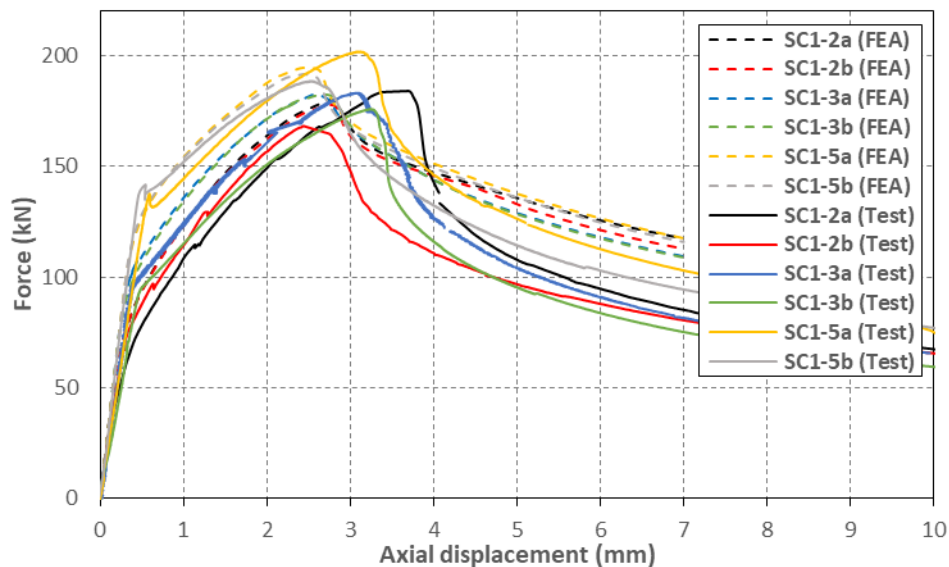


Figure 7.21: Numerical and experimental load vs. axial shortening curves of columns SC1

Table 7.14: Numerical and experimental ultimate loads of columns SC2

Specimen	Test ult. load (kN)	FEA ult. load (kN)	FEA/Test	Stabilization scheme	
				Step 1	Step 2
SC2-2a	213.32	226.89	1.064	cc 0.0002	-
SC2-2b	200.34	226.63	1.131	cc 0.0002	-
SC2-4a	238.00	232.56	0.977	cc 0.0002	-
SC2-4b	233.39	233.13	0.999	cc 0.0002	-
SC2-6a	220.24	239.86	1.089	cc 0.0002	-
SC2-6b	232.62	238.56	1.026	cc 0.0002	-
Avg.			1.048		
St. dev.			0.058		

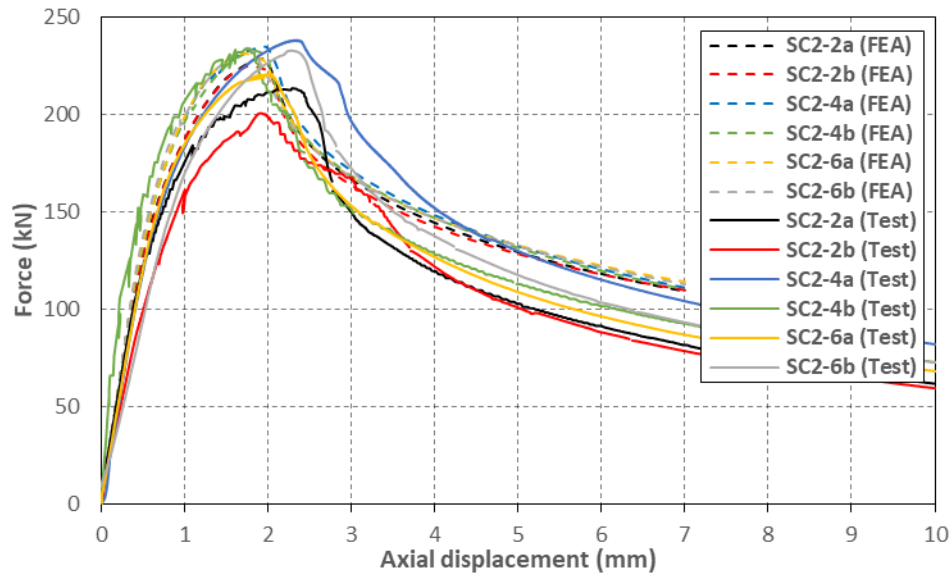


Figure 7.22: Numerical and experimental load vs. axial shortening curves of columns SC2

Table 7.15: Numerical and experimental ultimate loads of columns SC3

Specimen	Test ult. load (kN)	FEA ult. load (kN)	FEA/Test	Stabilization scheme	
				Step 1	Step 2
SC3-2a	139.30	134.69	0.967	cc 0.0002	-
SC3-2b	138.53	133.61	0.964	cc 0.0002	-
SC3-5a	138.77	142.14	1.024	cc 0.0002	sc 0.002
SC3-5b	143.40	142.27	0.992	cc 0.0002	-
Avg.			0.987		
St. dev.			0.028		

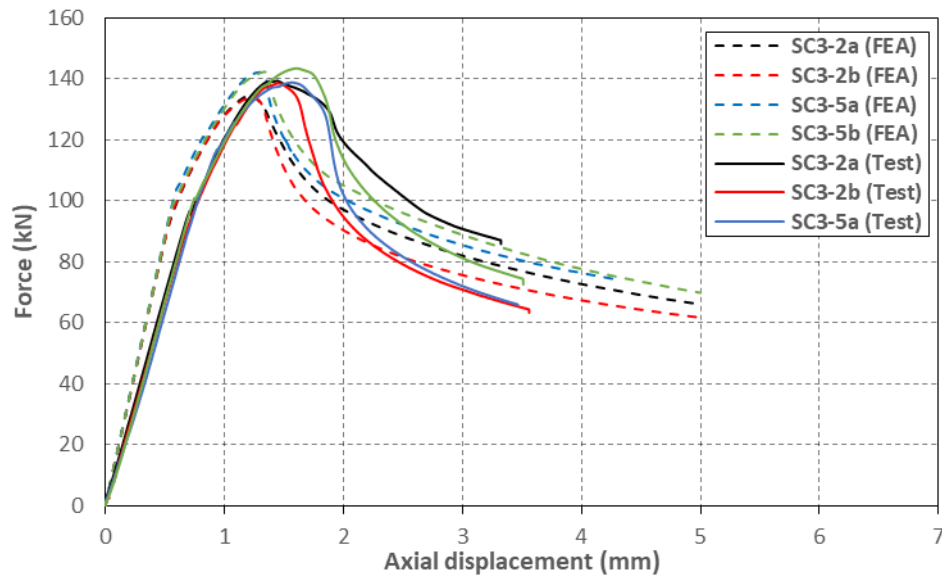


Figure 7.23: Numerical and experimental load vs. axial shortening curves of columns SC3

Table 7.16: Numerical and experimental ultimate loads of columns SC4

	Test ult. load (kN)	FEA ult. load (kN)	FEA/Test	Stabilization scheme	
				Step 1	Step 2
SC4-2a	148.09	135.84	0.917	cc 0.0002	sc 0.002
SC4-2b	147.03	135.47	0.921	cc 0.0002	sc 0.002
SC4-5a	141.23	141.58	1.002	cc 0.0002	sc 0.002
SC4-5b	137.74	142.74	1.036	cc 0.0002	sc 0.002
Avg.			0.969		
St. dev.			0.059		

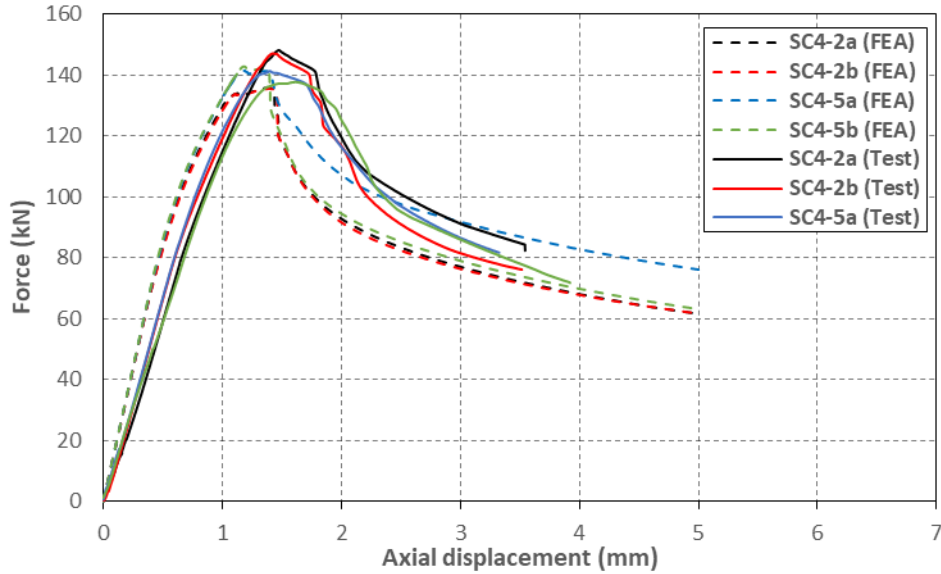


Figure 7.24: Numerical and experimental load vs. axial shortening curves of columns SC4

7.3.2 Deformed shape

The FE models were able to accurately replicate the initial buckled shape of the tested columns for each of the built-up geometries and connector spacings. As examples, Figure 7.25a and Figure 7.26a compare the initial buckled shapes obtained from the FE models with those observed during the tests for columns SC1-2a and SC1-5a, respectively, while Figure 7.27a and Figure 7.28a do the same for columns SC2-2a and SC2-5a, respectively. For geometries SC3 and SC4, Figure 7.29a and Figure 7.30a compare the initial buckling deformations predicted by the FE models with the deformations observed during the tests in columns SC3-5a and SC4-5a, respectively.

A fairly good agreement was also achieved between the yield line mechanisms predicted by the FE models and those observed in the tested columns. However, as Figure 7.25b, Figure 7.26b, Figure 7.27b and Figure 7.28b show, the yield line mechanism predicted by the FE models often developed in a different location along the column.

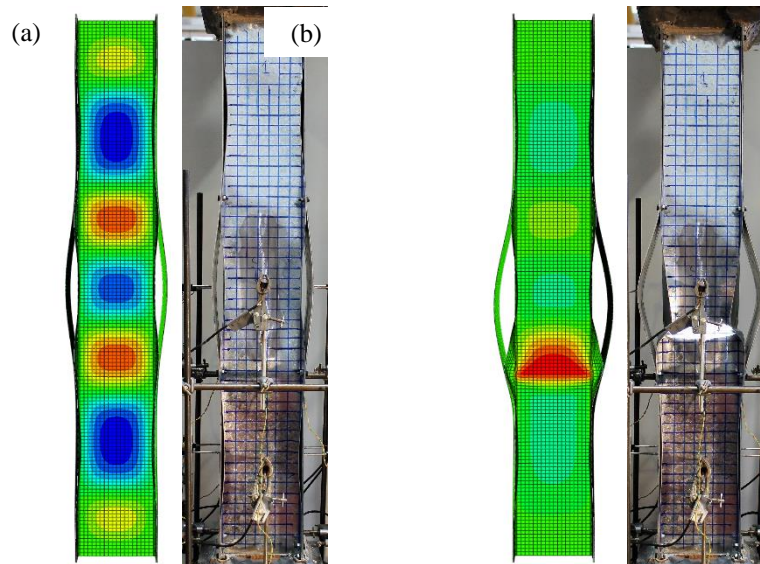


Figure 7.25: Deformed shape of SC1-2a: a) before peak load; b) after peak load

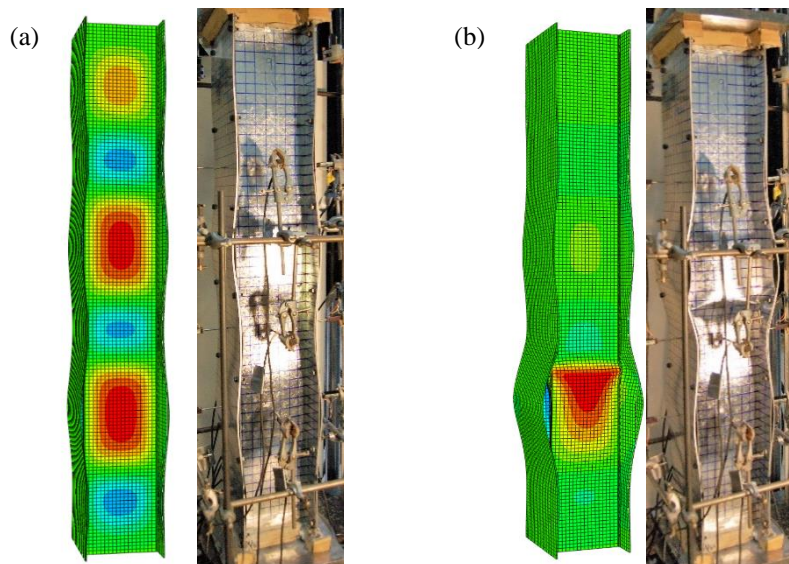


Figure 7.26: Deformed shape of SC1-5a: a) before peak load; b) after peak load

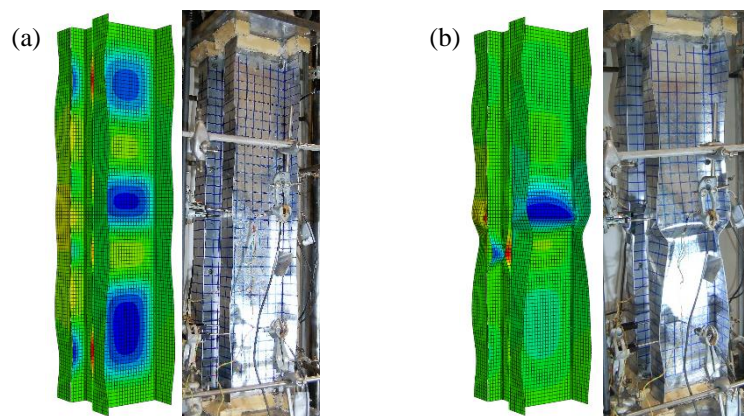


Figure 7.27: Deformed shape of SC2-2a: a) before peak load; b) after peak load

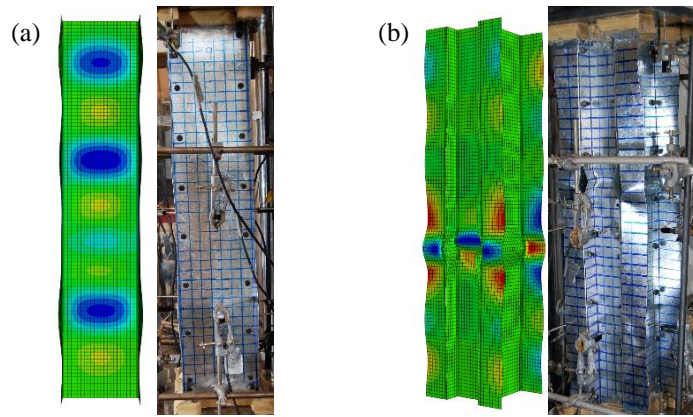


Figure 7.28: Deformed shape of SC2-6a: a) before peak load; b) after peak load

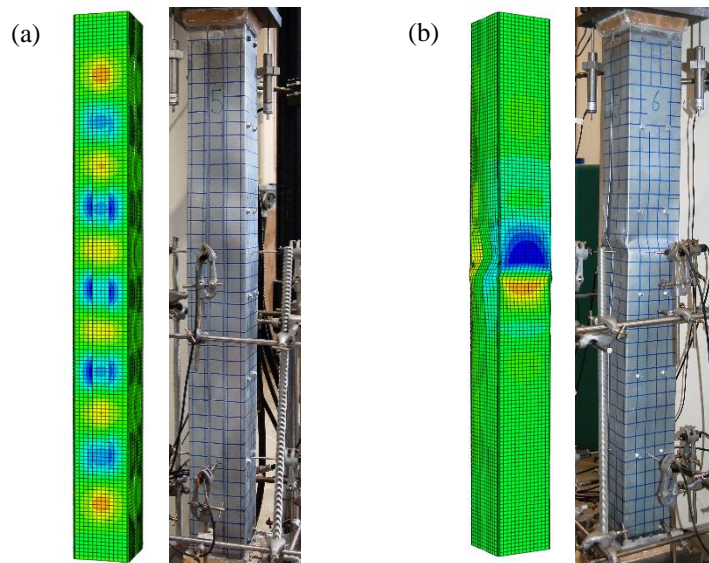


Figure 7.29: Deformed shape of SC3-5a: a) before peak load; b) after peak load

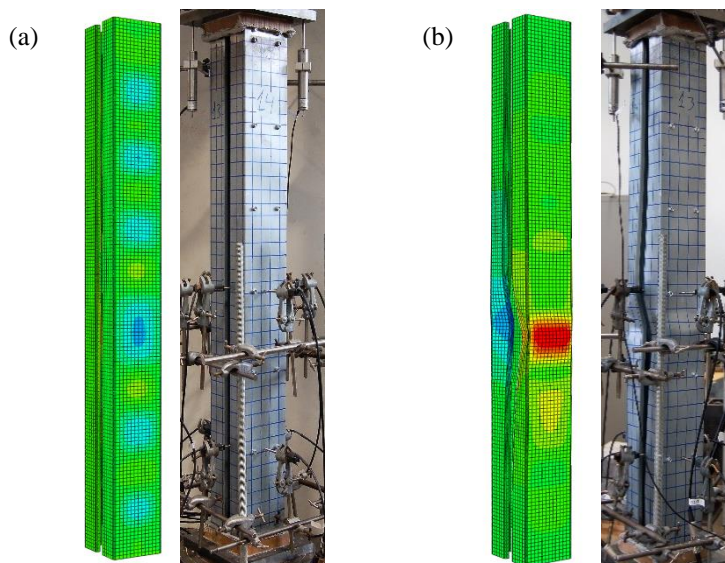


Figure 7.30: Deformed shape of SC4-5a: a) before peak load; b) after peak load

In order to further assess the accuracy of the FE models in predicting the initial deformed shape of the stub columns, the readings obtained from the potentiometers used to record the out-of-

plane deformations of the components of each tested column were compared to the out-of-plane displacements of the nodes in the FE models which were at the same location as the potentiometers. Figure 7.31, Figure 7.32, Figure 7.33 and Figure 7.34 compare the out-of-plane deformations obtained from the FE models to those from the tests for a representative column with geometry SC1, SC2, SC3 and SC4, respectively. The figures show an excellent agreement between the numerical and experimental out-of-plane deformation curves. Curves comparing the numerical and experimental out-of-plane deformations of the components of each tested column are included in Appendix L.

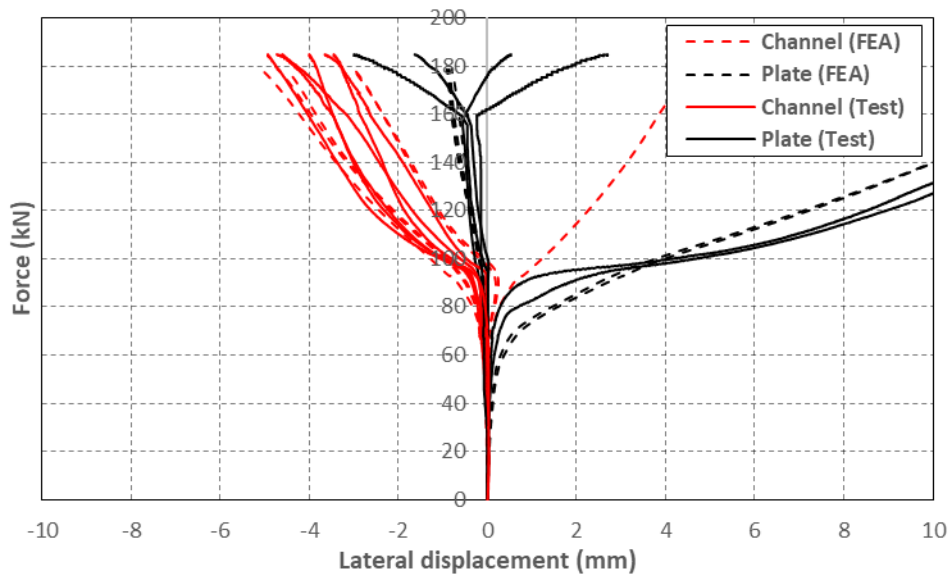


Figure 7.31: Experimental and numerical axial load vs lateral displacement curves of SC1-3b

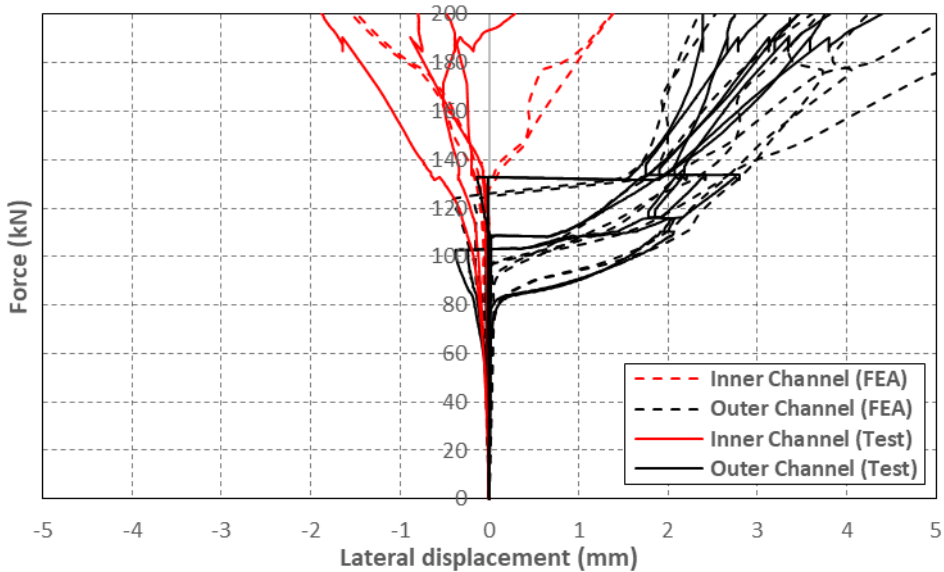


Figure 7.32: Experimental and numerical axial load vs lateral displacement curves of SC2-2a

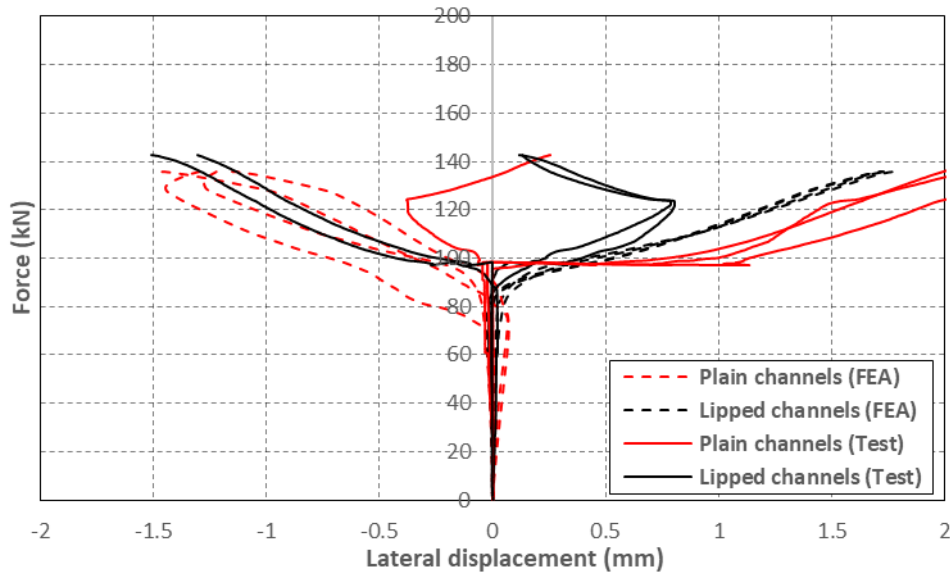


Figure 7.33: Experimental and numerical axial load vs lateral displacement curves of SC3-2a

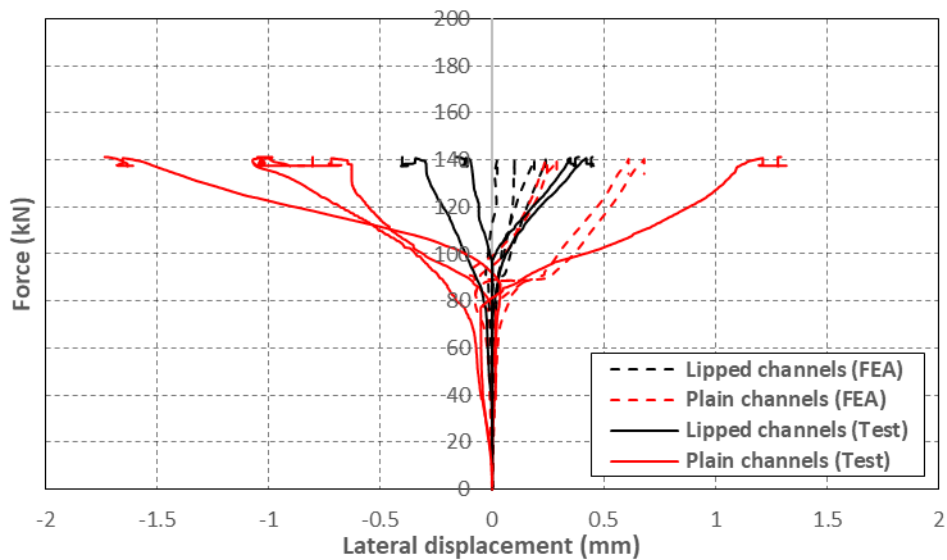


Figure 7.34: Experimental and numerical axial load vs lateral displacement curves of SC4-5b

It is worth mentioning that, in agreement with the observations made during the tests of columns SC3, the FE models showed no sign of distortional buckling in the lipped channels of these columns. For columns SC4, on the other hand, the experiments showed some minor participation of distortional buckling in the lipped channels. However, the FE models did not confirm this and did not show any sign of this buckling mode in these columns. For example, Figure 7.35 shows the deformed shape of one of the lipped channels of columns SC3-2a and SC4-2a, amplified five times, shortly before the columns reached their ultimate load.

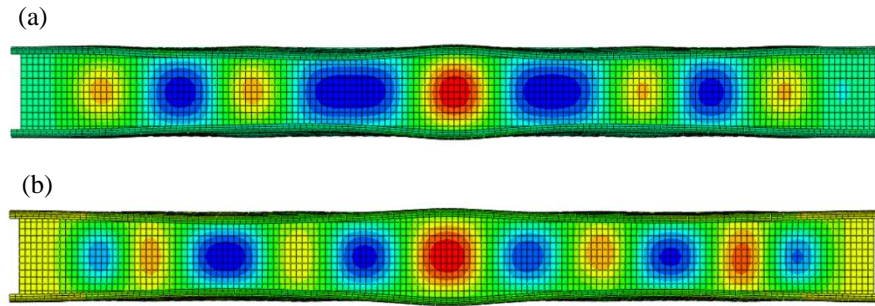


Figure 7.35: Amplified deformed shape of one of the lipped channels of: a) SC3-2a; b) SC4-2a

7.3.3 Critical buckling stresses

The accuracy of the FE models in predicting the critical buckling stresses of the different components of the stub columns was assessed by comparing the experimentally derived buckling stresses with those obtained from the FE models. Load-lateral displacement curves, similar to those shown in Figures 7.31-7.34, were used to calculate the experimental and numerical critical buckling stresses of the components of each tested column using the same assumptions as previously described in Section 3.8.3 of Chapter 3. The critical buckling stresses obtained from the tests and the corresponding FE models are reported in Table 7.17, Table 7.18, Table 7.19 and Table 7.20 for columns with geometry SC1, SC2, SC3 and SC4, respectively.

For columns SC1, Table 7.17 shows that the average difference between the experimentally derived critical buckling stresses and those obtained from the FE models was around 15 % for the plate sections and around 7 % for the channel sections. For columns SC2, Table 7.18 shows that the average difference between the experimentally and numerically derived critical buckling stresses of the outer channels was around 5 %, while for columns SC3 and SC4 Table 7.19 and Table 7.20 show that these differences were around 5 % and 11 %, respectively.

Table 7.17: Numerical and experimental buckling stresses of the components of columns SC1

Column	Buckling stress from test (MPa)		Buckling stress from FEA (MPa)	
	Channel	Plate	Channel	Plate
SC1-2a	65	28	71	21
SC1-2b	72	19	70	24
SC1-3a	70	46	72	42
SC1-3b	69	45	72	40
SC1-5a	69	69	59	59
SC1-5b	67	67	61	61

Table 7.18: Numerical and experimental buckling stresses of the components of columns SC2

Column	Buckling stress from test (MPa)		Buckling stress from FEA (MPa)	
	Inner Channel	Outer Channel	Inner Channel	Outer Channel
SC2-2a	-	77-95	-	82-90
SC2-2b	-	79	-	76-90
SC2-4a	-	69-86	-	86
SC2-4b	-	86	-	86
SC2-6a	-	105	-	97
SC2-6b	-	105	-	101

Table 7.19: Numerical and experimental buckling stresses of the components of columns SC3

Column	Buckling stress from test (MPa)		Buckling stress from FEA (MPa)	
	Plain Channel	Lipped Channel	Plain Channel	Lipped Channel
SC3-2a	103	103	96	96
SC3-2b	84-96	96	101	101
SC3-5a	-	96-117	108	105
SC3-5b	108	108	105	105

Table 7.20: Numerical and experimental buckling stresses of the components of columns SC4

Column	Buckling stress from test (MPa)		Buckling stress from FEA (MPa)	
	Plain Channel	Lipped Channel	Plain Channel	Lipped Channel
SC4-2a	87	-	74	-
SC4-2b	88	-	73	-
SC4-5a	73-91	91	91	91
SC4-5b	93-104	104	93	93

From the above it can be concluded that the FE models which included material non-linearity derived from coupon tests, measured geometric imperfections and actual experimentally determined connector behaviour were able to accurately replicate the behaviour of the tested stub columns and they were therefore further used in parametric studies.

7.4. Parametric study

7.4.1 Effect of fastener modelling

In order to study the way in which different connector modelling approaches affect the predicted response of the FE model, the ultimate loads obtained from the validated FE models were compared to the results obtained from FE models in which the connectors behaviour was modelled in three different ways.

The first and simplest approach to model the connectors was using BEAM multi-point constraints (MPCs). MPC constraints eliminate the degrees of freedom of a particular node, in this case by coupling the degrees of freedom of the fastening points on both surfaces. They have been used in the past to model the behaviour of screw connectors in CFS built-up specimens (Anapayan and Mahendran, 2012; Zhang and Young, 2015). This approach has the advantage of reducing the size of the model. However, it does not allow any output to be obtained from the connectors (e.g. the connector shear forces), and since the constraints are imposed by eliminating the degrees of freedom of one of the fastening nodes, it cannot be used to model more complex connector behaviour such as slip or bearing deformations of the connected plates.

In the remaining two modelling approaches the fasteners were modelled using either HINGE or PLANAR connector elements. HINGE connectors constrain all components of relative motion (CRMs) between the surfaces, apart from the rotational component normal to the fastened surfaces, while PLANAR connectors constrain all CRMs apart from the rotation normal to the surfaces and the translational CRMs tangential to the surfaces. It is worth noting that this last modelling approach is similar to the approach used to model the connectors in the validated models. However, in this case neither elastic nor plastic behaviour was added to the tangential CRMs. The ‘HINGE’ and ‘PLANAR’ models can be seen as opposite ends of a spectrum. In the former, slip at the connectors is completely prevented, while in the latter infinite and unrestrained slip is allowed.

Figure 7.36 shows, for each column, the ultimate load obtained from the HINGE, PLANAR and MPC FE models, normalized against the ultimate load obtained with the validated FE models. Figure 7.36 shows that the most significant effect of the connector behaviour on the ultimate load occurred in columns SC1, in which the MPC models predicted the highest ultimate loads and the PLANAR models the lowest. The HINGE models predicted slightly lower ultimate loads than the MPC models. This may be attributed to the additional in-plane rotational restraint the MPC model exerted between the fastened surfaces at the connecting points. The average difference between the peak loads predicted for columns SC1 by the HINGE and PLANAR FE models was around 16 %, while the average difference between the MPC and PLANAR FE models was around 20 %. In columns SC2, SC3 and SC4 the effect of the connector behaviour was less noticeable. However, for columns SC2 the predictions of the ultimate loads given by the PLANAR models were consistently lower than those of the HINGE and MPC FE models, with an average difference of around 5 %. In columns SC3 and SC4, on the other hand, some of the PLANAR models predicted ultimate loads which were slightly larger than those predicted by the HINGE and MPC models. However, the difference in the ultimate load predicted with the different modelling approaches was less than 3 %.

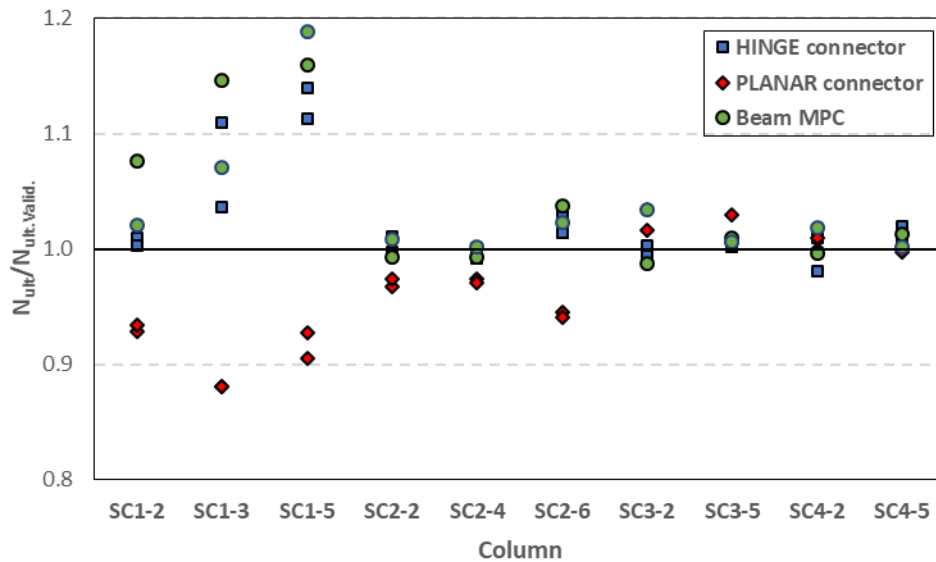


Figure 7.36: Ultimate load comparison for different connector modelling approaches

Figure 7.36 also shows that for columns SC1 the predictions given by the validated FE models lay somewhere in between those of the HINGE/MPC and PLANAR FE models, while in columns SC2, SC3 and SC4 the predictions given by the validated FE models were in much better agreement with those of the HINGE/MPC FE models. To explain this, Figure 7.37 and Figure 7.38 show the maximum shear force and associated slip which developed at the connector points for all geometries. Figure 7.37 also shows the slip force of the bolts used to assemble columns SC1 and SC2, as measured from single lap shear tests (in solid line). Figure 7.37 shows that in columns SC1 the shear forces which developed at the connector points as a result of flexural buckling of the plate sections were larger than the force which causes the bolts to slip. Slip deformations of the connectors reached up to 0.9 mm in these columns before the peak load was reached, as shown in Figure 7.38. In columns SC2, the shear forces which originated at the connectors as a result of local buckling of the channels were lower than the slip force and the relative deformations at the connector points in these columns were significantly smaller (less than 0.3 mm). Columns SC3 and SC4 showed the lowest shear forces as a result of local buckling of the components, with almost no slip predicted by the validated FE model.

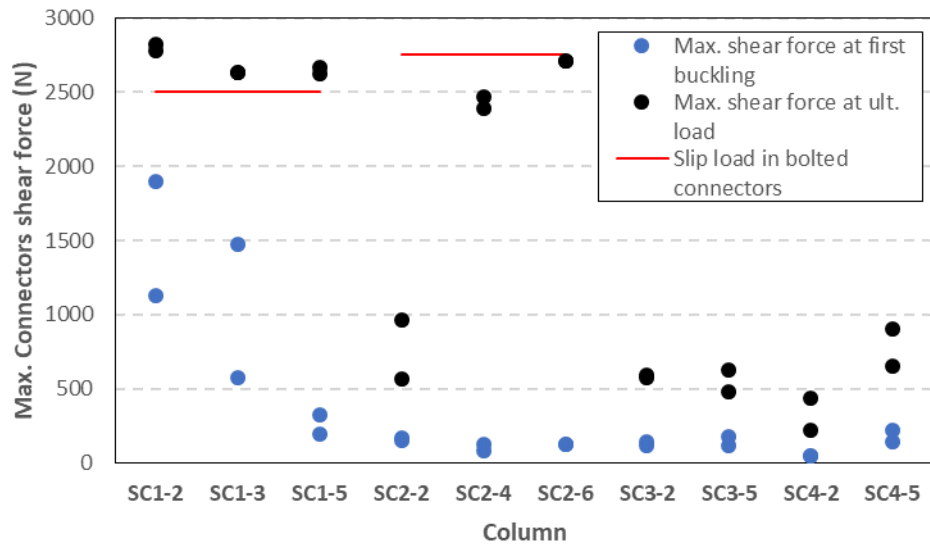


Figure 7.37: Maximum connector shear force

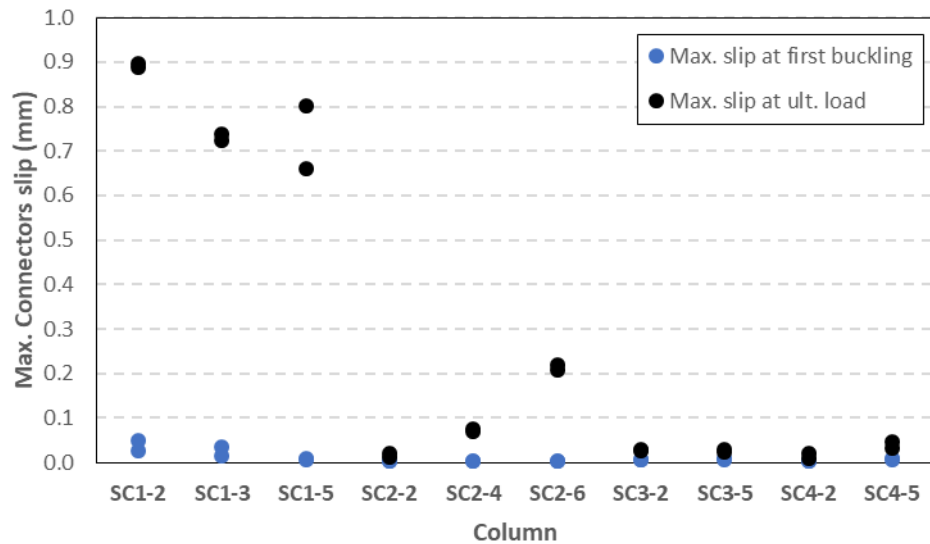


Figure 7.38: Maximum connector slip

The large differences in the ultimate load predicted for columns SC1 by the different modelling approaches is due to the fact that in these columns the plate sections, which account for almost 60 % of the built-up cross-section, buckled in a global-type flexural mode, so that their critical buckling stress was inversely proportional to the square of the buckle half-wave length. This buckle half-wave length was increased in the PLANAR FE model due to slip which, in the case of columns SC1-2 and SC1-3, allowed the plates to remain unbuckled in some fields between connectors, while the channels buckled in all the fields. This allowed the plates to increase their half-wave length in the fields where they buckled as a result of some minor rotation of the channel flanges at the connectors, as shown in Figure 7.39 and Figure 7.40 for columns SC1-2a and SC1-3a, respectively. In columns SC1-5 the channels and the plates buckled synchronously, with identical half-wave lengths, irrespective of whether the FE models allowed slip between

the components or not. However, in the PLANAR FE model, in which the components were free to slip, the channel sections were less restrained by the plates and were able to buckle with a slightly larger half-wave length than in the HINGE/MPC FE models, in which slip was completely prevented, as illustrated in Figure 7.41 for column SC1-5b. The effect in the reduction of the buckle half-wave length of the plate sections was more pronounced in the columns with a larger number of intermediate connectors, since in these columns the buckle half-wave length in the plate sections was shorter, and therefore their critical buckling stress was more sensitive to variations in their buckle half-wave length. As an example of the effect of the connector behaviour on the critical buckling stress of the plate and channel sections, Figure 7.42 compares the load-lateral deformation curves for column SC1-5b obtained from the HINGE and PLANAR FE models. Note that the load at which the channels buckled in a local mode was also increased in the HINGE model. This was partly due to the additional restraint provided by the plates and partly due to the fact that in this model the plate sections were able to carry more load than in the PLANAR model as a result of the increase in their critical buckling stress.

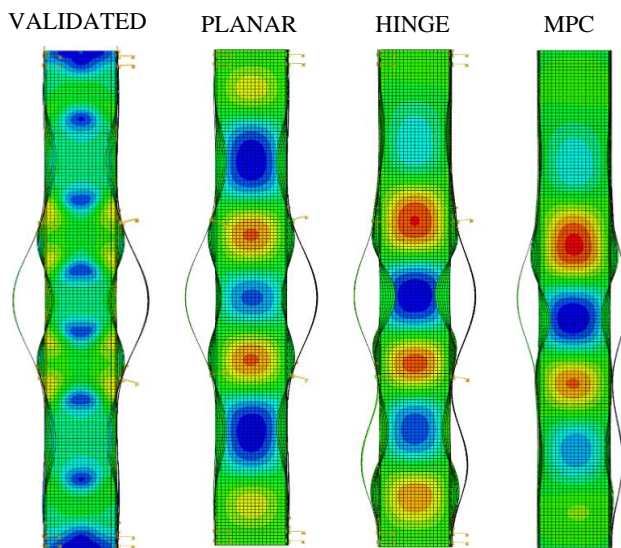


Figure 7.39: FE models: deformed shape of SC1-2a

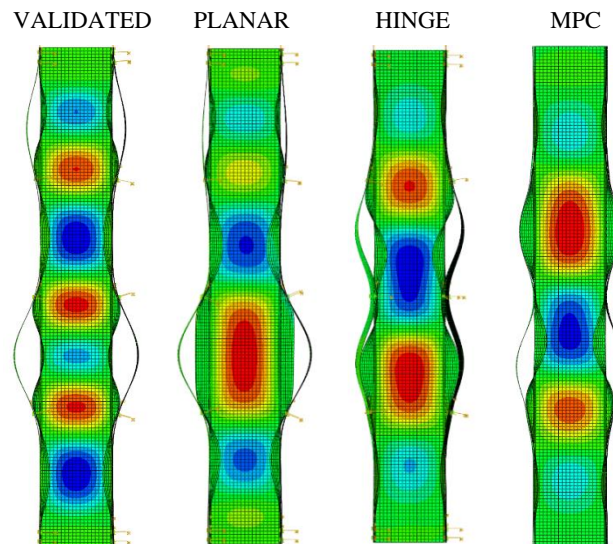


Figure 7.40: FE models: deformed shape of SC1-3a

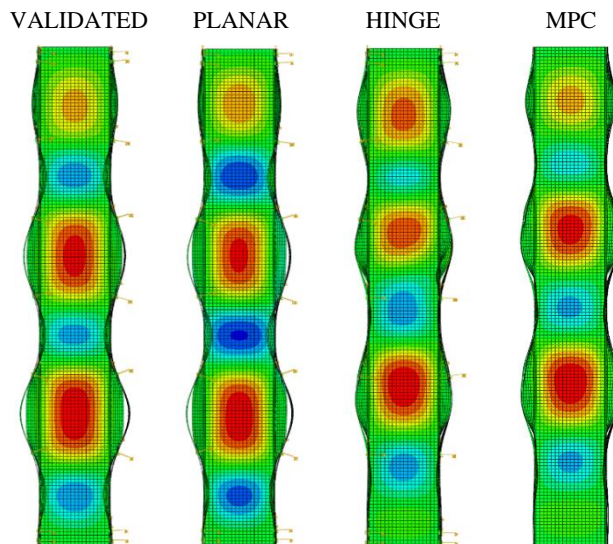


Figure 7.41: FE models: deformed shape of SC1-5a

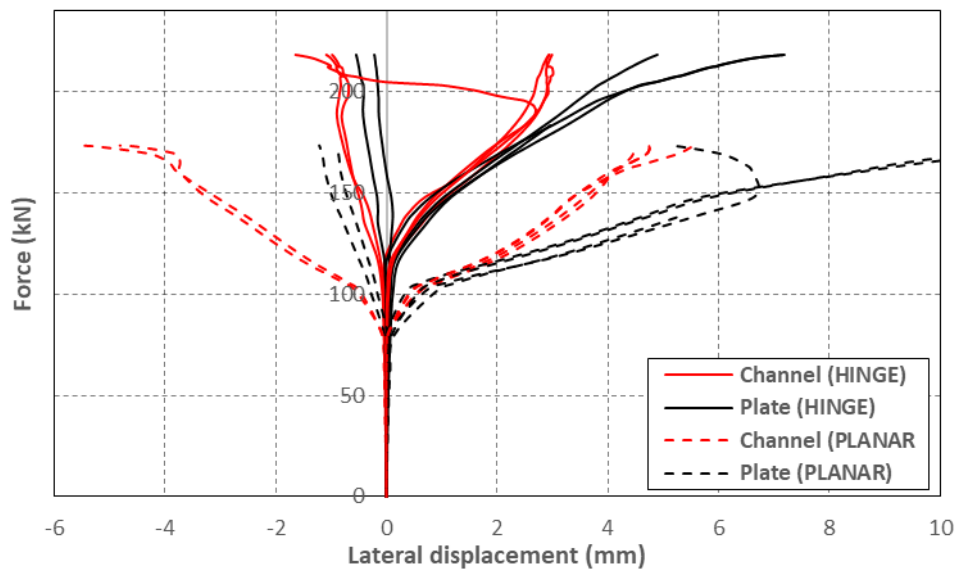


Figure 7.42: Load-lateral displacement curves from Hinge and Planar FE models of SC1-5b

For columns SC2, although the HINGE/MPC models predicted a slightly different buckled shape compared to the validated and PLANAR model (see Figure 7.43 for column SC2-6a, which was the column which showed the largest difference in ultimate load), this did not result in a significant variation in their critical buckling stresses, as shown in Figure 7.44 for column SC2-6a. In columns SC2 the slight decrease in the ultimate load predicted with the PLANAR model compared to the predictions given by the HINGE/MPC models was due to the slip experienced by the components at the connector points after they buckled, which slightly facilitated the formation of the yield line mechanisms in the column.

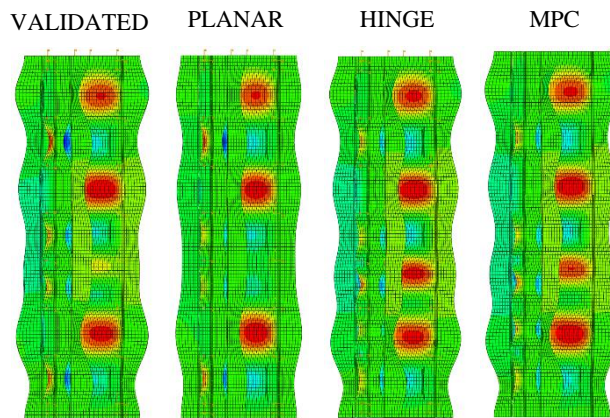


Figure 7.43: FE models: deformed shape of SC2-6a

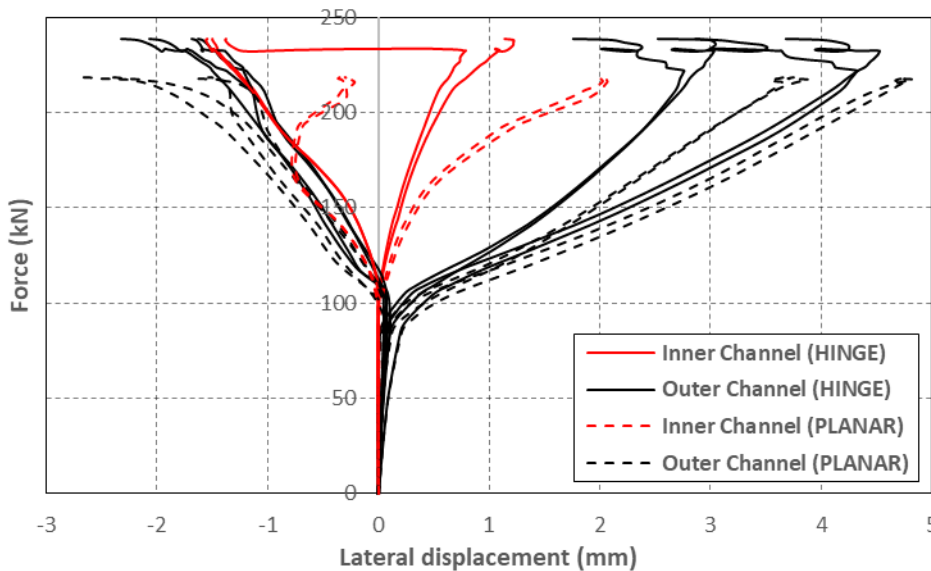


Figure 7.44: Load-lateral displacement curves from Hinge and Planar FE models of SC2-6a

7.4.2 Connector spacing and contact interaction

Parametric studies were also carried out to study the way in which the ultimate capacity of the CFS built-up stub columns is affected by the connector spacing and by contact interaction between the components.

For each built-up geometry simulations were run with and without contact between the components, while varying the number of equally spaced intermediate connectors along the column from zero to 31 (i.e. without counting the connectors at the end cross-sections of the column). This corresponded to a connector spacing which varied from 1000 mm to around 30 mm for columns SC1, SC3 and SC4, and from 700 mm to around 20 mm for column SC2. In addition to this, in order to establish an upper-bound for the ultimate capacity when the connector spacing is reduced to zero, an additional column was modelled for each built-up geometry, in which the connector points were replaced by smeared TIE constraints between the component surfaces along the whole column length, as illustrated in Figure 7.45 for column SC3. All numerical simulations included the initial geometric imperfections of a representative column and the material non-linearity obtained from the tensile coupons.

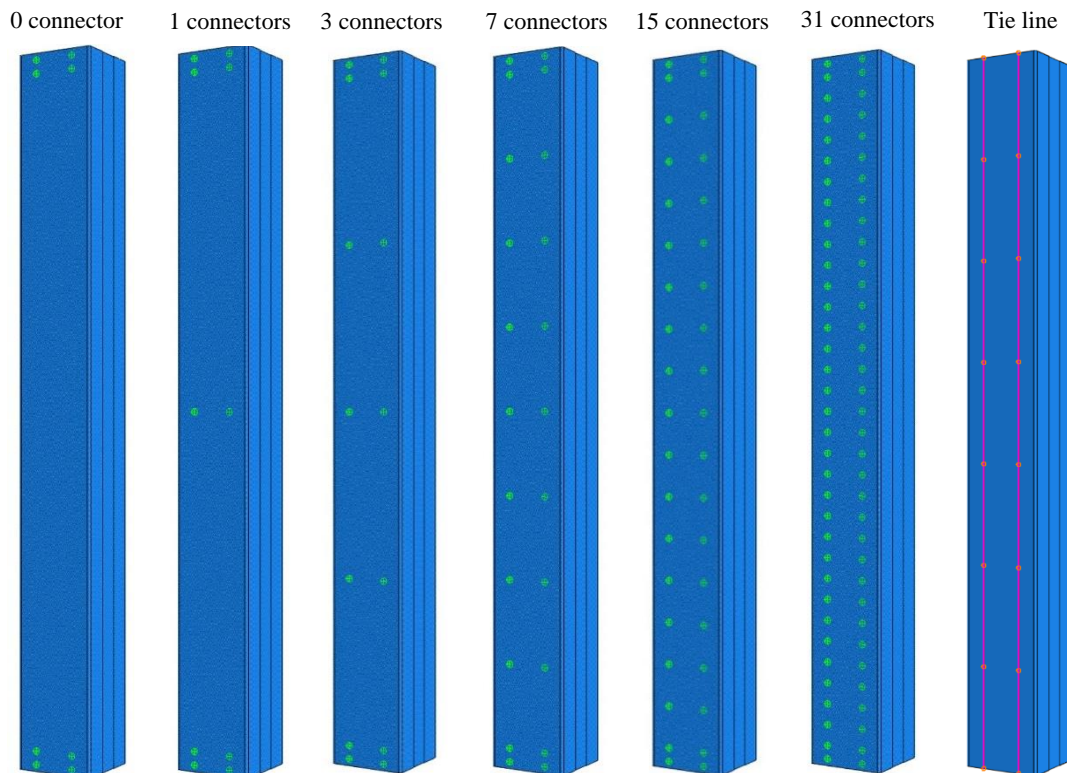


Figure 7.45: FE models with varying number of connectors and Tie constraint for column SC3

The load vs. axial shortening curves obtained from the FE models including contact and with varying connector spacing are shown in Figure 7.46a, Figure 7.47a, Figure 7.48a and Figure

7.49a for the columns with geometries SC1, SC2, SC3 and SC4, respectively, while the load vs. axial shortening curves obtained from the FE models in which contact was deactivated are shown in Figure 7.46b, Figure 7.47b, Figure 7.48b and Figure 7.49b.

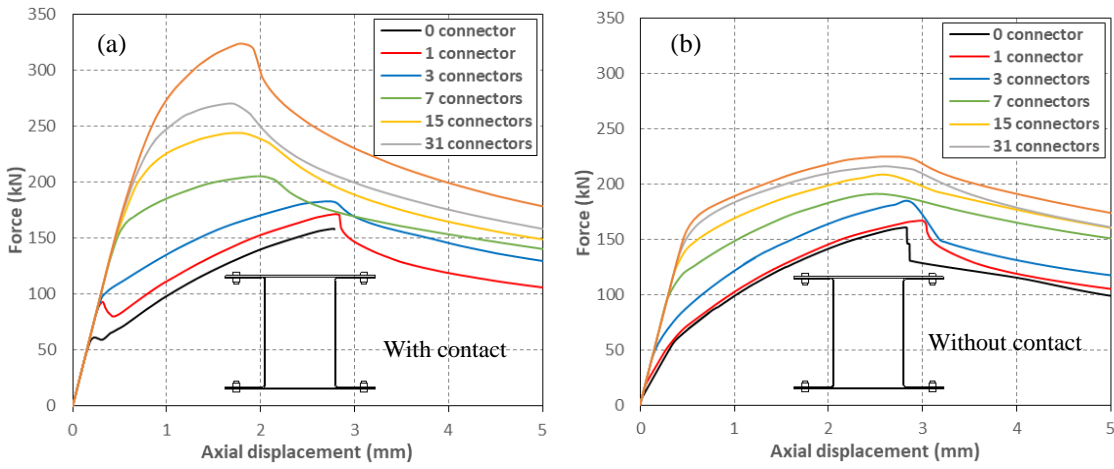


Figure 7.46: Load-axial deformation curve of SC1: a) with contact; b) without contact

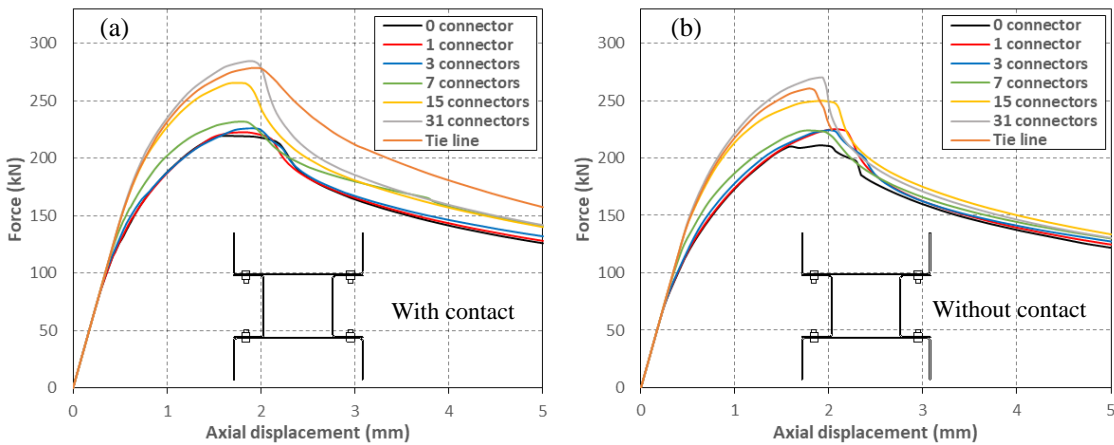


Figure 7.47: Load-axial deformation curve of SC2: a) with contact; b) without contact

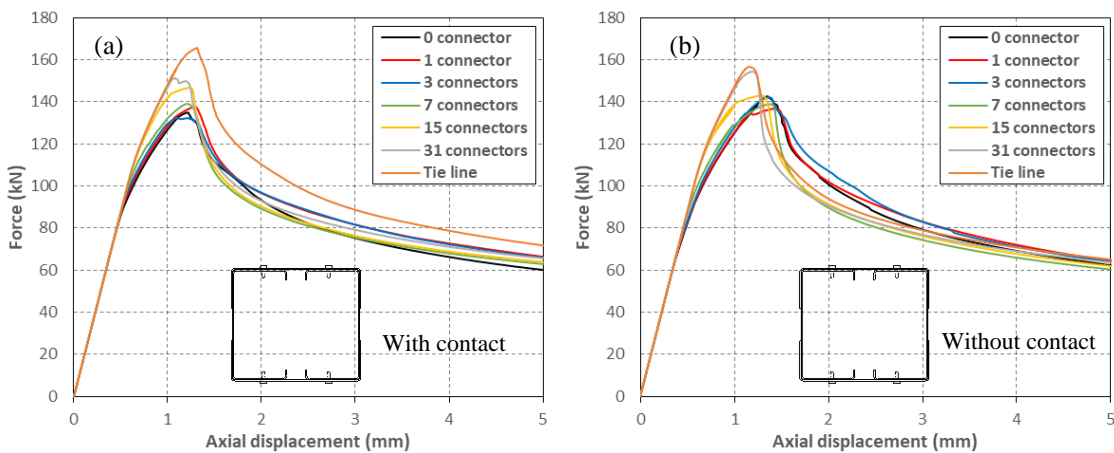


Figure 7.48: Load-axial deformation curve of SC3: a) with contact; b) without contact

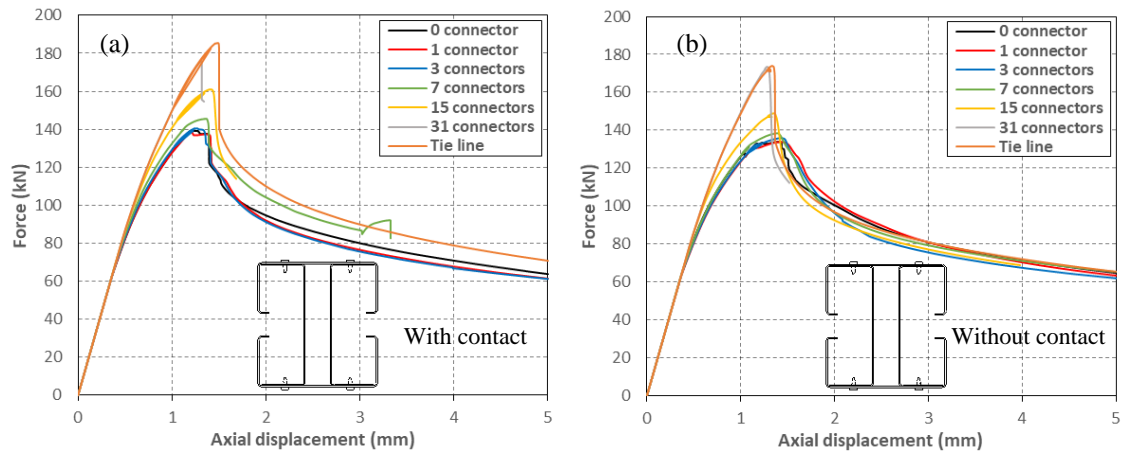


Figure 7.49: Load-axial deformation curve of SC4: a) with contact; b) without contact

The ultimate load predicted by the FE models as a function of the connector spacing is shown in Figure 7.50 for all geometries considered. Figure 7.50a illustrates the results for the models in which contact was activated, while Figure 7.50b shows the ultimate loads obtained from the FE models in which contact was not considered. In the figures, the ultimate loads are normalized with respect to the predictions given by the same models in which the connectors were modelled with smeared TIE constraints.

Figure 7.50a shows that for connector spacings larger than around 125 mm the ultimate load remained almost unaffected by the connector spacing in most of the built-up geometries. Only columns SC1 showed a noticeable increase in the ultimate load of around 30 % when reducing the connector spacing from 1000 mm to 125 mm. This is attributed to the fact that reducing the connector spacing in these columns results in a reduction in the buckle half-wave length of the plate sections, which buckle in a global-type flexural mode. This is clearly illustrated in Figure 7.46 by the first change in stiffness in the built-up columns which was delayed towards higher loads when the connector spacing was reduced. For columns SC3 and SC4, reducing the connector spacing from 1000 mm to 125 mm only resulted in increases in the ultimate load of around 3 % and 4 %, respectively, while for columns SC2 reducing the connector spacing from 700 mm to 88 mm resulted in an increase in the ultimate load of around 6 %.

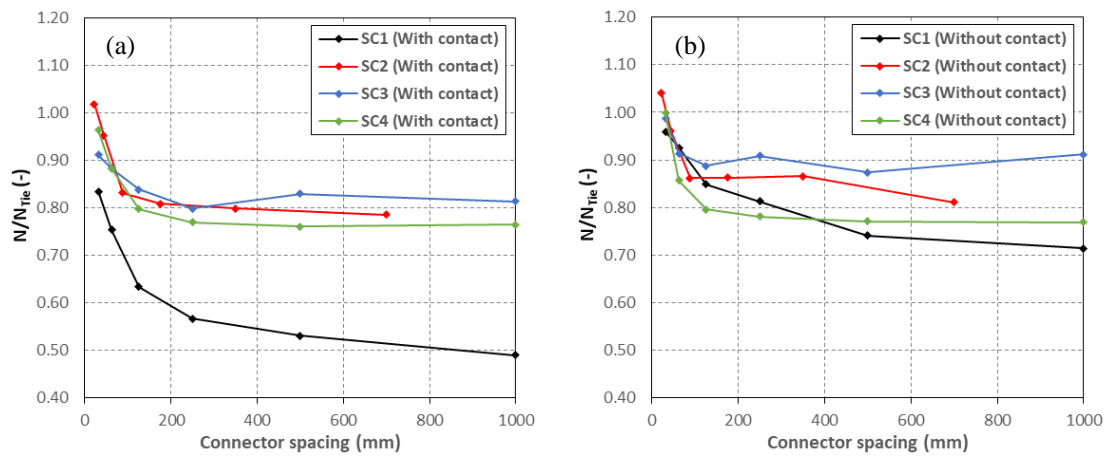


Figure 7.50: Ultimate load vs. connector spacing obtained from FE models: a) with contact; b) without contact

An amplified buckled shape obtained from the FE models of columns SC1, SC2, SC3 and SC4, in which contact between the components was included, is illustrated in Figure 7.51, Figure 7.52, Figure 7.53 and Figure 7.55, respectively, for each connector spacing considered in the parametric study. In Figure 7.55, two of the components of column SC4 were removed in order to show the deformed shape of the interior (plain) channel.

Figure 7.51 shows that in columns SC1 with zero, 1 and 3 rows of intermediate connectors the plate and the channel sections buckled with different half-wave lengths. In the column without intermediate connectors the channels were not constrained by the plate sections and they buckled in a local mode with their flanges and web moving alternately inwards and outwards along the column. As the connector spacing was reduced, the buckling pattern in the channels became increasingly restrained by the plate sections. The reduction of the connector spacing also resulted in a reduction of the buckle half-wave length of the plate sections. For the columns with connector spacings smaller or equal to 125 mm (i.e. the columns with 7, 15 and 31 intermediate rows of connectors, as well as the column in which the connectors were modelled with Tie constraints) the connector spacing was smaller than the buckle half-wave length of the plate and the channel sections. As a result, the plates and the channels were forced by the connectors to buckle synchronously with a half-wave length of around 155 mm. This half-wave length is relatively close to the natural local buckle half-wave length of the channels of 170 mm. It is worth pointing out that despite the small variation in the buckle half-wave length in the columns with more than 15 intermediate set of connectors, it was in these columns in which the ultimate load showed the largest sensitivity to the connector spacing. However, this range of connector spacings is of little practical importance in construction due to the amount of labour required to assemble columns with such a large number of connectors.

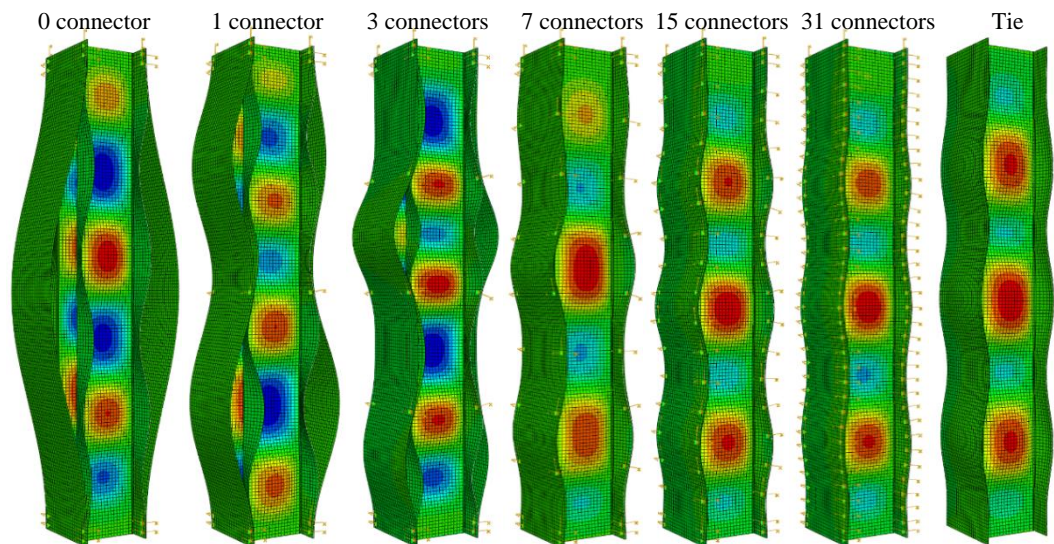


Figure 7.51: Amplified buckled shape of columns SC1

For geometry SC2 the different components in the columns with zero, 1, 3 and 7 intermediate rows of connectors buckled in a local mode with different half-wave lengths, as shown in Figure 7.52. For this range of connector spacings the ultimate capacity of the column showed little sensitivity to the distance between connectors. The effect of the connector spacing was more noticeable in the columns with a connector spacing smaller than or equal to 44 mm (i.e. the columns with 15 and 31 rows of connectors, as well as in the column in which the connectors were modelled with Tie constraints). In these columns, the connector spacing was small enough to force the different components of the built-up geometry to buckle with the same half-wave length of around 80 mm, which was slightly shorter than the natural local buckle half-wave length of the inner channels (100 mm) and less than half the natural local buckle half-wave length of the outer channels (170 mm).

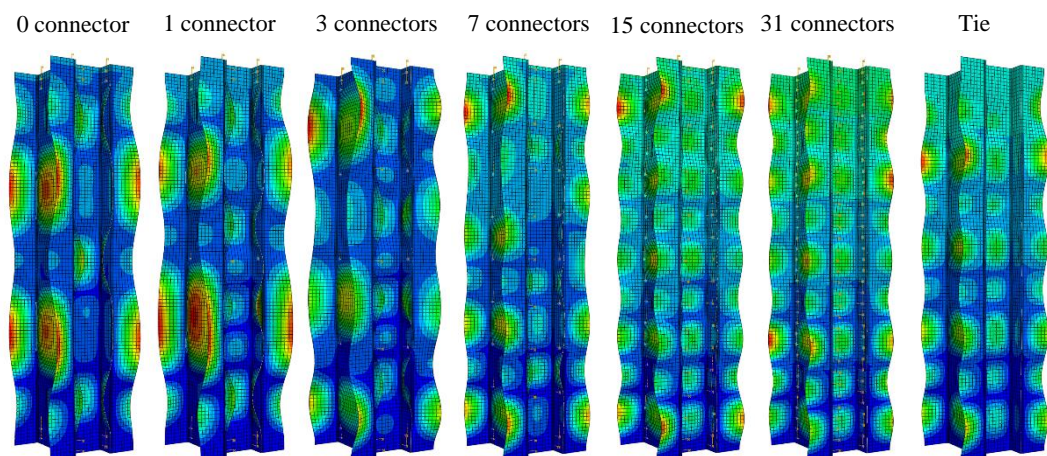


Figure 7.52: Amplified buckled shape of columns SC2

In the case of geometry SC3, both the plain and lipped channels buckled in a local mode. In the column without intermediate connectors the components forced each other to buckle with the

same half-wave length of around 100 mm, as shown in Figure 7.53. It is worth mentioning that the natural local buckle half-wave length of the lipped channels was 90 mm, while the natural buckle half-wave length of the plain channels was 130 mm. However, due to the lack of intermediate connectors in this column, discontinuous gaps were formed between the web of the plain channels and the flanges of the lipped channels as they buckled. This is illustrated in Figure 7.54, which shows a cut of columns SC3 through a plane containing the connectors. In the columns with 1, 3 and 7 intermediate sets of connectors, the connectors forced the components to adjust their buckling pattern so that the cross-sections containing connectors could fall inside a concave buckle of the plain channels. As a result of this imposition, the plain and lipped channels displayed buckles with slightly varying half-wave lengths along the column. The gaps between the components were also reduced in both length and amplitude when the connector spacing was reduced. In the column with 15 intermediate rows of connectors, where the connector spacing was smaller than the local buckle half-wave length of the components, the flanges of the lipped channels and the web of the plain channels were forced to buckle synchronously with a half-wave length of around 85 mm and without any gaps between the components, as shown in Figure 7.54. This resulted in a noticeable increase in the ultimate capacity of the column, which further increased for even shorter connector spacings, as shown in Figure 7.50a.

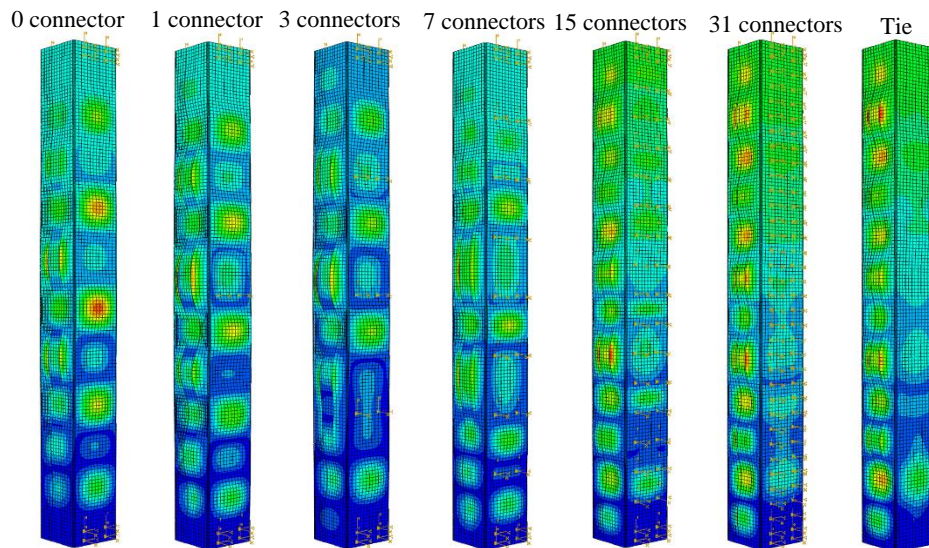


Figure 7.53: Amplified buckled shape of columns SC3

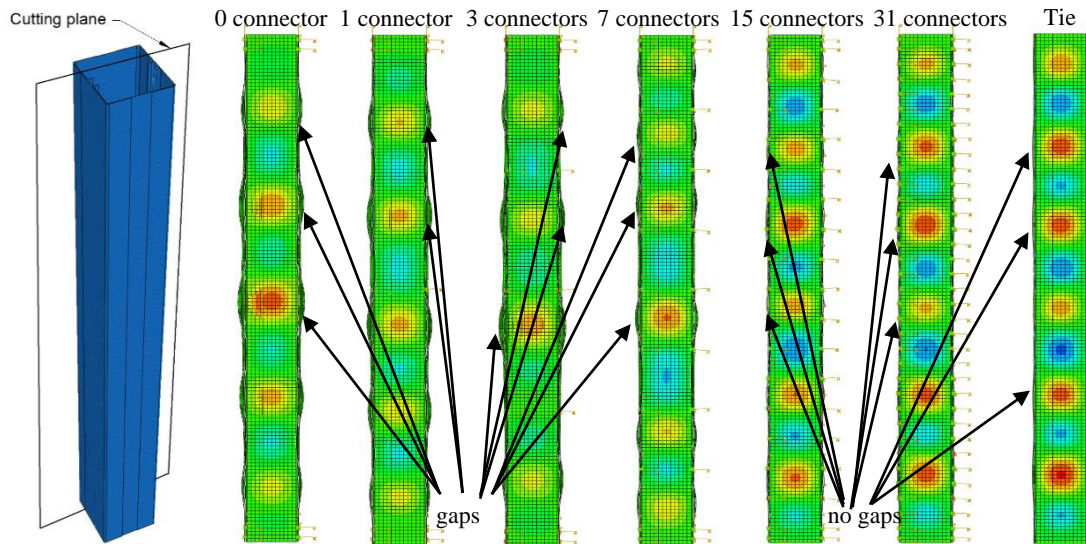


Figure 7.54: Gap formation between the web of the plain channels and the flanges of the lipped channels in columns SC3

For columns SC4, in the specimen without intermediate connectors the plain and lipped channels buckled with a regular half-wave length along the column. The plain channels buckled with eight half-waves, while the lipped channels buckled with ten half-waves. As rows of connectors were added along the column, the regularity in the buckling pattern in the lipped and plain channels was lost, as their buckles became enlarged or shortened as a result of the enforcement of deformational compatibility between the components at the connector points. The amplitude of the buckles was also reduced as the number of intermediate connectors increased. In the column with 31 intermediate sets of connectors, the amplitude of the buckles was almost imperceptible and the inner and outer channels buckled in a perfectly synchronous manner with a buckle half-wave length of around 85 mm.

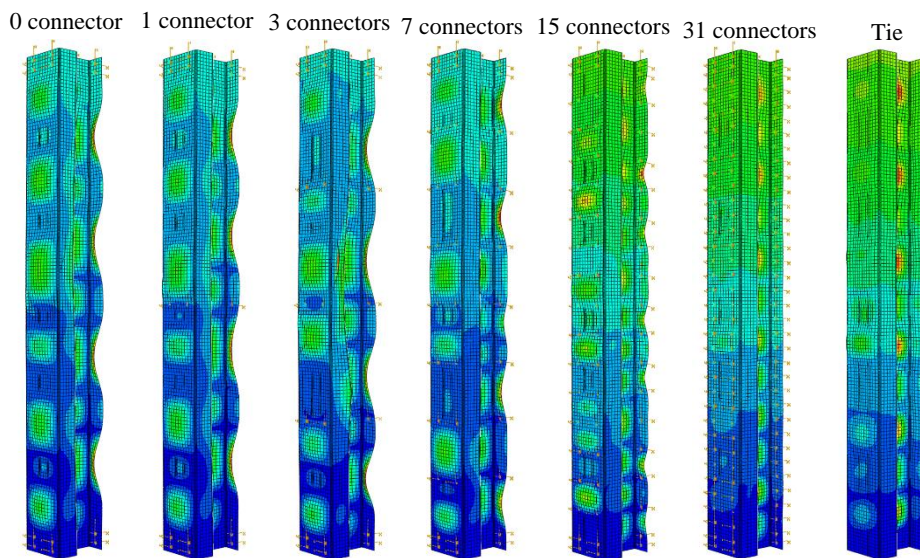


Figure 7.55: Amplified buckled shape of two of the components of columns SC4

The way in which the ultimate capacity is affected by contact pressures between the components is illustrated in Figure 7.56 for each built-up geometry. The figure shows the ratio of the peak load obtained from the FE models with contact to the corresponding value without contact for each connector spacing. For the columns in which all the components buckled in a local mode (i.e. columns SC2, SC3 and SC4), the effect of contact on the ultimate capacity of the column was relatively small, irrespective of the connector spacing. The maximum increase in the ultimate capacity as a result of contact was 7 % for columns SC2, 6 % for columns SC3 and 8 % for columns SC4. However, in columns SC1, where the plate sections buckled in a global-type flexural mode, the effect of contact on the ultimate capacity of the column was almost negligible when the connector spacing was larger than the buckle half-wave length of the components, while for shorter connector spacings it resulted in an increase in the ultimate capacity of the column. Its effect rapidly increased as the connector spacing was further reduced, resulting in an increase in the ultimate load of up to 36 % in the model in which the connectors were represented by smeared TIE constraints along the column.

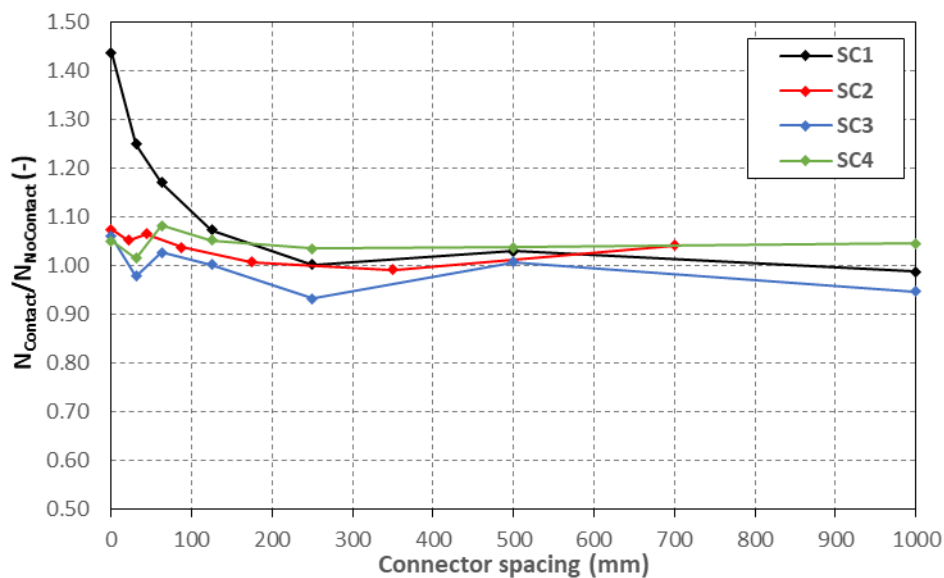


Figure 7.56: Effect of contact interaction on the ultimate capacity

7.5. Summary and conclusions

Detailed FE models were developed of the 20 built-up stub columns with four different cross-sectional geometries presented in Chapter 3 using the software package Abaqus v.6.14. The initial geometric imperfections measured on the tested columns, as well as non-linear material properties obtained from tensile coupons, were incorporated into the FE models. In addition, the connectors used to assemble the stub columns were modelled using mesh-independent fasteners

and they included the load-elongation behaviour of the connectors which was previously obtained from single lap shear tests. The effects of using two simplified material modelling approaches on the ultimate capacity of the built-up stub columns was investigated by carrying out a material modelling study.

The column models presented significant convergence issues which were overcome by modifying some solution control parameters and by introducing artificial damping through either the contact or the automatic stabilization mechanisms. A stability analysis was carried out to ensure that the amount of damping introduced into the model was sufficiently low not to significantly alter the ultimate capacity predicted by the models. The accuracy of the FE models was verified by comparing their predictions with the experimental data obtained from the tested stub columns, which included the ultimate capacity and initial buckled deformed shape of the columns, as well as the experimentally derived critical buckling stresses of some of the components of the built-up geometries. The validated models were further used in parametric studies to investigate the way in which the connector modelling approach and the connector spacing, as well as contact between components affect the response of the built-up stub columns.

The following conclusions could be drawn from the numerical investigation:

- The material modelling study revealed that substituting the actual stress-strain behaviour by a simplified bilinear stress-strain curve resulted in an overestimation of the ultimate capacity of the stub columns of around 4.4 % for the studied geometries, while the effect of not modelling the enhancement of the mechanical properties in the corner regions of the components was less significant, resulting in an average reduction in the peak load of 1.2 % for the studied geometries. However, the effect of the corner enhancement became more noticeable as the number of corners in the built-up cross-section increased.
- The FE models were able to accurately predict the ultimate capacity of the tested columns for all studied geometries, with average predicted errors of 2.88 % for columns SC1, 4.37 % for columns SC2, 2.52 % for columns SC3 and 5.02 % for columns SC4. The FE models were also able to accurately replicate the initial buckled shape of the tested columns for each geometry and connector spacing considered, while predicting fairly similar critical buckling stresses of the components. The average differences between the numerically and experimentally derived critical buckling stresses were 11 % for columns SC1, 5 % for columns SC2, 5 % for columns SC3 and 11 % for columns SC4.
- For the columns in which all components buckled in a local mode (columns SC2, SC3 and SC4), the connector behaviour did not have a significant effect on the

ultimate capacity of the built-up column and good agreement was achieved between the models in which no slip was allowed at the connector points (the HINGE model and the MPC model) and the validated model, irrespective of whether the column was assembled using bolts or screws. In these columns the shear forces introduced at the connector points as a result of local buckling of the components were sufficiently low not to cause significant slip. In the case of columns SC2, which were assembled with bolts, the shear forces remained below the slip force, while in columns SC3 and SC4, which were assembled with screws, the shear forces remained below 1 kN. In columns SC1, which were constructed with channel and plate sections bolted together, the connector behaviour showed a more noticeable effect on the ultimate capacity of the column. This was attributed to the reduction in the buckle half-wave length of the plate sections when preventing slip at the connector points, which buckled in a global-type flexural mode.

- For columns SC2, SC3 and SC4, in which all components buckled in a local mode, the ultimate load remained almost unaffected by the connector spacing when this spacing was larger than the buckle half-wave length of the components. For columns SC1, on the other hand, a more noticeable increase in the ultimate capacity was observed within the range of connector spacings which were larger than the buckle half-wave length of the components when the connector spacing was reduced. This increase in the ultimate capacity was attributed to a reduction of the buckle half-wave length of the plate sections when the connector spacing was reduced. In all the studied geometries, the ultimate capacity of the column became significantly more sensitive to the distance between connectors when this distance was shorter than the buckle half-wave length of the components. In these columns the components were forced by the connectors to buckle synchronously with an identical half-wave length. It is worth pointing out that exploiting this range of connector spacings would be impractical in construction due to the large amount of labour involved in assembling specimens with such a large number of connectors.
- Contact pressure between the components was found to have a modest effect on the ultimate capacity of those columns in which all the components buckled in a local mode (i.e. columns SC2, SC3 and SC4), irrespective of the connector spacing. The maximum increase in the ultimate capacity in these columns as a result of contact was less than 8 %. In columns SC1, where the plate sections buckled in a global-type flexural mode, contact only resulted in an appreciable increase in the ultimate capacity of the column when the connector spacing was shorter than the buckle half-wave length of the components. Over this range of connector spacings the effect of contact rapidly increased as the connector spacing was reduced, resulting

in an increase in the ultimate load of up to 36 % for the model in which the connectors were represented by smeared TIE constraints along the column.

Chapter 8

Numerical Study of Cold-Formed Steel Built-up Beams

8.1. Introduction

This chapter presents the development of both detailed and simplified finite element (FE) models of the built-up beams presented in Chapter 4. Figure 8.1 illustrates the cross-sectional geometries of the beams. All test specimens were assembled using M6 bolts.

Both the detailed and the simplified FE models were validated against the tested beams, considering the ultimate moment capacity, the initial buckling shape and the critical buckling stresses of the (compressive) top channel of the built-up geometries. The simplified model was further used in parametric studies to investigate the way in which the connector modelling approach and connector spacing, as well as contact between the individual components affects the buckling response of the built-up beams.

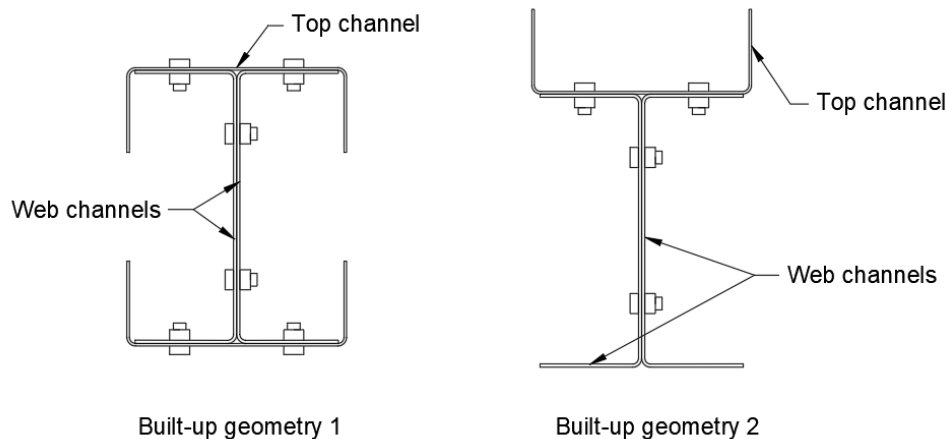


Figure 8.1: Built-up cross-sections

8.2. FE modelling details

The finite element (FE) models of the built-up beams presented in Chapter 4 were developed using the software package Abaqus v.6.14 (Dassault Systemes, 2014). The models were constructed using structural shell elements and the three-dimensional geometry of each component was represented by its mid-surface. The default five integration points through the thickness of the shell in combination with Simpson's rule were used. The models incorporated the measured cross-sectional dimensions of the components, the initial geometric imperfections as measured on the beams and material non-linearity as obtained from the tensile coupons. In addition, the connectors used to assemble the built-up beams were modelled using mesh-independent fasteners which accounted for their actual behaviour.

For each built-up geometry both a detailed and a simplified FE model were developed. The detailed FE model intended to replicate the four-point loading configuration used to test the built-up beams presented in Chapter 4 as much as possible, inclusive of any possible slip between the components of the built-up beam, particularly within the shear span. In the simplified FE models, only the constant moment span of the beam was modelled and the load was introduced as prescribed rotations at the ends of the beam. The purpose of the simplified FE model was to use a less computationally demanding numerical model to carry out the parametric studies, as well as to have easily identifiable boundary conditions.

The labelling used to refer to the FE models is consistent with the one used for the tested beams: 'B1' or 'B2' refers to the geometry of the beam, with reference to Figure 8.1, while the number following the hyphen indicates the number of intermediate rows of connectors along the constant moment span. For example, the label 'B1-2' refers to an FE model of a beam with cross-sectional geometry 1 and two intermediate rows of connectors along the constant moment span.

8.2.1 Boundary conditions

Different boundary conditions were defined for the detailed and simplified FE models. A detailed description is given below.

8.2.1.1 Detailed FE model

The loading and support conditions in the detailed FE models were defined to replicate the actual conditions in the tested beams as accurately as possible. In the tests the beams were simply supported on rollers located 3000 mm apart, while being loaded at two points 1600 mm apart through a spreader beam, as shown in Figure 8.2. The spreader beam was restrained near its ends against any out-of-plane displacement. The end sections of the built-up specimens

above the supports were tightly packed with wooden blocks to prevent distortion of the cross-section, as described in Section 4.7.2.4 of Chapter 4. Figure 8.3 shows an overview of the boundary conditions applied to the detailed FE model of a representative beam belonging to geometry 1, while a detailed description of the way in which the loading and support conditions were defined in the FE models is presented below.

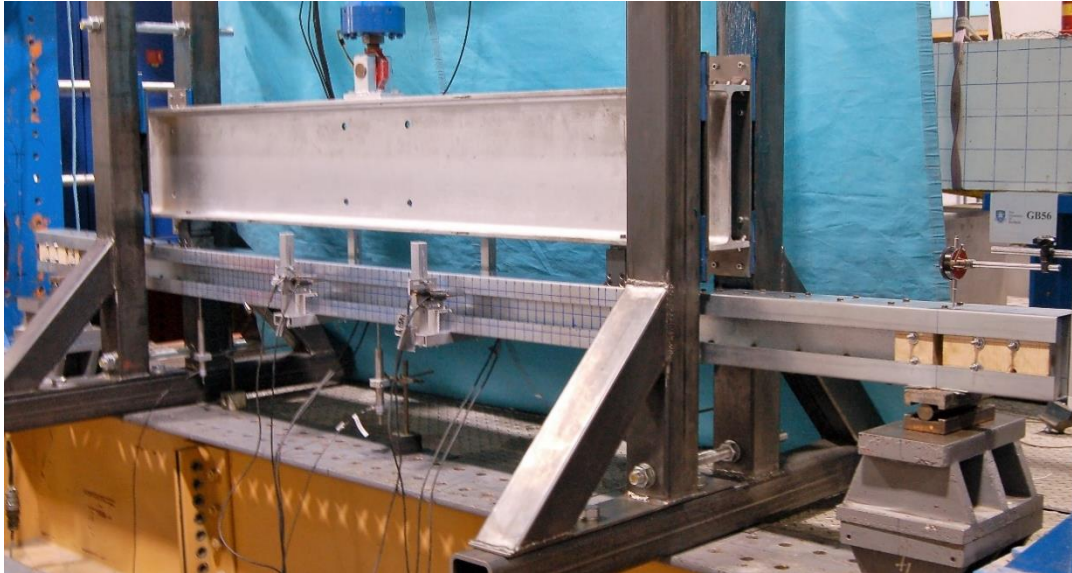


Figure 8.2: Loading and support conditions in test set-up

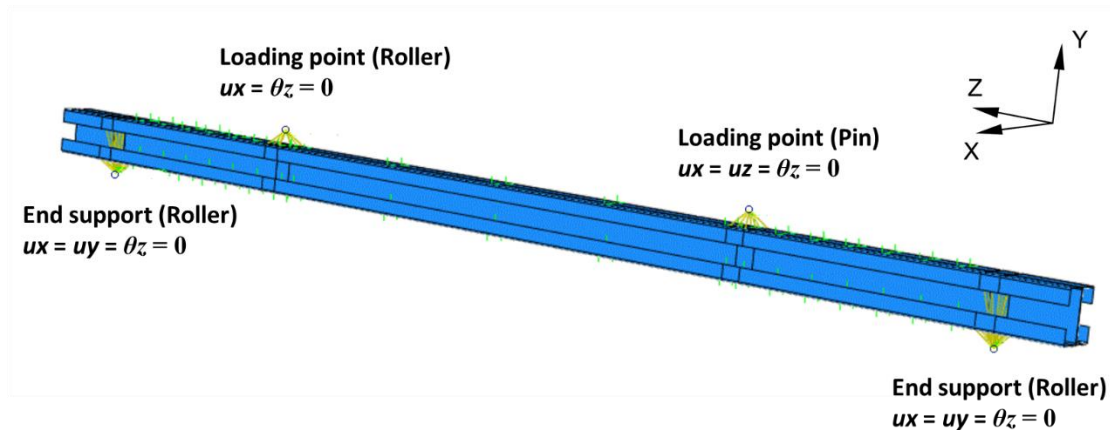


Figure 8.3: Loading and support conditions in FE model

8.2.1.2 Modelling of the loading points

In the test the load was transferred from the spreader beam to the built-up specimens through loading assemblies which simulated a pin and a roller and which were bolted to the top channel of the specimens, preventing any out-of-plane displacement of the tested beam at the loading points. In the FE model each loading point was modelled by creating a BEAM MPC constraint between a reference point and a small area in the web of the top channel, as shown in Figure 8.4

for beams B1 and B2. The area covered the entire width of the web and had a width of 50 mm, identical to the experiment. The reference points coincided with the axes of the pins of the loading assemblies. At the pinned loading point, the translational degrees of freedom along the x - and z -axis, as well as the rotational degree of freedom about the z -axis of the reference point were constrained, while at the roller the translational degree of freedom along the x -axis and the rotational degree of freedom about the z -axis of the reference point were constrained, as shown in Figure 8.3.

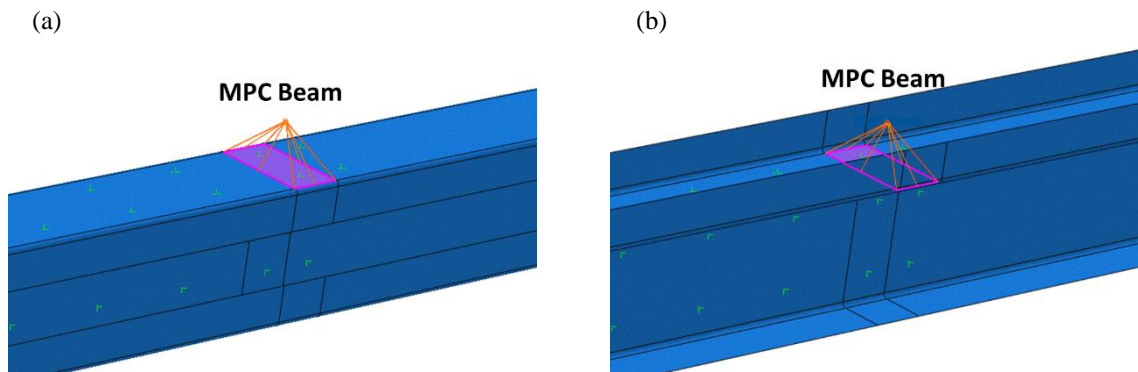


Figure 8.4: Modelling of the loading points of beam: a) B1; b) B2

8.2.1.3 Modelling of the end supports

To model the end support conditions, a reference point of which the location coincided with the axis of the pin of the roller support, was created at each end. The reference points had their translational degrees of freedom along the x - and y -axis, as well as their rotational degree of freedom about the z -axis restrained.

In the beams with geometry B1, MPC BEAM constraints were defined between each reference point and an area of the bottom channel right above the support, which covered the entire width of the channel web and had a width of 50 mm, as shown in Figure 8.5a. The stiffening effect of the wooden blocks at each end of the beam was modelled by coupling the translational degrees of freedom along the x - and y -axis of the nodes in a 50 mm wide strip of the web channels above the roller supports to the respective degrees of freedom of the reference point, as illustrated in Figure 8.5b. This prevented any distortion of the end cross-sections while still allowing slip between the components of the built-up beam,

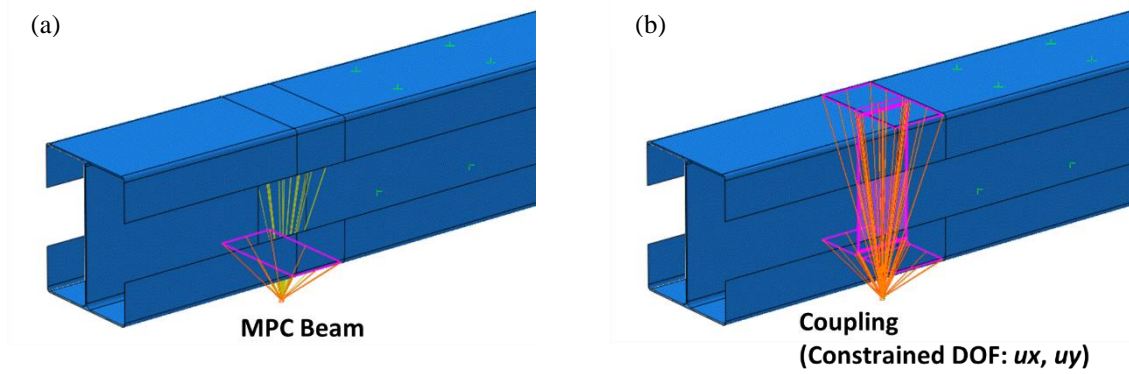


Figure 8.5: End support modelling of beam B1

In the beams with geometry B2, the end support conditions, including the stiffening effect of the wooden blocks was modelled by creating an MPC BEAM constraint between the reference point and a strip of the web above the support, which had a width of 50 mm, as shown in Figure 8.6.

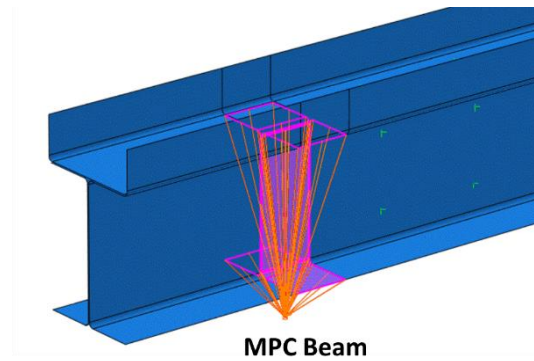


Figure 8.6: End support modelling of beam B2

8.2.1.4 Simplified FE model

The simplified FE model only included the constant moment span of the beam. The boundary conditions were modelled by creating a reference point at each end of the span, which coincided with the centroid of the built-up cross-section. A Beam MPC constraint was then defined between the end cross-sections and the respective reference points, as illustrated in Figure 8.7.

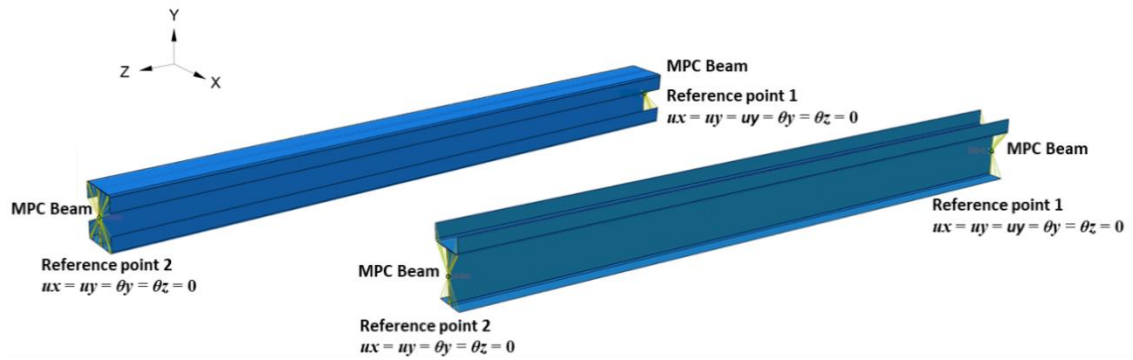


Figure 8.7: Boundary conditions in simplified FE models

The boundary conditions were then applied to the reference points. The reference point at the right end of the beam (Reference point 1) had all its translational and rotational degrees of freedom constrained, apart from the rotational degree of freedom about the x -axis. At the reference point at the left end of the beam (Reference point 2) all degrees of freedom were constrained apart from the rotational degree of freedom about the x -axis and the translational degree of freedom along the z -axis. A sagging moment was applied to the beams by imposing a rotation about the x -axis at the reference points. It is worth pointing out that these boundary conditions restrained warping at the ends of the moment span, which is not strictly the same case as in the experiments, where warping was only partially restrained by continuity with the shear spans. However, the moment span was long enough to allow for the formation of several local half-waves and therefore the difference in the warping conditions at the end of the moment span can be expected to have a negligible effect on the local buckling behaviour of the specimens.

8.2.2 Geometric imperfections

The initial geometric out-of-plane imperfections present in the tested beams were incorporated into the FE models by modifying the coordinates of the nodes in the input file (*.inp) of a geometrically perfect FE model generated in Abaqus/Standard. Adjustment of the node coordinates was carried out using a specially developed Matlab code.

The imperfection data used in the FE models was recorded by moving a laser displacement sensor over the specimen along discrete longitudinal lines, as indicated by the arrows in Figure 8.8. The out-of-plane imperfections were only recorded within the constant moment span. A detailed description of the way in which the out-of-plane imperfections were measured is included in Section 4.6 of Chapter 4.

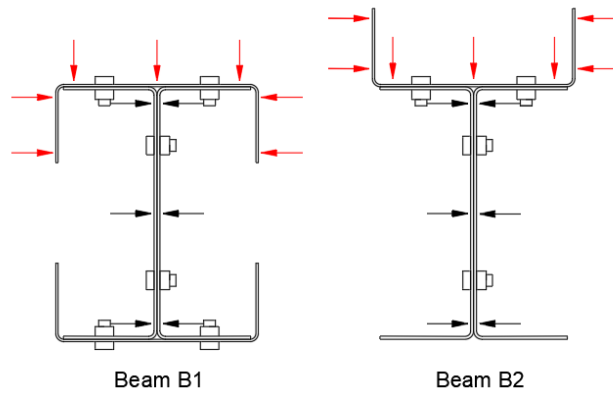


Figure 8.8: Location of the imperfection measurements

The imperfections at the exact locations of the nodes of the FE model were obtained by interpolating between the actual imperfections measurements taken on the test specimen. Linear interpolation was used to determine the nodal imperfections in the flanges of the channels, while quadratic interpolation was used for the web of the channels, as illustrated in Figure 8.9. As an example, Figure 8.10 shows an FE model of beam B2 including the initial geometric imperfections which were amplified 50 times.

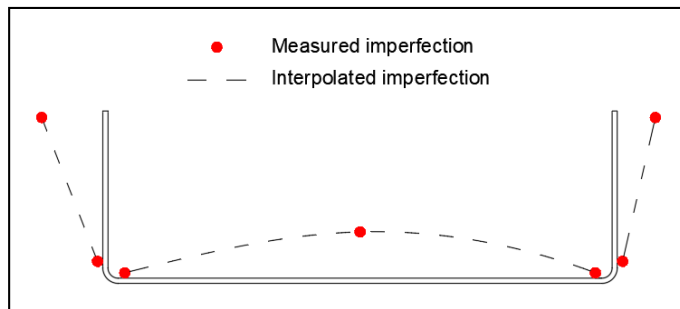


Figure 8.9: Interpolated imperfections

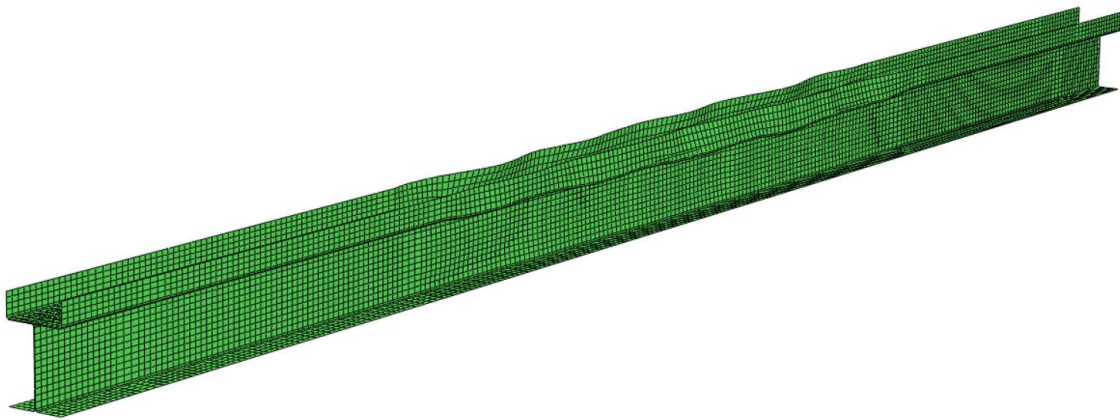


Figure 8.10: Beam B2 FE model incorporating out-of-plane imperfections (amplified x50)

8.2.3 Material properties

The material behaviour was modelled following the same approach described in Section 7.2.3 of Chapter 7 using the data obtained from tensile coupons taken from the flat and corner regions of the channels. Details of the tensile coupons result are included in Section 4.3.3 of Chapter 4.

8.2.3.1 Simplified approaches to model material properties

The first simplified material modelling approach consisted of using a bilinear stress-strain diagram, in which the elastic range was defined in the same way as in the actual material modelling approach, while the plastic range was defined using the 0.2 % proof strength and neglecting any strain hardening. The second simplified material modelling approach was identical to the actual material modelling approach, apart from the fact that the enhancement of the material properties in the corner regions was not considered.

Figure 8.11 shows the moment vs. vertical displacement curves obtained using the two simplified modelling approaches, together with the curve obtained using the actual material modelling approach, for a representative beam of each geometry (B1 and B2). In addition, Table 8.1 reports, for each geometry, the difference in the ultimate moment predicted by the FE models incorporating the simplified material modelling approaches with respect to the FE models including the actual material properties. The figure shows that the effect of both simplified modelling approaches on the behaviour of the studied beams was, in general, fairly small. The only noticeable difference with respect to the predictions given by the FE model including the actual material properties was the stiffer post-buckling response predicted by the FE model in which the material properties were approximated by a bilinear stress-strain curve. However, for both geometries, the ultimate capacities obtained using the bilinear stress-strain curve were only around 2 % higher than those obtained using the actual material properties, while the ultimate capacities obtained from the FE models in which the enhancement of the material properties in the corner regions was ignored were around 2 % lower.

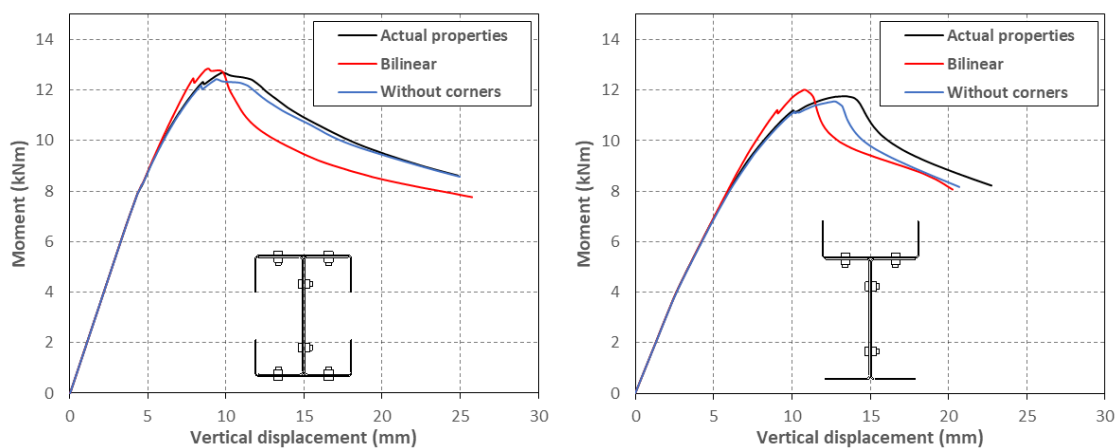


Figure 8.11: Effect of material properties modelling approaches on beams: a) B1-3a; b) B2-3a**Table 8.1: Difference in ultimate moment with respect to FE model with actual material properties**

Beam	Difference in ult. moment with respect to actual material properties (%)	
	Bilinear	Without corners
B1-3a	1.3	-2.1
B2-3a	2.2	-1.8

8.2.4 Contact interaction

Contact between the components of the built-up beams was defined using the general contact formulation available in Abaqus/Standard which employs the surface-to-surface contact discretization and the finite-sliding tracking approach, as described in 7.2.4 of Chapter 7. The contact interaction was defined as ‘frictionless’ in the tangential direction, while a ‘hard’ pressure-overclosure relationship was defined in the normal direction. The ‘hard’ pressure-overclosure behaviour was approximated using the ‘Augmented Lagrange’ constraint enforcement method.

Contact was activated only between those surfaces of the components which were likely to interact with each other during the analysis. In particular, in the beams with built-up geometry 1 and 2 contact interaction was defined between the top flange of the web channels and the web of the top channel, and between the webs of the web channels, while in the beams with built-up geometry 1 contact interaction was also defined between the bottom flange of the web channels and the web of the bottom channel, as shown in Figure 8.12. It is worth noting that, in the beams with geometry 1, defining contact between the top flange of the web channels and the web of the top channel only (without including the flanges of the top channel) implies that the tip of the top flange of the web channels can penetrate the flanges of the top channel. However, adding the flanges of the top channel to the contact interaction as an edge-to-surface contact required a noticeable additional computational time and resulted in significant convergence issues. It was therefore decided not to include the flanges of the top channel in the contact interaction. Moreover, penetration of the tip of the top flange of the web channels into the flanges of the top channel was only observed in the FE models of the beams without any intermediate connectors in the constant moment span and only after the beams reached their ultimate moment capacity. Therefore, it did not affect the pre-peak behaviour of the beams.

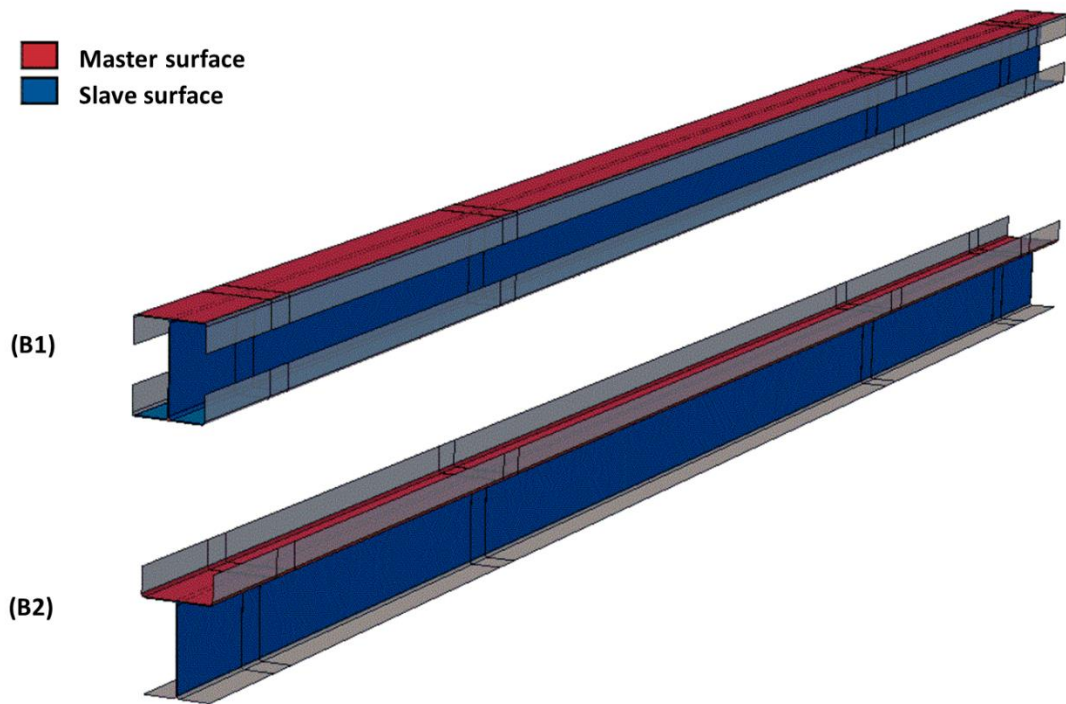


Figure 8.12: Master and slave surfaces in contact interaction

Some penetration of the slave nodes into the master surface was likely to occur between contacting surfaces in the initial analysis stage due to the introduction of the measured out-of-plane imperfections into the FE models. These initial overclosures were resolved at the beginning of the analysis using the strain-free adjustment method. The default search zone for the strain-free adjustment was increased to 2 mm to ensure all the penetrating slave nodes were adjusted. To ensure that the adjusted nodes did not belong to the surface in which the out-of-plane imperfections were introduced, the ‘master’ and ‘slave’ role for the surfaces involved in a contact interaction was manually assigned. The only contact interaction where the nodes of a surface including measured out-of-plane imperfections had to be readjusted occurred in the interaction between the webs of the web channels, as in this case both contacting surfaces included out-of-plane imperfections.

8.2.5 Connector modelling

The bolts used to assemble the components of the built-up beams were modelled using mesh-independent fasteners, which create a point-to-point connection between fastening points on both surfaces, as described in Section 7.2.5 of Chapter 7. The fastening points were connected to the neighbouring nodes on the respective surfaces using a structural coupling method together with the uniform weighting scheme, and defining a physical radius for the fastener of 5 mm.

In between the fastening points PLANAR connector elements were used, which were orientated with their rotational component of relative motion (CRM) normal to the surfaces in contact and

the two translational CRMs tangential to the plane of contact. Elastic and plastic properties, derived from the single lap shear tests carried out on the bolted connections, were assigned to the two translational CRMs of the PLANAR connector. This permitted to include the effects of slip, tilting of the bolts and the bearing deformations in the steel plate into the FE model.

8.2.6 Type of analysis

The analysis of the built-up beams was carried out using the General Static solver available in Abaqus/Standard, with the inclusion of artificial damping to stabilize the solution. This modelling approach was found to be suitable for modelling the response of built-up specimens in which various instabilities and contact discontinuities may result in severe convergence errors. The analyses included geometric and material non-linearity. The time increments in the analysis were automatically adjusted by Abaqus/Standard using the automatic incrementation control algorithm.

8.2.7 Stabilization study

Both the detailed and the simplified FE models presented some convergence issues, which originated mainly as a result of instabilities and contact discontinuity between the components of the built-up geometry. These issues were overcome by employing a similar strategy to the one used to stabilize the stub column models described in Section 7.2.7 of Chapter 7, which consisted in adding artificial damping forces into the model either through the automatic stabilization or the contact stabilization schemes together with adjusting some non-default solution control parameters.

The solution control parameters which were modified included the time incrementation parameters I_0 and I_R , which control the frequency with which Abaqus/Standard checks whether the solution converges monotonically and quadratically. The values of these parameters were increased from 4 and 8 to 8 and 10, respectively. In addition, all simulations were run with the 'line search algorithm' activated. This algorithm helps prevent divergence by applying a scale factor to the displaced configuration of the nodes computed within each iteration of a given time increment. The scale factor is calculated in order to minimize the residual forces at the nodes. A maximum of 40 line search iterations were allowed to calculate the scale factor, while the tolerance for the change of the scale factor between successive iterations was set to 0.001.

The automatic stabilization mechanism is intended to address convergence issues mainly related to geometric and material non-linearity. In this method viscous damping forces are applied to all the nodes of the model with a magnitude proportional to the absolute velocity of each node. The automatic stabilization mechanism can be defined by either directly specifying a damping

factor, or by using the adaptive automatic stabilization scheme in order to minimize the amount of artificial damping introduced into the numerical models. The first option was used in some of the detailed FE models of beam B1, where convergence issues arose during the first increment. In this case, a small step was created during which the beam was only deflected by 1 mm while using a damping factor of 4×10^{-4} . After that, the stabilization scheme was deactivated and the analysis was continued using contact stabilization alone, as explained below. This stabilization scheme is further referred to as ‘Stabilization 1’. The adaptive stabilization scheme was used in some of the simplified FE models of beam B2, where contact interaction between the components of the built-up geometry was not considered. In the adaptive automatic stabilization scheme the amount of damping introduced into the model varies throughout the simulation and can be different for each node of the model. Abaqus/Standard automatically calculates an initial damping factor for the first increment based on the ‘dissipated energy fraction’ (DEF), which is the ratio between the energy dissipated through artificial damping and the total strain energy. This damping factor is adjusted in the subsequent increments based on the convergence history and is limited by an accuracy tolerance (AT). In all the models where the adaptive automatic stabilization scheme was activated, the DEF and the AT were set to 2×10^{-4} and 5×10^{-3} , respectively. This stabilization scheme is further referred to as ‘Stabilization 2’.

Contact stabilization is only meant to address convergence issues due to contact discontinuities and therefore the viscous damping forces are only applied to the nodes of a slave surface in a contact interaction and are made proportional to the relative motion between the surfaces in contact. Contact stabilization was used through the *CONTACT CONTROL keyword while specifying a constant scale factor of 2×10^{-4} on the magnitude of the viscous stresses normal to the surfaces. Since the tangential viscous stresses are likely to absorb significant amount of energy when slip occurs and this was undesirable, no artificial damping was used in the direction tangential to the surfaces. This stabilization scheme is further referred to as ‘Stabilization 3’.

To ensure that the amount of artificial damping introduced into the model is small enough not to affect the accuracy of the solution, Abaqus/Standard recommends checking whether the amount of viscous damping energy (ALLSD) is a small enough fraction of the total strain energy (ALLIE). Figure 8.13 and Figure 8.14 plot the ALLSD/ALLIE ratio against the vertical deflection at mid-span of representative FE models with geometries B1 and B2, which were stabilized using the Stabilization 1 and Stabilization 3 schemes. The vertical dashed line indicates the approximate deflection at which the ultimate load was reached. Figure 8.13 and Figure 8.14 show that ALLSD is several orders of magnitude smaller than ALLIE. For beams B1 the maximum ALLSD/ALLIE ratio is less than 0.6 %, while for beam B2 the ratio is less than 0.2 %. This shows that ALLSD is negligible compared to ALLIE, and that the ultimate

moment capacity of the beams is virtually unaffected by using stabilization schemes Stabilization 2 and Stabilization 3.

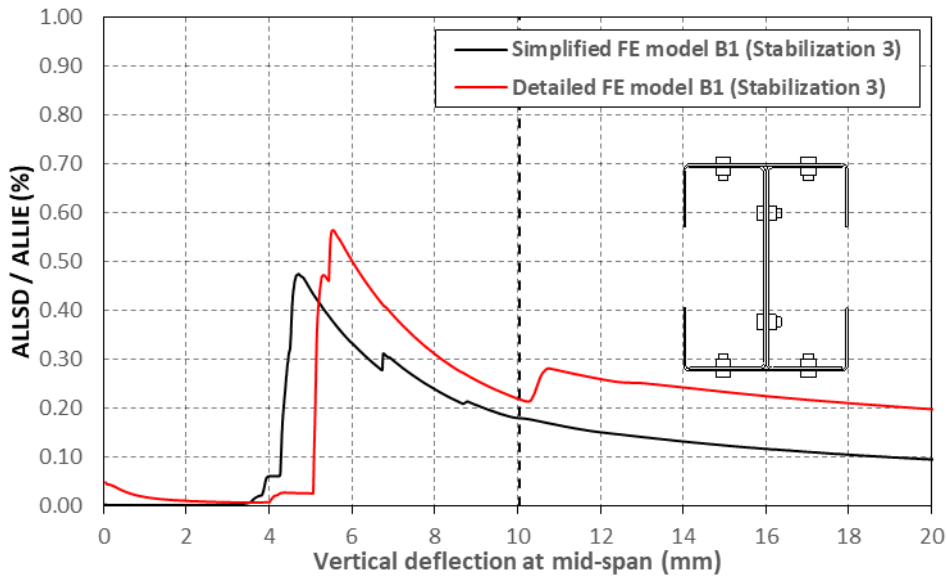


Figure 8.13: Dissipated viscous energy relative to total strain energy using Stabilization 3 in beams B1

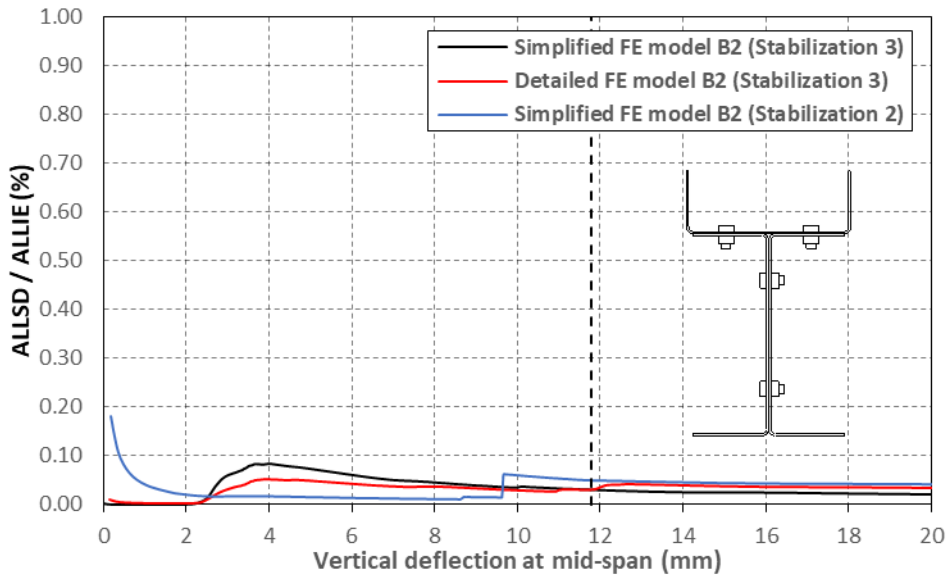


Figure 8.14: Dissipated viscous energy relative to total strain energy using Stabilization 2 and Stabilization 3 in beams B2

To assess the effect of the Stabilization 1 scheme on the detailed FE models of beam B2, Figure 8.15 compares the ALLSD/ALLIE ratio obtained for the same FE model when using Stabilization 1 and Stabilization 3, while Figure 8.16 compares the corresponding moment vs. mid-span deflection curves. When using Stabilization 1, ALLSD was more than twice as large as ALLIE during the first step, during which the automatic stabilization mechanism was used with a constant damping coefficient of 4×10^{-4} . As mentioned above, this step was only created

to get the analysis underway and only lasted until the beam deflected up to 1 mm at the loading points. The effect of the large damping forces introduced during this stabilizing step can be seen in Figure 8.16 near the origin of the moment vs. deflection curve. However, this figure also shows that after the first step was completed, the effect of the artificial damping essentially disappeared. The moment vs. deflection curve obtained when using Stabilization 1 followed the curve obtained when using Stabilization 3 very closely up to the peak. After the first step in Stabilization 1 the artificial damping forces in the model became negligible and the ALLSD/ALLIE ratio decreased exponentially as ALLIE increased, as shown in Figure 8.15 by the black curve. The ultimate moment capacities obtained with Stabilization 1 and Stabilization 3 only differed by about 1 %.

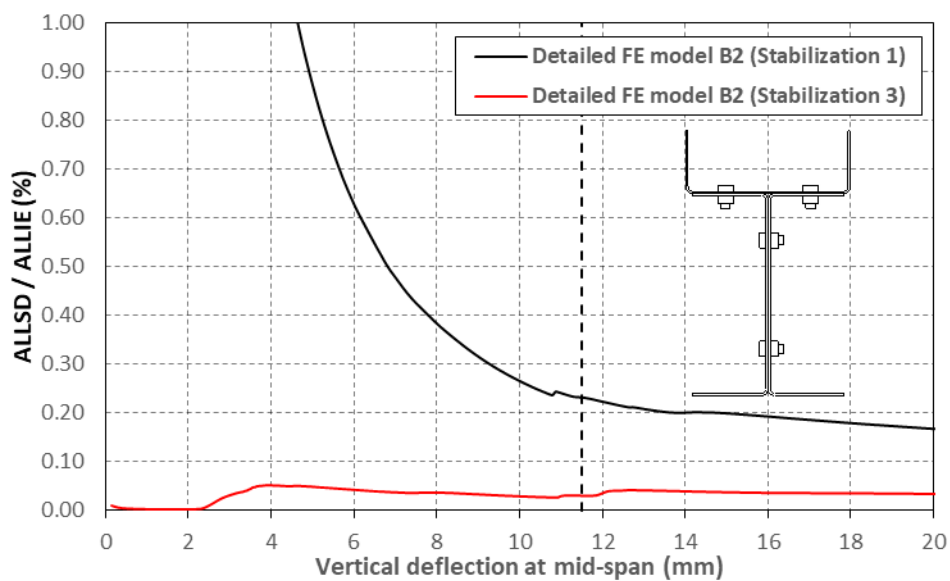


Figure 8.15: Dissipated viscous energy relative to total strain energy using Stabilization 1 and Stabilization 3 in beams B2

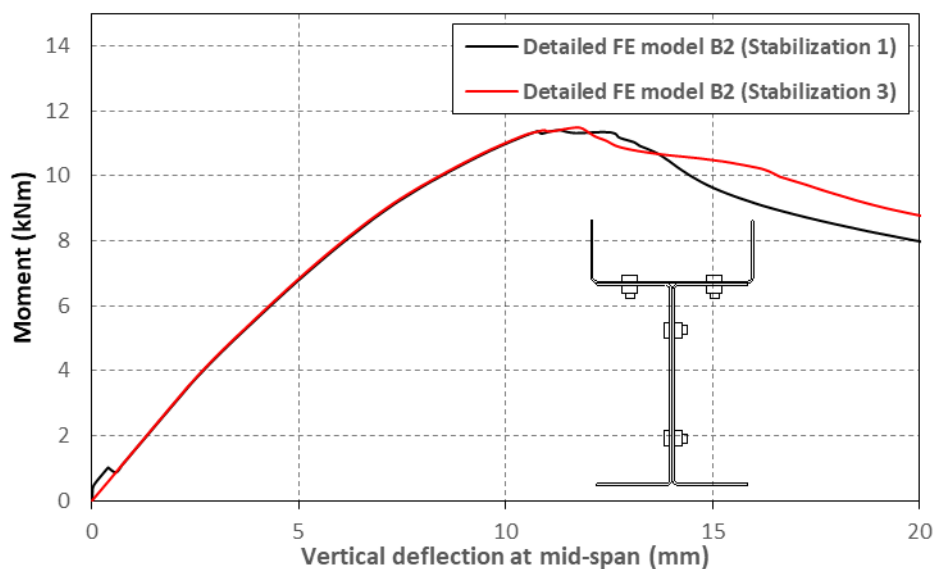


Figure 8.16: Moment-deflection curve using Stabilization 1 and Stabilization 3 in beams B2

8.2.8 Mesh analysis

A suitable mesh configuration was established by carrying out a mesh sensitivity analysis. All FE models were built using S4R elements with five integration points through the shell thickness.

For each built-up geometry a representative beam with three sets of intermediate connectors along the constant moment was chosen for the study. The beams were modelled using the nominal dimensions of the component sections and the FE models included material non-linearity obtained from the results of tensile coupons and the recorded geometric imperfections of a representative test specimen of each geometry. The FE models used for the mesh analysis included contact stabilization with a damping factor of 0.0002 applied to the normal direction of the surfaces, while no contact stabilization was used in the tangential direction. The connectors were modelled using ‘HINGE connectors’, which did not allow slip at the connector points.

In a first step four different uniform mesh densities were studied. The size of the elements in the flanges and the web of the channels was chosen to be as similar as possible, while the number of elements along the length of the beam was determined by limiting the aspect ratio of the elements in the flanges and the web to a maximum of 2, following the recommendations by Schafer (1997). The aspect ratio of the elements contained within the corner regions of the channels was limited to a maximum of 4 in order to avoid an extremely dense mesh. Table 8.2 and Table 8.3 show the total number of elements and nodes used in each mesh for the beams with geometries B1 and B2, respectively, while Table 8.4 lists the maximum aspect ratios in the flat and corner regions of beams with geometries B1 and B2.

Table 8.2: Mesh configurations for built-up beam 1

Mesh	Number of elements							along moment span	Total	Number of nodes
	Flange Channel			Web Channel						
	Flange	Web	Corner	Flange	Web	Corner				
Mesh 1	2	4	2	2	6	2	116	13312	14392	
Mesh 2	4	10	2	4	12	2	116	23552	24672	
Mesh 3	6	14	4	6	18	4	232	74880	77108	
Mesh 4	8	18	4	8	24	4	232	93600	95864	

Table 8.3: Mesh configurations for built-up beam 2

Mesh	Number of elements							along moment span	Total	Number of nodes
	Flange Channel			Web Channel						
	Flange	Web	Corner	Flange	Web	Corner				
Mesh 1	2	4	2	2	6	2	116	10240	11051	
Mesh 2	4	10	2	4	12	2	116	17920	18761	

Mesh 3	6	14	4	6	18	4	232	57200	58873
Mesh 4	8	18	4	8	24	4	232	71760	73461

Table 8.4: Maximum aspect ratios in built-up beams 1 and 2

Mesh	Max. Aspect ratio	
	Flat regions	Corner regions
Mesh 1	1.71	4.00
Mesh 2	1.57	4.00
Mesh 3	1.18	4.00
Mesh 4	1.57	4.00

All simulations for the mesh analysis were run using the University of Sheffield's central High Performance Computing Resource. The most suitable mesh configuration to model the beams with geometries 1 and 2 was determined by comparing the average CPU time required per increment and the ultimate moment capacity obtained with each mesh configuration.

The ultimate load and the total CPU time required to complete the simulations for different mesh densities are listed in Table 8.5 and Table 8.6 for beams B1 and B2, respectively. The tables also show the total number of increments and the average CPU time required to solve each increment.

Table 8.5: Effect of mesh size on the ultimate load and total CPU time for beam B1

Element type	Mesh	Ultimate Moment (kNm)	Total CPU time (s)	Number of increments	CPU time per increment (s)
S4R	Mesh 1	14.45	48555	318	153
	Mesh 2	13.66	45632	276	165
	Mesh 3	13.33	228369	336	680
	Mesh 4	13.30	351507	323	1088
	Mesh 3A	13.27	132004	314	420
	Mesh 3B	13.34	103022	287	359

Table 8.6: Effect of mesh size on the ultimate load and total CPU time for beam B2

Element type	Mesh	Ultimate Moment (kNm)	Total CPU time (s)	Number of increments	CPU time per increment (s)
S4R	Mesh 1	12.93	24921	307	81
	Mesh 2	12.58	19760	188	105
	Mesh 3	12.34	97623	271	360
	Mesh 4	12.27	147359	265	556
	Mesh 3A	12.34	48737	235	207

Figure 8.17 and Figure 8.18 plot the ultimate moment and the CPU time per increment as a function of the number of nodes in each mesh configuration. The figures show that for both beams B1 and B2, Mesh 3 predicted an ultimate moment capacity which differed from the value obtained with the finest mesh considered (Mesh 4) by only 0.24 % and 0.61 %, respectively. However, the computational cost required by these mesh densities was excessively high, especially for the FE model of beam B1. For this reason, additional meshes were considered in which the size of the mesh varied along the length of the beam.

Mesh 3A conserved the density of Mesh 3 in the constant moment span, while having elements with twice the length and width in the shear spans. The transition from the finer mesh in the constant moment span to the coarser mesh in the shear spans was achieved by partitioning narrow strips across the beam next to the loading points, which were meshed with triangular S3 elements, as shown in Figure 8.19 and Figure 8.20 for beams B1 and B2, respectively. This mesh configuration can be justified by the fact that failure was expected to occur within the constant moment span in all FE models. Furthermore, since in beam B1 the bottom channel was mainly subject to tensile stresses and therefore not subject to buckling, an additional mesh (Mesh 3B) was investigated. Mesh 3B was similar to Mesh 3A, however, the entire bottom channel was meshed using the same mesh density as the shear spans, as shown in Figure 8.21.

The results obtained for the additional meshes are also included in Figure 8.17 and Figure 8.18 for beams B1 and B2, respectively. For beam B1, the difference between the ultimate moments predicted by the models with Mesh 3A and Mesh 3 was only 0.45 %, while for beam B2, the model with Mesh 3A predicted virtually the same ultimate moment as the model with Mesh 3. However, the number of nodes in Mesh 3A was around 39 % less than in Mesh 3 for both beams B1 and B2, and the CPU time per increment was reduced by 38 % and 42 % for beams B1 and B2, respectively. For beam B1, the ultimate moment predicted by the FE model with Mesh 3B was almost the same as that predicted by the model with Mesh 3. Mesh 3B resulted in a 0.29 % difference with respect to the prediction given by the model with the finest mesh, as opposed to the 0.24 % difference obtained with Mesh 3. Both the CPU time per increment and the number of nodes in the model with Mesh 3B were reduced by around 47 % with respect to the model with Mesh 3. It was therefore decided to use Mesh 3B for modelling beams B1 and Mesh 3A for modelling beams B2.

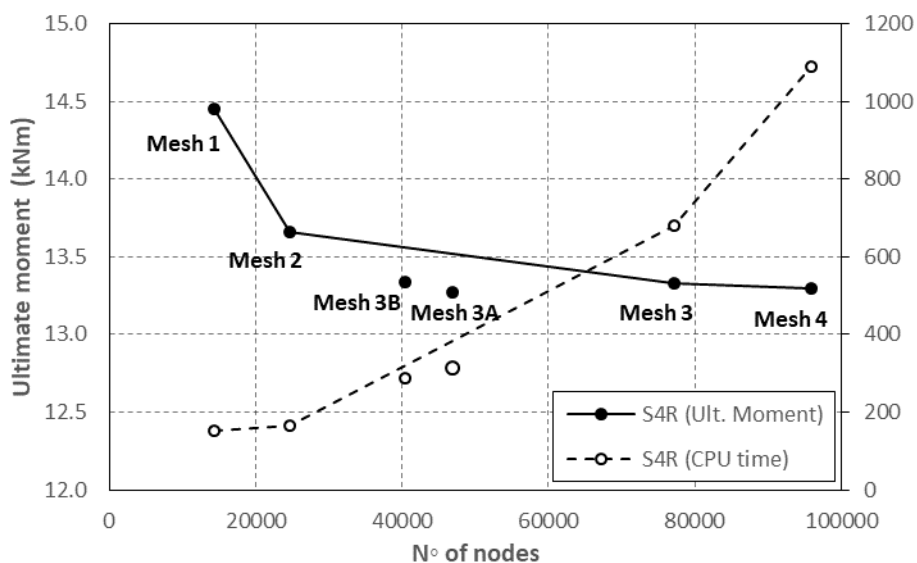


Figure 8.17: Effect of mesh size on the ultimate moment and total CPU time for beam B1

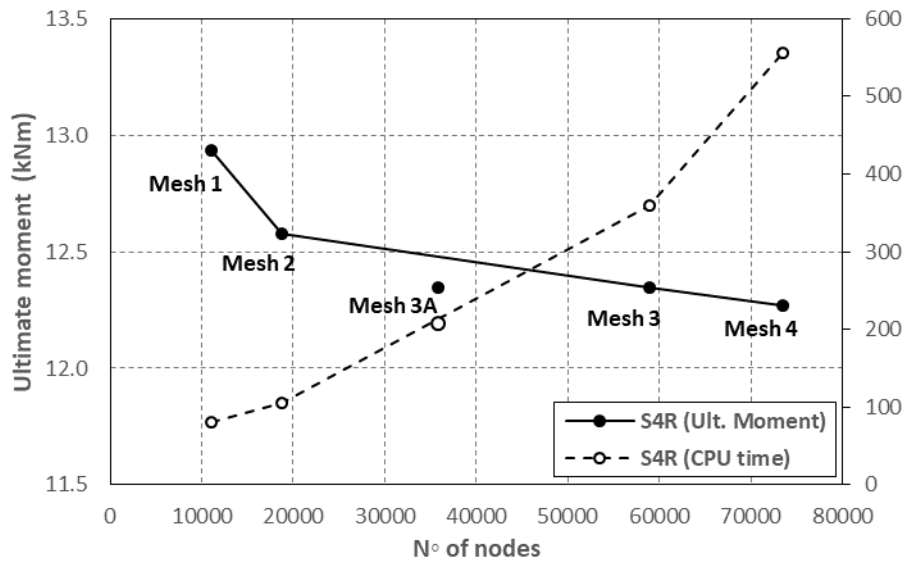


Figure 8.18: Effect of mesh size on the ultimate moment and total CPU time for beam B2

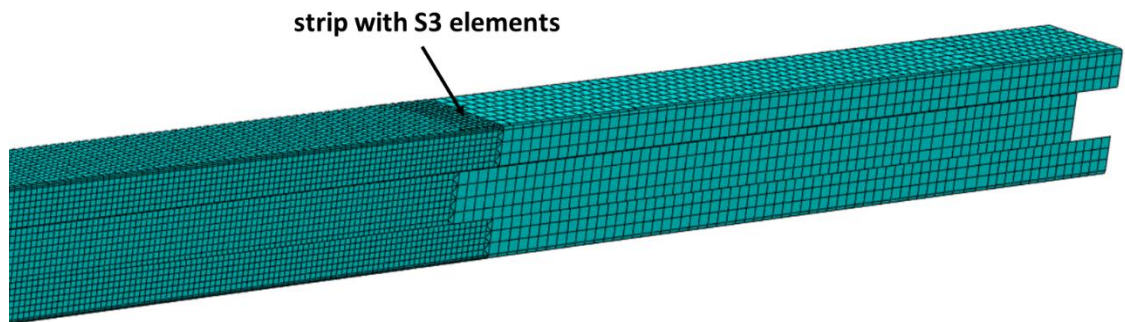


Figure 8.19: Mesh 3A configuration in beam B1

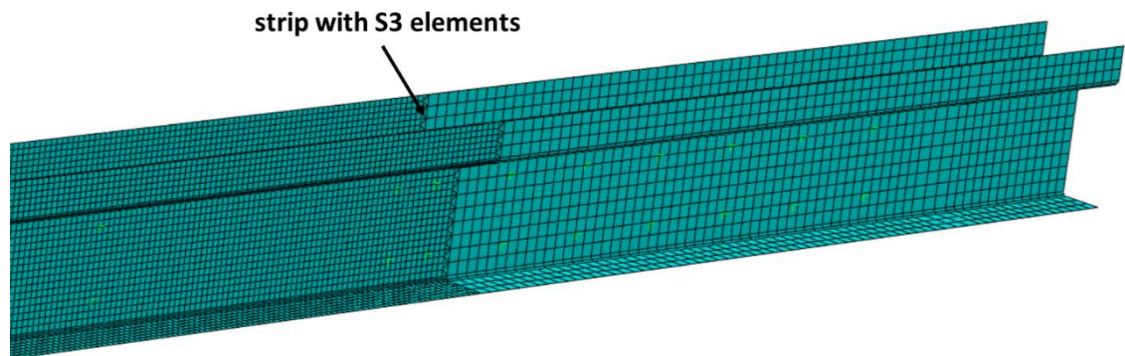


Figure 8.20: Mesh 3A configuration in beam B2

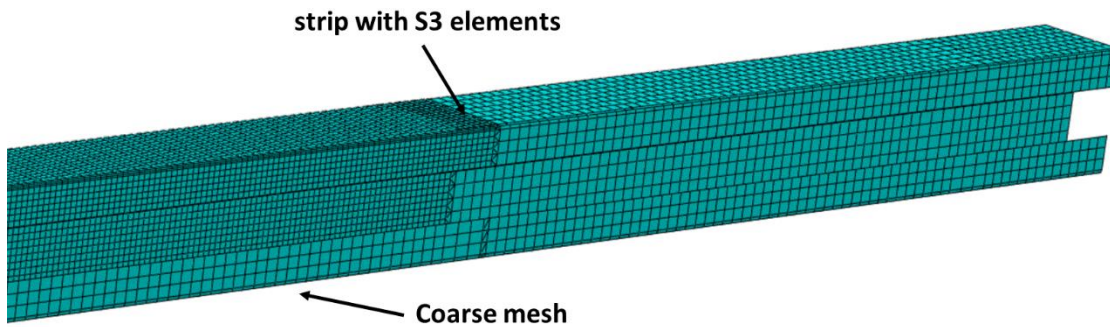


Figure 8.21: Mesh 3B configuration in beam B1

8.3. Detailed FE model: verification

8.3.1 Ultimate moment capacity

The ultimate capacities obtained from the detailed FE models are compared against the experimental results in Table 8.7 and Table 8.8 for the beams with geometry B1 and B2, respectively. The tables also include the stabilization settings used to help Abaqus/Standard achieve a converging solution. The tables show that the detailed FE models were able to provide a reasonable prediction of the ultimate capacity of the built-up beams, with an average error of 3.98 % and 6.85 % for beams B1 and B2, respectively. It is worth pointing out that for beams B2 the FE models predicted similar ultimate capacities in the beams with 2 and 3 intermediate rows of connectors along the constant moment span (less than 2 % difference), as opposed to the results obtained from the experiments, which showed an average increase of 11 % in the ultimate capacity of beams B2-3 with respect to beams B2-2.

The moment vs. mid-span deflection curves obtained from the detailed FE models and from the experiments are plotted in Figure 8.22 and Figure 8.23 for beams B1 and B2, respectively.

Table 8.7: Ultimate moment capacity obtained from tests and detailed FE models for beams B1

Specimen	Test ult. moment (kNm)	FEA ult. moment (kNm)	FEA/Test	Contact control	Automatic stabilization	
					DEF	AT
B1-0b	11.837	11.701	0.988	2×10^{-4}	-	-
B1-2a	12.509	12.783	1.022	2×10^{-4}	-	-
B1-2b	11.830	13.102	1.108	2×10^{-4}	-	-
B1-3a	13.282	12.849	0.967	2×10^{-4}	-	-
B1-3b	13.007	12.675	0.974	2×10^{-4}	-	-
Avg.			1.012			
St. dev.			0.057			

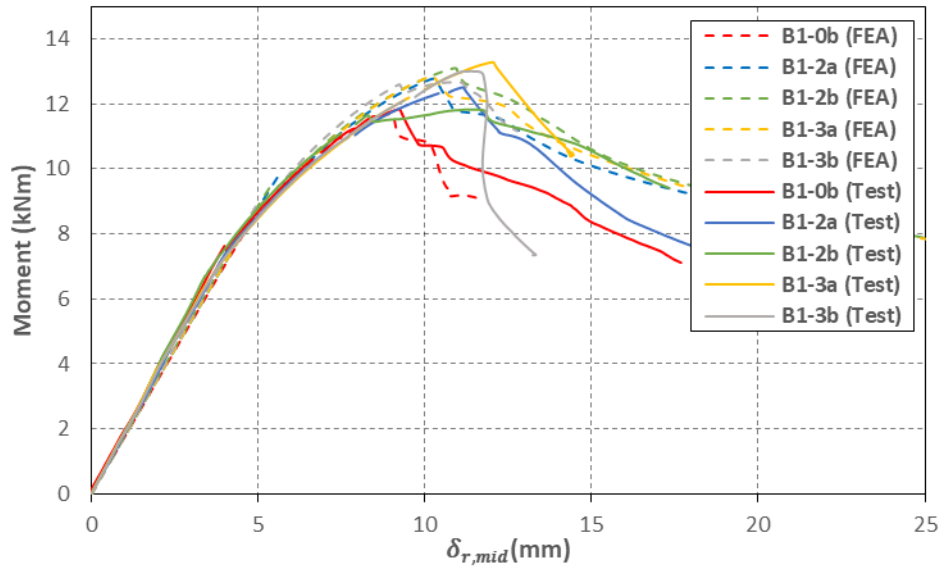


Figure 8.22: Moment vs. mid-span deflection curve obtained from tests and detailed FE models for beams B1

Table 8.8: Ultimate moment capacity obtained from tests and detailed FE models for beams B2

Specimen	Test ult. moment (kNm)	FEA ult. moment (kNm)	FEA/Test	Contact control	Automatic stabilization	
					DEF	AT
B2-0a	9.077	9.526	1.049	2×10^{-4}	-	-
B2-0b	8.190	9.630	1.176	2×10^{-4}	-	-
B2-2a	10.413	11.366	1.092	2×10^{-4}	-	-
B2-2b	10.645	11.306	1.062	2×10^{-4}	-	-
B2-3a	11.658	11.510	0.987	2×10^{-4}	-	-
B2-3b	11.740	11.513	0.981	2×10^{-4}	-	-
Avg.			1.058			
St. dev.			0.072			

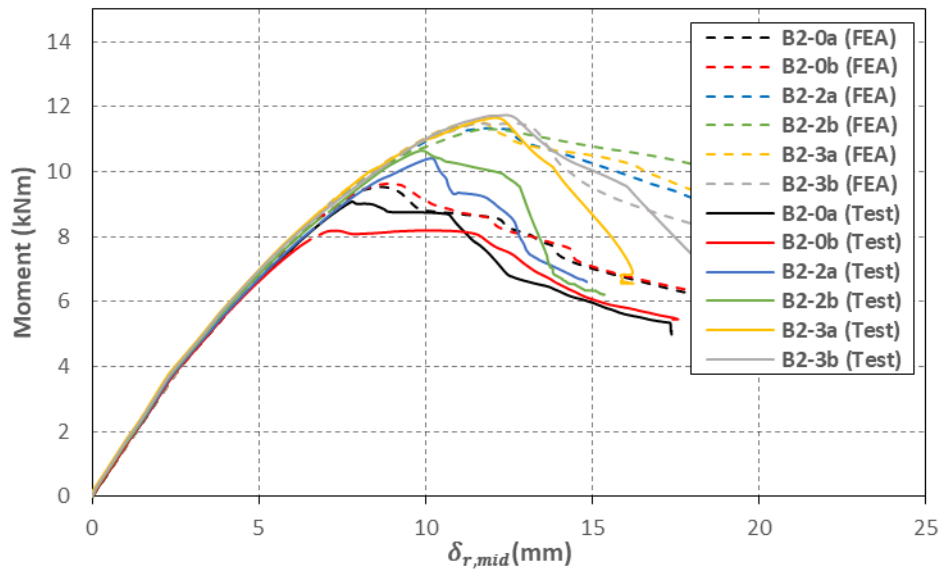


Figure 8.23: Moment vs. mid-span deflection curve obtained from tests and detailed FE models for beams B2

8.3.2 Deformed shape

The FE models were able to accurately replicate the deformations, including the initial buckled shape, and the failure mode of the tested beams. As examples, Figure 8.24, Figure 8.26 and Figure 8.27 compare the deformed shapes obtained from the FE models with those observed during the test (before and after the peak load) for beams B1-0b, B1-2b and B1-3b, respectively, while Figure 8.28, Figure 8.29 and Figure 8.30 do the same for beams B2-0b, B2-2b and B2-3b, respectively. In the figures, the deformed shapes obtained from the FE models before the peak load was reached is amplified for clarity.

For beam B1-0b, although the experiment showed that the beam failed purely by local buckling, the deformed shape obtained from the FE model after the peak load showed that the top channel experienced some flexural-torsional buckling, as shown in Figure 8.24b. However, the moment vs. deflection curves obtained from the FE model and the experimental test were almost identical, as shown in Figure 8.22, with a difference in the ultimate moment capacity of only 1.16 %. Close examination of the failure mode of the FE model revealed that failure originated in the top flanges of the web channels, as a result of local buckling (see Figure 8.25), and that flexural-torsional buckling of the top channel only occurred after the beam reached its ultimate moment capacity.

In general, a fairly good agreement was also achieved between the yield line mechanisms predicted by the FE models and those observed in the tested beams. However, the plastic mechanism predicted by the FE models often developed in a different location along the constant moment span.

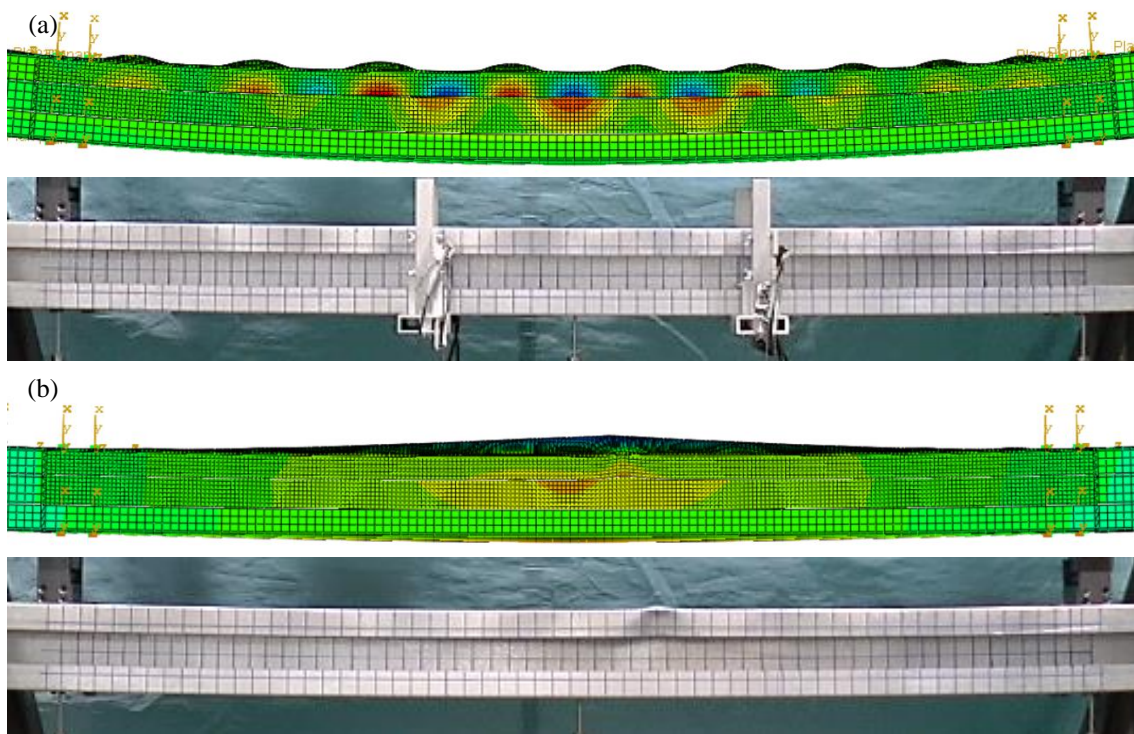


Figure 8.24: Deformed shape of B1-0b: a) before peak load (amplified); b) after peak load

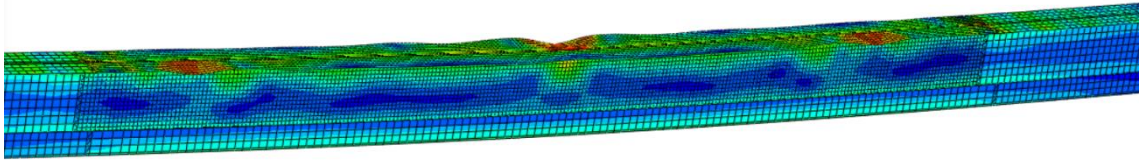


Figure 8.25: Deformed shape of the web channels of B1-0b at the peak load

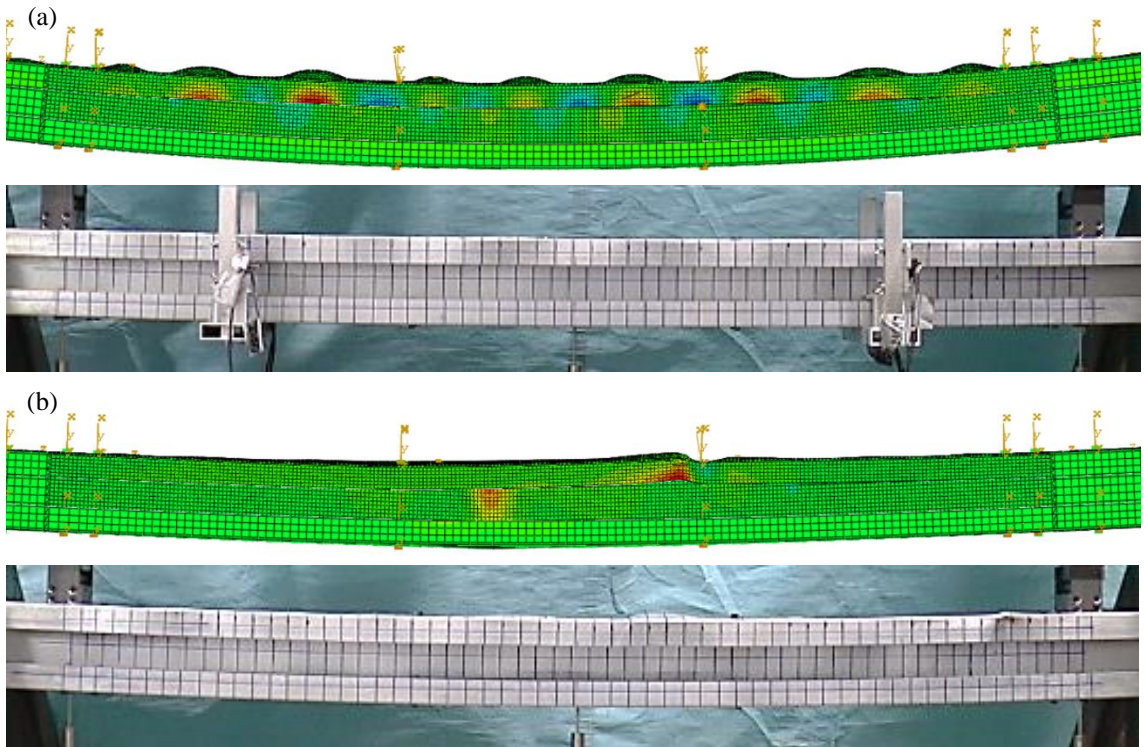


Figure 8.26: Deformed shape of B1-2b: a) before peak load (amplified); b) after peak load

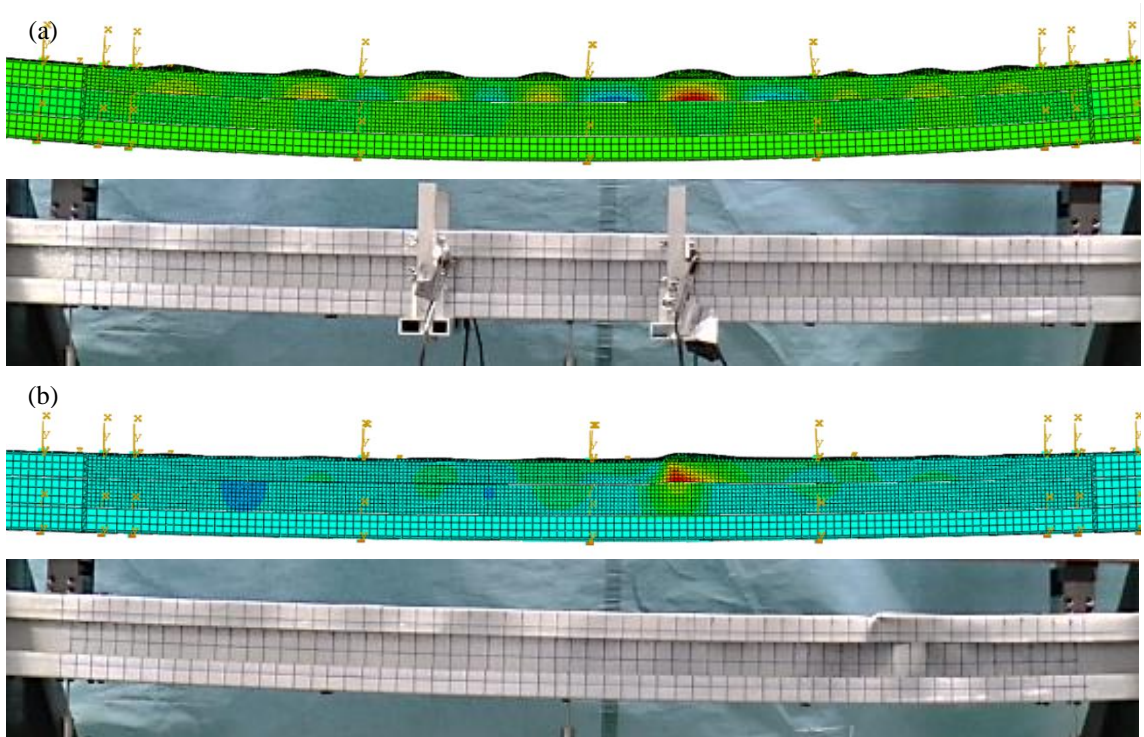


Figure 8.27: Deformed shape of B1-0b: a) before peak load (amplified); b) after peak load

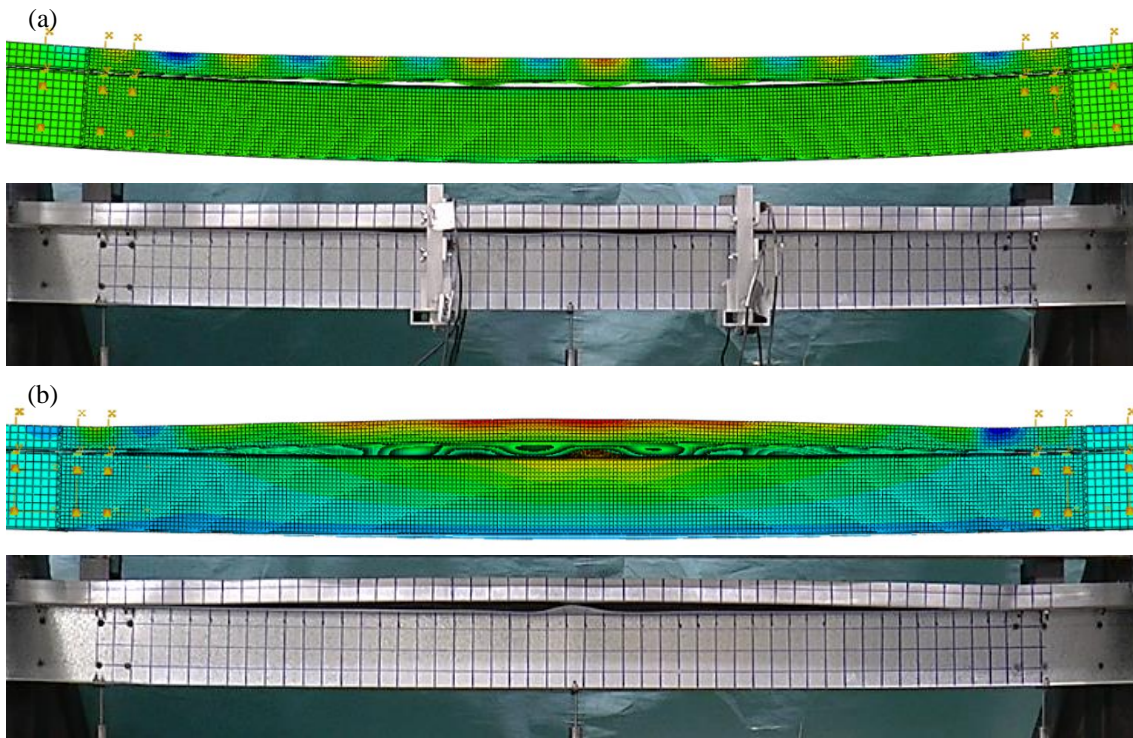


Figure 8.28: Deformed shape of B2-0b: a) before peak load (amplified); b) after peak load

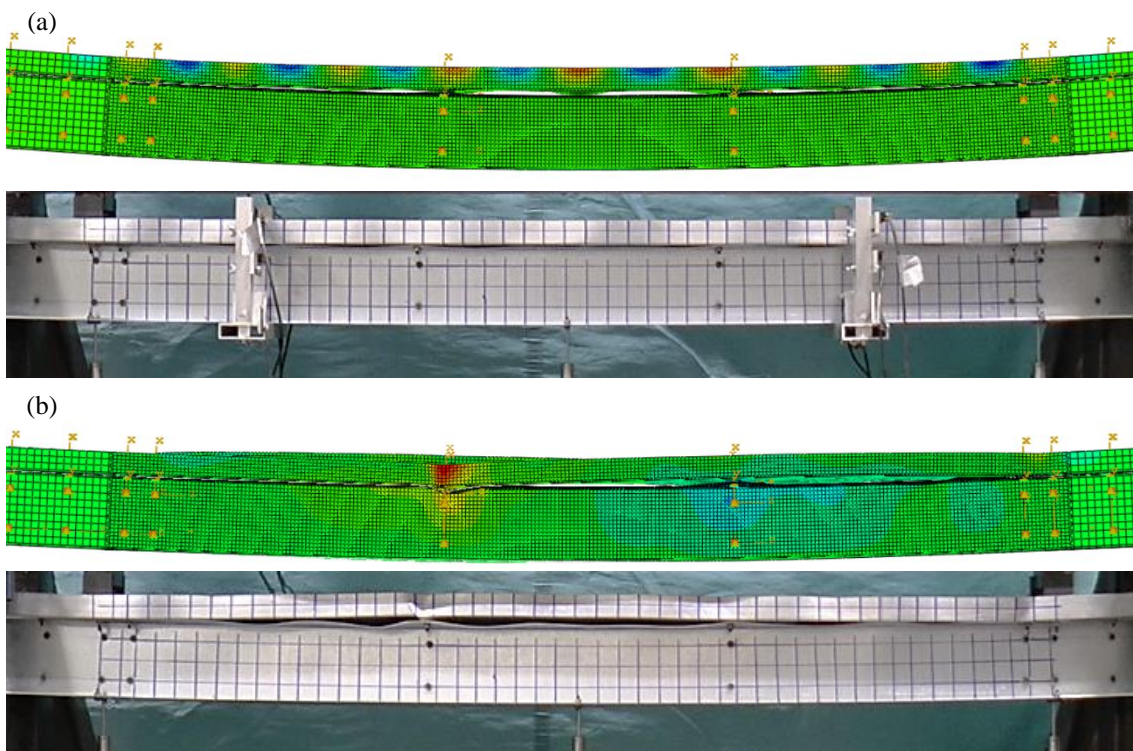


Figure 8.29: Deformed shape of B2-2b: a) before peak load (amplified); b) after peak load

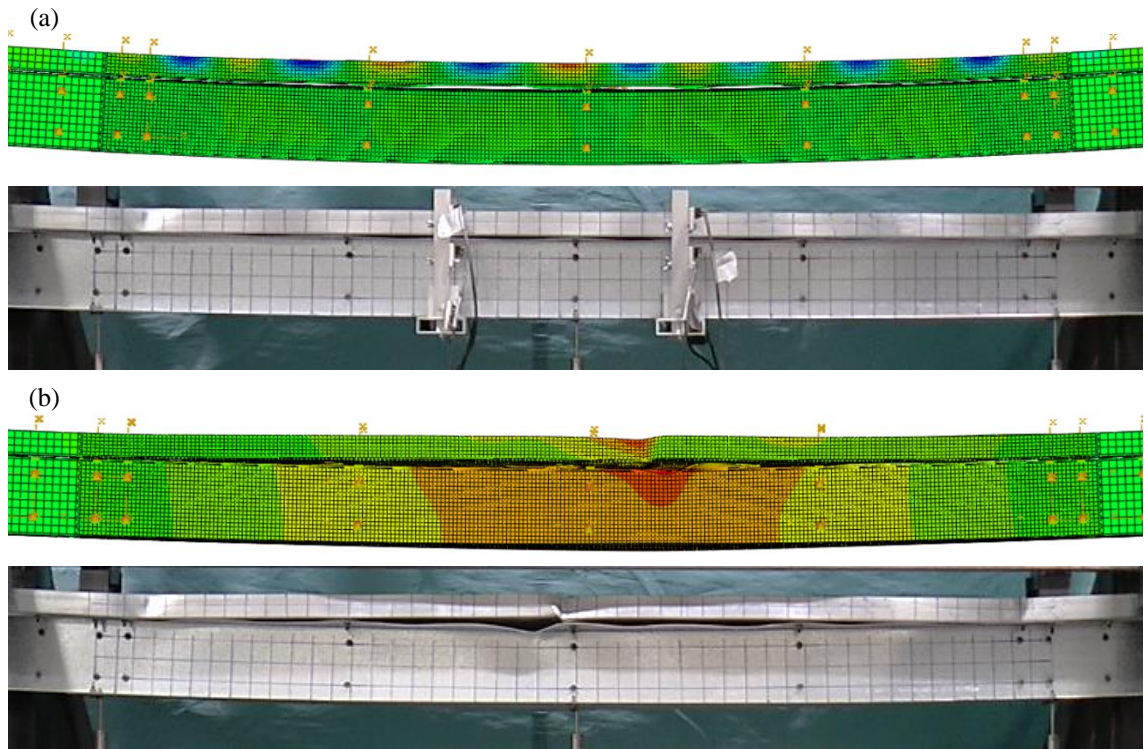


Figure 8.30: Deformed shape of B2-3b: a) before peak load (amplified); b) after peak load

8.3.3 Critical buckling stresses

The out-of-plane deformations of the channel components of beams B1 and B2 due to local buckling were experimentally recorded with eight potentiometers mounted on two identical yokes located within the constant moment span, as shown in Figures 8.24-8.30. These out-of-plane deformations were also extracted from the FE models at the same locations. A comparison between the out-of-plane deformations obtained experimentally and predicted by the FE models is shown in Figure 8.31 and Figure 8.32 for two representative beams with geometry B1, and in Figure 8.33 and Figure 8.34 for two representative beams with geometry B2. In all figures the out-of-plane deformations are plotted against the total load applied to the beam. Curves comparing the numerical and experimental out-of-plane deformations for each tested beam are included in Appendix M.

The load vs. out-of-plane displacement curves were used to calculate the experimental and numerical critical buckling stresses of the top channel of each tested beam, using the same assumptions as previously described in Section 4.8.2 of Chapter 4. The critical buckling stresses obtained from the tests and the respective FE models are reported in Table 8.9 and Table 8.10 for beams B1 and B2, respectively.

For beams B1, Table 8.9 shows that the critical buckling stresses obtained from the FE models are consistently larger than the experimentally derived ones, with an average difference of around 30 %. This difference is also evident in Figure 8.31 and Figure 8.32 for the two

representative beams. It is worth pointing out that despite the noticeable difference between the numerical and experimental critical buckling stresses, the ultimate moment capacity obtained from the FE models and the tests show a fairly good agreement for all beams with geometry B1.

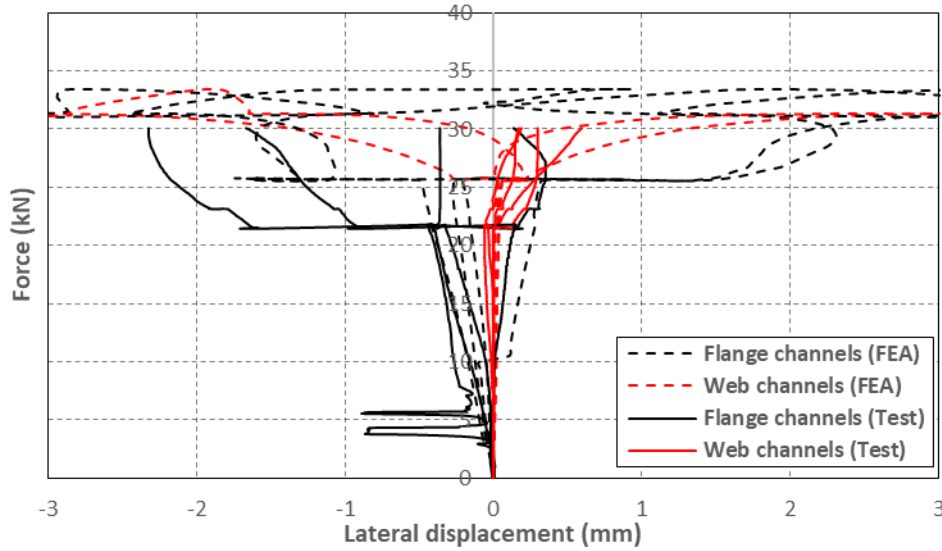


Figure 8.31: Axial load vs lateral displacements curve of B1-0b obtained from the test and the detailed FE model

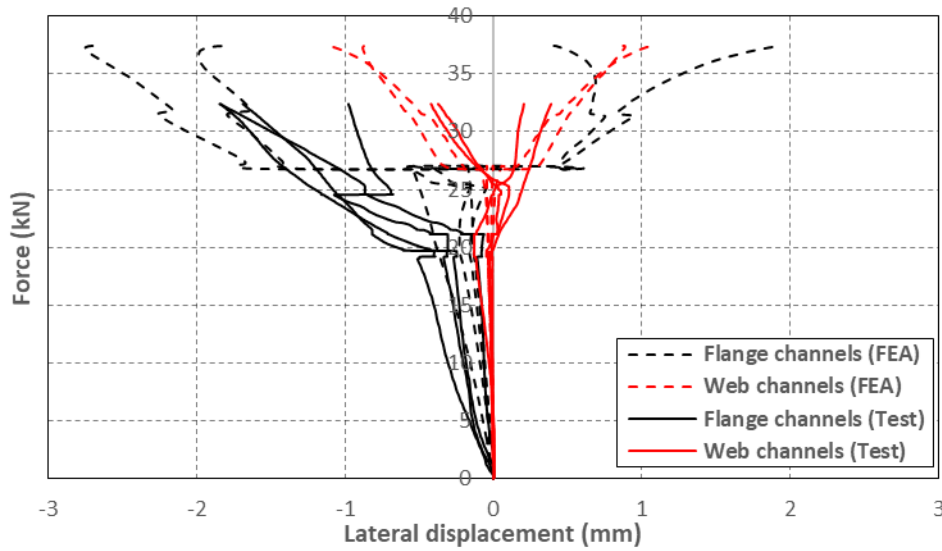


Figure 8.32: Axial load vs lateral displacements curve of B1-2b obtained from the test and the detailed FE model

Table 8.9: Buckling stresses of the top channel of beams B1 obtained from the tests and the detailed FE models

Specimen	Component section	Buckling stress from test (MPa)	Buckling stress from FEA (MPa)
B1-0b	T10412-3	170	203
B1-2a	T10412-5	170	220
B1-2b	T10412-7	154-166	211
B1-3a	T10412-9	142	162
B1-3b	T10412-11	126-134	201

For beams B2, the critical buckling stresses of the top channel obtained from the FE models were slightly larger than those obtained from the tests. However, in this case the agreement was considerably better than for beams B1, with an average difference between the numerical and experimental buckling stresses of around 7 %. This good agreement is also revealed in Figure 8.33 and Figure 8.34, which show how the out-of-plane deformations of the top channel obtained from the FE model follow the deformations recorded by the potentiometers almost perfectly.

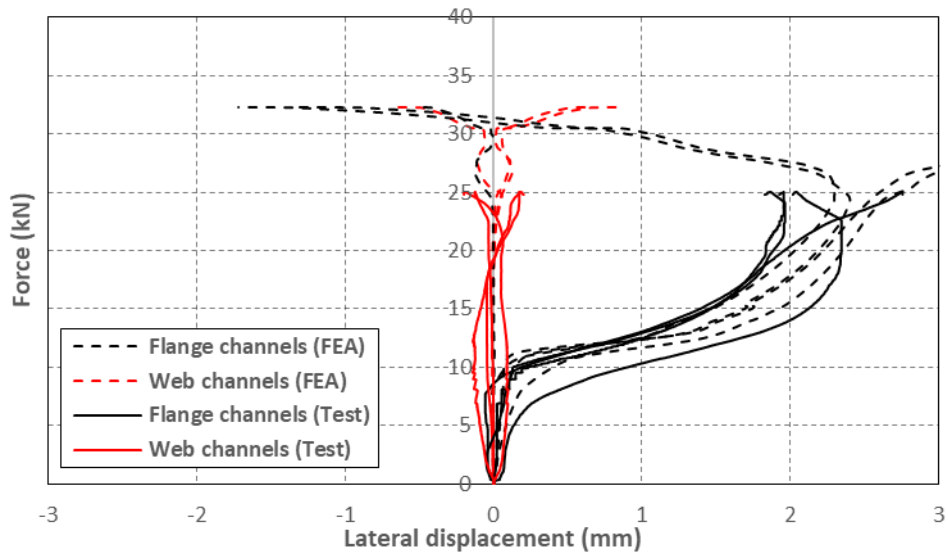


Figure 8.33: Axial load vs lateral displacements curve of B2-2b obtained from the test and the detailed FE model

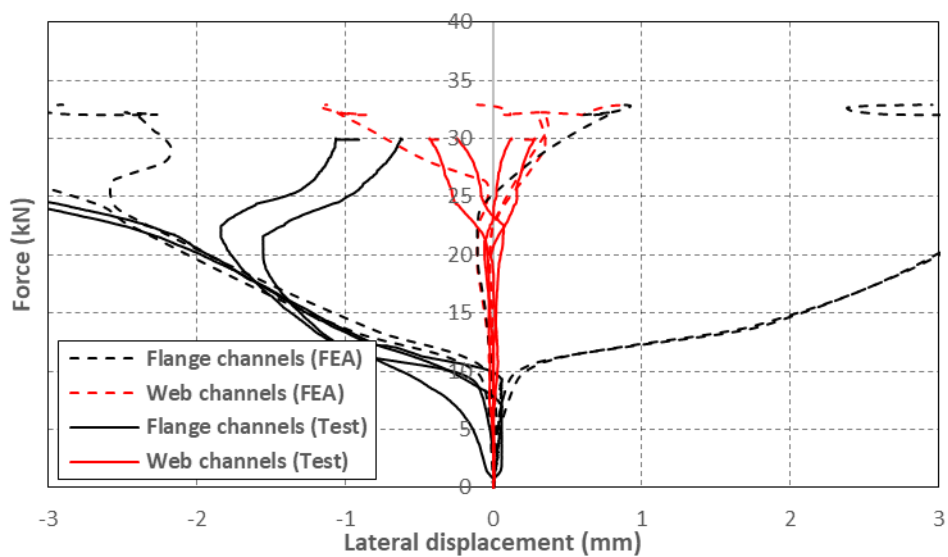


Figure 8.34: Axial load vs lateral displacements curve of B2-3b obtained from the test and the detailed FE model

Table 8.10: Buckling stresses of the top channel of beams B2 obtained from the tests and the detailed FE models

Specimen	Component section	Buckling stress from test (MPa)	Buckling stress from FEA (MPa)
B2-0a	T10412-1	127	147
B2-0b	T10412-2	120-142	138
B2-2a	T10412-3	133-152	152
B2-2b	T10412-4	121-136	140
B2-3a	T10412-5	133	133
B2-3b	T10412-6	128	139

8.4. Simplified FE model: verification

8.4.1 Ultimate moment capacity

The simplified FE models were able to accurately replicate the buckling behaviour of the tested beams. Table 8.11 and Table 8.12 compare the ultimate moment capacities obtained from the simplified models against the experimental results for the beams with geometry B1 and B2, respectively. For beams B1, the average error in the ultimate moment predictions was 3.99 %, which is virtually the same error as obtained with the detailed FE models, while for beams B2 this value was 7.67 %, which is slightly larger than the average error of 6.85 % obtained with the detailed FE models. As with the detailed FE models, the simplified FE models predicted very similar ultimate moment capacities in beams B2 with 2 and 3 intermediate rows of connectors along the constant moment span, which differed from the experimental observations. The moment vs. vertical deflection curves obtained from the simplified FE models, as well as those measured in the experiment are plotted in Figure 8.35 and Figure 8.36 for beams B1 and B2, respectively.

Table 8.11: Ultimate moment capacity obtained from tests and simplified FE models for beams B1

Specimen	Test ult. moment (kNm)	FEA ult. moment (kNm)	FEA/Test	Contact control	Automatic stabilization	
					DEF	AT
B1-0b	11.837	11.996	1.013	2×10^{-4}	-	-
B1-2a	12.509	12.814	1.024	2×10^{-4}	-	-
B1-2b	11.830	12.916	1.092	2×10^{-4}	-	-
B1-3a	13.282	12.600	0.949	2×10^{-4}	-	-
B1-3b	13.007	12.731	0.979	2×10^{-4}	-	-
Avg.			1.011			
St. dev.			0.054			

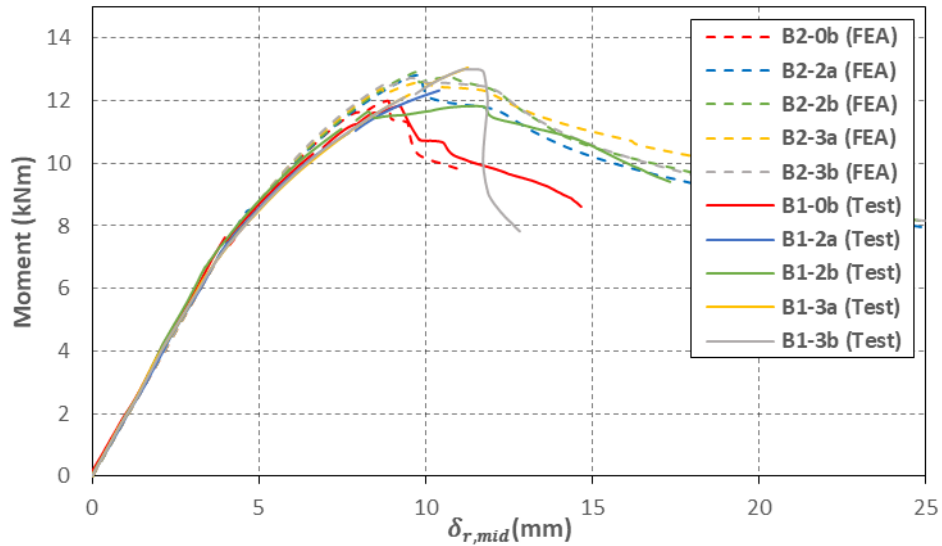


Figure 8.35: Moment vs. mid-span deflection curve obtained from tests and simplified FE models for beams B1

Table 8.12: Ultimate moment capacity obtained from tests and simplified FE models for beams B2

Specimen	Test ult. moment (kNm)	FEA ult. moment (kNm)	FEA/Test	Contact control	Automatic stabilization	
					DEF	AT
B2-0a	9.077	9.705	1.069	2×10^{-4}	-	-
B2-0b	8.190	9.647	1.178	2×10^{-4}	-	-
B2-2a	10.413	11.545	1.109	2×10^{-4}	-	-
B2-2b	10.645	11.678	1.097	2×10^{-4}	-	-
B2-3a	11.658	11.660	1.000	2×10^{-4}	-	-
B2-3b	11.740	12.148	1.035	2×10^{-4}	-	-
Avg.			1.081			
St. dev.			0.062			

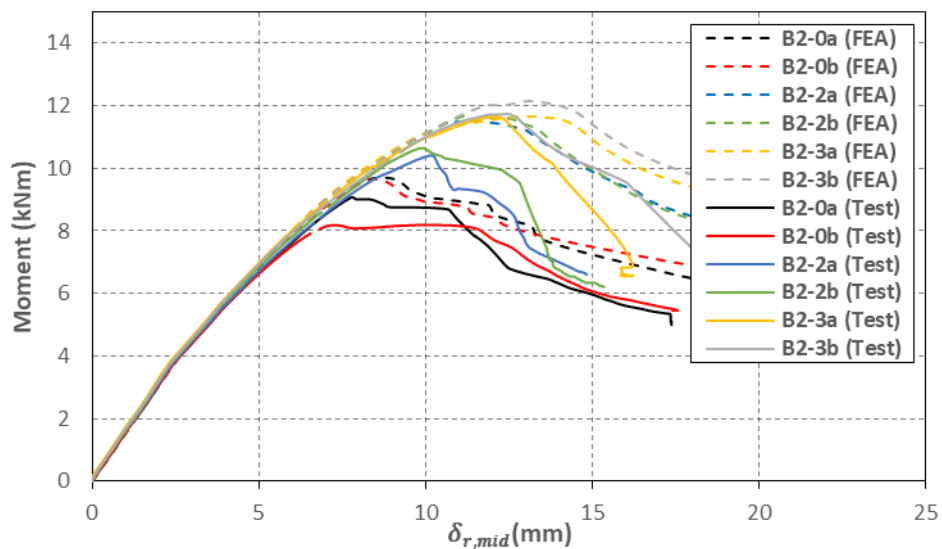


Figure 8.36: Moment vs. mid-span deflection curve obtained from tests and simplified FE models for beams B2

8.4.2 Deformed shape and critical buckling stresses

The simplified FE models were able to predict deformed shapes and failure modes for beams B1 and B2 similar to those predicted by the detailed FE models. In addition, for beams B1 the out-of-plane deformations in the simplified FE models were in better agreement with those recorded in the tested beams than in the detailed FE models. Figure 8.41 and Figure 8.42 compare the out-of-plane deformations obtained from the simplified FE models with those obtained experimentally for the components of beams B1-0b and B1-2b, respectively. A comparison involving the predictions obtained from the detailed FE models of the same beams was previously presented in Figure 8.31 and Figure 8.32. For beams B2, the out-of-plane deformations predicted by the simplified FE models were very similar to those predicted by the detailed FE models. For example, Figure 8.39 and Figure 8.40 compare the experimental out-of-plane deformations with those predicted by the simplified FE models for beams B2-2b and B2-3b, respectively. The deformations of the same beams were previously compared to the predictions of the detailed FE models in Figure 8.33 and Figure 8.34. Figures comparing the experimental out-of-plane deformations with those predicted by the simplified FE models are included in Appendix M for each tested beam.

The critical buckling stresses of the top channel of beams B1 and B2 derived from the simplified FE models are listed in Table 8.13 and Table 8.14, respectively. For beams B1 the agreement between the numerical and the experimental critical buckling stresses was better in the simplified FE models than in the detailed FE models, with an average difference in the former of 9 % (compared to around 30 % difference in the latter). For beams B2, the critical buckling stresses derived from the simplified and detailed FE models were virtually the same, with an average difference with respect to the experimentally derived ones of around 7 %.

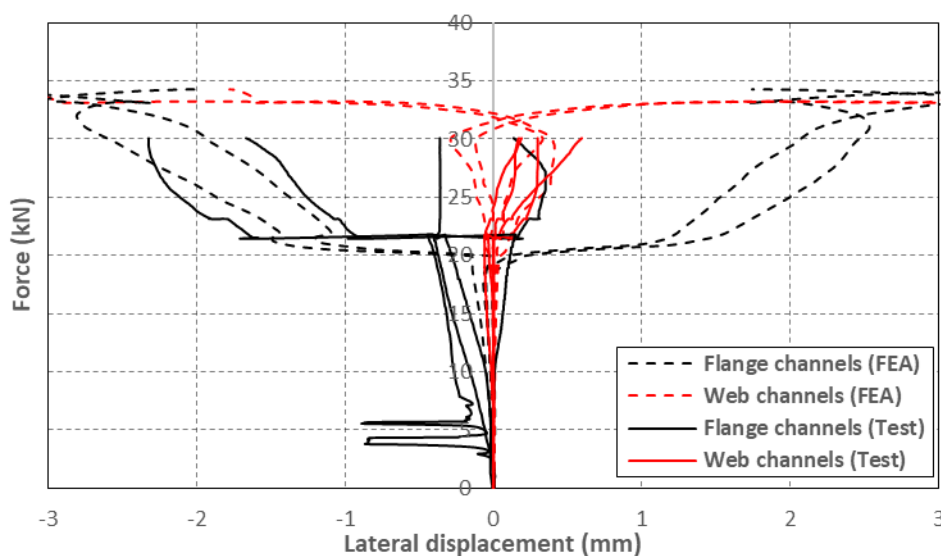


Figure 8.37: Axial load vs lateral displacements of B1-0b obtained from the tests and the simplified FE models

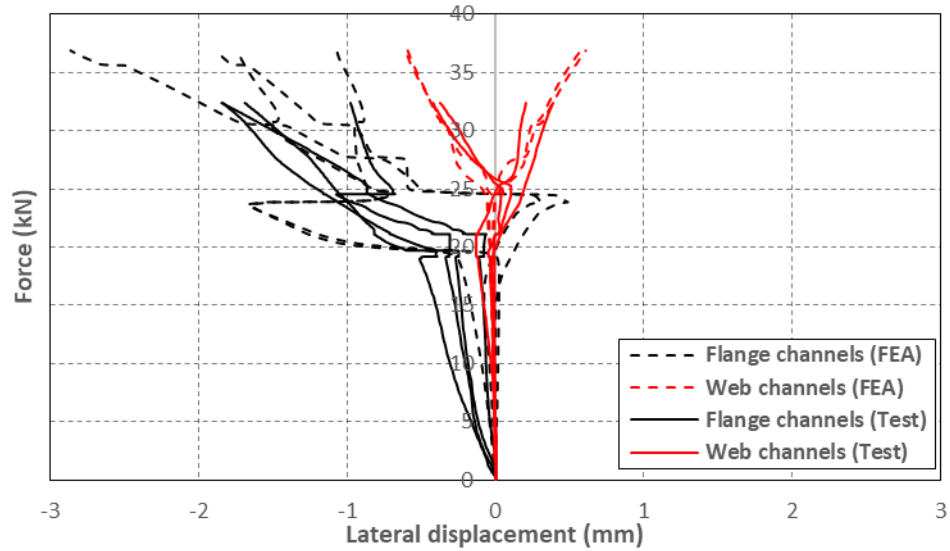


Figure 8.38: Axial load vs lateral displacements of B1-2b obtained from the tests and the simplified FE models

Table 8.13: Buckling stresses of the top channel of beams B1 obtained from the tests and the simplified FE models

Specimen	Component section	Buckling stress from test (MPa)	Buckling stress from FEA (MPa)
B1-0b	T10412-3	170	161
B1-2a	T10412-5	170	155-169
B1-2b	T10412-7	154-166	156-189
B1-3a	T10412-9	142	146
B1-3b	T10412-11	126-134	160

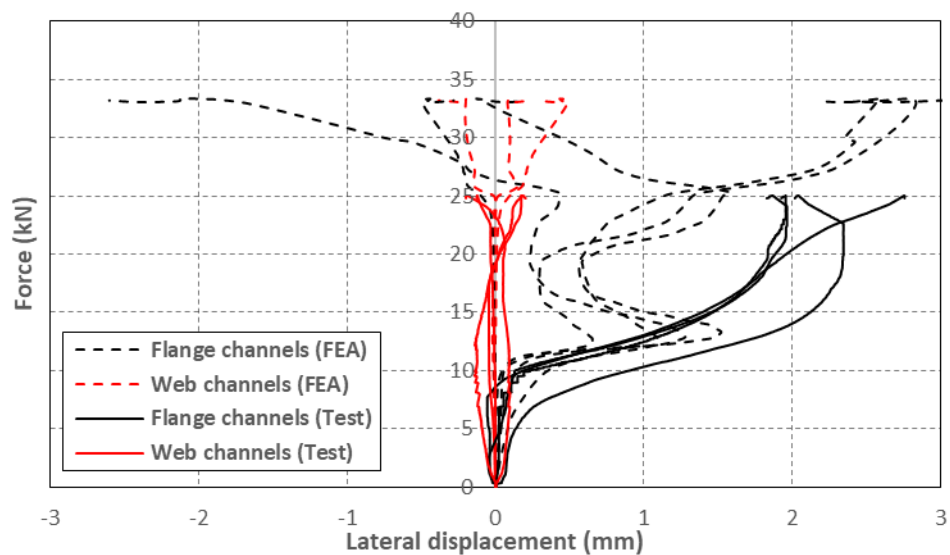


Figure 8.39: Axial load vs lateral displacements of B2-2b obtained from the tests and the simplified FE models

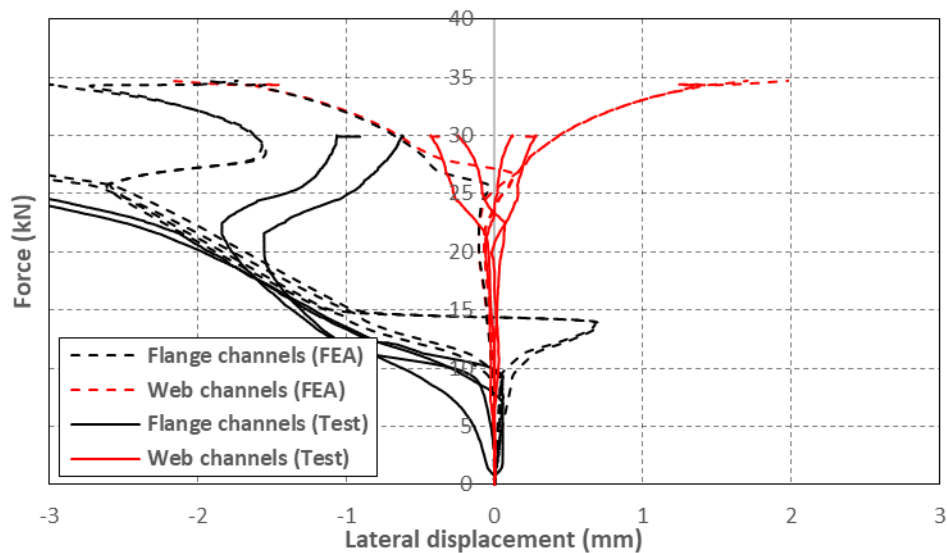


Figure 8.40: Axial load vs lateral displacements of B2-3b obtained from the tests and the simplified FE models

Table 8.14: buckling stresses of the top channel of beams B2 obtained from the tests and the simplified FE models

Specimen	Component section	Buckling stress from test (MPa)	Buckling stress from FEA (MPa)
B2-0a	T10412-1	127	147
B2-0b	T10412-2	120-142	138
B2-2a	T10412-3	133-152	152
B2-2b	T10412-4	121-136	140
B2-3a	T10412-5	133	133
B2-3b	T10412-6	128	139

8.5. Parametric study

8.5.1 Effect of fastener modelling

The simplified FE models were used to study the effect of the connector behaviour on the buckling behaviour and ultimate capacity of CFS built-up beams. To this end additional FE models were created in which the behaviour of the connectors was modelled using three different approaches. The ultimate moment capacities obtained with each modelling approach were then compared with the predictions given by the validated FE models.

The simplest approach to model the connectors consists of using BEAM multi-point constraints (MPCs). This approach has the advantage of reducing the size of the model. However, since BEAM MPCs eliminate the degrees of freedom of one of the fastening nodes at the connecting points, they have the disadvantage that it is not possible to obtain output from the connectors

(for instance with respect to their internal forces). Moreover, they cannot be used to model more complex connector behaviour such as slip or bearing deformations of the connecting plates.

The other two approaches which were considered consisted of using connector elements to model the fasteners, namely HINGE and PLANAR connectors. In the FE model with HINGE connector elements all CRMs (Components of Relative Motion) between the surfaces were constrained, apart from the rotational component about the normal to the fastened surfaces, while in the FE models with PLANAR connector elements all CRMs were constrained apart from the rotation about the normal to the surfaces and the translational CRMs tangential to the surfaces. This last modelling approach was similar to the approach used to model the fasteners in the validated model. However, in this case neither elastic nor plastic behaviour was added to the tangential CRMs, allowing the fastened surfaces to freely slide relative to each other. Therefore, the 'HINGE' and 'PLANAR' models can be seen as idealized extreme opposites in terms of the surface sliding behaviour.

The ultimate moment capacities obtained from the FE models incorporating HINGE, PLANAR and MPC approaches, normalized against the predictions given by the validated FE models, are shown in Figure 8.41 for beams B1 and B2 with 2 and 3 intermediate rows of connectors along the constant moment span.

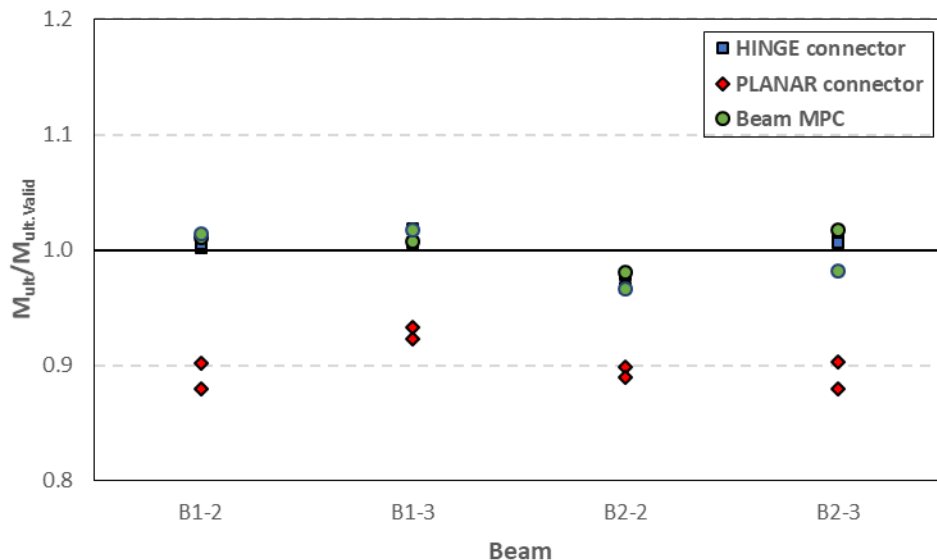


Figure 8.41: Ultimate moment comparison for different connector modelling approaches

Figure 8.41 shows that the HINGE and MPC models predict virtually identical ultimate moment capacities for both built-up geometries and that these predictions are very similar to those given by the validated FE models, with an average difference of 1 % for beams B1 and 2 % for beams B2. This can be attributed to the fact that the connectors were not subject to large shear forces because the simplified FE models were subject to a constant moment. Consequently, shear

forces in the connectors only originated as a result of local buckling of the components of the built-up geometry. These shear forces were smaller than the slip force of around 3 kN obtained from the single lap shear tests on the bolted connectors, as illustrated in Figure 8.42a and Figure 8.42b for representative beams with geometries B1 and B2. Therefore, the relative motion of the surfaces at the connector points in the validated FE models was negligible.

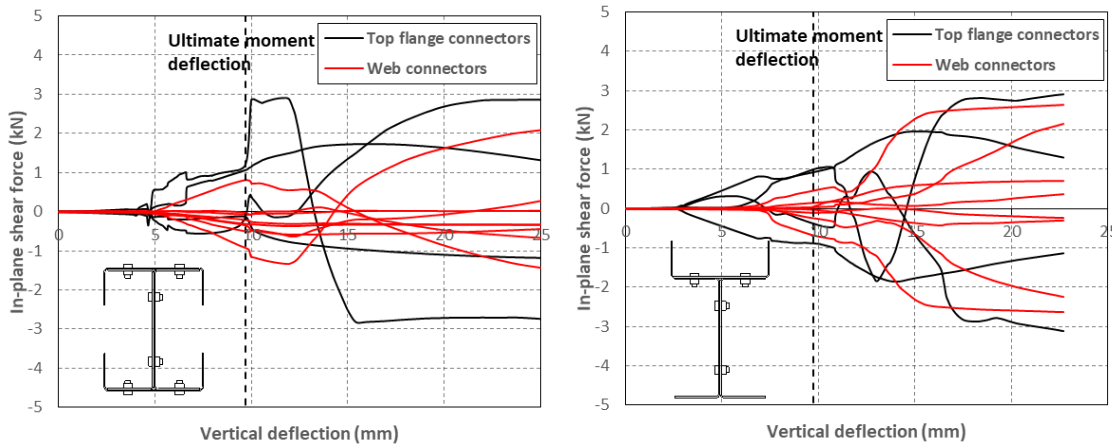


Figure 8.42: Shear forces in the connectors: a) B1-2a; b) B2-2a

The ultimate moment capacities predicted by the PLANAR models, on the other hand, were significantly lower than those predicted by the validated FE models, with average differences of 10 % and 11 % for the beams with geometries B1 and B2, respectively. This was due to the fact that in the PLANAR models, slip between the components of the built-up geometry was completely unrestrained, and therefore the top channel was not able to restrain the lateral movement of the top flange of the web channels. As a result, the web channels failed prematurely in a lateral-distortional buckling mode, as shown in Figure 8.43a and Figure 8.44a for beams B1-2a and B2-2a, respectively. In the validated FE models, on the other hand, the built-up beams failed due to local buckling of the components, with global instabilities of the individual components being prevented by the bolts (see Figure 8.43b and Figure 8.44b for beam B1-2a and B2-2a, respectively).

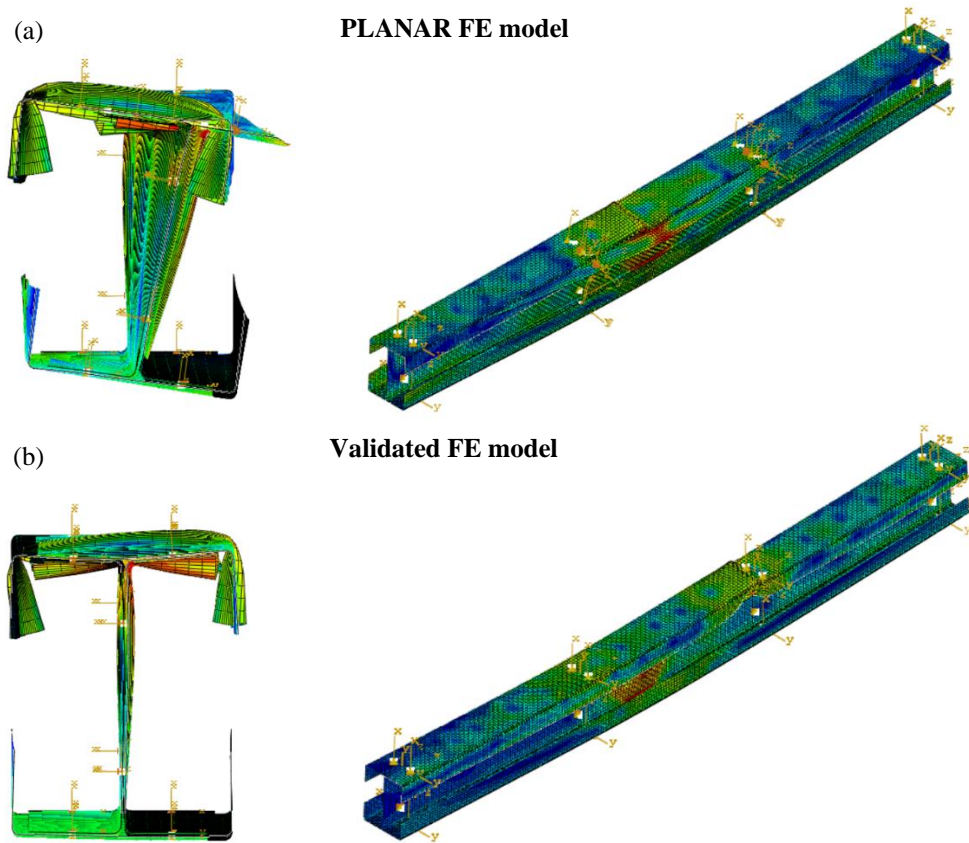


Figure 8.43: Failure mode of beam B1-2a:a) PLANAR model; b) Validated model

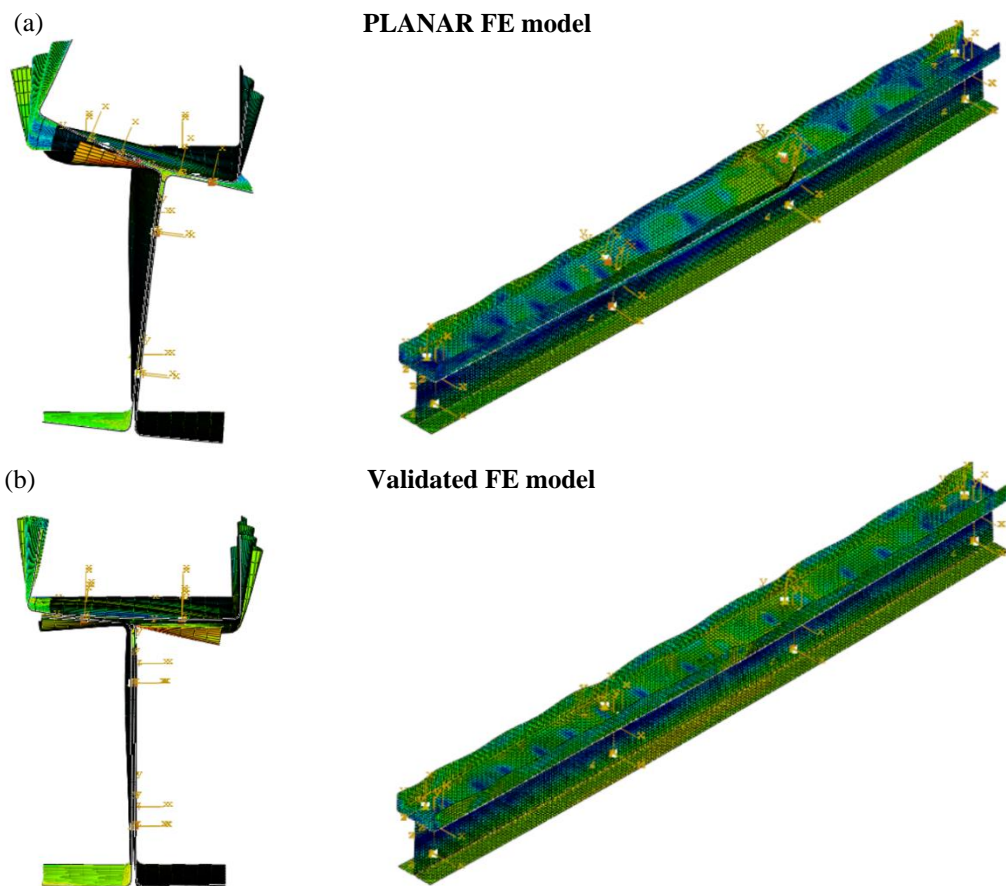


Figure 8.44: Failure mode of beam B2-2a:a) PLANAR model; b) Validated model

8.5.2 Connector spacing and contact interaction

The validated FE models were further used to study the way in which the ultimate capacity of CFS built-up beams is affected by the connector spacing and by contact between the component sections. For each built-up geometry, the number of equally spaced rows of intermediate connectors along the beam (without counting the connectors at the end cross-sections) was varied from zero to 31. This corresponded to a connector spacing which varied from 1500 mm to around 50 mm. For each connector spacing, simulations were run with and without contact interaction between the components of the built-up geometry. In addition, in order to establish an upper-bound for the moment capacity, corresponding to the connector spacing being reduced to zero, FE models were created (with and without contact between the components) in which the connector points were replaced by smeared TIE constrains between the component surfaces all along the beam length. All the FE models in this study included the initial geometric imperfections of a representative beam, the material non-linearity obtained from tensile coupons and the actual connector behaviour as determined from single lap shear tests.

The moment vs. mid-span deflection curves obtained from the FE models for a varying connector spacing are illustrated in Figure 8.45 and Figure 8.46 for beams B1 and B2, respectively. Figure 8.45a and Figure 8.46a show the results obtained when contact interaction between the components of the built-up geometry was activated, while Figure 8.45b and Figure 8.46b show the results obtained when contact was not activated. The failure modes of beams B1 and B2, obtained with and without contact are listed in Table 8.15 for different connector spacings.

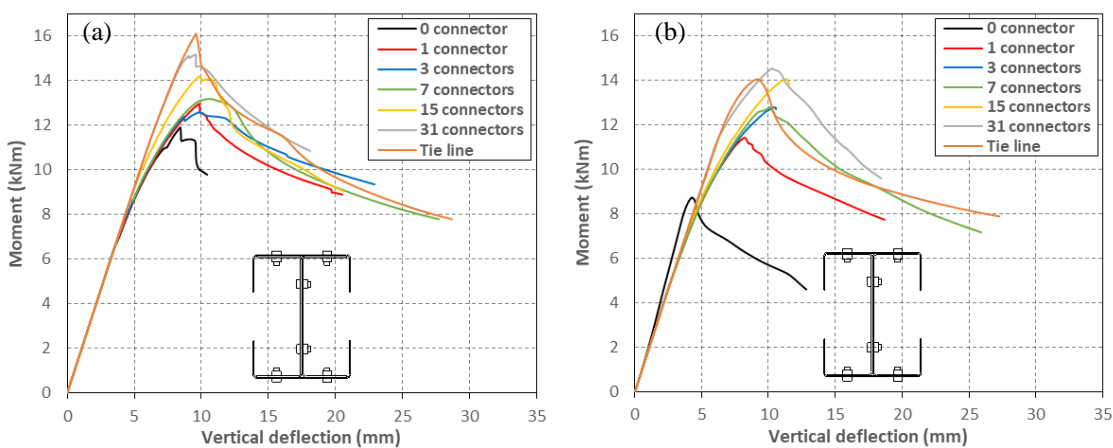


Figure 8.45: Moment vs. mid-span deflection of B1: a) with contact; b) without contact

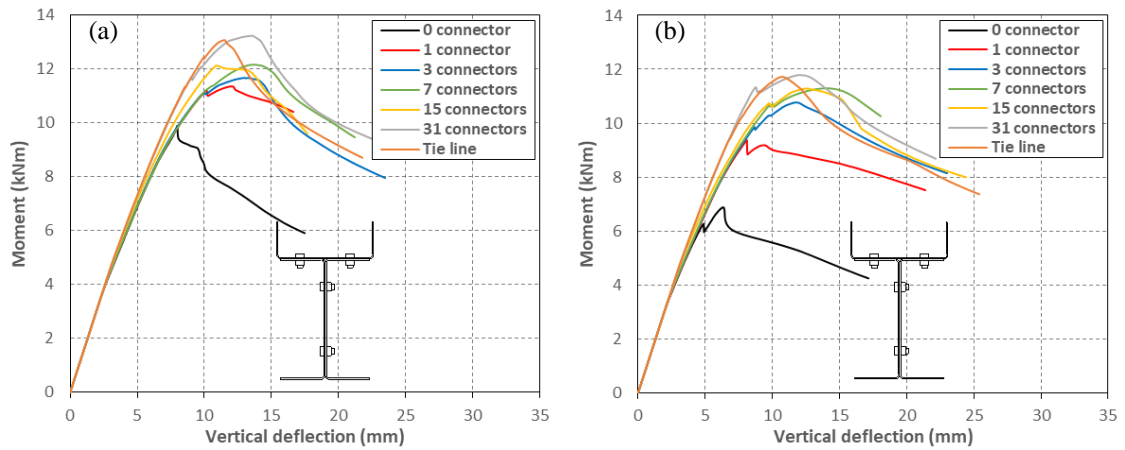


Figure 8.46: Moment vs. mid-span deflection of B2: a) with contact; b) without contact

Table 8.15: Failure modes beams B1 and B2

Beam	Failure mode at peak moment					
	With contact			Without contact		
	Top channel	Web channels	Built-up	Top channel	Web channels	Built-up
B1-0	L	L+LTB	-	L+F	L+LTB	-
B1-1	L	-	-	L	L+LTB	-
B1-3	L	L	-	L	L	-
B1-7	L	L	-	L	L	-
B1-15	L	L	-	L	L	-
B1-31	L	L	-	L	L	-
B1-Tie	L	L	-	L	L	-
B2-0	-	L+LTB	-	L+F	L+LTB	-
B2-1	L	L	-	L+F	-	-
B2-3	L	L	-	L	L	-
B2-7	L	L	-	L	L	-
B2-15	L	L	-	L	L	-
B2-31	L	L	-	L	L	-
B2-Tie	L	L	-	L	L	-

L = Local buckling; F = Flexural buckling; LTB = Lateral-torsional buckling

Table 8.15 shows that, in beams B1 and B2 without connectors along the constant moment span, failure of the built-up specimen was triggered as a result of the web channels failing by interaction of local and lateral-torsional buckling. By activating contact and adding one row of connectors at mid-span the components were able to mutually prevent each other from undergoing global instabilities between connector points. In beams B1 and B2 with three or more rows of intermediate connectors, the connector spacing was small enough to prevent global buckling of the components between connector points, irrespective of whether contact was activated or not, and failure occurred as a result of local buckling of the component sections.

The ultimate moment capacities predicted by the FE models including contact are plotted against the connector spacing in Figure 8.47a for beams B1 and B2, while the ultimate moment capacities obtained from the FE models in which contact interaction between the components was not activated are plotted in Figure 8.47b. In these figures, the ultimate moments are

normalized against the predictions given by the models in which the connectors were modelled with smeared TIE constraints along the beam.

Figure 8.47a and Figure 8.47b show, as could be expected, that preventing global instabilities of the component sections between connector points resulted in an increase in the ultimate moment capacity of the built-up specimen. This increase was especially pronounced in the FE models in which contact between components was not considered. This is due to the fact that the absence of contact interaction allowed the component sections to buckle individually in a global mode between connector points without any restraint. In the beams without intermediate connectors, the web channels buckled in a lateral-torsional buckling mode irrespective of whether contact was activated or not. However, when contact was not activated, the two web channels buckled independently from each other, while they were forced to buckle together when contact was activated, as shown in Figure 8.48 for beam B2.

Figure 8.47a also shows that once the global instabilities of the components between connector points are completely restrained by a sufficiently small connector spacing, there is a range of spacings in which the ultimate capacity of the beams does not vary significantly. For example, reducing the connector spacing from 750 mm to around 94 mm resulted in an increase in the ultimate capacity of only 10 % and 7 % for beams B1 and B2, respectively.

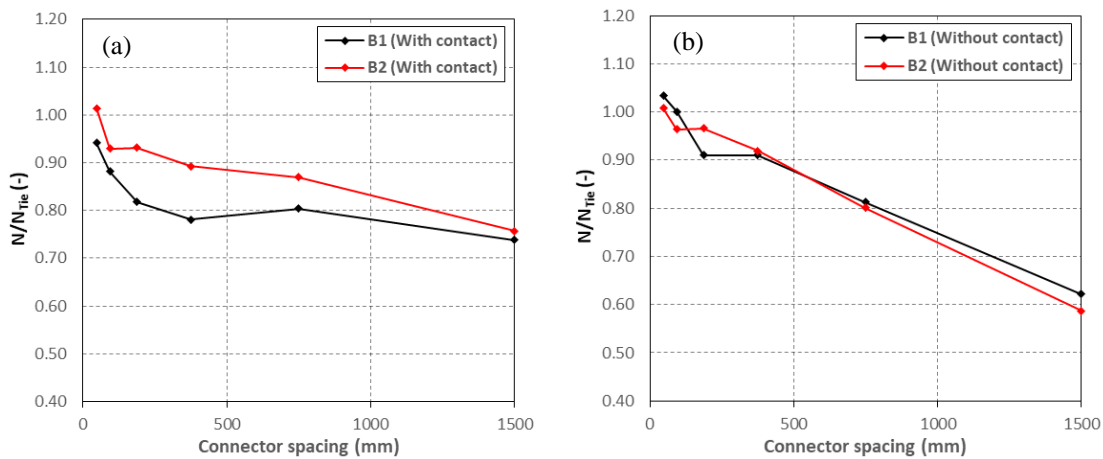


Figure 8.47: Ultimate load vs. connector spacing for FE models: a) with contact; b) without contact

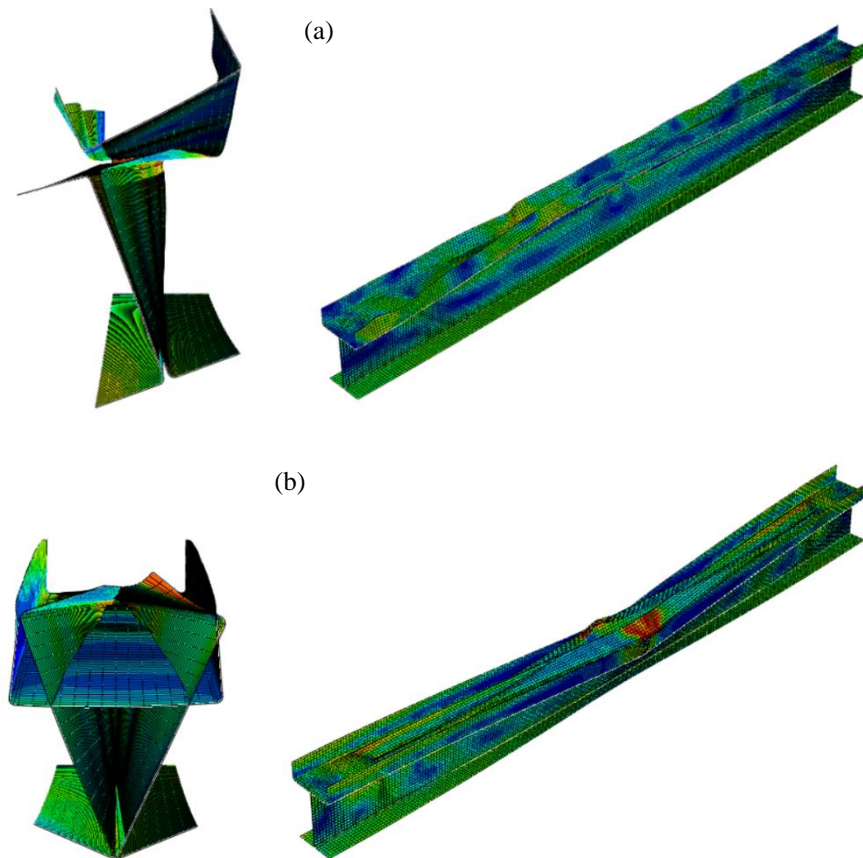


Figure 8.48: Deformed shape of beam B2-0: a) with contact; b) without contact

The initial buckled shape obtained for beams B1 and B2 is shown amplified in Figure 8.49 and Figure 8.50, respectively, for different connector spacings. The local buckling pattern was most noticeable in the top channel, while in the web channels it was only visible in the top flange of the channels, as expected.

In the beams without intermediate connectors the top channel exhibited a regular buckling pattern along the beam with a half-wave length very close to 110 mm, which is the natural local buckling half-wave length of the channel. The presence of the web channels forced the top channel to buckle upwards. This can be clearly appreciated in Figure 8.50 for beams B2. In the beams with 1 and 3 intermediate rows of connectors, the connector spacing was large enough for the top channel to buckle generating several half-waves between connector points. However, the presence of the connectors forced the top channel to adjust its preferred buckle half-wave length so that the cross-sections containing connectors fell inside a concave buckle. This imposition obliged the top channel to generate an even number of half-waves between connector points. Considering the beams with 3 intermediate rows of connectors, neither a half-wave length of 188 mm, resulting from generating two half-waves between connectors, nor a half-wave length of 94 mm, resulting from generating four half-waves between connectors, was optimal for the top channel, which preferred to buckle with a half-wave length of 110 mm, as shown in Figure 8.51a and Figure 8.51b for beams B1-3 and B2-3, respectively. As a result, while the top channel buckled with four half-waves between connectors in one of the fields,

with a half-wave length slightly larger than 94 mm, in the adjacent fields the top channel buckled with two half waves with a half-wave length slightly shorter than 188 mm. The cross-section containing connectors consequently did no longer exactly coincide with the centre of a concave buckle, but was slightly shifted towards one side. As Figure 8.51a and Figure 8.51b show, this buckling pattern with two different half-wave lengths along the beam required a lower stress than those where the top channel buckled while consistently generating either two or four half-waves between connectors. A similar explanation applies to the beams with one row of connectors in the moment span.

As the connector spacing was further reduced the buckles in the top channel became more regular again. In the beams with 7 intermediate rows of connectors the buckle half-wave length in the top channel approximately coincided with half the distance between connectors, while in the beams with 15 intermediate rows of connectors the distance between connectors was almost the same as the buckle half-wave length of the top channel and the gap between the top channel and the web channels, which was present in the beams with larger connector spacings, became almost undetectable. In the beams with 31 intermediate rows of connectors the connector spacing was smaller than the buckle half-wave length of the top channel, and the connectors forced the top and web channels to buckle in a synchronous manner. At these short connector spacings the ultimate capacity of the built-up beams became more sensitive to the distance between connectors compared to the cases where the connector spacing was larger than the buckle half-wave length of the components. However, it should be noted that this range of connector spacings is not practical in construction due to the large amount of labour involved in assembling specimens with such a large number of connectors.

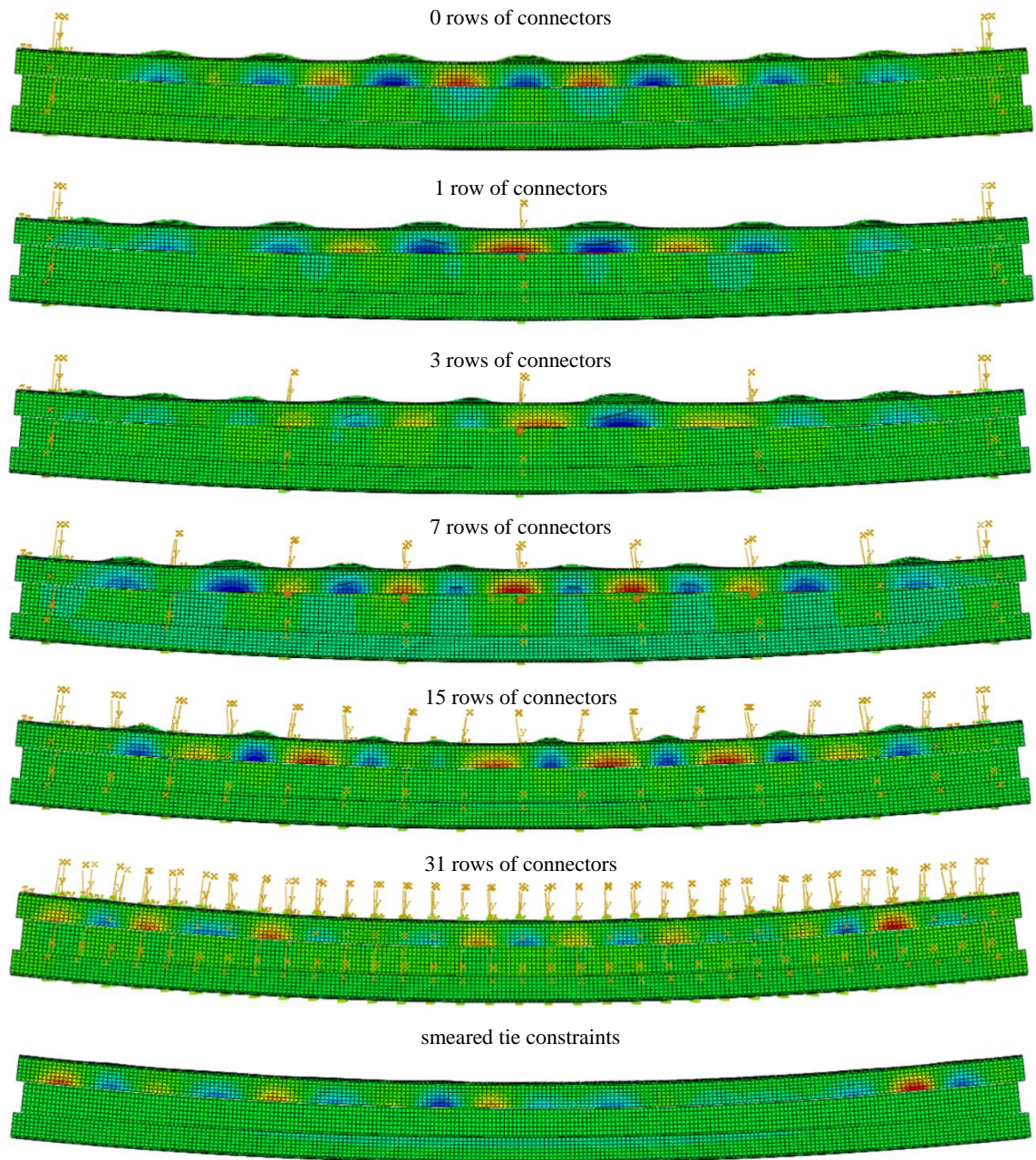


Figure 8.49: Amplified buckling deformed shape of beams B1

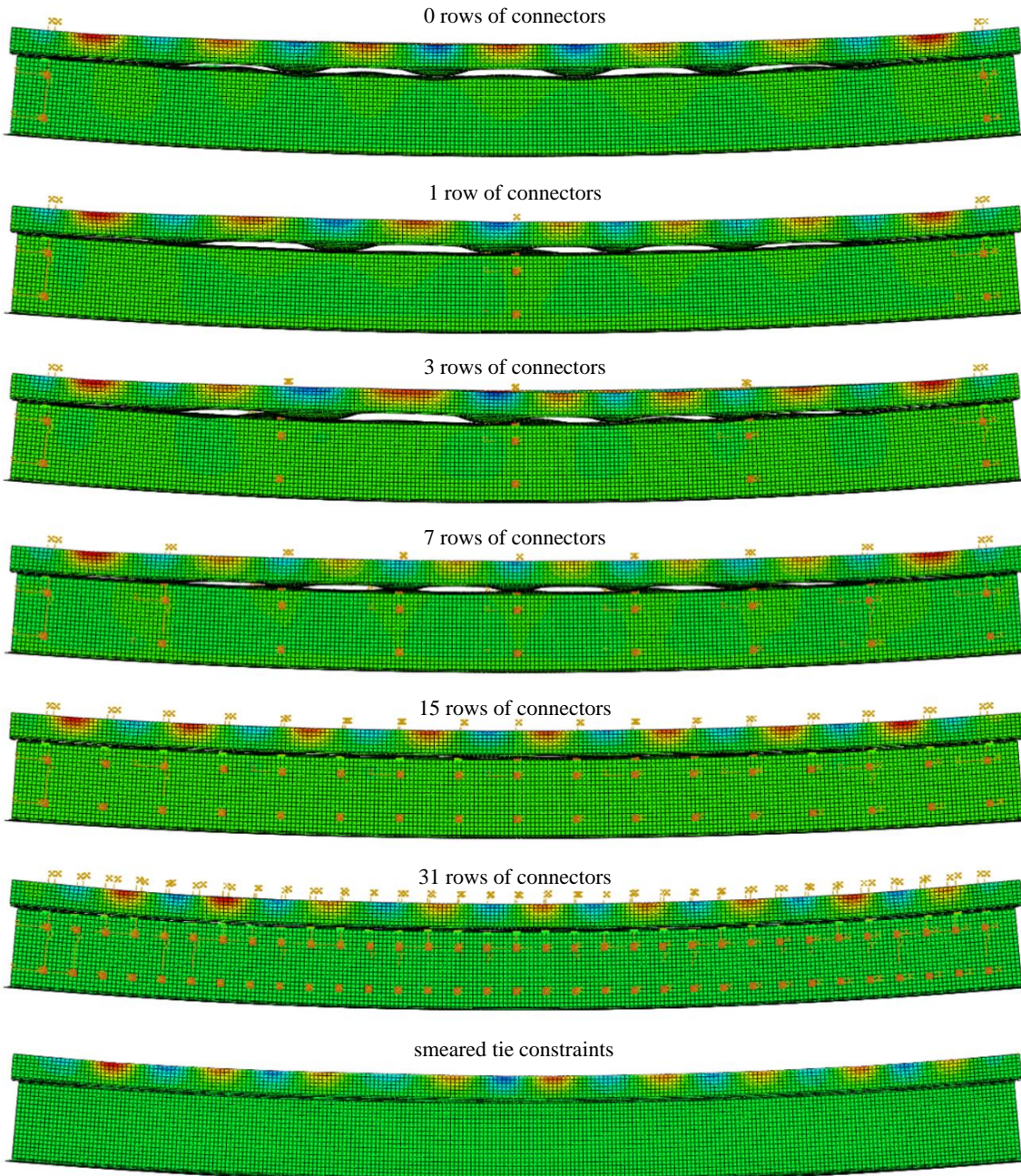


Figure 8.50: Amplified buckled shape of beams B2

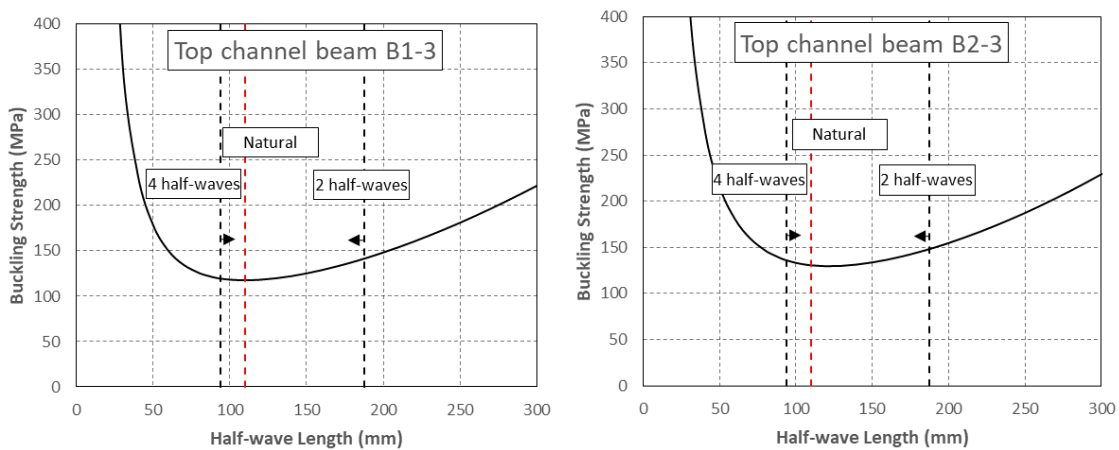


Figure 8.51: Signature curve top channel in: a) B1-3; b) B2-3

The effect of contact between the components on the ultimate capacity of beams B1 and B2 is illustrated in Figure 8.52, which shows the ratio between the ultimate moment capacities obtained from the FE models with contact activated and deactivated as a function of the connector spacing. The figure shows that for the geometries studied the effect of contact was only important in those beams in which the connector spacing was large enough for the components to undergo global instability between connector points when no contact was considered (i.e. beams with zero or one row of connectors). In this case, the different components in the built-up specimen restrained each other through contact, delaying or even preventing global instabilities. An example is found in beam B1-1, where contact between the web channels prevented them from buckling in a lateral-torsional mode. For shorter connector spacings, on the other hand, the effect of contact became less significant, resulting, on average, in an increase in the ultimate capacity of less than 5 % for beams B1 and less than 10 % for beams B2.

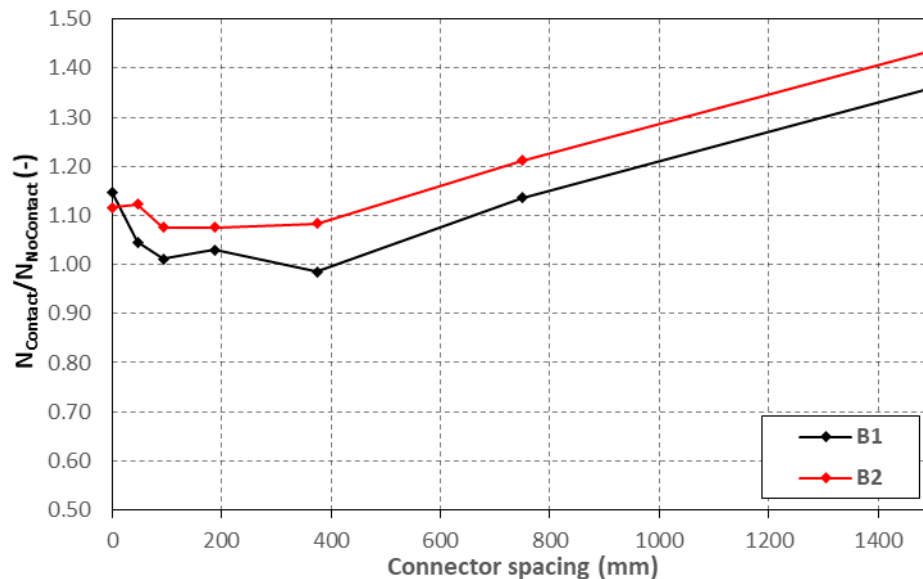


Figure 8.52: Effect of contact interaction on the ultimate capacity

8.6. Summary and conclusions

Both detailed and simplified FE models were developed for the 11 built-up CFS beams with two different cross-sectional geometries presented in Chapter 4, using the software package Abaqus v.6.14. The beams were assembled with bolts which were modelled using mesh-independent fasteners. The models included the initial geometric imperfections, as measured on the tested beams, material non-linearity obtained from tensile coupons extracted from the flat portions and

the corner regions of the components of the tested beams, and the actual load-elongation behaviour of the connectors, which was determined from single lap shear tests.

Both the detailed and simplified FE models were validated against the experimental data. The validation included a comparison of the ultimate moment capacities, the initial buckled shapes and the critical buckling stresses derived for the top channel of the built-up geometries. The simplified model was further used in parametric studies to investigate the way in which the connector modelling approach and connector spacing, as well as contact between components affect the behaviour and capacity of the built-up beams.

The following conclusions could be drawn from the numerical investigation:

- A material modelling study showed that either approximating the actual stress-strain behaviour in the FE model by a simplified bilinear stress-strain curve or neglecting the enhancement of the material properties in the corner regions only had a minor effect on the predicted behaviour and ultimate capacity of the built-up geometries. While the former simplification resulted in a stiffer post-buckling response and an overestimation of the ultimate capacity by around 2 %, the latter only affected the ultimate capacity, underestimating it by approximately the same amount.
- Both the detailed and the simplified FE models were able to accurately predict the initial stiffness of the beams and provided reasonable predictions of their ultimate moment capacities. For beams B1 the average error in the ultimate moment predictions given by the detailed and simplified models were virtually the same (around 4 %), while for beams B2 the predictions given by the detailed model were slightly more accurate than those given by the simplified one, with an average error of 6.85 % for the former and 7.67 % for the latter. The detailed and simplified FE models were also able to predict local buckling patterns similar to those observed in the tested beams. However, while the critical buckling stresses in the top channel of beam B2 derived from the detailed FE model were in good agreement with those determined from the tested beams (with an average error of 7 %), for beams B1 the detailed model consistently predicted larger critical buckling stresses, with an average error of around 30 %. On the other hand, the critical buckling stresses derived from the simplified model were in good agreement with those observed experimentally, with an average difference of 9 % for beams B1 and 7 % for beams B2.
- The ultimate capacities predicted by the validated FE models were in good agreement with the predictions given by the HINGE and MPC models, in which bolt slip was prevented. This was attributed to the fact that no shear forces were present in the beams within the constant moment span. Therefore, shear forces in the connectors only originated as a result of local buckling of the components and these forces were smaller

than the bolt slip load. The bolts in beams B1 and B2 were also instrumental in enabling the top channel to completely restrain the web channels from buckling in a lateral-torsional mode. This could be verified with the PLANAR model, in which slip without any resistance was allowed at the connector points. This model predicted ultimate capacities which were on average around 10 % lower than those predicted by the validated FE model for beams B1 and B2 as a result of premature global buckling of the web channels.

- The effect of the connector spacing on the ultimate moment capacity of the beams was found to be important only when the connectors were necessary to restrain global instabilities of the individual components between connector points. Within the range of connector spacings where the components buckled in a local mode, reducing the connector spacing only resulted in a modest increase in the ultimate capacity. For example, reducing the connector spacing from 750 mm to around 94 mm resulted in an increase in the ultimate capacity of less than 10 % in both built-up geometries. For connector spacings shorter than the local buckle half-wave length of the components the ultimate capacity of the built-up beams became slightly more sensitive to the distance between connectors. However, this range of connector spacings is impractical for construction purposes due to the large amount of labour involved.
- For the geometries studied contact between the components was seen to be important mainly when it contributed to partially or completely restraining global instabilities of the components of the built-up geometry between connector points. When the connector spacing became small enough to prevent global instabilities of the individual components the effect of contact became less significant, resulting, on average, in an increase in the ultimate capacity of less than 5 % for beams B1 and less than 10 % for beams B2. The effect of contact was also seen to be slightly more important for connector spacings shorter than the local buckle half-wave length of the components. However, its effect remained relatively modest.

Chapter 9

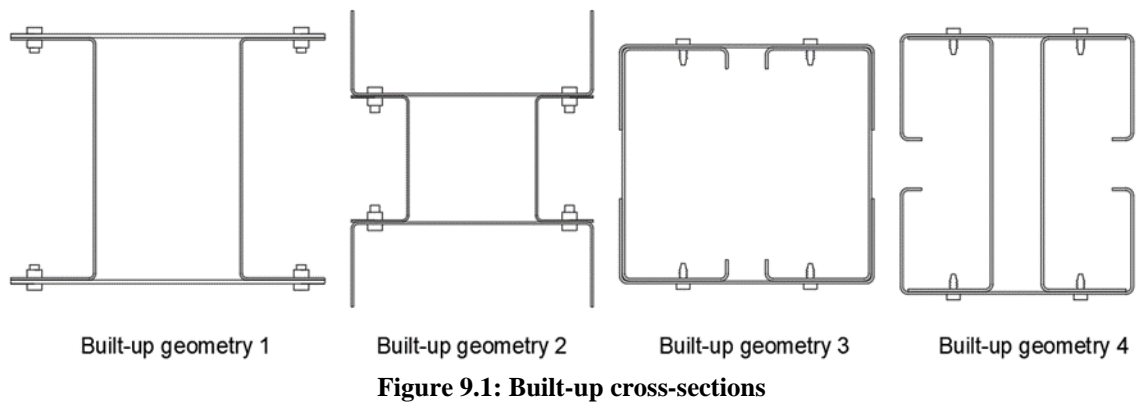
Numerical Study of Long Cold-Formed Steel Built-up Columns

9.1. Introduction

This chapter is devoted to the development of detailed finite element (FE) models of the long built-up columns presented in Chapter 5. Figure 9.1 illustrates the four different cross-sectional geometries which were investigated. The columns with geometries 1 and 2 were assembled using M6 bolts, while the columns with geometries 3 and 4 were assembled using M5.5 self-drilling screws.

The FE models presented significant convergence issues, which often resulted in the analysis being terminated before the peak load of the column was reached. These convergence issues were overcome by adjusting some of the default solution control parameters Abaqus/Standard uses to solve a non-linear analysis together with adding artificial damping to the model. The amount of artificial damping introduced into the FE models was determined by carrying out a stabilization analysis, which paid special attention to the way in which the ultimate capacity of the columns was affected by the artificial damping forces.

The FE models were verified using the experimental data gathered from the long built-up columns presented in Chapter 5, which included the ultimate capacity of the column, the deformed shape after buckling and the critical buckling stresses obtained for some of the component sections. The validated models were further used to carry out parametric studies with the aim of investigating the way in which the connector modelling approach and connector spacing, as well as contact between components affects the buckling response of built-up columns subject to interaction between cross-sectional buckling of the components, global instabilities of the components between connector points and global instabilities of the built-up member as a whole.



9.2. Details of the FE models

The FE models were created using the software package Abaqus v.6.14 (Dassault Systemes, 2014). The columns were discretized using structural shell elements with the default five integration points through the thickness and using Simpson's rule. The models were constructed based on the measured cross-sectional dimensions of the components. They incorporated the initial geometric imperfections measured on the columns and material non-linearity obtained from tensile coupons, while the connectors used to assemble the columns were modelled using mesh-independent fasteners which accounted for their actual behaviour.

Similarly to the tested columns, the numerical models were labelled with the letters 'LC' to indicate that the model corresponded to a long column, and the numbers 1 to 4 to indicate its cross-sectional geometry (with reference to Figure 9.1). The number of intermediate rows of connectors along the column was indicated after a hyphen at the end of the label. As an example, the label 'LC1-2' refers to an FE model of a long column with cross-sectional geometry 1 and two intermediate rows of connectors.

9.2.1 Boundary conditions

The pin-ended boundary conditions in the long columns were simulated by defining a reference point at each end of the column, which coincided with the rotational axis of the end support. This axis was located 73.5 mm away from the end cross-section of the column, as illustrated in Figure 9.2b. Since in the experiments the columns were welded at each end to endplates, BEAM MPC constraints were used to couple the rotational and translational degrees of freedom of the nodes of the bottom and top end cross-sections of the column to the degrees of freedom of the reference points. The boundary conditions were applied to the reference points by constraining

all of their rotational degrees of freedom, apart from the rotational degree of freedom about the x -axis, as shown in Figure 9.2a. In addition, the bottom reference point also had all of its translational degrees of freedom restrained, while the top reference point had all of its translational degrees of freedom restrained apart from the vertical degree of freedom. The compressive force was applied to the model by imposing a vertical displacement to the top reference point, with the load eccentricity accounted for by adjusting the position of the reference points in the y -direction respect to the centroid of the built-up cross-section (see Figure 9.2 for the axis convention).

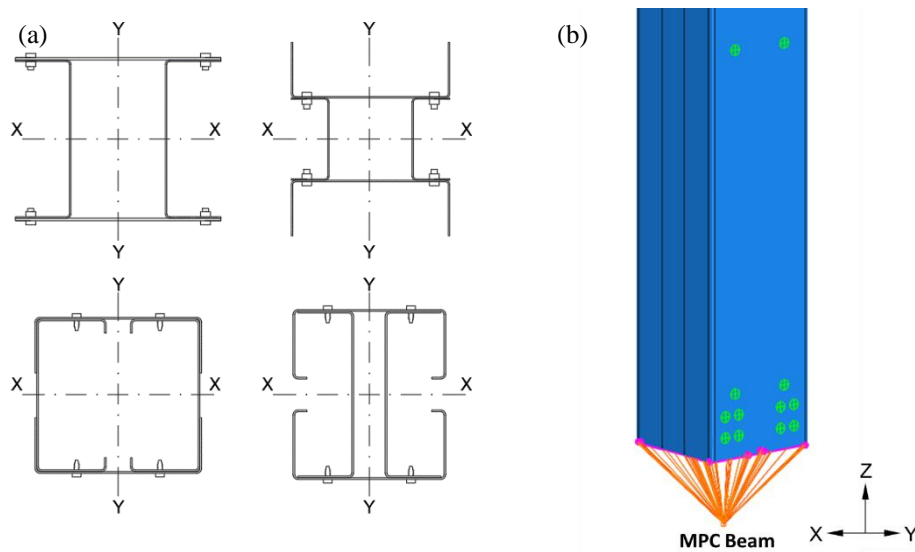


Figure 9.2: FE model boundary conditions

9.2.2 Geometric imperfections

All FE models included the initial geometric out-of-plane imperfections as measured on the tested columns presented in Chapter 5 after the components were assembled into their final configuration. The imperfections were incorporated into the FE models using a specially developed Matlab code, which was used to modify the coordinates of the nodes in the input file (*.inp) of a geometrically perfect FE model generated in Abaqus/Standard.

The imperfection data used in the FE models was recorded by moving a laser displacement sensor along several lines on each face of each column, as indicated by the arrows in Figure 9.3. A detailed description of the way in which the out-of-plane imperfections in the tested columns were recorded is included in Section 5.6.2 of Chapter 5.

On each measured plate element of the built-up cross-sections (i.e. web and flanges of the components) the imperfections were recorded along four lines. Third order polynomial

interpolation was therefore carried out to obtain the imperfections at the nodes of the FE model, as illustrated in Figure 9.4.

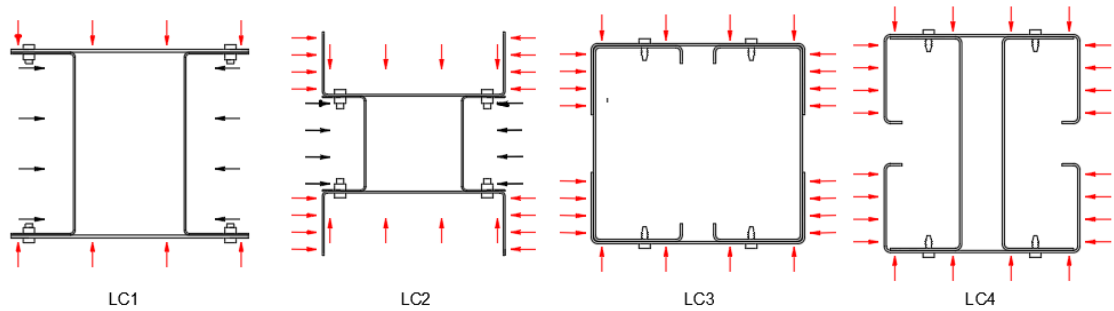


Figure 9.3: Location of measured imperfections in stub columns

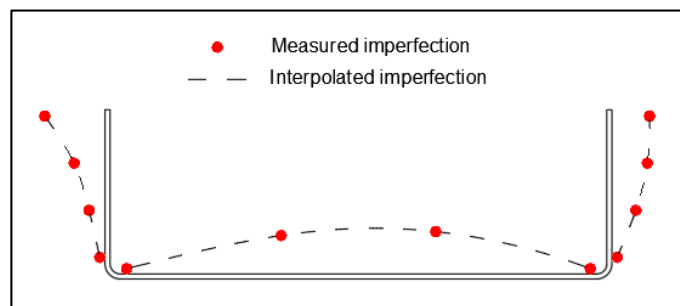


Figure 9.4: Interpolated imperfection

9.2.3 Material properties

The material behaviour was modelled following the same approach described in Section 7.2.3 of Chapter 7 using the data obtained from tensile coupons taken from the flat and corner regions of the channels. This approach to represent the material properties in the FE models is further referred to as the ‘actual material’ modelling approach. Details of the tensile coupon tests and full results are provided in Section 5.3 of Chapter 5.

9.2.3.1 Simplified approaches to model material properties

In order to quantify the degree to which the ultimate capacity of the studied built-up geometries is affected by simplifications in representing the material behaviour in the numerical models, a series of non-linear analyses were carried out for a representative column belonging to each built-up geometry using the two simplified material modelling approaches described in Section 7.2.3.1 of Chapter 7, and their ultimate capacities were compared to the predictions given by the FE models including the actual material properties.

Figure 9.5 and Table 9.1 show that the FE models in which the material properties are approximated by a bilinear stress-strain curve consistently predict higher ultimate capacities than the FE models incorporating the actual material properties, with an average increase in the ultimate load of 5.3 %, and a maximum increase of 8.8 % (for the column with geometry LC3). On the other hand, the effect of ignoring the enhancement of the mechanical properties in the corner regions of the FE models was less significant, resulting in an average reduction of the predicted ultimate capacity of 1.5 %. It is worth pointing out, however, that in the columns assembled with lipped channels (columns LC3 and LC4) the effect of ignoring the corner enhancement was noticeably larger than in the other geometries, with a maximum reduction in the ultimate capacity of 3 % in the columns with geometry LC4. This suggests that, as the number of corners in a cross-section increases (as may be the case in optimized cross-sections with edge and intermediate stiffeners), the error in the ultimate load prediction introduced in the FE model by ignoring the enhancement of the mechanical properties in the corner regions may not be negligible.

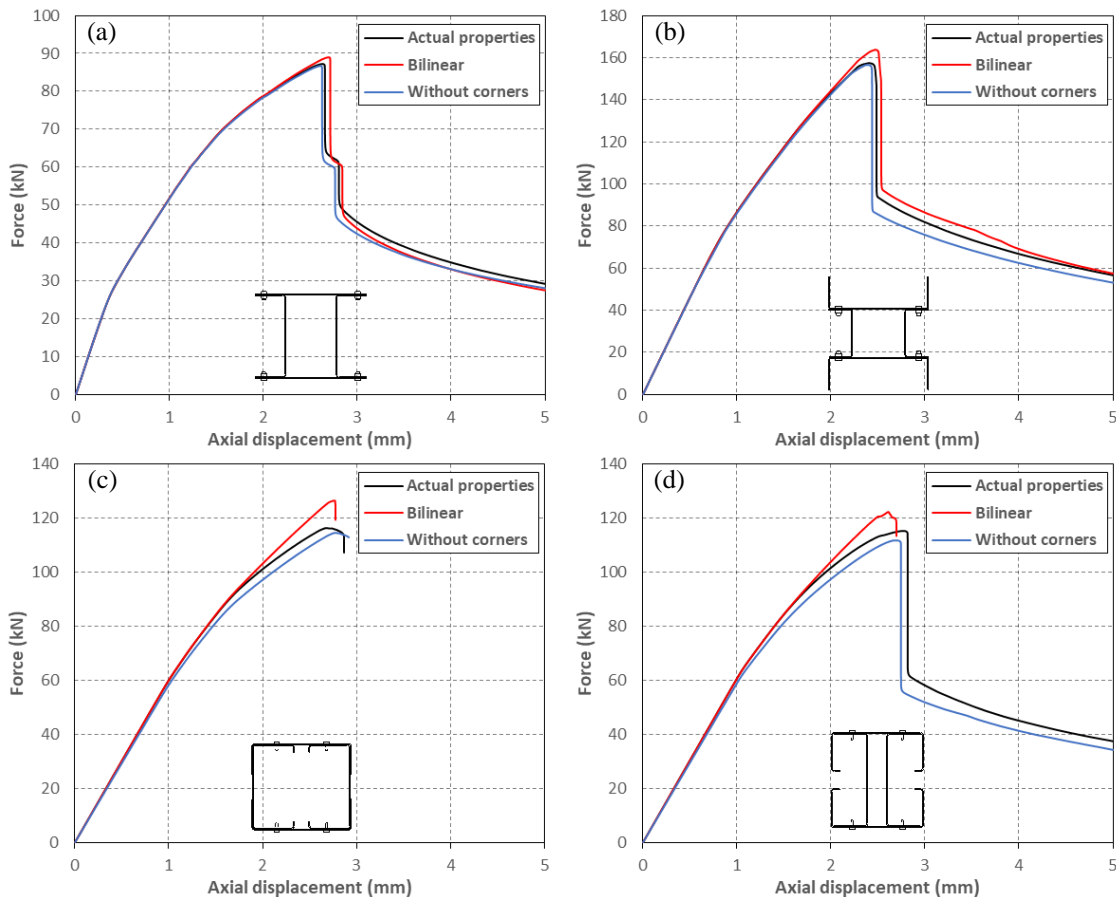


Figure 9.5: Effect of material properties modelling approaches on columns: a) LC1-8a; b) LC2-6a; c) LC3-2a; d) LC4-3a

Table 9.1: Difference in ultimate load with respect to FE model with actual material properties

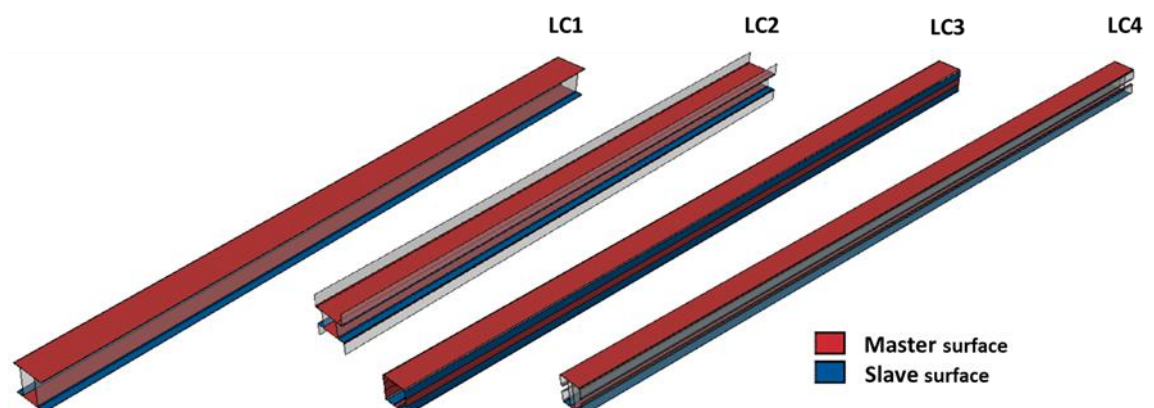
Column	Difference in ult. load with respect to actual material properties (%)	
	Bilinear	Without corners
LC1-8a	1.9	-0.7
LC2-6a	4.1	-0.6
LC3-2a	8.8	-1.5
LC4-3a	6.2	-3.0

9.2.4 Contact interaction

Contact between the components of the built-up columns was defined using the finite-sliding surface-to-surface contact formulation available with the General Contact implementation in Abaqus/Standard, which allows for arbitrarily large relative motion between the interacting surfaces, as described in Section 7.2.4 of Chapter 7. Contact between the surfaces was defined as ‘frictionless’ in the tangential direction, while a ‘hard’ pressure-overclosure behaviour was approximated in the direction normal to the surfaces using the ‘Augmented Lagrange’ constraint enforcement method.

In order to reduce the computational cost, contact was only defined between those surfaces of the components which were likely to interact with each other during the analysis. Figure 9.6 shows the surfaces which were involved in the contact interactions, indicating whether the surfaces were assigned the master or the slave role in the interaction.

The strain-free adjustment method was used to correct for any possible penetration of the slave nodes into the master surfaces at the beginning of the analysis, which was likely to occur due to the introduction of the measured geometric imperfections into the FE model. Since the default strain-free adjustment available in Abaqus/Standard is designed to only remove small initial overclosures measuring up to the average thickness of the connected surfaces, the default search zone for the strain-free adjustment method was increased to 2 mm.

**Figure 9.6: Master and slave role in contact interaction**

It is worth noting that for built-up column 4 the edges of the plain channel flanges were allowed to penetrate the flanges of the lipped channels since only the web of the lipped channels was included in the contact interactions. This option was adopted to avoid edge-to-surface contact, which was noted to result in significant convergence issues. On the other hand, penetration of the edges of the plain channel flanges into the lipped channels flanges was noted to only occur after the columns reached their peak load, and was not considered to affect their buckling capacity or initial buckling behaviour.

9.2.5 Connector modelling

The bolts and screws used to assemble the components of the built-up columns, as well as the spot welds which were added at the ends of the columns to ensure a uniform distribution of the load to all the components, were modelled using mesh-independent fasteners, as described in Section 7.2.5 of Chapter 7. The fastening points were connected to the neighbouring nodes on the respective surfaces using the structural coupling method, which was implemented using the uniform weighting scheme and defining a physical radius for the fastener of 5 mm.

All mesh-independent fasteners were modelled with discrete fasteners. PLANAR connector elements were used to replicate the behaviour of the bolts and screws used to assemble the columns, while BEAM connectors were used to simulate the spot welds which were used to connect the components at each end of the column. The PLANAR connectors were orientated so that their available rotational component of relative motion (CRM) was normal to the surfaces in contact and the two available translational CRMs were tangential to the plane of contact. Elastic and plastic properties, obtained from single lap shear tests, were assigned to the two available translational CRMs of the PLANAR connectors in order to replicate the actual behaviour of the screws and bolts.

9.2.6 Type of analysis

The non-linear buckling analysis of the built-up columns was carried out using the General Static solver available in Abaqus/Standard, with the inclusion of artificial damping to stabilize the solution. The analyses included geometric and material non-linearity. The time increments in the analysis were automatically adjusted by Abaqus/Standard using the automatic incrementation control algorithm.

9.2.7 Overcoming convergence issues in Abaqus/Standard

The unstable character of the non-linear problem, as well as the presence of contact between the components of the built-up geometry resulted in significant convergence issues, which were

overcome by adjusting some of the solution control parameters, together with adding artificial damping to the FE models, either through the automatic stabilization or the contact stabilization schemes available in Abaqus/Standard.

The strategy followed to achieve a convergent solution in all models presented in this chapter consisted of first running the model using the contact control mechanism together with the non-default time incrementation control parameters described in Section 7.2.7 of Chapter 7. If the simulation terminated before the peak load was reached, an additional step was added to the simulation, in which the contact control mechanism was removed and replaced with the adaptive automatic stabilization mechanism. Also, in this second step the maximum displacement correction check was removed by setting C_n^α to 1. A description of this solution control parameter is given in Section 7.2.7 of Chapter 7 together with a discussion about its effect on the convergent solution. A description of the contact control and adaptive automatic stabilization mechanism is also given in Section 7.2.7.

The following section presents a stabilization study carried out to determine the appropriate settings to be used with the contact control and the automatic stabilization schemes to ensure that the amount of damping introduced into the models was sufficiently low not to significantly alter the solution.

9.2.8 Stabilization study

9.2.8.1 Contact control

A stabilization study was carried out to ensure that the amount of artificial damping introduced in the FE models through the contact control mechanism available in Abaqus/Standard was sufficiently low to have a negligible effect on the final solution. The study was carried out for one representative column of each built-up geometry. The constant factor Abaqus/Standard uses to scale the magnitude of the viscous stresses normal to the surfaces in contact was increased from zero to 8×10^{-4} . In all models, the ‘tangent fraction’ parameter, which specifies the amount of artificial damping applied to the relative motion of the surfaces in the tangential direction was set to zero. This option was chosen because tangential viscous stresses would be likely to absorb a significant amount of energy when the contact surfaces slip relative to each other.

Table 9.2 lists the ultimate loads obtained for each built-up geometry, as well as the corresponding value given to the scale factor. Column LC1 was the only geometry where a converging solution past the peak load could be achieved by only adjusting the solution control parameters. For the other geometries, a post-peak solution was only possible after activating the contact control scheme. Figure 9.7a, Figure 9.8a, Figure 9.9a and Figure 9.10a show the ratios between the energy dissipated through artificial damping (ALLSD) and the total strain energy

(ALLIE) for different values of the constant scale factor, obtained for a representative column with geometries LC1, LC2, LC3 and LC4, respectively. In the figures, a vertical dashed line shows the approximate axial deformation at which the column reached its ultimate capacity. The load-axial shortening curves obtained for different values of the scale factor are shown in Figure 9.7b, Figure 9.8b, Figure 9.9b and Figure 9.10b for a representative column with geometry LC1, LC2, LC3 and LC4, respectively.

Table 9.2: Ultimate load comparison with contact control schemes

Specimen	Stabilization scheme	Contact control	Ult. Load (kN)
LC1-2a	No stabilization	-	74.95
	cc 0.0002	2×10^{-4}	74.92
	cc 0.0005	5×10^{-4}	74.96
	cc 0.0008	8×10^{-4}	75.37
LC2-2a	No stabilization	-	Divergence
	cc 0.0002	2×10^{-4}	153.40
	cc 0.0005	5×10^{-4}	154.07
	cc 0.0008	8×10^{-4}	154.43
LC3-2a	No stabilization	-	Divergence
	cc 0.0002	2×10^{-4}	116.11
	cc 0.0005	5×10^{-4}	116.25
	cc 0.0008	8×10^{-4}	116.36
LC4-2a	No stabilization	-	Divergence
	cc 0.0002	2×10^{-4}	112.75
	cc 0.0005	5×10^{-4}	112.70
	cc 0.0008	8×10^{-4}	112.91

Table 9.2 shows that for the selected range of values of the scale factor, the ultimate load is not significantly affected by the contact control mechanism for any of the studied geometries. For column LC1, the difference in the ultimate load achieved with a scale factor equal to 2×10^{-4} was only 0.04 % relative to the model in which no stabilization was used, while for columns LC2, LC3 and LC4 the maximum variations in the ultimate load when varying the scale factor from 2×10^{-4} to 8×10^{-4} were 0.67 %, 0.22 % and 0.19 %, respectively.

As Figures 9.7-9.10 show, the largest amount of artificial damping was introduced in the column with geometry LC1 at the moment when the plate sections started buckling in a global-type flexural mode between connectors. It is worth pointing out that this column had only two intermediate sets of connectors along the column (at a distance of 960 mm), which caused the plate sections to buckle almost from the onset of loading in the model without stabilization. The large connector spacings also implied that the forces required to prevent the plate sections from buckling were relatively small, and therefore in all the FE models in which the contact control mechanism was activated the viscous forces delayed the onset of global buckling of the plates between connector points. This is evidenced by the distortion of the load-axial deformation curve of column LC1 shown in Figure 9.7b. In addition, Figure 9.11 shows the load-lateral deformation curve of the plate sections at mid-distance between connectors for the different

values of the scale factor. Despite artificial damping delaying the onset of global buckling of the plate sections between connector points, after the plate buckled the load-lateral deformation curves obtained for different values of the scale factor converged to the curve obtained from the FE model in which no artificial damping was added. This explains why, despite the clear influence of the artificial damping forces on the initial buckling load, the ultimate capacity of the columns remained almost unaltered.

Based on the results obtained from this stabilization study, it was decided not to use the contact control mechanism in the LC1 columns with two and three intermediate set of connectors in order to avoid altering the critical buckling stresses of the plate sections. For the remaining columns the models were run with the contact control mechanism activated, using a scale factor equal to 2×10^{-4} , since this resulted in a negligible change in the ultimate capacity of the studied geometries.

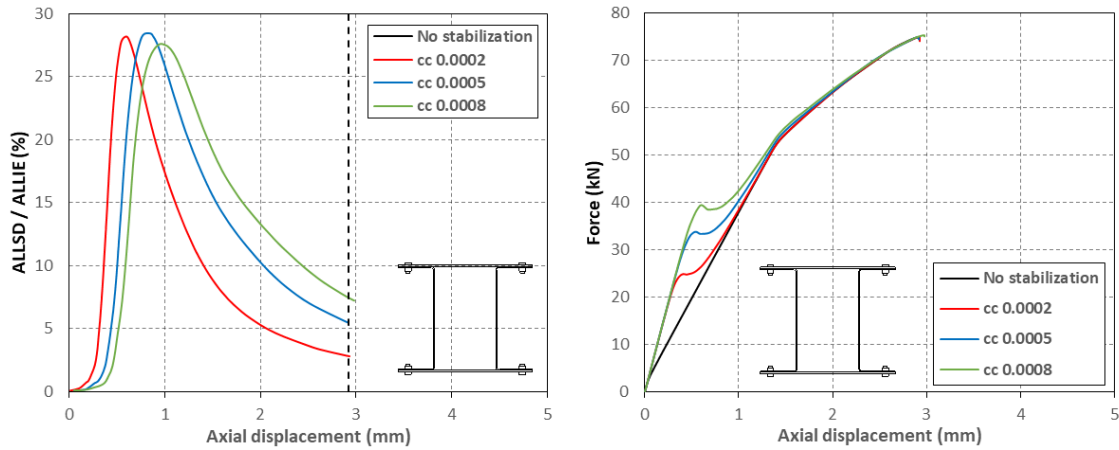


Figure 9.7: Contact stabilization in columns LC1: a) Dissipated energy over total strain energy; b) Load-axial shortening curve

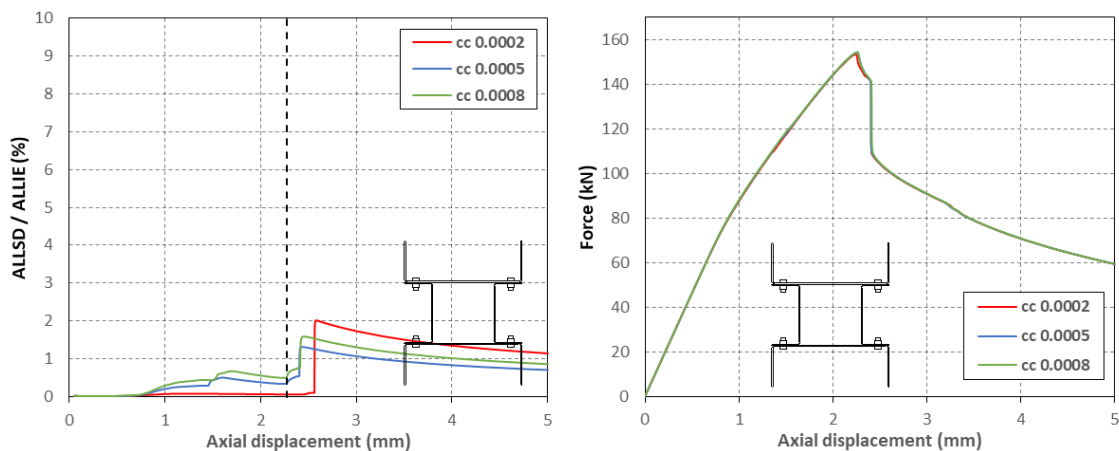


Figure 9.8: Contact stabilization in columns LC2: a) Dissipated energy over total strain energy; b) Load-axial shortening curve

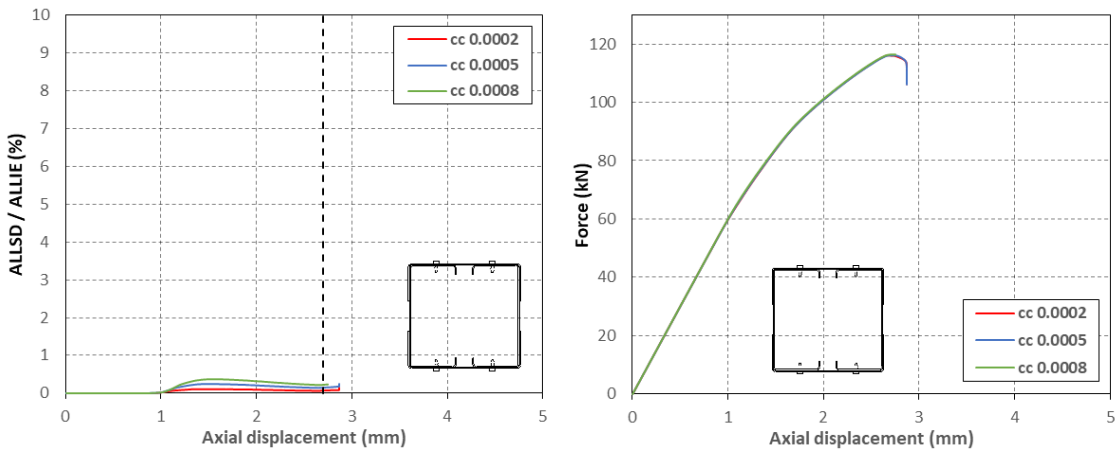


Figure 9.9: Contact stabilization in columns LC3: a) Dissipated energy over total strain energy; b) Load-axial shortening curve

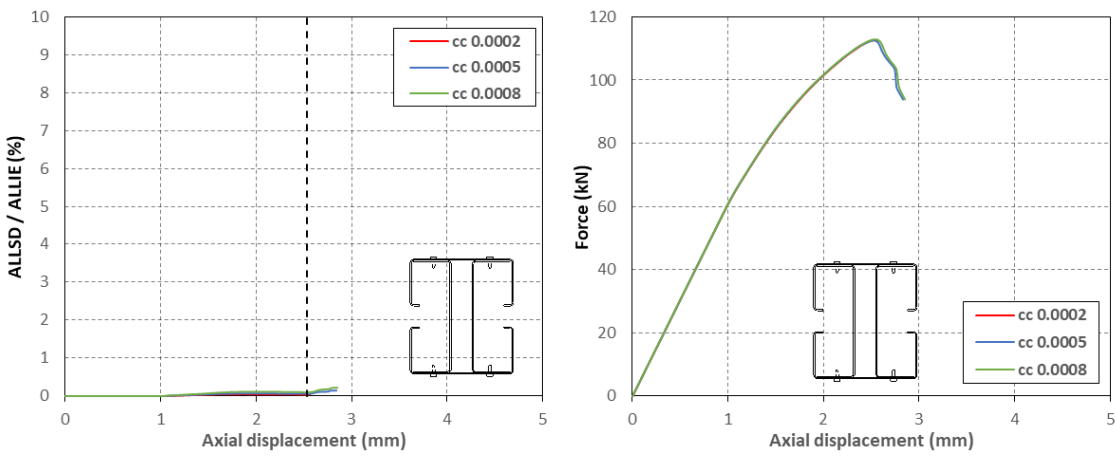


Figure 9.10: Contact stabilization in columns LC4: a) Dissipated energy over total strain energy; b) Load-axial shortening curve

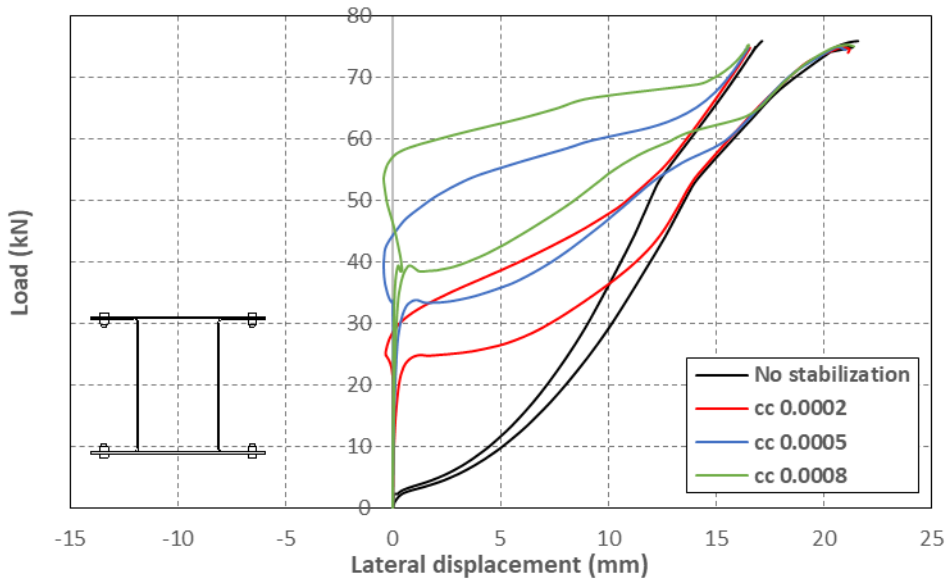


Figure 9.11: Load-lateral displacement curves of plate sections in column LC1-2a for different scale factors

9.2.8.2 Automatic stabilization

In the adaptive automatic stabilization scheme available in Abaqus/Standard the amount of damping introduced into the model varies for each node of the model and depends on the 'dissipated energy fraction' (DEF), the convergence history and the accuracy tolerance (AT). The DEF is the ratio between the energy dissipated through artificial damping and the total strain energy in the first increment of the step. It is used by Abaqus/Standard to calculate the initial static stabilization damping factor. The DEF was set to 2×10^{-5} for all the models in which automatic stabilization was activated. The initial stabilization factor is automatically adjusted throughout the step based on the convergence history and the accuracy tolerance (AT). To ensure that the solution predicted by the model was not significantly altered by the artificial damping introduced through the automatic stabilization scheme, a suitable value of the AT was determined by carrying out a stabilization study, which included one representative column of each built-up geometry. In this study the AT was varied from zero (no artificial damping added to the model) to 8×10^{-3} .

The ultimate loads obtained for each built-up geometry, as well as the values given to the DEF and the AT are reported in Table 9.3, while Figure 9.12a, Figure 9.13a, Figure 9.14a and Figure 9.15a plot the ratio between the energy dissipated through artificial damping (ALLSD) and the total strain energy (ALLIE) for columns LC1, LC2, LC3 and LC4, respectively. The vertical dashed line shows the approximate axial deformation at which the column reached its ultimate capacity. The load-axial shortening curve obtained for the different values of the AT are shown in Figure 9.12b, Figure 9.13b, Figure 9.14b and Figure 9.15b for columns LC1, LC2, LC3 and LC4, respectively.

As previously mentioned, only the FE model of the column with geometry LC1 was able to converge without having to add artificial damping. For this geometry, the addition of artificial damping forces through the automatic stabilization scheme had a minimal effect on the ultimate capacity for the chosen range of AT values. For example, setting the AT equal to 2×10^{-3} resulted in an increase in the ultimate capacity of only 0.04 %, while the increase in the ultimate capacity as a result of setting the AT equal to 8×10^{-3} was only 0.33 %. Figure 9.12 shows that, for this geometry, artificial damping is introduced only at the beginning of the loading process, when the plate sections start buckling, and immediately after the peak load is reached. The ultimate capacity of the column with geometry LC4 also showed little sensitivity to the addition of artificial damping forces through the automatic stabilization scheme, with a maximum variation of 0.56 % over the chosen range of AT values. On the other hand, the ultimate capacity of the columns with geometries LC2 and LC3 showed a more noticeable sensitivity. For example, increasing the AT from 2×10^{-3} to 8×10^{-3} in the columns with geometries LC2 and LC3 resulted in an increase in the ultimate capacities of 7.67 % and 5.71 %, respectively. In these columns

artificial damping was introduced into the model shortly before the ultimate capacity was reached.

In section 9.2.8.1 it was shown that the ultimate capacities obtained from the FE models when the contact control mechanism was activated with a scale factor equal to 2×10^{-4} were almost identical to those obtained without adding artificial damping. Since for the columns with geometries LC2, LC3 and LC4 a converging solution could not be obtained without adding artificial damping to the FE model, for these columns the ultimate capacity obtained with a small scale factor of 2×10^{-4} was used as a reference to assess the effect of the automatic stabilization mechanism on the ultimate capacity of the column. This comparison showed that the increases in the ultimate capacities of the columns with geometries LC2, LC3 and LC4 obtained with the FE models in which the AT was set to 2×10^{-3} were 0.61 %, 1.83 % and 0.33 %, respectively. These errors were considered acceptable, given the great complexity of the models. Therefore, for all the built-up geometries presented in this chapter, those models requiring a second step with the automatic stabilization scheme activated in order to achieve a converging solution past the peak load were defined with an AT equal to 2×10^{-3} .

Table 9.3: Ultimate load comparison with automatic stabilization schemes

Specimen	Stabilization scheme	DEF	AT	Ult. Load (kN)
LC1-2a	No stabilization	-	-	74.95
	sc 0.002	2×10^{-5}	2×10^{-3}	74.98
	sc 0.005	2×10^{-5}	5×10^{-3}	75.02
	sc 0.008	2×10^{-5}	8×10^{-3}	75.20
LC2-2a	No stabilization	-	-	Divergence
	sc 0.002	2×10^{-5}	2×10^{-3}	154.33
	sc 0.005	2×10^{-5}	5×10^{-3}	160.39
	sc 0.008	2×10^{-5}	8×10^{-3}	166.17
LC3-2a	No stabilization	-	-	Divergence
	sc 0.002	2×10^{-5}	2×10^{-3}	118.23
	sc 0.005	2×10^{-5}	5×10^{-3}	120.47
	sc 0.008	2×10^{-5}	8×10^{-3}	124.98
LC4-2a	No stabilization	-	-	Divergence
	sc 0.002	2×10^{-5}	2×10^{-3}	113.12
	sc 0.005	2×10^{-5}	5×10^{-3}	113.37
	sc 0.008	2×10^{-5}	8×10^{-3}	113.76

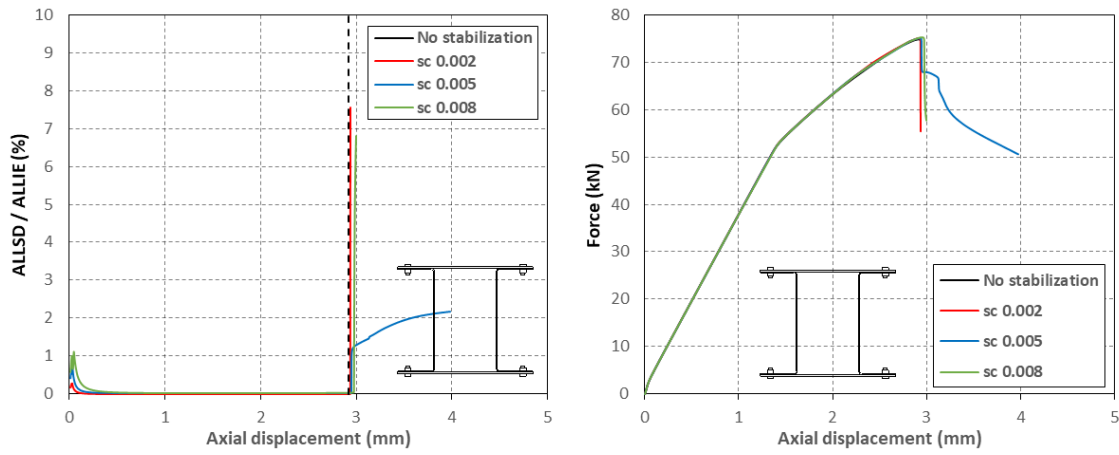


Figure 9.12: Automatic stabilization in columns LC1: a) Dissipated energy over total strain energy; b) Load-axial shortening curve

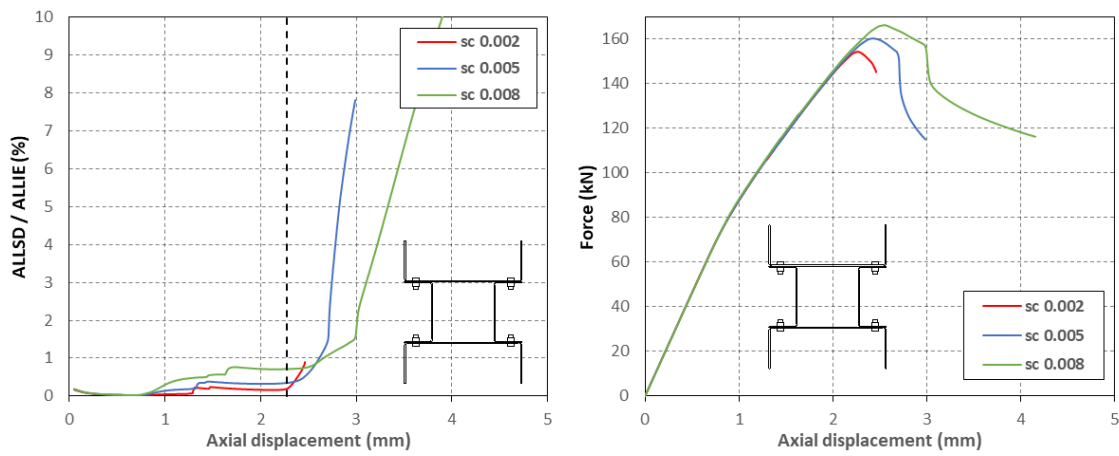


Figure 9.13: Automatic stabilization in columns LC2: a) Dissipated energy over total strain energy; b) Load-axial shortening curve

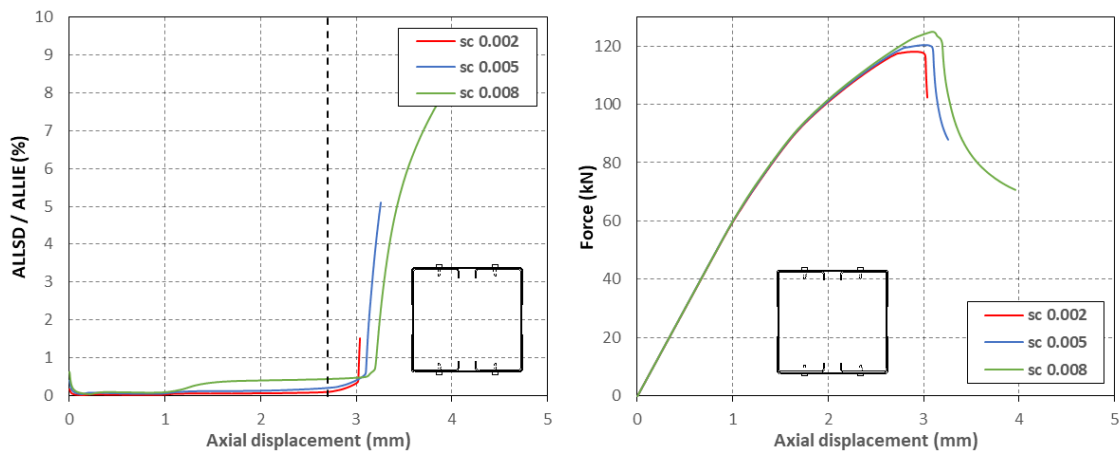


Figure 9.14: Automatic stabilization in columns LC3: a) Dissipated energy over total strain energy; b) Load-axial shortening curve

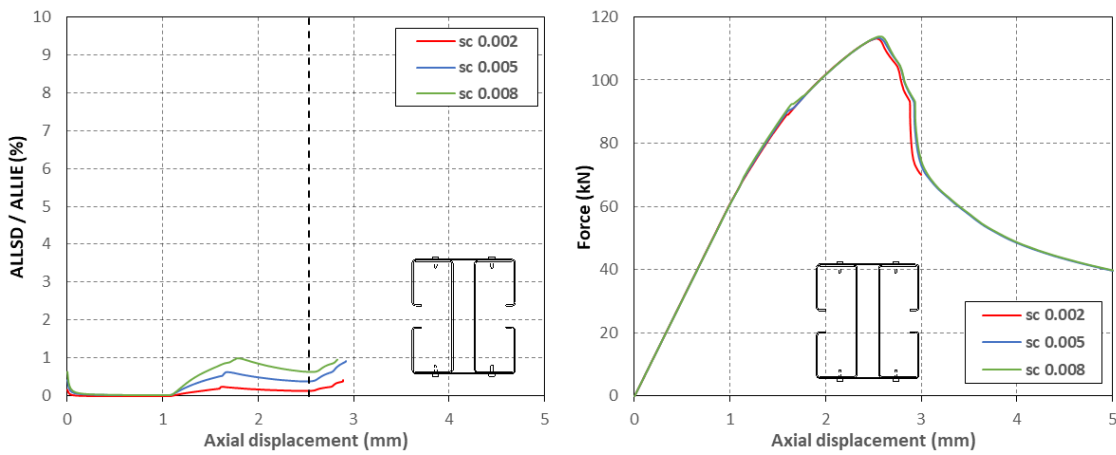


Figure 9.15: Automatic stabilization in columns LC4: a) Dissipated energy over total strain energy; b) Load-axial shortening curve

9.2.9 Mesh analysis

The long column models were developed using S4R elements with five integration points through the shell thickness. A mesh analysis was performed to determine a suitable mesh density, which does not require excessive computational time and does not compromise the accuracy of the solution. The study was carried out using one representative column of each of the geometries LC1, LC2 and LC3. Since geometries LC3 and LC4 were assembled using component sections with the same nominal dimensions, but arranged in a different configuration, the mesh density obtained for column LC3 was considered to also be applicable to columns LC4. The columns were modelled using the nominal cross-sectional dimensions of the components, representative initial geometric imperfections as measured on one of the tested columns, the non-linear material properties obtained from the tensile coupons, and while modelling the connectors using HINGE connector elements. For geometries LC1 and LC3, the columns chosen for the mesh study had a 3 m length and eight intermediate sets of connectors, while for geometry LC2 the chosen column had a length of 2.5 m and six intermediate sets of connectors. Both the total CPU time required to run the analysis and the peak load were considered as criteria in the study.

Four different mesh densities were included for each built-up geometry. The size of the elements in the flanges and the web of the channels, as well as in the plate section of LC1 was chosen to be as uniform as possible. The aspect ratio of these elements was kept below 2, following the recommendations given by Schafer (1997). The number of elements across the corner region of the channels was varied from two to four. The aspect ratio of the elements located in these regions was limited to less than 4 (rather than 2) in order to avoid an overly dense mesh. In the lipped channels, two elements were used across the lips in all the studied meshes.

Table 9.4, Table 9.6 and Table 9.8 show the number of elements and nodes used in the different mesh configurations for columns LC1, LC2 and LC3, respectively, while Table 9.5, Table 9.7 and Table 9.9 show the aspect ratios of the meshes studied.

Table 9.4: Mesh configuration for column LC1

Mesh	N of elements						N of nodes
	Channel			Plate	column	Total	
	Flange	Web	Corner	Width	Length		
Mesh 1	2	7	2	9	214	10272	11180
Mesh 2	4	14	2	18	214	18832	19780
Mesh 3	6	21	4	27	429	58344	60200
Mesh 4	7	28	4	36	429	73788	75680

Table 9.5: Mesh aspect ratio in column LC1

Mesh	Aspect ratio			
	Channels			Plates
	Flange	Web	Corner	Width
Mesh 1	0.903	0.817	4.000	0.841
Mesh 2	1.805	1.634	4.000	1.682
Mesh 3	1.351	1.223	4.000	1.259
Mesh 4	1.576	1.630	4.000	1.678

Table 9.6: Mesh configuration for columns LC2

Mesh	N of elements							N of nodes	
	Inner Channel			Outer Channel			column		Total
	Flange	Web	Corner	Flange	Web	Corner	Length		
Mesh 1	1	3	2	2	6	2	179	8234	9000
Mesh 2	3	6	2	4	12	2	179	14320	15120
Mesh 3	5	10	4	7	22	4	358	51552	53132
Mesh 4	7	15	4	10	30	4	358	68020	69646

Table 9.7: : Mesh aspect ratio in columns LC2

Mesh	Aspect ratio					
	Inner Channels			Outer Channels		
	Flange	Web	Corner	Flange	Web	Corner
Mesh 1	0.436	0.606	4.000	0.569	0.581	0.436
Mesh 2	1.307	1.213	4.000	1.139	1.163	1.307
Mesh 3	1.089	1.010	4.000	0.996	1.066	1.089
Mesh 4	1.525	1.516	4.000	1.423	1.454	1.525

Table 9.8: Mesh configuration for column LC3

Mesh	N of elements								N of nodes	
	Plain Channel			Lipped Channel				column		Total
	Flange	Web	Corner	Flange	Web	Lip	Corner	Length		
Mesh 1	2	4	2	2	4	2	2	205	13120	14008
Mesh 2	3	9	2	3	8	2	2	205	18450	19364
Mesh 3	4	13	4	5	12	2	4	416	59072	60882
Mesh 4	6	19	4	7	17	2	4	416	74880	76728

Table 9.9: Mesh aspect ratio in columns LC3

Mesh	Aspect ratio						
	Plain Channels			Lipped Channels			
	Flange	Web	Corner	Flange	Web	Lip	Corner
Mesh 1	0.831	0.530	4.000	0.726	0.583	5.672	4.000
Mesh 2	1.247	1.193	4.000	1.089	1.167	5.672	4.000
Mesh 3	0.819	0.849	4.000	0.895	0.863	2.795	4.000
Mesh 4	1.229	1.241	4.000	1.252	1.222	2.795	4.000

9.2.9.1 Mesh analysis results

The ultimate load and the CPU time required to complete the simulation for the different mesh configurations considered in the mesh study are listed in Table 9.10, Table 9.11 and Table 9.12 for columns LC1, LC2 and LC3, respectively. The tables also show the total number of increments Abaqus/Standard needed to complete the simulation and the average CPU time required for each increment. The CPU times listed in brackets correspond to simulations in which, although the peak load was reached, the analyses were not completed.

Table 9.10: Effect of the mesh size on the ultimate load and total CPU time for columns LC1

Element type	Mesh	Ultimate Load (kN)	Total CPU time (s)	N of increments	CPU time per increment (s)
S4R	Mesh 1	88.88	7957	148	54
	Mesh 2	89.86	14208	151	94
	Mesh 3	87.34	45171	133	340
	Mesh 4	87.31	115862	133	871

Table 9.11: Effect of the mesh size on the ultimate load and total CPU time for columns LC2

Element type	Mesh	Ultimate Load (kN)	Total CPU time (s)	N of increments	CPU time per increment (s)
S4R	Mesh 1	144.63	3045	42	72
	Mesh 2	146.81	6437	64	101
	Mesh 3	146.10	19655	86	229
	Mesh 4	146.08	62718	95	660

Table 9.12: Effect of the mesh size on the ultimate load and total CPU time for columns LC3

Element type	Mesh	Ultimate Load (kN)	Total CPU time (s)	N of increments	CPU time per increment (s)
S4R	Mesh 1	142.86	31069	514	60
	Mesh 2	135.60	39300	443	89
	Mesh 3	136.59	163200	446	366
	Mesh 4	135.69	(242942)	433	561

The ultimate load and the CPU time per increment are plotted, for each mesh configuration, against the number of nodes in Figure 9.16, Figure 9.17 and Figure 9.18 for columns LC1, LC2 and LC3, respectively. The figures show that, for all geometries considered, the ultimate load predictions obtained with Mesh 3 are relatively close to the predictions obtained with the finest

mesh (Mesh 4). For column LC1, the difference between the ultimate load predicted with these mesh configurations was 0.04 %, while for columns LC2 and LC3 the differences were 0.02 % and 0.66 %, respectively. This range of accuracy was considered satisfactory given the complexity of the models and all the models were meshed using a Mesh 3 configuration.

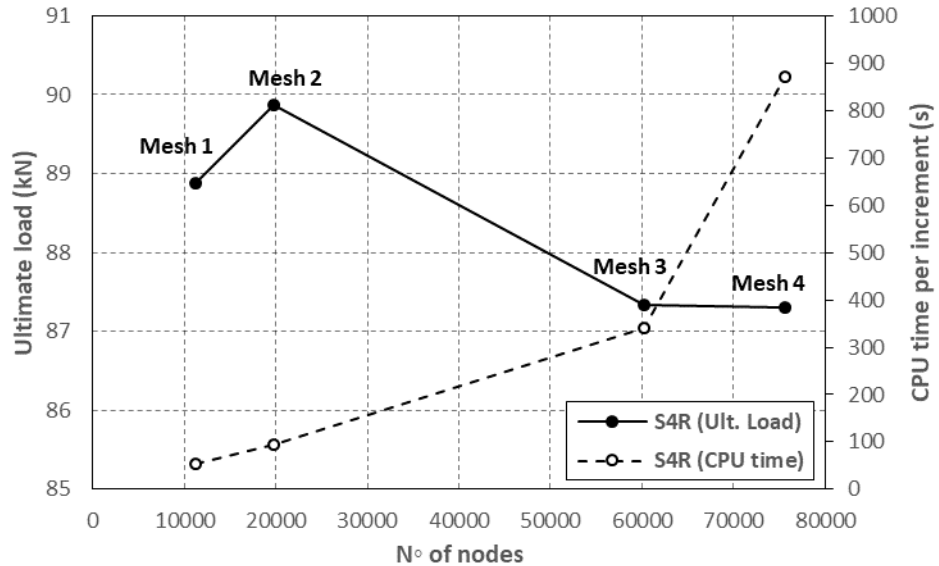


Figure 9.16: Effect of mesh size on the ultimate load and total CPU time for columns LC1

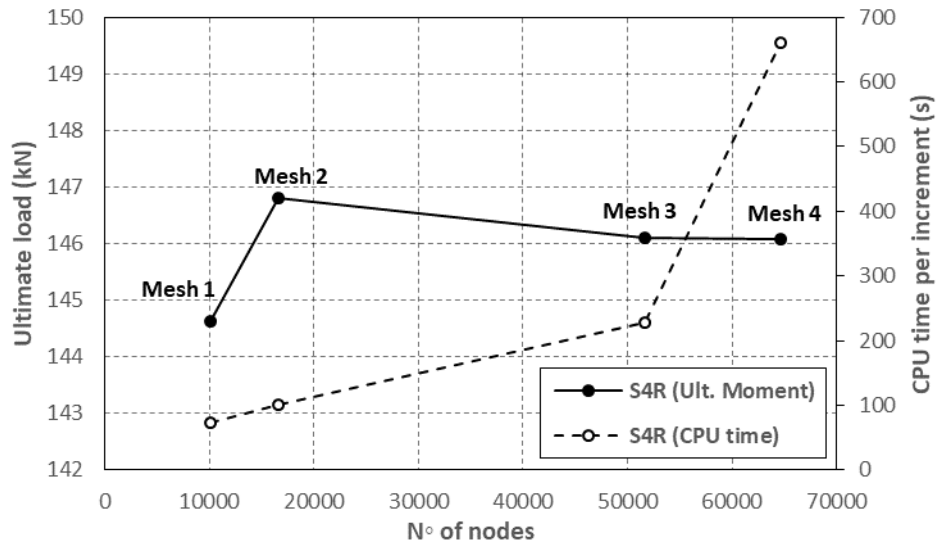


Figure 9.17 Effect of mesh size on the ultimate load and total CPU time for columns LC2

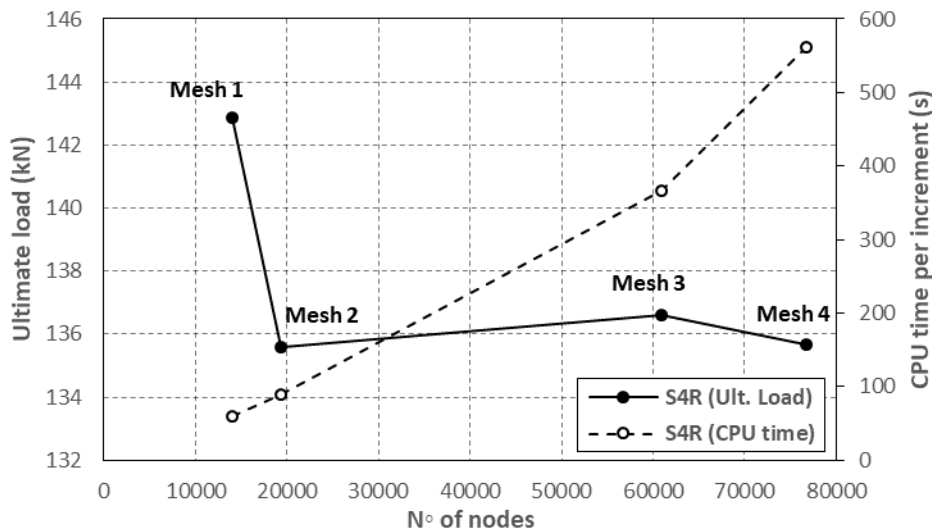


Figure 9.18: Effect of mesh size on the ultimate load and total CPU time for columns LC3

9.3. FE model verification

9.3.1 Ultimate load

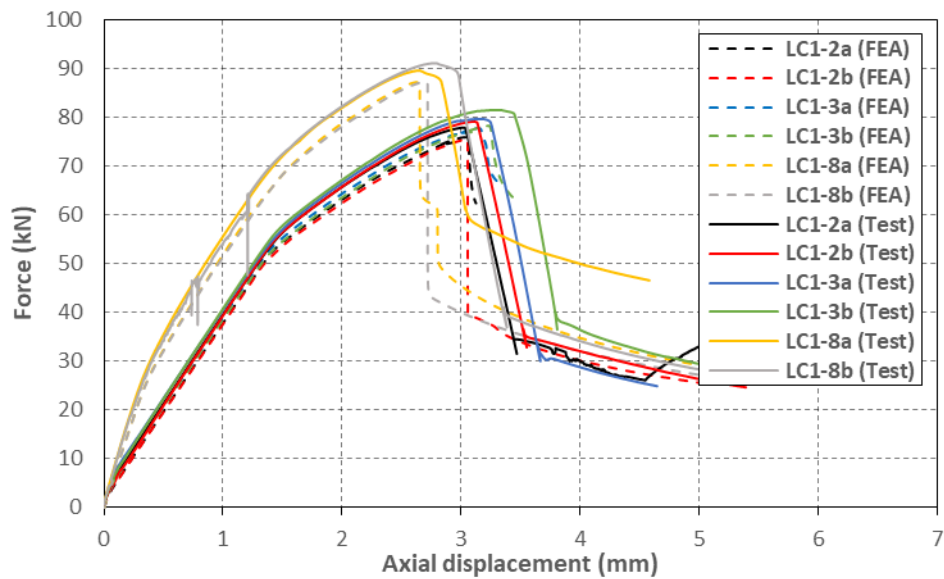
Table 9.13, Table 9.14, Table 9.15 and Table 9.16 compare the ultimate loads predicted by the FE models with those obtained from the tests for columns LC1, LC2, LC3 and LC4, respectively. The tables also show the stabilization scheme which was used to achieve the numerical solution.

For columns LC1 and LC2, Table 9.13 and Table 9.14 show that the ultimate loads predicted by the FE models were consistently lower than those obtained from the tests. For columns LC1 the numerical ultimate loads were, on average, 3.4 % lower than the experimental ones, while for columns LC2 the numerical predictions were, on average, 5.5 % lower. A better agreement was achieved between the numerical and experimental ultimate loads of columns LC3 and LC4, as shown in Table 9.15 and Table 9.16. For columns LC3, the average difference between the numerical and experimental ultimate loads was 1.3 %, while for columns LC4 the average difference was 2.6 %. Excluding columns LC1-2, the numerical models agreed with the test results in predicting larger ultimate capacities for the columns tested with a load eccentricity of $L/1500$ compared to those tested with a load eccentricity of $L/1000$.

The load vs. axial shortening curves predicted by the FE models and those obtained from the experiments are shown in Figure 9.19, Figure 9.20, Figure 9.21 and Figure 9.22 for columns LC1, LC2, LC3, and LC4, respectively. The figures show that the FE models were able to accurately replicate the initial stiffness as well as the post-buckling stiffness of the column for all the geometries studied.

Table 9.13: Numerical and experimental ultimate loads of columns LC1

Specimen	Test ult. load (kN)	FEA ult. load (kN)	FEA/Test	Stabilization scheme	
				Step 1	Step 2
LC1-2a	77.94	75.98	0.975	None	sc 0.002
LC1-2b	79.18	75.57	0.954	sc 0.002	-
LC1-3a	79.73	77.85	0.976	None	sc 0.002
LC1-3b	81.57	78.32	0.960	None	sc 0.002
LC1-8a	89.66	87.28	0.973	cc 0.0001	-
LC1-8b	91.17	87.34	0.958	cc 0.0001	-
Avg.			0.966		
St. dev.			0.010		

**Figure 9.19: Numerical and experimental load vs. axial shortening curves of columns LC1****Table 9.14: Numerical and experimental ultimate loads of columns LC2**

Specimen	Test ult. load (kN)	FEA ult. load (kN)	FEA/Test	Stabilization scheme	
				Step 1	Step 2
LC2-2a	160.90	153.27	0.953	cc 0.0002	-
LC2-2b	171.82	157.47	0.916	cc 0.0002	-
LC2-6a	165.15	157.39	0.953	cc 0.0002	-
LC2-6b	166.88	159.93	0.958	cc 0.0002	-
LC2-4a	-	161.35	-	cc 0.0002	-
LC2-4b	-	164.83	-	cc 0.0002	-
Avg.			0.945		
St. dev.			0.019		

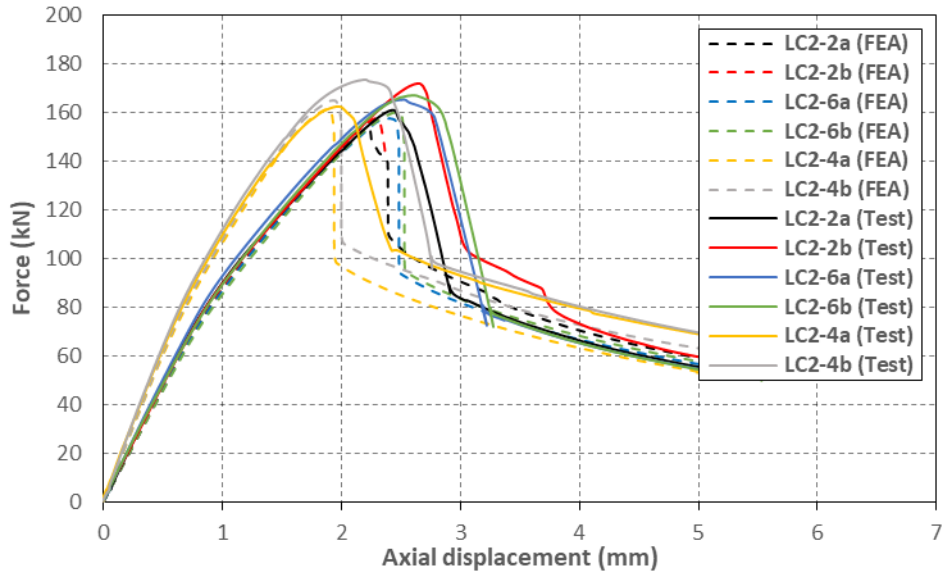


Figure 9.20: Numerical and experimental load vs. axial shortening curves of columns LC2

Table 9.15: Numerical and experimental ultimate loads of columns LC3

Specimen	Test ult. load (kN)	FEA ult. load (kN)	FEA/Test	Stabilization scheme	
				Step 1	Step 2
LC3-2a	119.04	116.15	0.976	cc 0.0002	-
LC3-2b	123.48	123.40	0.999	cc 0.0002	sc 0.002
LC3-3a	118.88	118.48	0.997	cc 0.0002	-
LC3-3b	122.94	121.26	0.986	cc 0.0002	-
LC3-8a	120.22	122.52	1.019	cc 0.0002	sc 0.002
LC3-8b	-	123.99	-	cc 0.0002	-
Avg.			0.995		
St. dev.			0.016		

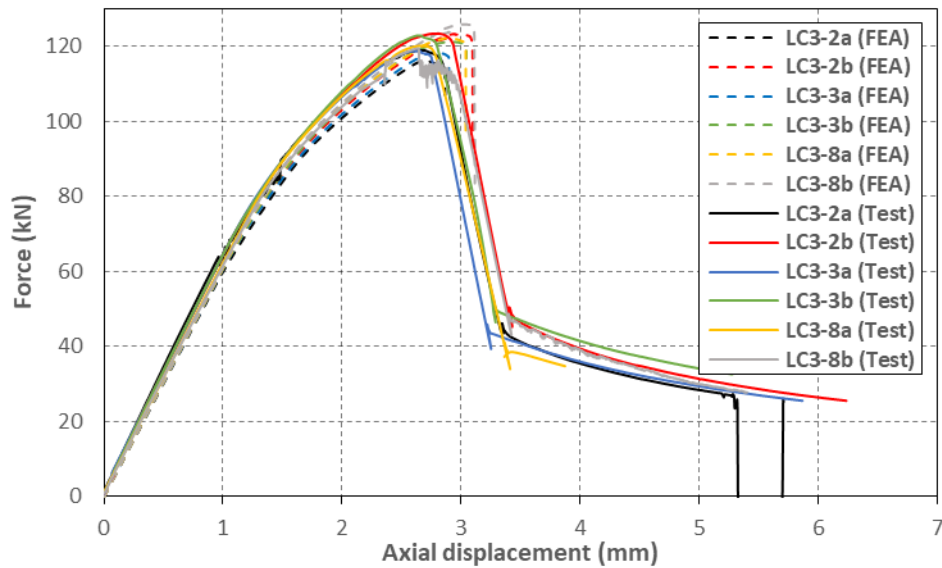
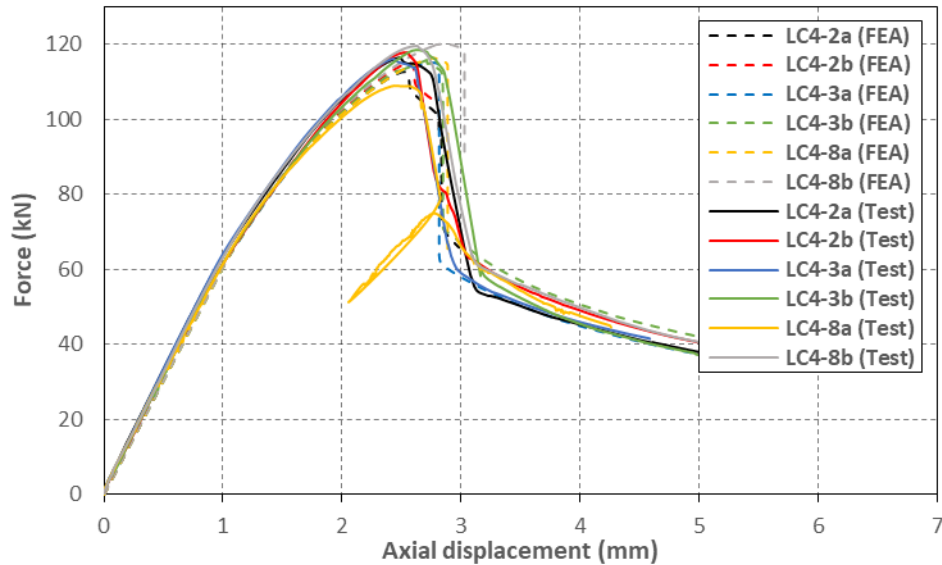


Figure 9.21: Numerical and experimental load vs. axial shortening curves of columns LC3

Table 9.16: Numerical and experimental ultimate loads of columns LC4

	Test ult. load (kN)	FEA ult. load (kN)	FEA/Test	Stabilization scheme	
				Step 1	Step 2
LC4-2a	116.53	112.76	0.968	cc 0.0002	-
LC4-2b	117.90	115.04	0.976	cc 0.0002	-
LC4-3a	116.19	113.70	0.979	cc 0.0002	-
LC4-3b	118.57	115.97	0.978	cc 0.0002	sc 0.002
LC4-8a	109.06	117.34	1.076	cc 0.0002	sc 0.002
LC4-8b	119.65	120.13	1.004	cc 0.0002	sc 0.002
Avg.			0.997		
St. dev.			0.041		

**Figure 9.22: Numerical and experimental load vs. axial shortening curves of columns LC4**

9.3.2 Deformed shape

In general, the FE models were able to accurately replicate the initial buckled shape of the tested columns, while for most columns the failure mode and yield line mechanism observed in the experiments also agreed well with those predicted by the FE models. However, the plastic deformations predicted by the FE models often concentrated in a location different from the one observed in the tested columns.

For columns LC1, the experiments showed that the channels buckled in a local mode with 22 half-waves, irrespective of the number of connectors along the column, while the plate sections buckled outward in each field in columns LC1-2 and LC1-3. This was accurately replicated by the FE models, as shown in Figure 9.23a and Figure 9.23b for columns LC1-2a and LC1-3a, respectively. For columns LC1-8 (the columns with eight intermediate sets of connectors) the experiments showed that the plate sections initially buckled in every other field, while remaining straight in the adjacent fields. In the corresponding FE model, however, the plate sections only remained unbuckled in two fields along the column, as shown in Figure 9.23c.

The experiments also showed that in columns LC1-2 failure was triggered by flexural-torsional buckling of the channels between connectors, which interacted with local buckling of the channels, global-type flexural buckling of the plates between connectors and flexural buckling of the whole built-up geometry. This type of failure could only be accurately replicated by the FE models in column LC1-2b, which was tested with a load eccentricity of $L/1500$ (Figure 9.24b). For column LC1-2a, which was tested with a load eccentricity of $L/1000$, the FE models only predicted a minor participation of flexural-torsional buckling of the channels between connectors, as shown in Figure 9.24a. In column LC1-3b the channels were also seen experimentally to fail due to buckling interaction involving flexural-torsional buckling between connectors, with both channels deforming in a point-symmetric pattern relative to each other. However, the corresponding FE model predicted the channels to fail predominantly due to interaction between local buckling and global flexural buckling of the built-up column, as shown in Figure 9.25a. Columns LC1-3a and LC1-8 failed experimentally due to interaction between local buckling of the channels, global-type flexural buckling of the plates between connectors and global flexural buckling of the built-up specimen. The failure mode of these columns was accurately replicated by the FE models, as shown in Figure 9.25b for column LC1-8b.

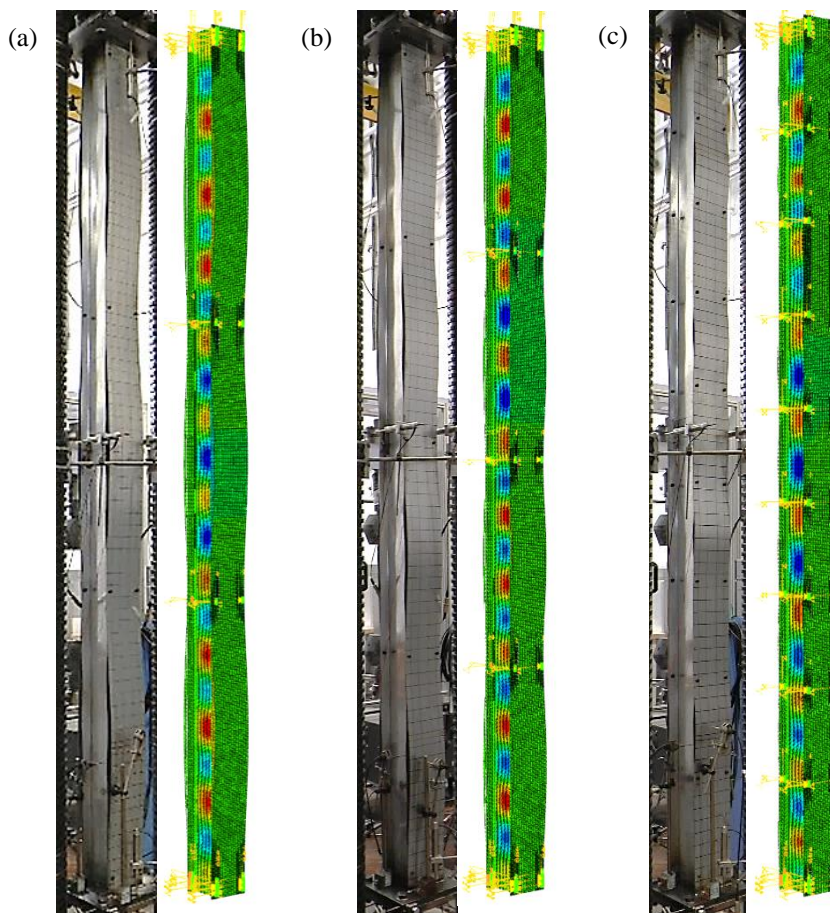


Figure 9.23: Comparison of the buckled shape: a) LC1-2a; b) LC1-3a; c) LC1-8a

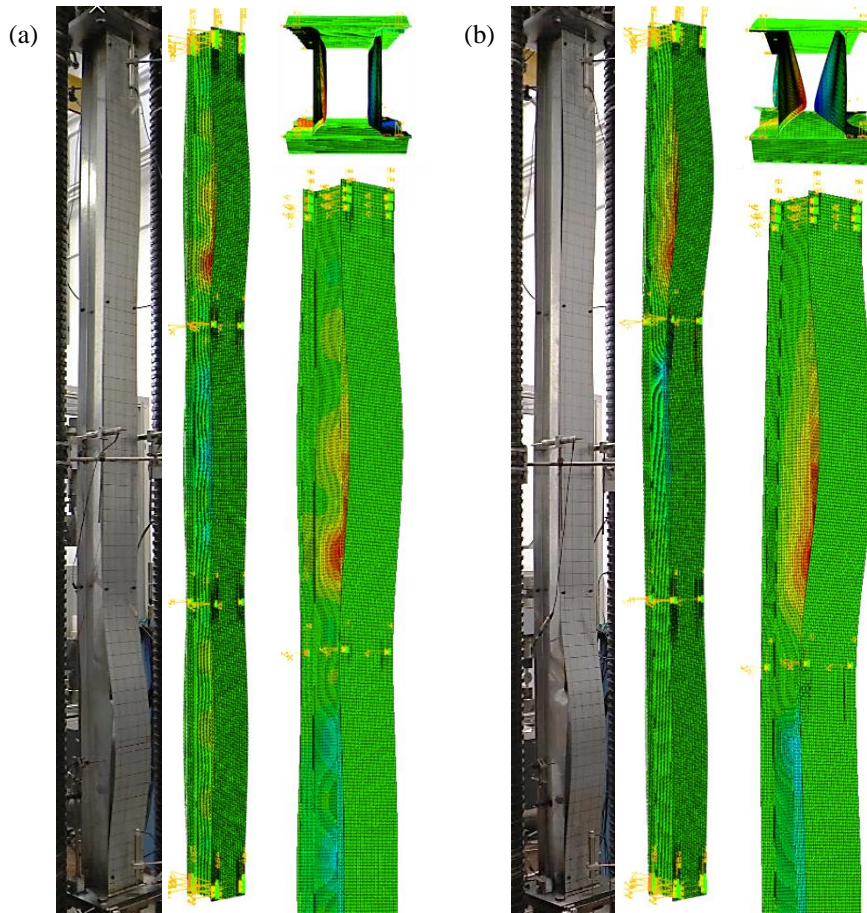


Figure 9.24: Comparison of localized plastic deformations: a) LC1-2a; b) LC1-2b

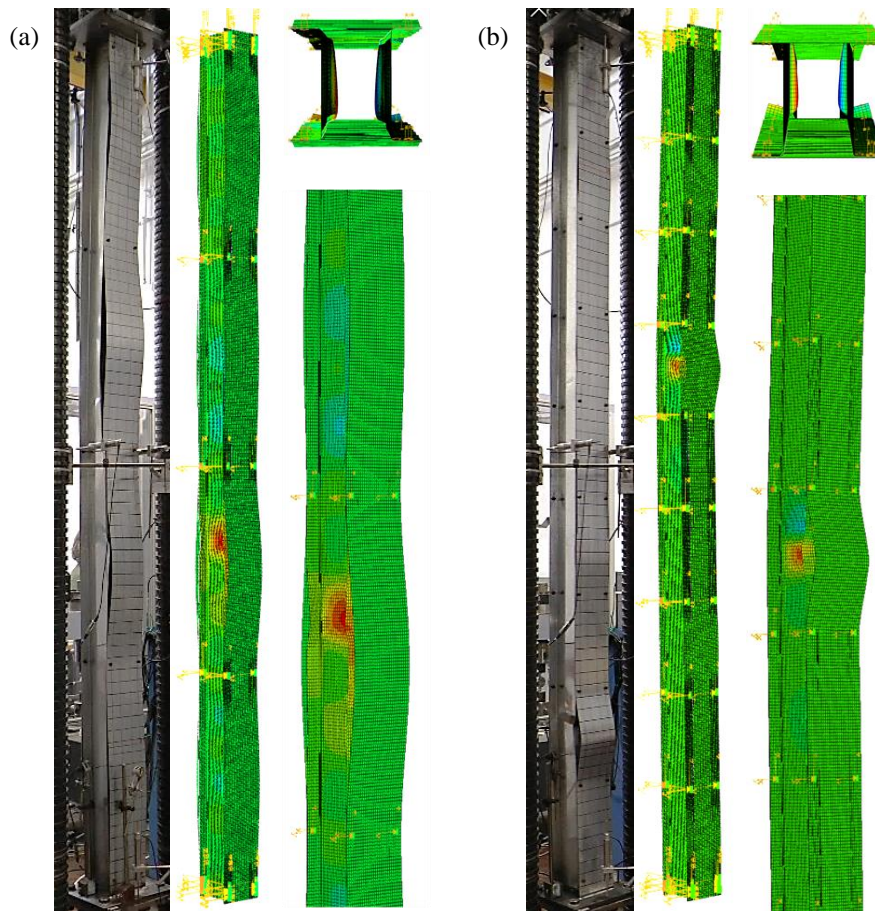


Figure 9.25: Comparison of localized plastic deformations: a) LC1-3b; b) LC1-8b

With respect to columns LC2, the FE models predicted less buckles in the outer channels of column LC2-2 than the number observed in the tested columns, as shown in Figure 9.26a for column LC2-2b. This was due to the fact that in the tested columns with geometry LC2 the flanges of the outer channels were significantly distorted at each end of the column due to the welding of the endplates, as described in Section 5.5 of Chapter 5. These distortions, which were not included in the FE models, resulted in buckles with a smaller half-wave length at each end of the column and therefore the outer channels in the tested columns were able to accommodate one or two additional buckles. In columns LC2-6 and LC2-4, the outer channels buckled with two half-waves between connectors in both the FE model and the tested column, as shown in Figure 9.26b and Figure 9.26c for columns LC2-6a and LC2-4a, respectively. The FE models only predicted some minor local buckling in the inner channels of columns LC2-6 and LC2-4 shortly before the ultimate load was reached, consistent with the experiments.

Figure 9.27 compares the yield line mechanisms which were observed during the experiments in columns LC2-2b and LC2-6b with those predicted by the FE models.

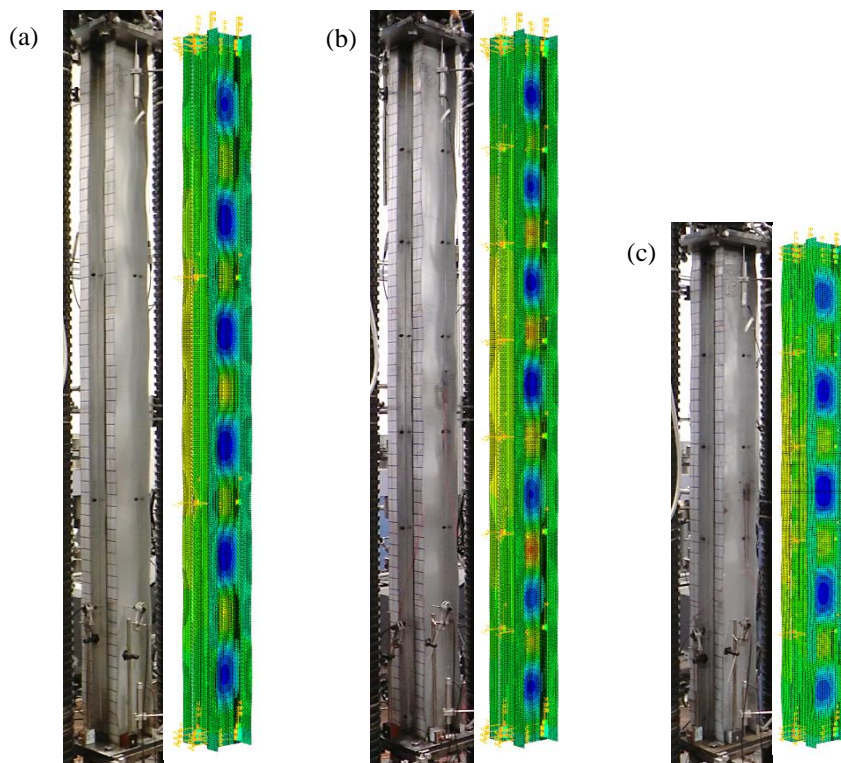


Figure 9.26: Comparison of the buckled shape: a) LC2-2b; b) LC2-6a; c) LC2-4a

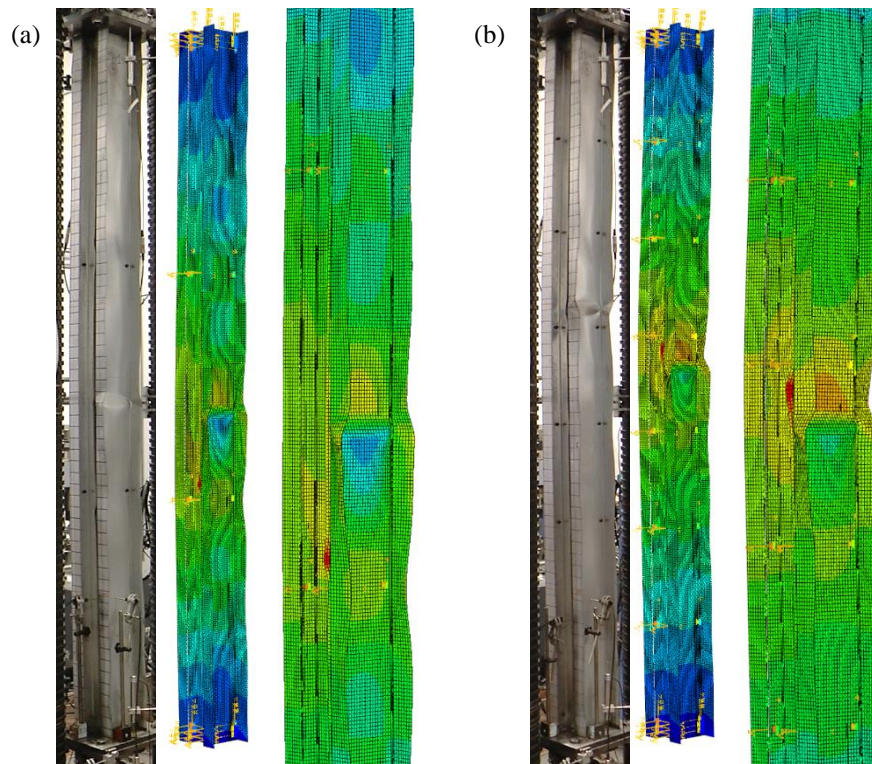


Figure 9.27: Comparison of localized plastic deformations: a) LC2-2b; b) LC2-6b

In the columns with geometry LC3 the plain channels were experimentally observed to buckle with eight half-waves between connector points in columns LC3-2, six in columns LC3-3 and between two and four in columns LC3-8, while the cross-sections containing connectors were always seen to fall within a concave buckle. The lipped channels, on the other hand, were seen to buckle in a local mode with between 10 and 12 half-waves between connectors in columns LC3-2, eight half-waves between connectors in columns LC3-3 and between two and four half-waves between connectors in columns LC3-8. These buckling patterns were accurately replicated by the FE models, as shown in Figure 9.28.

Figure 9.29 compares the yield line mechanisms observed during the experiments in columns LC3-2a and LC3-8a with those predicted by the FE models.

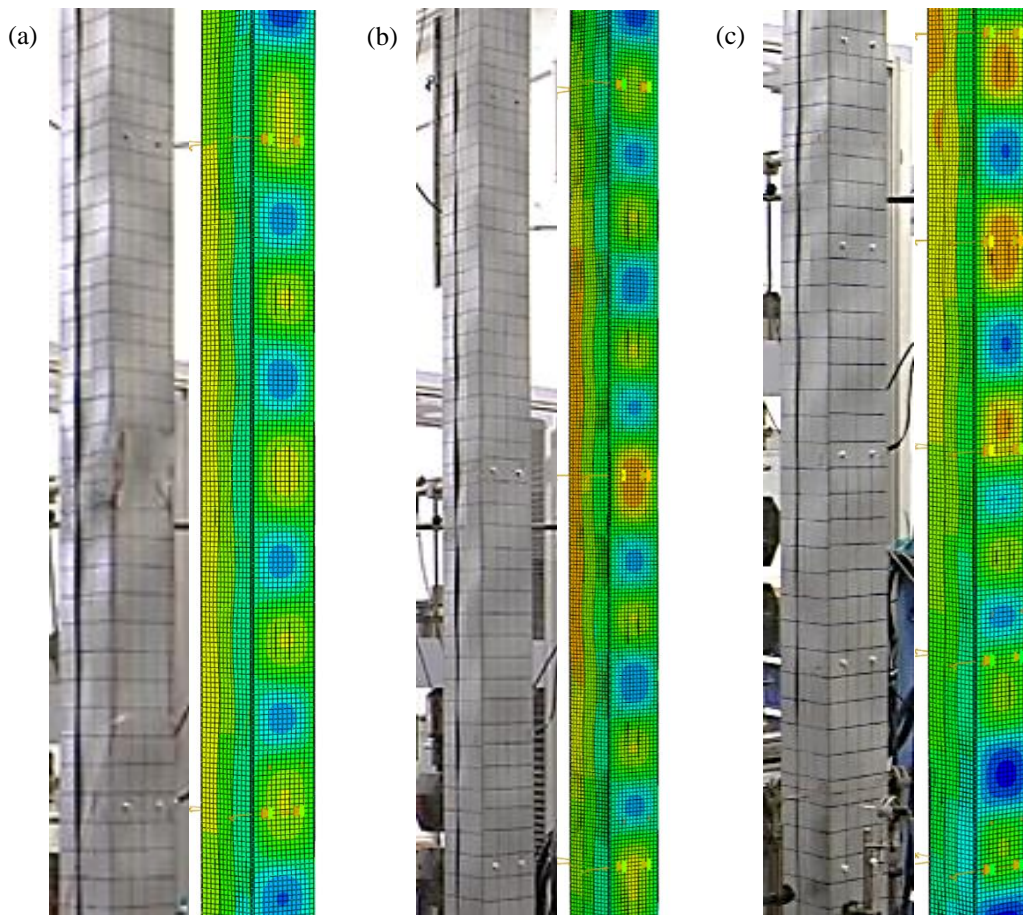


Figure 9.28: Comparison of the buckled shape: a) LC3-2a; b) LC3-3b; c) LC3-8b

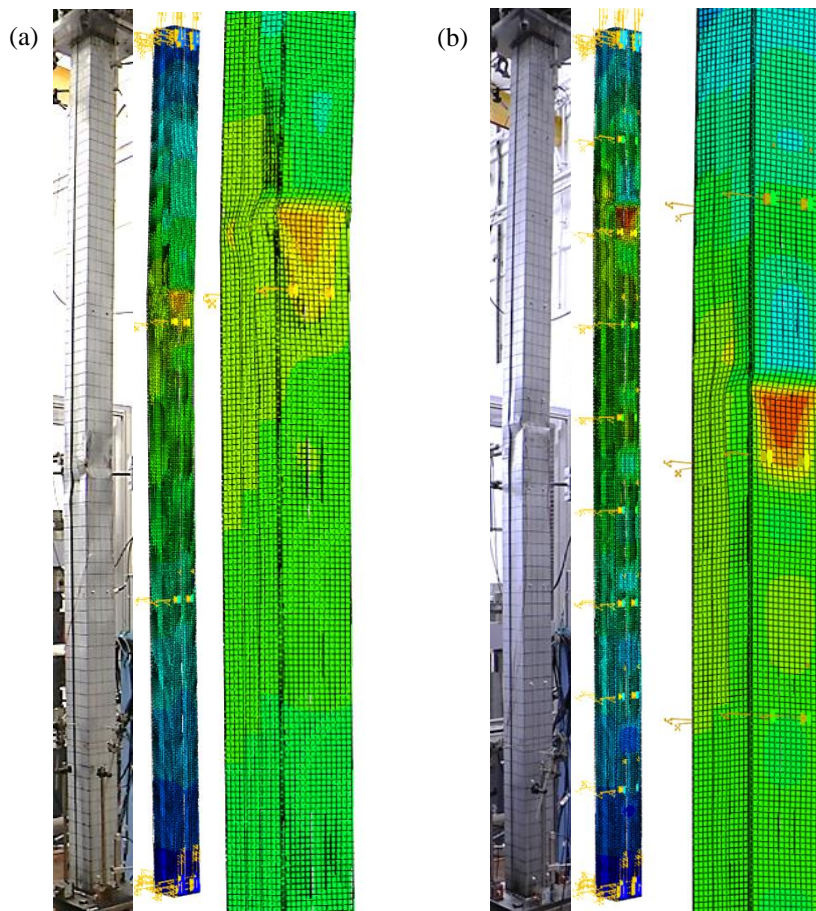


Figure 9.29: Comparison of localized plastic deformations: a) LC3-2a; b) LC3-8a

The FE models were also able to accurately replicate the buckled shape of the lipped channels in columns LC4. The buckled shape of the plain channels of columns LC4 could not be observed in the experiments and was therefore not compared. Consistent with the experiments, the lipped channels in the FE models buckled with a half-wave length which ranged from 80 to 90 mm and the cross-sections containing connectors fell inside a concave buckle. The lipped channels buckled with between 10 and 12 half-waves between connectors in columns LC4-2, between eight and ten half-waves between connectors in columns LC4-3 and four half-waves between connectors in columns LC4-8, as shown in Figure 9.30.

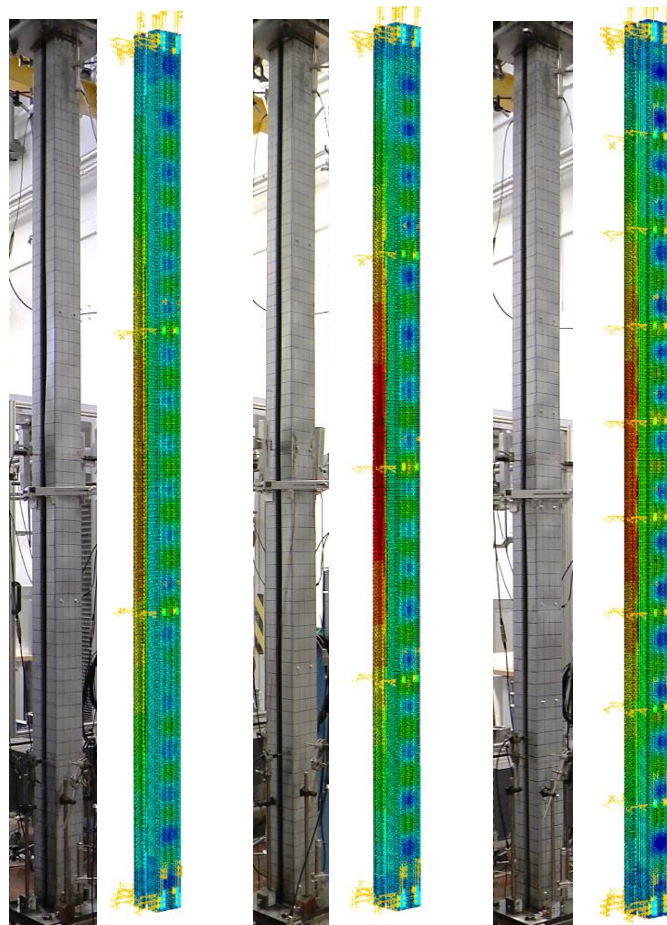


Figure 9.30: Comparison of the buckled shape: a) LC4-2a; b) LC4-3b; c) LC4-8b

Similarly to what was observed in the experiments, the FE models revealed that distortional buckling of the lipped channels only had a minor participation before the ultimate capacity of the column was reached. However, the participation predicted by the FE models was even less significant. Figure 9.31 shows the deformed shape of the lipped channel located on the compression side of the built-up geometry when the load in the column was around 90 % of the ultimate capacity for all the columns with geometry LC4.

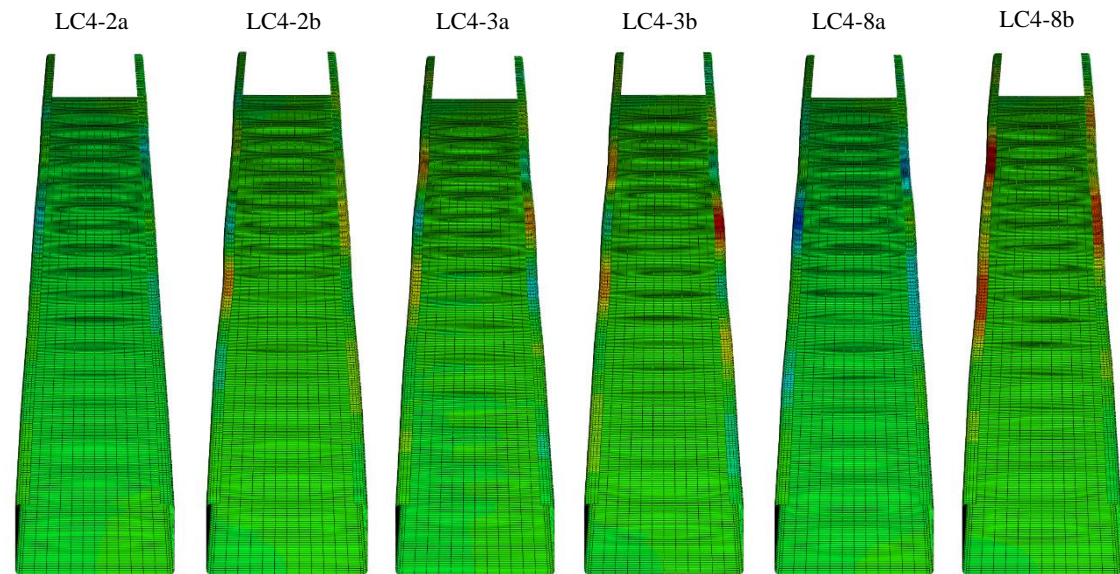


Figure 9.31: Deformed shape of lipped channel on compression side

A comparison between the yield line mechanisms observed during the experiments and those predicted by the FE models is shown in Figure 9.32 for columns LC4-2b, LC4-3b and LC4-8b.

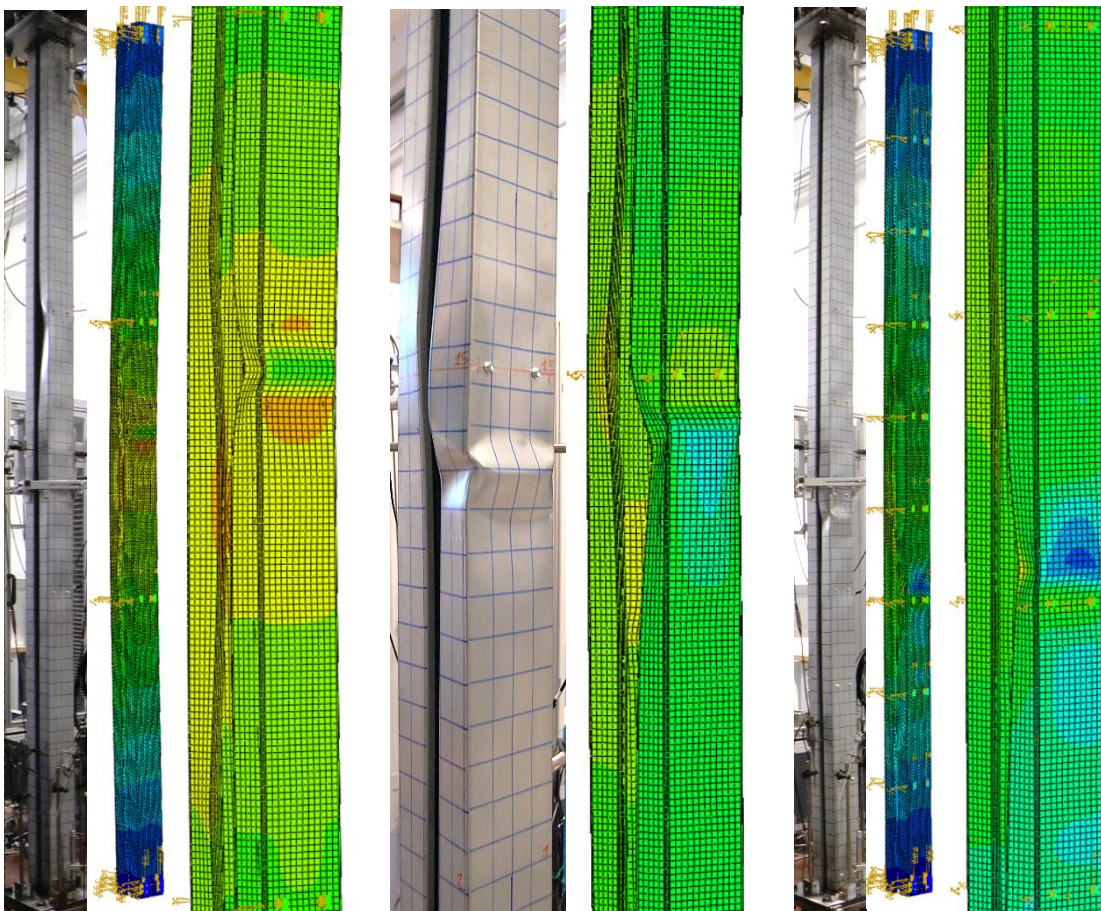


Figure 9.32: Comparison of localized plastic deformations: a) LC4-2b; b) LC4-3b; c) LC4-8b

9.3.3 Critical buckling stresses

The out-of-plane buckling deformations of the different components of the tested columns were recorded in the experiments using four potentiometers located near the bottom end of the column, as shown in Figures 9.23-9.32. These out-of-plane deformations were also extracted from the FE models at the corresponding locations and a comparison is presented in Figure 9.33, Figure 9.34, Figure 9.35 and Figure 9.36 for a representative column with geometry LC1, LC2, LC3 and LC4, respectively. Curves comparing the experimental and numerical out-of-plane deformations for each tested column are included in Appendix N.

The experimental and numerical critical buckling stresses of the components of each tested column were derived from the load vs. out-of-plane displacement curves using the same assumptions described in Section 5.8.3 of Chapter 5, and are reported in Table 9.17, Table 9.18, Table 9.19 and Table 9.20 for the columns with geometries LC1, LC2, LC3 and LC4, respectively.

Figures 9.33-9.36 show that, similarly to what was observed in the experiments, the FE models predicted that in most columns the component located on the side of the built-up specimen where global flexural buckling introduced additional compressive stresses buckled before the twin component located on the opposite side. Therefore the critical buckling stress was taken as the average value.

Table 9.17 shows that for columns LC1, the average difference between the experimentally derived critical buckling stresses and those obtained from the FE models was around 20.8 % for the plates and 4.2 % for the channel sections. The relatively large difference between the experimental and numerical buckling stresses calculated for the plate sections is due to the fact that in columns LC1-2 and LC1-3 the plates buckled at very low stresses. In absolute value the average difference is only 2 MPa. The critical buckling stresses obtained from the FE models for the channel sections were, on average, 5 % larger than the natural local buckling stress of the channel considered in isolation. For columns LC2, Table 9.18 shows that, on average, the numerically derived critical buckling stresses of the outer channels were 12.6 % lower than the experimentally derived ones and were, on average, 9 % larger than the natural local buckling stress of outer channel considered in isolation. Table 9.19 also shows that the average difference between the experimental and numerical buckling stresses in the plain channels of columns LC3 was 13.0 %, with the largest difference (25.5 %) obtained for columns LC3-8. For columns LC3-2 and LC3-3 the average difference was only 6.8 %. For columns LC4, Table 9.20 shows that the average difference between the experimentally and numerically derived critical buckling stresses of the plain channels was 8.3 %. The critical buckling stresses obtained from the FE models for columns LC3 and LC4 were, on average, 14 % larger than the natural local buckling stress of the channel considered in isolation.

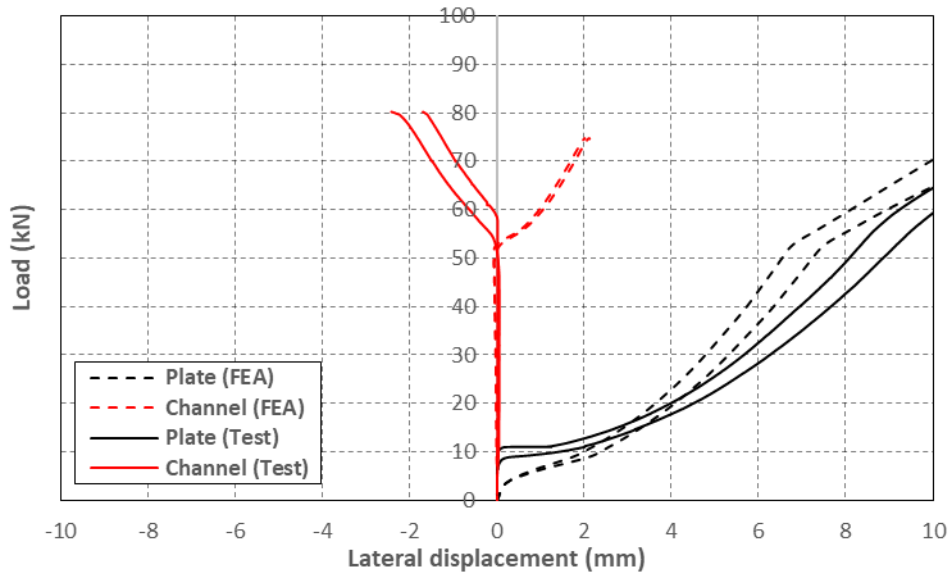


Figure 9.33: Experimental and numerical axial load vs lateral displacement curves of LC1-3a

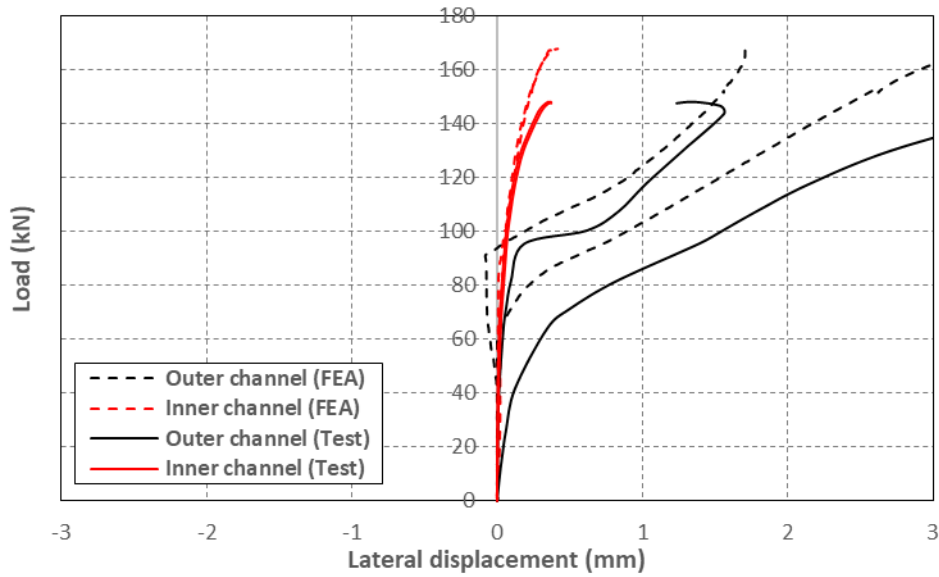


Figure 9.34: Experimental and numerical axial load vs lateral displacement curves of LC2-6b

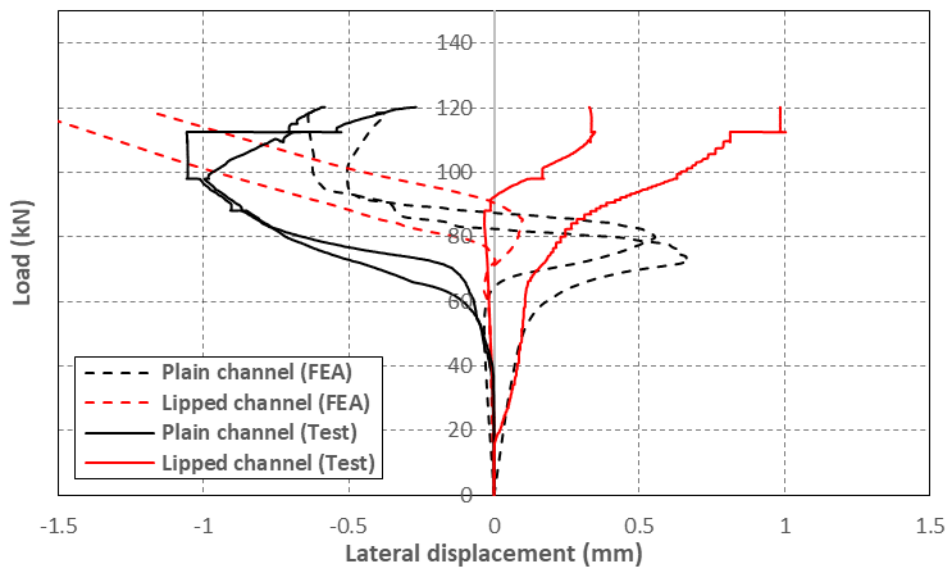


Figure 9.35: Experimental and numerical axial load vs lateral displacement curves of LC3-3a

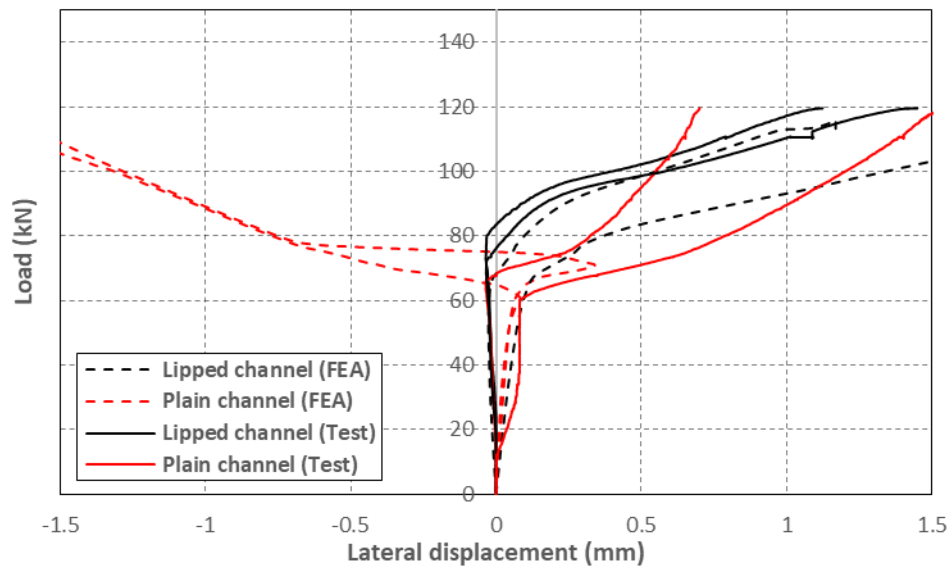


Figure 9.36: Experimental and numerical axial load vs lateral displacement curves of LC4-3b

Table 9.17: Numerical and experimental buckling stresses of the components of columns LC1

Column	Buckling stress from test (MPa)		Buckling stress from FEA (MPa)	
	Channel	Plate	Channel	Plate
LC1-2a	99	6	97	3
LC1-2b	98	5	90	5
LC1-3a	97	8	93	6
LC1-3b	101	8	95	4
LC1-8a	100	23	102	23
LC1-8b	106	23	103	23

Table 9.18: Numerical and experimental buckling stresses of the components of columns LC2

Column	Buckling stress from test (MPa)		Buckling stress from FEA (MPa)	
	Inner Channel	Outer Channel	Inner Channel	Outer Channel
LC2-2a	-	83	-	66
LC2-2b	-	77	-	62
LC2-6a	-	74	-	68
LC2-6b	-	78	-	76
LC2-4a	-	83	-	70
LC2-4b	-	76	-	69

Table 9.19: Numerical and experimental buckling stresses of the components of columns LC3

Column	Buckling stress from test (MPa)		Buckling stress from FEA (MPa)	
	Plain Channel	Lipped Channel	Plain Channel	Lipped Channel
LC3-2a	82	-	69	-
LC3-2b	83	-	78	-
LC3-3a	74	-	73	-
LC3-3b	79	-	76	-
LC3-8a	82-105	99	68	-
LC3-8b	88-109	109	75	-

Table 9.20: Numerical and experimental buckling stresses of the components of columns LC4

Column	Buckling stress from test (MPa)		Buckling stress from FEA (MPa)	
	Plain Channel	Lipped Channel	Plain Channel	Lipped Channel
LC4-2a	74	-	68	-
LC4-2b	63	-	68	-
LC4-3a	78	-	70	-
LC4-3b	73	-	73	-
LC4-8a	63-85	-	72	-
LC4-8b	67	-	81	-

9.4. Parametric study

9.4.1 Effect of fastener modelling

Additional FE models were created of the built-up columns presented in Chapter 5, in which the connector behaviour was modelled using either HINGE or PLANAR connector elements, without adding any elastic or plastic behaviour to the available components of relative motion. These two connector modelling approaches represent two opposite ends of the spectrum in terms of surface sliding behaviour. In the former, slip at the connectors is completely prevented while in the latter infinite and unrestrained slip is allowed. In addition, both modelling approaches allow free rotation of the fastened surfaces about the axis normal to the surfaces.

The buckling response and ultimate capacities obtained with the ‘HINGE’ and ‘PLANAR’ models were compared to the predictions obtained from the validated FE models in order to study the effect the connector modelling approach has on the buckling response of CFS built-up columns subject to buckling of the individual components, as well as global instabilities of the built-up geometry.

Figure 9.37 shows the ultimate capacities obtained from the HINGE and PLANAR FE models, normalized against the ultimate loads obtained with the validated FE models for all geometries. The figure shows that the HINGE FE models predicted almost identical ultimate capacities to those predicted by the validated FE models. This can be attributed to the low shear forces and deformations present at the connectors over the load-deformation history of the specimens. This is illustrated in Figure 9.38 and Figure 9.39, respectively, which show the maximum shear force and slip at the connectors when the first component buckled and when the ultimate load was reached. In fact, it has already been shown in Section 7.4.2 of Chapter 7 that the shear forces which developed at the connector points when the components buckled in a local mode were relatively small. In the case of the columns assembled with bolts they were typically smaller than the force which caused the connectors to slip. As Figure 9.38 and Figure 9.39 show, only

columns LC1-8 developed some slip at the connector points after the plate sections buckled in a global-type flexural mode between connector points. This slip, which was also evident during the tests from the fact that the plate sections buckled only in some of the fields along the column, had a small effect on the ultimate capacity of the column, reducing it by around 3 % with respect to the case where slip was prevented (HINGE FE model), as shown in Figure 9.37. Global flexural buckling of the built-up geometry as a whole also resulted in small shear forces. However, this could be attributed to the fact that in these columns slip between the components at each end of the column was completely prevented. This suggests that if the shear slip between the components is prevented at the column ends, the shear flexibility of the connectors located along the column can be ignored when computing the global flexural buckling load of the built-up column.

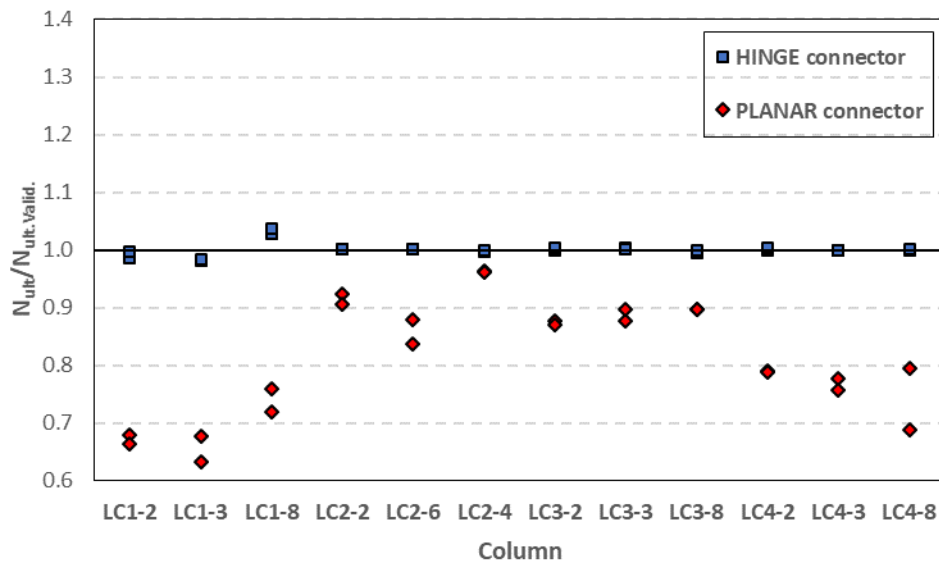


Figure 9.37: Ultimate load comparison for different connector modelling approaches

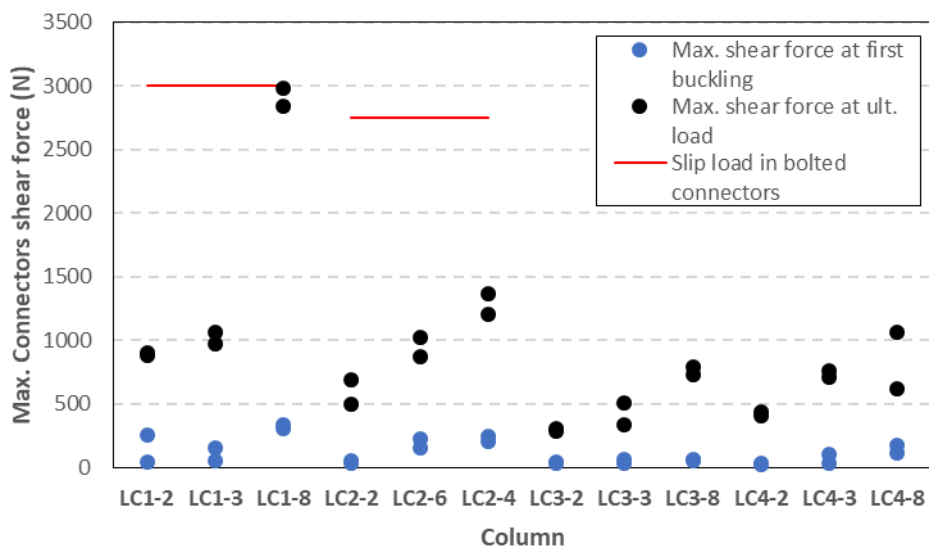


Figure 9.38: Maximum connector slip

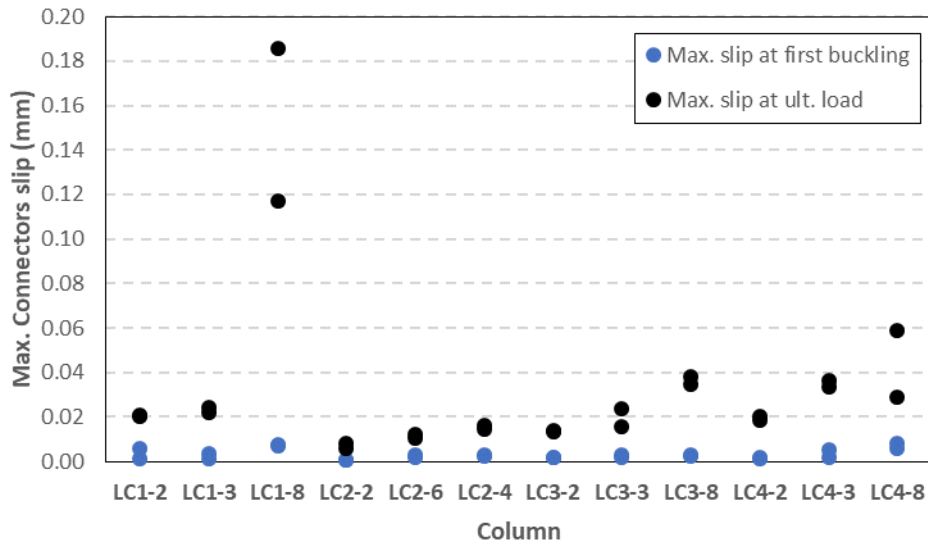


Figure 9.39: Maximum connector slip

The PLANAR models, on the other hand, predicted ultimate capacities which were noticeably lower than those predicted by the validated FE models. For columns LC1 and LC2 the average reductions in the ultimate capacity were 31 % and 9 %, respectively, while for columns LC3 and LC4 the average reductions in ultimate capacity were 11 % and 23 %, respectively. This consistent reduction in ultimate capacity was due to the fact that in the PLANAR models some of the components of each built-up geometry failed prematurely due to global instabilities, which were not prevented by the connectors as in these FE models slip between the components of the built-up geometry was completely unrestrained, as shown in Figure 9.40, for a representative column with geometry LC1, LC2, LC3 and LC4.

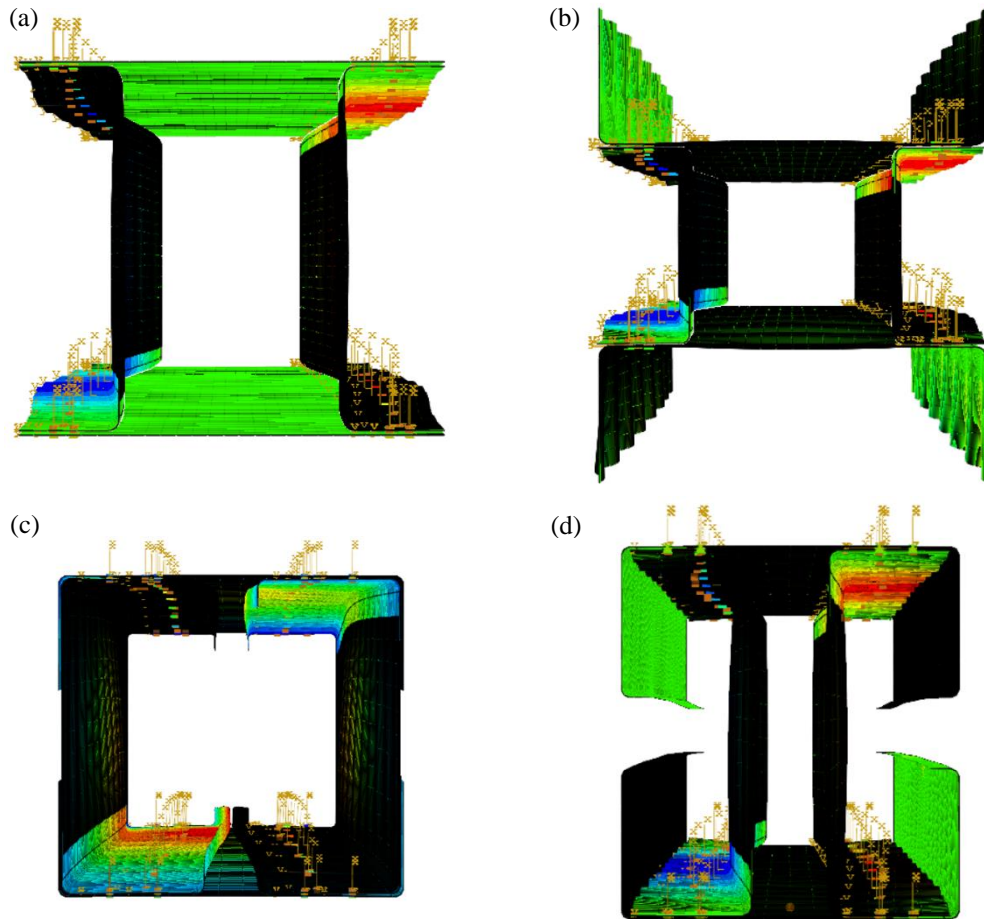


Figure 9.40: Failure mode in PLANAR FE model: a) LC1-8a; b) LC2-6a; c) LC3-8a; d) LC4-8a

9.4.2 Connector spacing and contact interaction

The effect which both the connector spacing and contact between the components have on the ultimate capacity of the four built-up geometries when subject to cross-sectional and global buckling interaction was investigated by running a series of numerical simulations in which the number of equally spaced rows of intermediate connectors along the column was varied from zero to 63, corresponding to a connector spacing which ranged from 2880 mm to 45 mm in columns LC1, LC3 and LC4 and from 2380 mm to 37 mm in column LC2. For each connector spacing, the models were run with and without including contact interactions between the components of the built-up geometry. In addition, both for the models with and without contact an upper bound of the ultimate capacity was established by considering the case where the connector spacing was reduced to zero. This was achieved by replacing the connector points with smeared TIE constraints between the component surfaces along the column length. All numerical models used in the parametric study included the initial geometric imperfections of a representative column, the material non-linearity obtained from the tensile coupons and the actual connector behaviour as determined from single lap shear tests.

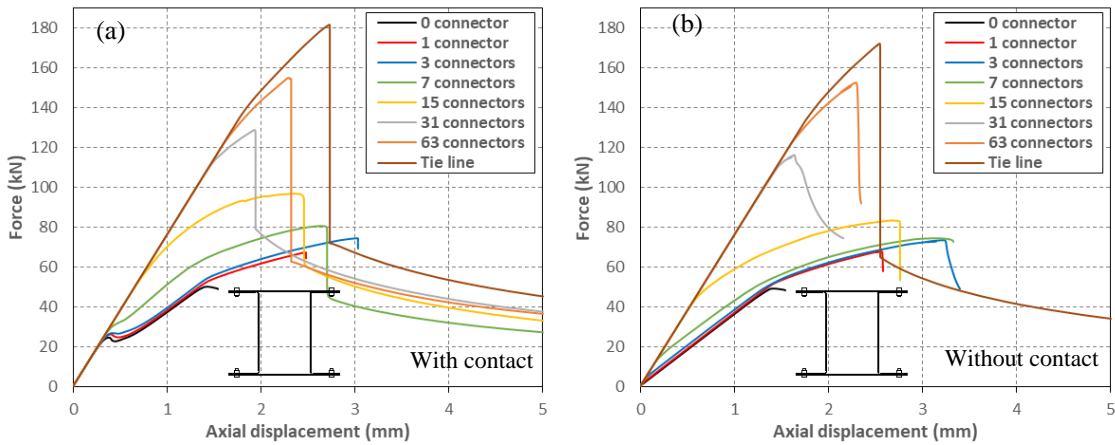


Figure 9.41: Load-axial deformation LC1: a) with contact; b) without contact

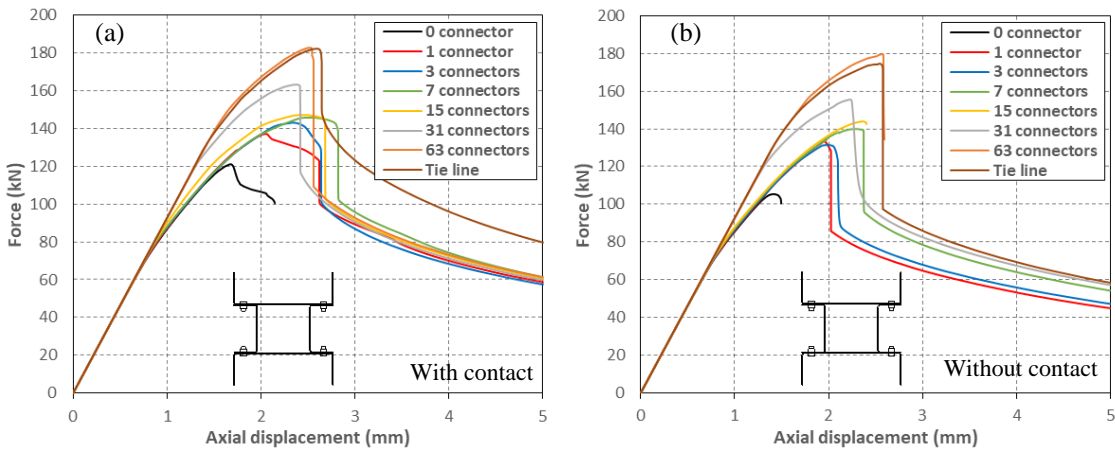


Figure 9.42: Load-axial deformation LC2: a) with contact; b) without contact

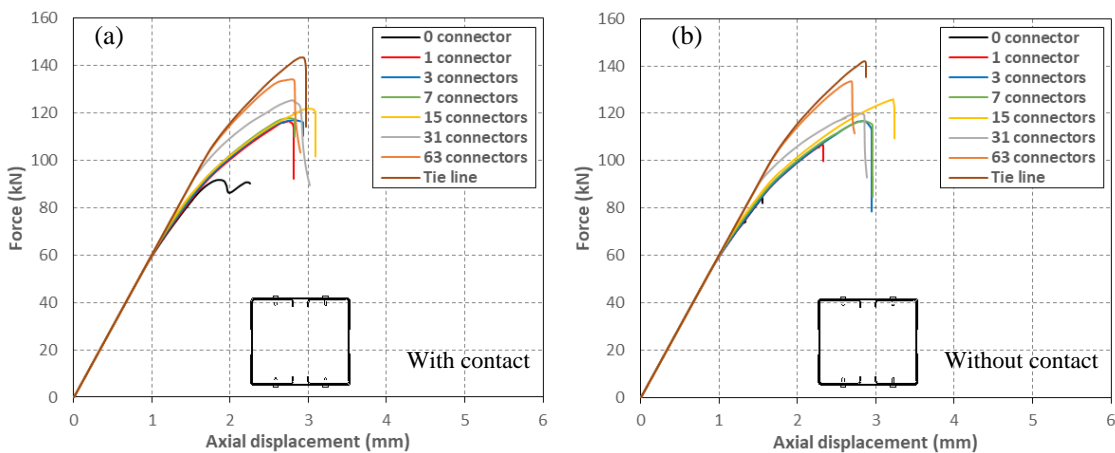


Figure 9.43: Load-axial deformation LC3: a) with contact; b) without contact

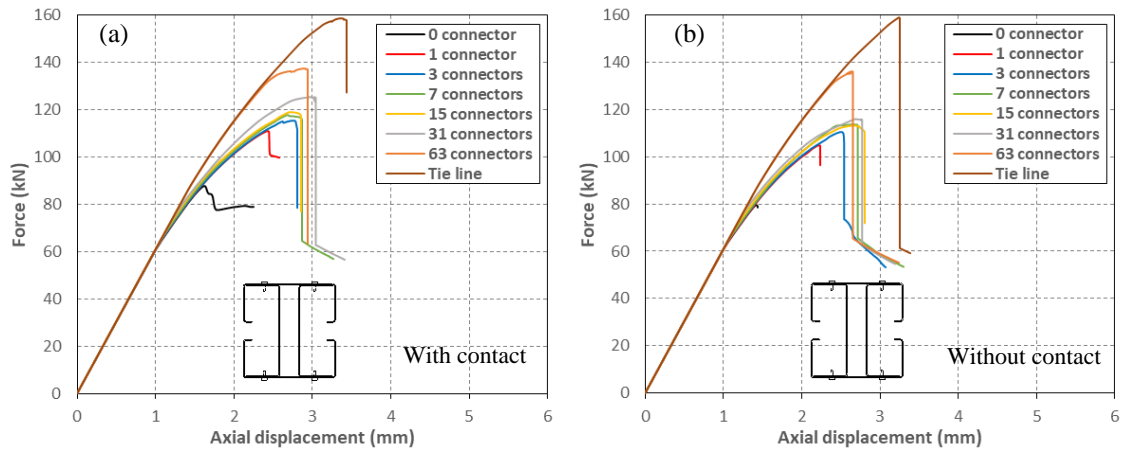


Figure 9.44: Load-axial deformation LC4: a) with contact; b) without contact

Figure 9.41, Figure 9.42, Figure 9.43 and Figure 9.44 show the load vs. axial shortening curves obtained for columns LC1, LC2, LC3 and LC4, respectively, with varying connector spacings and for the cases where contact was activated or deactivated, while Tables 9.21-9.24 list the failure modes obtained for each built-up geometry.

Table 9.21: Failure modes in columns LC1

Column	Failure mode at peak load					
	With contact			Without contact		
	Channels	Plates	Built-up	Channels	Plates	Built-up
LC1-0	F	F	-	F	F	-
LC1-1	L+FT	F	F	L+FT	F	-
LC1-3	L	F	F	L	F	-
LC1-7	L	F	F	L	F	F
LC1-15	L*	F*	F	L*	F*	F
LC1-31	L*	F*	F	L*	F*	F
LC1-63	L*	F*	F	L*	F*	-
LC1-Tie	L*	F*	F		F	-

L = Local buckling; F = Flexural buckling; LTB = Lateral-torsional buckling
 *Same buckle half-wave length in each component

Table 9.22: Failure modes in columns LC2

Column	Failure mode at peak load					
	With contact			Without contact		
	Inner channels	Outer channels	Built-up	Inner channels	Outer channels	Built-up
LC2-0	FT	L	F	FT	L	-
LC2-1	-	L	F	-	L	F
LC2-3	-	L	F	-	L	F
LC2-7	L	L	F	L	L	F
LC2-15	L	L	F	L*	L*	F
LC2-31	L*	L*	F	L*	L*	F
LC2-63	L*	L*	F	L*	L*	F
LC2-Tie	L*	L*	F	L*	L*	F

L = Local buckling; F = Flexural buckling; LTB = Lateral-torsional buckling
 *Same buckle half-wave length in each component

Table 9.23: Failure modes in columns LC3

Column	Failure mode at peak load					
	With contact			Without contact		
	Plain channels	Lipped channels	Built-up	Plain channels	Lipped channels	Built-up
LC3-0	L+F	L+FT	F	L+FT	-	-
LC3-1	L	L	F	L+F	L	F
LC3-3	L	L	F	L	L	F
LC3-7	L	L	F	L	L	F
LC3-15	L	L	F	L	L	F
LC3-31	L*	L*	F	L*	L*	F
LC3-63	L*	L*	F	L*	L*	F
LC3-Tie	L*	L*	F	L*	L*	F

L = Local buckling; F = Flexural buckling; LTB = Lateral-torsional buckling
 *Same buckle half-wave length in each component

Table 9.24: Failure modes in columns LC4

Column	Failure mode at peak load					
	With contact			Without contact		
	Plain channels	Lipped channels	Built-up	Plain channels	Lipped channels	Built-up
LC4-0	L+FT	L	F	L+FT	-	-
LC4-1	L+FT	L	F	L+FT	L	F
LC4-3	L	L	F	L	L	F
LC4-7	L	L	F	L	L	F
LC4-15	L	L	F	L	L	F
LC4-31	L*	L*	F	L*	L*	F
LC4-63	L*	L*	F	L	L	F
LC4-Tie	L*	L*	F	L*	L*	F

L = Local buckling; F = Flexural buckling; LTB = Lateral-torsional buckling
 *Same buckle half-wave length in each component

The tables show that when contact was included between the components of geometry LC1, failure originated due to global instabilities of the channel sections between connector points in the columns with zero and one intermediate sets of connectors. For geometries LC2 and LC3, when contact was included, global instabilities of the individual components between connector points occurred only in those columns with zero rows of intermediate connectors, while for geometry LC4 the plain channels buckled in a global mode between connector points in the columns with zero and one row of connectors. As the connector spacing was reduced, in all geometries the global instabilities of the individual channels were suppressed and they were only allowed to buckle in a local mode before failure occurred due to global flexural buckling of the built-up specimen. For relatively large connector spacings each channel in the built-up specimen buckled in a local mode with a half-wave length close to its natural half-wave length, while the plate sections in columns LC1 buckled in a global-type flexural mode with a half-wave length between half the distance and the distance between connectors. When the connector spacing was further reduced, typically below the shortest natural half-wave length of the components, the built-up geometry behaved more like a solid cross-section and all components buckled with the same half-wave length.

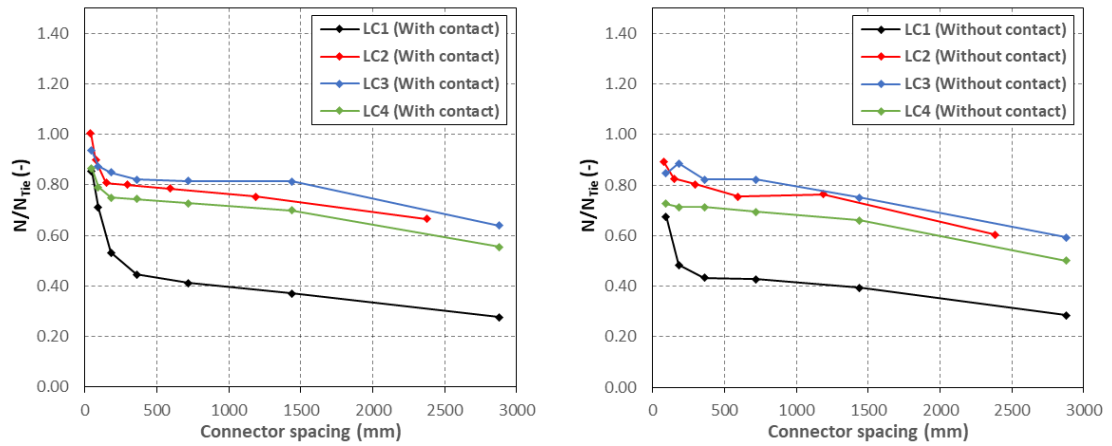


Figure 9.45: Ultimate load vs. connector spacing for FE models: a) with contact; b) without contact

The ultimate load predicted by the FE models as a function of the connector spacing for the case in which contact was activated is plotted Figure 9.45a for each built-up geometry, while Figure 9.45b provides the corresponding information for the case in which contact was not activated. The ultimate loads are normalized against the predictions given by the models in which the connectors were modelled with smeared TIE constraints. The figures show that, similar to the observations obtained from the FE models of the stub columns described in Chapter 7, the largest sensitivity of the ultimate load to the connector spacing occurs when the connector spacing is short enough to force the different components of the built-up geometry to buckle with the same half-wave length. For larger connector spacings, in all columns except LC1, the load remained almost unaffected by the connector spacing once global instabilities of the individual channels were restrained. For example, reducing the connector spacing in columns LC2 from 1190 mm to 149 mm resulted in an increase in the ultimate load of 7 %, while reducing the connector spacing from 1440 mm to 180 mm in columns LC3 or from 720 mm to 180 mm in columns LC4 resulted in increases in the ultimate load of only 4 % and 3 %, respectively. For columns LC1, a more noticeable sensitivity of the ultimate load to the connector spacing was observed. For example, reducing the connector spacing from 720 mm to 360 mm resulted in an increase of the ultimate load of 8 %. As discussed in Section 7.4.2 of Chapter 7, this is due to the reduction of the half-wave length of the plate sections which buckled in a global-type flexural mode. Consequently, the load bearing capacity of the plates was inversely proportional to the square of their effective length.

Figure 9.46 illustrates the effect of contact on the ultimate capacity of each built-up geometry for different connector spacings. The figure shows the ratio between the peak load obtained from the FE models in which contact was activated and deactivated for each built-up geometry and connector spacing. In columns LC2, LC3 and LC4, in which all the components buckled in a local mode, contact between the components had a modest effect on the ultimate capacity once the connector spacing was short enough to suppress global instabilities of the individual components between connector points. For these geometries, the maximum increase in the

ultimate capacity obtained due to the inclusion of contact in the FE models was less than 10 %. Contact had a slightly more noticeable effect on the ultimate capacity of columns LC1, resulting in a maximum increase in the ultimate capacity of 16 %.

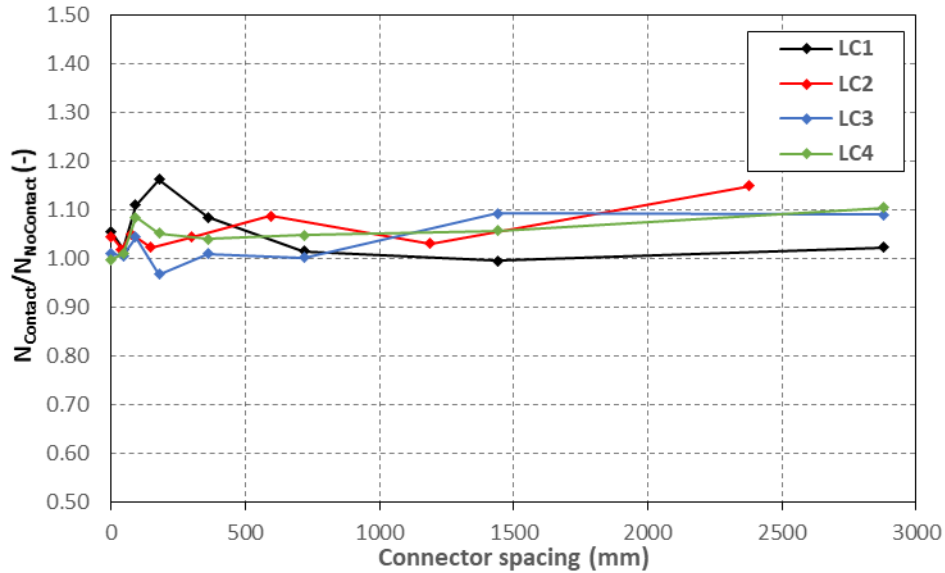


Figure 9.46: Effect of contact interaction on the ultimate capacity

9.5. Summary and conclusions

Detailed FE models were developed of the 24 long built-up CFS columns with four different cross-sectional geometries presented in Chapter 5 using the software package Abaqus v.6.14. The models incorporated the initial geometric imperfections measured on the tested columns, the non-linear material properties obtained from tensile coupons, as well as the actual load-elongation behaviour of the connectors used to assemble the columns, which were modelled using mesh-independent fasteners.

Convergence issues arising while running the models were overcome by modifying some solution control parameters and introducing artificial damping through either the contact control or the automatic stabilization mechanism. A sensitivity analysis was carried out to ensure the amount of artificial damping introduced into the models was sufficiently low not to alter the ultimate capacity predicted by the models. The FE models were verified against the experimental data gathered from the experiments on the long columns presented in Chapter 5, which included the ultimate capacity, the initial buckled shape of the columns and the critical buckling stresses determined for some of the components of the built-up geometries. The validated models were further used in parametric studies to investigate the way in which the connector modelling approach and the connector spacing, as well as contact between components affect the buckling response of the long built-up columns.

The most relevant conclusions which were drawn from this numerical investigation are listed below:

- A material modelling study revealed that substituting the actual stress-strain behaviour by a simplified bilinear stress-strain curve in the FE model resulted in an overestimation of the ultimate capacity by amounts which ranged from 1.9 % to 8.8 % for the studied columns. On the other hand, not accounting for the enhancement of the material properties in the corner regions of the channels had a less significant effect, resulting in an underestimation of the ultimate capacity of the built-up columns by amounts which ranged from 0.6 % to 3.0 %.
- The validated FE models were able to accurately predict the ultimate capacities of the tested columns for all the investigated geometries, with average errors of 3.4 % for columns LC1, 5.5 % for columns LC2, 1.3 % for columns LC3 and 2.6 % for columns LC4. The FE models were also able to accurately replicate the initial buckled shape of the tested columns, while for most columns the failure mode and yield line mechanism observed in the experiments were also seen to agree with those predicted by the FE models. A fairly good agreement was obtained between the experimentally and numerically derived critical buckling stresses of the components of each built-up geometry, with average differences of around 20.8 % and 4.2 % for the plate and channel sections of columns LC1, 12.6 % for the outer channels of columns LC2, and 13.0 % and 8.3 % for the plain channels of columns LC3 and LC4, respectively. For all the studied geometries, the numerically derived critical buckling stresses of the channels were, on average, around 10 % larger than those expected from a finite strip analysis when the channels were considered in isolation.
- The HINGE FE models, in which slip at the connector points was completely restrained, predicted almost identical ultimate capacities to the validated FE models. This can be explained by the negligible amount of slip which developed at the connector points as the built-up columns buckled. As previously shown in Section 7.4.2 of Chapter 7, the shear forces which develop at the connector points as a result of local buckling of the components are very small. In addition, since slip between the components was completely restrained at each end of the column, the shear forces at the connector points resulting from global flexural buckling of the built-up geometry were minimal. On the other hand, the PLANAR FE models, in which infinite and unrestrained slip was allowed at the connector points, predicted noticeably lower ultimate capacities than the validated FE models, due to premature global instabilities of the components which were not restrained by the connectors.

- Regarding the effect of the connector spacing on the ultimate capacity of the built-up geometries, for the columns assembled from channel sections only (columns LC2, LC3 and LC4), once the connector spacing was short enough to prevent global instabilities of the channel sections between connector points, there was a wide range of connector spacings for which the ultimate capacity of the built-up specimen remained almost unaffected by the connector spacing. In these columns the components buckled with half-wave lengths independent from each other. As the connector spacing was reduced, typically below the shortest natural local half-wave length of the components, the built-up geometry behaved more like a solid cross-section and all components buckled with the same half-wave length. In this range, the ultimate capacity of the built-up column showed the largest sensitivity to the connector spacing, displaying an increasing capacity when the connector spacing was reduced. A similar behaviour was also observed in columns LC1, in which the plate sections buckled in a global-type flexural mode. However, in this case, the ultimate capacity of the column still showed a moderate increase as the connector spacing was reduced, even when the connector spacing was larger than the natural local buckling half-wave length of the channels. This increase in the ultimate capacity was due to the reduction of the global buckling effective length of the plate sections
- With respect to the effect of contact on the ultimate capacity of the built-up geometries, once the connector spacing was short enough to prevent global instabilities of the individual components between connector points, the increase in ultimate capacity resulting from the effect of the contact pressure exerted between the components was generally modest. In columns LC2, LC3 and LC4, in which all the components buckled in a local mode, contact resulted in a maximum increase in the ultimate capacity of less than 10 %, while for columns LC1, the maximum increase in the ultimate capacity was 16 %.

Chapter 10

Conclusions and Recommendations

10.1. Summary and conclusions

The main purpose of this study was to develop an improved understanding of the behaviour, stability and capacity of built-up cold-formed steel members in compression and bending, paying special attention to the various interactions resulting from buckling of the individual components in between connector points, cross-sectional instabilities of the components and global buckling of the built-up member, as well as the role played by the connector spacing in these interactions. To achieve this, a series of laboratory tests on cold-formed steel built-up columns and beams were conducted and their behaviour was subsequently replicated and further studied by means of finite elements simulations. This chapter presents a brief summary of the work undertaken and reports the main conclusions.

10.1.1 Experimental studies

10.1.1.1 Column and beam tests

20 stub columns with four different built-up geometries were tested between fixed end conditions. The specimens were each constructed from four individual components, assembled with either bolts or self-drilling screws at varying spacings. The columns were designed to fail by cross-sectional instability and buckling of the individual components between connectors, while excluding global instabilities of the built-up specimen as a whole.

24 long column tests with built-up cross-sectional geometries almost identical to those of the stub columns and assembled with the same types of connectors were also conducted. The columns were compressed between pin-ended boundary conditions, while the load was applied with eccentricities of $L/1000$ or $L/1500$. Each built-up geometry was tested with three different connector spacings, and this time the columns were designed to exhibit global buckling of the

whole column in addition to cross-sectional buckling of the components and possible global buckling of the components in between connector points.

A series of 12 four-point bending tests was conducted on beams with two different cross-sectional geometries. The specimens were constructed from three or four channel sections, connected with bolts at varying spacings, and were designed to fail by local buckling of their component sections. Lateral restraint was provided at the locations where the concentrated loads were applied in order to avoid global instability.

The material properties of the test specimens were determined by means of test coupons taken from the corners and flat portions of the constituent sections, while detailed measurements of the geometric imperfections of each specimen were carried out using a laser displacement sensor mounted on a specially designed measuring rig. In addition, the mechanical behaviour of the connectors used to assemble the built-up specimens was determined by means of single lap shear tests.

The following are the main conclusions which were drawn from these experiments:

- The connectors were observed to rotate and/or translate in order to accommodate the buckling pattern of the connected components and could not be considered as fixed points in space. In addition, in some of the columns bolted together from channels and plate sections, the tests showed clear evidence of slip between the components as a result of a global-type flexural buckling of the plate sections between connector points.
- The buckling pattern of the individual components was seen to be subject to considerable restraint resulting from the presence of the connectors and contact with the adjacent components. The amount of restraint depended on the number of connectors, the built-up configuration and the loading condition.
- In the long columns, interaction between global buckling of the built-up specimen and cross-sectional buckling of the components was evidenced by an amplification of the amplitude of the buckles of the component located on the most compressed side of the built-up specimen. This component section was also recorded to buckle slightly before its twin counterpart located on the opposite side.
- By comparing the theoretical buckling stresses of the component sections, calculated under the assumption that they were isolated from the rest of the specimen, to the experimental values obtained from the stub column tests, the long column tests and the beam tests it was observed that the buckling stress of the most slender components was increased by up to 44 %, 34 % and 54 %, respectively, as a result of the restraint provided by the remainder of the cross-section.

- Both the stub column tests and the long column tests showed that when the cross-sectional buckling mode of all the components of the built-up geometry is a local mode (i.e. the columns with geometries 2, 3 and 4), the effect of the connector spacing on the ultimate capacity of the column is very small or negligible. In the beam tests the specimens with geometry B1 showed a relatively modest increase in the ultimate capacity when reducing the connector spacing, while the ultimate capacity of the specimens with geometry B2 was more significantly affected by the connector spacing.

10.1.1.2 Imperfection measurements of the components of the long columns

An imperfection measuring rig able to perform measurements over a length of 3000 mm was specifically designed to record the geometric imperfections of the plate and channel sections used to assemble the long built-up columns. The measuring rig consisted of a laser displacement sensor moved by two electric motors along high precision guiding bars. The geometric imperfections of the component sections were recorded along several lines before and after they were assembled into their final configuration in order to study the effect of the assembly process on the magnitude and shape of the imperfections. The imperfections recorded on the components of the built-up geometries were classified into out-of-plane imperfections and global imperfections.

A simple and inexpensive calibration technique was developed to achieve imperfection measurements with sufficient accuracy to capture both the global and the cross-sectional imperfections of the specimens. The technique consisted of using a reflective liquid to create a virtually perfectly flat surface which could be measured by the laser sensor in order to use it as a reference surface for all the measurements taken of the specimens.

The following are the main conclusions which were drawn from this study:

- The accuracy of the imperfection readings was found to be limited by the out-of-straightness of the guiding bars along which the laser sensor was moved. After accounting for this out-of-straightness, the accuracy of the imperfection measurements was estimated to be ± 0.06 mm over the full 3 m length.
- The imperfection measurements recorded on each type of channel section revealed a similar out-of-plane imperfection profile along the respective web, flanges and lips before they were assembled into their built-up configuration. This consistency in the imperfection shape was attributed to the fact that each type of channel section was presumably fabricated from the same steel coil and followed the same type of cold-forming process and handling.

- The fabrication process was also considered to be responsible for the consistency in the minor axis global flexural imperfection recorded in all the channels before they were assembled, which closely resembled a ‘Bow imperfection’ towards the web of the channel. The major axis global flexural imperfections present in the channels before they were assembled could be less accurately approximated by a ‘Chamber imperfection’, with the maximum imperfection amplitude generally not coinciding with the mid-length of the channel. These global imperfections were significantly smaller than those recorded about the minor axis of the channels.
- By decomposing the out-of-plane imperfections recorded in the channels before they were assembled into a constant and an undulating component along the channel, it was found that the constant component may be up to twice as large as the undulating component. This shows that characterising imperfections related to local or distortional buckling using the maximum out-of-plane imperfection can yield exceedingly conservative imperfection values. This is exacerbated by the fact that the profile of the undulating component will not necessarily resemble the longitudinal shape of the critical cross-sectional buckling mode of the channel.
- Assembling the channels into their final configuration significantly altered the amplitude and shape of the out-of-plane imperfections along the web of the channels as a result of direct contact with the adjacent components of the built-up geometry and the presence of the connectors, or due to rotational compatibility at the junction with the flanges, which were themselves in contact with or connected to other components. The former resulting in a greater modification of the out-of-plane imperfections. The assembly process was found to have a lesser effect on the out-of-plane imperfections recorded along the flanges of the channels, which in most cases resulted from rotational compatibility at the web-flange junction.
- The assembly process was also found to significantly affect the minor axis global flexural imperfection of the channels, reducing its magnitude at mid-length by 48 % on average and in some cases reversing the direction of the global imperfection. The shape of these imperfections was also affected, resembling less of a sinusoidal bow imperfection. The effect of the assembly process on the major axis global flexural imperfections of the channels was less clear, increasing the magnitude of the imperfections in some cases and reducing it or even inverting it in others.

10.1.1.3 Single lap shear tests

A series of single lap shear tests was carried out to determine the behaviour and the capacity of the connectors used to assemble the built-up columns and beams. The specimens were

fabricated with the aim of replicating the conditions in the actual built-up members as much as possible, in terms of dimensions, material properties, fabrication and torque. The connector behaviour was recorded using LVDTs attached to the test specimens and also using Digital Image Correlation (DIC), an alternative non-contact measuring technique of which the reliability was assessed by comparing the results with those obtained from the transducers. The following conclusions were drawn from this study:

- The tests allowed to successfully obtain the load-deformation curves of the connectors, which were further used as input data in detailed FE models.
- Assessment of two DIC algorithms suggested that both algorithms can successfully be used to measure deformations in CFS sections, provided that the deformations are contained within a plane.
- Out of the two codes assessed, Ncorr v.1.2 showed a significantly higher accuracy than Jones' (Jones, 2015) DIC code. Moreover, the accuracy of the measurements obtained from Ncorr v.1.2 was at least of the same order as the accuracy of the LVDTs.

10.1.2 Numerical studies

Detailed finite element models were developed of the tested built-up beams and columns, which incorporated the material non-linear behaviour obtained from the tensile coupons, the geometric imperfections recorded on the test specimens and the connector behaviour obtained from the single lap shear tests.

The models were validated against the data gathered from the experiments and were further used in parametric studies to investigate the way in which the connector modelling approach and the connector spacing, as well as contact between components affect the buckling response of the built-up specimen.

The main conclusions drawn from the numerical studies are as follows:

- A material modelling study revealed that substituting the actual stress-strain behaviour by a simplified bilinear stress-strain curve in the FE model generally resulted in a noticeably stiffer post-buckling response and an increase in the ultimate capacity of up to 8.8 %. The post-buckling stiffness and the ultimate capacity of the specimens were generally less sensitive to the enhancement of the material properties in the corner regions.
- The FE models were able to provide fairly accurate predictions of the ultimate capacity of the tested columns and beams for all studied geometries. For the stub columns and the long columns, the average predicted errors in the ultimate capacity were 3.7 % and

3.2 %, respectively, while for the beams the average error in the ultimate capacity predicted with a simplified FE model was 5.8 %. The FE models were also able to replicate the initial buckled shape of the tested specimens for each geometry and connector spacing, while predicting critical buckling stresses of the components which, on average, differed by less than 10 % from those experimentally determined.

- The FE models showed that the shear forces, which developed at the connectors as a result of local buckling were sufficiently low not to cause significant slip. Therefore, preventing slip when modelling the connectors can be expected to lead to accurate predictions of the ultimate capacity when the individual components buckle in a local mode, irrespective of whether the specimen is assembled using bolts or screws. On the other hand, the connectors were found to be instrumental in preventing global instabilities of the individual components in relatively long specimens. Therefore, allowing slip without any resistance at the connector points may result in a premature failure of the built-up specimen.
- For the columns and beams assembled only with channel sections, once the connector spacing was short enough to prevent global instabilities of the channels between connector points, there was a wide range of connector spacings for which the ultimate capacity of the built-up specimen was not significantly affected by the connector spacing. In this range, the components generally buckled with half-wave lengths independent from each other. In all the studied geometries it was observed that as the distance between connectors was typically reduced below the shortest buckle half-wave length of the components, the built-up geometry behaved more like a solid cross-section and all components buckled with the same half-wave length. In this range, the ultimate capacity of the built-up specimen became significantly more sensitive to the distance between connectors, displaying an increasing capacity when the connector spacing was reduced. However, due to the large amount of labour required to achieve these reduced connector spacings, it may prove more economical to assume that the connector spacing does not have an effect on the ultimate capacity of the built-up geometry and to use a longer connector spacing which is still short enough to prevent global instabilities or excessive separation of the components between connector points.
- For the studied geometries contact between the components was seen to be mainly important when it contributed to partially or completely restraining global instabilities of the components of the built-up geometry between connector points. When the connector spacing became small enough to prevent global instabilities of the individual components, the effect of contact became less significant, typically resulting in an increase in the ultimate capacity of less than 10 %. For those specimens in which global instabilities of the entire member were excluded (i.e. the stub columns and the beams),

the effect of contact was also seen to be slightly more important for connector spacings shorter than the local buckle half-wave length of the components. However, its effect remained relatively modest.

10.2. Recommendations for future work

The numerical models developed as part of this research have been proved to accurately replicate the ultimate capacity and behaviour of the built-up beams and columns investigated. These FE models can be used in future parametric studies where the material grade, the cross-sectional dimensions of the components and the overall length of the built-up specimen are varied in order to cover different local and global slenderness. These additional data points could then be used to complement the experimental data reported in this thesis to establish a potential relationship between the ultimate capacity and relevant key parameters which may affect it, such as the critical buckling stress or the yield stress of the different components. The numerical models can also be used together with the geometric imperfection data recorded in this research to study the effect which the shape and magnitude of geometric imperfections may have on the ultimate capacity of CFS built-up members.

Regarding the experiments presented in this study, it is worth emphasizing that in the long column tests, slip between the components at each end of the column was intentionally suppressed. This decision was taken so that the effect of the connector spacing along the column could be better studied and to ensure that the load was evenly distributed to all the components of the built-up specimen. However, it is acknowledged that slip between the components at the column ends due to global instabilities of the built-up geometry or due to a slight difference in length between the components may significantly reduce the ultimate capacity of the column. More research should be directed towards quantifying the degree to which this slip may affect the ultimate capacity of built-up columns and towards exploring different ways to remove or limit it. Using spot welds to connect the different components at each end of the column may be a good way to prevent them from slipping. The operation can be easily applied on site by one operator and the equipment required is relatively inexpensive. However, research should be conducted to determine the appropriate number of spot welds to be used. The NAS (AISI, 2016a) specifies that: *“The ends of a built-up compression member are connected by a weld having a length not less than the maximum width of the member or by connectors spaced longitudinally not more than 4 diameters apart for a distance equal to 1.5 times the maximum width of the member”*. This specification seems excessive, especially if spot welds are used as connectors, and it is only applicable for built-up members composed of two sections.

The column tests presented in this thesis were designed to exhibit interaction between various types of buckling modes, including local buckling of the components, global flexural buckling of the built-up geometry and global buckling of the individual components between connectors. While distortional buckling was also observed in one of the built-up geometries, its presence was only minor. Additional tests focusing on interactions involving distortional buckling and how this is affected by the connector spacing should also be considered. The effect of the connector spacing on other types of global buckling modes such as torsional or flexural-torsional buckling of the built-up specimen should be also investigated.

The beam specimens presented in this thesis were tested while providing lateral restraint in order to avoid lateral-torsional buckling of the built-up specimen. This decision was taken after considering that in most practical applications the beams are restrained by the presence of the bridging and a roof or floor. However, there are situations in which this is not the case, and lateral-torsional buckling of the built-up specimen may interact with cross-sectional buckling of the components. Experiments should be designed and conducted to study this type of interaction, as well as the role played by the connector spacing.

In addition, the beams presented in this thesis were tested in a four-point bending configuration, which resulted in no shear force being introduced in the region of interest. This type of loading is hardly encountered in practical situations, where beams are typically subjected to a combination of moment and shear. The interaction effect of bending and shear could be studied by conducting three-point bending tests, in which the amount of shear can be varied by changing the span of the beam. Also, tests in which the load is applied to only one individual component of the beam could be conducted to simulate the case in which a secondary cross-beam is eccentrically connected to the primary beam, initially transferring its load to a single component of the built-up specimen. These tests would permit to study the effectiveness of the load sharing between components as a function of the connector spacing.

Regarding the imperfection measuring rig which was presented in this thesis, a clear improvement which could significantly reduce the number of scans required to capture the 3D imperfection profile of the specimens and allow for a direct and easier measurement of the corner regions of the cross-section would consist of replacing the 1D laser by a 2D laser. More than one laser sensor could also be mounted on the measuring rig, as shown in Figure 10.1, in order to further reduce the number of scans required to carry out the measurements. The direction of the measurements could also be changed so that, instead of taking measurements in the vertical direction, as in the presented measuring rig, measurements are taken in a horizontal direction, as shown in Figure 10.2. This would automatically remove the effect of the self-weight of the specimen from the measurements. Finally, it is worth highlighting the importance of investing in a motion system for the measuring rig in which all the moving components are covered and protected from dust. This will help reduce the vibrations while moving the laser

sensor to minimum levels and will prolong the life span of the measuring rig. This is especially important in cases where the measuring rig has to coexist in an environment with dust producing materials, such as concrete, which is likely to be the case in a structural laboratory.

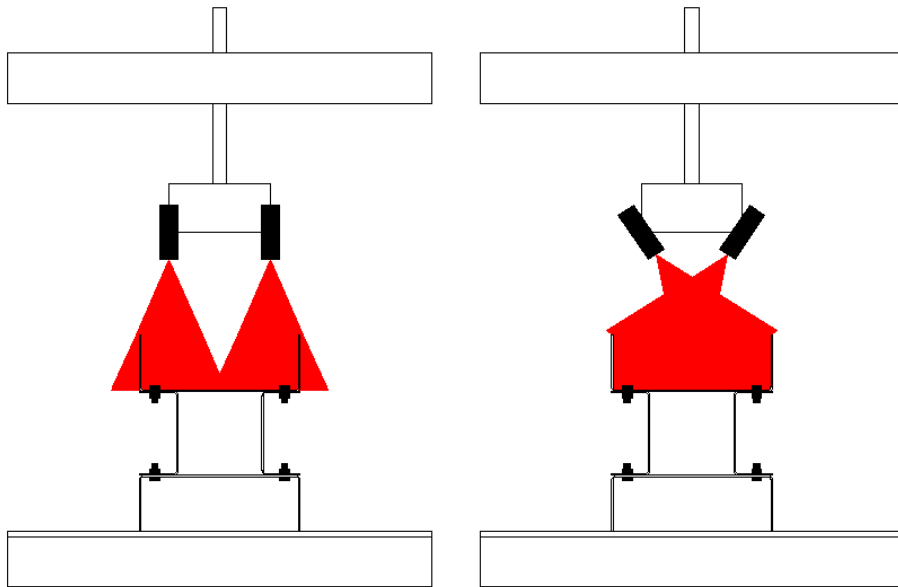


Figure 10.1: Arrangements of two 2D laser sensors taking measurements in the vertical direction

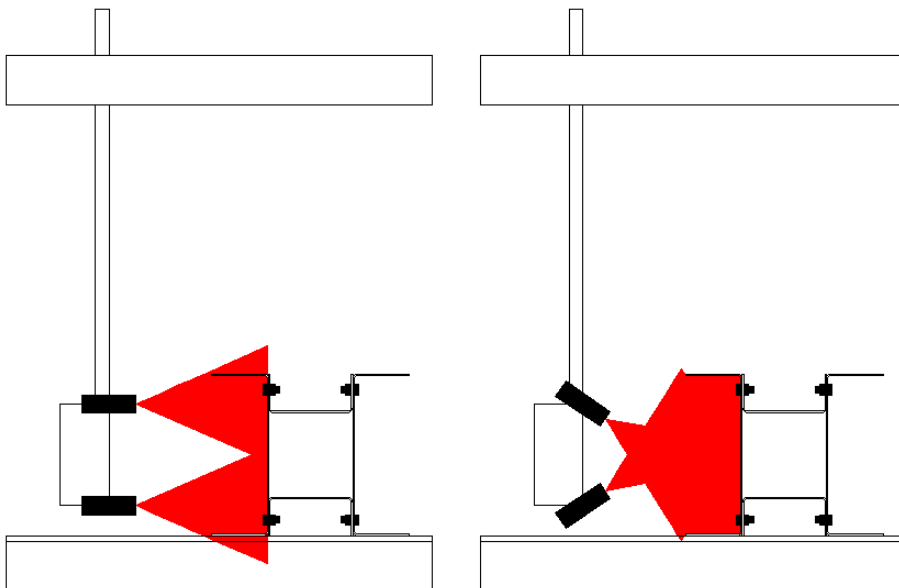


Figure 10.2: Arrangements of two 2D laser sensors taking measurements in a horizontal direction

References

- Abbasi, M., Khezri, M. and Rasmussen, K.J.R. (2017), "On extending the direct strength method to the design of cold - formed steel built - up columns", *EUROSTEEL 2017*. Copenhagen, Denmark.
- Abbasi, M., Khezri, M., Rasmussen, K.J.R. and Schafer, B.W. (2018) "Elastic buckling analysis of cold-formed steel built-up sections with discrete fasteners using the compound strip method", *Thin-Walled Structures*, 124, 58–71.
- Abdel-Rahman, N. and Sivakumaran, K.S. (1997), "Material Properties Models for Analysis of Cold-Formed Steel Members", *Journal of Structural Engineering*, 123, 1135–1143.
- Ádány, S. (2004), "Buckling Mode Classification of Members With Open Thin-Walled Cross-Sections By Using The Finite Strip Method", Report, Johns Hopkins University.
- Adany, S. and Schafer, B.W. (2006), "Buckling mode decomposition of single-branched open cross-section members via finite strip method: Derivation", *Thin-Walled Structures*, 44, 563.584.
- Ádány, S. and Schafer, B.W. (2008), "A full modal decomposition of thin-walled, single-branched open cross-section members via the constrained finite strip method", *Journal of Constructional Steel Research*, 64, 12–29.
- Ádány, S. and Schafer, B.W. (2014a), "Generalized constrained finite strip method for thin-walled members with arbitrary cross-section: Primary modes", *Thin-Walled Structures*, 84, 150–169.
- Ádány, S. and Schafer, B.W. (2014b), "Generalized constrained finite strip method for thin-walled members with arbitrary cross-section: Secondary modes , orthogonality , examples", *Thin Walled Structures*, 84, 123–133.
- AISI (2016a), North American Specification for the Design of Cold-Formed Steel Structural Members.
- AISI (2016b), Commentary on North American Specification for the Design of Cold-Formed

Steel Structural Members.

- Anapayan, T. and Mahendran, M. (2012), "Numerical modelling and design of LiteSteel Beams subject to lateral buckling", *Journal of Constructional Steel Research*, 70, 51–64.
- Anbarasu, M. (2016), "Local-distortional buckling interaction on cold-formed steel lipped channel beams", *Thin-Walled Structures*, 98, 351–359.
- Ashraf, M., Gardner, L. and Nethercot, D.A. (2006), "Finite element modelling of structural stainless steel cross-sections", *Thin-Walled Structures*, 44, 1048–1062.
- Bambach, M.R. and Rasmussen, K.J.R. (2002), "Effective Widths of Unstiffened Elements Under Combined Compression and Bending", *Sixteenth International Specialty Conference on Cold-Formed Steel Structures*, Orlando, Florida USA.
- Batista, E.D.M. and Rodrigues, F.G. (1992), "Residual Stress Measurements on Cold-Formed Profiles", *Experimental Techniques*, pp. 25–29.
- Becque, J. (2008), "The Interaction of Local and Overall Buckling of Cold-Formed Stainless Steel Columns", PhD thesis, The University of Sidney.
- Becque, J. and Rasmussen, K.J.R. (2008), "Numerical Investigation and Design Methods for Stainless Steel Columns Failing by Interaction of Local and Overall Buckling", Report No 888, The University of Sidney.
- Becque, J. and Rasmussen, K.J.R. (2009a), "Numerical Investigation of the Interaction of Local and Overall Buckling of Stainless Steel I-Columns", *Journal of Structural Engineering*, 135, 1349–1356.
- Becque, J. and Rasmussen, K.J.R. (2009b), "Experimental investigation of local-overall interaction buckling of stainless steel lipped channel columns", *Journal of Constructional Steel Research*, 65, 1677–1684.
- Becque, J. and Rasmussen, K.J.R. (2009c), "A numerical investigation of local-overall interaction buckling of stainless steel lipped channel columns", *Journal of Constructional Steel Research*, 65, 1685–1693.
- Bernard, E.S., Bridge, R.Q. and Hancock, G.J. (1993), "Tests of Profiled Steel Decks With V-Stiffeners", *Journal of Structural Engineering*, 119, 2277–2293.
- Bjorhovde, R. (1972), "Deterministic and probabilistic approaches to the strength of steel columns", PhD thesis, Lehigh University.
- Blaber, J., Adair, B. and Antoniou, A. (2015), "Ncorr: Open-Source 2D Digital Image Correlation Matlab Software", *Experimental Mechanics*, 55, 1105–1122.

-
- Bleich, F. (1952), *Buckling strength of metal structures*, McGraw-Hill Book Company Inc., New York.
- Brueggen, B. and Ranrseyel, C. (2005), "Capacity of built-up cold-formed steel axial compression members", *Proceeding of the Annual Stability Conference*, Missouri, pp. 89–103.
- Bryan, G.H. (1891), "On the Stability of Plane Plate under Thrusts in its own Plate, with Applications to the "Buckling" of the Sides of a Ship", *Proceedings of the London Mathematical Society*, pp. 54–67.
- BSI (2008), BS 817:2008 - Specification for surface plates.
- Bulson, P.S. (1970), *The Stability of Flat Plates*, Chatto & Windus, London.
- Camotim, D., Silvestre, N., Basaglia, C. and Bebiano, R. (2008), "GBT-based buckling analysis of thin-walled members with non-standard support conditions", *Thin-Walled Structures*, 46, 800–815.
- CEN (1995), BS EN 10142: 1991 - Specification for Continuously hot-dip zinc coated mild steel strip and sheet for cold forming - Technical delivery conditions.
- CEN (2005), Eurocode 3: Design of steel structures — Part 1-1: Genral rules and rules for buildings. British Standard Institution.
- CEN (2006), Eurocode 3 — Design of steel structures — Part 1-3: General rules — Supplementary rules for cold-formed members and sheeting. British Standard Institution.
- CEN (2009a), Eurocode 3 — Design of steel structures — Part 1-5 : Plated structural elements. British Standard Institution.
- CEN (2009b), BS EN ISO 6892-1:2009 - Metallic materials — Tensile testing — Part 1 : Method of test at ambient temperature. British Standard Institution.
- Chajes, A., Britvec, S.J. and Winter, G. (1963), "Effects of Cold-Straining on Structural Sheet Steels", *Journal of the Structural Division Proceedings of the American Society of Civil Engineers*, 89, 1–32.
- Charnvarnichborikarn, P. and Polyzois, D. (1992), "Distortional Buckling of Cold-Formed Steel Z-Section Columns", *Eleventh International Specialty Conference on Cold-Formed Steel Structures*, St. Louis, Missouri, USA.
- Cheung, Y.K. (1976), *Finite Strip Method in Structural Analysis*, Pergamon Press, Oxford.
- Craveiro, H.D., Paulo, J., Rodrigues, C. and Laím, L. (2016), "Buckling resistance of axially loaded cold-formed steel columns", *Thin-Walled Structures*, 106, 358–375.

- Dai, M. (2017), "The effect of connectors behaviour on the capacity of built-up cold-formed steel structural elements", The University of Sheffield.
- Dassault Systemes (2014), Abaqus 6.14 Analysis User's Guide: Analysis II, 14.
- Davids, A. and Hancock, G. (1986), "Compression Tests of Long Welded I-Section Columns", *American Society of Civil Engineers*, 112, 2281–2297.
- Davies, J.M. and Leach, P. (1994), "First-order generalised beam theory", *Journal of Constructional Steel Research*, 31, 187–220.
- Davies, J.M., Leach, P. and Heinz, D. (1994), "Second-order generalised beam theory", *Journal of Constructional Steel Research*, 31, 221–241.
- Desmond, T.P., Pekoz, T. and Winter, G. (1981), "Intermediate Stiffeners for Thin-Walled Members", *Journal of Structural Engineering*. 107, 329–353.
- Dilorenzo, G., Portioli, F. and Landolfo, R. (2006), "Experimental Investigation on the Load Bearing Capacity of Built-up Cold-Formed Steel Beams", *Proceedings of International Colloquium on Stability and Ductility of Steel Structures*, Lisbon.
- Dinis, P.B. and Camotim, D. (2015), "Cold-formed steel columns undergoing local-distortional coupling: Behaviour and direct strength prediction against interactive failure", *Computers and Structures*, 147, 181–208.
- Dinis, P.D. and Camotim, D. (2010), "Local/distortional mode interaction in cold-formed steel lipped channel beams", *Thin-Walled Structures*, 48, 771–785.
- Dubina, D. and Ungureanu, V. (2000), "Elastic-plastic interactive buckling of thin-walled steel compression members", *Fifteenth International Specialty Conference on Cold-Formed Steel Structures*, St. Louis, Missouri, pp. 223–237.
- Dubina, D. and Ungureanu, V. (2002), "Effect of imperfections on numerical simulation of instability behaviour of cold-formed steel members", *Thin-Walled Structures*, 40, 239–262.
- Dubina, D., Ungureanu, V. and Landolfo, R. (2012), *Design of Cold-Formed Steel Structures - Eurocode 3: design of Steel Structures Part 1-3: Design of Cold-formed Steel Structures*, ECCS - European Convention for Constructional Steelwork.
- ECCS, 1978. European recommendations for steel construction, Publication P022, Experimental Techniques. Brussels, Belgium.
- ECCS TC7 (2009), The Testing of Connections with Mechanical Fasteners in Steel Sheeting and Sections.

-
- Fang, P.J. and Winter, G. (1965), "Torsional-flexural buckling of thin-walled open sections", Report No 320A, Cornell University, Ithaca, NY.
- Fisher, G.P. and Bijlaard, P.P. (1953), "Column Strength of H-sections and Square Tubes in Postbuckling Range of Component Plates", *National Advisory Comettee for Aeronautics*, TN 2994.
- Fratamico, D.C., Torabian, S., Zhao, X., Rasmussen, K.J.R. and Schafer, B.W. (2018a), "Experimental study on the composite action in sheathed and bare built-up cold-formed steel columns", *Thin-Walled Structures*, 127, 290–305.
- Fratamico, D.C., Torabian, S., Zhao, X., Rasmussen, K.J.R. and Schafer, B.W. (2018b), "Experiments on the global buckling and collapse of built-up cold-formed steel columns", *Journal of Constructional Steel Research*, 144, 65–80.
- Galambos, T. V. (1998), *Guide to stability Design Criteria for Metal Structures*, Fifth edit. ed. John Wiley & Sons, Inc.
- Gardner, L. and Nethercot, D.A. (2004), "Numerical Modeling of Stainless Steel Structural Components — A Consistent Approach", *Journal of Structural Engineering*, 130, 1586–1601.
- Georgieva, I., Schueremans, L., Roeck, G. De and Pyl, L. (2011), "Experimental Investigation of the Deformation of Built-up Members of Cold-formed Steel Profiles", *Applied Mechanics and Materials*, 70, 416–421.
- Georgieva, I., Schueremans, L. and Pyl, L. (2012a), "Composed columns from cold-formed steel Z-profiles: Experiments and code-based predictions of the overall compression capacity", *Engineering Structures*, 37, 125–134.
- Georgieva, I., Schueremans, L., Pyl, L. and Vandewalle, L. (2012b), "Experimental investigation of built-up double-Z members in bending and compression", *Thin-Walled Structures*, 53, 48–57.
- Georgieva, I., Schueremans, L., Pyl, L. and Vandewalle, L. (2012c), "Numerical study of built-up double-Z members in bending and compression", *Thin-Walled Structures*, 60, 85–97.
- Gonçalves, R., Ritto-Corrêa, M. and Camotim, D. (2010), "A new approach to the calculation of cross-section deformation modes in the framework of generalized beam theory", *Computational Mechanics*, 46, 759–781.
- Goodier, J.N. (1941), "The Buckling of Compressed Bars by Torsion and Flexure", Bulletin, Cornell University, Engineering Experiment Station, Ithaca, NY.
- Graves Smith, T.R. (1967), "The Ultimate Strength of Locally Buckled Columns of Arbitrary
-

-
- Length", *Proceeding, 18 Symposium on Thin-Walled Structures*, Swansea, pp. 35–60.
- Hancock, G.J. (1981), "Non-Linear Analysis of Thin Sections in Compression", *Journal of the Structural Division: Proceedings of the ASCE*, 107, 455–471.
- Hancock, G.J. (1985), "Distortional Buckling of Steel Storage Rack Columns", *Journal of Structural Engineering*, 111, 2770–2783.
- Hancock, G.J. (1997), "Design for distortional buckling of flexural members", *Thin-Walled Structures*, 27, 3–12.
- Hancock, G.J., Kwon, Y.B. and Bernard, E.S. (1994), "Strength Design Curves for Thin-Walled Sections Undergoing Distortional Buckling", *Journal of Constructional Steel Research*, 31, 169–186.
- Hancock, G.J., Rogers, C.A. and Schuster, R.M. (1996), "Comparison of the Distortional Buckling Method for Flexural Members With Tests", *Thirteenth International Specialty Conference on Cold-Formed Steel Structures*, St. Louis, Missouri, USA, pp. 125–140.
- Huang, Y. and Young, B. (2014), "The art of coupon tests", *Journal of Constructional Steel Research*, 96, 159–175.
- Ingvarsson, L. (1975), "Cold-Forming Residual Stresses. Effect on Buckling", *In: Proceedings of the 3rd International Specialty Conference on Cold-Formed Steel Structures*.
- Jeyaragan, S. and Mahendran, M. (2008a), "Experimental Investigation of the New Built-up LiteSteel Beams", *Fifth International Conference on Thin-Walled Structures*, Brisbane, Australia.
- Jeyaragan, S. and Mahendran, M. (2008b), "Numerical Modelling and Design of the New Built-up LiteSteel Beams", *Fifth International Conference on Coupled Instability in Metal Structures*, Sidney, Australia.
- Jiahui, Z. (2014), "Cold-Formed Steel Built-Up Compression Members with Longitudinal Stiffeners", PhD thesis, The University of Hong Kong.
- Jones, E.M.C. (2015), Documentation for Matlab-based DIC code.
- Kalyanaraman, V., Pekoz, T. and Winter, G. (1977), "Unstiffened Compression Elements", *Journal of the Structural division: Proceedings of the ASCE*, 103, 1833–1848.
- Karren, K.W. (1967), "Corner Properties of Cold-formed Steel Shapes", *Journal of the Structural Division Proceedings of the American Society of Civil Engineers*, 93, 401–432.
- Kenneth, W.K. and Winter, G. (1965), "Effects of Cold-Forming on Light-Gage Steel Members", Report No. 318, Cornell University.
-

-
- Kenneth, W.K. and Winter, G. (1967), "Effects of Cold-forming on Light-gage Steel Members", *Journal of the Structural Division Proceedings of the American Society of Civil Engineers*, 93, 433–469.
- Key, P.W. and Hancock, G.J. (1993), "A Theoretical Investigation of the Column Behaviour of Cold-Formed Square Hollow Sections", *Thin-Walled Structures*, pp. 31–64.
- Kwon, Y.B. and Hancock, G.J. (1992a), "Design of Channels Against Distortional Buckling", *Eleventh International Specialty Conference on Cold-Formed Steel Structures*, St. Louis, Missouri, USA.
- Kwon, Y.B. and Hancock, G.J. (1992b), "Tests of Cold-Formed Channels with Local and Distortional Buckling", *Journal of Structural Engineering*, 118, 1786–1803.
- Kwon, Y.B. and Hancock, G.J. (1993), "Post-buckling analysis of thin-walled channel sections undergoing local and distortional buckling", *Computers and Structures*, 49, 507–516.
- Kwon, Y.B., Kim, B.S. and Hancock, G.J. (2009), "Compression tests of high strength cold-formed steel channels with buckling interaction", *Journal of Constructional Steel Research*, 65, 278–289.
- Landolfo, R., Mammana, O., Portioli, F., Di Lorenzo, G. and Guerrieri, M.R. (2008), "Laser welded built-up cold-formed steel beams: Experimental investigations", *Thin-Walled Structures*, 46, 781–791.
- Landolfo, R., Mammana, O., Portioli, F., Di Lorenzo, G. and Guerrieri, M.R. (2009), "Experimental investigation on laser welded connections for built-up cold-formed steel beams", *Journal of Constructional Steel Research*, 65, 196–208.
- Lau, S.C.W. and Hancock, G.J. (1987), "Distortional Buckling Formulas for Channel Columns", *Journal of Structural Engineering*, 113, 1063–1078.
- Lau, S.C.W. and Hancock, G.J. (1988), "Distortional buckling tests of cold-formed channel sections", *Ninth International Specialty Conference on Cold-Formed Steel Structures*, St. Louis, Missouri, USA, pp. 45–74.
- Lau, S.C.W. and Hancock, G.J. (1990), "Inelastic Buckling of Channel Columns in the Distortional Mode", *Thin-Walled Structures*, 10, 59–84.
- Li, Y., Li, Y., Wang, S. and Shen, Z. (2014), "Ultimate load-carrying capacity of cold-formed thin-walled columns with built-up box and I section under axial compression", *Thin-Walled Structures*, 79, 202–217.
- Li, Z., Ádány, S. and Schafer, B.W. (2013), "Modal identification for shell finite element models of thin-walled members in nonlinear collapse analysis", *Thin-Walled Structures*,
-

67, 15–24.

- Li, Z. and Schafer, B.W. (2013), "Constrained Finite Strip Method for Thin-Walled Members with General End Boundary Conditions", *Journal of Engineering Mechanics*, 139, 1566–1576.
- Liao, F., Wu, H., Wang, R. and Zhou, T. (2017), "Compression test and analysis of multi-limbs built-up cold-formed steel stub columns", *Journal of Constructional Steel Research*, 128, 405–415.
- Lorenzo, G. Di, Portioli, F. and Landolfo, R. (2004), "On the Characterization of the Material Properties for Cold-Formed Steel Members", *Fourth International Conference On Thin-Walled Structures*, pp. 251–258.
- Lu, Y., Zhou, T., Li, W. and Wu, H. (2017), "Experimental investigation and a novel direct strength method for cold-formed built-up I-section columns", *Thin-Walled Structures*, 112, 125–139.
- Lundquist, E.E., Stoweix, E.Z. and Schuette, E.H. (1945), "Principles of Moment Distribution Applied to Stability of Structures Composed of Bars or Plates", Report No. 809, National Advisory Committee for Aeronautics.
- Marguerre, K. (1938), "Zur Theorie der gekremmter Platte grosser Formaenderung", *Proceedings of 5th Congress for Applied Mechanics*, Cambridge.
- Martins, A.D., Camotim, D. and Dinis, P.B. (2017), "Local-distortional interaction in cold-formed steel beams: Behaviour, strength and DSM design", *Thin-Walled Structures*, 119, 879–901.
- Moen, C.D., Igusa, T. and Schafer, B.W. (2008), "Prediction of residual stresses and strains in cold-formed steel members", *Thin-Walled Structures*, 46, 1274–1289.
- Pastor, M.M., Bonada, J., Roure, F. and Casafont, M. (2013), "Residual stresses and initial imperfections in non-linear analysis", *Engineering Structures*, 46, 493–507.
- Pastor, M.M., Casafont, M., Bonada, J. and Roure, F. (2014), "Imperfection amplitudes for nonlinear analysis of open thin-walled steel cross-sections used in rack column uprights", *Thin-Walled Structures*, 76, 28–41.
- Piyawat, D. (2011), "A Suggested Design Approach for Built-up Cold-Formed Columns Based on Research Using Nonlinear Finite Element Method", PhD thesis, University of Oklahoma.
- Piyawat, K., Ramseyer, C. and Kang, T.H. (2011), "Nonlinear buckling of built-up cold-formed sections", *International Journal of Theoretical and Applied Multiscale Mechanics*, 2, 145–

164.

- Piyawat, K., Ramseyer, C. and Kang, T.H. (2013), "Development of an Axial Load Capacity Equation for Doubly Symmetric Built-Up Cold-Formed Sections", *Journal of Structural Engineering*, 139, 1–13.
- Portioli, F., Lorenzo, G. Di, Landolfo, R. and Mazzolani, F.M. (2012), "Contact Buckling Effects in Built-up Cold-Formed Steel Beams", *The 6th International Conference on Coupled Instabilities in Metal Structures*, pp. 1–8.
- Puckett, J.A. and Cutkowski, R.M. (1986), "Compound strip method for analysis of plate systems", *Journal of Structural Engineering*, 112, 121–138.
- Quach, W., Teng, J. and Chung, K. (2004), "Residual stresses in steel sheets due to coiling and uncoiling: a closed-form analytical solution", *Engineering Structures*, 26, 1249–1259.
- Quach, W.M., Teng, J.G. and Chung, K.F. (2010), "Effect of the manufacturing process on the behaviour of press-braked thin-walled steel columns", *Engineering Structures*, 32, 3501–3515.
- Quach, W.M., Teng, J.G. and Chung, K.F. (2006), "Finite element predictions of residual stresses in press-braked thin-walled steel sections", *Engineering Structures*, 28, 1609–1619.
- Rasmussen, K.J.R. and Hancock, G.J. (1988), "Geometric Imperfections in Plated Structures Subject to Interaction between Buckling Modes", *Thin-Walled Structures*, 6, 433–452.
- Rasmussen, K.J.R. and Hancock, G.J. (1992), "Design of Thin-Walled Plain Channel Section Columns Against Flexural Buckling", *First International Specialty Conference on Coupled Instabilities in Metal Structures*.
- Rasmussen, K.J.R. and Hancock, G.J. (1993), "Design of Cold-Formed Stainless Steel Tubular Members. I: Columns", *Engineering Structures*, 119, 2349–2367.
- Rasmussen, K.J.R. (1994), "Design of thin-walled columns with unstiffened flanges", *Engineering Structures*, 16, 307–316.
- Rasmussen, K.J.R. (2006), "Bifurcation of locally buckled point symmetric columns-Analytical developments", *Thin-Walled Structures*, 44, 1161–1174.
- Reyes, W. and Guzmán, A. (2011), "Evaluation of the slenderness ratio in built-up cold-formed box sections", *Journal of Constructional Steel Research*, 67, 929–935.
- Rondal, J. (1987), "Residual stresses in cold-rolled profiles", *Construction and Building Materials*, 1, 150–164.

-
- Saint-Venant (1883), "Discussion in Théorie de l' élasticité des corps solides" by Clebsch, 704.
- Schafer, B.W. (1997), "Cold-Formed Steel Behavior and Design: Analytical and Numerical Modeling of Elements and Members with Longitudinal Stiffeners", PhD thesis, Cornell University.
- Schafer, B.W. (2000), "Distortional Buckling of Cold-formed Steel Columns", The American Iron and Steel Institute.
- Schafer, B.W. (2002), "Local, Distortional, and Euler Buckling of Thin-Walled Columns", *Journal of Structural Engineering*, 128, 289–299.
- Schafer, B.W. (2006), "Buckling analysis of cold-formed steel members using CUFSM: conventional and constrained finite strip methods", *18th International Specialty Conference on Cold-Formed Steel Structures*, Orlando, Florida.
- Schafer, B.W. (2011), "Cold-formed steel structures around the world", *Steel Construction*, 4, 141–149.
- Schafer, B.W., Grigoriu, M. and Pekoz, T. (1998), "A probabilistic examination of the ultimate strength of cold-formed steel elements", *Thin-Walled Structures*, 31, 271–288.
- Schafer, B.W., Li, Z. and Moen, C.D. (2010), "Computational modeling of cold-formed steel", *Thin-Walled Structures*, 48, 752–762.
- Schafer, B.W. and Pekoz, T. (1998), "Computational modeling of cold-formed steel: characterizing geometric imperfections and residual stresses", *Journal of Constructional Steel Research*, 47, 193–210.
- Schafer, B.W. and Pekoz, T. (1998), "Direct Strength Prediction of Cold-Formed Steel Members Using Numerical Elastic Buckling Solutions", *Fourteenth International Specialty Conference on Cold-Formed Steel Structures*, St. Louis, Missouri.
- Schafer, B.W. and Pekoz, T. (1999), "Laterally braced cold-formed steel flexural members with edge stiffened flanges", *Journal of Structural Engineering*, 125, 118–127.
- Schardt, R. (1989), *Verallgemeinerte Technische Biegetheorie*, Springer, Berlin.
- Silvestre, N. and Camotim, D. (2003), "Non-linear generalised beam theory for cold-formed steel members", *International Journal of Structural Stability and Dynamics*, 3, 461–490.
- Silvestre, N. and Camotim, D. (2003), "GBT buckling analysis of pultruded FRP lipped channel members", *Computers and Structures*, 81, 1889–1904.
- Silvestre, N., Camotim, D. and Dinis, P.B. (2009), "Direct strength prediction of lipped channel columns experiencing local-plate/distortional interaction", *Advanced Steel Construction*, 5,
-

49–71.

Sivapathasunderam, J. (2009), "Flexural Behaviour and Design of the New LiteSteel Beams", PhD thesis, Queensland University of Technology.

Stone, T.A. and LaBoube, R.A. (2005), "Behavior of cold-formed steel built-up I-sections", *Thin-Walled Structures*, 43, 1805–1817.

Timoshenko, S.P. (1945), "Theory of bending, torsion and buckling of thin-walled members of open cross section", *Journal of The Franklin Institute*, 239, 249–268.

Timoshenko, S.P. and Gere, J.M. (1963), *Theory of Elastic Stability*, McGraw-Hill.

Van der Neut, A. (1969), "The interaction of local buckling and column failure of thin-walled compression members", *Proceedings 12th International Congress of Applied Mechanics*, pp. 389–399.

Venkataramaiah, K.R. and Roorda, J. (1982), "Analysis of Local Plate Buckling Experimental Data", *Sixth International Specialty Conference on Cold-Formed Steel Structures*, St. Louis, Missouri, pp. 45–73.

Vlasov, V.Z. (1961), *Thin-Walled Elastic Beams*.

von Karman, T., Sechler, E.E. and Donnell, L.H. (1932), "The Strength of Thin Plates in Compression", *ASME*, 54, 53-70.

Walker, A.C. (1975), *Design and Analysis of Cold-Formed Sections*, International Textbook Company Ltd., London.

Wang, L. and Young, B. (2015), "Beam tests of cold-formed steel built-up sections with web perforations", *Journal of Constructional Steel Research*, 115, 18–33.

Wang, L. and Young, B. (2016a), "Behavior of Cold-Formed Steel Built-Up Sections with Intermediate Stiffeners under Bending. I: Tests and Numerical Validation", *Journal of Structural Engineering*, 142.

Wang, L. and Young, B. (2016b), "Behavior of Cold-Formed Steel Built-Up Sections with Intermediate Stiffeners under Bending. II: Parametric Study and Design", *Journal of Structural Engineering*, 142.

Weng, B.C.C. and White, R.N. (1990), "Residual Stresses in Cold-Bent Thick Steel Plates", *Journal of Structural Engineering*, 116, 24–39.

Weng, C.C. and Pekoz, T. (1990), "Residual Stresses in Cold-Formed Steel Members", *Journal of Structural Engineering*, 116, 1611–1625.

Whittle, J. and Ramseyer, C. (2009), "Buckling capacities of axially loaded, cold-formed, built-

-
- up C-channels", *Thin-Walled Structures*, 47, 190–201.
- Yan, J. and Young, B. (2004), "Numerical investigation of channel columns with complex stiffeners—part I: test verification", *Thin-Walled Structures*, 42, 883–893.
- Yang, D. and Hancock, G.J. (2004), "Compression Tests of High Strength Steel Channel Columns with Interaction between Local and Distortional Buckling", *Journal of Structural Engineering*, 130, 1954–1963.
- Yang, D. and Hancock, G.J. (2006), "Numerical Simulation of High-Strength Steel Box-Shaped Columns Failing in Local and Overall Buckling Modes", *Journal of Structural Engineering*, 132, 541–549.
- Yap, D.C.Y. and Hancock, G.J. (2008), "Experimental study of complex high-strength cold-formed cross-shaped steel section", *Journal of Structural Engineering*, 134, 1322–1333.
- Young, B. and Chen, J. (2008), "Design of Cold-Formed Steel Built-Up Closed Sections with Intermediate Stiffeners", *Journal of Structural Engineering*, 134, 727–737.
- Young, B., Silvestre, N. and Camotim, D. (2013), "Cold-Formed Steel Lipped Channel Columns Influenced by Local-Distortional Interaction: Strength and DSM Design", *Journal of Structural Engineering*, 139, 1059–1074.
- Young, B. and Yan, J. (2004), "Numerical investigation of channel columns with complex stiffeners—part II: parametric study and design", *Thin-Walled Structures*, 42, 895–909.
- Yu, W. (2000), *Cold-Formed Steel Design*, Third Edit. ed. John Wiley and sons, Inc.
- Yu, W. and LaBoube, R.A. (2010), *Cold-Formed Steel Design*, 4th editio. ed. John Wiley and Sons, Inc., Hoboken, NJ, USA.
- Zandonini, R. (1985), "Stability of compact built-up struts: experimental investigation and numerical simulation", *Costruzioni metalliche*, No. 4, 1985.
- Zeinoddini, V. and Schafer, B.W. (2011), "Global Imperfections and Dimensional Variations in Cold-Formed Steel Members", *International Journal of Structural Stability and Dynamics*, 11, 829–854.
- Zeinoddini, V. and Schafer, B.W. (2012), "Simulation of geometric imperfections in cold-formed steel members using spectral representation approach", *Thin-Walled Structures*, 60, 105–117.
- Zhang, J. and Young, B. (2012), "Compression tests of cold-formed steel I-shaped open sections with edge and web stiffeners", *Thin-Walled Structures*, 52, 1–11.
- Zhang, J.H. and Young, B. (2015), "Numerical investigation and design of cold-formed steel
-

-
- built-up open section columns with longitudinal stiffeners", *Thin Walled Structures*, 89, 178–191.
- Zhang, J.H. and Young, B. (2018), "Experimental investigation of cold-formed steel built-up closed section columns with web stiffeners", *Journal of Constructional Steel Research*, 147, 380–392.
- Zhang, X. and Rasmussen, K.J.R. (2014), "Tests of cold-formed steel portal frames with slender sections", *Steel Construction*. 7, 199–203.
- Zhao, X., Tootkaboni, M. and Schafer, B.W. (2015), "Development of a Laser-Based Geometric Imperfection Measurement Platform with Application to Cold-Formed Steel Construction", *Experimental Mechanics*, 55, 1779–1790.
- Zhao, X., Tootkaboni, M. and Schafer, B.W. (2017), "Laser-based cross-section measurement of cold-formed steel members: Model reconstruction and application", *Thin-Walled Structures*, 120, 70–80.
- Ziemian, R.D. (2010), Appendix B - Technical Memoranda of Structural Stability Research Council.